SAND2014-18303R

Evaluation of Used Fuel Disposition in Clay-Bearing Rock

(FCRD-UFD-2014-000056)

Fuel Cycle Research & Development

Prepared for
U.S. Department of Energy
Used Fuel Disposition Campaign

Carlos F. Jové Colón, Philippe F. Weck, David H. Sassani (SNL)

Liange Zheng, Jonny Rutqvist, Carl I. Steefel, Kunhwi Kim, Seiji Nakagawa, James Houseworth, Jens Birkholzer, (LBNL)

Florie A. Caporuscio, Michael Cheshire, Michael S. Rearick, Mary K. McCarney (LANL)

Mavrik Zavarin, Ana Benedicto, Annie B. Kersting, Mark Sutton (LLNL)

James Jerden, Kurt E. Frey, Jacqueline M. Copple, William Ebert (ANL)

August 29th, 2014

SAND2014-18303 R

Prepared by:

Sandia National Laboratories

Albuquerque, New Mexico 87185

Sandia National Laboratories is a multi-program laboratory managed and operated by Sandia Corporation, a wholly owned subsidiary of Lockheed Martin Corporation, for the U.S. Department of Energy's National Nuclear Security Administration under contract DE-AC04-94AL85000.

U.S. DEPARTMENT OF ENERGY

Sandia National Laboratories

APPENDIX E
FCT DOCUMENT COVER SHEET [1]

Name/Title of Deliverable/Milestone/Revision No. Evaluation of Used Fuel Disposition in Clay-Bearing Rock (M2FT-14SN0806051)

Work Package Title and Number Argillite Disposal R&D – SNL

Work Package WBS Number 1.02.08.06

Responsible Work Package Manager Carlos F. Jove Colon (Name/Signature)

Date Submitted

Quality Rigor Level for Deliverable/Milestone[2]	☒ QRL-3	☐ QRL-2	☐ QRL-1 Nuclear Data	☐ Lab/Participant QA Program (no additional FCT QA requirements)

This deliverable was prepared in accordance with Sandia National Laboratories
(Participant/National Laboratory Name)

QA program which meets the requirements of

☒ DOE Order 414.1 ☐ NQA-1-2000 ☐ Other

This Deliverable was subjected to:

☐ Technical Review ☐ Peer Review

Technical Review (TR)
Review Documentation Provided

☐ Signed TR Report or,

☐ Signed TR Concurrence Sheet or,

☒ Signature of TR Reviewer(s) below

Peer Review (PR)
Review Documentation Provided

☐ Signed PR Report or,

☐ Signed PR Concurrence Sheet or,

☐ Signature of PR Reviewer(s) below

Name and Signature of Reviewers

Yifeng Wang

8/28/2014

NOTE 1: *Appendix E should be filled out and submitted with the deliverable. Or, if the PICS:NE system permits, completely enter all applicable information in the PICS:NE Deliverable Form. The requirement is to ensure that all applicable information is entered either in the PICS:NE system or by using the FCT Document Cover Sheet.*

NOTE 2: *In some cases there may be a milestone where an item is being fabricated, maintenance is being performed on a facility, or a document is being issued through a formal document control process where it specifically calls out a formal review of the document. In these cases, documentation (e.g., inspection report, maintenance request, work planning package documentation or the documented review of the issued document through the document control process) of the completion of the activity, along with the Document Cover Sheet, is sufficient to demonstrate achieving the milestone. If QRL 1, 2, or 3 is not assigned, then the Lab / Participant QA Program (no additional FCT QA requirements) box must be checked, and the work is understood to be performed and any deliverable developed in conformance with the respective National Laboratory / Participant, DOE or NNSA-approved QA Program.*

AKNOWLEDGEMENTS

The authors acknowledge our gratitude to Yifeng Wang (SNL), Ernest Hardin (SNL), Kevin McMahon (SNL), Geoff Freeze (SNL), David Sevougian (SNL), Victor Figueroa (SNL), Thomas J. Wolery (retired from LLNL), William Spezialetti (DOE NE-53), Prasad Nair (DOE NE-53), Mark Tynan (DOE NE-53), and Tim Gunther (DOE NE-53) for their helpful discussions and contributions on various topics covered in this report.

SUMMARY

Radioactive waste disposal in shale/argillite rock formations has been widely considered given its desirable isolation properties (low permeability), geochemically reduced conditions, anomalous groundwater pressures, and widespread geologic occurrence. Clay/shale rock formations are characterized by their high content of clay minerals such as smectites and illites where diffusive transport and chemisorption phenomena predominate. These, in addition to low permeability, are key attributes of shale to impede radionuclide mobility. Shale host-media has been comprehensively studied in international nuclear waste repository programs as part of underground research laboratories (URLs) programs in Switzerland, France, Belgium, and Japan. These investigations, in some cases a decade or more long, have produced a large but fundamental body of information spanning from site characterization data (geological, hydrogeological, geochemical, geomechanical) to controlled experiments on the engineered barrier system (EBS) (barrier clay and seals materials). Evaluation of nuclear waste disposal in shale formations in the USA was conducted in the late 70's and mid 80's. Most of these studies evaluated the potential for shale to host a nuclear waste repository but not at the programmatic level of URLs in international repository programs. This report covers various R&D work and capabilities relevant to disposal of heat-generating nuclear waste in shale/argillite media. Integration and cross-fertilization of these capabilities will be utilized in the development and implementation of the shale/argillite reference case planned for FY15.

Disposal R&D activities under the UFDC in the past few years have produced state-of-the-art modeling capabilities for coupled Thermal-Hydrological-Mechanical-Chemical (THMC), used fuel degradation (source term), and thermodynamic modeling and database development to evaluate generic disposal concepts. The THMC models have been developed for shale repository leveraging in large part on the information garnered in URLs and laboratory data to test and demonstrate model prediction capability and to accurately represent behavior of the EBS and the natural (barrier) system (NS). In addition, experimental work to improve our understanding of clay barrier interactions and TM couplings at high temperatures are key to evaluate thermal effects as a result of relatively high heat loads from waste and the extent of *sacrificial zones* in the EBS. To assess the latter, experiments and modeling approaches have provided important information on the stability and fate of barrier materials under high heat loads. This information is central to the assessment of thermal limits and the implementation of the reference case when constraining EBS properties and the repository layout (e.g., waste package and drift spacing).

This report is comprised of various parts, each one describing various R&D activities applicable to shale/argillite media. For example, progress made on modeling and experimental approaches to analyze physical and chemical interactions affecting clay in the EBS, NS, and used nuclear fuel (source term) in support of R&D objectives. It also describes the development of a reference case for shale/argillite media. The accomplishments of these activities are summarized as follows:

- **Development of a reference case for shale/argillite (Part I)**
    - A generic shale/argillite repository reference case is presented.
    - Waste inventory, waste form, waste package, repository layout, EBS backfill and host rock properties, and biosphere have been described to accommodate 12-PWR and 32-PWR waste packages.

- Some aspects of the reference case for disposal in shale (e.g., waste inventory, waste form) are consistent with that for disposal in salt and crystalline host-rock media.
- The planned implementation of the reference case will use information gauged from Parts II, III, IV, and V of this report.

- **Investigation of Reactive Transport and Coupled THM Processes in EBS: FY14 (Part II)**
  - Development and validation of constitutive relationships for permeability, porosity and effective stress:
    - Development of a new theoretical approach, a two-part Hooke's Model (TPHM) based on the basic concept that the elastic deformation in a rock can be more accurately represented as a combination of two material types, a harder (or stiffer) material and a softer material.
    - Existing stress-dependent formulations for porosity and permeability were reviewed, along with relationships between porosity and permeability.
    - Preliminary evaluation of the model against published data produced on silty-shale samples with encouraging results.
  - Discrete fracture network (DFN) approach for fractures in argillaceous rock - The use of the rigid-body-spring network (RBSN) approach to model geomechanical behavior including fracturing:
    - Linkage between TOUGH2 for simulating heat and mass transport and the RBSN method.
    - A simulation of fracture damage around the excavated disturbed zone (EDZ) of the HG-A microtunnel has been conducted and qualitatively agrees with physical observations.
    - TOUGH-RBSN simulator capabilities for strongly coupled hydro-mechanical processes have been shown through a simulation of hydraulic fracturing.
  - THM Modeling of Underground Heater Experiments:
    - Completed implementation of constitutive models for the coupled geomechanical behavior of bentonite-based buffer material (i.e., dual-structure model in the Barcelona Basic Model (BBM)).
    - Verification and testing of the implemented geomechanical constitutive models for bentonite-based buffer material by modeling laboratory experiments and long-term behavior of a generic repository.
    - Validation of TOUGH-FLAC and characterization of THM properties for two types of bentonite-based buffer materials through modeling of CIEMAT laboratory column experiments.

        - Development of full-scale 3D TOUGH-FLAC models of the Horonobe EBS experiment and Mont Terri FE experiment.
        - Benchmarking associated with the Horonobe EBS experiment achieving good agreement with the results of other international modeling teams.
        - Published one journal paper (Rutqvist et al., 2014) on THM modeling of nuclear waste disposal in argillite and submitted one journal paper on the use of the dual-structure model for modeling long-term behavior of a nuclear waste repository (Vilarrasa et al., 2014).
    - Investigation of the maximum allowable temperature and detailed impacts of a high temperature on repository performance:
        - Coupled THMC models were developed, with properties of clay formation from Opalinus Clay, and two types of EBS bentonite—Kunigel-VI and FEBEX bentonites.
        - Two main scenarios were developed: a "high T" case where temperature near the waste package can reach about 200°C and a "low T" scenario where temperature peaks at about 100°C. Also conducted sensitivity analyses to key parameters.
        - Laboratory investigations: Results suggest the likelihood of heat-induced changes in the strength and failure behavior of the compacted bentonite and the Opalinus Clay from Mont Terri were caused by decrease of water content from samples during heating.
    - Transport in clay and clay rock:
        - Two complementary approaches to modeling ion diffusion through clays have been developed: (1) Donnan Equilibrium or Mean Electrostatic Approach and (2) Nernst-Planck and Poisson-Boltzmann equation (termed the PNP method).
        - Benchmark studies using the software codes CrunchEDL versus PHREEQC: Differences between the calculations are a result of the neglect of the longitudinal gradient in the mean electrostatic potential in CrunchEDL. A fix to this problem will be completed soon.

- **Update on Experimental Activities on Buffer/Backfill Interactions at elevated Pressure and Temperature (Part III)**
    - Peak temperature conditions (currently unknown and will be determine during repository design) drives the formation of possible zeolite reactions (mordenite, laumontite, analcime, wairakite formation) at the expense of kaolinite in the host rock. This is indicative of repository conditions shifting towards the zeolite metamorphic facies.
    - Zeolite reactions, along with silica saturation reactions, will control the porewater solution chemistry and determine any further mineral alteration.
    - Illite formation can still progress, if a K-source is available. K-source stability with respect to the repository conditions will determine the illitization rates.

- **Thermodynamic Database Development: Evaluation Strategy, Modeling Tools, First-Principles Modeling of Clay, and Sorption Database Assessment (Part IV)**
    - Assessment and retrieval strategies of thermodynamic data for mineral and aqueous species:
        - Evaluation of a thermodynamic data "deconstruction" from the "ground-up" approach to establish consistency links with key reference data.
    - Analysis of thermodynamic data and mineral phase stability relations of clays and zeolites at elevated temperatures with the CHNOSZ software:
        - Chemographic analysis of equilibrium phase relations in the Na-Ca-Mg-K-Si-Al-H_2O system for clay and zeolite using the CHNOSZ package.
        - Incorporation of recent literature thermodynamic (calorimetric) data for smectite (MX-80), illite (IMt-2), and Na-saponite (Sap-Ca-1) phases, relevant to clay barrier interactions at elevated temperatures.
    - Comprehensive approaches to developing ion exchange and surface complexation models for nuclear waste repository conditions:
        - Development of a self-consistent surface complexation/ion exchange models: Expansion of the RES^{3}T database to include raw sorption data to allow user-choice of model fitting.
        - An example of this approach is the extraction of uranium sorption data for quartz from the RES^{3}T database fitted with a non-electrostatic model with promising results.
        - Development of ion exchange mechanism of Np(V) sorption to montmorillonite: Experimental work described in a manuscript recently published in Applied Geochemistry (Benedicto et al., 2014)
    - Application of first-principles computational approaches in the retrieval of thermodynamic properties for kaolinite clay ($Al_2Si_2O_5(OH)_4$) and bischofite salt plus its dehydrated phases [$MgCl_2 \cdot nH_2O$ (n=6, 4, 2, 1)]:
        - Application of the density functional theory corrected for dispersion (DFT-D) with the generalized gradient approximation (GGA) describes the van der Waals interactions in layered silicate structures like kaolinite.
        - Analysis of two types of cell deformation was investigated (hydrostatic and uniaxial deformation) along the z-axis normal of the layers.
        - Bulk moduli hydrostatic compression in close agreement with the experimental values.
        - Computed isobaric heat capacity using uniaxial deformation of the cell reproduces handbook calorimetric data.

- **ANL Mixed Potential Model For Used Fuel Degradation: Application to Argillite and Crystalline Rock Environments (Part V)**
    - Added a working noble metal particle (epsilon phase) domain on fuel surface to account for the protective hydrogen effect.
    - Incorporated the radiolysis model subroutine in MPM (using an analytical function provided by PNNL)
    - Performed systematic sensitivity runs that identify and quantify the processes that affect the fuel dissolution rate.
    - Compared sensitivity results with available experimental data (ongoing).
    - Developed a research priority list based on results from sensitivity study and comparison with experimental results.
    - Converted the MPM from MATLAB to Fortran to facilitate integration with PA codes (PFLOTRAN) (ongoing)

TABLE OF CONTENTS

TABLE OF FIGURES

(Part I) Evaluation of Used Fuel Disposition in Clay-Bearing Rock: Conceptual Description of an Argillite Reference Case

(Part II) Investigation of Coupled Processes and Impact of High Temperature Limits in Argillite Rock

(Part III) Update on Experimental Activities on Buffer/Backfill Interactions at Elevated Pressure and Temperature

(Part IV) Thermodynamic Database (TDB): Recommendations and Guidelines on Future TDB Development

(Part V) ANL Mixed Potential Model For Used Fuel Degradation: Application to Argillite and Crystalline Rock Environments

LIST OF TABLES

(Part I) Evaluation of Used Fuel Disposition in Clay-Bearing Rock: Conceptual Description of an Argillite Reference Case

(Part II) Investigation of Coupled Processes and Impact of High Temperature Limits in Argillite Rock

(Part III) Update on Experimental Activities on Buffer/Backfill Interactions at Elevated Pressure and Temperature

(Part IV) Thermodynamic Database Development: Evaluation Strategy, Modeling Tools, First-Principles Modeling of Clay, and Sorption Database Assessment

(Part V) ANL Mixed Potential Model (MPM) For Used Fuel Degradation: Application to Argillite and Crystalline Rock Environments

ACRONYMS

1D	One Dimensional
2D, 2-D	Two Dimensional
3D, 2-D	Three Dimensional
ADSM	advanced disposal system modeling
BBM	Barcelona Basic Model
BExM	Barcelona Expansive Model
BWR	Boiling Water Reactor
CEC	Cation Exchange Capacity
DECOVALEX	DEvelopment of COupled Models and their VALidation against EXperiments
DFN	Discrete Fracture Network
DI	Deionized
DOE	Department of Energy
DOE-NE	Department of Energy, Office of Nuclear Energy
DOE-EM	Department of Energy, Office of Enviromental Management
DOE-FE	Department of Energy, Office of Fossil Energy
DPC	Dual Purpose Canister
DRZ	Disturbed Rock Zone
DSEF	Disposal Systems Evaluation Framework
EBS	Engineered Barrier System
EC	European Community
EDL	Electric Double Layer
EDX	Energy dispersive X-ray spectroscopy
EDZ	Excavated Disturbed Zone
ENRESA	Empresa Nacional de Residuos Radioactivos SA
EoS	Equation of State
EPCA	Elasto-Plastic Cellular Automata
FCRD	Fuel Cycle Research and Development
FDM	Fuel Degradation Model
FE	Full-Scale Emplacement Experiment
FEBEX	Full-scale Engineered Barriers Experiment
FEP	Features, Events, and Processes

FY	Fiscal Year
GDSA	Generic Disposal System Analysis
GEM	Gibbs Energy Minimization
GW	Gigawatt
GWd	Gigawatt days
GWd/MT	Gigawatt (thermal) - days per Metric Ton
HC	Hydrological and Chemical
HKF	Helgeson-Kirkham-Flowers
HLW	High-Level nuclear Waste
HM	Heavy Metal
HMech	Hydro-Mechanical
IAEA	International Atomic Energy Association
IC	Ion Chromatography
IRF	Instant Release Fraction
I-S	Illite-Smectite
IUPAC	International Union of Pure and Applied Chemistry
JAEA	Japan Atomic Energy Agency
JANAF	Join-Army-Navy-Air Force
JNC	Japan Nuclear Cycle Development Institute
LAMMPS	Large-scale Atomic/Molecular Massively Parallel Simulator
LANL	Los Alamos National Laboratory
LBNL	Lawrence Berkeley National Laboratory
LC	Load Collapse
LLNL	Lawrence Livermore National Laboratory
MC	Mechanical Chemical
MCC	Modified Cam Clay
MD	Molecular Dynamics
MT	Metric Ton
MTHM	Metric Tons Heavy Metal
NAGRA	National Cooperative for the Disposal of Radioactive Waste
NE	DOE-Nuclear Energy
NEA	Nuclear Energy Agency

NIST	National Institute of Standard and Technology
NS	Natural (Barrier) System
NW	Nuclear Waste
OECD	Organization for Economic Co-operation and Development
OoR	Out-of-Reactor
PA	Performance Assessment
PB	Poisson-Boltzmann
PNP	Poisson-Nernst-Planck
PWR	Pressurized Water Reactor
QA	Quality Assessment
QC	Quality Control
R&D	Research and Development
RBSN	Rigid-Body-Spring Network
RH	Relative Humidity
SEM	Scanning Electron Microscopy
SIT	Specific Interaction Theory
SNF	Spent Nuclear Fuel
SNL	Sandia National Laboratories
SRA	Strategic Research Agenda
T	Temperature
TC	Thermal and Chemical
TDB	Thermodynamic Database
TEM	Transmission Electron Microscopy
TH	Thermal and Hydrological
THM	Thermal-Hydrological-Mechanical
THMC	Thermal-Hydrological-Mechanical-Chemical
TIC	Total Inorganic Carbon
TM	Thermal-Mechanical
TPHM	Two-Part Hooke's Model
UNF	Used Nuclear Fuel
UFD	Used Fuel Disposition
UFDC	Used Fuel Disposition Campaign

UOX	Uranium Oxide Fuel
UOX-40	UOX with 40-GWd/MTU burnup
UOX-60	UOX with 60-GWd/MTU burnup
UPC	University of Catalonia
URL	Underground Research Laboratory
WIPP	Waste Isolation Pilot Plant
WP	Waste Package
XRD	X-ray Diffraction
XRF	X-ray Fluorescence

Evaluation of Used Fuel Disposition in Clay-Bearing Rock:
Conceptual Description of an Argillite Reference Case
(Part I)

1. Evaluation of Used Fuel Disposition in Clay-Bearing Rock

1.1 Introduction

Radioactive waste disposal in a deep subsurface repository hosted in shale/argillite rock formations has been widely considered given the desirable isolation properties (low permeability), geochemically reduced deep-seated groundwaters, anomalous groundwater pressures, and widespread geologic occurrence (Bianchi et al., 2013; Gonzales and Johnson, 1984; Hansen et al., 2010; Mazurek et al., 2003; Neuzil, 2013; Schurr, 1977). In addition to shale media being nearly impermeable, the predominance of diffusive transport and chemisorption phenomena are other key attributes of shale to impede radionuclide mobility making these formations target sites for disposal of high-level radioactive waste (Horseman et al., 1996). Evaluation of shale formations in the USA with potential to host nuclear waste were conducted in the late 70's and mid 80's. Gonzales and Johnson (1984) provide a comprehensive review of the distribution and type of shale formations in the U.S.A. Schurr (1977) describes the potential for the Late Cretaceous Pierre shale (northern Great Plains) to host a nuclear waste repository. Hansen et al. (2010) provides a review of the limited shale repository studies related to two small-scale heater tests conducted in the USA: (1) the Eleana argillite (McVey et al., 1979) and (2) the Conasauga shale near Oak Ridge, TN (Krumhansl, 1983). The former was a preliminary study towards a full-scale heater test whereas the latter, similarly, aimed at characterizing thermally-induced phenomena on shale. One interesting conclusion on the study by Krumhansl (1983) was that, in general, clay minerals were "unreactive" when exposed to high temperatures. Similar conclusions have been obtained in laboratory experiments on clay interactions including pyrite oxidation (Jové Colón et al., 2013).

Clay/shale rock formations are characterized by high content of clay minerals such as smectites and illites. From here on, the term 'shale'and/or 'argillite' will be used interchangeably and generically to delineate mudrock composed primarily of clay minerals plus other minor phases such as quartz, Fe oxides, pyrite, and feldspar. Common definitions of clay/shale rock are based on mineralogical content and textural features such as grain size, fisillity, and the presence of laminations. For simplicity, no rigorous distinction between shale and argillite on the basis of metamorphic grade or level of clay induration will be made in this report. It should be noted that the term 'argillite' is commonly referred in sedimentology to a mud- or clay-shale having a low degree of metamorphism (Boggs, 2006). This is different from 'argillaceous' rock where this term refers to sedimentary rocks having argillite components. Hansen et al. (2010) summarizes the classification of clay-bearing rocks on the basis of texture and level of induration.

There is large body of nuclear waste disposal research on shale media and related disposal concepts (Hansen et al., 2010) and such information will be deferred to the existing literature. For example, the reports by Hansen et al. (2010) and those from numerous studies in shale-hosted underground research laboratories (URLs) in Belgium, France and Switzerland (ANDRA, 2005; NAGRA, 2002; Wickham, 2008) outline the extensive scientific knowledge obtained to assess the long-term repository isolation performance of nuclear waste in shale. In the past few years, under the UFDC disposal R&D activities, coupled Thermal-Hydrological-Mechanical (THM) and Thermal-Hydrological-Mechanical-Chemical (THMC) models have been developed for shale repository and tested against URL and laboratory data to demonstrate: model capability, understand spatio-temporal behavior of the Engineered Barrier System (EBS), bentonite barrier material, and evaluate different disposal scenarios in argillite (Liu et al. 2013; Rutqvist et al. 2014a, Zheng et al. 2014a). A large scale 2-D hydrogeologic model by Bianchi et al. (2013)

investigated the hydraulic connection between an emplacement drift and surrounding hydrogeological units. The Disposal Systems Evaluation Framework (DSEF) (Greenberg et al. 2013) has been used to evaluate the repository thermal evolution as a thermal conduction problem approximated by line and point sources to facilitate the analysis of disposal design options in shale and other host rock media. In addition, a brief description of the history of shale consideration in the U.S. is also given by Hansen et al. (2010). Bianchi et al. (2013) provides a description of diffusive transport in a clay-hosted repository based on single-phase flow and full saturation using parameter data based on documented studies in European repository programs.

Hardin et al. (2012) provides descriptions of reference disposal concepts on the basis of host media and thermal load management analysis. The report also evaluates reference disposal concepts according to geologic host-rock media, waste type (thus inventory), and mode of operation. The latter refers to whether repository will be backfilled at closure (enclosed) or ventilated for many years either without backfilling openings or backfilling at closure. Schurr (1977), Hansen et al. (2010), and Hardin et al. (2012) emphasize on the main criteria for site suitability for long-term radioactive waste disposal in shale: formation thickness, depth, low hydraulic conductivity, areal coverage, self-healing, mineralogy, stratigraphic and structural uniformity, hydrogeochemistry, and tectonic and/or seismogenic activity. These items will be discussed further in a later section. These criteria items can be met by a large suite of shale formations in the continental U.S. Gonzales and Johnson (1984) provide a comprehensive evaluation of the distribution and type of shale formations in the U.S.A. Schurr (1977) describes the potential for the Late Cretaceous Pierre shale (northern Great Plains) to host a nuclear waste repository.

The establishment of a reference case, based on the acquired knowledge and methods developed in the Used Fuel Disposition Campaign (UFDC), is an important phase in setting up a baseline for model development to evaluate repository performance. A generic salt repository reference case was developed in Freeze et al. (2013) and a generic shale repository reference case is presented in this report. The definition of a reference case requires the characterization of the waste inventory, waste form, waste package, repository layout, EBS backfill, host rock, and biosphere. Emphasis is given to properties and processes of the EBS and natural barrier (bentonite and host rock) that are key to performance assessment (PA). Brief descriptions are given for other components of the reference case such as waste inventory, waste form, waste package, repository layout, and biosphere.

2. Generic Argillite Repository Disposal Concept

The reference case for shale/argillite is largely based and consistent with that developed for the generic salt repository disposal concept (Freeze et al. 2013), with some modifications to meet the requirements for a repository hosted in shale. Specific assumptions of the generic disposal concept in shale are the following:

- Waste disposal capacity is 70,000 metric tons of heavy metal (MTHM).
- Waste packages (canister/container plus disposal overpack) will be sealed permanently to avoid any risk of additional exposure during handling operations. As described in Hardin et al. (2012), disposal overpacks are cost effective in satisfying the operational requirements for heat dissipation, impact damage, and corrosion resistance.

- Horizontal repository layout consists of excavated emplacement drifts or tunnels separated by the shale host rock, connected (laterally) with an operations tunnel between two vertical shaft facilities (Figure 1):
    - Waste package spacing and drift spacing are dictated by thermal loading, total radionuclide inventory, waste package size, and EBS configuration. Hardin et al. (2013) (Figure 2) determined drift and waste package spacing based on a thermal limit at the rock wall of 100°C.
    - The repository layout option of a centralized access hallway with disposal galleries on each side similar to that advanced by Freeze et al. (2013) for disposal in salt could be considered as an alternative.
- Horizontal disposal galleries (Figure 2) are emplaced end-to-end with waste packages in drifts that are lined with cement (see Figure 3) and/or metal support structures. Disposal galleries are then backfilled with clay material. The space between waste packages can be backfilled with clay rock or cement. Multilayered backfilling is part of the EBS configuration (Figure 3).
- Ground support structures and cement linings (Figure 3) are needed for structural integrity of the disposal gallery. The lining properties (rigidity, pervious/impervious) depend on the mechanical and hydrologic properties of the clay rock.
- Drifts and access/operations tunnels are sealed at closure. Drift and operations tunnel design layout can vary depending on waste type, heat loads, and canister size.
- Access shafts are used for construction, waste handling/emplacement operations, and ventilation. These will be sealed at closure.
- Excavated drifts will be emplaced at a depth of about 650 meters within a clay rock unit. Given the anticipated heterogeneities in shale formations, the presence of either bentonite clay strata or other lithologic units should be accounted for.

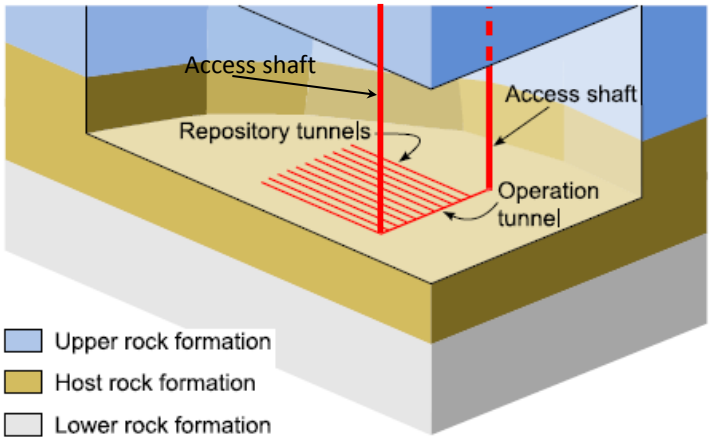

Figure 1. Generic design for a deep geological nuclear waste repository in shale (Modified after Bianchi et al. (2013)).

Repository design will meet operational requirements to guarantee safe pre- and post-closure performance. Pre-closure operational constraints encompass shaft dimensions for access and ventilation during mining activities, transport, emplacement of waste packages, sealing, and monitoring. Hardin (2014) provides a review of excavation and construction practices of underground tunnels in clay/shale rock media. This study is part of a feasibility evaluation for the direct disposal of SNF in large heat-generating DPCs. The report summarizes the experience (about 50 years or more) and technological viability garnered in the construction of large-diameter and long tunnels for vehicle transportation (highways, railroads) and underground water passages in the USA and Europe. Einstein (2000) provides a good summary of tunneling activities and potential issues (clay softening and swelling) in the construction of tunnels in Opalinus clay/shale. Einstein (2000) also provides important points of consideration on recent tunnel construction methods such as the use of circular tunnel cross-sections (reduced shear stress) and the emplacement of pre-fabricated liners that are evenly-arranged and water-tight to preclude water ponding and its movement from the rock.

Drift spacing will be constrained by the dimensions of pillar structures to support safe underground tunneling (preclude drift collapse) and pre-closure operations during emplacement. Drift spacing and in-drift spacing between waste packages will be constrained by thermal loading on compliance points relative to coordinate locations of waste packages in the drift and the clay host rock. At this point, compliance points are defined as 'observation' points for temperature-time profiles located within the drift (e.g., drift wall, buffer, and waste package surface) or within the host rock at a defined distance from the drift wall represented by temperatures at a given time. The current treatment of compliance points is arbitrary and it is used mainly for evaluation of thermal loads for a given type of waste and package size (Greenberg et al. 2013). The use of compliance points would be key to the evaluation of thermal limits combined with other knowledge on EBS material properties and thermal characteristics, and host-rock thermal-hydrologic (TH) properties.

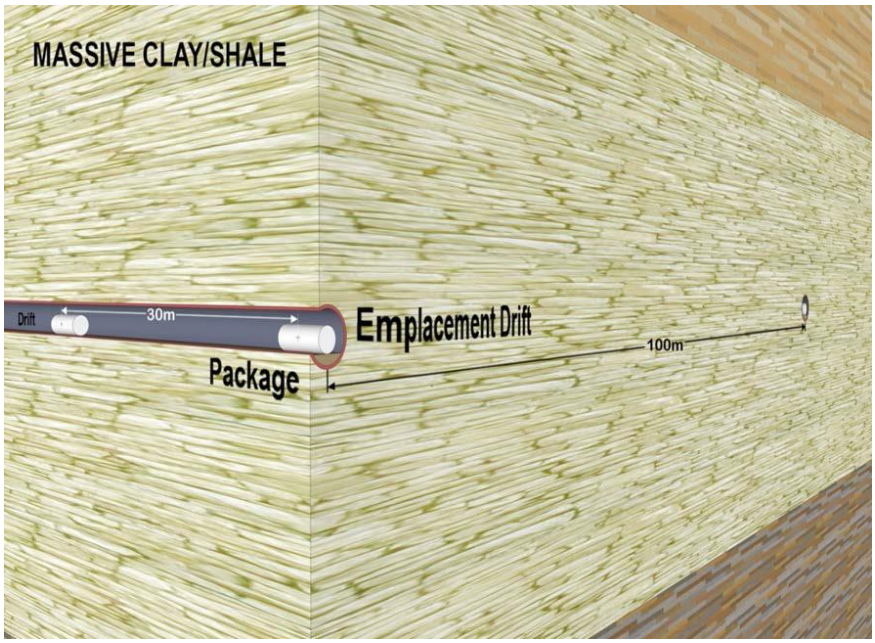

Figure 2. Schematic illustration of an emplacement drifts for an argillite-hosted repository (Hardin et al. 2013).

3. Generic Argillite Repository Reference Case

The generic crystalline repository reference case has the following major elements:

- Waste inventory
- Engineered barrier system (EBS)
  - Waste form
  - Waste package
  - Repository layout
  - Backfill
  - Seals
- Natural barrier system
- Biosphere

Here we briefly describe components of the reference case such waste inventory, waste form, waste package, repository layout, and biosphere following the structure and details of the salt disposal reference case. The biosphere will not be treated in much detail at this point since it depends on receptor scenarios (pumping well from an aquifer) and "fast" upward transport through shafts among other parameters that may be site specific.

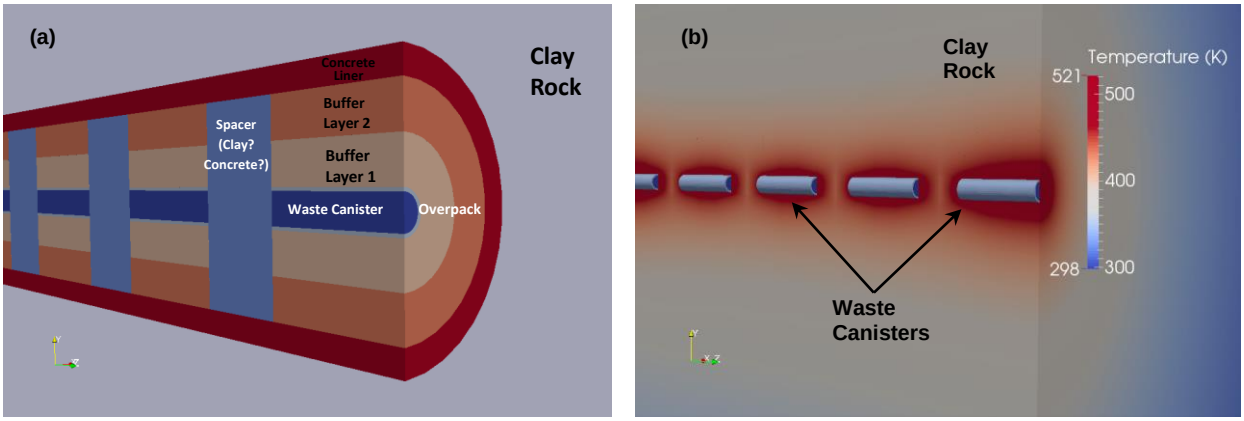

Figure 3. (a) Schematic representation of a longitudinal section of a backfilled single drift with multiple waste canisters and a multi-layered EBS; (b) results of the Albany 3D-FEM thermal model showing temperatures distributions for a single-drift multiple-waste-package case (Jové Colón et al. (2013); 12-PWR UOX, 40 GWd/MT burnup, 50 years time out of the reactor). Temperature color mapping does not apply to waste canisters shown here for schematic purposes.

3.1 Waste Inventory

The waste inventory assumed for the shale the reference case is the same as that for the salt disposal system as discussed in Freeze et al. (2013). We therefore summarize the waste inventory in this section and refer to further details in Freeze et al. (2013).

Just like the salt reference case, repository capacity for the argillite reference case for is 70,000 metric tons heavy metal (MTHM). For simplicity, the entire single-repository inventory is assumed to consist of pressurized water reactor (PWR) used nuclear fuel (UNF) assemblies. Each PWR UNF assembly contains 0.435 MTHM (91,000 MTHM/209,000 assemblies). The

single-repository reference case PWR inventory assumes a bounding fuel burn-up 60 GWd/MTHM. The isotopic composition of the reference case 60 GWd/MTHM PWR inventory assumes an initial enrichment of 4.73% and 30-year out-of-reactor (OoR) decay storage, as reported in Carter et al. (2012, Table C-1). This reference case inventory can be augmented with boiling water reactor (BWR) and high-level waste (HLW) inventories as the performance assessment (PA) model matures.

The reference case PWR UNF inventory includes approximately 450 isotopes with a total mass of 1.44×10^6 g/MTHM and a decay heat of 1.438 kW/MT (Carter et al. 2012, Table C-1). The total mass of the PWR inventory includes actinides (dominated by ^{238}U), oxygen from the UO_2, zirconium from cladding, and other fission and activation products. The mass inventory of these selected radionuclides in a reference case PWR UNF assembly (60 GWd/MTHM burn-up, 30-year OoR, 4.73% initial enrichment) is shown in Table 1. Smaller subset of radionuclides that are considered in the salt reference case (Freeze et al. 2013) are also assumed for the argillite reference case, including neptunium series alpha-decay chain, uranium series alpha-decay chain, and ^{129}I, a non-sorbing radionuclide with a long half-life. Details of their half-life and decay constants are given in Freeze et al. (2013).

Information regarding heat loads according to fuel type and burnup can be retrieved from the DSEF catalog. Also, thermal properties of barrier materials and host-rock can be also obtained from the information available in DSEF. Such information can be used in other models such as the Albany 3D finite element model (FEM) as described in Jové Colón et al. (2013). Albany is a multi-physics FEM code based on the Agile Components vision built almost entirely from the functionality obtained in reusable libraries. In expanding activities started in FY13, the Albany 3D FEM thermal model was extended to a single-drift multi-waste-package scenario as depicted in Figure 3b. 3D FEM models are suitable for this type of thermal problem given the thermal heterogeneities in the EBS materials and the natural barrier plus geometrical asymmetries in the disposal gallery configuration. Zheng et al. (2014c) concluded that a 3-D thermal model is needed to accurately compute the maximum temperature in the disposal system given the accuracy limitations in a 2-D model for the longitudinal configuration of waste packages spaced from each other. This is still an ongoing effort and there are plans to expand the 3D mesh to a multi-drift multi-waste-package scenario where sensitivities to drift and waste package spacing can be evaluated.

Table 1. UNF Radionuclide Inventory for the Reference Case (same as Table 3-1 in Freeze et al., 2013)

Isotope	Waste inventory mass[1] (g/MTHM)	Molecular weight[2] (g/mol)	Mass fraction[2] (g / g UNF)	Mole fraction (mol / g UNF)
^{238}U	9.10×10^{5}	238.05	6.32×10^{-1}	2.66×10^{-3}
^{237}Np	1.24×10^{3}	237.05	8.61×10^{-4}	3.63×10^{-6}
^{241}Am	1.25×10^{3}	241.06	8.68×10^{-4}	3.60×10^{-6}
^{242}Pu	8.17×10^{2}	242.06	5.68×10^{-4}	2.34×10^{-6}
^{129}I	3.13×10^{2}	129.00	2.17×10^{-4}	1.69×10^{-6}
^{234}U	3.06×10^{2}	234.04	2.13×10^{-4}	9.08×10^{-7}
^{230}Th	2.28×10^{-2}	230.03	1.58×10^{-8}	6.89×10^{-11}
^{233}U	1.40×10^{-2}	233.04	9.73×10^{-9}	4.17×10^{-11}
^{229}Th	6.37×10^{-6}	229.03	4.43×10^{-12}	1.93×10^{-14}
^{226}Ra	3.18×10^{-6}	226.03	2.21×10^{-12}	9.77×10^{-15}

[1]from Carter et al. (2012, Table C-1)

[2]from Sevougian et al. (2013, Table 1)

3.2 Engineered Barrier System (EBS)

The description of EBS for the argillite reference case includes the following components:

- Waste Form
- Waste Package
- Repository Layout
- Backfill
- Seals

3.2.1 Waste Form

As described above, the reference case inventory is limited to PWR UNF waste. Each irradiated PWR assembly is assumed to contain 0.435 MTHM and 1.44×10^{6} g/MTHM of isotopes, with mass fractions of the selected radionuclides as listed in Table 1. This corresponds to a total mass of 6.27×10^{5} g of isotopes per PWR assembly. The PWR waste forms are assumed to be predominantly UO_2 with zircaloy cladding. UO_2 has a solid density of 10.97 g/cm^3 (Lide 1999, p. 4-94). Therefore, the solid volume of a PWR assembly can be approximated by (6.27×10^{5} g/assembly)/(10.97×10^{6} g/m^3) = 0.057 m^3.

Typical dimensions for unirradiated PWR assemblies are lengths of 111.8 to 178.3 in (2.84 – 4.53 m) and widths of 7.62 – 8.54 in (0.19 – 0.22 m) (Carter et al., 2012, Table A-1). Based on these dimensions, the total volume of a PWR assembly can range from about 0.10 – 0.22 m^3. The

uranium loading (0.435 MTHM per assembly) is consistent with loadings, burn-ups, and enrichments of PWR assemblies listed in Carter et al. (2012, Table A-3).

The release of radionuclides from UNF includes a fast/instant release fraction (IRF) – predominantly from radionuclides and fission gases located in the fuel and cladding gap, rod plenum regions (fission gases like Kr and Xe), and grain boundaries. Then a slower fraction – from radionuclides released from the UO_2 matrix through dissolution/conversion of the matrix. Sassani et al. (2012) describes the current state of knowledge of IRF processes in irradiated used fuels, structural considerations (e.g., accessible and inaccessible grain boundaries; Figure 4), and IRF models, and distributions for the IRF of radionuclides. The IRF distributions are based largely on empirical correlations depending on the state of the fuel and cladding, burnup rates, and irradiation history. For PA sampling, Sassani et al. (2012) advances the IRF implementation in two sets of distributions: (a) triangular distributions representing minimum, maximum, and mean (apex) values for LWR used fuel with burnup at or below 50 GWd/MT, and (b) a process model has yet to be developed with functional parametrics. Table 3.2 1 of Sassani et al. (2012) provides model and values of IRF (% of radioelement inventory) for spent fuel pellets of various burnups, for a variety of environment conditions, and from various regions of the fuel pellet samples.

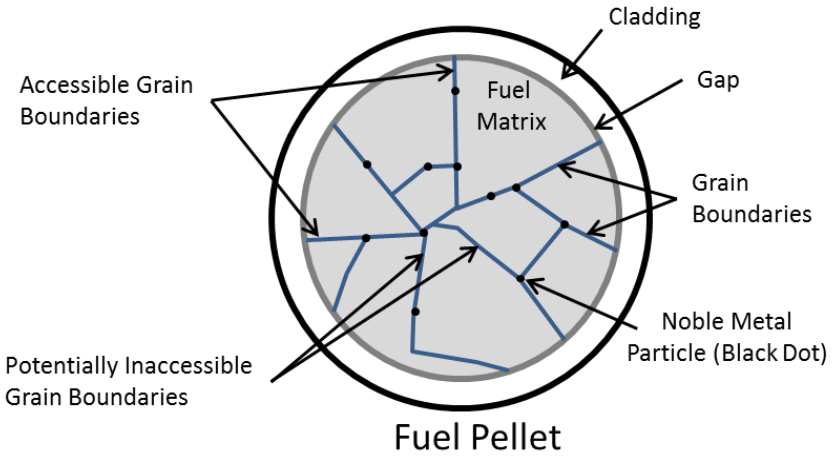

Figure 4. Schematic of a fuel pellet cross section showing the relative locations of radionuclide inventories for the gap, grain boundaries, fuel matrix, and noble metal particles. Also shown are the general locations of accessible grain boundaries and inaccessible grain boundaries (after Sassani et al. 2012).

3.2.2 Waste Package

The reference case considers the design for two types of waste packages: the dual-purpose canister (DPC) that contains a used fuel waste inventory of 32-PWR UNF assemblies (Pressurized Water Reactor) and 12-PWR UNF assemblies. Waste package is composed of the stainless steel canister/container plus enclosing disposal overpack. Various types of disposal overpacks have been proposed in U.S. and international repository programs. Materials for disposal overpack can range from stainless steel, copper, and carbon steel depending on the barrier operational design (e.g., corrosion allowance) within the EBS concept. No decision on the disposal overpack material has been advanced so far but likely candidates are carbon- and stainless-steel. It is expected that implementation of the shale reference case with the generic disposal system analysis (GDSA) will consider waste package failure and thus provide the basis to make decisions on the disposal overpack material. Section 4.3.1 of Hardin et al. (2011) provides more details on waste packages for SNF and HLW.

3.2.2.1 12-PWR Waste Package

Similar to the reference case for disposal in salt (Freeze et al. 2013), the reference case for disposal in shale considers a waste package consisting of a canister containing a 12 PWR UNF assemblies with a disposal overpack. The 12-PWR waste package has a length of 5.0 m and a diameter of 1.29 m (Hardin et al., 2012, Table 1.4-1). These outer dimensions include a 5.0 cm thick disposal overpack. Waste package dimensions are summarized in Table 2. This overpack thickness is considered sufficient to withstand general corrosion and ensure a retrievability period (if considered) of 50 years (Sevougian et al. 2013, Section 2.2.3). More details of 12-PWR waste package are given in Freeze et al. (2013). A burnup of 60 GWd/MT for 12-PWR UNF is also assumed (Freeze et al. 2013).

3.2.2.2 32-PWR Dual Purpose Canister (DPC) Waste package

Hardin et al. (2013) discussed the characteristics of DPC while presenting the concept of direct disposal of DPC. The design capacity of a DPC can accommodate 32-PWR assemblies or 68-BWR assemblies. The average burnup for existing spent nuclear fuel (SNF) in dry storage is nominally 40 GWd/MT. We therefore assume a burnup of 40 GWd/MT for 32-PWR DPCs. Also, many of the cases developed by Greenberg et al. (2013) for scoping thermal calculations for DPCs use a 40 GWd/MT burnup. The nominal dimensions of DPCs have a length of 5 m and a diameter of 1.74 m based on the HI-STAR 100 Multi-Purpose Canister (MPC-32) (Greene et al. 2013). The exterior dimensions of the MPC-32 should include an additional 5.0 cm thick overpack for a total outer diameter of about 1.79 m. It should be noted that the HI-STAR 100 design includes a storage overpack with a wall thickness of 34.5 cm (Greene et al. 2013). Figure 5 shows a cross-section view of the MPC-32 for the HI-STAR 100 system. According to Hardin et al. (2013), DPCs having a 5 cm steel overpack would add about 30 MT in addition to approximately 50 MT of a fully loaded DPC.

Table 2. Canister dimensions for the waste package types considered in the shale reference case. Waste package diameter includes overpack (see text).

Canister type	Dimensions, m	Remarks
12-PWR	1.29 m (diameter) 5.0 m (length)	Source: (Hardin et al., 2012, Table 1.4-1)
32-PWR	1.79 m (diameter) 5.0 m (length)	Source: Greene et al. 2013

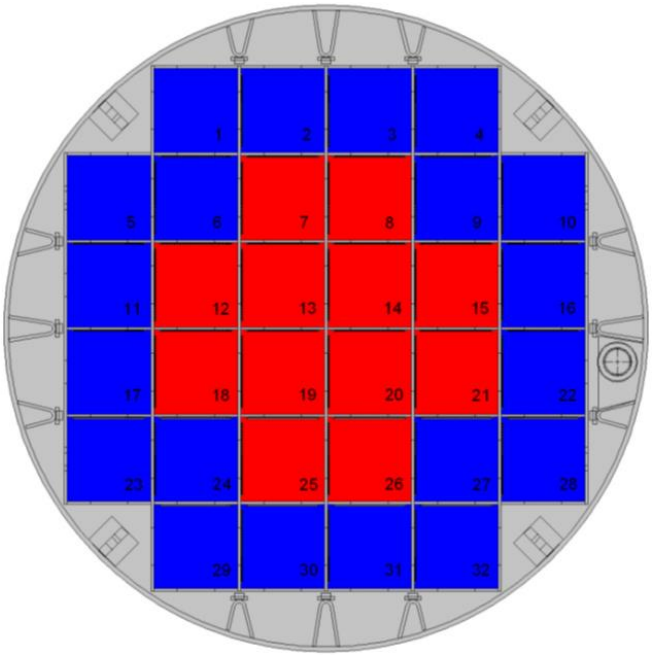

Figure 5. Cross-section view of the multi-purpose canister MPC-32 for the HI-STAR 100 system (after Greene et al. 2013). Red and blue represent younger (higher dose) and older (lower dose) fuel assemblies, respectively.

3.2.3 Repository Layout

The repository layout must consider various operational, mechanical, and thermal design constraints. Liu et al. (2013) summarized the thermal constraints on EBS bentonite imposed in disposal concepts throughout the world for disposal in argillite and crystalline host-rock media. A 100^{o}C thermal limit is imposed unanimously in all these disposal concepts despite their differences in EBS design concepts. The same thermal limit was used when presenting the generic repository design concepts for clay (shale/argillite) repository (e.g. Hardin et al., 2011; 2012). As a result, in order to address assumed thermal constraints imposed on the buffer materials and shale/argillite host-rock media, waste packages that can accommodate 4-PWR or 9-BWR assemblies have been evaluated for this disposal concept (Hardin et al., 2011). Subsequently, thermal analysis for UNF disposal in shale was performed for 4-PWR waste package scenarios given their maximum thermal limit of 100^{o}C for the waste package surface in

their analysis. However, the basis for a 100°C thermal limit is not backed up by rigorous scientific studies (Liu et al., 2013; Jove Colon et al. 2012). Reviews of the performance of bentonite backfill at temperatures above 100°C (e.g., Wersin et al., 2007; Pusch et al., 2010), modeling (Liu et al., 2013; Zheng et al., 2014a), and experimental studies (e.g. Pusch et al., 2003; Caporuscio et al., 2012; Cheshire et al., 2013; Cheshire et al., 2014) describing the mechanical and chemical changes showed little or moderate deterioration of bentonite. While further analyses of the THMC alteration of EBS bentonite and argillite at high temperatures are warranted, these modeling and experimental studies (e.g. Zheng et al., 2014a; Cheshire et al., 2014) in the UFDC suggest that an argillite repository EBS with bentonite clay could sustain temperatures exceeding 100°C. Thermal analyses with the Disposal System Evaluation Framework (DSEF) or other codes (e.g., Albany 3-D FEM thermal analysis) are needed to determine the effects of drift and waste package spacing under thermal loads higher than a 100°C in the vicinity of the waste package surface, drift wall, and compliance points at distance within the rock.

3.2.3.1 Layout for 12-PWR Waste Package

The repository layout dimensions for shale/argillite hosting drifts with 12-PWR waste packages are given in Table 3. Estimated values for the repository dimensions were approximated by the UNF loading, and waste package and drift spacings consistent with the reference case for disposal in salt. There are differences between the disposal concept in salt and shale/argillite, for example, with respect to specified thermal limits in the salt host rock (200°C) and the EBS configuration (e.g., crushed salt backfill). Therefore, evaluation of thermal responses to the proposed shale repository layout and the analysis of thermal limits in the EBS and the natural barrier will be investigated. This could lead to modifications on the proposed layout prior to implementation in GDSA.

Layout dimensions include a drift diameter of 4.5 m with waste package (end-to-end) and drift spacings of 5 m and 20 m, respectively. UNF storage and ventilation times of 50 years are assumed for the reference case. As expected, there are close similarities in the values to those listed in Table 3-3 of Freeze et al. (2013). However, it should be noted that the repository design for the disposal concept in salt includes a central hallway for waste emplacement and disposal drifts on each side. The shale disposal concept only accounts for a series of emplacement drifts on one side of the access tunnel. Therefore, repository length dimensions and thus the overall footprint geometry will be different.

Table 3. Layout Dimensions for the Shale Repository Reference Case for 12-PWR Waste Package.

12-PWR Waste Package

Parameters	Value	Source
Waste Package (WP)		
WP length (m)	5	Freeze et al. 2013, Table 3-3
WP outer diameter (m)	1.29	Freeze et al. 2013, Table 3-3
Overpack thickness (alloy steel) (cm)	5	Hardin et al. 2012
WP end-to-end spacing (in-drift) (m)	5	This work; 10 m center-to-center
Inventory per 12-PWR WP (MTHM)	5.225	Freeze et al. 2013, Table 3-3
Approx. number of WPs for 70,000 MTHM	13,397.40	Freeze et al. 2013, Table 3-3
Emplacement Drift		
Drift diameter (m)	4.5	Jove Colon et al. 2013; Part IV Table 1
Drift center-to-center spacing (m)	20	This work
Number of WPs per drift	80	Freeze et al. 2013, Table 3-3
Drift seal length (m)	10	Freeze et al. 2013, Table 3-3; Bianchi et al. 2013 Table 1
Drift length, including seals (m)	805	Freeze et al. 2013, Table 3-3
Shaft access height (m)	5	This work
Shaft access diameter (m)	5.4	Bianchi et al. 2013 Table 1
Access tunnel height (m)	5	This work
Access tunnel width (m)	8	Freeze et al. 2013 uses 8.0 m
Approx. number of drifts needed for 70,000 MTHM (rounded)	167	Freeze et al. 2013, Table 3-3
Repository		
Approx. repository length (m)	813	This work
Approx. Repository width (m)	3320.0	This work
Repository Depth (m)	600	This work.
Total length of all drifts (m)	134435	This work

3.2.3.2 Layout for 32-PWR DPCs

The drift layout dimensions for disposal of DPCs in shale/argillite host-rock is given in Hardin et al. (2013, Table 4-1). A drift of 5 m high by 7 m wide or a circular cross-section with a diameter of 5.5 m was proposed in the report. Greenberg et al. (2013) did a series of thermal analyses for 32-PWR waste packages with a burnup of 40 GWd/MT and with different drift and waste package spacings and ventilation times. In the shale reference case, we assume a drift spacing of 70 m, waste package spacing of 20 m, and a ventilation time of 50 years.

Table 4 lists parameters and corresponding values used to estimate the overall repository layout dimensions for disposal of DPCs. The temperature at the waste package surface and additional compliance points calculated by DSEF (Greenberg et al., 2013, case 500-11) are given in Table 5. This is just an example of how compliance points can be defined in accord with canister dimensions, EBS geometry, and thermal loads. Zheng et al. (2014) provides a THM evaluation of disposal of DPCs in argillaceous host rock. The thermal part of this evaluation consisted in model comparisons between Disposal Systems Evaluation Framework (DSEF) using analytical solutions for heat conduction and the TOUGH numerical simulator. Although some of the layout characteristics are somewhat similar to those adopted here for a 32-PWR DPC (e.g., waste package spacing), other key parameters like drift spacing are different. Still, the analysis provides model comparisons between analytical and numerical methods and also delineates important bounding cases to evaluate sensitivities to ventilation scenarios and hydrological parameters. Notice also (from Table 4) that a 32-PWR canister configuration yields a much lower number of drifts (~63 drifts) relative to the 12-PWR case (~167 drifts) needed to accommodate 70,000 MTHM of UNF. However, the areal repository footprint for the 32-PWR case is larger than the 12-PWR scenario mainly due to larger drift and waste package spacings. Drift and waste package spacings are influenced by the thermal load in the disposal galleries. Therefore, a more integrated evaluation of thermal limits is needed and based on information obtained from high temperature clay interaction experiments and thermodynamic analysis of phase stability relations.

Table 4. Layout Dimensions for the Shale Repository Reference Case for 32-PWR Waste Package.

32-PWR Waste Package

Parameters	Value	Sources
Waste Package (WP)		
WP length (m)	5	Freeze et al. 2013, Table 3-3
WP outer diameter (m) (inc. overpack)	1.79	after Greene et al. 2013
Overpack thickness (alloy steel) (cm)	5	Hardin et al. 2012
WP end-to-end spacing (in-drift) (m)	15	This work; 20 m center-to-center
Inventory per 12-PWR WP (MTHM)	13.92	Freeze et al. 2013, Table 3-3
Approx. number of WPs for 70,000 MTHM	5,028.74	Freeze et al. 2013, Table 3-3
Emplacement Drift		
Drift diameter (m)	5.5	Hardin et al., 2013
Drift center-to-center spacing (m)	70	Zheng et al. 2014c; This work
Number of WPs per drift	80	Freeze et al. 2013, Table 3-3
Drift seal length (m)	10	Freeze et al. 2013, Table 3-3; Bianchi et al. 2013 Table 1
Drift length, including seals (m)	1595	This work
Shaft access height (m)	5	This work
Shaft access diameter (m)	5.4	Bianchi et al. 2013 Table 1
Access tunnel height (m)	5	Freeze et al. 2013
Access tunnel width (m)	8	Freeze et al. 2013
Approx. number of drifts needed for 70,000 MTHM (rounded)	63	This work
Repository		
Approx. repository length (m)	1603	This work
Approx. Repository width (m)	4340.0	This work
Repository Depth (m)	600	This work.
Total length of all drifts (m)	100485	This work

Table 5. The peak temperature at several compliance points for a argillite repository with a waste package of 32 PWR, 40 GWd/MT, drift spacing of 70 m, waste package spacing of 20 m, and ventilation time of 50 years (case 500-11 in Greenberg et al., 2013)

Location	Radius, m	Peak temperature, ^{o}C
Second compliance point	3.25	103.8
Peak rock	2.25	125.8
Liner inner surface	2.225	125.8
Backfill inner surface	1	233.9
Envelope inner surface	1	233.9
Waste package surface	1	233.9

3.2.4 Bentonite Backfill

As described earlier, two different waste-package designs are considered: (1) a DPC that contains a larger waste inventory of 32-PWR fuel assemblies, and (2) a 12-PWR canister. An engineered clay buffer backfill can be emplaced in a multi-layered configuration to optimize thermal, flow, and sorption properties of the buffer/backfill media. Figure 6 shows a double layer backfill configuration having two clay buffer materials for the 12-PWR canister. The choice of a double layer permits the use of two different clay buffer materials that can be tailored to optimize the barrier physical and chemical properties, while maintaining a low level of complexity in the overall EBS design. While the double layer backfill configuration can certainly be applied to the disposal of DPCs, a single layer backfill configuration (as shown in Figure 7) could also be another option. It may be operationally challenging to install a two-layer backfill to accommodate the relatively large dimensions and substantial weight of a DPC. On the other hand, the high thermal load of a DPC would impose the partial sacrifice of the inner buffer layer closest to the waste package surface. The extent of such a "sacrificial layer" can be engineered with a tailored inner clay backfill layer as part of a double-layer system.

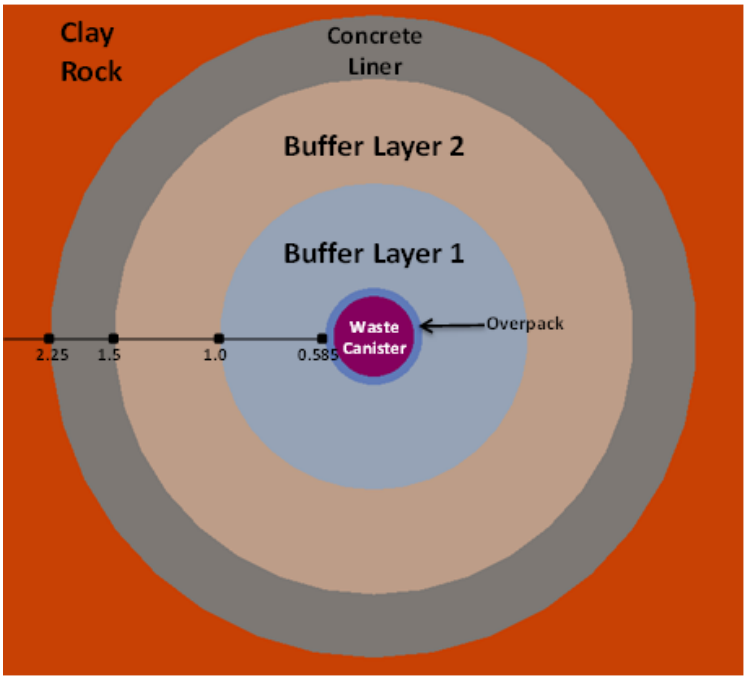

Figure 6. 2-D schematic diagram two-clay buffer layer EBS geometry used in 12-PWR thermal calculations. Point values are radial distances in meters from the center of the waste canister (Jové Colón et al. 2013).

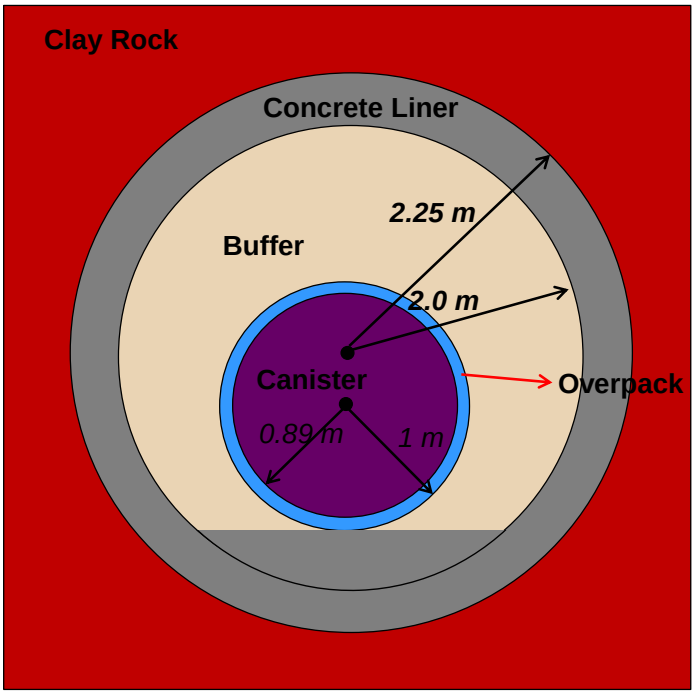

15

Figure 7. Geometry of a cross section of a drift for the disposal of DPC, largely based on Hardin et al (2013) and Greenberg et al. (2013).

3.2.4.1 Relevant Processes

Numerous modeling studies have been conducted by international research groups and by the UFDC. Some processes have long been identified as of great importance for the performance of a repository, such as diffusion and sorption. But the importance of some processes is not clear and requires more modeling and experimental studies. Here are the processes that are thought to be important and, therefore, have to be considered in the reference case:

- Heat transport by advection and conduction. An accurate prediction of the temperature profile in EBS is clearly important. The thermal limit in many countries (Hicks et al., 2009) is based on the temperature of the EBS.
- Fluid (water and vapor) flow by advection and diffusion. The hydrological condition is also obviously important, because they affect heat transport, mechanical changes, and chemical reactions in the EBS.
- Mechanical changes in the EBS, which are also important because they affect the long-term stability of the EBS and drift.
- Chemical reactions including mineral precipitation/dissolution, sorption, and cation exchange are very important because they either directly control the migration of radionuclides or affect radionuclide transport indirectly through changes in the chemical conditions within the EBS. Cation exchange reactions also affect the volumes of the clay phase and thus the swelling properties.
- Interactions between the EBS and the canister materials, which have a significant impact on the redox environment and thus radionuclide solubility.

While the coupling between TH (e.g., heat transport by the advection of water), TC (e.g., change of mineral solubility with temperature), TM (e.g., thermal expansion and pressurization), and HC (e.g., solute transport by advection) are known to be important, recent modeling work sheds light on the importance of HMech (such as swelling due to moisture change) and MC (e.g. change in swelling pressure due to pore-water chemistry changes) couplings. Coupled THM models have been developed in Rutqvist et al. (2009, 2011, 2014a, 2014b). The results from the model developed in Rutqvist et al. (2014b) show that it takes about 2780 years to fully saturate the EBS bentonite if the interaction between micro- and macro-structures is considered. This is much longer than the saturation time for the EBS predicted with single-structure models. Coupled THMC models have also been developed (Liu et al. 2013; Zheng et al. 2014a) to evaluate the impact of chemical processes on mechanical behavior, specifically the effect of illitization, pore-water chemistry changes, and cation exchange on the swelling of EBS bentonite. Liu et al. (2013) showed that chemical changes result in a decrease in swelling pressure of 0.2–0.3 MPa (about 20–30% of the swelling capacity) for Kunigel-VI bentonite (JNC 2000). In one extreme case, Kunigel-VI bentonite could loss up to 70% of its swelling capacity, which suggests that MC coupling is important for Kunigel-VI bentonite. Zheng et al. (2014a) conducted modeling studies which consider FEBEX bentonite (ENRESA, 2000) as the EBS buffer/backfill material. Model results showed only a moderate decrease in swelling stress of about 0.08 MPa, accounting for just 2% of the swelling capacity of FEBEX bentonite. The possible reasons for FEBEX bentonite experiencing less swelling pressure loss than Kunigel-VI bentonite are as follows: (a) less illitization is predicted for FEBEX bentonite, and (b) FEBEX bentonite has much higher swelling capacity (5–8 MPa) than Kunigel-VI bentonite (around 1MPa). The tentative conclusion

from current THMC models is that MC coupling does not necessarily need to be included in a performance assessment model. However, before making the determination that MC coupling could be neglected, coupled THMC modeling is warranted when site-specific data are available. The bentonite properties that need to be specified to address these processes are given the following section.

3.2.4.2 Thermal, Hydrological and Mechanical Properties

The basic material in the backfill is typically bentonite which is an impure clay consisting mostly of smectite (montmorillonite), along with small amounts of other minerals such as quartz and feldspar. In some disposal concepts (ENRESA 2000; SKB 2006), the backfill contains bentonite exclusively, but mixtures of bentonite with graphite or silica phases (e.g., quartz) have also been considered in some disposal concepts to enhance thermal conductivity (e.g., JNC 2000). Here we focus on the properties of two widely studied bentonites: FEBEX (ENRESA 2000) and MX-80 (SKB 2006) bentonites. The properties of bentonite mixtures with other materials are not discussed here.

Table 6 lists typical thermal, hydrological and mechanical parameters for the two bentonites that have been studied as the backfill material for nuclear waste disposal. Thermal, hydrological and mechanical properties for bentonite vary a great deal with degree of compaction (dry density). Those properties listed in Table 6 are for the dry density range that is widely used in tests of different scales and are considered candidates for use in a future repository. For example, a dry density of around 1650 kg/m^3 for FEBEX bentonite bricks has been used in the Mockup and In Situ test (ENRESA 2000) and it is also the design used in the Spanish reference concept for high level nuclear waste disposal (ENRESA 2000). Properties for FEBEX and MX-80 bentonite (see Table 6) are largely from ENRESA (2000) and SKB (2006), respectively, but some are taken from various other sources as noted below.

Saturated permeability for FEBEX bentonite is typically around 2–3×10^{-21} m^2, but a summary from various sources (ENRESA 2000; Börgesson and Hernelind 2005; Zheng et al. 2011a) leads to a larger range of permeabilities.

The relative permeability curve for FEBEX bentonite is typically given as:

$$K_{rl} = S^n \tag{1}$$

where K_{rl} is the relative permeability, S is the water saturation, and n is a constant. The exponent n ranges from 3 to 4.5 (ENRESA 2000), but most models (Zheng et al. 2011a; Sánchez et al. 2012) have used 3. The relative permeability curve for MX-80 bentonite is the same as in equation (1), with n ranging from 2 to 4 (Hökmark 2004).

Typically the van Genuchten (van Genuchten 1980) function is used for water retention curve, which expresses the capillary pressure, s, as a function of water saturation, S.

$$S_w = S_r + (S_m - S_r)\left[1 + \left(\frac{s}{P_0}\right)^{\frac{1}{1-\lambda}}\right]^{-\lambda} \tag{2}$$

where S_r and S_m are the residual and maximum degree of water saturation, P_0 is the material property that represents capillary strength, and λ is m in van Genuchten's notation, which represents the effects of the pore-size distribution. ENRESA (2000) lists a quite large range of

λ and $P_{0,}$ but in some modeling works (Zheng et al. 2011a; Sánchez et al. 2012), λ is 0.18 and P_0 is 2×10^7 Pa; Villar et al. (2008) used the same value of λ but a slightly different value for P_0 (2.8×10^7 Pa). The parameters λ and P_0 for MX-80 bentonite are from Hökmark (2004). The specific heat capacity for MX-80 bentonite is from Man and Martino (2009).

Table 6. Thermal, hydrological and mechanical parameters for two bentonites.

Parameter	**FEBEX bentonite**	**MX-80 bentonite**
Grain density [kg/m^3]	2700	2700
Dry density [kg/m^3]	1650-1700	1650-1700
Porosity ϕ	0.41	0.41
Thermal conductivity [W/m ^{o}C] dry/wet	0.57/1.28	0.3/1.3
Saturated permeability [m^2]	1.75×10^{-21} - 8×10^{-21}	2.0×10^{-21}
Relative permeability, k_{rl}	$K_{rl} = S^3$	$K_{rl} = S^3$
van Genuchten P_0 (Pa)	2×10^7 to 1×10^8	0.9×10^7 to 2×10^7
van Genuchten *m* (or λ)	0.18-0.475	0.4-0.45
Compressibility, β [1/Pa]	3.2×10^{-9}	3.2×10^{-9}
Thermal expansion coeff., [1/^{o}C]	1.0×10^{-5}	1.0×10^{-5}
Dry specific heat, [J/kg ^{o}C]	767-939	800
Tortuosity for vapor phase	$\phi^{1/3}S_g^{10/3}$	$\phi^{1/3}S_g^{10/3}$
Swelling pressure (MPa)	5-10	7.5-8

3.2.4.3 Chemical Properties

The chemical properties of the buffer layer are critical for the performance of a repository. First, these properties significantly affect the chemical environment in which canisters or overpack react with incoming formation water, particularly at elevated temperatures. Second, the buffer layer serves as the first barrier for retarding radionuclide migration, the effectiveness of that retardation is highly sensitive to the chemical conditions in the buffer. The most relevant chemical properties of bentonite buffer are the initial-state mineral and aqueous compositions.

Mineralogical Composition

The most prominent mineral in bentonite backfill is smectite clay, which typically accounts for 40% to 95% of the total mass of bentonite. Table 7 lists the mineral compositions of FEBEX and MX-80 bentonites. In addition to smectite, quartz, K-feldspar, and oxides are common accessory minerals. Highly soluble minerals such as calcite and gypsum could also be present. These minerals could have a significant impact on the pore-water chemistry during the hydration of EBS bentonite.

Table 7. Mass fraction (%) of minerals for FEBEX (ENRESA 2000; Fernández et al. 2004) and MX-80 bentonite (Börgesson et al. 2006).

Mineral	FEBEX bentonite	MX-80 bentonite
Calcite	trace	0
Dolomite	0.0	0
Illite	0.0	1
Kaolinite	0.0	0
Smectite	92 ± 3	87
Chlorite	0.8	0
Quartz	2 ± 1	3
K-Feldspar	trace	3
Siderite	0.0	0
Ankerite	0.0	0
Cristobalite	2 ± 1	0
Plagioclase	2 ± 1	0
pyrite	0.02	0.25
Mica		4
Gypsum	0.14	0.7

Bentonite pore-water Chemistry at the Initial State

Pore-water chemistry at the initial state of bentonite backfill is very important, because it affects the chemical environment in which the radionuclides migrate. The initial state of bentonite backfill for the repository conditions is typically characterized by the dry density and water content, or solid/liquid ratio. For example, FEBEX bentonite blocks have an initial gravimetric water content of 13.5–14% (ENRESA 2000), which is about 56% in terms of volumetric water content (Zheng et al. 2011a). However, as mentioned in Bradbury and Baeyens (2003a), obtaining the pore-water chemistry of compacted bentonite is not a straightforward task, and therefore there is considerable uncertainty associated with the concentrations of ions in the pore-water. Major uncertainties are as follows:

1. The concentration of ions for the initial state of compact bentonite cannot be measured directly; therefore indirect measurement methods have to be used. Squeezing and aqueous extract are the most commonly used methods. Pore-water squeezed out of the rock in sufficient amounts provide aqueous solution concentrations. However, squeezing does not allow extracting pore-water from clay samples with gravimetric water contents less than 20% (Fernández et al. 2001, 2004). This means that this method cannot be used for FEBEX bentonite blocks, which initially have a water content of 14% (ENRESA 2000). In an aqueous extract test, a crushed sample is placed in contact with water at a low solid/liquid ratio (ranging from 1:16 to 1:1). After establishing equilibrium, the solid phase is separated and the liquid phase is analyzed (Fernández et al. 2001). Because of the low water content (high solid/liquid ratio as well), the pore-water chemistry at the initial state can only be measured indirectly by squeezing conducted at higher water content or aqueous extract. Both methods introduce artifacts that result in scattered data and geochemical modeling is therefore needed to constrain aqueous ion concentrations at low water content (Zheng et al. 2008). Any uncertainties associated with the geochemical models affect concentration levels at low water content (the water content at the initial state).
2. It is generally agreed that there are two types of pore-water in compacted bentonite: (1) external or intergranular water that resides in large pores and (2) interlayer water located in the interlayer spaces of the swelling smectite (e.g., Bradbury and Baeyens 2003a). External water can be viewed as two types: (1) bulk or "free" water and (2) diffuse double layer (DDL) water adsorbed on the mineral surface. Typically the "pore-water" refers to the free water, whose concentrations are for the ions present in the bulk aqueous solution.
3. Compacted bentonite blocks are typically fabricated by adding a small amount of water to dry bentonite power. Sometimes deionized water is used but in some cases the water from the potential host formation is used, which affects the pore-water chemistry.

Table 8 lists the concentration of major ions in compacted MX-80 and FEBEX bentonites as examples. The pore-water for FEBEX bentonite is calculated from measured concentrations at different solid/liquid ratios with bentonite being mixed with granite water from the Grimsel test site (ENRESA 2000). Pore-water for MX-80 bentonite is calculated from data obtained by mixing MX-80 bentonite powder with Opalinus Clay pore-water (Curtis and Wersin 2002).

Table 8. Pore-water composition of FEBEX bentonite (Fernández et al. 2001) and MX-80 bentonite (Curtis and Wersin 2002).

Species	MX-80 Bentonite	FEBEX Bentonite
pH	7.25	7.72
Cl	1.91E-1	1.60E-01
SO_4^{-2}	6.16E-2	3.20E-02
HCO_3^-	2.83E-03	4.1E-04
Ca^{+2}	1.32E-02	2.2E-02
Mg^{+2}	7.64E-03	2.3E-02
Na^+	2.74E-01	1.3E-01
K^+	1.55E-03	1.7E-03
Fe^{+2}	4.33E-05	NR*
SiO_2(aq)	1.80E-04	1.1E-04
AlO_2^-	1.92E-08	NR*

*not reported

Sorption Properties

Cation exchange capacity (CEC) is usually needed for reactive transport modeling of a repository system: it generally represents the sorption capacity of bentonite. FEBEX bentonite has a CEC of ~102 meq/100 g (ENRESA 2000; Fernandez et al. 2001) and MX-80 bentonite has a CEC of ~78.7 meq/100 g (Bradbury and Baeyens 2002). Table 9 shows the cation occupancies of the exchangeable sites.

Table 9. The CEC and exchangeable cations for FEBEX bentonite (Fernández et al. 2001) and MX-80 bentonite (Bradbury and Baeyens 2002).

Cations (meq/100 g)	MX-80 Bentonite	FEBEX Bentonite
Ca^{+2}	6.6	34.6
Mg^{+2}	4.0	34.0
Na^+	66.8	31.1
K^+	1.3	1.94
CEC (meq/100 g)	78.7	102

The radionuclide sorption properties of the clay material are represented in the form of K_d (distribution coefficients) or retardation factor, R_d. K_d is defined as the ratio of the sorbed radionuclide mass per unit mass of solid divided by the radionuclide solution mass concentration. R_d is defined as:

$$R_d = 1 + \frac{\rho_d}{\theta} K_d \tag{3}$$

where ρ_d is the dry bulk density of the soil and θ is the volumetric water content.

The K_d approach and its variants have been widely adopted in transport calculations and have been calibrated to capture dependencies, such as aqueous phase and bulk rock chemistry. K_d values for various radionuclides have been determined for various types of materials. Current UFD work (experimental and modeling) is under way to assess diffusion data for U and other radionuclides in clay material. Reactive diffusion through clay is also part of this effort to mechanistically represent the effect of compacted porous clay on diffusive fluxes, particularly for charged species. Sorption data (expressed as a retardation factor, R_d) for MX-80 bentonite were tabulated in Bradbury and Baeyens (2003b), with a subset of those tables shown in Table 10. A critical review of K_d for several bentonites and argillites are given in Miller and Wang (2012).

Table 10. In situ retardation factor R_d value (m^3/kg) for the MX-80 bentonite at pH = 7.2 (Bradbury and Baeyens 2003b)

Species	**Retardation factor**	**Species**	**Retardation factor**
Cs(I)	0.12	Ra(II)	0.0021
Ce(III)	4.7	Ac(III)	26.8
PM(III)	4.7	Th(IV)	63
Sm(III)	4.7	Pa(V)	5
Eu(III)	4.7	U(IV)	49.1
Ho(III)	4.7	Np(IV)	63
Hf(IV)	81	Pu(III)	26.8
Pb(II)	7.9	Am(III)	26.8
Po(IV)	0.068	Cm(III)	26.8

Diffusion coefficients are important parameters that control the migration of radionuclides. Although the diffusion coefficient for major cations such as Na and trace elements such Sr and Cs have been widely studied—for example, García-Gutiérrez et al. (2001) for FEBEX bentonite and Ochs et al. (2001) for MX-80 bentonite—the diffusion coefficients for radionuclides are not widely reported. Table 11 lists the effective diffusion coefficients of several radionuclides for MX-80 bentonite (Brandberg and Skagius 1991).

Table 11. Effective diffusion coefficient for some elements for MX-80 (Brandberg and Skagius 1991).

Species	**Effective diffusion coefficient (m^2/s)**
C-14	10^{-10}
I-129	2×10^{-12}
Sr-90	2×10^{-8}
Cs-137	2×10^{-9}
Na-22	2×10^{-9}
Pu-238	10^{-10}
Am-234	10^{-10}

Radionuclide Solubilities

Radionuclide solubility must be considered as a key limiting mechanism to arrest species mobility. These solubilities can be estimated through chemical equilibrium calculations using existing thermodynamic data. Some limitations exist with regard to temperature and the effects of ionic strength. However, such calculations have been performed and embedded in PA calculations with uncertainty bounds to address some of these limitations. Current efforts directed at describing used fuel interactions and the effects of radiolytic phenomena will provide a comprehensive analysis of source term releases (Buck et al. 2013). An update of those efforts is discussed in another part of this report. Bernot (2005) provides an evaluation of radionuclide solubilities for implementation into PA. Recent efforts in thermodynamic database development, along with tools for computing solution-mineral equilibria, are being assessed for a more rigorous computation of solubility limits. Such type of evaluation could be used to bound solubilities of actinides like plutonium, neptunium, uranium, thorium, americium, actinium, and protactinium.

3.2.5 Concrete Liner

Ground support for the drift is generally needed, especially for the disposal of DPCs. Hardin et al. (2013) mentioned that steel sets or shotcrete could be used, with the latter probably being more economically viable. Currently, for the reference case, a 25 cm thick shotcrete layer (Figure 7) is considered. Similar to the bentonite backfill, shotcrete undergoes simultaneous

THMC alterations. Those processes that are relevant for the bentonite backfill are also important for the concrete liner. Because coupled THMC models for shotcrete were not found in the literature, the importance of some coupled processes such as HMech and MC couplings cannot be evaluated. HMech and MC presumably might not be too important for the safety assessment. For example, moisture-induced stress changes, the predominant HMech coupling, might not be important because concrete is much more rigid than bentonite. Chemically-induced stress effects, a typical MC coupling, would not be significant unless concrete undergoes significant chemical changes. However, modeling of coupled processes needs to be performed before making decisions on whether to neglect HMech and MC couplings. Because a concrete liner is emplaced between the bentonite backfill and argillite host rock, concrete/bentonite and concrete/argillite interactions are potentially important. Experimental and modeling studies of concrete/bentonite interaction are extensively reviewed in Gaucher and Blanc (2006). Kosakowski and Berner (2013), Gaboreau et al. (2012), and De Windt et al. (2008) provide modeling studies of concrete/argillite interactions. The parameters needed to describe those processes are given below.

3.2.5.1 Thermal, Hydrological and Mechanical Properties

Shotcrete has been used in the Full-Scale Emplacement Experiment (FE) at the Mont Terri URL, Switzerland (Vietor 2012) and models for scoping calculations and benchmarking have been developed in Houseworth et al. (2013). Table 12 lists the thermal and hydrological parameters for shotcrete used in these models. The relative permeability and retention curve for shotcrete are described by the van Genuchten relationship, with formats shown in Equations (4) and (5). The parameters for Equations (4) and (5) are given in Table 12:

The water relative permeability in the shotcrete is given by:

$$k_{rw}(S_w) = \left(\frac{S_w - S_r}{S_m - S_r}\right)^{1/2} \left[1 - \left\{1 - \left(\frac{S_w - S_r}{S_m - S_r}\right)^{1/m}\right\}^{m}\right]^2$$

Capillary pressure in the shotcrete is given by:

$$\psi(S_w) = \frac{1}{\alpha}\left\{\left(\frac{S_w - S_r}{S_m - S_r}\right)^{-1/m} - 1\right\}^{1-m}$$

where $\frac{1}{\alpha}$ is equivalent to P_0 in Equation (2).

Table 12. Thermal and hydrological parameters for shotcrete (Houseworth et al. 2013).

Parameters	**Shotcrete**
Solids density (kg/m^3)	2700.
Porosity	0.15
Permeability (m^2)	3.5 x 10^{-21}
Thermal conductivity (saturated) (W/m)	1.7
Specific heat (solids)	800.
Thermal conductivity (desaturated) (W/m)	1.06
Tortuosity	1.
Water relative permeability parameter *m*, (Equation (4))	0.52
Water relative permeability residual saturation, S_r (Equation (4))	0.0071
Water relative permeability maximum saturation, S_m (Equation (4))	1.
Capillary pressure parameter, α (Pa^{-1}) (Equation (5))	9.091 x 10^{-8}
Capillary pressure parameter, *m*, (Equation (5))	0.29
Capillary pressure residual saturation, S_r (Equation (5))	0.0071
Capillary pressure maximum saturation, S_r (Equation (5))	1.
Vapor and air diffusion coefficients (D in Equation (6)) (m^2/s)	2.68 x 10^{-5}
Vapor and air diffusion temperature exponents, (n in Equation (6))	2.3

The vapor and air diffusion coefficients are both given by, D_g^w, which is modeled as a function of temperature and gas-phase saturation using the following relationship,

$$D_g^w = \tau S_g D \frac{P_{g0}\left(273.15+T\right)^n}{P_g\left(273.15\right)^n} \quad (1)$$

where P_g is the gas phase pressure, T is the temperature in Celsius, P_{g0} is the gas-phase pressure at a temperature of zero Celsius, τ is the tortuosity, S_g is the gas saturation, and D is the diffusion coefficient at a temperature of zero Celsius, and n is an empirical coefficient.

3.2.5.2 Chemical Properties

The properties of concrete vary according to the locations where the cement is fabricated. De Windt et al. (2008) modeled reactive transport at the concrete/argillite interface. Table 13 lists the mineralogical composition of concrete used in their model. The extensive review of Pabalan et al. (2009) discusses important characteristics of cement degradation relevant to engineered barriers in radioactive waste disposal. For example, chemical degradation processes such cement corrosion, carbonation, and leaching. Mechanical effects include thermal cracking or shrinkage as a result of desiccation. Pore-water composition data for concrete phases is scarce and it's usually specific to certain types of cementitious materials. Still, bounding pore water compositions can be estimated through geochemical modeling and through knowledge of the cement phase composition.

Table 13. Mineralogical composition of concrete after De Windt et al. (2008).

Mineral	Shotcrete
Calcite (aggregate)	66.5
CSH 1.8	23
Ettringite	1.5
Hydrotalcite	0.5
Monosulfoaluminate	1.5
Portlandite	0.8

An example of concrete pore water composition calculated by equilibrating unhydrated cements with water is given in Kosakowski and Berner (2013). A thermodynamic database compilation for clay and cementitious materials has been compiled in a previous report (Jové Colón et al, 2011) along with modeling tool development of C-S-H solid solution and computation of equilibrium aqueous species concentrations (Jové Colón et al, 2012). Sorption onto concrete is also an important process for migration of radionuclides. McKinley and Scholits (1993) compiled and compared different sorption databases for cements.

3.3 Seals

Seals comprise the isolation system emplaced in deep repository structures — such as shaft/tunnel/disposal gallery accesses and drift linings and/or support assemblies — to limit radionuclide mobility and fluid flow beyond the confines of the near-field environment. The shaft seal system is designed to limit access of formation water into the repository and disposal galleries. Conversely, it is also designed to restrict the outflow of contaminated fluids from the repository. Extensive work conducted at the WIPP repository provides the basis for the evaluation of the expected performance depending on the seal configuration and materials to be considered.

The design guidance items for a shaft seal system are given by Hansen et al. (2010):

• Limit waste constituents reaching regulatory boundaries

• Restrict formation water flow through the sealing system

• Use materials possessing mechanical and chemical compatibility

• Protect against structural failure of system components

• Limit subsidence and prevent accidental entry

• Utilize available construction methods and materials.

Seal materials include cement and clay that are consistent with shaft sealing material specifications and the repository makeup. In general, small amounts of groundwater (if any) are expected to percolate into the repository even with distal or proximal aquifers. Although cement and bentonite clay are regarded as stable seal materials, potential processes such as thermally-induced phase transformations and interactions with intrinsic or extrinsic fluids may cause degradation. However, significant degradation of this type is not expected to occur in a clay/shale repository, given the expected level of isolation. Another aspect of seals is its close relationship to the excavated disturbed zone (EDZ) as described by Bianchi et al. (2013). Permeability ranges for seals can be obtained from existing literature sources for cement and clay materials.

3.4 Natural Barrier System

The natural (barrier) system (NS) for the reference case includes the unaltered host rock and the excavation damaged zone (EDZ) around the tunnels and access shafts of the repository. The host rock is represented by an argillaceous formation characterized by low permeability, high retention capacity for radionuclides, and potential self-sealing of fractures. Geological formations with similar properties are currently under consideration for disposal of HLW by several countries such as France (argillite), Belgium (plastic clay), and Switzerland (claystone). Argillaceous or clay-rich formations can have a wide range of lithologies in terms of degree of consolidation, textural parameters (e.g., presence of lamination), and mineralogical composition (i.e., type of clay minerals, percentage of carbonate or quartz particles). Moreover, the term "clay" is often ambiguous, since it can be used to refer to a group of minerals (clay minerals), rock fragments rich in clay minerals, or sediment grains smaller than fine silt (< 2 μm). Because of the wide range of clay-rich formations in the United States, and the fact that a specific site has not been yet identified, the generic term *argillaceous formation* is used to describe a clay-bearing host rock in the reference case. This term indicates a generic sedimentary formation with a lithological composition of at least 50% clay. More specific details on the argillaceous formation considered in the reference case are presented in the next section.

3.4.1 Relevant Processes

Those processes relevant to the performance of EBS bentonite are also important for the argillite host rock, including heat transport by advection and conduction, water flow by advection, vapor flow by advection and diffusion, mechanical changes, and chemical reactions. Vapor flow by diffusion is of particular importance for argillite in the short term. Argillite near the

concrete/argillite might become unsaturated for a short period for the disposal of 12-PWR canisters whereas argillite undergoes a desaturation during ventilation for the disposal of DPCs (Zheng et al. 2014c). Concrete/argillite interactions could have significant impact on the migration of the radionuclides because minerals precipitation in concrete might cause pore clogging (Gaboreau et al. 2012).

Coupled THM models for argillite have been developed in Rutqvist et al. (2014a) and coupled the THMC models have also been developed (Liu et al. 2013; Zheng et al. 2014a, 2014b). Because of significant increases in stress due to thermal pressurization (Rutqvist et al. 2014a), the stress change due to illitization caused by MC couplings (Liu et al. 2013; Zheng et al. 2014a) seems not to be very important. However, the effect of illitization on the sorption capacity of argillite still requires further study. MC couplings are therefore not deemed indispensable in the performance assessment model. However, when site-specific data are available, the use of a coupled THMC model is warranted before deciding to neglect MC couplings.

3.4.2 Properties of the Argillaceous Host Formation

For the reference case, the stratigraphic setting and hydrogeological properties of a generic argillaceous formation are made consistent with the characteristics of argillaceous units in four major shale provinces in the United States based on the classification of Gonzales and Johnson (1984): Eastern Interior, Great Plains, Rocky Mountains, and Colorado Plateau. These provinces were chosen because of the higher number of units with potential for HLW storage (Table 1-1 in Hansen et al. 2010). Figure 8 shows the areal distribution of shale in the USA along with depth to top mapping of formation units. In collecting data from several potential units, we also considered the recommendations of Hansen et al. (2010) and Shurr (1977):

- **Formation thickness:** Formation thickness should be at a minimum 150 meters. Lesser values have been proposed (75 meters) but larger thicknesses are desirable depending on formation stratigraphic uniformity.
- **Depth:** The repository horizon should be at a depth between 300 to 900 meters. A depth of ~600 meters is considered in generic disposal concepts. The report by Perry et al (2014a) provides an analysis of shale formation depths and thicknesses distributed along continental USA.
- **Low hydraulic conductivity:** Shale media is highly desirable for its very low permeability with small values in the order of $10^{-14} – 10^{-22}$ m^2.
- **Areal coverage:** Widespread distributions of sedimentary basins in the continental USA contain thick shale sequences extending hundreds of kilometers. Gonzales and Johnson (1985) and more recently Perry et al. (2014a) provide a comprehensive description of shale distribution in the USA.
- **Self-healing:** A key property of shale is plasticity (along with swelling) allowing for healing or self-sealing (used here interchangeably) of fractures as a result of burial processes or during excavation activities. Self-healing leads to reduction to hydraulic conductivity of fracture and can occur through chemo-mechanical (swelling), chemical

(fracture filling and mineral precipitation), and mechanical closure of fracture through rock deformation (Mazurek et al. 2003).

- **Mineralogy:** Shale formations can have variable mineralogy and organic content. The desirable mixed-clay fraction (illite/smectite) should exceed 85% where the remainder is usually as assemblage of accessory minerals such as quartz, Fe oxides, pyrite, and feldspar.
- **Stratigraphic and structural uniformity (bedding and faulting):** Uniform stratigraphy (e.g., lack of sandstone lenses, and allocthonous materials) with low bedding angle or flat-lying sequences and marginal thick sedimentary layering within the repository horizon. Minimal structural geologic features such as folding, faulting, and joint/fractures is desirable within the extent of the repository footprint.
- **Hydrogeochemistry:** The hydrochemistry of deep-seated clay-bearing is often represented by reduced aqueous fluids with bulk chemistries enriched in Na-Ca-Cl-SO_4 and often saline. Salinity tends to increase with depth due increase fluid isolation. Therefore, mixing with more diluted waters from overlying or much shallower formations is usually not observed.
- **Tectonic and/or seismogenic stability:** Preference is given to areas that are seismically quiet, devoid of active faults or far from major tectonic lineaments.
- **Borehole activity:** Oil and gas drilling targets for hydrocarbon resource exploration and production in shale are unwanted, particularly in the exploitation of unconventional (often deep) shale reservoirs.

In the Eastern Interior Province, the characteristics of the Upper Ordovician Black River Group and Middle Ordovician Trenton Group of the Michigan Basin were considered (Clark et al. 2013; Beauheim et al. 2014) . In the Great Plains Province, most of the data analyzed refers to the Pierre Shale (Neuzil 1986; 1993; Bredehoeft et al. 1983; Olgaard et al. 1995; Smith et al. 2013). Based on this information, the reference case assumes a depth for the top of the argillite host formation of 450 m (with a range of ~300 m to 900 m), a thickness of 150 m (with a range of ~75 m to 300 m), and an extent of 300 km x 300 km (with a range of ~100 km × 100 km to 500 km × 500 km). There are several locations in the Eastern Interior, Great Plains, Rocky Mountains, and Colorado Plateau shale provinces that have argillaceous formations with these ranges of depth, thickness, and areal extent, such that they can be targeted for HLW disposal. It is also assumed that the argillaceous formation is bounded at the top and at the bottom by two geological units with permeability 4 to 5 orders of magnitude higher than the argillaceous host rock. The lithology of these surrounding units is not specified at this stage, but will be specified when a site will be selected.

As for the structural and stratigraphic setting, the values assumed for the hydrogeological properties of the argillaceous host formation in the reference case are based on available data from argillaceous formations in the U.S. (Table 14). The permeability of the unaltered argillaceous rock is assumed equal to 5×10^{-20} m^2 (with a range of 1×10^{-19} m^2 to 1×10^{-21} m^2). This value is also consistent with the range of permeability values measured in argillaceous formations currently under investigation as potential host rock for HLW disposal, such as the Callovo-Oxfordian Argillites (e.g., ANDRA 2005, Armand et al. 2013), and the Opalinus Clay

(e.g., NAGRA 2002; Croisé et al. 2004). The same value was also adopted by Bianchi et al. (2013; 2014). The total porosity is assumed equal to 0.15 (with a range of 0.1 – 0.4), while the accessible porosity—that is, the fraction of pore space that actually accessible to diffusion—is assumed equal to 0.08 (with a range of 0.04 to 0.1).

3.4.3 Hydraulic Conditions in the Argillaceous Formation

The reference case formation is assumed saturated with a specific storativity of 1.0×10^{-5} m^{-1} (with a range of 8.0×10^{-6} m^{-1} to 4.0×10^{-5} m^{-1}). A vertical upward hydraulic gradient equal to 1 m/m is assumed. At this stage, the hydraulic head distribution in the reference case is assumed at equilibrium relative to the hydraulic heads in the overlying and underlying formations with higher permeability. However, an anomalous head distribution within the host formation is expected since this phenomenon is typically observed in several argillaceous formations. For example, hydraulic head measurements in the Callovo-Oxfordian argillite at Bure, France, revealed overpressures between 20 to 40 meters water column equivalent relative to the upper and lower surrounding formations (ANDRA 2005). Similarly, the Opalinus Clay near Benken, Switzerland (NAGRA 2002) is overpressurized. In the U.S., the Middle Ordovician Trenton Group in the Michigan Basin is significantly underpressurized (Beauheim et al. 2014). Hydraulic head data for the Pierre Shale in South Dakota also provide evidence of underpressurized conditions with head values as much as 125 m below hydrostatic level (Neuzil, 1993). As shown recently by Bianchi et al. (2014), pressure anomalies within the host argillaceous formation can have an impact on radionuclide transport from the repository toward the biosphere. In particular, inward flow induced by negative pressure anomalies in the host rock can delay radionuclide transport therefore enhancing the performance of the geological barrier to confine radioactive waste in a deep subsurface shale repository (Neuzil, 2013). Conversely, local high gradients, owing to the presence of overpressures, can speed up the transport process. Pressure conditions within the host rock will be thoroughly assessed once more specific details of the argillaceous host formation become available through site characterization.

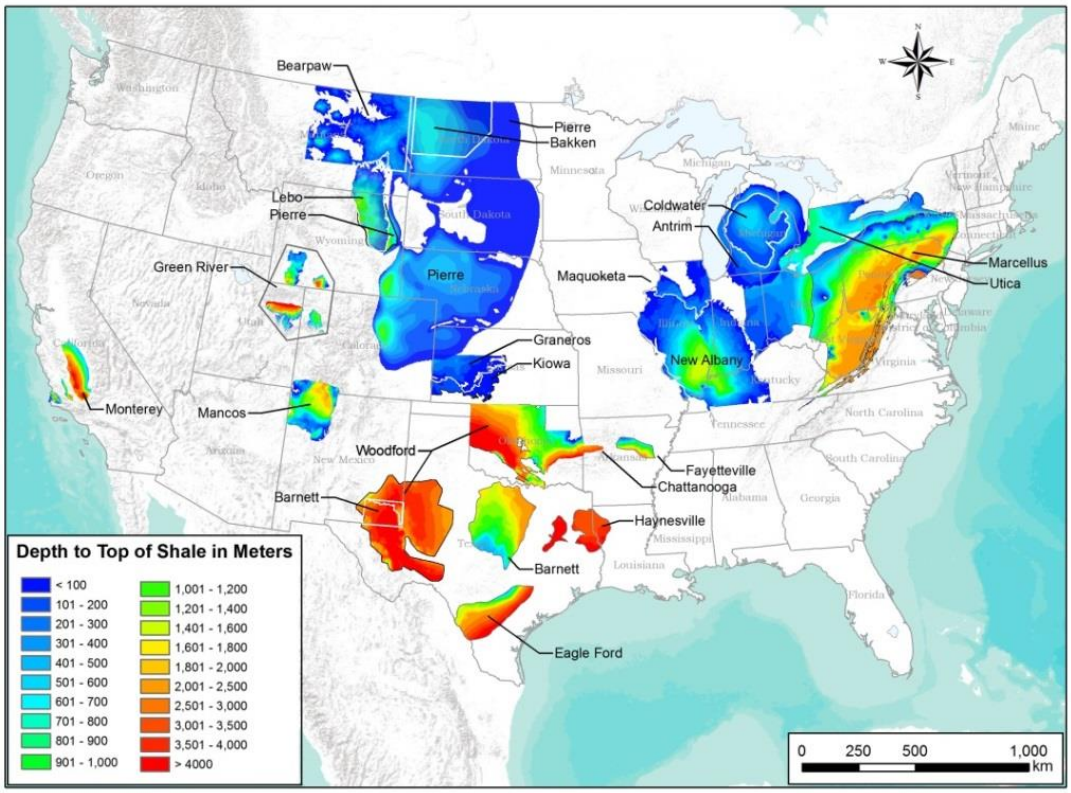

Figure 8. Distribution of the clay-rich formations in the USA along with depth to top mapping (updated from Perry (2014a))

Table 14. Properties and distribution of the clay-rich formations in the USA (adapted from Gonzales and Johnson (1984) and other studies)

Property	Value	Formation	Location	Source
Total porosity (-)	0.05 to 0.18	Huron member Ohio Shale	Ohio-Kentucky	Soeder (1988)
	0.02 to 0.11	Ordovician	Ontario	Sykes et al. (2008)
	0.134	Pierre Shale	South Dakota	Olgaard et al. (1995)
	0.35 to 0.45	Pierre Shale	Saskatchewan	Smith et al. (2013)
	0.02 to 0.01	Trenton Group	Ontario	Gartner Lee Limited (2008)
Accessible porosity (-)	0.07 to 0.08	Wilcox	Louisiana	Kwon et al. (2004)
	0.04 to 0.1	Pierre Shale	South Dakota	Bredehoeft et al. (1983)
Hydraulic conductivity ($m\ s^{-1}$)	8e-12 to 5.2e-11	Ordovician	Ontario	Sykes et al. (2008)
	4e-12 to 1e-11	Pierre Shale	South Dakota	Bredehoeft et al. (1983)
	1e-14 to 1e-13	Pierre Shale	South Dakota	Neuzil (1993)
	2E-12	Pierre Shale	South Dakota	Neuzil (1986)
	2e-16 to 2e-10	Trenton Group	Ontario	Beauheim et al. (2014), Clark et al. (2013)
	8e-13 to 2e-12	Trenton Group	Ontario	Gartner Lee Limited (2008)
	7.9e-14 to 8.2e-11	Huron member Ohio Shale	Ohio-Kentucky	Soeder (1988)
	5.8e-11 to 1.9e-10	Marcellus	West Virginia	Soeder (1988)
	3e-15 to 3e-12	Wilcox	Louisiana	Kwon et al. (2004)
Specific storativity (m^{-1})	1.3e-6 to 1.2e-4	Ordovician	Ontario	Sykes et al. (2008)
	8.0e-7	Pierre Shale	South Dakota	Neuzil (1986)
	2.69e-5 to 3.60e-5	Pierre Shale	South Dakota	Bredehoeft et al. (1983)
	1.1e-5 to 2.4 e-5	Pierre Shale	Saskatchewan	Smith et al. (2013)
	1.2e-6 to 1.3e-6	Trenton Group	Ontario	Gartner Lee Limited (2008)

3.4.4 Excavated Disturbed Zone (EDZ)

A major concern in post-closure safety evaluations of the repository system is the potential for hydro-mechanical perturbations caused by excavation. These perturbations are found within the excavation damaged zone (EDZ) around the repository tunnels and access shaft. The EDZ is primarily caused by redistribution of *in situ* stresses and rearrangement of rock structures (Tsang et al. 2012). Field investigations conducted at underground laboratories such as at Mont Terri (Switzerland) and Bure (France) have shown that the permeability of the EDZ can be one or more orders of magnitude higher than the unaltered argillaceous rock. This is primarily caused by the higher concentration of macro- and micro-fractures. For these conditions, the EDZ could then act as a preferential flow path for advective transport and thereby speed up radionuclide migration toward the biosphere. The EZD properties and their evolution over time have been analyzed in laboratory and field studies (Bossart et al. 2004; Baechler et al. 2011; Armand et al. 2013). These investigations suggest that a partial or complete self-sealing of fractures due to clay swelling and creep within the EDZ is possible after a certain amount of time. The self-sealing process can potentially decrease the EDZ permeability over time, which may eventually return to the values of the unaltered rock. However, the mechanisms and the time evolution of self-healing is still a matter of research, and at this point models simply assign constant permeability values for base-case scenarios. For the reference case described in this report, we followed the same simplified approach: the permeability in the EDZ is assumed constant in time with a value equal to 1×10^{-18} m^2. This value, which is 20 times higher than the unaltered argillaceous rock permeability, was used in previous performance assessment studies (ANDRA 2005; Genty et al. 2011), and more recently by Bianchi et al. (2013; 2014) The thicknesses of the EDZ around horizontal tunnels and the shaft in the reference case is assumed equal to 1.2 times the radius of the corresponding excavation (with a range of 0.8 to 1.6). This value is comparable to observations conducted at the Mont Terri in the Opalinus Clay (Bossart et al. 2004). The same thickness was also used in the simulations presented in Bianchi et al. (2013; 2014).

3.4.5 Radionuclide Transport Mechanisms in the Host Formation and EDZ

Bianchi et al. (2013; 2014) conducted numerical simulations of groundwater flow and radionuclide transport to understand factors controlling transport behavior within a generic HLW repository in an argillaceous formation. These simulations are based on simplified 2-D representation of the repository, including one horizontal emplacement tunnel, a vertical shaft, and cross section of the argillaceous host formation. Several scenarios were simulated to study the influence of several factors on transport behavior, including the hydraulic gradient in the host rock, the presence of pressure anomalies, the thickness of the EDZ, and its hydraulic properties. In their base case, these authors considered a vertical upward hydraulic gradient (1 m/m) resulting from imposing specified heads as boundary conditions at the top and bottom of the argillaceous formation, as well as hydrogeological parameters with values analogous to those presented for this reference case. The simulated flow field and the spatial distribution of the Peclet number (*Pe*) for the base-case scenario is considered in Bianchi et al. (2013; 2014), as shown in Figure 9.

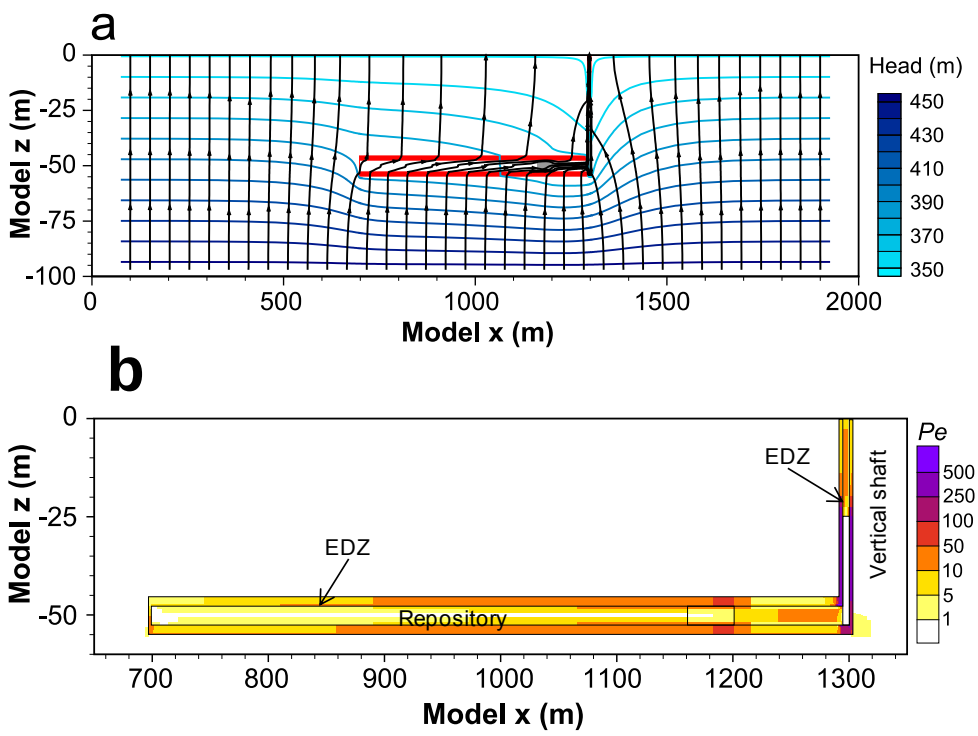

Figure 9. Simulated steady-state flow field (a) and Pe spatial distribution (b) in the base case scenario considered in Bianchi et al. (2013, 2014). The EZD is shown in red (a). (Modified from Bianchi et al. 2014).

The Peclet number was used to investigate whether and where transport in the simulated flow fields is driven by advection ($Pe > 10$) or molecular diffusion ($Pe < 1$). Results show that radionuclide transport is driven by molecular diffusion in the argillaceous formation and (mostly) by advection in the EDZ. Diffusion is predominant in the emplacement tunnel and in the bentonite seals, while advective transport is prevalent in the more permeable tunnels backfill. In most of the simulated scenarios, the EDZ plays a major role as a preferential flow path for radionuclide transport. When the EDZ is not taken into account, transport is dominated by molecular diffusion in almost all the components of the simulated domain. On the other hand, in these simulations, the host rock, EDZ, and EBS are assumed to be fully saturated, and therefore these results have to be considered conservative with respect to the safety performance of the repository system. In particular, processes such as the self-sealing of the EDZ and consolidation of clay components in the EBS, may prevent preferential flow along the EDZ (Hansen et al. 2010). Moreover, advective transport along the EDZ and the access shaft may be insignificant due to a limited amount of water inflow from the argillite formation (Blümling et al., 2007; Hansen et al. 2010). All these aspects need to be further investigated after a site is identified. At this stage, the presented reference case considers diffusive transport in the argillaceous formation. This scenario corresponds to the "Nominal Scenario, Pathway 2" proposed by Hansen et al. (2010), in which diffusion is the prevalent mechanism moving radionuclides upward from the repository, through the NS, to a shallow aquifer from which they are pumped to the

biosphere. In this scenario, radionuclide transport is expected to be delayed by the reducing environment in the host rock and by sorption. Radioactive decay is also taken into account.

3.4.6 Chemical Properties

Chemical properties including mineralogical composition, water chemistry, diffusion, and sorption coefficients are critical for evaluating the migration of radionuclides in host rocks. Some reference values of these properties are given below. More detailed information can be found in the sources given below, particularly in the case of mineralogical characterization and chemisorption properties.

3.4.6.1 Mineralogical Composition

As previously mentioned, some shales and argillites that are candidate host rocks for HLW disposal have been studied extensively, such as the Opalinus Clay at Mont Terri (Switzerland) (Thury 2002). Table 15 lists the mineralogical composition of Opalinus Clay. The measured mineralogical composition of Opalinus Clay varies remarkably, probably because of the spatial heterogeneity in mineralogical composition and the analytical method used. For example, Bossart (2011) summarized measured mineralogical composition from Waber et al. (1998), De Canniere (1997), Thury and Bossart (1999), and NAGRA (2003), and reported the mixed layer illite/smectite ranging from 5% to 11%. However, Lauber et al. (2000) reported the illite/smectite mixed layer ranging from 14% to 22%. The mineralogical compositions listed in Table 15 are the average of the Bossart (2011) and Lauber et al. (2000).

Table 15. Mineral volume fraction (dimensionless, ratio of the volume for a mineral to the total volume of medium) of Opalinus Clay (Bossart 2011; Lauber et al. 2000).

Mineral	Opalinus Clay
Calcite	0.093
Dolomite	0.050
Illite	0.273
Kaolinite	0.186
Smectite	0.035
Chlorite	0.076
Quartz	0.111
K-Feldspar	0.015
Siderite	0.020
Ankerite	0.045

3.4.6.2 Pore-water Chemistry

Pore-water chemistry in shale formations can be variable and hard to obtain, due to their low volumes and difficulties in extraction from rock. Most pore waters compositions found in the literature are extracted from shale samples found in weathered zones (e.g., Cody shale), groundwater from seeps and springs (e.g., Mancos shale), and production waters from oil field wells (e.g., Pierre shale). Water chemistries should preferably be limited to careful extractions from rock samples obtained at repository depths. Moreover, samples should be well characterized and obtained at various formations depths to resolve chemical variability (both major elements and isotopes) and the extent of or lack of mixing with shallower groundwaters. Studies by Fernández et al. (2007) and Turrero et al. (2006) provide fairly comprehensive chemical characterizations of pore-waters for the Opalinus Clay (Switzerland) and an Oligocene-Miocene Clay from Spain. Very few sources of pore water chemistry data relevant to clay formations in the USA can be found. However, the majority of deep-seated pore water chemistries tend to be briny with Na-Ca-Cl as the main components but with K and SO_4 in relatively lower concentrations depending on the geologic setting. The data given by Fernández et al. (2007) and Turrero et al. (2006) will be used to constrain nominal pore water chemistries in the reference case. Perry (2014b) reported Cl concentrations for a wide array of shale/argillite pore waters showing an increasing concentration trend with depth. Such trend resembles that of seawater evaporation; however, a complete analysis of aqueous species (cations and anions) is necessary to accurately assess pore-water compositional trends. Fernandez et al. (2007) presented another study that provides data on the pore-water composition of the Opalinus Clay. These authors conducted five onsite water sampling campaigns from borehole BDI-B1. The average concentrations of these five campaigns are shown in Table 16.

Another important aspect of deep-seated groundwaters to a nuclear waste repository is the redox state of the natural barrier pore waters and the EBS. Jové Colón et al. (2010) discusses the importance of redox conditions to nuclear waste disposal from the standpoint of natural analogs and the EBS. Groundwater interaction with metallic barrier components in the EBS leads to consumption of available O_2. Corrosion of iron present in the form of barrier materials could exert a strong influence on $H_{2(g)}$ partial pressures and thus dissolved $O_{2(aq)}$ in solutions contacting a corroding waste canister. Figure 10 (Jové Colón et al. 2010) shows the redox stability of iron-bearing phases as function of pH for common corrosion products of potential metallic barrier materials such as steels. The strong agreement depicted by the Eh-pH relations for the ferric-ferrous iron system and measured Eh-pH reported for the Pu solubility experiments (Rai et al. 2001 and Neck et al. 2007) suggests overall solution redox could be controlled by equilibria with phase like green rust. The figure also shows the solution redox of subsurface waters for three types of host-rock environments: salt, clay rock, and granite. The redox relations for solutions sampled in these environments indicate a consistent reduced state which is a common trend for deep subsurface waters. Such a reduced state in the pore waters is key in mitigating radionuclide transport by lowering solubilities. Moreover, the equilibria of reduced solutions with potential corrosion products could also serve as an enhanced redox barrier to further reduce radionuclide mobility. The trend depicted in Figure 10 indicates a close similarity in Eh-pH relations for the three host-rock settings where the redox state of these waters falls within the "green rust" stability field. Such relation will be used to bound Eh-pH in the adopted pore water chemistries.

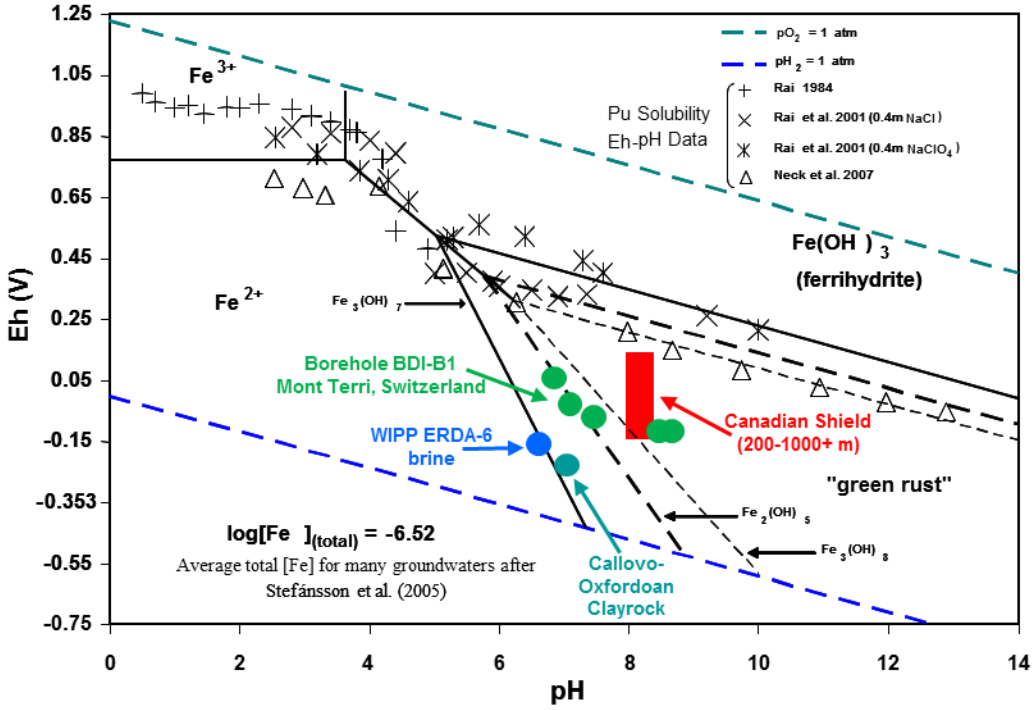

Figure 10. Plot of Eh versus pH relationships for the iron system with relevance to solution redox control for a corroding metallic barrier material (see text). Diagram was constructed using thermodynamic data from Bourrie et al, (1999, 2004) for green rust phases, YMP Pitzer thermodynamic database (Mariner, 2007) for ferrihydrite (Fe(OH)3(s)), and ancillary data used obtained from the YMP thermodynamic database (Wolery and Jové-Colón, 2007), Robie et al. (1979), Stefansson et al. (2005), and Parker and Khodakovskii (1995). The Eh-pH data depicted in the diagram for the Canadian Shield waters, WIPP ERDA-6 brine, Callovo-Oxfordian clayrock, and Mont Terri Opalinus Clay (borehole BDI-B1) are from Gascoyne et al. (2004), D'Appolonia Consulting Engineers (1983), Gaucher et al. (2009), and Turrero et al. (2006), respectively.

Table 16. Average pore water composition of Opalinus Clay.

Opalinus Clay – Average Concentrations (Fernandez et al., 2007)	
pH	7.40
Eh(V)	0.268
Cl (mol/L)	3.32E-01
SO_4^{-2} (mol/L)	1.86E-02
HCO_3^- (mol/L)	5.18E-03
Ca^{+2} (mol/L)	2.26E-02
Mg^{+2} (mol/L)	2.09E-02
Na^+ (mol/L)	2.76E-01
K^+ (mol/L)	2.16E-03
Fe^{+2} (mol/L)	3.46E-06
SiO_2(aq) (mol/L)	1.10E-04
AlO_2^- (mol/L)	3.89E-08
F^- (mol/L)	1.68E-05
Br^- (mol/L)	3.2E-04
O_2(aq) (mol/L)	1.07E-41
UO_2^{+2} (mol/L)	1E-10

3.4.7 Diffusion Coefficients in the Argillaceous Host Rock

Diffusive transport of sorbing radionuclides in the reference argillaceous formation is defined by Fick's second law:

$$\varepsilon R \frac{\partial C}{\partial t} = \nabla \cdot (D_e \nabla C) \tag{2}$$

where C is concentration, t is the time, ε is the effective porosity, D_e is effective diffusion coefficient and R is retardation factor.

The effective diffusion coefficient takes into account the fact that in porous media the diffusion process is slower than in free water due to longer diffusive paths. D_e can then be described by the following equation:

$$D_e = \varepsilon D_p = \varepsilon \tau D_w \quad (3)$$

where D_p is the pore-water diffusion coefficient, τ is a geometrical factor representing the tortuosity of the diffusive paths in the porous medium, and D_w is the molecular diffusion coefficient in water. A uniform value equal to 0.1 is specified for tortuosity in the reference case.

Previous studies collected and reported datasets of diffusive parameters from argillaceous formations (e.g., Aertsens et al. 2004; van Loon et al. 2004a and 2004b; Descostes et al. 2008; Appelo et al. 2007). A summary of the diffusion parameters collected in clay-rock formations available in the literature was presented by Zheng et al. (2011b). For example, the D_e of ^{22}Na and ^{85}Sr in the Opalinus Clay range from 1.20×10^{-11} m^2/s to 6.0×10^{-11} m^2/s for ^{22}Na and from 1.4×10^{-11} m^2/s to 2.4×10^{-11} m^2/s for ^{85}Sr. Measurements of D_e of iodide in the Boom Clay along a depth interval of about 100 m range between 9.1×10^{-11} m^2/s and 5.2×10^{-10} m^2/s, with an average value of 1.6×10^{-10} m^2/s and a standard deviation of 9.0×10^{-11} m^2/s (Huysmans and Dassargues 2006). Laboratory scale experiments also showed that D_e is anisotropic; Samper et al. (2008), for instance, found that the anisotropy ratio e of D_e for HTO in a cylindrical rock sample of Callovo-Oxfordian argillite is between 0.26 and 0.56.

For the reference case described in this report, the water diffusion coefficient of generic radionuclide is assumed to be equal to 1.08×10^{-9} m^2/s (Bianchi et al. 2013; 2014), and with radionuclide-specific effects (e.g., due to size and charge) not considered at this stage. This value is similar to the diffusion coefficient of iodine, which is abundant in radioactive waste. Since iodine is also highly mobile in the solute phase, the assumed value is a conservative choice with respect to the safety performance of the repository system. Compound-specific diffusion coefficients will be considered in future stages of the repository performance assessment. Part II, Section 6) of this report describes reactive diffusion modeling for clay and clay rock. This model adopts different approaches from Fick's law that are based on ion diffusion through clay.

3.4.7.1 Sorption Data

Modeling sorption via linear sorption isotherm, i.e. distribution coefficient (K_d) is widely used in PA-level models. Because K_d depends not only on the properties of the adsorbate (i.e., radionuclides) but also adsorbents (i.e. host rock), it varies a great deal and is affected by many factors. For example, the plutonium K_d value was correlated to parameters specifying the aqueous chemical conditions and solid characteristics, using the data from Glover et al. (1976). This data set provides sorption data and a quantitative specification of the mineral phase and solution chemistry associated with each sorption experiment. The correlation indicates that the main controls on sorption are the soluble (or dissolved) carbon content (DC) of the clay, the inorganic carbonate content (i.e., the $CaCO_3$ content) (IC), pH, and the solution electrical conductivity (EC). Such correlations can be useful as guidance on potential factors controlling radionuclide sorption. McKinley and Scholits (1993) compiled and compared different sorption databases for argillites. More recently, Miller and Wang (2012) also reviewed sorption coefficients for some argillites. The information compiled by these authors on K_d data will be important to determine the adequate bounds and ranges when developing distributions to represent these data. Part IV of this report documents the advances of thermodynamic database developments including that applicable to sorption models (ion exchange and surface complexation) for nuclear waste repository conditions.

4. Biosphere

The biosphere representation is usually dependent on regulatory guidance and specific scenarios for potential pathways towards near-surface receptors of contaminants (e.g., shallow aquifers, well water). The conceptualization of the biosphere is typically specified by regulation and can vary between different national radioactive waste disposal programs. For the reference case, the biosphere conceptualization is based on the International Atomic Energy Agency (IAEA) BIOMASS Example Reference Biosphere 1B (ERB 1B) dose model (IAEA 2003, Sections A.3.2 and C.2.6.1). The ERB 1B dose model assumes that the receptor is an individual adult who obtains drinking water from a pumping well drilled into the aquifer above the argillaceous host rock. Dissolved radionuclide concentrations in the aquifer are converted to estimates of annual dose to the receptor (dose from each radionuclide and total dose) using ERB 1B dose model parameters, which include the well pumping rate, the water consumption rate of the receptor, and radionuclide-specific dose conversion factors. Determination of dose model parameter values depends on the characteristics of the biosphere (e.g., climate) and the habits of the population (receptor) in that biosphere. Dose model parameters are not currently specified, but will be determined as the PA model matures.

5. Concluding Remarks

A generic argillite repository reference case is presented in this part of the report. In the past several years, under the auspices of the UFDC, various kinds of models have been developed for repositories in argillaceous rock to demonstrate the modeling capability, understand the spatial and temporal alteration in the EBS bentonite and host rock, and evaluate different disposal scenarios. The establishment of a reference case requires the description of waste inventory, waste form, waste package, repository layout, properties of EBS backfill and host rock, and biosphere. Some of these parameters needed to represent repository components such as waste inventory, waste form, and waste package dimensions (12-PWR only) are consistent with those adopted for disposal in salt by Freeze et al. (2013). The description of the reference case for shale focuses on relevant processes and properties of EBS bentonite and host rock, it proposes a repository layout for 12-PWR and 32-PWR waste packages, and provides a brief description of the biosphere. The latter is specific to certain parameters to be defined in the evolving PA model and characteristics of the site hydrogeology along with receptor consumption rates.

Some processes, including heat transport by advection and conduction, water flow by advection, vapor flow by diffusion, mechanical changes, and chemical reactions are known to be important for the EBS and host rock. Recent coupled THM and THMC simulations of these subsystems (Rutqvist et al. 2014a, 2014b; Zheng et al. 2014a, 2014b, 2014c) are very helpful in evaluating the importance of HMech and MC couplings. The HMech coupling could be important because of its relevance to the time needed to fully saturate the EBS bentonite. The tentative conclusion from current THMC models is that MC couplings need not necessarily be directly included in the PA model. However, the variation in clay swelling capacity resulting from THMC couplings in the EBS should be included for uncertainty analysis in the PA model. Moreover, when site-specific data are available, coupled THMC models are warranted before determining whether to neglect certain couplings. Figure 11 shows a stylized chronological evolution of a coupled THMC processes in a shale disposal environment (Jové Colón et al. 2013). Such a schematic diagram or “whiteboard” approach allows for a high-level evaluation of the importance of coupled processes like, for example, HMech and MC throughout the repository timeline. The precise timing of these coupled processes is a gross estimate based on the expected repository

thermal behavior and the projected impact on other phenomena. Thermally-driven processes such as moisture transport (desiccation) affects chemical processes like water uptake from clay and thus would impact swelling. Then most of the clay swelling "performance" would be more important during the post thermal period (after ~1000 years) where relative humidity is high. Leveraging on both modeling and experimental studies would provide enhanced confidence on delineating the extent of these processes to inform decisions on exclusion or inclusion into PA models. Integration of information obtained from other UFDC activities (e.g., clay interaction and thermo-mechanical experiments) is key to the evaluation of thermal limits in the EBS and the natural barrier. Such thermal constrains will determine the various repository layout options through thermal evaluation of the proposed reference case for shale.

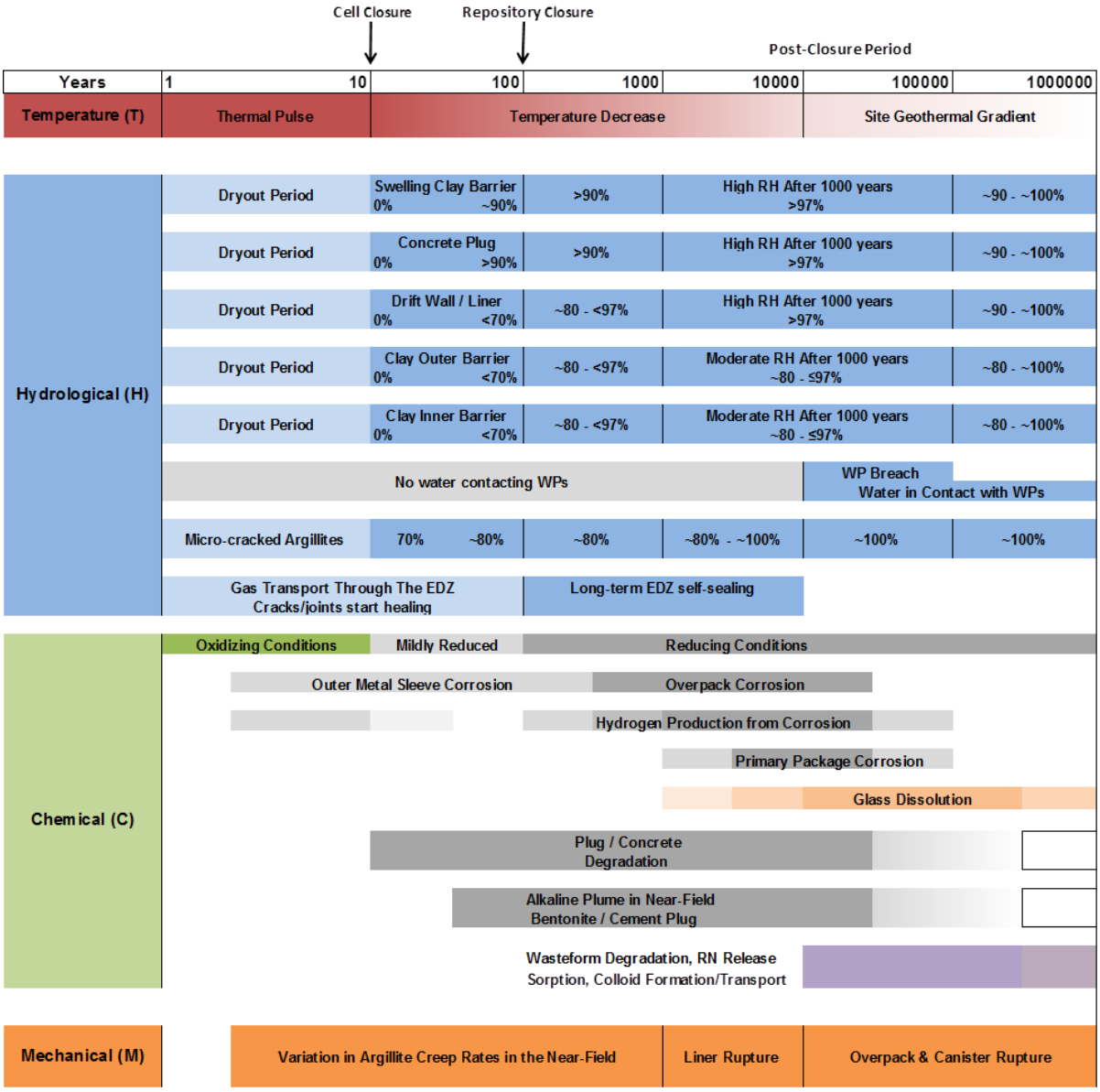

Figure 11. Chronological evolution of coupled processes in a shale/argillite repository.

6. Plans for FY15

The main goals for FY15 related to the reference case for disposal in shale are:

- Implementation of the shale reference case. This will be a concerted effort between SNL and LBNL in which strategies for reference case implementation into GDSA framework will be evaluated.
- THMC analysis will be conducted in support of reference case implementation activity. This may also include the thermodynamic analysis of clay-fluid interaction to evaluate the extent of MC effects.
- Expand the 3-D FEM thermal model to a multi-drift and multi-waste-package scenario using the Albany platform suitable for large-scale parallel computation. Such model would be more accurate to capture peak temperatures and the effects of geometric asymmetries in the EBS configuration of a DPC, for example.

7. References

Aertsens, M., I. Wemaere and L. Wouters (2004). Spatial variability of transport parameters in the Boom Clay. Applied Clay Science 26: 37–45.

Allard, B. (1985). Radionuclide sorption on concrete. NAGRA (Natl. Coop. Disposal Radioactive Waste), Baden. Nagra NTB 85-21. 13 pp.

ANDRA (2005). "Dossier 2005 Argile", Tome: Evaluation of the feasibility of a geological repository in an argillaceous formation. Andra Report Series.

Appelo, C. A. J. and P. Wersin (2007). Multicomponent diffusion modeling in clay systems with application to the diffusion of tritium, iodide, and sodium in opalinus clay. Environmental Science & Technology 41: 5002–5007.

Armand, G., A. Noiret, J. Zghondi, and D.M. Seyedi. (2013). Short- and long-term behaviors of drifts in the Callovo-Oxfordian claystone at the Meuse/Haute-Marne Underground Research Laboratory. Journal of Rock Mechanics and Geotechnical Engineering 5, no. 3: 221-230.

Baechler, S., J.M. Lavanchy, G. Armand, M. Cruchaudet. (2011). Characterisation of the hydraulic properties within the EDZ around drifts at level -490 m of the Meuse/Haute-Marne URL: a methodology for consistent interpretation of hydraulic tests. Physics and Chemistry of the Earth, no. 17: 1922-1931.

Beauheim R. L., R.M. Roberts, J.D. Avis (2014). Hydraulic testing of low-permeability Silurian and Ordovician strata, Michigan Basin, southwestern Ontario, Journal of Hydrology, Volume 509, 13 Pages 163-178.

Bernot P. (2005). Dissolved concentration limits for radioactive elements. ANL-WIS-MD-000010. July 2005.

Bianchi, M., H.-H., Liu, and J. T. Birkholzer. (2013). Diffusion Modeling in a Clay Repository: FY13 Report. . FCRD-UFD-2013-000228 Report, Lawrence Berkeley National Laboratory, Berkeley, USA.

Bianchi, M., H.-H., Liu, and J. T. Birkholzer. (2014). Radionuclide Transport Behavior in a Generic Geological Radioactive Waste Repository. Groundwater. doi: 10.1111/gwat.12171.

Blümling, P., F. Bernier, P. Lebon, and C.D. Martin. (2007). The excavation damaged zone in clay formations: Time-dependent behaviour and influence on performance assessment. Physics and Chemistry of the Earth 32: 588–599.

Boggs, S., 2006, Principles of Sedimentology and Stratigraphy, Pearson Prentice Hall.

Börgesson, L. and J. Hernelind. (2005). Hydraulic bentonite/rock interactions in FEBEX experiment. In: Advances in Understanding Engineered Clay Barriers (E.E. Alonso and A. Ledesma, eds), pp. 391-412. Taylor & Francis Group, London, ISBN 04 1536 544 9.

Börgesson, L., O. Karnland, L. E. Johannesson and D. Gunnarsson. (2006). Current Status of SKB's Research, Development and Demonstration Programme on Buffer, Backfill and Seals. A report prepared by SKB for United Kingdom Nirex Ltd., SKB IC-122.

Bossart P. (2011). Characteristics of the Opalinus Clay at Mont Terri, http://www.mont-terri.ch/internet/mont-terri/en/home/geology/key_characteristics.html

Bossart, P., T. Trick, P.M. Meierand, and J.-C. Mayor. (2004). Structural and hydrogeological Characterization of the excavation-disturbed zone in the Opalinus Clay, Mont Terri Project, Switzerland. Applied Clay Science 26, no. 1-4: 429– 448.

Bourrie, G., Trolard, F., Genin, J.M.R., Jaffrezic, A., Maitre, V., and Abdelmoula M. (1999). Iron control by equilibria between hydroxy-Green Rusts and solutions in hydromorphic soils.‖ Geochimica Cosmochimica Acta, 63(19-20), 3417-3427.

Bourrie, G., F. Trolard, P. Refait, and F. Feder, A solid-solution model for Fe(II)-Fe(III)-Mg(II) green rusts and fougerite and estimation of their Gibbs free energies of formation (2004) Clays and Clay Minerals, 52(3): p. 382-394.

Brandberg, F. and K. Skagius. (1991). Porosity, sorption and diffusivity data complied for the SKB 91 study. SKB technical report 91-16.

Bradbury, M.H. and B. Baeyens. (2002). Porewater chemistry in compacted re-saturated MX-80 bentonite: physico-chemical characterisation and geochemical modelling. PSI Bericht 02–10, Villigen PSI and NTB 01–08, Nagra, Wettingen, Switzerland.

Bradbury, M. H. and B. Baeyens. (2003a). Porewater chemistry in compacted re-saturated MX-80 bentonite. Journal of Contaminant Hydrology 61(1–4): 329-338.

Bradbury M. and B. Baeyens. (2003b). Near Field Sorption Data Bases for Compacted MX-80 Bentonite for Performance Assessment of a High- Level Radioactive Waste Repository in Opalinus Clay Host Rock. PSI Bericht Nr. 03-07 August 2003 ISSIN 1019-0643.

Bredehoeft, J. D., C. E. Neuzil, and P. C. D. Milly. (1983). Regional flow in the Dakota Aquifer: A study of the role of confining layers, U.S. Geol. Surv. Water Supply Pap., 2237, 1-45.

Buhmann. D., A. Nies and R. Storck. (1991). Systemanalyse Mischkonzept, Technischer Anhang 7. GSF (Ges. Strahlen-/Unweltforsch.), Braunschweig, KWA No. 5702A, 200 pp.

Buck, E. C., J. L. Jerden and R. S. Wittman. (2013). Coupling the Mixed Potential and Radiolysis Models for Used Fuel Degradation, FCRD-UFD-2013-000290, PNNL Report PNNL-22701, 30 pp.

Caporuscio F.A., Cheshire, M. C., McCarney, M. (2012). Bentonite Clay Evolution at Elevated Pressures and Temperatures: An experimental study for generic nuclear repositories, 2012 AGU fall meeting.

Carter, J. T., A. J. Luptak, J. Gastelum, C. Stockman, and A. Miller 2012. Fuel Cycle Potential Waste Inventory for Disposition. FCRD-USED-2010-000031, Rev. 5. U.S. Department of Energy, Office of Used Nuclear Fuel Disposition, Washington, DC.

Cheshire, M. C., Caporuscio, F. A., Jové-Colon, C. and McCarney, M. K. (2013). Alteration of clinoptilolite into high-silica analcime within a bentonite barrier system under used nuclear fuel repository conditions. International High-Level Radioactive Waste Management (2013 IHLRWM). Albuquerque, NM.

Cheshire, M., F. Caporuscio, M. Rearick, C. Jové Colón and M. K. McCarney (2014). Bentonite evolution at elevated pressures and temperatures: an experimental study for generic nuclear repository designs. American Mineralogist: in press.

Carter, J. T., A. J. Luptak, J. Gastelum, C. Stockman, and A. Miller (2012). Fuel Cycle Potential Waste Inventory for Disposition. FCRD-USED-2010-000031, Rev. 5. U.S. Department of Energy, Office of Used Nuclear Fuel Disposition, Washington, DC.

Clayton, D., G. Freeze, T. Hadgu, E. Hardin, J. Lee, J. Prouty, R. Rogers, W.M. Nutt, J. Birkholzer, H.H. Liu, L. Zheng, and S. Chu (2011). Generic Disposal System Modeling – Fiscal Year 2011 Progress Report. FCRD-USED-2011-000184, SAND2011-5828P. U.S. Department of Energy, Office of Nuclear Energy, Used Fuel Disposition Campaign, Washington, DC.

Croisé, J., L. Schlickenrieder, P. Marschall, J.Y. Boisson, P. Vogel, and S. Yamamoto. (2004). Hydrogeological investigations in a low permeability claystone formation: the Mont Terri Rock Laboratory. Physics and Chemistry of the Earth Parts A/B/C 29, no. 1:3-15.

Clark I.D., T. Al, M. Jensen, L. Kennell, M. Mazurek, R. Mohapatra, K.G. Ravent (2013). Paleozoic-age brine and authigenic helium preserved in an Ordovician shale aquiclude. Geology, 41, pp. 951–954.

Curtis, E. and Wersin, P. (2002). Assessment of porewater chemistry in the bentonite buffer for the Swiss SF/HLW repository. PSI Bericht, Paul Scherrer Institut, Villigen, Nagra Technical Report NTB 02-09, Nagra, Wettingen, Switzerland.

Descostes, M., V. Blin, F. Bazer-Bachi, P. Meier, B. Grenut, J. Radwan, M.L. Schlegel, S. Buschaert, D. Coelho E. and Tevissen (2008). Diffusion of anionic species in Callovo-Oxfordian argillites and Oxfordian limestones (Meuse/Haute–Marne, France). Applied Geochemistry 23: 655–677.

D'Appolonia Consulting Engineers, Inc. (1983). Brine reservoirs in the Castile Formation Waste Isolation Pilot Plant (WIPP) project, Southeastern New Mexico.‖ Westinghouse Electric Corporation – Waste Isolation Division Carlsbad, NM., report TME 3153.

De Canniere, P. (1997). Measurements of Eh on slurries of Opalinus Clay, Mont Terri. SCK•CEN. Mont Terri Project, Technical Note TN 96-32 (internal unpublished report).

De Windt, L., F. Marsal, E. Tinseau and D. Pellegrini (2008). Reactive transport modeling of geochemical interactions at a concrete/argillite interface, Tournemire site (France). Physics and Chemistry of the Earth, Parts A/B/C 33, Supplement 1(0): S295-S305.

Einstein, H., (2000). Tunnels in Opalinus Clayshale—a review of case histories and new developments. Tunnelling and Underground Space Technology, 15(1): p. 13-29.

ENRESA (2000). Full-scale engineered barriers experiment for a deep geological repository in crystalline host rock FEBEX Project, European Commission**:** 403.

Ewart. F.T.. Pugh, S.Y.R., Wisbey. S.J. and Woodwark. D.R.. (1988). Chemical and microbiological effects in the near field - Current status. Nirex Ltd., Harwell, NSS/G103. 32 pp.

Fernández, A., Cuevas, J., Rivas, P., (2001). Pore-water chemistry of the FEBEX bentonite. Mat. Res. Soc. Symp. Proc. 663, 573–588.

Fernández, A. M., B. Baeyens, M. Bradbury and P. Rivas (2004). Analysis of the porewater chemical composition of a Spanish compacted bentonite used in an engineered barrier. Physics and Chemistry of the Earth, Parts A/B/C 29(1): 105-118.

Fernández, A. M., M. Turrero, D. Sánchez, A. Yllera, A. Melón, M. Sánchez, J. Peña, A. Garralón, P. Rivas and P. Bossart (2007). On site measurements of the redox and carbonate system parameters in the low-permeability Opalinus Clay formation at the Mont Terri Rock Laboratory. Physics and Chemistry of the Earth, Parts A/B/C 32(1): 181-195.

Freeze, G., M. Voegele, P. Vaughn, J. Prouty, W.M. Nutt, E. Hardin, and S.D. Sevougian (2013). Generic Deep Geologic Disposal Safety Case. FCRD-UFD-2012-000146 Rev. 1, SAND2013-0974P. Sandia National Laboratories, Albuquerque, NM.

Gaboreau, S., C. Lerouge, S. Dewonck, Y. Linard, X. Bourbon, C. Fialips, A. Mazurier, D. Prêt, D. Borschneck and V. Montouillout (2012). In-situ interaction of cement paste and shotcrete with claystones in a deep disposal context. American Journal of Science 312(3): 314-356.

García-Gutiérrez, M., T. Missana, M. Mingarro, J. Samper, Z. Dai and J. Molinero (2001). Solute transport properties of compacted Ca-bentonite used in FEBEX project. Journal of Contaminant Hydrology 47(2–4): 127-137.

Gartner Lee Limited (2008). Phase I Regional Geology, Southern Ontario. OPG's Deep Geologic Repository for Low & Intermediate Level Waste, Supporting Techinical Report. GLL 61-123; OPG 00216-REP-01300-00007-R00.

Gascoyne, M. (2004). Hydrogeochemistry, groundwater ages and sources of salts in a granitic batholith on the Canadian Shield, southeastern Manitoba. Applied Geochemistry, 19, 519–560.

Gaucher, E. C. and P. Blanc 2006. Cement/clay interactions – A review: Experiments, natural analogues, and modeling. Waste Management 26(7): 776-788.

Gaucher, E.C., Tournassat, C., Pearson, F.J., Blanc, P., Crouzet, C., Lerouge, C., and Altmann, S. (2009). A robust model for pore-water chemistry of clayrock, Geochimica et Cosmochimica Acta, 73, 6470–6487.

Genty, A., C. Le Potier, and S. Gounand. (2011). Analysis of the Excavation Deviations Impact on Geological Radioactive Waste Repository Performance. Geotechnical and Geological Engineering 29, no. 4: 537-554.

Glover P. A., Miner F. J. and Polzer W. O. (1976). Plutonium and Americium behavior in the soil/water environment. I. sorption of Plutonium and Americium by soils. In Proceedings of Actinide-Sediment Reactions Working Meeting, Seattle, Washington. pp. 225-254, BNWL-2117, Battelle Pacific Northwest Laboratories, Richland, Washington.

Greenberg, H. R. J. Wen, T. A. Buscheck, (2013). Scoping Thermal Analysis of Alternative Dual-Purpose Canister Disposal Concepts. LLNL-TR-639869.

Greene, S.R., J.S. Medford, and S.A. Macy, (2013). Storage and Transport Cask Data For Used Commercial Nuclear Fuel (2013 U.S. Edition), Report ATI-TR-130472013, EnergX, LLC: Oak Ridge, TN. 314 pp.

Gonzales, S. and K.S. Johnson, (1984). Shale and other argillaceous strata in the United States. Oak Ridge National Laboratory. ORNL/Sub/84-64794/1.

Hansen, F.D., E.L. Hardin, R. P. Rechard, G. A. Freeze, D.C. Sassani, P.V. Brady, C. M. Stone, M. J. Martinez, J. F. Holland, T. Dewers, K.N. Gaither, S. R. Sobolik, and R. T. Cygan,

(2010). Shale Disposal of U.S. High-Level Radioactive Waste. SAND2010-2843. Albuquerque, NM: Sandia National Laboratories.

Hardin, E., J. Blink, H. Greenberg, M. Sutton, F. Massimiliano, J. Carter, M. Dupont, R. Howard, (2011). Generic Repository Design Concepts and Thermal Analysis (FY11). Sandia report SAND2011-6202.

Hardin, E., T. Hadgu, D. Clayton, R. Howard, H. Greenberg, J. Blink, M. Sharma, M. Sutton, J. Carter, M. Dupont, and P. Rodwell, (2012). Repository Reference Disposal Concepts and Thermal Load Management Analysis. FCRD-UFD-2012-000219 Rev. 2. U.S. Department of Energy, Office of Used Nuclear Fuel Disposition, Washington, DC.

Hardin, E., Clayton, D., Howard, R., Scaglione, J.M., Pierce, E., Banerjee, K., Voegele, M.D., Greenberg, H., Wen, J., Buscheck, T.A., Carter, J.T., Severynse, T., Nutt, W.M., (2013). Preliminary Report on Dual-Purpose Canister Disposal Alternatives (FY13), August, 2013, FCRD-UFD-2013-000171 Rev. 0.

Hardin, E., (2014). Review of Underground Construction Methods and Opening Stability for Repositories in Clay/Shale Media (FCRD-UFD-2014-000330), Sandia National Laboratories: Albuquerque, NM. 48 pp.

Hicks, T.W., White, M.J. and Hooker, P.J. (2009). Role of Bentonite in Determination of Thermal Limits on Geological Disposal Facility Design, Report 0883-1, Version 2, Falson Sciences Ltd., Rutland, UK, Sept. 2009.

Horseman, S. T., Higgo, J. J. W., Alexander, J., and Harrington, R., 1996, Water, Gas and Solute Movement Through Argillaceous Media, NEA Working Group on Measurement and Physical Understanding of Groundwater Flow Through Argillaceous Media ("Clay Club"), Report CC-96/1: Paris, France, NEA-OECD, 306 pp.

Hökmark, H. (2004). Hydration of the bentonite buffer in a KBS-3 repository. Applied Clay Science 26(1–4): 219-233.

Houseworth J., Jonny Rutqvist, Daisuke Asahina, Fei Chen, Victor Vilarrasa, H.H Liu, Jens Birkholzer. (2013). International Collaborations on FE Heater and HG-A Tests. Lawrence Berkeley National Laboratory November, 2013. FCRD-UFD-2014-000002.

Huysmans, M. and A. Dessargues (2006). Stochastic analysis of the effect of spatial variability of diffusion parameters on radionuclide transport in a low permeability clay layer. Hydrogeology Journal 14: 1094–1106.

Jové Colón, C.F., F.A. Caporuscio, S.S. Levy, J.A. Blink, H.R. Greenberg, W.G. Halsey, M. Fratoni, M. Sutton, T.J. Wolery, J. Rutqvist, H.H. Liu, J. Birkholzer, C.I. Steefel, and J. Galindez, (2011). Disposal Systems Evaluations and Tool Development - Engineered Barrier System (EBS) Evaluation, p. 1-192.

Jové Colón, C.F., J.A. Greathouse, S. Teich-McGoldrick, R.T. Cygan, T. Hadgu, J.E. Bean, M.J. Martinez, P.L. Hopkins, J.G. Argüello, F.D. Hansen, F.A. Caporuscio, and M. Cheshire, et al. (2012). Evaluation of Generic EBS Design Concepts and Process Models: Implications to EBS Design Optimization (FCRD-USED-2012-000140), U.S. Department of Energy, Washington DC., 250 pp.

Jové Colón, C. J. A. Greathouse, S. Teich-McGoldrick, Cygan, R. T., Weck, P. F., Hansen, G. A., Criscenti, L. J., Caporuscio, F. A., Cheshire, M., Rearick, M. S., McCarney, M. K.,

Greenberg, H. R., Wolery, T. J., Sutton, M., Zavarin, M., Kersting, A. B., Begg, J. B., Blink, J. A., Buscheck, T., Benedicto-Cordoba, A., Zhao, P., Rutqvist, J., Steefel, C. I., Birkholzer, J., Liu, H-H, Davis, J. A., Tinnacher, R., Bourg, I., Zheng, L., Vilarrasa, V.et al. (2013) EBS Model Development and Evaluation Report, FCRD-UFD-2013-000312, U.S. Department of Energy, Washington D.C., 508 pp.

JNC (2000). H12: Project to Establish the Scientific and Technical Basis for HLW Disposal in Japan. Second Progress Report on Research and Development for the Geological Disposal of HLW in Japan. Supporting Report 2: Repository Design and Engineering Technology. JNC TN1410 2000-003.

Kosakowski, G. and U. Berner (2013). The evolution of clay rock/cement interfaces in a cementitious repository for low- and intermediate level radioactive waste. Physics and Chemistry of the Earth, Parts A/B/C 64(0): 65-86.

Krumhansl, J. L., 1983, Near-surface heater test results: Environmental implications for the disposal of high-level waste: Radioactive Waste Management and the Nuclear Fuel Cycle, v. 4, no. 1, p. 1-31.

Kwon, O., A. K. Kronenberg, A. F. Gangi, B. Johnson, and B. E. Herbert (2004). Permeability of illite-bearing shale: 1. Anisotropy and effects of clay content and loading, J. Geophys. Res., 109, B10205, doi:10.1029/2004JB003052.

Lauber, M., B. Baeyens and Bradbury, M. H. (2000). Physico-Chemical Characterisation and Sorption Measurements of Cs, Sr, Ni, Eu, Th, Sn and Se on Opalinus Clay from Mont Terri. PSI Bericht Nr. 00-10 December 2000 ISSN 1019-0643.

Lide, D.R., ed. (1999). CRC Handbook of Chemistry and Physics, CRC Press, Boca Raton, FL.

Liu, H.H., J. Houseworth, J. Rutqvist, L. Zheng, D.e Asahina, L. Li, V. Vilarrasa, F. Chen, S. Nakagawa, S. Finsterle, C. Doughty, T. Kneafsey and J. Birkholzer. (2013). Report on THMC modeling of the near field evolution of a generic clay repository: Model validation and demonstration, Lawrence Berkeley National Laboratory, August, 2013, FCRD-UFD-2013-0000244.

Man A. and Martino J.B. (2009). Thermal , hydraulic and mechanical properties of sealing materials. NWMO TR-2009-20. December 2009, Atomic Energy and Canada Limited.

Mariner, P.E. (2007). In-Drift Precipitates/Salts Model‖, ANL-EBS-MD-000045 (Rev.03), Sandia National Laboratories, Albuquerque, NM.

Mazurek, M., F.J. Pearson, G. Volckaert, and H. Bock, Features, Events and Processes Evaluation Catalogue for Argillaceous Media, (2003). Organisation for Economic Co-operation and Development (OECD) - Nuclear Energy Agency (NEA): Paris, France. 379 pp.

McKinley, I. G. and A. Scholits (1993). A comparison of radionuclide sorption databases used in recent performance assessments. Journal of Contaminant Hydrology 13(1–4): 347-363.

McVey, D. F., Thomas, R. K., and Lappin, A. R., 1979, Small Scale Heater Tests in Argillite if the Eleana Formation at the Nevada Test Site, Volume 5AND79-0344: Albuquerque, NM, Sandia National Laboratories, p. 61.

Miller, A. W. and Y. Wang (2012). Radionuclide interaction with clays in dilute and heavily compacted systems: a critical review. Environmental Science & Technology 46(4): 1981-1994.

Nacarrow, D.J., Sumerling, T.J. and Ashton, J., (1988). Preliminary radiological assessments of low-level waste repositories. U.K. DOE (Dep. Environ.), London, Rep. DOE/RW/88.084,62 pp.

NAGRA (2002). Project Opalinus Clay: safety report. Demonstration of disposal feasibility for spent fuel, vitrified high-level waste and long-lived intermediate level waste (Entsorgungsnachweis). Nagra Technical Report NTB 02-05, Wettingen, Switzerland.

NAGRA (2003). Geosynthese. Nagra Technical Report NTB 02-03. Nagra, Wettingen, Switzerland.

Neuzil, C. E. (1986). Groundwater flow in low-permeability environments, Water Resour. Res., 22(8), 1163-1195.

Neuzil, C. E. (1993). Low fluid pressure within the Pierre Shale: A transient response to erosion, Water Resour. Res., 29(7), 2007–2020, doi:10.1029/ 93WR00406.

Neuzil, C. (2013). Can Shale Safely Host US Nuclear Waste? Eos, Transactions American Geophysical Union 94(30): 261-262.

Olgaard, D.L. Nueesch, R., Urai, J., (1995). Consolidation of water saturated shales at great depth under drained conditions. In: Fujii, T. (Ed.), Proceedings of the Congress of the International Society for Rock Mechanics, vol. 8, pp. 273– 277.

Ochs, M., B. Lothenbach, H. Wanner, H. Sato and M. Yui (2001). An integrated sorption–diffusion model for the calculation of consistent distribution and diffusion coefficients in compacted bentonite. Journal of Contaminant Hydrology 47(2–4): 283-296.

Pabalan, R.T., F.P. Glasser, D.A. Pickett, G.R. Walter, S. Biswas, M.R. Juckett, L.M. Sabido, and J.L. Myers, Review of Literature and Assessment of Factors Relevant to Performance of Grouted Systems for Radioactive Waste Disposal (CNWRA 2009-001), Report prepared for the U.S. Nuclear Regulatory Commission by the Center for Nuclear Waste Regulatory Analyses: San Antonio, Texas, 359 pp.

Parker, V.B. and Khodakovskii, I.L. (1995). Thermodynamic properties of the aqueous ions (2+ and 3+) of iron and the key compounds of iron. Journal of Physical and Chemical Reference Data, 24(5), 1699-1745.

Perry, F.V., (2014a). Regional Geology: A GIS Database for Alternative Host Rocks and Potential Siting Guidelines (FCRD-UFD-2014-000068), LANL Unlimited Release Report LA-UR-14-203682014, Los Alamos National Laboratory: Los Alamos, NM.

Perry, F.V., (2014b). Survey of chloride concentrations in formation (pore) waters of crystalline rocks and shale, Fuel Cycle R&D, FCRD-UFD-2014-000514, Los Alamos Unlimited Release LA-UR-14-24761, 14 pp.

Pusch, R., Bluemling, P. and Johnson, L. (2003). Performance of strongly compressed MX-80 pellets under repository-like conditions, Applied Clay Science 23: 239– 244.

Pusch, R., Kasbohm, J. and Thao, H. T. M. (2010). Chemical stability of montmorillonite buffer clay under repository-like conditions—A synthesis of relevant experimental data. Applied Clay Science 47(1–2): 113-119.

Robie, R.A., Hemingway, B.S., and Fisher, J.R. (1979) Thermodynamic properties of minerals and related substances at 298.15 K and 1 Bar (10^5 Pascals) pressure and at higher temperatures. U.S. Geological Survey Bulletin 1452, Washington, D.C.: U.S. Government Printing Office.

Rutqvist, J., D. Barr, J. Birkholzer, K. Fujisaki, O. Kolditz, Q.-S. Liu, T. Fujita, W. Wang and C.-Y. Zhang (2009). A comparative simulation study of coupled THM processes and their effect on fractured rock permeability around nuclear waste repositories. Environmental Geology 57(6): 1347-1360.

Rutqvist, J., Y. Ijiri and H. Yamamoto (2011). Implementation of the Barcelona Basic Model into TOUGH–FLAC for simulations of the geomechanical behavior of unsaturated soils. Computers & Geosciences 37(6): 751-762.

Rutqvist, J., L. Zheng, F. Chen, H.-H. Liu and J. Birkholzer (2014a). Modeling of Coupled Thermo-Hydro-Mechanical Processes with Links to Geochemistry Associated with Bentonite-Backfilled Repository Tunnels in Clay Formations. Rock Mechanics and Rock Engineering 47(1): 167-186.

Rutqvist, J., L. Zheng, F. Chen, H.-H. Liu and J. Birkholzer (2014b). Investigation of coupled THMC process and reactive transport: FY14 progress. FCRD-UFD-2014-000497

Samper, J., Q. Yang, S. Yi, M. García-Gutiérrez, T. Missana, M. Mingarro, Ú. Alonso and J.L. Cormenzana (2008). Numerical modelling of large-scale solid-source diffusion experiment in Callovo-Oxfordian clay. Physics and Chemistry of the Earth 33 (Suppl. 1): S208–S215.

Sánchez, M., A. Gens and S. Olivella (2012). THM analysis of a large-scale heating test incorporating material fabric changes. International Journal for Numerical and Analytical Methods in Geomechanics 36(4): 391-421.

Sassani, D.C., C.F. Jové Colón, P. Weck, J.L. Jerden, K.E. Frey, T. Cruse, W.L. Ebert, E.C. Buck, R.S. Wittman, F.N. Skomurski, K.J. Cantrell, B.K. McNamara, and C.Z. Soderquist (2012) Integration of EBS Models with Generic Disposal System Models (FCRD-UFD-2012-000277), U.S. Department of Energy: Washington D.C.

Schultz, L. G., (1965). Mineralogy and stratigraphy of the lower part of the Pierre Shale, South Dakota and Nebraska: U.S. Geol. Survey Prof. Paper 392-B, p. B1-B19.

Sevougian, S.D., G.A. Freeze, P. Vaughn, P. Mariner, and W.P. Gardner (2013). Update to the Salt R&D Reference Case. FCRD-UFD-2013-000368, SAND2013-8255P. Sandia National Laboratories, Albuquerque, NM.

Shurr, G.W. (1977). The Pierre Shale, Northern Great Plains; A Potential Isolation Medium for Radioactive Waste. United States Geological Survey Open File Report 77-776.

SKB (Svensk Kärnbränslehantering AB) (2006). Buffer and backfill process report for the safety assessment SR-Can, SKB Technical Report TR-06-18.

SKB (Svensk Kärnbränslehantering AB) (2010). Data Report for the Safety Assessment SR-Site. Technical Report TR-10-52. Swedish Nuclear Fuel and Waste Management Co., Stockholm, Sweden.

SNL (Sandia National Laboratories) 2007. Radionuclide Screening. ANL-WIS-MD-000006 REV 02, U.S. Department of Energy, Office of Civilian Radioactive Waste Management, Las Vegas, Nevada.

Smith, L. A., G. van der Kamp, M. J. Hendry (2013). A new technique for obtaining high-resolution pore pressure records in thick claystone aquitards and its use to determine in situ compressibility, Water Resour. Res., 49, 1–12, doi:10.1002/wrcr.20084.

Soeder, D.J., (1988). Porosity and permeability of eastern Devonian gas shale: Society of Petroleum Engineers Formation Evaluation, Society of Petroleum Engineers, v. 3, no. 2, p. 116–124, DOI 10.2118/15213–PA.

Stefánsson, A.; Anórsson, S.; and Sveinbjörnsdóttir, A.E. (2005). Redox reactions and potentials in natural waters at disequilibrium. Chemical Geology, Vol. 221(3-4), p. 289-311

Sykes E. A., J. F. Sykes, S. D. Normani, E. A. Sudicky and Y. J. Park. (2008). Phase I Hydrogeologic modelling. OPG's Deep Geologic Repository for Low & Intermediate Level Waste, Supporting Techinical Report. GLL 61-123; OPG 00216-REP-01300-00009-R00.

Thury, M. and Bossart, P. (1999). Results of the hydrogeological, geochemical and geotechnical experiments performed in the Opalinus Clay (1996-1997). Chapter 6.4 Organic Matter Characterisation of Rocks and Pore-waters. Geological report No. 23. Swiss Geological Survey.

Toutelot, H. A., (1962). Preliminary Investigation of the Geologic Setting and Chemical Composition of the Pierre Shale Great Plains Region, UNITED STATES GEOLOGICAL SURVEY PROFESSIONAL PAPER 390, 81 pp.

Tsang, C.-F., J.D. Barnichon, J.T. Birkholzer, , X.L. Li, H.H. Liu, X. Sillen, and T. Vietor. (2012). Coupled Thermo-Hydro-Mechanical Processes in the Near-Field of a High-Level Radioactive Waste Repository in Clay Formations. International Journal of Rock Mechanics and Mining Sciences 49: 31-44.

Turrero et al., (2006). M.J. Turrero, A.M. Fernández, J. Peña, M.D. Sánchez, P. Wersin, P. Bossart, M. Sánchez, A. Melón, A. Yllera, A. Garralón, P. Gómez, P. Hernán. Pore-water chemistry of a Paleogene continental mudrock in Spain and a Jurassic marine mudrock in Switzerland: sampling methods and geochemical interpretation. J. Iberian Geol., 32 (2006), pp. 233–258.

van Genuchten, M. T. (1980). A closed-form equation for predicting the hydraulic conductivity of unsaturated soils. Soil science society of America journal 44(5): 892-898.

van Loon, L.R., J.M. Soler, W. Muller and M.H. Bradbury (2004a). Anisotropic diffusion in layered argillaceous rocks: a case study with opalinus clay. Environmental Science & Technology 38: 5721–5728.

van Loon, L.R., P. Wersin, J.M. Soler, J. Eikenberg, T. Gimmi, P. Hernan, S. Dewonck and S. Savoye (2004b). In-situ diffusion of HTO, $^{22}Na^{+}$, Cs^{+} and I^{-} in Opalinus Clay at the Mont Terri underground rock laboratory. Radiochimica Acta 92: 757–763.

Vietor, T. (2012). Mont Terri Project - FE Experiment Modelling Kick-off Meeting. February 9, 2012, Mont Terri, Switzerland. NAGRA Technical Discussion TD-217.

Vieno, T. and Nordman, H., (1991). Safety analysis of the VLJ repository. Nuclear Waste Commission of Finnish Power Companies, Helsinki, Rep. YJT-91-12, 14 pp. (in Finnish).

Villar, M. V., M. Sánchez and A. Gens (2008). Behaviour of a bentonite barrier in the laboratory: Experimental results up to 80 years and numerical simulation. Physics and Chemistry of the Earth, Parts A/B/C 33, Supplement 1(0): S476-S485.

Waber, H.N., Mazurek, M. and Pearson, F.J. (1998). Opalinus Clay: reference porewater, mineralogy and porosity. NAGRA Internal Report.

Wersin P., Johnson, L.H. and McKinley, I.G. (2007). Performance of the bentonite barrier at temperature beyond 100°C: A critical review, Physics and Chemistry of the Earth 32: 780-788.

Wiborgh, M. and Lindgreen, M., (1987). SKA progress report. SKB (Swed. Nucl. Fuel & Waste Manage. Co.), Stockholm, SFR 87-09, 63 pp.

Wolery, T.J. and Jové-Colón, C.F. (2007). Qualification of Thermodynamic Data for Geochemical Modeling of Mineral–Water Interactions in Dilute Systems, ANL-WIS-GS-000003 (Rev.01), Sandia National Laboratories, Albuquerque, NM.

Zheng, L., J. Samper and L. Montenegro (2008). Inverse hydrochemical models of aqueous extracts tests. Physics and Chemistry of the Earth, Parts A/B/C 33(14–16): 1009-1018.

Zheng, L., J. Samper and L. Montenegro (2011a). A coupled THC model of the FEBEX in situ test with bentonite swelling and chemical and thermal osmosis. Journal of Contaminant Hydrology 126(1–2): 45-60.

Zheng, L., H.H. Liu, J. Birkoltzer and W.M. Nutt (2011b). Diffusion modeling in a generic clay repository. FCRD-LBNL-2011-SLM: 25

Zheng, L., James Houseworth, Carl Steefel, Jonny Rutqvist, Jens Birkholzer (2014a), Investigation of Coupled Processes and Impact of High Temperature Limits in Argillite Rock. FCRD-UFD-2014-000493, U.S. Department of Energy, Washington DC.

Zheng, L., J. Rutqvist, H.-H. Liu, J. T. Birkholzer and E. Sonnenthal (2014b). Model evaluation of geochemically induced swelling/shrinkage in argillaceous formations for nuclear waste disposal. Applied Clay Science 97–98(0): 24-32.

Zheng, L., Jonny Rutqvist, Harris Greenberg, Jens Birkholzer. (2014c). Model Evaluation of the Thermo-Hydrological-Mechanical Response in Argillaceous Sedimentary Rock Repository for Direct Disposal of Dual-Purpose Canisters. FCRD-UFDC-2014-000515, U.S. Department of Energy, Washington DC.

Investigation of Coupled Processes and Impact of High Temperature Limits in Argillite Rock

(Part II)

1. Introduction

Shale and clay-rich geological formations have been considered as potential host rock for geological disposal of high-level radioactive waste throughout the world, because of their low permeability, low diffusion coefficient, high retention capacity for radionuclides, and capability to self-seal fractures. Permeabilities arising from the primary porosity of these rock types are low because of the extremely fine-grained constituents and the very small pores associated with the fine-grained material. Permeability values are typically less than 10 microdarcies (10^{-17} m^2 or about 10^{-10} m/s equivalent hydraulic conductivity) and are often two to four orders of magnitude lower. While fractures can occur, clay and shale often demonstrate the tendency to self-seal fractures, which reduces the effects of fractures on bulk permeability. This occurs as a result of swelling from the increased water potential in fractures, the generation of fracture infilling materials and mineral precipitation, and plastic deformation of the rock (Mazurek et al., 2003). The low permeability of clay and shale rock are well-known in the hydrogeology community where these rock types represent aquitards that severely limit groundwater movement, and in petroleum geology, where they act as caprocks limiting the rise of buoyant petroleum fluids. Other favorable characteristics of clay/shale rock are the strong sorptive behavior for many radionuclides and (in saturated systems) the low flow rates, which typically lead to reducing conditions because of the lack of oxygen transport from the surface. Clay and shale rock also act to chemically buffer the effects of materials introduced through repository construction, operation, and emplaced materials (Arcos et al., 2008).

A large body of information concerning the behavior of clay/shale geologic environments using bentonite backfill/buffers for nuclear waste disposal has been developed through the repository programs with underground research laboratories in Switzerland, France, Belgium, and Japan. At Switzerland's Mont Terri underground rock laboratory, experiments are being carried out to investigate the geological, hydrogeological, geochemical and rock mechanical properties of the Opalinus Clay formation, an indurated clay (also referred to as shale) (Meier et al., 2000). Experimentation is ongoing in a variety of areas including hydrogeology, geomechanics, geochemistry, characterization of the excavation damaged zone (EDZ), heater testing, radionuclide diffusion and retention, cement-clay interactions, and self-sealing behavior. The Callovo-Oxfordian clay formation, an indurated clay at Bure in France, is used for research emphasizing reversible geologic disposal of high-level and long-term intermediate level radioactive waste (Fouche et al., 2004). The program is investigating the role of faults or fractures in hydrogeologic behavior, geochemical properties of water and gas and interpretations of system connectivity, geochemical properties affecting radionuclide mobility, and feasibility of excavation. The program is also addressing complex issues concerning bentonite backfill and material interactions with cement and metallic components. The Toracian clay at Tournemire, France, is an indurated clay that is used for scientific evaluation of argillaceous formations for nuclear waste disposal but is not a candidate disposal site (Patriarche et al., 2004). Investigations include the effects of hydro-geochemical properties, rheological properties, excavation effects, the role of fractures in argillaceous formations, and interactions with concrete. The underground laboratory at Mol in Belgium conducts experiments to investigate the geological, hydrogeological, geochemical, and rock mechanical properties of the Boom Clay formation (Barnichon and Volckaert, 2003). This is softer clay than the Opalinus, Callovo-Oxfordian, or Toracian clays, and its geomechanical behavior is described as "plastic." Experiments include studies of the damage zone around drifts, thermal impact of the waste, radionuclide migration,

and backfill characterization. The Koetoi and Wakkanai Formations at Horonobe, Japan, have been recently developed as a URL (Hama et al., 2007). The argillaceous rock at this location consists of mechanically soft to indurated, highly porous diatomaceous mudstone.

In addition to the favorable characteristics of and international interest in argillaceous rocks for nuclear waste disposal, another reason for considering this rock type for the U.S. nuclear waste disposal program is the abundance of clay/shale geologic resources in the United States. Recent work on the UFD Campaign has updated shale resource estimates and identified extensive regions within sedimentary basins where shale formations are present, as shown in Figure 1.1.

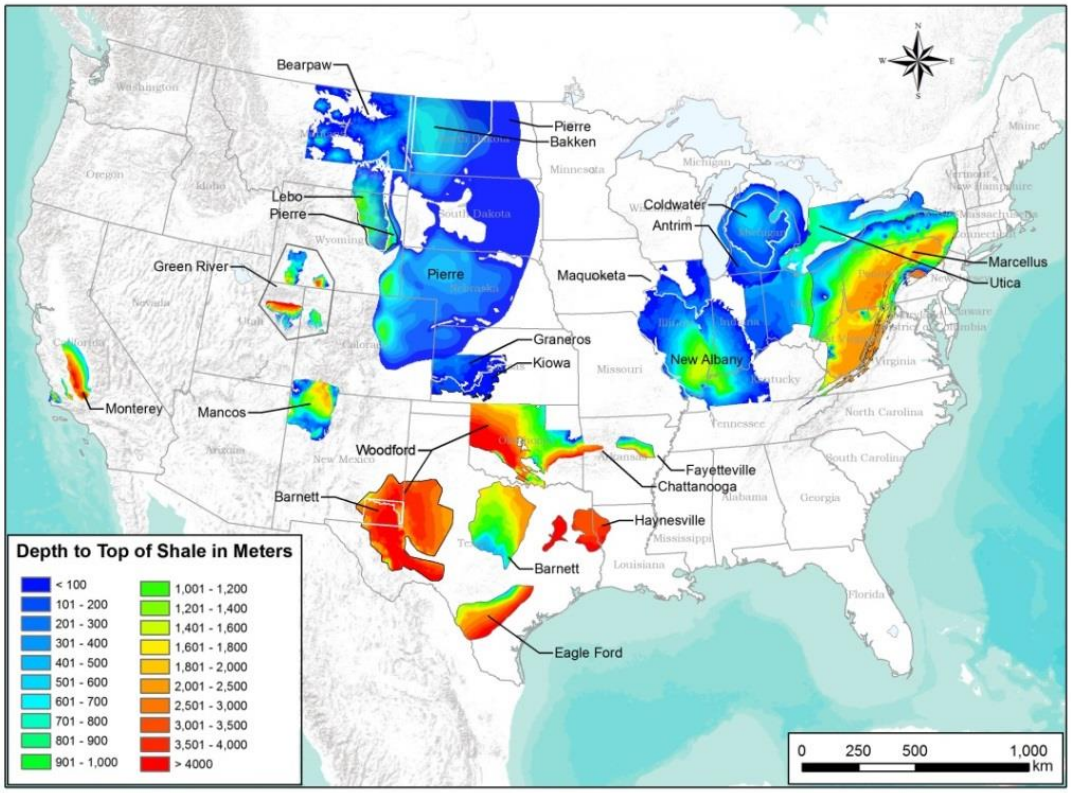

Figure 1.1. Summary of GIS data for depth to top of shale formations within major sedimentary basins in the US currently incorporated in the LANL GIS database. Figure produced by LANL from shale data populated into the GIS database. (updated after Perry et al., 2014).

The focus of research within the UFD Campaign is on repository-induced interactions that may affect the key safety characteristics of an argillaceous rock. A nuclear-waste-repository excavation causes changes in mechanical stress and water saturation, and introduces air into the underground environment. These changes have been observed in URLs discussed above and have been found to lead to fracture formation around the drift in a region called the excavation damaged zone (EDZ). The formation of fractures and increased permeability of the EDZ needs to be evaluated for its potential effects on repository performance. The behavior of the EDZ has

also been observed to change rapidly over time in response to changes in mechanical and hydrological conditions, including fracture self-sealing. Therefore, the formation and evolution of fractures in an argillaceous rock is a dynamic process.

Maximum allowable temperature is one of the most important design variables for a geological repository, because it determines waste-package spacing, distance between disposal galleries, and therefore the overall size (and cost) of the repository for a given amount of waste. This is especially important for a clay repository, because clay rock has relatively low thermal conductivity. However, data and knowledge gaps exist in establishing a scientific basis for determining this temperature for a clay repository.

Within the natural (barrier) system (NS) group of the Used Fuel Disposition (UFD) Campaign at the Department of Energy's (DOE) Office of Nuclear Energy, LBNL's research activities have focused on understanding and modeling EDZ evolution and the associated coupled processes, and impacts of high temperature on parameters and processes relevant to performance of a clay repository to establish the technical base for the maximum allowable temperature. This report documents results from some of these activities. These activities address key Features, Events and Processes (FEPs), which have been ranked in importance from medium to high, as listed in Table 7 of the *Used Fuel Disposition Campaign Disposal Research and Development Roadmap* (FCR&D-USED-2011-000065 REV0) (Nutt, 2011). Specifically, they address FEP 2.2.01, Excavation Disturbed Zone, for clay/shale, by investigating how coupled processes affect EDZ evolution; FEP 2.2.05, Flow and Transport Pathways; and FEP 2.2.08, Hydrologic Processes, and FEP 2.2.07, Mechanical Processes and FEP 2.2.09, Chemical Process—Transport, by studying near-field coupled THMC processes in clay/shale repositories. The activities documented in this report also address a number of research topics identified in *Research & Development (R&D) Plan for Used Fuel Disposition Campaign (UFDC) Natural System Evaluation and Tool Development* (Wang, 2011), including Topics S3, Disposal system modeling – Natural system; P1, Development of discrete fracture network (DFN) model; P14, Technical basis for thermal loading limits; and P15 Modeling of disturbed rock zone (DRZ) evolution (clay repository).

This report documents progress made in LBNL's FY14 research activities, including development and validation of rock stress-porosity and stress-permeability relationships based on the two-part Hooke's model, a new constitutive relationship for coupled hydromechanical processes (Section 2), development of capabilities to treat anisotropic properties in a discrete-fracture network, a fracture-damage model for investigating coupled processes in the EDZ (Section 3), modeling of THM processes for the HE-E and FE heater tests at Mont Terri, Switzerland (Section 4), the effects of strongly elevated temperature on the bentonite backfill and near-field clay host rock (Section 5), and modeling of reactive diffusive transport with application to the DR-A test at Mont Terri, Switzerland (Section 6). A summary and discussion of future work activities are given in Section 7.

2. Relationships among Permeability, Porosity and Effective Stress for Low-Permeability Sedimentary Rock Based on the Two-Part Hooke's Model

2.1 Introduction

One of the major concerns in post-closure safety evaluations of the repository system is the potential for hydromechanical perturbations caused by excavation, which is of particular importance for argillite repository. These perturbations are found within the excavation damaged

zone (EDZ) around the repository drifts and access shaft. The EDZ is primarily caused by redistribution of *in situ* stresses and rearrangement of rock structures (Tsang et al., 2012). Field investigations conducted at underground laboratories such as at Mont Terri (Switzerland) and Bure (France) have shown that the permeability of the EDZ can be one or more orders of magnitude higher than the unaltered argillaceous rock. For these conditions, the EDZ could then act as a preferential flow path for advective transport and thereby speed up radionuclide migration toward the biosphere. The EDZ properties and their evolution over time have been analyzed in laboratory and field studies (Bossart et al., 2004; Baechler et al., 2011; Armand et al., 2013). These investigations suggest that a partial or complete self-sealing of fractures due to clay swelling and creep within the EDZ is possible after a certain amount of time. The self-sealing process can potentially decrease the EDZ permeability over time, which may eventually return to the values of the unaltered rock. Stress change during excavation is the mainly driving force for the changes in permeability in EDZ, and stress recovery is also one of the major causes for the self-healing, with the other one being chemical changes such as mineral precipitation. An accurate mathematical representation of the permeability-stress relationship is therefore critical for understanding the evolution of permeability and predicting the permeability changes during excavation and self-healing stages.

The changes in permeability with stress in EDZ is a phenomenon (so called "stress-dependence of permeability") that is also widely observed for other low-permeability sedimentary rock and in other engineering applications, such as fossil-fuel exploitation (McLatchie et al., 1958; Vairogs et al., 1971; Jones and Owens, 1980; Walls et al., 1982; McKee et al., 1988; Brighenti, 1989; Spencer, 1989; Lei et al., 2008; Li et al., 2008), CO_2 geological sequestration (Rutqvist and Tsang, 2002; Cui et al., 2007), coal-mining safety (Somerton et al., 1975; Jasinge et al., 2011; Konecny and Kozusnikova, 2011), modeling fluid percolation and pore-pressure evolution in the crust (David et al., 1994; Wibberley and Shimamoto, 2005; Ghabezloo et al., 2009a; Dong et al., 2010). The low-permeability sedimentary rock typically refers to those with permeability less than 0.1 mD under reservoir conditions (Byrnes, 1996; Shanley et al., 2004; Holditch, 2006). Nowadays, hydraulic fracturing is widely used to extract oil and natural gas from tight sandstone and shale gas reservoirs, which usually show highly stress-sensitive mechanical and/or hydraulic properties. Knowledge of the dependence of such properties on stress is critical for productivity estimation and recovery-method design (Jones and Owens, 1980; Walls et al., 1982). The stress-dependence of porosity and permeability in argillite, especially in EDZ, as mentioned above, is of great importance for the performance assessment of the disposal site (Tsang et al., 2005), which motivate the study of an accurate mathematical representation of the permeability-stress, porosity-stress relationship as presented in this report.

The permeability and porosity change with effective stress are quite different for low-permeability rock. With an increase in effective stress, low-permeability rock undergoes fairly small porosity changes, typically less than 10% (Thomas and Ward, 1972; Jones and Owens, 1980; Byrnes, 1996; 1997; Byrnes and Castle, 2000). Some empirical relationships have been established between porosity and effective stress based on laboratory-measured data (Athy, 1930; Hoholick et al., 1984; Shi and Wang, 1986; Davies and Davies, 2001; Rutqvist et al., 2002). In contrast, significant permeability changes have been observed with relatively small increases in effective stress. For example, with the effective stress increases from zero to around 15 MPa (McLatchie et al., 1958; Thomas and Ward, 1972; Jones and Owens, 1980; Kilmer et al., 1987; David et al., 1994; Ghabezloo et al., 2009a; Dong et al., 2010; Metwally and Sondergeld,

2011), the permeability of this type of rock decreases more than one order of magnitude. Such a phenomenon is usually referred to as stress-sensitive rock permeability at low effective stress levels. Furthermore, as pointed out by McLatchie et al. (1958) and Vairogs et al. (1971), for tight sandstone, the lower the reference permeability (routinely tested permeability), the greater the permeability reduction under increasing effective stress. Some empirical relationships were established between permeability and effective stress based on laboratory-measured data. Representative relationships include exponential law (David et al., 1994; Evans et al., 1997; Mohiuddin et al., 2000; Jones, 2013) and power law (Shi and Wang, 1986; Lei et al., 2008; Ghabezloo et al., 2009a; Dong et al., 2010). However, the exponential law yields poor fitting in low effective-stress ranges, and the power law gives unreasonable predictions for certain effective-stress values. To describe the relationship between the significant permeability drop and the insignificant porosity reduction under effective stress has been a great challenge for scientists over a long period of time. Up to now, empirical relationships, usually in the form of a power law, were established based on laboratory-measured data to relate permeability and porosity. For example, Dong et al. (2010) systematically measured the porosity and permeability change with increasing effective stress. The relationship between permeability and porosity was represented by a power law, i.e. $k/k_0 = (\phi/\phi_0)^m$, where ϕ and ϕ_0 are the porosity under the current stress state and ambient conditions, respectively; k and k_0 are the permeability under the current stress state and ambient conditions, respectively; m is a material constant named porosity sensitivity exponent of permeability. The underlying assumption in relating permeability changes to the total porosity change is that the reduction of the total volume of pore space is the only driver for the permeability change—an assumption that leads to some problems with these relationships, one of which is the abnormally high m. If the flow path is largely controlled by slot-like micro-crack networks (as has been postulated by many researchers (Somerton et al., 1975; Jones and Owens, 1980; David and Darot 1989; David et al., 1994; Byrnes 1997; Evans et al., 1997; Byrnes and Castle 2000; Lei et al., 2008; Dong et al., 2010; Soeder and Randolph, 2013), the permeability change with the crack aperture reduction (reflected by porosity reduction) should obey the "cubic law" (Witherspoon et al., 1980; Zimmerman and Bodvarsson, 1996) which implies that m should be around 3. However, the calculated values of m based on the experimental data for low-permeability samples were much higher than 3, with values up to 70 (David et al., 1994; Dong et al., 2010). The extremely high exponent in the current power law for the relationship between permeability and porosity suggests that relating permeability changes to the total porosity changes is not a valid assumption. In this report we therefore attempt to establish relationships that are more physically robust for low permeability rock.

This study is based on the concept of the two-part Hooke's model (TPHM). Natural rock, which contains different mineral compositions, pores, micro-cracks and fractures, are inherently heterogeneous and will experience non-uniform deformation under uniform stress. Based on this consideration, Liu et al. (2009; 2011) conceptually divided the rock body into "soft" and "hard" parts. As they pointed out, the natural strain (volume change divided by rock volume at the current stress state), rather than the engineering strain (volume change divided by the unstressed rock volume), should be employed in Hooke's law for accurately modeling the elastic deformation, unless the two strains are essentially identical (as they might be for small mechanical deformations in the "hard" part). Based on this concept, a series of constitutive relations between stress and a variety of hydromechanical rock properties can be derived, e.g., stress-dependent rock bulk compressibility, pore compressibility, rock porosity and fracture aperture (Liu et al., 2009; Zhao and Liu, 2012; Liu et al., 2013a). These theoretically derived

relationships could represent the experimental data in literature very well. However, the TPHM based stress-dependent permeability relationship is not covered in the scientific literature. In this report, we will derive the stress-dependence of permeability based on the concept of TPHM. The derived relationships explain well the permeability stress-sensitive phenomena in the low effective-stress ranges. As demonstrated later in the report the soft part, while only a small portion of the low-permeability rock, plays a critical role in the stress-dependence of permeability.

In the next section (Section 2.2), the empirical relationships between porosity and stress and permeability and stress are reviewed and discussed. In Section 2.3, the theoretical development of the TPHM is provided for the sake of completeness. In Section 2.4, we derive the stress-dependence relationship for porosity and permeability based on the TPHM. In Section 2.5, the proposed relationships are used to match the experimental measured data.

2.2 Existing relationships for stress-dependent rock properties

The stress-dependent rock mechanical and/or hydraulic properties have been extensively studied, due to their importance in engineering applications (Walsh and Brace, 1984; McKee et al., 1988; Dewhurst et al., 1998; Louis et al., 2005; Sadhukhan et al., 2012; Wu and Dong, 2012). In this section, we discuss the existing empirical relationships for describing the stress-dependence of rock porosity and permeability. Also presented is the relationship between permeability and porosity as permeability changes occur via porosity changes with effective stress. Note that the effective stress refers to the confining pressure minus the pore pressure.

2.2.1 Relationship between porosity and effective stress

The influence of effective stress on porosity for low permeability rock is small, usually with less than 10 percent change of the total porosity (Byrnes, 1997; Byrnes and Castle, 2000). The relationship between porosity and effective stress, albeit in a slightly different form, can be described by exponential function, as shown in the following equations.

After studying the porosity of relatively pure shale samples from various depths, Athy (1930) presented the compaction induced porosity-depth relationship using an exponential equation:

$$\phi = \phi_0 \exp(-bx) \tag{2.1}$$

where ϕ is porosity at depth x, ϕ_0 is the porosity of surface sample, and b is a constant. This relationship could also be applied to sandstones (Hoholick et al., 1984). Because the equivalent effective stress can be deduced from burial depth, Shi and Wang (1986) reformat Equation (2.1) to relate the porosity to effective stress:

$$\phi = \phi_0 \exp(-\beta\sigma) \tag{2.2}$$

where σ is effective stress, and β is a material constant.

Based on laboratory experiments on sandstone by Davies and Davies (2001), Rutqvist et al. (2002) proposed a modified empirical stress-porosity expression that added an additional parameter called “residual porosity”:

$$\phi = \phi_r + (\phi_0 - \phi_r)\exp(-\beta\sigma) \tag{2.3}$$

where ϕ_r is the residual porosity at high effective stress. With the presence of residual porosity, Equation (2.3) can better characterize the relatively large degree of stress dependency on porosity in the lower effective-stress ranges.

2.2.2 Relationship between permeability and effective stress

It has been well-recognized that the effective stress has a huge influence on rock permeability. Many empirical relationships have been put forward to describe permeability changes with effective stress. In general, these relationships can be divided into exponential law and power law.

2.2.2.1 Empirical exponential law for stress-dependency of permeability

Generally, the exponential law for describing stress-dependent permeability takes the form of (David et al., 1994):

$$k = k_0 \exp[-\gamma(\sigma - \sigma_0)] \tag{2.4}$$

where k is the permeability at the effective stress σ, k_0 is the permeability at ambient stress σ_0, and γ is the stress sensitivity coefficient.

In the study of generation and maintenance of pore-pressure excess in the crust, David et al. (1994) conducted stress-dependent permeability experiments for five sandstones with effective stress from 3 MPa to about 600 MPa, using water as the test fluid. The ambient porosities of these samples range from 14% to 35%. The steady-state method and transient pulse method were employed for permeabilities higher and lower than 10 μD, respectively. As indicated by David et al. (1994) a typical permeability-effective stress curve has a sigmoidal shape, with an inflection point called a "critical pressure" at which pore collapse occurs. The "critical pressures" for the five sandstones vary from 75 MPa to 380 MPa. As also noted in David et al. (1994), the permeability reduction caused by mechanical compaction (effective stress ranging from 3 MPa to the "critical pressure") could be approximated using Equation (2.4). This relationship was suitable for the relatively high-stress part of the focused effective stress range. However, the permeability of two out of five sandstones exhibits high stress-sensitivity at low effective-stress range, which as argued by David et al. (1994) was related to closure of the micro-cracks. Equation (2.4) cannot reflect the permeability change at this effective-stress range.

Evans et al. (1997) measured the stress-dependent permeability of intact core, fault core, and damaged zone core of granite rock collected from outcrops, with ambient porosity ranging from 0.143% to 3.706%. Four intact cores, three fault cores, and five damage-zone cores were subjected to a series of effective stresses ranging from 2.07–10.34 MPa, 2.07–33.10 MPa, and 2.07–46.89 MPa, respectively. The tests were conducted at room temperature using nitrogen and a transient pulse method. An exponential equation, similar to Equation (2.4), was used to fit the stress-dependency of permeability data. However, it should be noted that the data used in the curve-fitting for the intact rock was only in the relatively low effective-stress range, i.e., from 2.07 MPa to 10.34 MPa. The other two have wider ranges of effective stress data. However, the fitted curves underestimated the permeability in effective stresses lower than 5 MPa. The fitted stress-sensitive coefficient for intact core was much higher than the other two, which the authors speculated was due to the micro-crack closure in the intact rock.

The major caveat of the exponential law for permeability-effective stress is that it yields poor fittings in low effective-stress ranges. When the measured permeability spans large ranges of

effective stress, it is very hard to find one permeability-stress function to fit all the data. Evans et al. (1997) seemed to be able to fit their data with one equation, but only because their data (for intact rock) is only for low effective stress.

2.2.2.2 Empirical power law for stress-dependent permeability

A simple power law described by Equation 2.5 has also been used to fit measured permeability with effective stress (Morrow et al., 1984; Shi and Wang 1986; Ghabezloo et al., 2009b):

$$k = a\sigma^{-b} \tag{2.5}$$

where a and b are material constants, σ is effective stress.

Ghabezloo et al. (2009b) studied the effective-stress law of permeability for limestone with effective porosity (connected porosity) between 13.4% and 17.6%. A series of steady-state permeability tests were performed for different combinations of pore pressure and confining pressure, using water as the test fluid. The authors used Equation (2.5) to describe the variation in permeability, with the effective stress ranging from ~1 MPa to ~ 8 MPa. However, as indicated by the authors, this power law cannot be accepted as a general stress-permeability relationship, due to the infinite permeability value at zero effective stress.

Shi and Wang (1986) also use Equation (2.5) to describe the relationship between effective stress and the permeability of fault gouge measured by Morrow et al. (1984). Morrow et al. (1984) studied the permeability changes in clay-rich, non-clay, and pure-clay artificial gouges under an effective stress ranging from 5 MPa to 200 MPa. The artificial fault gouge was comprised of two pieces of very permeable saw-cut Berea sandstone and 1-mm-thick-layer tested material. The tests were conducted at a temperature of 27 ± 0.5 ℃, using distilled water and a steady-state method.

A slightly different form of power law, as shown in Equation 2.6, was employed by Kwon et al. (2001) to fit the measured permeability of illite-rich shale with different effective stresses ranging from 3 MPa to 12 MPa.

$$k = k_0[1 - (\sigma/P_1)^m]^3 \tag{2.6}$$

where k_0 is the reference permeability at zero effective pressure, σ is effective stress, P_1 is the effective modulus of the equivalent asperities, and m is a constant between 0 and 1. Kwon et al. (2001) took samples from a depth around 3955 m in West Baton Rouge Parish, Louisiana, with effective porosities from 7% to 8%. The transient pulse method was employed in a permeability test using 1*M* NaCl solution as the test fluid. Equation (2.6) has the advantage that it relates permeability with the equivalent fracture aperture, which provided a possible explanation for the permeability change with effective stress through the "cubic law." However, the flaw in the equation is also obvious, in that it gives negative k when σ is larger than P_1. The value of P_1 is only 19.3 ± 1.6 MPa for shale, based on the fitting of the measured data (Kwon et al., 2001). Jones and Owens (1980) also used a similar relationship to describe permeability reduction with increasing effective stress for tight sandstone. A comprehensive review of stress-dependent permeability based on the equivalent fracture models could be found in Ostensen (1983). The common flaw of this type of relationship is that above a certain effective stress, the predicted permeability gives negative values.

In summary, while the power law can provide a reasonable description of the permeability-stress relationship at relatively low effective stress ranges, its flaw is quite obvious—Equation (2.5)

yields infinite permeability at zero effective stress, and Equation (2.6) yields negative permeability when effective stress is larger than a certain value.

2.3 Relationship between permeability and porosity

Porosity acts as a bridge between permeability changes and changes in effective stress when assuming the mechanical compaction of the flow path as the main factor in causing permeability reduction. Thus, researchers have tried to construct permeability-porosity relationships in describing mechanical compaction. It is generally believed that the relationship between permeability and porosity of a rock undergoing mechanical compaction could be expressed by a power law:

$$k/k_0 = (\phi/\phi_0)^{\alpha} \tag{2.7}$$

where k_0 and ϕ_0 are permeability and porosity under ambient stress state, and α is a material constant.

David et al. (1994) used Equation (2.7) to describe permeability and porosity data under different effective stress for five types of sandstones, with exponent value α ranging from 4.6 to 25.4. They also reviewed a batch of publish data on the permeability-porosity relationship for different geomaterials, and with α varying from 1.11 to 25.4.

Ghabezloo et al. (2009b) measured the permeability-porosity relationship for oil-well cement paste using a single transient method which allows the porosity and permeability data to be measured in a single test. The permeability-porosity relationships obeyed a power law identical with Equation (2.7), with α value equal to 11.

Dong et al. (2010) conducted a series of permeability and porosity tests under different effective stresses. Equation (2.7) was also employed in these tests to describe the permeability-porosity relationship, with exponent α value ranging from 2.04 to 5.04 for fine-grained sandstone, and from 9.92 to 70.17 for silty-shale samples.

As shown above, the value of exponent α for most low-permeability rock is very large, which means that a small change in porosity (due to the applied stress) causes a huge decrease in permeability. This was first noticed by David et al. (1994), who noted that the theoretical models that used low values of α would underestimate the permeability reduction induced by compaction. Dong et al. (2010) observed even higher values of α, and postulated that it was caused by the effect of micro-crack closure. It is known that permeability is largely determined by the pore throat, or the slot-like micro-cracks that connect large pores to form a flow network (Byrnes, 1996; Dewhurst et al., 1998). This supports the applicability of a "cubic law" (Zimmerman and Bodvarsson, 1996; Liu et al., 2013a) derived for a fractured medium. However, the fact that an exponent α up to 70 has to be used to fit the measured data suggests that relating permeability changes to total porosity is fundamentally flawed.

Using total porosity in Equation (2.7) is essentially assuming that all pores, both large pores and micro-cracks, have equal contribution to permeability, which runs contrary to the fact that micro-cracks actually control the connectivity of pores and subsequently control permeability. Another fact is that the micro-cracks are generally more deformable, which means that they experience relatively large deformation at low effective stress range. Thus, the impropriety of homogenizing the contribution of different types of pores to permeability is more pronounced for low-permeability rock under low effective stress. When the rock is subject to compaction, the

deformation of micro-cracks, although insignificant in term of volume, is critical for permeability changes. It is therefore necessary to separate the contribution of micro-cracks and large pores, which can be done via the concept brought by TPHM, as described in detail in the following subsections.

2.4 A brief description of the TPHM

The TPHM proposed by Liu et al. (2009) is briefly described here for completeness. Liu et al. (2009) argued that the *true strain*, rather than the *engineering strain*, should be used in Hooke's law for accurately modeling elastic deformation of rock, unless the two strains are essentially identical (as they might be for small mechanical deformations). In terms of volumetric strain, the true strain refers to volume change divided by rock volume at the current stress state, and the engineering strain refers to volume change divided by the unstressed rock volume. (In the literature of rock mechanics and other related scientific fields, however, engineering strain is now used exclusively.) Liu et al. (2009) further argued that natural rocks are inherently heterogeneous, and thus different varieties of Hooke's law should be applied within ranges having significantly different stress–strain behavior. They conceptually divide the rock body into two parts, hard and soft, and hypothesize that the soft part obeys the true-strain-based Hooke's law, while the hard part approximately follows the engineering-strain based Hooke's law for mathematical convenience, because its deformation is small (true strain is practically identical to the engineering strain when the deformation is small). This conceptualization can be represented by the hypothesized composite spring system shown in Figure 2.1. These two springs are subject to the same stress, but follow different variations on Hooke's law. To be consistent with previous work, the subscripts $0, \mathrm{e}, \text{and } \mathrm{t}$ denote the unstressed state, the hard part and the soft part, respectively. For the soft part, Hooke's law could be expressed using the true strain:

$$\mathrm{d}\sigma = \mathrm{K}_t \mathrm{d}\varepsilon_{V,t} = -\mathrm{K}_t \frac{\mathrm{dV}_t}{\mathrm{V}_t} \tag{2.8}$$

where K_t is the elastic modulus of the soft part, and V_t is the volume of the soft part. Integrating Equation (2.8) and the initial condition $\mathrm{V}_t = \mathrm{V}_{0,t}$ for $\sigma = 0$, we have:

$$\mathrm{V}_t = \mathrm{V}_{0,t} \exp\left(-\frac{\sigma}{\mathrm{K}_t}\right) \tag{2.9}$$

For the hard part, using the engineering strain, we have:

$$\mathrm{d}\sigma = \mathrm{K}_e \mathrm{d}\varepsilon_{V,e} = -\mathrm{K}_e \frac{\mathrm{dV}_e}{\mathrm{V}_{0,e}} \tag{2.10}$$

where K_e is the elastic modulus of the hard part, and V_e is the volume of the hard part. Integrating Equation (2.9) and the initial condition $\mathrm{V}_e = \mathrm{V}_{0,\mathrm{e}}$ for $\sigma = 0$, we have:

$$\mathrm{V}_e = \mathrm{V}_{0,e}\left(1 - \frac{\sigma}{\mathrm{K}_e}\right) \tag{2.11}$$

By combining Equations (2.9) and (2.11), the TPHM-based stress-strain relationship under a hydrostatic state can be expressed by:

$$\varepsilon = -\frac{\mathrm{dV}}{\mathrm{V}_0} = -\frac{\mathrm{dV}_e + \mathrm{dV}_t}{\mathrm{V}_0} = \gamma_e \frac{\mathrm{d}\sigma}{\mathrm{K}_e} + \gamma_t \exp\left(-\frac{\sigma}{\mathrm{K}_t}\right)\frac{\mathrm{d}\sigma}{\mathrm{K}_t} \tag{2.12}$$

$$\gamma_t = \frac{V_{0,t}}{V_0} \tag{2.13}$$

$$\gamma_e = 1 - \gamma_t \tag{2.14}$$

where V_0 is the rock bulk volume under an unstressed state. Equation (2.12)-(2.14) together comprise the basic stress–strain relationship.

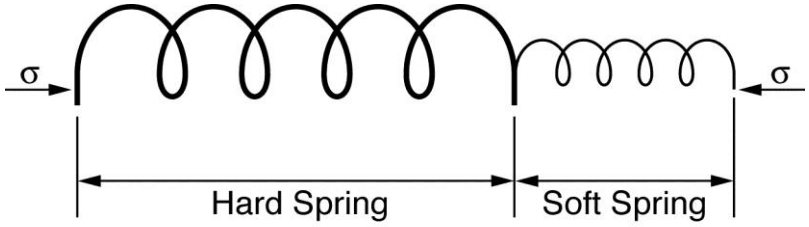

Figure 2.1. A composite spring system consisting of two springs. The hard and soft springs follow engineering-strain-based and natural-strain-based Hooke's law, respectively.

With the basic stress-strain relationship available, a number of rock mechanical and/or hydraulic properties subjected to elastic deformation can be developed. For example, Liu et al. (2009) derived the stress-dependent bulk rock compressibility, pore compressibility, rock porosity, and fracture aperture based on the TPHM. The derived relationships were compared with a variety of laboratory experimental data, which showed a great consistency. Furthermore, they argued that the proposed relationships are robust for engineering applications, because the parameter values estimated from different types of data are quite consistent for similar types of rocks. Zhao and Liu (2012) extended the stress-dependent relationships for porous rock under elastic and anisotropic conditions by assuming that the principal strain resulting from the soft part is a function of principal stress along the same direction only. These relationships also showed great consistency with the data gathered from the literature. Liu et al. (2013a) focused on the normal-stress dependent fracture hydraulic properties. The derived relationship between stress and fracture permeability (or related aperture and closure) based on the TPHM showed a satisfactory agreement with the datasets obtained from the literature. Li et al. (2014) incorporated the TPHM-based relationships into a geomechanical simulator to study the coupled hydromechanical behavior of the Opalinus Clay in responding to tunnel excavations. The simulation results obtained using the TPHM-based constitutive relationships are more consistent with the field observations than the results using the traditional constitutive relationships.

2.5 Stress-dependent relationships for rock porosity and permeability based on the TPHM

It is clear that the permeability changes in the low stress range are mainly due to the compaction of micro-cracks that experienced relatively large deformation. As pointed out by Liu et al. (2009; 2013a), some portion of the pores and microfractures in a rock body could be subjected to significant deformation due to their geometrical heterogeneity. Byrnes et al. (1997; 2000) found that the average pore-throat size in low-permeability sandstones under *in situ* stress decreased by as much as 50 to 70% (e.g., from 1 μm to 0.5–0.3 μm) compared with that under no confining stress, whereas, the porosity under in-situ stress were just several percent less than that under no confining stress. As indicated by Byrnes et al., the thin and sheet-like interconnecting throats, although constituting only a small portion of the porosity, make a significant contribution to

permeability reduction. More attention should be paid to the deformation of the more compliant part of the rock body (e.g., micro-cracks), since they act as critical fluid-flow paths that determine hydraulic properties. However, most previous studies (Gangi, 1978; Shi and Wang, 1986; Ghabezloo et al., 2009a; Dong et al., 2010) assumed homogeneity of the rock sample and ignored the likelihood that the different parts of the rock have different mechanical responses under stress and thus affect permeability differently. The division of hard and soft parts in THPM provides us with a framework to consider such heterogeneity development of stress-dependent permeability-porosity relationships. The derivations based on the TPHM are given below.

2.5.1 Stress-dependence of porosity

As discussed above, we conceptualize the pore structures into two parts. The hard part experiences small deformation, whereas the soft part undergoes relatively large deformation. The aforementioned micro-cracks correspond to the soft part, while the rest of the pores and solids belong to the hard part. Using the same notations as in Section 2.4, the porosity change could be defined as:

$$\mathrm{d}\phi \approx \frac{\mathrm{dV^p}}{\mathrm{V_0}} = \frac{\mathrm{dV_t^p} + \mathrm{dV_e^p}}{\mathrm{V_0}} = \frac{\mathrm{dV_t} + \mathrm{dV_e^p}}{\mathrm{V_0}} \tag{2.15}$$

where the superscript p refers to pore space. The soft part of rock body V_t is considered to be a portion of pore volume, which leads to $\mathrm{V}_t = \mathrm{V}_t^{\mathrm{p}}$. Liu et al. (2009) indicated that, for the purpose of calculating porosity, the changes in total rock volume V could be ignored, and its value could be approximated with the unstressed volume V_0. With this assumption, and following the same procedure used to derive Equation (2.12), we obtained:

$$\mathrm{d}\phi = -\phi_{e,0}\mathrm{C}_e\mathrm{d}\sigma - \frac{\gamma_t}{\mathrm{K}_t}\exp\left(-\frac{\sigma}{\mathrm{K}_t}\right)\mathrm{d}\sigma \tag{2.16}$$

$$\phi_{e,0} = \phi_0 - \gamma_t \tag{2.17}$$

where C_e is the compressibility for the hard fraction of pore volume.

Integrating Equation (2.16) and using $\phi = \phi_0$ for $\sigma = 0$ gives

$$\phi = \phi_{e,0}(1 - \mathrm{C}_e\sigma) + \gamma_t\exp\left(-\frac{\sigma}{\mathrm{K}_t}\right) \tag{2.18}$$

$$\phi_e = \phi_{e,0}(1 - \mathrm{C}_e\sigma) \tag{2.19}$$

$$\phi_t = \gamma_t\exp\left(-\frac{\sigma}{\mathrm{K}_t}\right) \tag{2.20}$$

As expressed by Equations (2.18)–(2.20), the porosity of a rock sample is divided into two parts. The hard-part porosity, i.e., $\phi_e = \phi_{e,0}(1 - \mathrm{C}_e\sigma)$, has a linear relationship with the effective stress. The soft-part porosity, i.e., $\phi_t = \gamma_t\exp\left(-\frac{\sigma}{\mathrm{K}_t}\right)$, changes exponentially with effective stress. The soft-part porosity corresponds to those more compliant, slot-like micro-cracks, which experience relatively large deformation under low effective stress. The two porosities experience different types of reduction with increasing effective stress. Specifically, the soft part is important in the low-stress range while negligible in the high stress range because K_t is relatively small (i.e., $\exp\left(-\frac{\sigma}{\mathrm{K}_t}\right) \approx 0$ when $\sigma \gg \mathrm{K}_t$).

2.5.2 Stress-dependence of permeability

The division of total porosity into a soft part and a hard part, which obey different relationships for effective stress, allows us to consider their respective effect on the total permeability.

The permeability changes in relatively high effective-stress ranges is controlled by the hard part with the consideration that the soft-part porosity could be neglected in this stress range (micro-crack closure). Mathematically, the stress-dependent permeability contributed by the hard part (referred to as "hard-part permeability" hereafter) could be written as:

$$\mathrm{k}_e = \mathrm{k}_{e,0}\exp\left[\beta\left(\phi_e - \phi_{e,0}\right)\right] = \mathrm{k}_{e,0}\exp\left[-\beta \mathrm{C}_e \phi_{e,0}\sigma\right] \tag{2.21}$$

where ϕ_e and k_e are the stress-dependent hard-part porosity and permeability, β is a constant that represents a stress-sensitive coefficient. Equation 2.21 is consistent with most of the experimental observations (David et al., 1994; Evans et al., 1997; David et al., 2001; Kwon et al., 2001), such that permeability changes linearly with the logarithm of effective stress within the relatively high effective stress range, as discussed in Section 2.2.2.1.

The stress-sensitive permeability changes in the low effective-stress range are mainly due to the deformation of the soft part (micro-cracks) porosity, which experienced relatively large deformation, despite the fact that the soft-part porosity makes up only a small portion of the total pore volume. The permeability contributed by the soft part, referred to as the "soft-part permeability" hereafter, could be considered as the total permeability minus the hard-part permeability:

$$\mathrm{k}_t = \mathrm{k} - \mathrm{k}_e \tag{2.22}$$

where k is the total permeability and k_t is the soft-part permeability.

Mathematically, we postulate the relationship between soft-part porosity and soft-part permeability as:

$$\mathrm{k}_t = \alpha {\phi_t}^{\mathrm{m}} \tag{2.23}$$

where ϕ_t, k_t are the soft-part porosity and permeability, respectively**;** and α and m are constants.

Combining Equations (2.20)-(2.23) yields the total permeability as:

$$k = \mathrm{k}_{e,0}\exp\left[-\beta \mathrm{C}_e \phi_{e,0}\sigma\right] + \alpha\left[\gamma_t \exp\left(-\frac{\sigma}{\mathrm{K}_t}\right)\right]^{\mathrm{m}} \tag{2.24}$$

In this report the soft part corresponds to those thin, slot-like micro-cracks. If such a hypothesis holds, the permeability change caused by the soft-part deformation should obey the "cubic law" (Witherspoon et al., 1980; Zimmerman and Bodvarsson, 1996; Kwon et al., 2001). In other words, the soft-part permeability should be well related with the soft-part porosity through a relationship similar to the "cubic law," i.e., m in Equation (2.23) should be around 3. In the next section, we will evaluate the equations proposed here using the experimental observations collected from the literature.

2.6 Verification of the proposed stress-dependent relationships for rock porosity and permeability based on the TPHM

Here we evaluate the proposed relationships using the experimental observations provided by Dong et al. (2010). Actually, there are a number of stress-dependent permeability data for low-

permeability rock in the literature (McLatchie et al., 1958; Vairogs et al., 1971; Thomas and Ward, 1972; Walls et al., 1982; Wei et al., 1986; Kilmer et al., 1987; Brighenti, 1989; Spencer, 1989; Kwon et al., 2001; Lei et al., 2008; Jasinge et al., 2011; Konecny and Kozusnikova, 2011; Metwally and Sondergeld, 2011). However, those that include stress-dependent porosity data are few. To the best of our knowledge, these data sets can be found in Wyble (1958), Jones and Owens (1980), Yale and Nur (1985), David et al. (1994), Mohiuddin et al. (2000); and Dong et al. (2010). In the selection of the experimental data sets we used to evaluate the proposed relationships, several criteria were considered. First of all, the samples and the measurement procedures had to be well documented. Second, we preferred that the permeability be measured by gas rather than liquid, because gas (e.g., nitrogen and helium) is more chemically inert than liquid (e.g., pure water and NaCl solution). Third, the samples collected from wells were preferred over outcrop rock samples, since the relationships of interest are mostly for underground engineering applications. Other selection considerations include sufficient data density and microscopic pore structure analysis. Given these considerations, we chose the data sets provided by Dong et al. (2010) to evaluate the proposed relationships.

2.6.1 Experiments description

Rock samples from depths of 900–1235 m were collected from a deep drilling project (Taiwan Chelungpu Fault Drilling Project, TCDP-A) in the Western Foothills of Taiwan. Only the relatively homogeneous cores were selected; cores with interbedded layers were discarded. The samples were carefully prepared to reduce the occurrence of micro-cracks during sample preparation. A series of stress-dependent porosity and permeability of dry rock samples were measured on an integrated porosity/permeability measurement system, i.e. YOYK2. A steady-state flow method was employed to assess the stress-dependent permeability, while stress-dependent porosity was measured by a gas-expansion method. Nitrogen was used as the test fluid for both tests. The experiments were conducted by first gradually increasing (loading) the confining pressure P_c from 3 to 5 MPa, then to 20 MPa (in 5 MPa increments), and finally to 120 MPa (in 10 MPa increments). P_c was then gradually reduced (unloaded) back to 3 MPa in the reverse order. The average pore pressures P_p were relatively low, i.e., 0.13–1.40 MPa for the permeability measurement and 0.3–1.41 MPa for the porosity measurement. The effective stress is defined as the difference between the P_c and P_p. Tested samples included Pliocene to Pleistocene fine-grained sandstone and silty-shale. The sandstone samples had relatively high permeability, exceeding the definition of low-permeability rock. In this study, we focused on the stress-dependent hydraulic properties of the silty-shale. The basic geophysical properties of the samples are listed in Table 2.1.

Table 2.1. Basic geophysical properties of silty-shale samples for permeability and porosity measurements

Sample name	Depth(m)	Dry density (g/cm3)	Rock type
R255_sec2	902.68	2.59	Silty-shale
R287_sec1	972.42	2.58	Silty-shale
R351_sec2	1114.33	2.59	Silty-shale
R390_sec3	1174.24	2.66	Silty-shale

2.6.2 Matching experiment data using TPHM based relationships

Since the porosity under zero effective stress ($\phi_{e,0}$) was not given due to the limitation of the experimental method, we simply used the porosity at lowest effective stress $\phi_{e,1}$ to substitute $\phi_{e,0}$. The subscript 1 hereafter refers to the lowest effective stress state. Equation (2.18) is therefore revised as:

$$\phi = \phi_{e,1}(1 - C_e\Delta\sigma) + \gamma_{t,1}\exp\left(-\frac{\Delta\sigma}{K_t}\right) \tag{2.25}$$

where $\Delta\sigma = \sigma - \sigma_1$, and $\gamma_{t,1}$ was the soft-part fraction at the lowest effective stress.

Similarly, the Equation (2.24) was revised as:

$$k = k_{e,1}\exp\left[-\beta C_e\phi_{e,1}\Delta\sigma\right] + \alpha\left[\gamma_{t,1}\exp\left(-\frac{\Delta\sigma}{K_t}\right)\right]^m \tag{2.26}$$

The matching process of stress-dependent porosity and permeability for the loading part of sample R255_sec2 was used to illustrate the determination of parameters in Equations (2.25) and (2.26). As shown in Figure 2.2(a), the porosity-effective stress relationship can be well represented by a straight line for the relatively high effective-stress range. In this study, we chose the effective-stress range 35 MPa–120 MPa as the relatively high effective stress range. The slope of the straight line was used to determine $(-\phi_{e,1}C_e)$, because the second term on the right hand side of Equation (2.25) is negligible for high effective stress values. The value of $\phi_{e,1}$ was determined by extrapolating the straight line to σ_1, as illustrated by the intersection of the red line and Y axis in Figure 2.2(a). The measured porosity ϕ_1 was equal to $\phi_{e,1} + \gamma_{t,1}$ as implied by Equation (2.25). The above procedure allowed for direct determination of values for $\phi_{e,1}$, C_e, and $\gamma_{t,1}$. The remaining parameter K_t could be estimated using the porosity data at relatively low effective stress, based on Equation (2.25). The effective stress range 3 MPa–15 MPa was chosen as the relatively low effective-stress range.

Figure 2.2(b) shows the permeability-effective stress relationship with permeability plotted in logarithm. A linear relationship exists for *log(K_e)* versus σ, as shown by the red straight line for the relatively high effective-stress range. In this effective-stress range, the contribution of the soft part to permeability is neglected, because the second term on the right-hand side of Equation (2.26) is negligible. The slope of the straight line in the relatively high effective-stress range yields the value of $(-\beta C_e\phi_{e,1})$, which leads to the determination of β as $\phi_{e,1}$ and C_e is known by fitting the porosity-stress data. $k_{e,1}$, the hard-part permeability at σ_1, is given by the intersection of the straight line with Y axis.

Once the hard-part permeability is known, the soft-part permeability is calculated by the total permeability minus the hard-part permeability. Then, the soft-part permeability is related to the soft-part porosity at corresponding stress with $k_t = \alpha\phi_t^m$, which yields the exponent *m*. The m value is marked out on the stress-permeability figure.

Experimental data matched with Equations 2.25 and 2.26 are shown in Figures 2.2–2.5. A close match between Equation (2.25) and (2.26) and the experimental data confirms the validity of these TPHM-based porosity-stress and permeability-stress relationships. As shown in the porosity- stress figures, the soft part mainly accounts for the nonlinear porosity reduction with effective stress in the low stress range. The porosity reduction in this range resulted mainly from

the deformation of slot-like micro-cracks. In addition, as shown in the permeability-stress figures, the soft part accounts for most of the permeability reduction in the low effective-stress range. The soft-part porosity, which occupied only a small portion of the total pore volume, acted as critical flow paths that connected the hard-part porosity. Thus, its deformation significantly affected the permeability. Using the concept of dividing the rock body into hard and soft parts, the stress-dependent rock porosity and permeability have a reasonable explanation.

The determined value of $\phi_{e,1}$, C_e, $\gamma_{t,1}$, K_t, $k_{e,1}$, β, α, m and its coefficient of determination R^2 are listed in Table 2.2. As listed, the soft-part porosity at lowest effective stress $\gamma_{t,1}$ was only a small portion of the total porosity (from 0.07% to 0.77%). The elastic modulus of the soft part (from 2.83 to 14.81 MPa) was significantly smaller than the general rock bulk modulus. The values of $k_{e,1}$ were significantly smaller than the total permeability, suggesting that the soft part makes the major contribution to the total permeability at low effective-stress range. In addition, the soft-part permeability is nicely correlated to the soft-part porosity by a power law with exponent m from 1.62 to 3.03, which validates our hypothesis that the soft-part permeability is controlled by the slot-like micro-cracks.

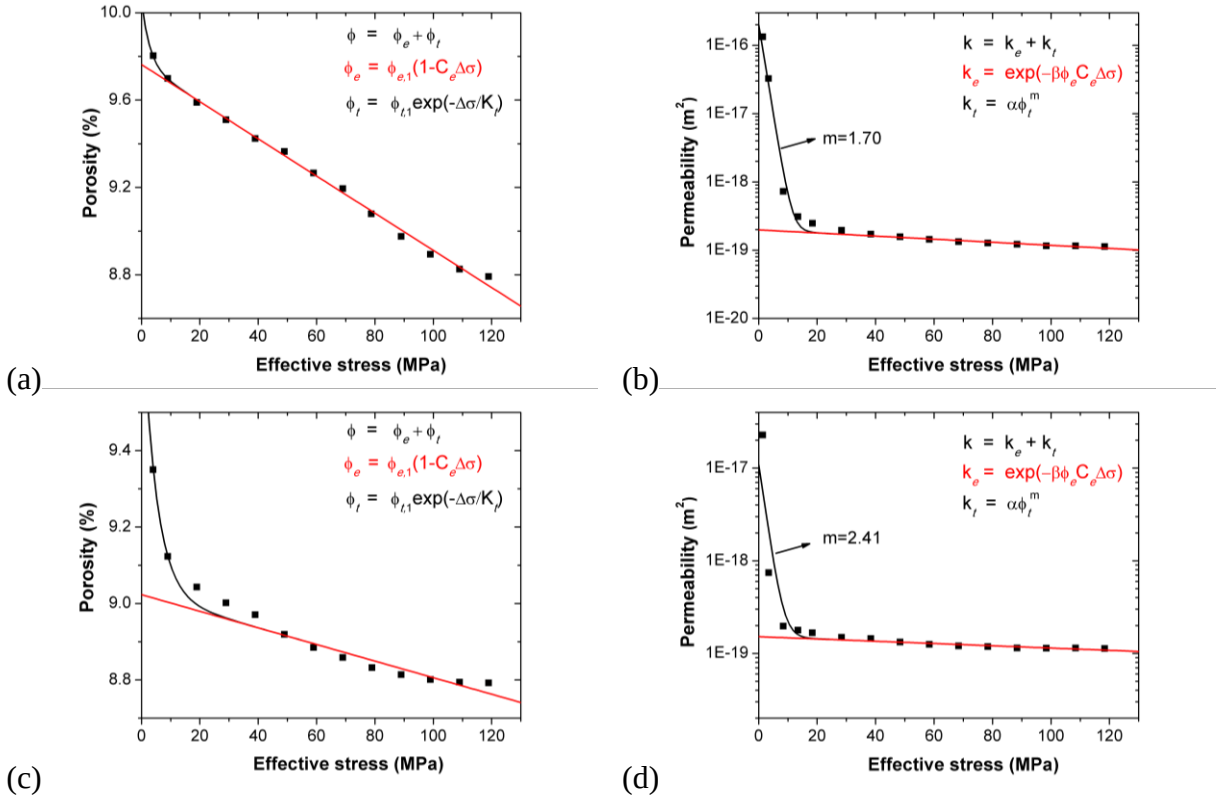

Figure 2.2. The matching result of the proposed relationships and the experimental test data for sample R255_sec2. (a) porosity-stress on loading stage. (b) permeability-stress permeability on loading stage. (c) porosity-stress on unloading stage. (d) permeability-stress permeability on unloading stage.

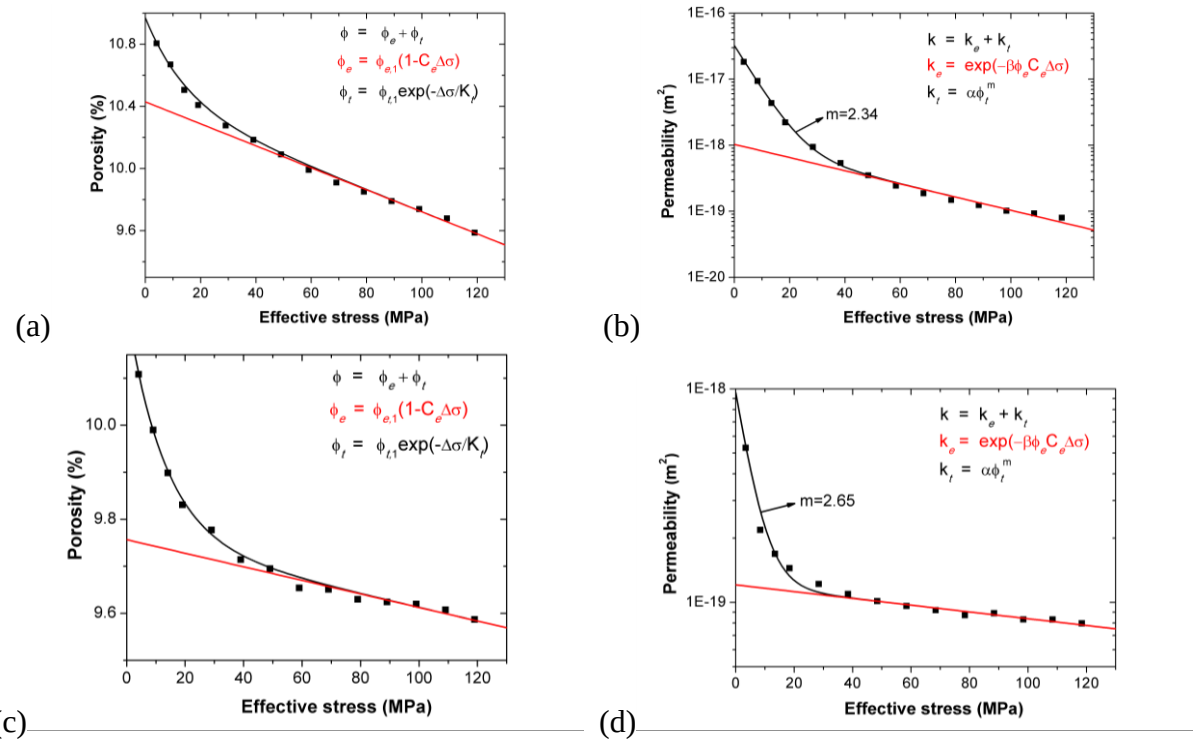

Figure 2.3. The matching result of the proposed relationships and the experimental test data for sample R287_sec1. (a) Stress-dependent porosity on loading stage. (b) Stress-dependent permeability on loading stage. (c) Stress-dependent porosity on unloading stage. (d) Stress-dependent permeability on unloading stage.

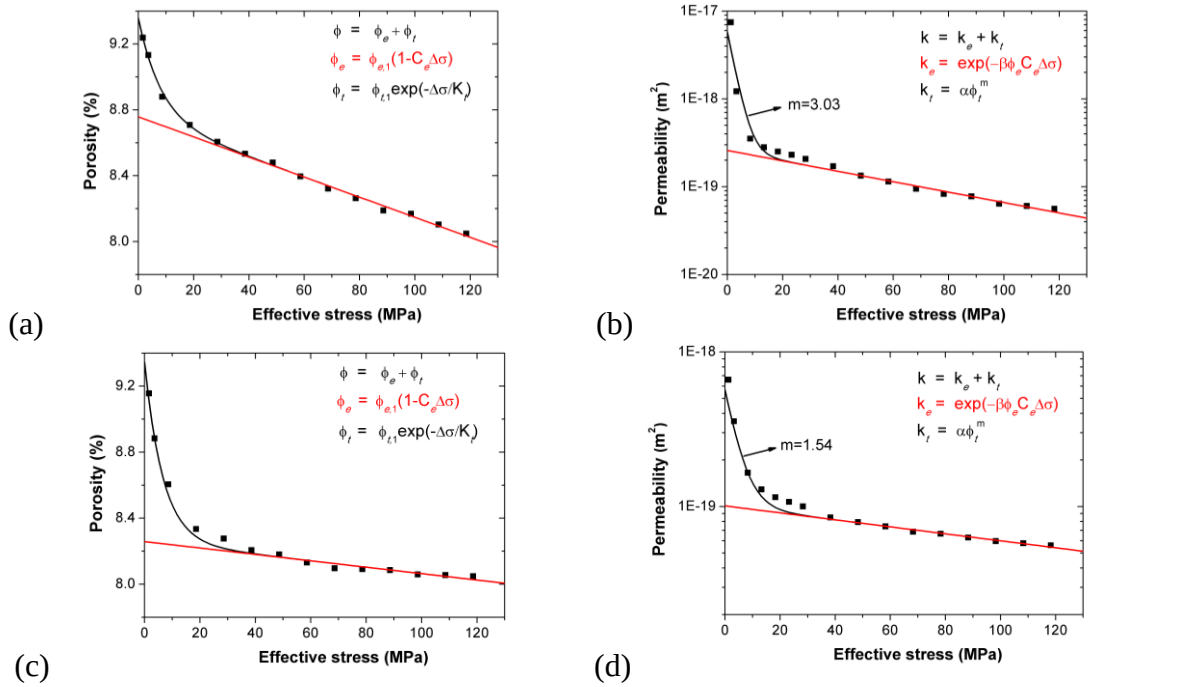

Figure 2.4. The matching result of the proposed relationships and the experimental test data for sample R351_sec2. (a) porosity-stress on loading stage. (b) permeability-stress permeability on loading stage. (c) porosity-stress on unloading stage. (d) permeability-stress permeability on unloading stage.

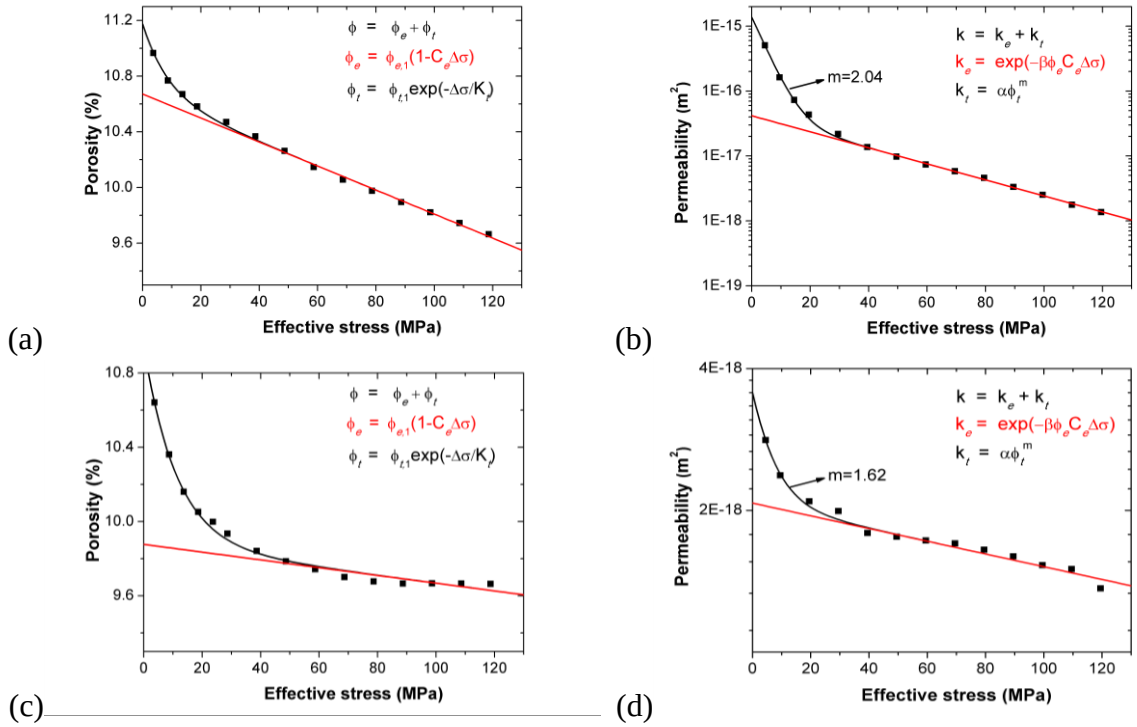

Figure 2.5. The matching result of the proposed relationships and the experimental test data for sample R351_sec3. (a) porosity-stress on loading stage. (b) permeability-stress permeability on loading stage. (c) porosity-stress on unloading stage. (d) permeability-stress permeability on unloading stage.

Table 2.2. Fitted parameter values from the experimental data of Dong et al. (2010).

Sample		$\phi_{e,1}$ (%)	$\gamma_{t,1}$ (%)	C_e (MPa^{-1})	K_t (MPa)	$k_{e,1}$ (m^2)	β	α (m^2)	m	R^2
R255_	Loading	9.73	0.07	8.75×10^{-4}	2.83	1.97×10^{-19}	0.61	1.66×10^{-15}	1.70	0.94
sec2	Unloading	9.01	0.34	2.41×10^{-4}	4.84	1.51×10^{-19}	1.30	1.99×10^{-17}	2.41	0.69
R287_	Loading	10.40	0.41	6.81×10^{-4}	14.81	9.54×10^{-19}	3.25	1.32×10^{-16}	2.34	0.99
sec1	Unloading	9.75	0.36	1.48×10^{-4}	13.04	1.19×10^{-19}	2.53	5.53×10^{-18}	2.65	0.91
R351_	Loading	8.75	0.49	6.97×10^{-4}	8.09	2.54×10^{-19}	2.24	2.61×10^{-17}	3.03	0.83
sec2	Unloading	8.26	0.90	2.35×10^{-4}	6.67	1.01×10^{-19}	2.68	4.12×10^{-19}	1.54	0.95
R390_	Loading	10.64	0.33	8.11×10^{-4}	8.74	3.66×10^{-17}	3.30	5.42×10^{-15}	2.04	0.99
sec3	Unloading	9.87	0.77	2.12×10^{-4}	11.30	2.04×10^{-18}	1.49	1.33×10^{-18}	1.62	0.95

2.6.3 Match of Klinkenberg corrected permeability data using TPHM based relationships

The permeability measured using gas as the test fluid is generally higher than when using water, due to the Klinkenberg gas slippage effect (Klinkenberg 1941). As discussed in Tanikawa and Shimamoto (2009), the Klinkenberg effect is important when the permeability is lower than 10^{-18} m^2 and when there is little pore-pressure difference on the different sides of the test sample. The

following equations, suggested by Tanikawa and Shimamoto (2009) and Dong et al. (2010), are used in this study to correct the measured permeability data.

$$k_g = k_l[1 + (b/P_{av})] \tag{2.27}$$

where k_g is the measured gas permeability, k_l is the corrected permeability using Klinkenberg correction, and P_{av} is the average pore pressure, which could be calculated using Dong et al. (2010):

$$P_{av} = 2(P_u^2 + P_u P_d + P_u^2)/3(P_u + P_d) \tag{2.28}$$

where P_u denotes upper-end pore pressure, P_d denotes the lower-end pore pressure, assumed at atmospheric pressure. b is the Klinkenberg slip factor and can be obtained using the following equation, based on the experimental data (Tanikawa and Shimamoto, 2009):

$$b = 0.15 \times k_l^{-0.37} \tag{2.29}$$

The same procedure is used to determine the parameters in the permeability-stress relationship for Klinkenberg corrected permeability. The matching results for the Klinkenberg corrected permeability are shown in Figures 2.6-2.9. The determined value of $k_{e,1}$, α, β, m and the coefficient of determination R^2 are listed in Table 2.3.

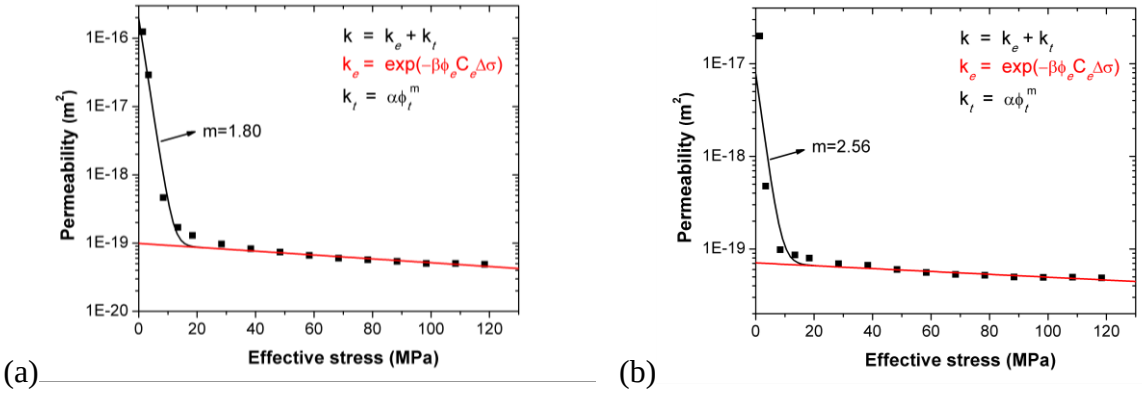

Figure 2.6. The Klinkenberg corrected permeability matching result of the proposed relationships and the experimental test data for sample R255_sec2. (a) Stress-dependent permeability on loading stage. (b) Stress-dependent permeability on unloading stage.

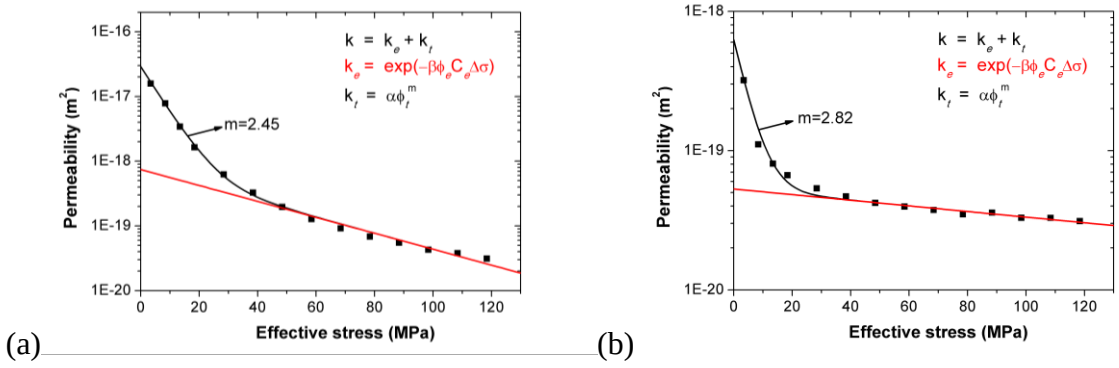

Figure 2.7. The Klinkenberg corrected permeability matching result of the proposed relationships and the experimental test data for sample R287_sec1. (a) Stress-dependent permeability on loading stage. (b) Stress-dependent permeability on unloading stage.

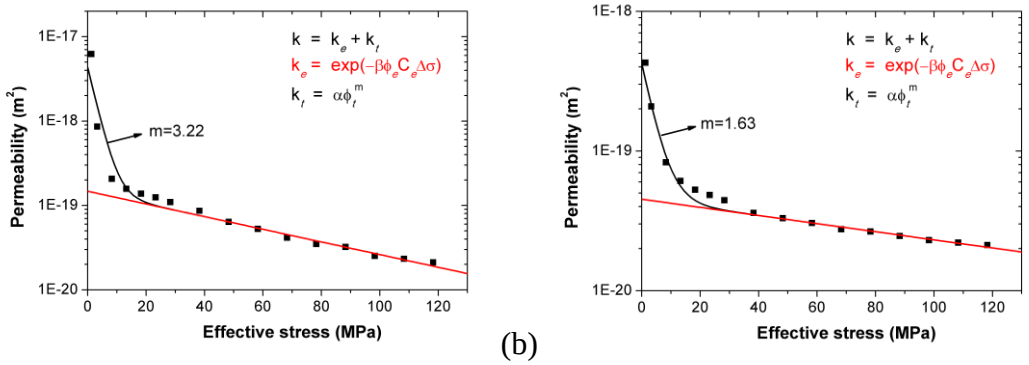

(a) (b)

Figure 2.8. The Klinkenberg corrected permeability matching result of the proposed relationships and the experimental test data for sample R351_sec2. (a) Stress-dependent permeability on loading stage. (b) Stress-dependent permeability on unloading stage.

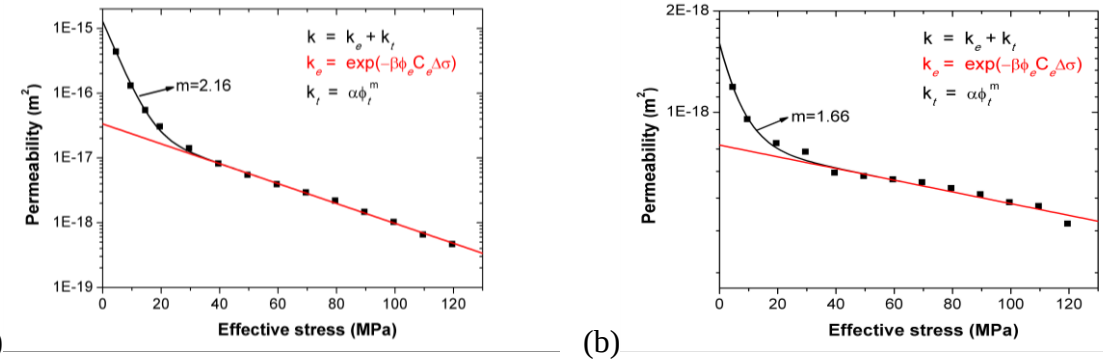

(a) (b)

Figure 2.9. The Klinkenberg corrected permeability matching result of the proposed relationships and the experimental test data for sample R390_sec3. (a) Stress-dependent permeability on loading stage. (b) Stress-dependent permeability on unloading stage.

Table 2.3. Fitted parameter values for stress-dependent relationship of Klinkenberg corrected permeability.

Sample		$k_{e,1}$ (m^2)	β	α (m^2)	m	R^2
R255_sec2	Loading	9.80×10^{-20}	0.76	1.82×10^{-15}	1.80	0.94
	Unloading	7.05×10^{-20}	1.64	1.70×10^{-17}	2.56	0.68
R287_sec1	Loading	6.75×10^{-19}	4.00	1.28×10^{-16}	2.45	0.99
	Unloading	5.22×10^{-20}	3.23	4.24×10^{-18}	2.82	0.91
R351_sec2	Loading	1.44×10^{-19}	2.83	2.39×10^{-17}	3.22	0.82
	Unloading	4.48×10^{-20}	3.45	3.30×10^{-19}	1.63	0.94
R390_sec3	Loading	2.85×10^{-17}	4.10	5.46×10^{-15}	2.16	0.99
	Unloading	7.85×10^{-19}	1.92	7.20×10^{-19}	1.66	0.95

In general, the Klinkenberg corrected permeability k_l is smaller than the gas-measured permeability k_g. After the Klinkenberg correction, the $k_{e,1}$ value decreases, and the stress sensitivity coefficient β for the hard part increases. In addition, the porosity sensitivity parameter for soft part m increases slightly, which means that the Klinkenberg corrected permeability drops quicker with the porosity decrease at low stress range. The coefficient of determination R^2 remains almost the same.

2.7 Concluding remarks

Redistribution of *in situ* stresses and rearrangement of rock structures leads to development of EDZ. In the one hand, field investigations conducted at underground laboratories have shown that the permeability of the EDZ can be one or more orders of magnitude higher than the unaltered argillaceous rock. For these conditions, the EDZ could then act as a preferential flow path for advective transport and thereby speed up radionuclide migration toward the biosphere. On the other hand, laboratory and field studies (Bossart et al., 2004; Baechler et al., 2011; Armand et al., 2013) suggest that a partial or complete self-sealing of fractures due to clay swelling and creep within the EDZ is possible after a certain amount of time. The self-sealing process can potentially decrease the EDZ permeability over time, which may eventually return to the values of the unaltered rock. In either case, permeability in EDZ shows strong stress-dependence. An accurate mathematical representation of the permeability-stress relationship is therefore critical for understanding the evolution of permeability and predicting the permeability changes during excavation and self-healing stages.

Because of its importance in other engineering applications such as fossil-fuel exploitation and CO_2 geological sequestration, the stress-dependence of permeability and porosity has been widely studied. The permeability and porosity change with effective stress for argillite is featured with significant permeability changes with relatively small changes in effective stress and porosity. Some empirical relationships were established between permeability and effective stress based on laboratory-measured data. Representative relationships include exponential law and power law. However, the exponential law yields poor fitting in low effective-stress ranges, and the power law gives unreasonable predictions for certain effective-stress values. Moreover, to describe the relationship between the significant permeability change and the insignificant porosity change has been a great challenge for scientists over a long period of time. Up to now, empirical relationships, usually in the form of a power law, were established based on laboratory-measured data to relate permeability and porosity. The underlying assumption in relating permeability changes to the total porosity change is that the reduction of the total volume of pore space is the only driver for the permeability change—an assumption that leads to some problems with these relationships, one of which is the abnormally high value for the exponent, which is up to 70 in some studies (David et al., 1994; Dong et al., 2010). The extremely high exponent in the current power law for the relationship between permeability and porosity suggests that relating permeability changes to the total porosity changes is not a valid assumption. In this report we established relationships that are more physically robust for low permeability rock.

Based on the concept of the two-part Hooke's model Liu et al. (2009; 2011), in which rock body is conceptually divided into "soft" and "hard" parts, we derived a series of stress-porosity, stress-permeability and permeability-porosity relationships. The derived relationships explain well the stress-dependence of permeability and porosity in the low effective-stress ranges for low-

permeability rock such as argillite, and they have been validated by the published data. These relationships provide a critical link between hydrological to mechanical properties and will greatly improve our capability of modeling the coupled processes for a radioactive waste repository.

In the future, we hope to further validate the derived constitutive relationships with more comprehensive experimental data. Then these relationships will be implemented in our simulator TOUGHREACT-FLAC3D to evaluate the evolution of the EDZ for an argillite repository.

3. Discrete Fracture Network (DFN) Approach for Fractures in Argillaceous Rock

Although clay-rich formations are usually characterized by low intrinsic rock permeability and very limited fracture permeability, observations indicate that permeable fracture networks can form for limited times (e.g., Bossart et al., 2004; Cosgrove, 2001). There are two classes of fracturing that require investigation: (1) fracturing around an excavation in the excavation damaged zone (EDZ) and (2) natural fracturing.

Fractures in the EDZ have been routinely observed in clay-rock underground research laboratories (URL) in Europe, including the Opalinus Clay in Switzerland, Boom Clay in Belgium, and the Callovo-Oxfordian Clay in France (Volckaert et al., 2004). These fractures form as a consequence of tectonic disturbance by excavation, shrinkage caused by ventilation dry-out, and other conditions that are expected during the pre-closure phase of a repository. However, post-closure effects, such as thermal pressuring and gas evolution may also result in fracturing (Blümling et al., 2007). The EDZ not only exhibits fracturing along tunnel surfaces, but can contain fracture damage in thin zones (<~1 m) around drifts, which has been verified from measurements of permeability in that area (Bossart et al., 2004). Finally, fractures in clay-rich formations also show significant self-sealing over a three-year period (Bossart et al., 2004). The connectivity of fractures along a tunnel has been observed in the HG-A test at Mont Terri, Switzerland, where a test tunnel section, sealed by a packer, was injected with fluid that showed preferential pressure increases along the packer where the most severe EDZ damage was observed (Lanyon et al., 2009).

Fracturing has also been observed in clay-rich formations as a result of natural processes, often associated with abnormal pore-pressure conditions. These can lead to fault reactivation and hydraulic fracturing. Geologic evidence suggests that the Mercia Mudstone within the Bristol Channel Basin in the UK was subject to repeated episodes of natural hydraulic fracturing over its 250 million year history (Cosgrove, 2001). This mudstone underwent 150 M years of burial followed by 100 million years of uplift. Outcrop evidence shows that natural fractures formed, conducted fluids, and then sealed at various points in time both during burial and uplift.

The main inference to be drawn from the observations is that fractures in argillaceous rocks are transient features that require a dynamic modeling approach. In this part of the report, we mainly focus on the first case of fracturing process, which undergoes relatively in a short period, such as the excavation damage fracturing. The TOUGH-RBSN model is applied to simulate coupled thermal-hydrological-mechanical (THM) processes including fracture initiation, propagation, and evolution in rock formations.

3.1 Overview of the RBSN Approach for Mechanical Damage Modeling of Geomaterials

Discrete models have been used to study the heterogeneous characteristics of geological systems, with advantages in modeling mechanical behavior accompanied by discontinuities, such as fracture processes. The Rigid-Body-Spring Network (RBSN) approach, as a kind of discrete model, represents the system behavior by simple two-node elements interconnected on a set of nodal points. The RBSN formulation is based on the concept of the Rigid-Body-Spring Model (RBSM), first introduced by Kawai (1978), in which the material constitution is represented as a collection of rigid bodies connected by spring sets.

The RBSN model adopts the Voronoi diagram for partitioning the domain and the dual Delaunay tessellation for constructing the assembly of lattice elements. A lattice element is formed from a spring set, which is connected to neighboring nodes *i* and *j* via rigid-body constraints (Figure 3.1). The spring set has zero size since the rigid arm constraints relate to the same position, *C* (the centroid of the common Voronoi cell boundary). For the case of 3-D modeling, three displacements and three rotations are defined at each node, and the rigid-body constraints link these nodal degrees of freedom to the generalized relative displacements of the spring set. The spring set consists of three axial springs and three rotational springs acting independently, with stiffnesses $\mathbf{D} = \mathrm{diag}[k_n, k_s, k_t, k_{\phi n}, k_{\phi s}, k_{\phi t}]$ in local *n*-*s*-*t* coordinates. The local spring coefficients are defined according to the geometrical features of Voronoi diagram:

$$k_s = k_t = \alpha_1 k_n = \alpha_1 \alpha_2 E \frac{A_{ij}}{h_{ij}}, \quad k_{\phi n} = E \frac{J_p}{h_{ij}}, \quad k_{\phi s} = E \frac{I_{ss}}{h_{ij}}, \quad k_{\phi t} = E \frac{I_{tt}}{h_{ij}} \tag{3.1}$$

in which *E* is the elastic modulus, J_p, I_{ss}, and I_{tt} are the polar and two principal moments of inertia of the Voronoi cell boundary with respect to the centroid, respectively. The axial and rotational springs are scaled in proportion to the lattice element length h_{ij}, and the area of the Voronoi cell boundary A_{ij}. Effective (i.e., macroscopic) Poisson ratio can be adjusted by setting α_1 and α_2 for the axial spring coefficients, but a local description of Poisson effect is not realized. For the special case of $\alpha_1 = \alpha_2 = 1$, the Voronoi scaling of the spring coefficients enables the model to be elastically homogeneous under uniform modes of straining, albeit with zero effective Poisson ratio (Bolander and Saito, 1998; Asahina et al., 2011).

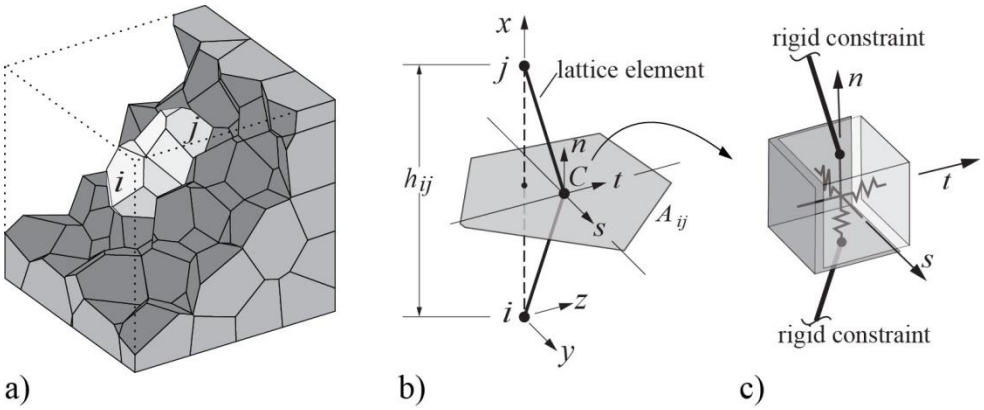

Figure 3.1. Typical RBSN element ij: a) within a Voronoi grid; b) isolated from the network; and c) a zero-size spring set located at centroid C of Voronoi cell boundary area A_{ij} (rotational springs have been omitted for clarity).

The RBSN model provides a discrete representation of fracture in the matrix material. Crack movement is constrained to occur along cell boundaries; therefore, the lattice orientation is important for the fracture representation. The random lattice geometry based on the Delaunay-Voronoi discretization reduces mesh bias on the cracking directions (Bolander and Saito, 1998).

Fracture is represented by the damage/breakage of the springs. For the damaged spring set, the local stiffness matrix is

$$\mathbf{D}' = (1 - \omega)\mathbf{D} \tag{3.2}$$

where ω is a scalar damage index with a range from 0 (undamaged) to 1 (completely damaged). In the modeling of brittle fracturing, which is applied to the cases presented in this report, ω is either 0 or 1. Fracture may initiate within a lattice element when the applied stress exceeds the given material strength. To determine the stress state, a stress ratio is calculated for each lattice element:

$$R_f = \sigma_e / \hat{\sigma} \tag{3.3}$$

where σ_e is the measure of the element stress and $\hat{\sigma}$ is the material strength. During iterative calculations, only one element, with the most critical stress state (i.e., the largest $R_f \geq 1$), is allowed to break per iteration, and the fracture event entails a reduction of spring stiffnesses (Equation (3.2)) and a release of the associated elemental forces.

In this study, a Mohr-Coulomb criterion is used to determine the fracture event. Figure 3.2 shows the fracture surface defined by three parameters: the angle of internal friction ψ (surface inclination with respect to σ_n-axis); cohesive strength c (surface intersection with the shear axes); and the tensile strength f_n (tension cut-off). Nodal displacements produce forces F_n, F_s, and F_t in the respective axial springs, and dividing these spring forces by the cell boundary area A_{ij} yields measures of stress $P(\sigma_n, \sigma_s, \sigma_t)$. The criticality of the stress state is assessed as $R_f = \overline{OP}/\overline{OP_O}$, where P_O is the point at which $\overline{OP}$ intersects the fracture surface.

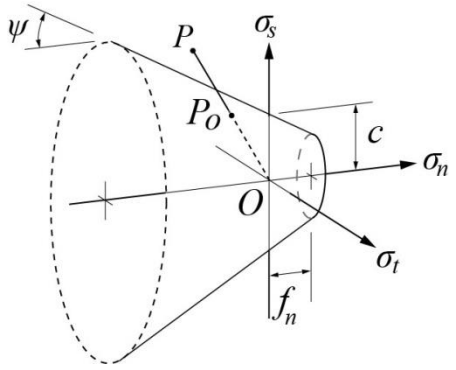

Figure 3.2. Mohr-Coulomb fracture surface with tension cut-off.

3.2 Representation of Anisotropy

Most sedimentary and metamorphic rocks (e.g., shales and slates) have directional features such as bedding, foliation, and flow structures that result in anisotropic mechanical behavior. These types of rocks usually exhibit transversely isotropic elastic properties in macro-scale. For example, Young's modulus parallel to bedding of the Opalinus Clay has been observed to be greater than normal to the bedding (Bossart, 2012). Anisotropic features may also be found in strength properties. In this section, a new scheme is proposed to represent the anisotropic rock properties in the RBSN model. The novelty of the new modeling scheme is the use of unstructured Voronoi grids without manipulating the mesh geometry, and straightforward formulations to construct the local stiffness matrix reflecting the anisotropy.

3.2.1 Anisotropic elastic properties

Figure 3.3 shows the arrangements of spring sets within a Voronoi grid and the corresponding lattice elements. A 2-D modeling case is illustrated to simplify visualization of the geometry, but the method is applicable to 3-D. In the ordinary RBSN model, the spring sets are oriented to their individual local coordinates defined by the Voronoi diagram (Figure 3.3a, and refer to Figure 3.1 for 3-D formations). In the new scheme, by comparison, all the spring sets are aligned to the principal bedding direction. The spring coefficients are defined in global fabric coordinates, where two orthogonal *N*- and *P*-axes are normal and parallel to bedding, respectively (Figure 3.3b). The formulation of the spring coefficients is based on the local geometry of the Voronoi diagram and a logical extension to Equation (3.1) for anisotropic materials. Transversely isotropic elastic properties are calculated by using two different Young's moduli related to the bedding direction:

$$k_N = E_N \frac{A_{ij}}{h_{ij}}, \quad k_P = E_P \frac{A_{ij}}{h_{ij}}, \quad k_\phi = E_N \frac{I_\phi}{h_{ij}} \tag{3.4}$$

where E_N and E_P are Young's moduli normal and parallel to bedding, respectively, which can be directly determined from laboratory measurements.

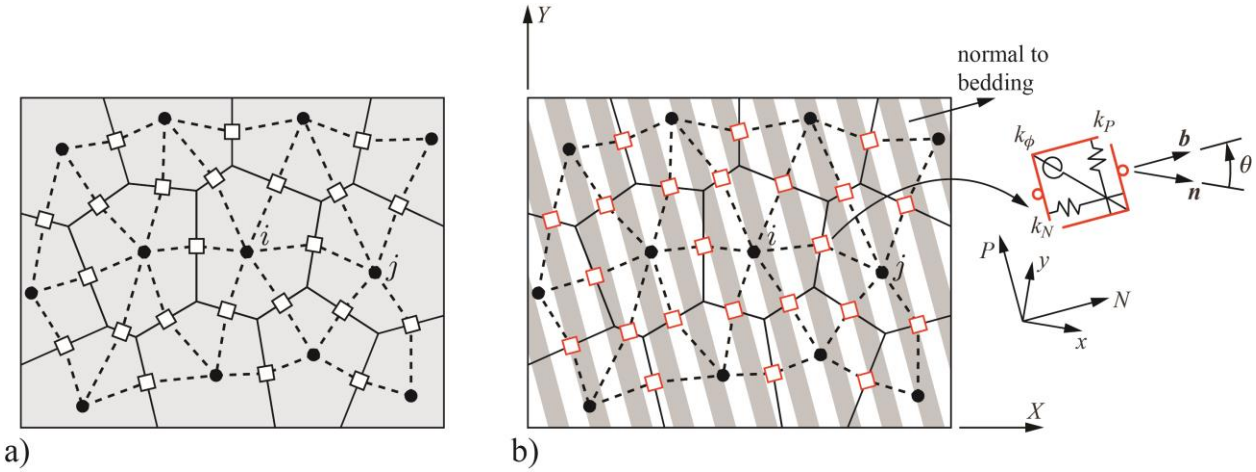

Figure 3.3. Arrangements of the spring sets in the identical lattice structure: a) the ordinary RBSN approach representing isotropic materials; and b) modified orientation of spring components with transversely isotropic elastic properties.

As seen in Figure 3.3b, three distinct coordinate systems are considered for representation of kinematic quantities: global *X*-*Y* coordinates based on domain construction; local *x*-*y* coordinates for individual elements; and global *N*-*P* coordinates related to the orientation of fabric. For each spring set, the spring stiffness matrix is established in *N*-*P* coordinates:

$$\mathbf{k}_b = \begin{bmatrix} k_N & & \\ & k_P & \\ & & k_\phi \end{bmatrix} \tag{3.5}$$

Although the derivation is invariant to coordinate systems, it is more convenient for matrix formulation to represent and manipulate the stiffness quantities in local *x*-*y* coordinates rather than in global *N*-*P* coordinates. Thus the spring stiffness matrix, $\mathbf{k}_b$, is transformed to local *x*-*y* coordinates using following coordinate transformation (McGuire and Gallagher, 1979):

$$\mathbf{k}_s = \boldsymbol{\gamma}^T \, \mathbf{k}_b \, \boldsymbol{\gamma} \tag{3.6}$$

where $\boldsymbol{\gamma}$ is the 3×3 coordinate transformation matrix from local (*x*-*y*) to global fabric (*N*-*P*) coordinates:

$$\boldsymbol{\gamma} = \begin{bmatrix} Nx & Ny & 0 \\ Px & Py & 0 \\ 0 & 0 & 1 \end{bmatrix} \tag{3.7}$$

The first 2×2 entries in $\boldsymbol{\gamma}$ are the direction cosines between the bedding direction and the local coordinate axes.

The element stiffness matrix, $\mathbf{k}_e$ (with respect to local *x*-*y* coordinates), is obtained by post- and pre-multiplication of $\mathbf{k}_s$ by the geometric transformation matrix that relates the generalized relative displacements at the spring set to the nodal displacements. Detailed formulation is presented elsewhere (Bolander and Saito, 1998; Berton and Bolander, 2006).

Finally, the element stiffness matrix is transformed to global coordinates in a similar way to Equation (3.6):

$$\mathbf{K}_e = \boldsymbol{\Gamma}^T \, \mathbf{k}_e \, \boldsymbol{\Gamma} \tag{3.8}$$

where $\boldsymbol{\Gamma}$ is the coordinate transformation matrix from global domain (*X*-*Y*) to local (*x*-*y*) coordinates. The transformed element stiffness matrices, $\mathbf{K}_e$, for individual lattice elements are assembled into the system stiffness matrix.

3.2.2 Anisotropic failure properties

Anisotropic strength in failure behavior is represented in the RBSN with an anisotropic version of the Mohr-Coulomb criterion. On the notion of microstructure of the RBSN model, the anisotropy of the strength parameters is represented based on the relative rotation θ, between normal to bedding and normal to the Voronoi cell boundary (Figure 3.3b). The dot product of the unit vectors in these two directions gives

$$\cos\theta = \boldsymbol{b} \cdot \boldsymbol{n} \tag{3.9}$$

Spatial variations of the strength parameters are calculated as linear scalar functions of the fabric tensors. The concept of the fabric tensor is introduced by Pietruszczak and Mroz (2001). The diagonal entries of the fabric tensor, representing the spatial bias of the strength parameters, are

summed to be zero. For the Mohr-Coulomb fracture criterion, the friction angle, cohesion, and tensile strength can be calculated respectively as

$$\psi = \psi_0[1 + \Omega^{\psi}(1 - 3\cos^2\theta)] \tag{3.10}$$

$$c = c_0[1 + \Omega^{c}(1 - 3\cos^2\theta)] \tag{3.11}$$

$$\sigma = \sigma_0[1 + \Omega^{\sigma}(1 - 3\cos^2\theta)] \tag{3.12}$$

where ψ_0, c_0, and σ_0 are constant coefficients; and Ω^{ψ}, Ω^{c}, and Ω^{σ} are the intensities of anisotropy. Equations (3.10), (3.11), and (3.12) can be written in a generalized form as

$$s = s_0[1 + \Omega(1 - 3\cos^2\theta)] \tag{3.13}$$

The strength parameter becomes the minimum $s_{min} = s_0(1 - 2\Omega)$ when the Voronoi cell boundary is parallel to the bedding plane (i.e., $\theta = 0^{\circ}$), and the maximum $s_{max} = s_0(1 + \Omega)$ when the Voronoi cell boundary and the bedding plane are orthogonal (i.e., $\theta = 90^{\circ}$). Then, Equation (3.13) can be rewritten as

$$s = s_{min}\cos^2\theta + s_{max}(1 - \cos^2\theta) \tag{3.14}$$

This spatial correlation function serves the local failure with some preferred characteristics in accordance with the orientation of fabric. By virtue of the random geometry of the Voronoi grid, the model can inherently represent heterogeneity as well as anisotropy in the failure behavior of geomaterials.

3.3 Coupled THM Models using TOUGH-RBSN Simulator

3.3.1 Coupling procedure

This section describes the linkage between the multiphase flow simulator TOUGH2 and the RSBN model. Several advantages of the coupled TOUGH-RBSN simulator stem from the availability of sharing the same geometrical mesh structure based on the Voronoi discretization techniques (Okabe et al., 2000), which allow representation of dynamically forming discrete fracture networks (DFNs) within a rock matrix in a simple and straightforward manner.

Rutqvist et al. (2002) have developed the TOUGH-FLAC software, which is based on linking TOUGH2 with FLAC3D, a continuum geomechanical modeling code. The general coupling procedure of TOUGH-RBSN is basically similar to that of the TOUGH-FLAC simulator, but the coupling modules to handle the thermal-hydrological and mechanical quantities are substantially modified and extended for modeling the existence of the DFNs. TOUGH2 is used to simulate scalar quantities (e.g., temperature, pressure, and degree of saturation) associated with fluid flow and heat transport, whereas RBSN accounts for mechanical quantities (e.g., displacement, strain, and stress) of interest. Such primary variables are coupled through simplified linear relationships or through nonlinear empirical expressions, which could be estimated by laboratory experiments with appropriate calibration. As previously noted, both models share the same unstructured, 3-D Voronoi grid and the same nodal information, which simplifies their data exchange.

Figure 3.4 shows a schematic flow diagram of the coupling procedure between TOUGH2 and RBSN, which are currently linked through external modules that handle two-way coupling of the relevant quantities at each time step. First, the TOUGH2 to RBSN link, shown on the left side of Figure 3.4, supplies multiphase pressure, temperature, and degree of saturation to update the mechanical quantities. For multiphase liquid, the choice of the definition of pore pressure is

problem-specific and depends on the target materials. Various approaches to determine the pore pressure have been exampled elsewhere (Rutqvist et al., 2001a; 2011; Vilarrasa et al., 2010).

The stress applied to the lattice element is modified by the general conventional effective stress law of Biot's theory (Biot and Willis, 1957):

$$\sigma' = \sigma + \alpha_p P \tag{3.15}$$

where σ is the total stress obtained from overall loading, including external loads; σ' is the effective (grain-to-grain) stress; α_p is the Biot effective stress parameter; and P is the pore pressure. Note that the effective stress concept is valid only for the normal stress terms, and tensile stress is taken to be positive. In incremental form, Equation (3.15) becomes

$$\Delta\sigma' = \Delta\sigma + \alpha_p(\Delta P_i + \Delta P_j)/2 \tag{3.16}$$

where ΔP_i and ΔP_j are the changes in pore pressures over the time step at neighboring nodes i and j.

It is assumed that the local changes in temperature and liquid saturation induce strain as follows:

$$\Delta\varepsilon_T = \alpha_T(\Delta T_i + \Delta T_j)/2 \tag{3.17}$$

$$\Delta\varepsilon_s = \alpha_s(\Delta S_i + \Delta S_j)/2 \tag{3.18}$$

where ε_T is thermal strain; ε_s is shrinkage/swelling strain; α_T is the coefficient of linear thermal expansion; and α_s is the hydraulic shrinkage coefficient. The changes in temperature and saturation are averaged from the variables at nodes i and j. If an expansible soil material is subjected to constant stress conditions in an elastic region, the effective stress due to thermal and swelling/shrinking strains can be calculated as

$$\Delta\sigma' = (\Delta\varepsilon_T + \Delta\varepsilon_s)E \tag{3.19}$$

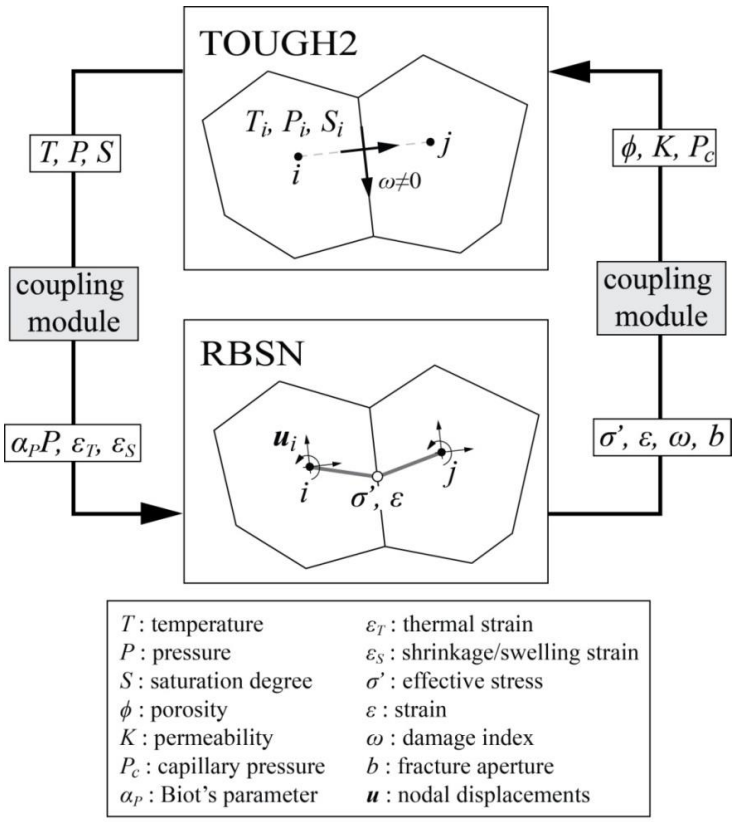

Figure 3.4. Flow diagram of the linkage between the TOUGH2 and the RBSN for coupled THM simulations.

Thereafter, the RBSN to TOUGH2 link, shown on the right side of Figure 3.4, supplies vectorial variables for the effective stress and the strain calculated at the lattice element to update the hydrogeological properties of the corresponding Voronoi cells *i* and *j* in the TOUGH2 model. The following general relations are considered (Rutqvist and Tsang, 2002):

$$\phi = \phi(\boldsymbol{\sigma}', \boldsymbol{\varepsilon}) \tag{3.20}$$

$$K = K(\boldsymbol{\sigma}', \boldsymbol{\varepsilon}) \tag{3.21}$$

$$P_c = P_c(\boldsymbol{\sigma}', \boldsymbol{\varepsilon}) \tag{3.22}$$

where ϕ is porosity, K is permeability, and P_c is capillary pressure.

In the TOUGH2 model using an ordinary Voronoi grid to represent an intact rock matrix, flow and mass transport are enacted only between nodes *i* and *j*, across the Voronoi cell boundary. However, if a fracture occurs within the matrix, substantial flow and mass transport may happen along the fracture length. As an integrated finite volume method, TOUGH2 allows for flexible gridding that can accommodate representation of fractures or fracture networks embedded within the matrix (Zhang et al., 2004; Rutqvist et al., 2013a). By utilizing a discrete fracture approach, continuity of the fracture is not assumed but rather explicitly modeled. A flow through the discrete fracture is activated in response to the damage/breakage of the lattice element from the RBSN simulation (i.e., $\omega \neq 0$). Following Darcy's law, the intrinsic permeability of an individual fracture can be based on a parallel-plate model which relates fracture permeability to

fracture aperture *b* (Bear, 1972). Details about forming fractures and their interconnections within Voronoi grids are presented in the next section.

3.3.2 Discrete representation of flow and mass transport in fractured media

In this study, a fracture is considered to be a discrete feature that facilitates flow and mass transport. Such crack-assisted flow and its permeation into the surrounding matrix are explicitly represented. Pre-existing or newly generated fractures are directly mapped onto the Voronoi grid representing the spatial domain of the geomaterial system. Descriptors of the fracture geometry (e.g., fracture orientation, length, width, shape) can be obtained by field mapping, computer-generated statistical representations, or the simulation outcomes of mechanical models. With reference to the 2-D case, a straight-lined fracture is discretized as follows (Figure 3.5):

- Discretize the spatial domain with an irregular Voronoi grid.
- Overlay the reference fracture onto the Voronoi grid.
- Select node-node (natural neighbor) connections that cross the reference fracture. The corresponding Voronoi cell boundaries of such nodal connections represent the reference fracture.

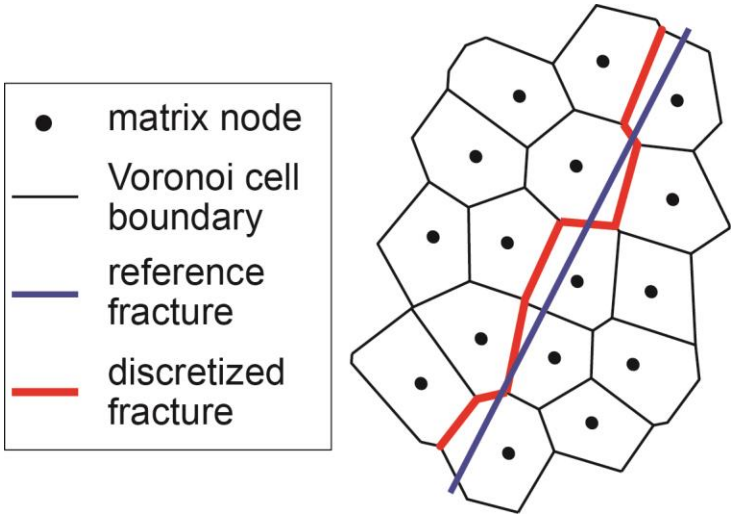

Figure 3.5. Mapping of a fracture geometry onto an irregular Voronoi grid.

The grid size should be selected to obtain a sufficiently accurate representation of the fracture line. As the density of nodal points increases, the discretized fracture path more closely resembles the reference line. By repeating the above process for multiple fractures, a network of discrete fractures can be generated. The advantages of this DFN generation approach include the abilities to: (1) simply activate and connect new discrete fractures; (2) automatically handle discrete fracture intersections; (3) control mesh size with a graded nodal density, which can be advantageous for reducing computational expense; and (4) straightforwardly extend to more complicated 3-D geometries.

Dynamically forming flow channels (i.e., discrete fractures) are implemented by introducing fracture nodes and the associated connections in addition to matrix nodes and connections within the Voronoi grid (Figure 3.6). A fracture node is inserted at the intersection of a Voronoi cell

boundary and a connection between two adjacent matrix nodes. The original matrix-matrix connection is divided into two matrix-fracture (and vice versa) connections by the newly generated fracture node. In addition, the connections between the fracture nodes are established to represent flow channels through the fracture networks. The hydrological properties of an individual fracture can be based on the grid geometry and the local fracture aperture computed by a mechanical-damage model. In the following simulations, however, the fracture permeability is simply assigned to be constant and very high relative to the permeability of the rock matrix.

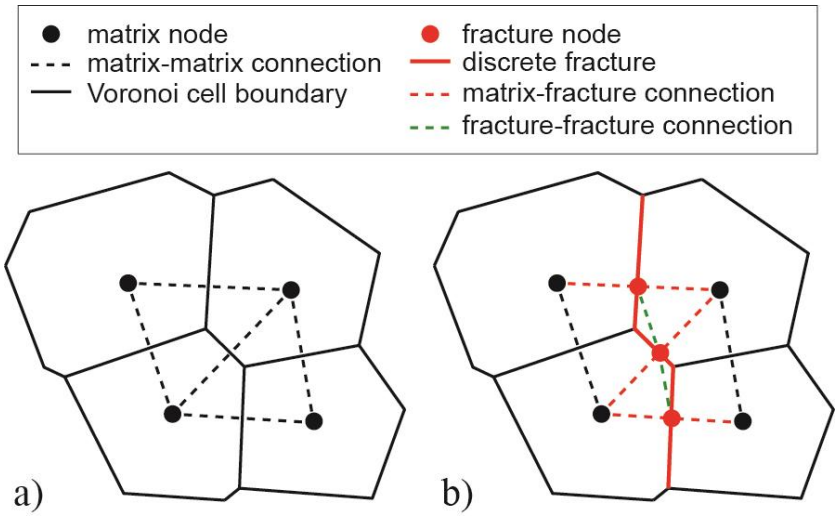

Figure 3.6. Nodal connectivity in the DFN approach for flow simulations: a) ordinary matrix nodes and connections; and b) additional fracture nodes and connections.

3.4 Mechanical Simulations of Transversely Isotropic Rock Formations

3.4.1 Uniaxial compression tests

The modeling scheme proposed in Section 3.2 is validated through uniaxial compression tests for transversely isotropic rock specimens. Consider 2-D configurations of a cylindrical core sample subjected to unconfined uniaxial compression, in which the loading direction forms an angle relative to the bedding plane, β (see Figure 3.7a). In laboratory experiments, the drilling direction for core sampling determines the angle between the axial loading direction and the bedding direction. The simulations consider seven cases of the orientation of fabric: $\beta = 0^{\circ}, 15^{\circ}, 30^{\circ}, 45^{\circ}, 60^{\circ}, 75^{\circ}, 90^{\circ}$. The model is discretized with about 3,800 nodal points and 10,000 elements. Boundary conditions are assigned at top and bottom layers of cells. Incremental loading is applied at the top layers by displacement control and the bottom layers are fixed. Herein the anisotropic mechanical properties of the rock material are adopted from the experimental results for the Opalinus Clay (Bossart, 2012), which are arranged in Table 3.1.

Table 3.1. Anisotropic mechanical properties of the Opalinus Clay (Bossart, 2012).

Rock mechanical properties	Parallel to bedding	Normal to bedding
Young's modulus [GPa]	15.5	9.5
Uniaxial tensile strength [MPa]	2.0	1.0
Cohesion (shear strength) [MPa]	5.5	2.2
Internal friction angle [°]	25	

Note: In Bossart (2012), the experiments on cohesion or shear strength are reported for three different parameters: minimum value of 2.2 MPa (normal bedding), maximum value of 5.5 MPa (parallel bedding), and the third value of 1 MPa (shear strength of bedding planes). In this study, 2.2 MPa is taken as cohesion normal to bedding as stated.

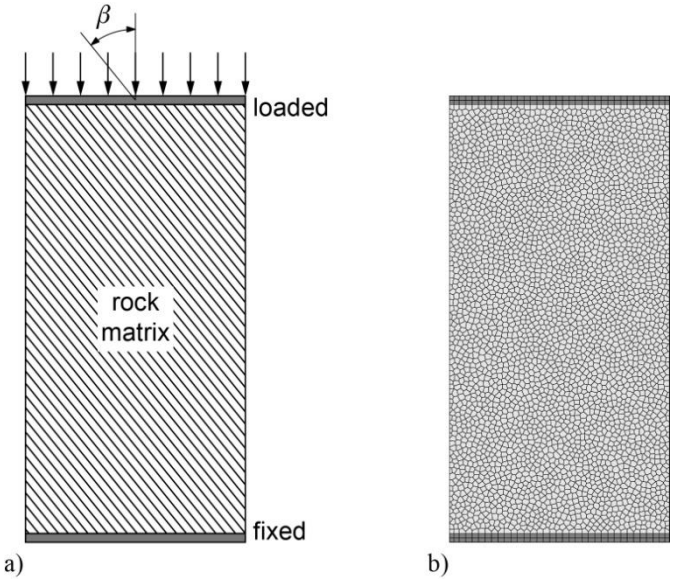

Figure 3.7. 2-D specimen for uniaxial compression test: a) schematic drawing of the test program; and b) model discretization.

The resulting stress-strain curves are plotted in Figure 3.8. The stress response is calculated by dividing the sum of reaction measured at the fixed layers of cells by the cross sectional area of the specimen. In the elastic region, the stress response linearly increases with strain. In the post-peak region, the models exhibit brittle behavior. Once the first breakage (i.e., fracture initiation) occurs at the most critical element, the neighboring elements undergo knock-on breakage even without increasing load/displacement. After sufficient elements have broken to release the energy in the fracture process, the fracture becomes stable in the sense that small load increments no longer produce bursts of elemental breakages. The unstable fracture process can be controlled by introducing softening/energy release rate of fracture in the post-peak behavior.

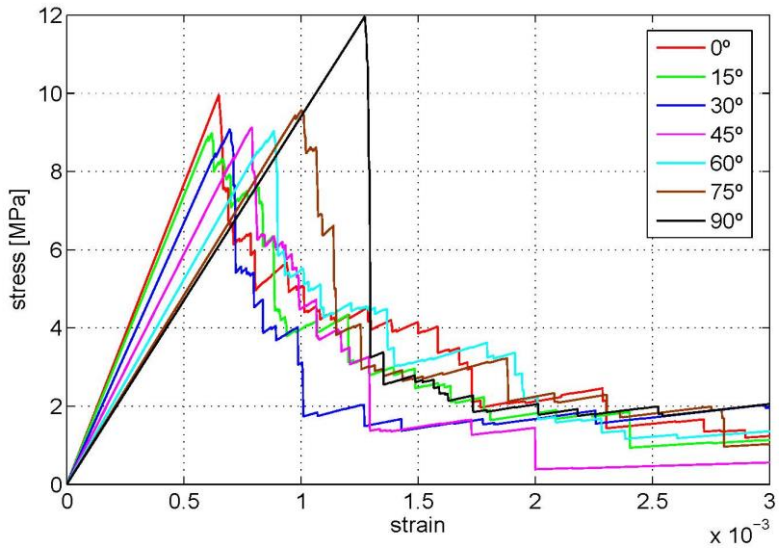

Figure 3.8. Stress-strain curves of transversely isotropic rock specimens with various orientations of bedding with regard to the loading direction.

The anisotropy of the elastic properties can be found in bulk Young's moduli, the slopes of linearly ascending branches in the stress-strain curves of Figure 3.8. Theoretically, the bulk Young's modulus at angle to bedding β can be obtained by (Pariseau, 2006):

$$\frac{1}{E} = \frac{\cos^4\beta}{E_P} + \left(\frac{1}{G_{12}} - \frac{2\nu_{12}}{E_P}\right)\sin^2\beta\ \cos^2\beta + \frac{\sin^4\beta}{E_N} \tag{3.23}$$

where G_{12} is shear modulus and ν_{12} is Poisson ratio. Equation (3.23) shows that the shear modulus greatly influences the variation in Young's modulus, so the shear modulus of anisotropic rock should be measured rather than estimated (Pariseau, 2006). However, the shear modulus can only be approximated in the RBSN model.

For an isotropic material, the shear modulus is derived from elasticity theory, which shows that

$$G = E/2(1+\nu) \tag{3.24}$$

For $\nu = 0$, $G = E/2$. An approximation of this relationship between shear modulus and Young's moduli for an anisotropic system with $\nu = 0$ is given as

$$G_{12} = 1/(\frac{1}{E_P} + \frac{1}{E_N}) \tag{3.25}$$

With this assumption for Equation (3.23), the variation in Young's modulus is depicted in Figure 3.9 and compared with the simulated bulk Young's moduli, where the two curves show a good agreement.

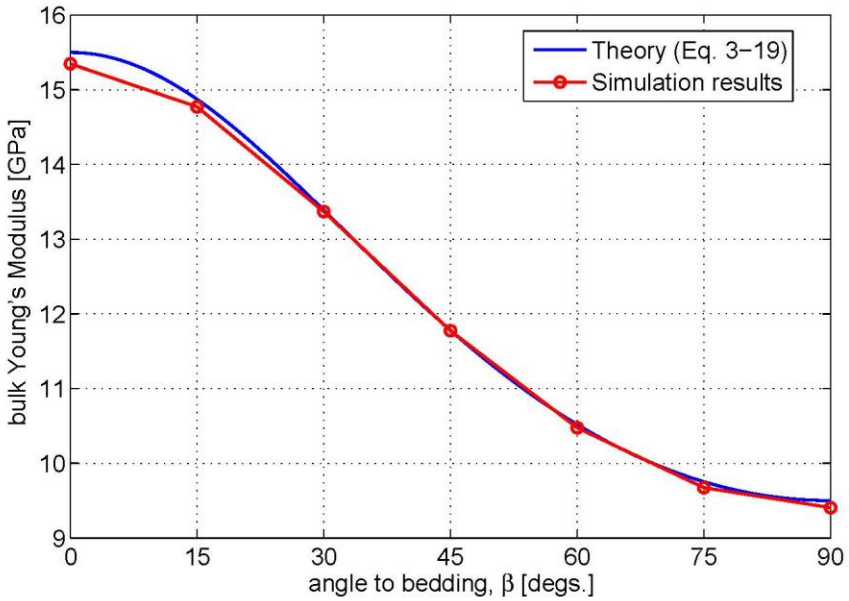

Figure 3.9. Variation of bulk Young's modulus of a transversely isotropic rock.

The peak stress values of the stress-strain curves, plotted in Figure 3.8, can be regarded as uniaxial compressive strengths. A comparison of the peak stresses indicates that the rock exhibits the maximum strength when the bedding is perpendicular to the axial loading (i.e., $\beta = 90^{\circ}$) and the minimum level of strength in cases of the bedding inclined to the loading direction. Similar interpretations of the compression failure of anisotropic rocks have been presented in other studies (Jaeger, 1960; McLamore and Gray, 1967; Kwaśniewski and Mogi, 2000). Quantitatively, however, the strength values are not accurately simulated. In the experiments, the compressive strengths parallel and normal to bedding are measured as 10.5 MPa and 25.6 MPa, respectively (Bossart, 2012). This discrepancy for the compressive strengths might result from the vague choice for the anisotropic shear strength parameters. Also, the RBSN model has been originally developed for simulating tension-dominated behavior, and the proposed fracture criteria generally account for tension failure, which could lead to some shortcomings in modeling of compression or multi-axial failure behavior (Bolander and Saito, 1998; Berton and Bolander, 2006). Currently, the failure is modeled to be brittle, which means the entire strength is lost at immediate failure. However, a more realistic failure response may result in gradual loss of strength during failure. In addition, contacts between fracture surfaces under compressive loads lead to friction along the fracture surface, which is not appropriately represented in the current model. This problem will be addressed in future studies.

Figure 3.10 shows deformed shapes and fracture patterns of the specimens at the final loading stage with the global strain of 0.003. The specimens with the bedding parallel and perpendicular to the loading direction do not demonstrate apparent directivity of the fracture patterns (Figure 3.10a and g). On the contrary, in the cases of the inclined orientations of fabric, the direction of fracturing appears biased towards the bedding direction (Figure 3.10b to f). This directivity of fracture pattern gets stronger with the bedding angle nearing 45°, in which the inclined major cracks are connected across the specimen. An additional case of the bedding angle $\beta = -15^{\circ}$ is considered (Figure 3.10h), in which the orientation of fabric has the same amount but the

opposite direction of rotation from the vertical axis. As expected, a symmetrical fracture pattern with respect to the vertical axis is presented, in comparison to the case of bedding angle $\beta = 15^{\circ}$ (Figure 3.10b).

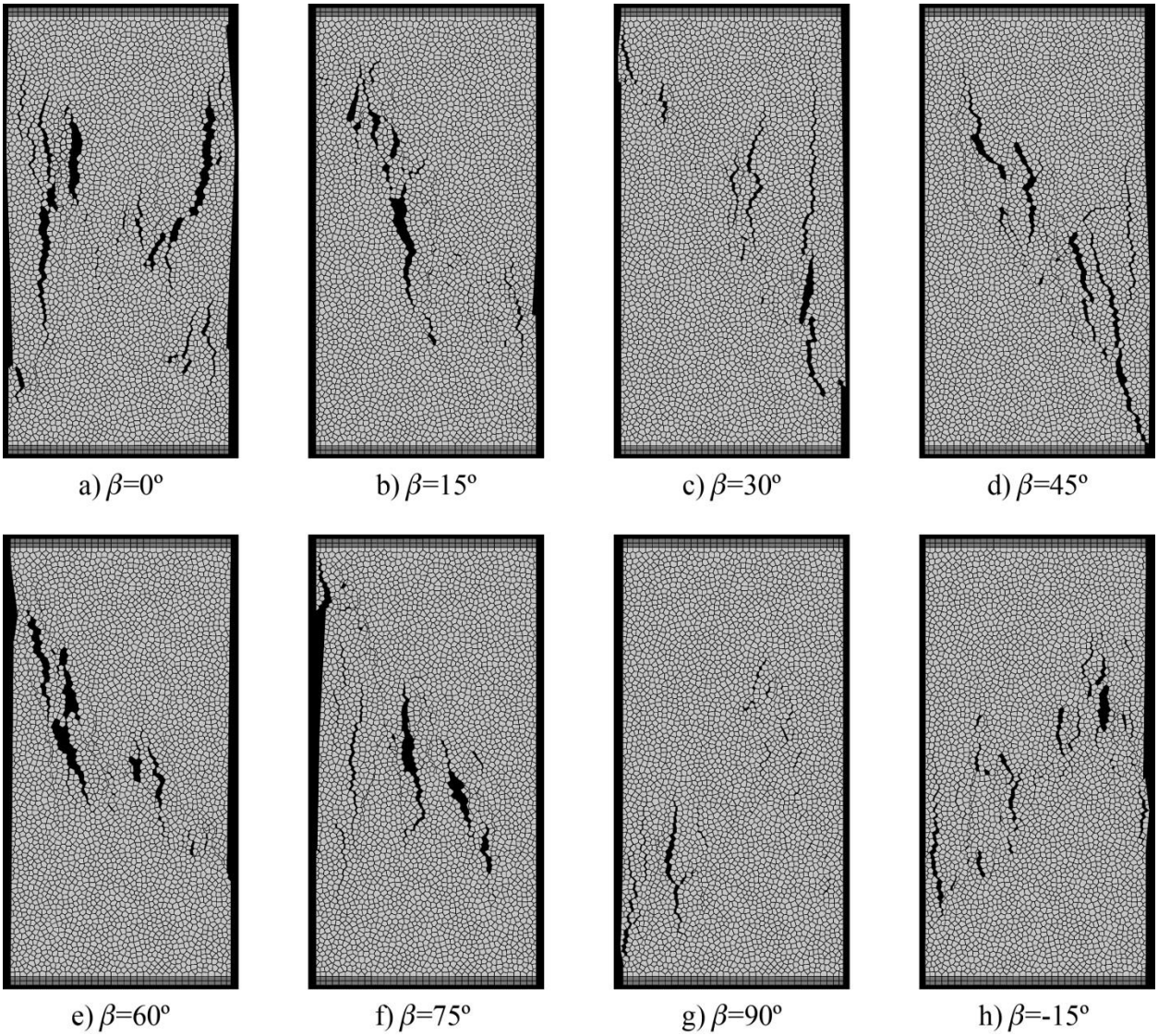

Figure 3.10. Fracture patterns of the specimens with various orientations of fabric forming the angle of β with the loading axis. Note that the positive angle indicates counter-clockwise rotation from the vertical orientation.

In the set of simulations for uniaxial compression tests, the anisotropic characteristics in elastic properties and failure properties are realistically demonstrated. Various bedding angles with respect to the axis of loading are represented by assigning global coordinates related to the orientations of fabric within the same Voronoi grid. By utilizing the proposed modeling scheme, rock materials are represented as macroscopically homogeneous, whereas microscopically, the anisotropic strength parameters, formulated by random local orientations of lattice elements, give intrinsic heterogeneity in failure behavior. This modeling scheme is applied to simulate fracture

processes in the excavation damage zone (EDZ) of the HG-A microtunnel, which is presented in the next section.

3.4.2 Fracture damage modeling of the HG-A test

The HG-A test is being conducted on a 13-m long microtunnel of 1 m diameter, located at the Mont Terri underground research laboratory (URL) near Saint-Ursanne, Switzerland. One main purpose of the HG-A test is to provide data on the geomechanical and hydrogeologic effects of the excavation damage zone (EDZ). The test is specifically targeted to observe how fluids injected into a test section sealed by a packer penetrate both into the rock and within the EDZ (Marschall et al., 2006). Although the long-term physical features observed in the test are related to coupled hydro-mechanical processes, as an initial study, herein the problem is simplified by assuming a constant uniform pore pressure such that fracture damage is simulated using the mechanical modeling of the RBSN approach exclusively. This assumption is valid up until the point at which mechanical deformation occurs much more quickly than water flow processes in the rock formation, where mechanical equilibrium is held within a rapid (undrained) excavation (Liu et al., 2013b).

The rock of the test site is relatively homogeneous in meter-scale, but pronounced bedding was discovered at finer scales (Marschall et al., 2006). The rock formation is highly fractured with frequencies of 0.3 to 1 m, although the fracture permeability is not significant, which indicates that fractures are mostly closed under natural stress conditions (Marschall et al., 2006; 2008).

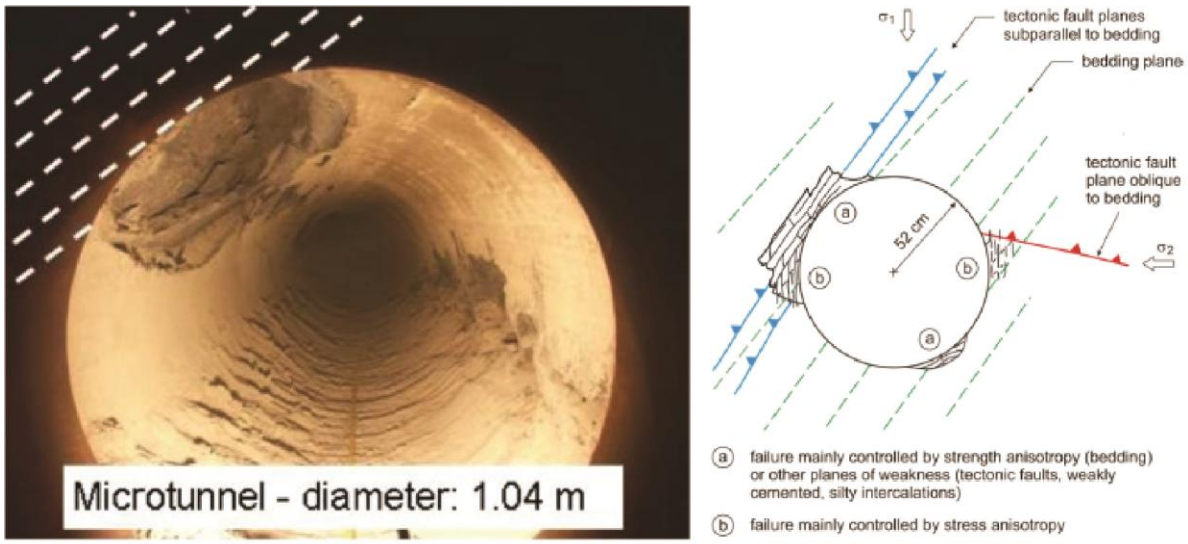

Figure 3.11. a) Excavation damage viewing from the HG-A Niche towards back end (Marschall et al., 2006); and b) Conceptual diagram of the damage zone (Lanyon et al., 2009; Marschall et al., 2006).

Figure 3.11 shows excavation damage of the microtunnel. Partial damage and exfoliations have occurred along the microtunnel wall (Figure 3.11a), which are mainly attributed to the anisotropic strength characteristics of the rock. Strength of an anisotropic rock is found to be a function of orientation relative to the bedding plane (Bock, 2001). The relative weakness

orthogonal to the bedding and the weakness near faults intercepting the tunnel, as depicted in Figure 3.11b, result in the nonuniform damage around the excavation wall.

The analyses start with the simulation of the elastic stress profiles around the microtunnel under compression condition. Figure 3.12a shows a 2-D square domain with a 10-m long side, where a circular opening with a radius of 0.5 m is placed at the center. The computational domain is discretized with 2044 nodes, and the nodal density is graded for computational efficiency. Far-field compressive stresses are 4.5 MPa in the horizontal direction and 6.5 MPa in the vertical direction (Martin and Lanyon, 2003). First, a homogeneous and isotropic material is considered in order that the simulation results can be verified with analytical solutions (Kirsch, 1898). Young's modulus and Poisson ratio are 15.5 GPa and 0.3, respectively. In Kirsch's solutions, the stress profiles are expressed as a function of the distance from the center, r and the normal angle, θ. Figure 3.12b compares the simulation results and the analytical solutions of stress profiles for $\theta = 0°$, which shows a good agreement between the two types of solutions.

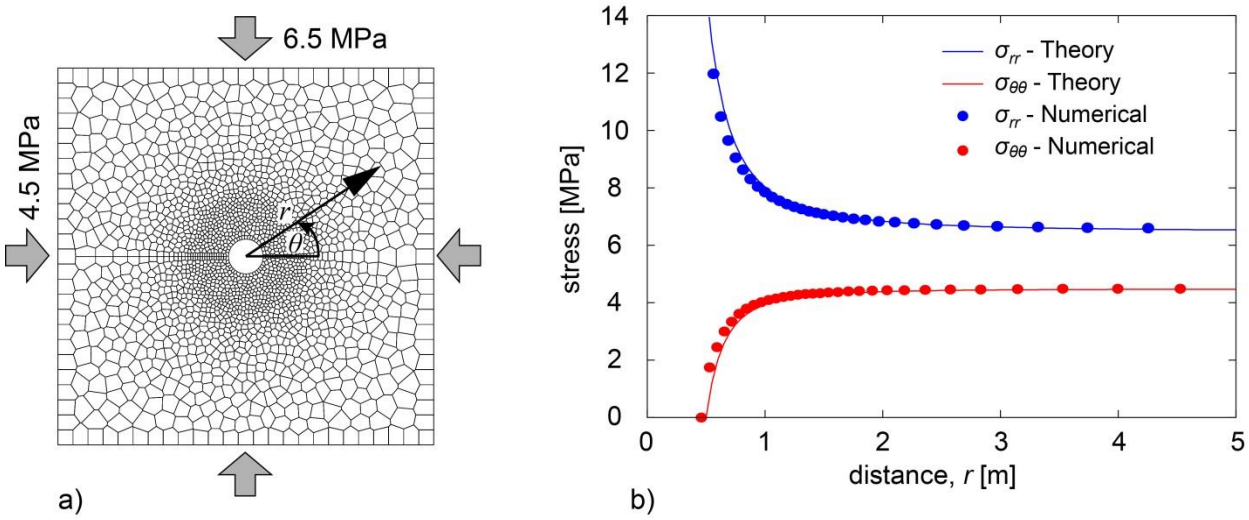

Figure 3.12. a) Discretization of the computational domain and loading configurations; and b) radial and tangential stress values versus the radial distance.

Next, the excavation damage of the HG-A microtunnel is simulated. In Figure 3.12b, we see that the asymptotic stress profiles approach sufficiently close to the far-field stresses at $r = 4$ m. For that reason, the dimension of the computational domain is reduced. Figure 3.13a shows the discretization of the reduced 8×8 m computational domain using a finer Voronoi grid (4042 nodes). External loading configurations are the same as in the previous simulation, and additionally, an internal pore pressure of 1.5 MPa is applied to the matrix volume. Mechanical properties of the Opalinus Clay, summarized in Table 3.1, are used to represent anisotropy of the on-site rock formation. The bedding planes are aligned at 45° from the horizontal axis, which is similar to the orientation of fabric shown in Figure 3.11. Figure 3.13b illustrates the fracture pattern, where the damage occurs mainly around the tunnel. Damaged zones are more prominent at the tunneling wall tangential to the bedding planes, similarly to the failure characteristics seen in Figure 3.11. For identification of failure modes, individual fracture segments are drawn in different colors: blue and red segments represent tensile and shear failure modes, respectively.

Tension fracturing is concentrated at the borehole boundary, due to the lack of constraints against the pore pressure acting towards the center of the tunnel. This failure feature can be supported by observation of the deformation around the borehole. Figure 3.13c depicts the deformed shape of the tunnel, in which the deformation is exaggerated for better visibility. Voronoi cells adjacent to the borehole come off the body, which indicates the tensile failure.

Figure 3.13. a) Discretization of the computational domain for the HG-A test simulation; b) nonuniform fracture pattern around the tunnel; and c) deformed shape of the borehole.

Although the tectonic faults around the tunnel are not modeled in this study, fracture damage process is in qualitative agreement with observations. In future study, the fracture damage process will be quantitatively analyzed along with long-term hydro-mechanical behavior, which is simulated by a coupled THM modeling approach, i.e. the TOUGH-RBSN simulator.

3.5 THM Simulations of Hydraulic Fracturing

This section provides an example application of the TOUGH-RBSN simulator for coupled THM processes, including hydraulic fracturing behavior within a geological system. Consider a 30×30 m domain with a relatively small borehole of 0.15 m diameter, subjected to respective far-field stresses of 45.5 MPa vertically and 34.5 MPa horizontally (Figure 3.14a). The Voronoi grid is generated with a graded nodal density, in which the mesh size around the expected fracturing path is controlled to be much finer (Figure 3.14b). The rock material is assumed to be homogeneous and isotropic with the following mechanical properties: Young's modulus $E = 11.0$ GPa; tensile strength $f_t = 15.0$ MPa; cohesion $c = 22.5$ MPa; and internal friction angle $\psi = 45°$. The hydrological properties are as follows: matrix density $\rho = 2{,}500$ kg/m^3; porosity $\phi = 0.06$; and permeability $K = 10^{-15}$ m^2. A pore pressure of 31.0 MPa is used throughout the matrix as the initial condition, and injection of water is conducted at a constant rate 0.18 kg/s per unit thickness.

If a fracture event occurs at a lattice element of the RBSN model, a fracture node and the connections to the surrounding nodes for the TOUGH2 simulation are activated as described in Section 3.3.2, and the porosity and permeability for the fracture node are drastically increased (e.g., $\phi_f = 1.0$ and $K_f = 10^{-6}$ m^2). These hydrological properties for individual fractures can be calculated as a function of fracture aperture; however, for simplicity, herein they are set to be constant, irrespective of the fracture geometries.

Two cases of rock formations are considered for simulations: (1) an intact medium without any pre-existing fracture or damage within the rock matrix, and (2) a fractured medium, in which a 3-m long inclined fracture is included (see Figure 3.14a), so that a newly generated fracture path will meet the pre-existing fracture during the hydraulic fracturing process. The pre-existing fracture retains high porosity and permeability from the initial stage of the simulation. The simulations are performed for a 600 s duration, when the steady-state pressure evolutions at the borehole are attained.

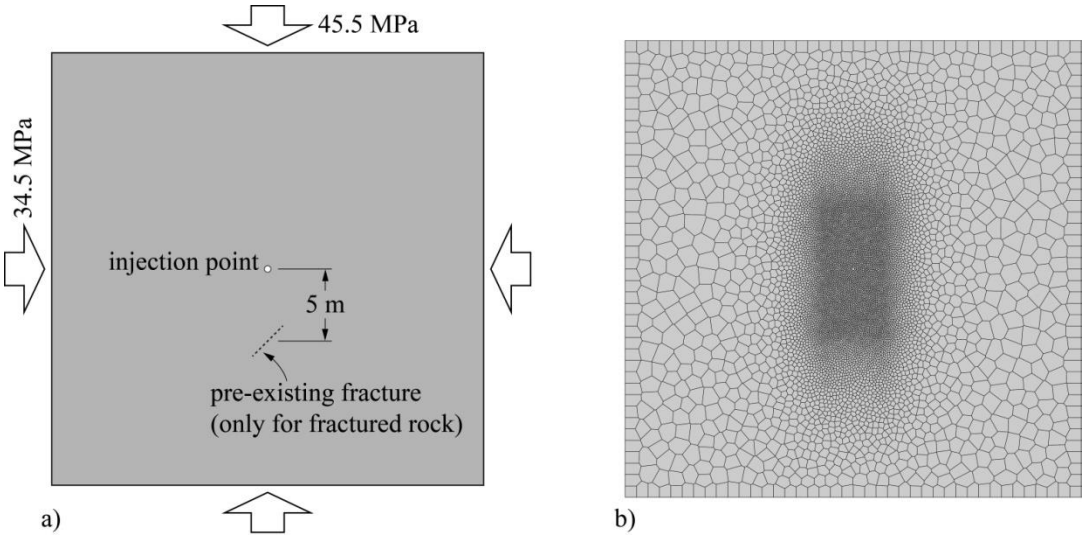

Figure 3.14. Hydraulic fracturing simulation: a) simulation configurations; and b) discretization of the computational domain.

Figure 3.15 compares the resulting fracture developments at the final stage for the two cases of simulations. In both cases, a single major crack stretching out from the borehole forms in the direction of maximum compressive stress, which represents tensile failure. As shown in Figure 3.15b, a distinctive bend in the fracture is observed near the inclined pre-existing fracture. The opening of the pre-existing fracture is not pronounced due to the shear movement along the fracture path.

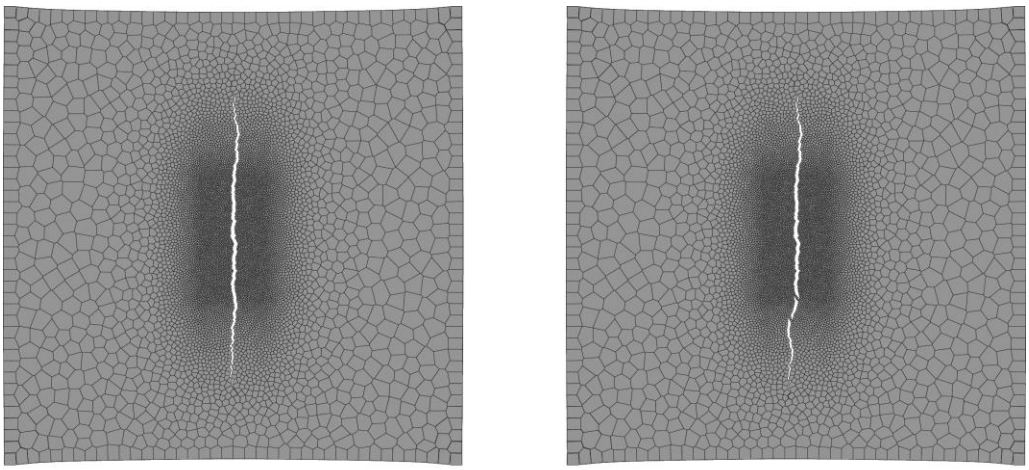

Figure 3.15. Comparison of fracture paths in deformed shapes of the domain: a) intact rock matrix; and b) fractured rock matrix.

Figure 3.16 arranges snapshots of pressure distributions, captured at the point of fracture initiation, at the early and the latter stages of fracture propagation, based on the length of the fracture, and at the final stage of the simulation, where the real time is specified in seconds. Up until fracture initiation, local pressure at the borehole increases due to the water injection (Figure 3.16a). The intact rock exhibits fracture initiation 16 s sooner than the fractured rock. The delayed fracture initiation results in greater energy stored in the matrix around the borehole for the case of the fractured rock. Therefore the fracture develops more rapidly after initiation. As the fracture propagates, the pressure at the borehole is directly transferred into the fracture path (Figure 3.16b). Figure 3.16c describes the effect of the pre-existing fracture on the hydraulic fracturing process. Hydraulic fracturing keeps proceeding through the intact rock matrix, whereas in the fractured rock, the propagation of downward fracture hitting the pre-existing fracture is arrested. The flow channels along the discrete fractures are connected to reduce the pressure gradient that promotes the fracturing process at the crack tip, thus the fracture development is slowed down. Figure 3.16d shows pressure contours in the shape of the final fracture path, in which the percolating water flow, from the fracture surface towards surrounding matrix, diffuses the concentrated pressure.

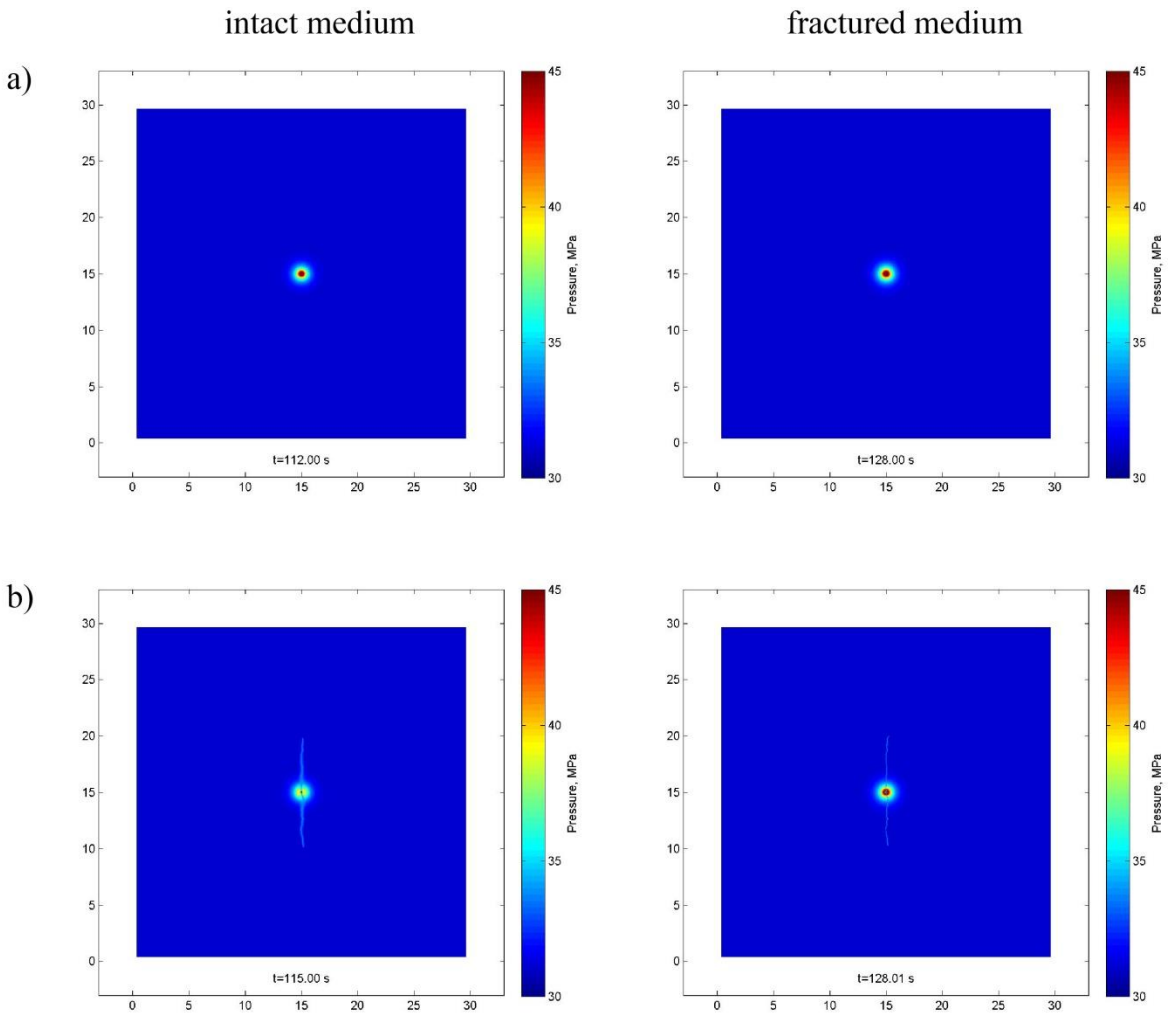

Figure 3.16. Pressure contour evolutions for intact and fractured rock formations: a) at the point of fracture initiation; and b) at the early stage of fracture propagation.

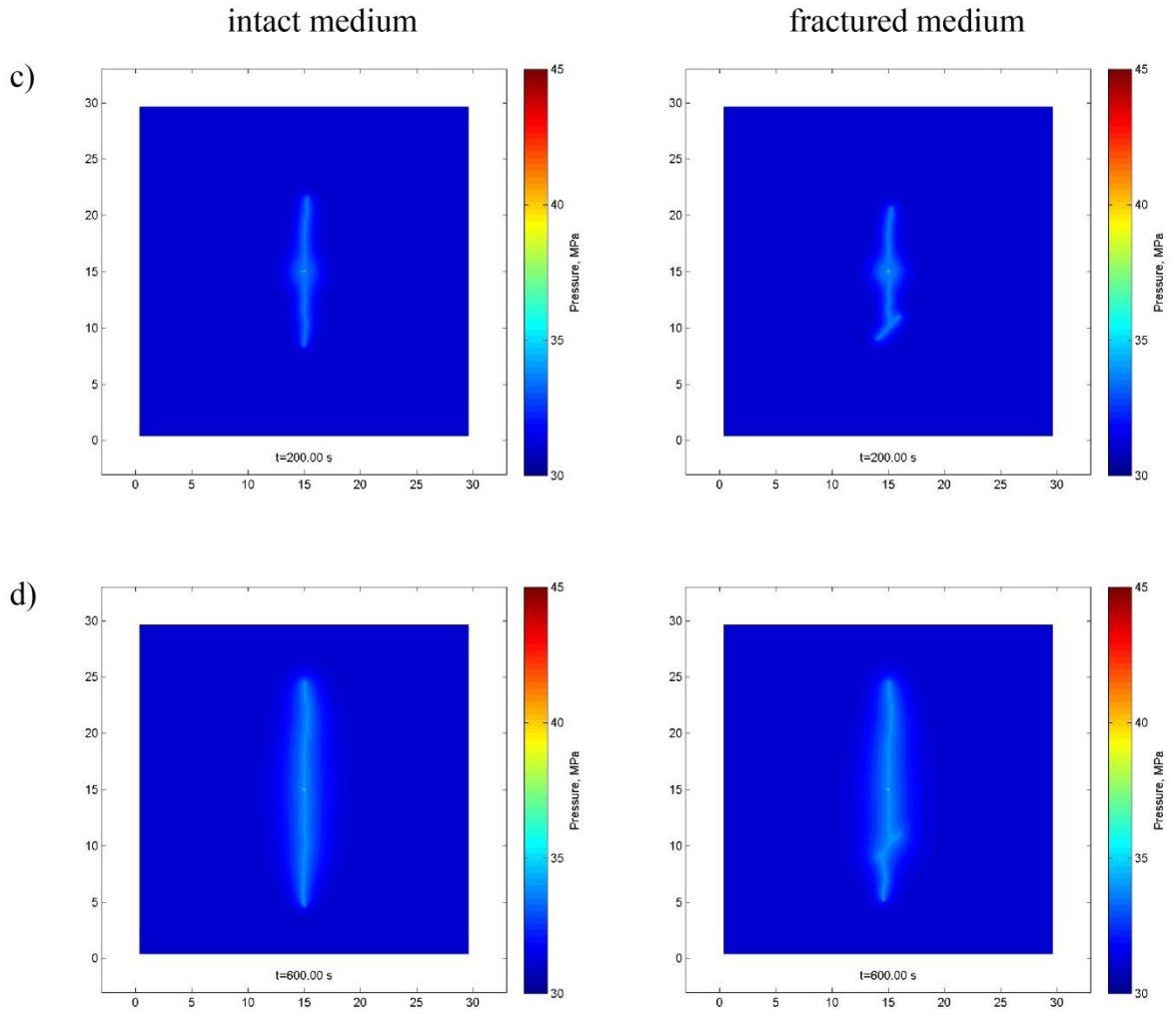

Figure 3.16. (continued). Pressure contour evolutions for intact and fractured rock formations: c) at the latter stage of fracture propagation; and d) at the final stage of the simulation.

This simulation example demonstrates the capabilities of the developed modeling approach for the coupled THM processes in geological systems. The mechanical effect of the excessive pressure produced by water injection (i.e., induced hydraulic fracturing) and the preferential flow features through the newly generated fracture path are realistically represented. As seen in the case of the fractured medium, the pre-existing fracture exerts a considerable influence on the flow behavior as well as on the mechanical behavior of the system, such that the fracturing process is disturbed. In the future, parametric studies on the hydro-mechanical effects of fracture networks can be done for various sizes, shapes, locations, and orientations of the fractures.

3.6 Conclusions

This study uses the RBSN approach to model geomechanical behavior including fracturing. The model provides a discrete representation of material elasticity and fracture development, and in that respect, it is considered to be suitable for the DFN approach to investigating fracturing processes. However, the original RBSN is limited to macroscopically modeling isotropic materials, or requires additional treatments in partitioning the domain (e.g., layering of individually isotropic materials) for introducing anisotropic mechanical properties.

To extend the applicability of the model to general anisotropic geomaterials, we propose a new modeling scheme. Elastic spring coefficients and strength parameters are systematically formulated for individual lattice elements based on the principal bedding direction, which facilitate a straightforward representation of anisotropy. Uniaxial compression tests are simulated for a transversely anisotropic material, the Opalinus Clay, to demonstrate the validity of the new modeling scheme. Thereafter, a simulation of fracture damage around the EDZ of the HG-A microtunnel is conducted. Qualitatively the simulation results closely match the physical observations, in which nonuniform damage, due to the anisotropic mechanical characteristics, forms around the excavation wall.

The behavior of strongly coupled THM processes has also been investigated using the TOUGH-RBSN simulator. We have established an effective linkage between the TOUGH2 code based on the finite volume method for simulating heat and mass transport within porous rock formations, and the RBSN method for simulating mechanical responses and fracture initiation and propagation. One main advantage of linking TOUGH2 and the RBSN is that both models utilize the same set of nodal points, along with the natural neighboring connections and the volume rendering definitions, according to the unstructured Voronoi discretization. The capabilities of the TOUGH-RBSN simulator are shown through simulation of hydraulic fracturing. In the simulations, two-way coupling of the THM variables produces realistic hydro-mechanical behavior in the fracturing process.

4. THM Modeling of Underground Heater Experiments

In this section, we present LBNL's activities related to THM modeling of underground heater experiments in clay formations, including studies related to the Development of Coupled Models and their Validation against Experiments (DECOVALEX)-2015 project and the Mont Terri FE (Full-scale Emplacement) Experiment.

DECOVALEX-2015 is an acronym for the 6th and current phase of the "Development of Coupled Models and their Validation against Experiments" project, ongoing from 2012 to 2015. In DECOVALEX-2015, LBNL participates in Task B, which includes:

Subtask B1—Mont Terri HE-E Experiment: A heating experiment to evaluate sealing and clay-barrier performance, in a micro-tunnel at the Mont Terri URL in Switzerland; and

Subtask B2—Horonobe Engineered Barrier System (EBS) Experiment: A heating experiment to study the thermo-hydro-mechanical-chemical (THMC) behavior of the EBS and its interaction with the mudstone host rock, in a vertical emplacement hole at the Horonobe URL in Japan

In addition to the modeling work in these two DECOVALEX tasks, LBNL participates in the Mont Terri FE Experiment as one of the participating modeling teams. The FE Experiment is undertaken as an ultimate test for the performance of geologic disposal in Opalinus Clay, with focuses on both the EBS components and the host-rock behavior; it will be one of the largest and longest running heater tests worldwide.

UFD objectives for participating in these international activities are to develop expertise and test advanced models on coupled processes in clay-based backfill in interaction with clay host rock. Through participation in modeling these field experiment, the models will be developed and experience will be gained for a range of different backfill materials (e.g., bentonite pellets and sand/bentonite mixture), as well as different host rocks (e.g., Opalinus clay and mudstone).

In the following Subsection 4.1, the modeling approach and the status of model development will be summarized. Then the modeling work conducted associated with field experiments are presented in Subsections 4.2 through 4.4. Finally, in Subsection 4.5, the current status and future plans for THM m modeling are summarized.

4.1 Modeling approach

LBNL uses two independent numerical simulators (TOUGH-FLAC and ROCMAS) for modeling of coupled THM processes associated with nuclear waste disposal and for modeling of the aforementioned heater experiments. The TOUGH-FLAC simulator developed at LBNL is the primary analysis tool, because this simulator has the required capabilities to model a large variety of problems associated with nuclear waste disposal for various engineering and natural systems. The ROCMAS code, also developed at LBNL, will in this project be used for confidence building through code-to-code verification. That is, models of a particular problem might be built in both TOUGH-FLAC and ROCMAS, and if the simulation results agree, that provides confidence in the models. Both the TOUGH-FLAC and ROCMAS codes solve THM coupled problems, but are two different codes with different characteristics. TOUGH-FLAC can simulate coupled THM processes under multiphase flow conditions through a sequential coupling of the TOUGH2 multiphase flow simulator with the FLAC3D geomechanical code (Rutqvist et al., 2002; Rutqvist 2011). TOUGH-FLAC has recently been modified for applications related with to bentonite-backfilled repositories in clay host formations (Rutqvist et al., 2014). ROCMAS simulates coupled THM processes in unsaturated media, including single-phase liquid flow and vapor diffusion in a static gas phase (Rutqvist et al., 2001a). The code has been extensively applied in earlier phases of the DECOVALEX project for THM analysis in bentonite-rock systems (Rutqvist et al., 2001b, 2005, 2009). In the following, the TOUGH-FLAC simulator (primary analysis tool) is described in more detail.

The TOUGH-FLAC simulator (Rutqvist 2011), is based on linking the TOUGH2 multiphase flow and heat transport simulator (Pruess et al., 2011) with the FLAC3D geomechanical simulator (Itasca 2011). In this approach, TOUGH2 (Pruess et al., 2011) is used for solving multiphase flow and heat transport equations, whereas FLAC3D (Itasca 2011) is used for solving geomechanical stress-strain equations. The two codes are sequentially coupled, but a TOUGH-FLAC simulation runs seamlessly. For analysis of coupled THM problems, the TOUGH2 and FLAC3D are executed on compatible numerical grids and linked through a coupled thermal-hydrological-mechanical (THM) model (Figure 4.1) with coupling functions to pass relevant information between the field equations that are solved in respective code. Depending on the problem and specific porous media (e.g., fractured rock, unsaturated clay, or hydrate-bearing sediments), a number of coupling functions have been developed.

In the coupling scheme between TOUGH2 and FLAC3D, the TOUGH2 multiphase pressures, saturation, and temperature are provided to update temperature, and pore pressure to FLAC3D (Figure 4.1). After data transfer, FLAC3D internally calculates thermal expansion, swelling, and effective stress. Conversely, element stress or deformation from FLA3D are supplied to TOUGH2 for correcting element porosity, permeability, and capillary pressure for the fluid-flow simulation in TOUGH2. The corrections of hydraulic properties are based on material-specific functions.

In a TOUGH-FLAC simulation, the calculation is stepped forward in time with the transient multiphase fluid flow analysis in TOUGH2, and at each time step or at the TOUGH2 Newton

iteration level, a quasi-static mechanical analysis is conducted with FLAC3D to calculate stress-induced changes in porosity and intrinsic permeability. In this scheme, the fluid-flow sequence is solved first under fixed stress, and the resulting pressure and temperature are prescribed in the mechanical sequence. This corresponds to so-called stress fixed iterations in the sequential scheme, in which the solution becomes unconditionally stable. The resulting THM analysis may be *explicit sequential*, meaning that the porosity and permeability is evaluated only at the beginning of each time step, or the analysis may be implicit sequential, with permeability and porosity updated on the Newton iteration level towards the end of the time step using an iterative process.

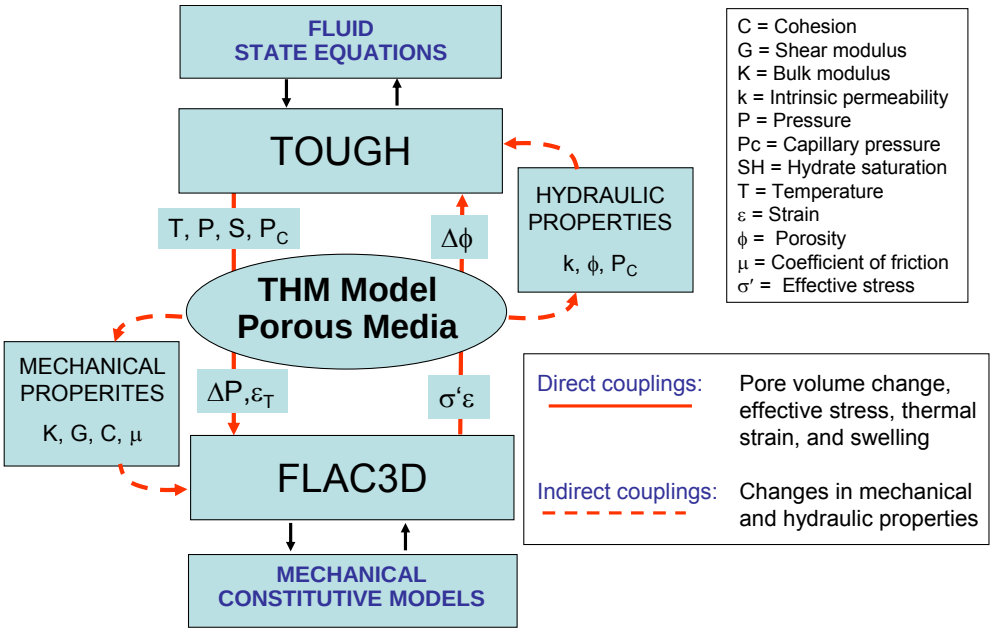

Figure 4.1. Schematic of linking of TOUGH2 and FLAC3D in a coupled TOUGH-FLAC simulation.

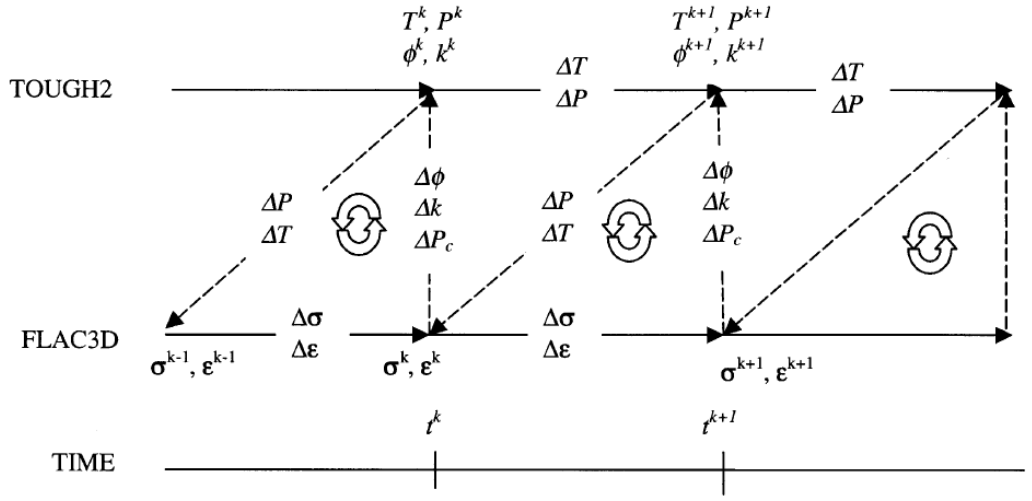

Figure 4.2. Numerical procedure of a linked TOUGH2 and FLAC3D simulation.

A great advantage with this adopted approach is that both codes are continuously developed and widely used in both academia and industry. In TOUGH2, a large number of fluid equation-of-state modules are available, while in FLAC3D, a large number of geomechanical constitutive models are available. This means that the simulator can be relatively easily extended to new application areas.

The TOUGH-FLAC simulator has in recent years been extended and applied to issues related to nuclear waste disposal with bentonite backfilled tunnels (Rutqvist et al., 2011; 2014). This includes implementation of the Barcelona Basic Model (BBM) (Alonso et al., 1990), for the mechanical behavior of unsaturated soils and applied for modeling of bentonite backfill behavior (Rutqvist et al., 2011). The BBM was first developed and presented in the early 1990s as an extension of the Modified Cam Clay (MCC) model to unsaturated soil conditions (Alonso et al., 1990). The model can describe many typical features of unsaturated-soil mechanical behavior, including wetting-induced swelling or collapse strains, depending on the magnitude of applied stress, as well as the increase in shear strength and apparent preconsolidation stress with suction (Gens et al., 2006). Figure 4.3 presents the yield surface of the BBM model in q-p-s space. The shaded surface corresponds to the elastic region at fully water-saturated conditions, which is equivalent to the modified MCC model. The figure also shows how the yield surface expands at unsaturated and dryer conditions when suction increases. There is an increase in both the apparent pre-consolidation pressure along the load collapse (LC) yield surface and by the increasing tensile strength, which in turn leads to an increased cohesion and shear strength.

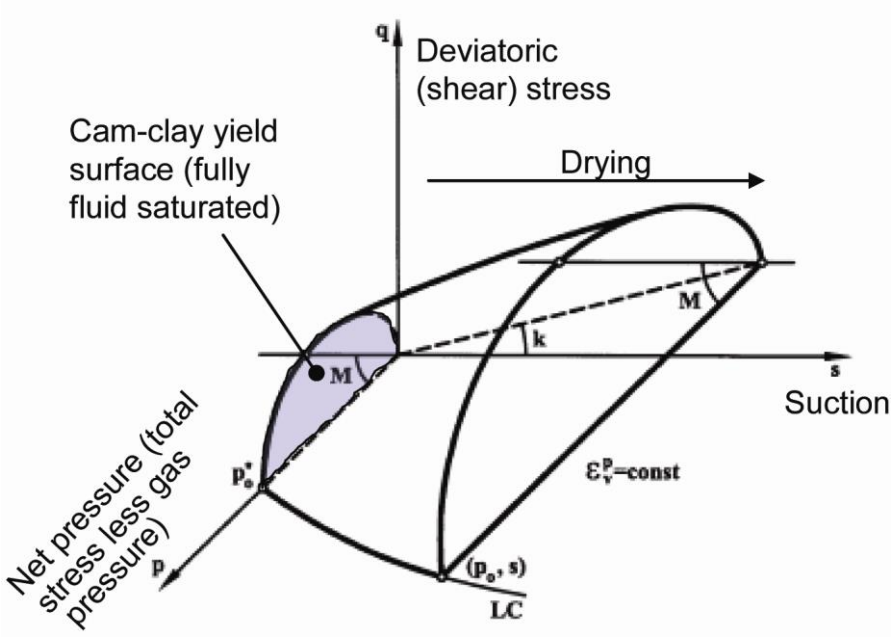

Figure 4.3. BBM constitutive model showing the yield surface in q-p-s space.

The BBM has been used for modeling of bentonite-buffer behavior in various national nuclear waste programs in Europe and Japan. For example, the BBM was successfully applied to model the coupled THM behavior of unsaturated bentonite clay associated with the FEBEX *in situ* heater test at the Grimsel Test Site, Switzerland (Gens et al., 2009). The BBM has also been applied to other types of bentonite-sand mixtures based on MX-80, considered as an option for an isolating buffer in the Swedish KBS-3 repository concept (Kristensson and Åkesson 2008). As part of the UFD program, the BBM was also used by Rutqvist et al. (2014), for the modeling of coupled THM processes around a generic repository in a clay host formation.

Recently, as part of the UFD EBS program, the BBM has been extended to a dual structure model, corresponding to the Barcelona Expansive Model (BExM). In a dual-structure model, the material consists of two structural levels: a microstructure in which the interactions occur at the particle level, and a macrostructure that accounts for the overall fabric arrangement of the material comprising aggregates and macropores (Figure 4.4) (Gens et al., 2006, Sánchez et al., 2005, Gens and Alonso 1992). A dual-structure model has important features for modeling the mechanical behavior of a bentonite buffer, such as irreversible strain during suction cycles. However, most importantly, a dual-structure model provides the necessary link between chemistry and mechanics, enabling us to develop a coupled THMC model for the analysis of long-term EBS behavior. This approach enables mechanistic modeling of processes important for long-term buffer stability, including effects of pore-water salinity on swelling (loss of swelling), conversion of smectite to nonexpansive mineral forms (loss of swelling), and swelling pressure versus exchangeable cations. The recent developments, testing and applications of the dual structure model, are presented in the upcoming FY2014 milestone report entitled “Investigation

of coupled THMC process and reactive transport", as well as in a new scientific article submitted to a journal (Vilarrasa et al., 2014)

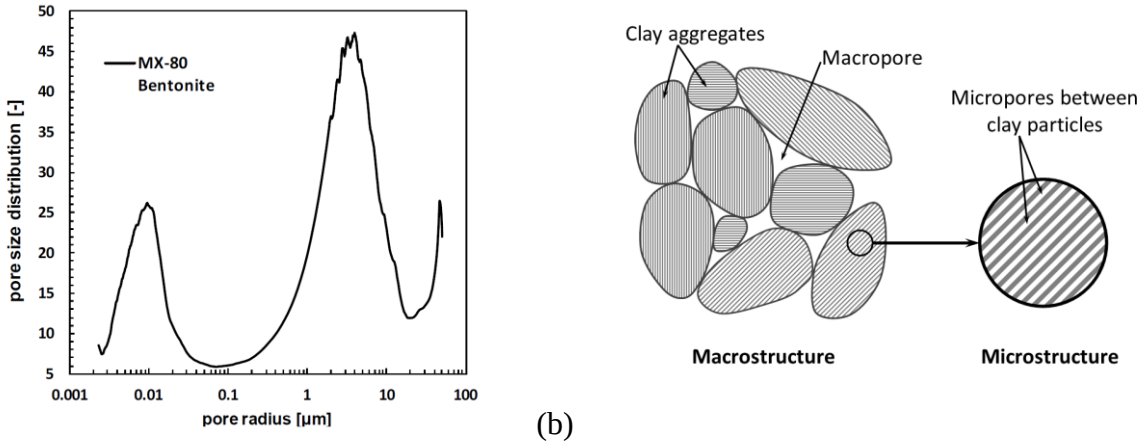

(a) (b)

Figure 4.4. (a) Pore size distribution and (b) schematic representation of the two structural levels considered in the dual structure model. Clay particles are represented by the gray lines.

4.2 Mont Terri HE-E Experiment (DECOVALEX)

The Mont Terri HE-E Experiment focuses on the THM behavior of bentonite barriers in the early nonisothermal resaturation stage and their THM interaction with Opalinus Clay (Figure 4.5). The objective is to better understand the evolution of a disposal system of high level waste in the early post-closure period, with emphasis on the thermal evolution, buffer resaturation (*in situ* determination of the thermal conductivity of bentonite and its dependency on saturation), pore-water pressure in the near field, and the evolution of swelling pressures in the buffer. Because the test is conducted in a micro-tunnel (at 1:2 scale), it is considered a validation, not a demonstration experiment. The heating test involves two types of bentonite buffer materials (Figure 4.5, left). The heater-buffer interface is heated to a maximum temperature of 135°C and a temperature of 60–70°C is expected at the buffer-rock interface. A dense instrumentation network was in place in the host rock surrounding the micro-tunnel from a previous experiment testing the impact of ventilation on the clay host rock, and has been improved for the purpose of the HE-E Heater Test (up to 40 piezometers in total); various sensors have also been placed in the buffer material. The heating phase started in the late summer of 2011 and is being continued for at least three years.

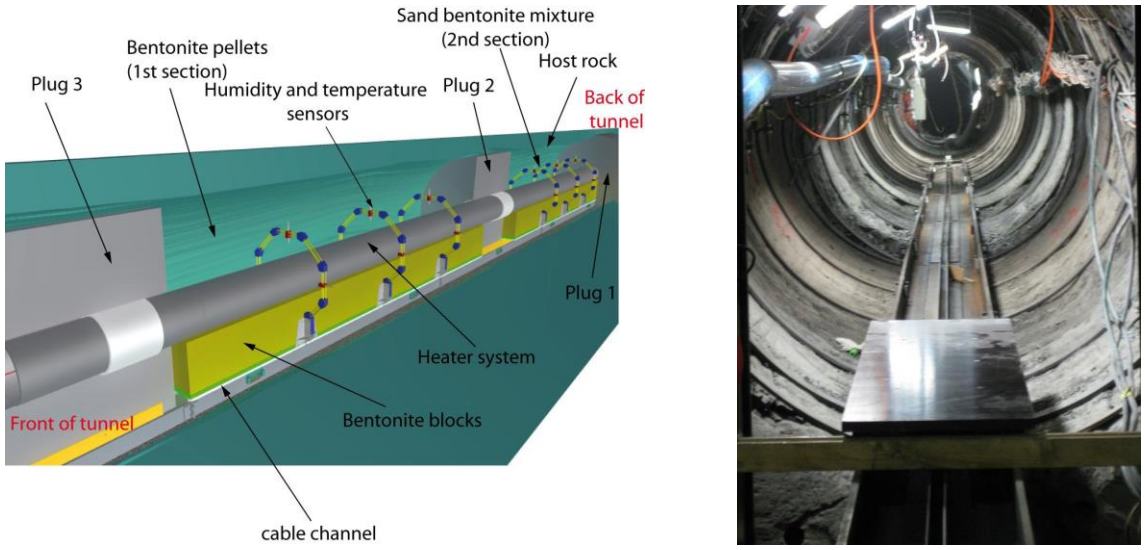

Figure 4.5. Schematic setup of HE-E experiment at Mont Terri and photo of micro-tunnel (Garritte, 2012).

In DECOVALEX-2015 (Task B1), eight international research teams are participating in the modeling of the HE-E experiment. Task B1, which is running over 3 years, is divided into the following steps:

- Step 1a: Opalinus Clay study including HE-D experiment, literature study, processes understanding and parameter determination.
- Step 1b: Buffer material study including CIEMAT column cells, literature study, processes understanding and parameter determination.
- Step 2: HE-E predictive modeling using as-built characteristics and true power load. Modeling is 2D (axisymmetric, plane strain or combination) and 3D.
- Step 3: HE-E interpretative modeling when data are made available.

Step 1a started in 2012 with the modeling of the previous HE-D experiment for *in situ* characterization of THM material parameters for the Opalinus Clay and was completed in November 2013. The HE-D experiment involved 1 year of heating of the Opalinus Clay without any bentonite buffer. The modeling of the HE-D experiment and comparison of the TOUGH-FLAC modeling results to the results of other modeling teams were reported in the FY2013 milestone report entitled "Report on THMC modeling of the near field evolution of a generic clay repository: Model validation and demonstration" (Liu et al., 2013b). Step 1b, which is a study of buffer material properties through modeling of laboratory experiments on buffer material samples, has recently been completed by all the modeling teams in DECOVALEX-2015, although the final comparison of the results between different teams is still ongoing. In this report, we present LBNL's final analysis of the CIEMAT column experiments, which has been substantially updated from last year. This update includes a more detailed analysis of transient temperature evolution, the heat loss through the experimental equipment, and more detailed consideration of the retention properties, including their temperature dependency. This also

resulted in a much improved agreement between simulated and observed THM responses. We have also begun Step 2 of Task B1, which is the HE-E predictive analysis, planned to be completed by October 2014.

4.3 Buffer characterization using CIEMAT column experiments

In this subsection, we present updated modeling of the CIEMAT column experiments (Villar 2012). The modeling of the CIEMAT column experiments are being done as part of DECOVALEX-2015 Task B1 for characterization of the buffer material associated with the Mont Terri HE-E experiment. However, the CIEMAT column experiments are also critical for the modeling of the Mont Terri FE experiment, because one of the bentonite materials studied in the column experiments will also be used for backfill at the FE experiment. In CIEMAT column experiments, two buffer materials, granular bentonite (or bentonite pellets) and sand/bentonite mixture, were tested (Figure 4.6). The design of the column experiments mimicked the HE-E conditions, with the height of the column equal to the thickness of the buffer filled between the canister and host rock. A heater was placed at the bottom and a cooler at the top of each column, so that the column was heated while the top remained at an ambient temperature of ~21.5°C. During the experiments, temperature and relative humidity were measured at three points along the axis of the column. The power input was monitored as well. In this study, our objectives are to model the fluid-flow and heat-transfer processes that occur in the experiment, and to calibrate the flow and thermal properties of the two buffer materials against the experimental measurements. In DECOVALEX-2015, only the granular bentonite experiment was required to be modeled by the research teams, whereas it was optional to model the sand/bentonite experiment.

The modeling of this experiment in the DECOVALEX-2015 project has revealed substantial heat loss through the equipment, such that it was decided at the last DECOVALEX-2015 workshop (in April 2014) that each research team should carefully look at both the heat power and temperature evolution, to properly consider the heat loss from the equipment. It is particularly important to quantify the heat loss if using this experimental data to determine the thermal conductivity of the tested bentonite material. LBNL has conducted model simulations of both experiments (both granular bentonite and sand/bentonite mixture). However, the main emphasis was placed on the modeling of the granular bentonite, because this was the main task in DECOVALEX-2015, and granular bentonite is the buffer material that will be used in the Mont Terri FE experiment.

4.3.1 Model setup of column experiment on granular bentonite

In the experiment, bentonite pellets were poured into a Teflon column without extra packing (Villar, 2012). A heater was placed at the bottom and a cooler at the top of the column (Figure 4.6). Sensors were installed at distances of 10 m, 22 m, and 40 cm from the heater to measure temperature and relative humidity. The Teflon column was wrapped with a layer of foam, which was later replaced with rock wool and another insulating material denoted in Villar (2012) as BT-LV.

After the system was assembled, the relative humidity and temperature were measured without heating the system. The measured initial relative humidity was uniformly 40% within the column. It remained unchanged until the start of heating, which was set to be the reference time (t=0). After the heater was turned on, the surface temperature of the heater reached the target temperature of 100°C within 33 minutes. By automatically adjusting the power into the heater,

the surface temperature of the heater remained at 100°C. By 1566 hours, the foam layer was replaced with a rock wool of 30 mm thickness, covering the entire column length, and a BT-LV of 25 mm thickness, covering the bottom 5 cm of the column (Figure 4.6). At 3527 hours, an adjustment of the target temperature was made for the heater, and its surface temperature increased to 140°C about 17 minutes after the adjustment. A hydration valve was opened by 5015 hours. Water flowed into the column from the top while the surface temperature of the heater remained at 140°C. During the hydration process, the changes in relative humidity and temperature along the column and the power input of the heater were monitored.

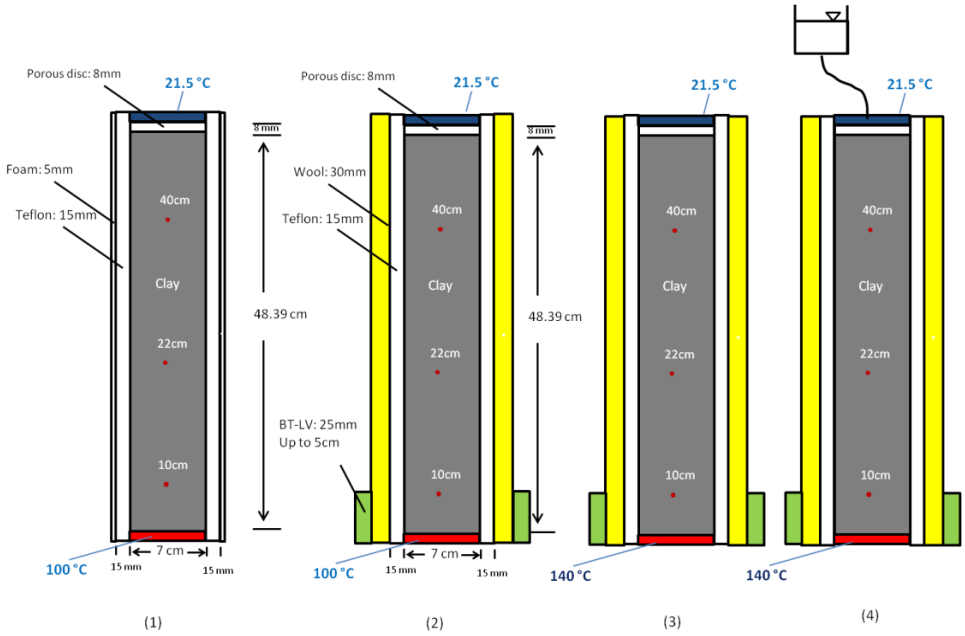

Figure 4.6. Schematic of experimental setups of column experiment in sequential steps: (1) Heating at temperature of 100 ˚C from 0 to 1566 hours, (2) heating with new insulation layer from 1566 to 3527 hours, (3) heating at 140 ˚C from 3527 to 5015 hours, (4) heating with hydration valve open after 5015 hours.

A 2D radial symmetric mesh of 9×28 elements was created for the modeling of this column experiment (Figure 4.7). Bentonite is represented in a zone of 4×25 elements (grey zone in Figure 4.7). The multiple stages of the experiment were simulated sequentially, and the boundary conditions of each step were adjusted according to the experiment. During the experiment, the hydration valve was closed, and therefore no water flowed into the column before the start of heating. Fixed temperature conditions at the heaters were simulated by assigning a large heat capacity to the heater elements. To simulate the temperature increase at the heater element, e.g., from 21.5 to 100°C, and from 100 to 140°C, a heating rate was applied to the heater element, such that the heating rate equal to the experiment. Hydration was simulated by assigning a constant absolute pressure of 1.1×10^4 Pa at the top boundary.

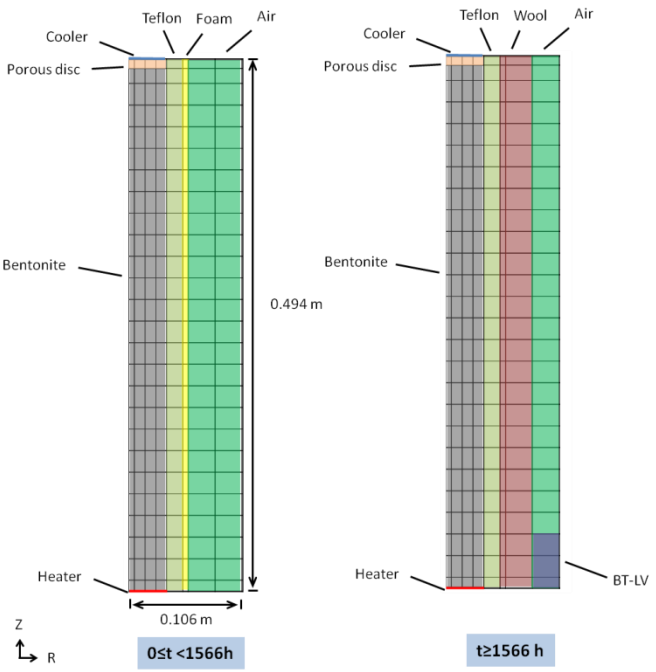

Figure 4.7. Model mesh and the materials represented in the model at different steps for column experiment on bentonite pellets. The reference time (t = 0) is the start of heating.

For assigning the initial properties we resorted to literature data of granular MX-80 bentonite or other similar bentonite materials. For example, properties for granular bentonite was defined by Nationale Genossenschaft für die Lagerung radioaktiver Abfälle (NAGRA) for a benchmark model problem associated with the Mont Terri FE experiment. These properties are listed Table 4.9 and an estimate of the properties. Here we complement these with new data from Villar, (2012) and Rizzi et al, (2011). The basic physical properties of the granular bentonite are presented in Table 4.1, including a solid grain density of 2700 kg/m^3 and a porosity of 0.46 (Villar, 2012). The specific heat of the bentonite is 950 J/kg°C (NAGRA best estimate, Table 4.9). The initial water saturation is 22% and the measured initial relative humidity was 40% uniformly along the column.

Table 4.1. Properties of bentonite pellets used in the modeling of the column experiment.

Properties	Values
Solid grain density	2700 kg/m^3
Porosity	0.46
Specific heat	950 J/kg^{o}C
Tortuosity	0.67

Transport of vapor in tight formation is enhanced by diffusion and Klinkenberg effects. Olivella and Gens (2000) reported that the measured permeabilities of FEBEX and Boom Clay samples to gas are about 6–7 orders of magnitude higher than those to liquid. To account for the increased gas permeability, we considered vapor and air diffusion and the Klinkenberg effect in the model.

A diffusion coefficient of 2.13×10^{5} m^2/s was used for both vapor and air, and a tortuosity factor of 0.67 was used in the model. A Klinkenberg parameter of 2.5×10^{11} Pa was used.

Gas phase is assumed to be perfectly mobile, and the relative permeability of liquid water is a power function of the degree of water saturation (NAGRA best estimate, Table 4.9).

$$k_{rl} = {s_l}^5 \tag{4.1}$$

$$k_{rg} = 1 \tag{4.2}$$

Typical values (Table 4.2) were used for the thermal conductivities of the Teflon wall and insulation layers, as described in Villar (2012).

Table 4.2. Properties of other materials used in the model for column experiment on bentonite pellets.

Materials	Thermal conductivity
Porous disc	3.5 W/mºC (wet and dry)
Teflon	0.25 W/mºC (wet and dry)
Foam	0.04 W/mºC (wet and dry)
Wool	0.03 W/mºC (wet and dry)
BT-LV	0.03 W/mºC (wet and dry)
Air	0.032 W/mºC (wet and dry)

4.3.2 Analysis of thermal conductivity of the granular bentonite

The analysis of the thermal conductivity of the granular bentonite was challenging, because the substantial heat loss from the test equipment affected the experimental results. We first investigated the possibility of calibrating the thermal conductivity of the granular bentonite using the temperature profile at steady-state conditions at the end of each heating step. The model for this analysis considered an insulation layer of 0.45 m in thickness (equals to the sum of Teflon and wool layers). The temperature was fixed at 140°C at the bottom, 21.5°C at the top, and 21.5°C at the sides. Both thermal conductivities of bentonite (λ) and insulation layer (h) were calibrated against the temperature profile at steady-state conditions.

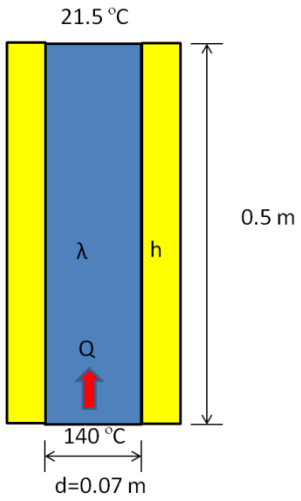

Figure 4.8. Schematic of the model for the calibration of thermal conductivity.

The analysis showed that steady-state temperature data alone do not contain enough information to calibrate the thermal conductivity of the benotonite. Different combinations of bentonite and insulation thermal conductivities can equally match the temperature profile measured at steady state (Figure 4.9). A thermal conductivity of 0.4 W/mK for bentonite and 0.032 W/mK for insulation layer produces the same temperature profile at λ=0.2 W/mK and h=0.016 W/mK or at λ=0.75 W/mK and h=0.06 W/mK. A thermal conductivity ratio (λ/h) of 12.5 is critical for matching the steady-state temperature data.

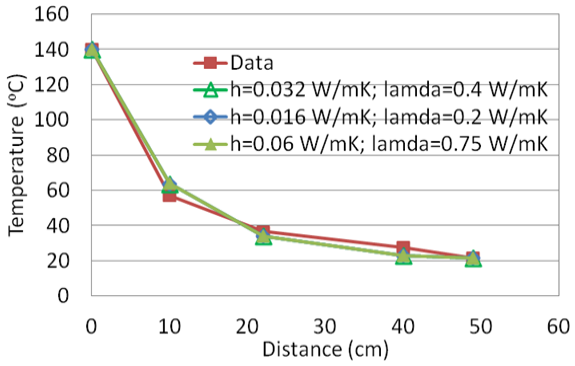

Figure 4.9. Simulated temperature profiles using different combinations of bentonite and insulation thermal conductivities and the measured temperature profile.

We then investigated the possibility of analyzing the transient temperature evolution in each step to calibrate the model for thermal conductivity of the bentonite. We found that when the temperature of heater is increased, the transient temperature data measured in the bentonite column contain information needed for the calibration of thermal conductivity of the bentonite and insulation layer, because the sensitivity of temperature response over thermal conductivities of the bentonite and insulation layer is time-dependent. When temperature at the heater is changed, the temperature evolution at the early stage is more sensitive to the thermal conductivity of the bentonite, while the impact of thermal conductivity of the insulation will

show up at later. As shown in Figure 4.10, thermal conductivities of 0.4 W/mK for bentonite and 0.04 W/mK for the insulation layer produce a temperature response that matches the transient temperature data well. Although changing the thermal conductivity of the insulation layer leads to a misfit in the temperature 2 hours after the start of heating, the match before that remains essentially the same. A change in thermal conductivity of the bentonite, however, results in a significant mismatch at the early time (Figure 4.11). Therefore, we conclude that the thermal conductivity of the granular bentonite in this experiment is 0.4 W/mK.

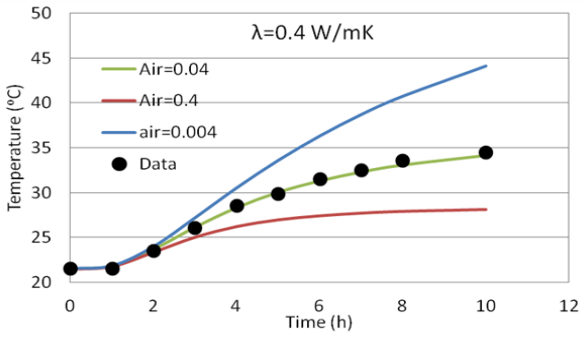

Figure 4.10. Sensitivity analysis over the amount of lateral heat loss on transient temperature data at t=0, where temperature increased from 21.5 to 100 ˚C at the surface of heater.

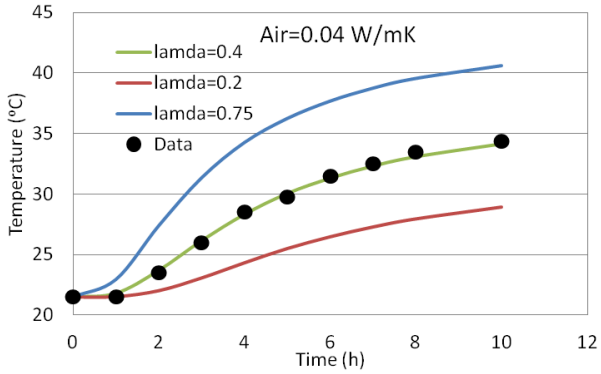

Figure 4.11. Sensitivity analysis over the thermal conductivity of bentonite on transient temperature data at t=0, where temperature increased from 21.5 to 100 ˚C at the surface of heater.

4.3.3 Dependency of thermal conductivity on water saturation

It is well known that thermal conductivity is a function of water saturation in porous soil. In this experiment, water saturation near the heater decreases with time as more water vaporized. A decrease in temperature in the first plateau (dashed box in Figure 4.12) was observed in the experiment. This phenomenon can be explained by the fact that even though the temperature at the heater surface remained unchanged, a sharper temperature gradient occurred near the heater, as the thermal conductivity in the region decreased with time. Using a constant thermal conductivity of 0.4 W/mK, the model failed to produce the decrease in temperature in the first plateau.

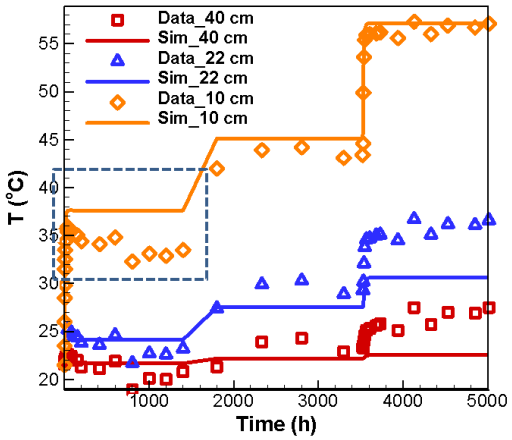

Figure 4.12. Simulated temperatures using constant thermal conductivity of 0.4 W/mK and measured temperatures.

The analysis showed that the match in temperature could be improved when the thermal conductivity varies as a function of water saturation (Figures 4.13 and 4.14). A linear function was used to describe the dependency of thermal conductivity on water saturation. With thermal conductivities of 0.28 W/mK under dry conditions and 0.825 W/mK under wet conditions, the initial thermal conductivity is still 0.4 W/mK (initial water saturation is 0.22). Considering the dependency of thermal conductivity on water saturation, the model not only reproduced the declining temperature in the first plateau (Figure 4.13), but also the transient temperature responses of two increases in temperature of the heater surface (Figure 4.14).

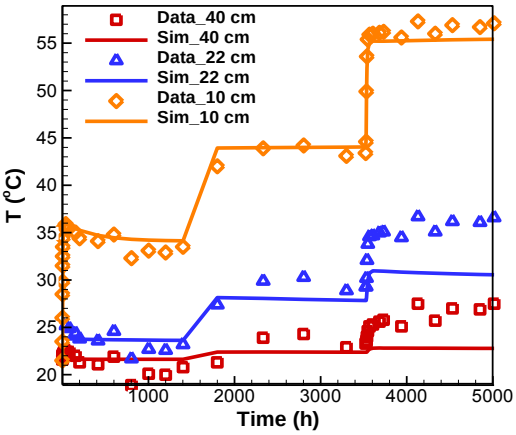

Figure 4.13. Measured temperatures and simulated temperatures with the thermal conductivity as a function of water saturation.

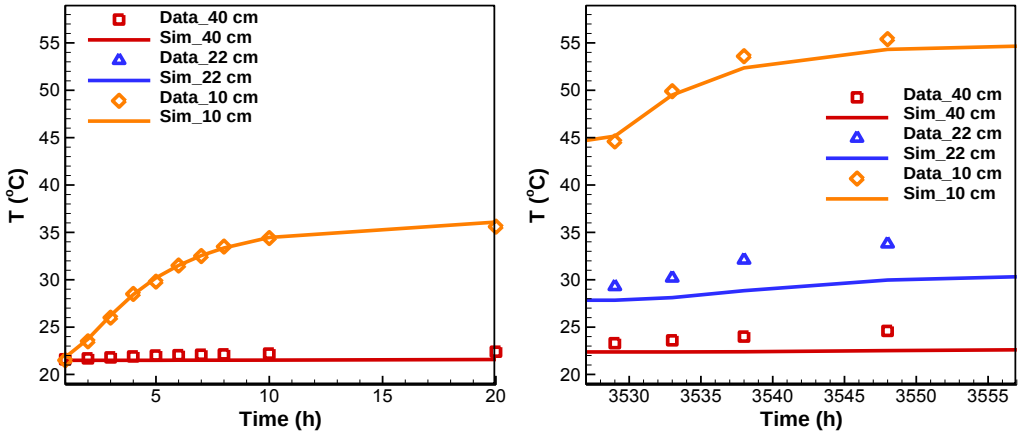

Figure 4.14. Simulated temperatures compared with the transient temperature data at t=0 and t=3527 h, when the temperature at heater surface was increased from 21.5°C to 100°C, and from 100°C to 140°C, respectively.

The calibration efforts show that the thermal conductivity of granular bentonite in this experiment is 0.28 W/mK under dry conditions and 0.825 W/mK under wet conditions. With an initial water saturation of 0.22, the bentonite in column B has an initial thermal conductivity of 0.4 W/mK. The calibrated value is consistent with the measured value by Wieczorek et al. (2013). These values were then used for the following simulations when calibrating the capillary pressure curve and analyzing the heat loss.

4.3.4 Calibration of Capillary Pressure Curve

The capillary pressure curve was described using the van Genuchten formula (van Genuchten 1980):

$$P_c = -P_0\left[(s^*)^{-1/\lambda} - 1\right]^{(1-\lambda)} \tag{4.3}$$

$$s^* = \frac{(s_l - s_{lr})}{(s_{ls} - s_{lr})} \tag{4.4}$$

where the curve fitting parameter, λ, is 0.55 (Table 4.3), residual water saturation, s_{lr}, is 0, reciprocal of entry pressure, $1/P_0$, is 2.7×10^{-8} 1/Pa, full saturation is 1.0.

The parameters were obtained by fitting the curve to the initial state (water saturation of 0.22 and capillary pressure of 1.06×10^{8} Pa) and the measurements at ambient temperature (Figure 4.15) (Rizzi et al. 2011), while matching the evolution in relative humidity in the column experiment (Figure 4.16). Note that in the column experiment, the relative humidity varies between 25 to 60%, which with the matched retention curve correspond to a saturation ranging from about 10 to 30%. Thus, we are only able to calibrate the dry end of the retention curve and this is also the range were the assumed retention curve matches the data the best in Figure 4.15.

According to the report by Rizzi et al. (2011), the capillary pressure of the bentonite sample was significantly lowered at 80°C. This temperature dependency of capillary pressure was taken into account using a simple square root function:

$$P_c(t) = P_c(t_0)\sqrt{t_0/t}, \tag{4.5}$$

where $P_c(t)$ is the capillary pressure at temperature, t; $P_c(t_0)$ is the capillary pressure at temperature, t_0.

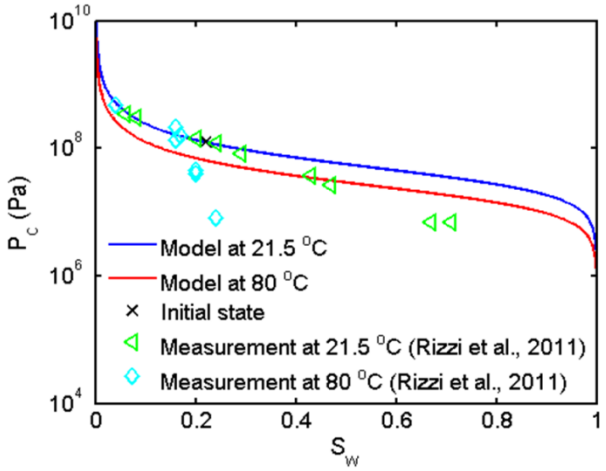

Figure 4.15. Capillary pressure curves in the model and measured capillary pressures at 21.5 and 80 ºC (Rizzi et al., 2011) for granular bentonite.

Assuming local thermodynamic equilibrium, we calculated the vapor pressure in the gas phase using the Kelvin's relationship, and the relative humidity (R_H) is therefore obtained as follows (e.g., Rutqvist et al., 2001a):

$$\ln(R_H) = \frac{P_c m^w}{\rho_l RT} \tag{4.6}$$

where P_c is the capillary pressure, ρ_l is the density of liquid water, e.g., $998.2\frac{kg}{m^3}\ at\ 20°C$ and $971.8\frac{kg}{m^3}\ at\ 80°C$, m_w is the molar mass of water, $18 \times 10^{-3}\ kg/mol$, R is the universal gas constant, which is $8.314\ J/(mol\ K)$, and T is the absolute temperature.

Table 4.3. Capillary pressure of granular bentonite used in the model.

Parameters	Values
λ	0.55
s_{lr}	0
$1/P_0$ (1/Pa)	2.7×10^{-8}
P_{max} (Pa)	3×10^{13}
s_{ls}	1.0

The simulated relative humidity is in good agreement with the measured relative humidity (Figure 4.16). After the heater was turned on, the simulated relative humidity increased rapidly at 10 cm. This is partially caused by the upward-flowing vapor from the heated zone beneath the

sensor. The other factor that contributes to increased relative humidity is the increased local temperature. At a higher temperature, the capillary pressure of the granular bentonite tends to be lower, even though the water saturation is the same. Such a phenomenon was evidenced by the measured capillary pressure at increased temperature by Rizzi et al. (2011). A lower capillary pressure, therefore, corresponds to a higher relative humidity. Over time, the relative humidity decreases at the 10 cm location, as a result of drying that occurred at the 10 cm location caused by continued heating. A discrepancy between the simulated and measured relative humidity appears after 3527 h, when insulation was improved. This is because the van Genuchten function overestimates the increase in capillary pressure at low water saturations, causing the underestimation of relative humidity at the 10 cm location. The upflow of vapor is evidenced by the continuous increases in relative humidity at the 22 cm and 40 cm locations. Overall, the simulated relative humidity is in good agreement with the measured ones at three locations.

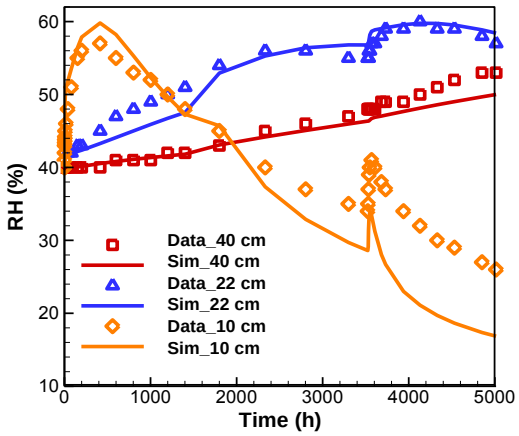

Figure 4.16. Simulated and measured relative humidity and temperature at 10, 22, and 40 cm from the heater in column experiment B.

4.3.5 Calibration of Intrinsic Permeability

Intrinsic permeability of bentonite was calibrated against the water-intake data of the hydration test. The amount of water flowing into the column was measured with time (Villar et al., 2014). Calibration results show that an intrinsic permeability of 5.5×10^{-21} m^2 produces a water intake consistent with the experiment (Figure 4.17).

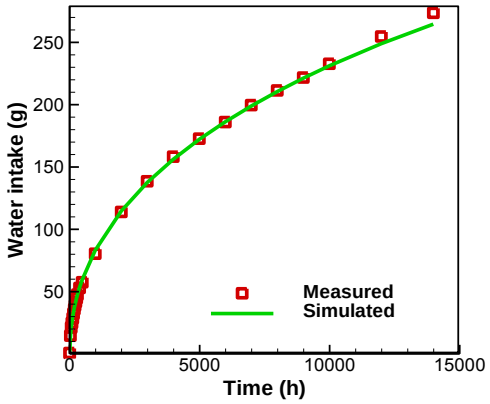

Figure 4.17. Simulated and measured water intake.

4.3.6 Analysis of Power Entering the Column

Power input was logged in the experiment to be 12 W at the end of heating (Villar et al., 2014). Our calibrated model shows that the power entering into the column at the end of heating is ~2.4 W, which is about 20% of the power input (Figure 4.18). During the experiment, heat loss occurred by means of thermal conduction through the lateral insulation layers and the bottom side of the heater and radiation.

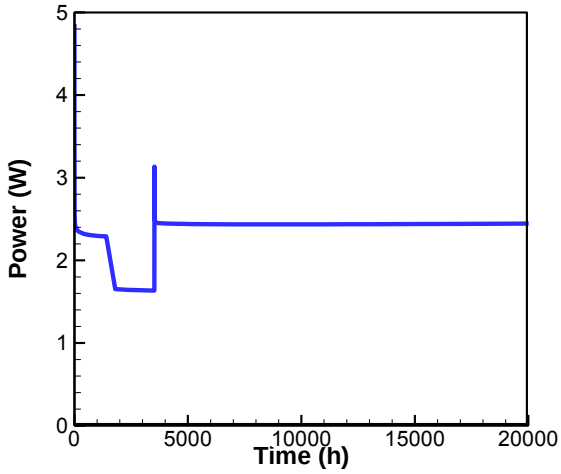

Figure 4.18. Calculated power entering the column during the heating test.

4.3.7 Model setup of column experiment on sand/bentonite mixture

For modeling of the column experiment with a sand/bentonite mixture, the same modeling approach was used. The experimental setup was also similar, but the insulation was different. In this case, the column was initially not wrapped with any insulation layers (Figure 4.19), but rather with a layer of foam 7 hours after the heater was turned on. The foam layer was later replaced with wool and BT-LV materials.

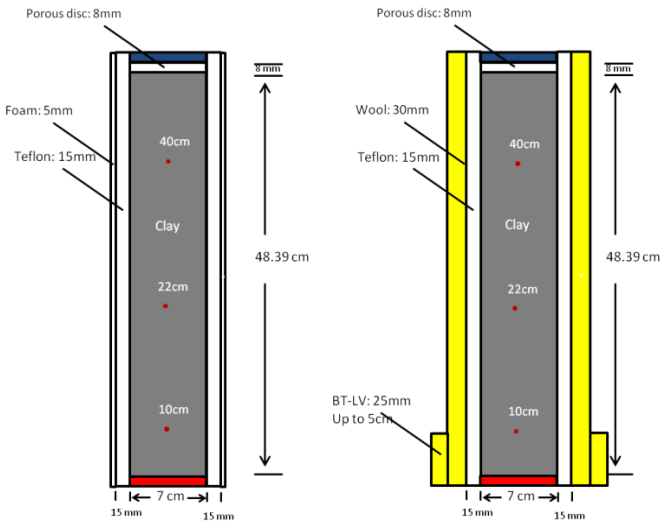

Figure 4.19. Schematic of the experimental setups before and after changing insulation.

The data acquisition system was turned on right after the system was assembled. Relative humidity and temperature were monitored for 260 hours without heating the system. The initial relative humidity is 0.46 uniformly within the column. After 95 hours, the hydration valve was accidentally opened, and water was flowing into the column until the valve was shut off ~5 minutes later. The measured relative humidity showed a steady increase from 0.46 to 0.52 at 40 cm, and an increase of 0.5% at the other two locations by 260 hours (Villar, 2012).

The heater was turned on at 260 hours and the target temperature was set at 100°C (t=0 in the simulation and the following experiment). The target temperature was reached after 25 minutes. The top of the column remained at 22.5°C. A foam layer was wrapped around the column 7 hours after the start of heating. After 1566 hours, the foam layer was replaced with wool of 30 mm thickness covering the entire column length and BT-LV of 25 mm thickness covering the bottom 8 cm. After 2498 hours, the target temperature of the heater was adjusted to 140°C. The temperature increased to 140°C 17 minutes after the adjustment was made. The experiment stopped after 3692 hours.

A 2D radial symmetric mesh was created to simulate the column experiment. The mesh has 9 columns and 28 rows (Figure 4.20). Materials used in the model include sand/bentonite mixture, porous disc, heater, cooler, Teflon, foam, wool, BT-LV, and air. The sand/bentonite mixture is represented by 4×25 elements (grey zone in Figure 4.20). Multiple steps were involved to simulate the experiment. Similar to the experimental procedure, we simulated the hydration process by assigning a slight overpressure (10^4 Pa, gauge pressure) to the cooler element. The duration of the hydration process was 5 min, as reported in the experiment. The calculated state variables (Pg, Sg, and Pa) of the system were used as the initial condition for the next step. We then simulated the heating experiment. Increasing temperature at the surface of heater was simulated by applying time-dependent heating rates to the “heater” element, with the heating rates being consistent with the experiment. During the experiment, the insulation around the column was changed. The change of insulation is considered in the model by assigning corresponding rock properties to the insulation elements.

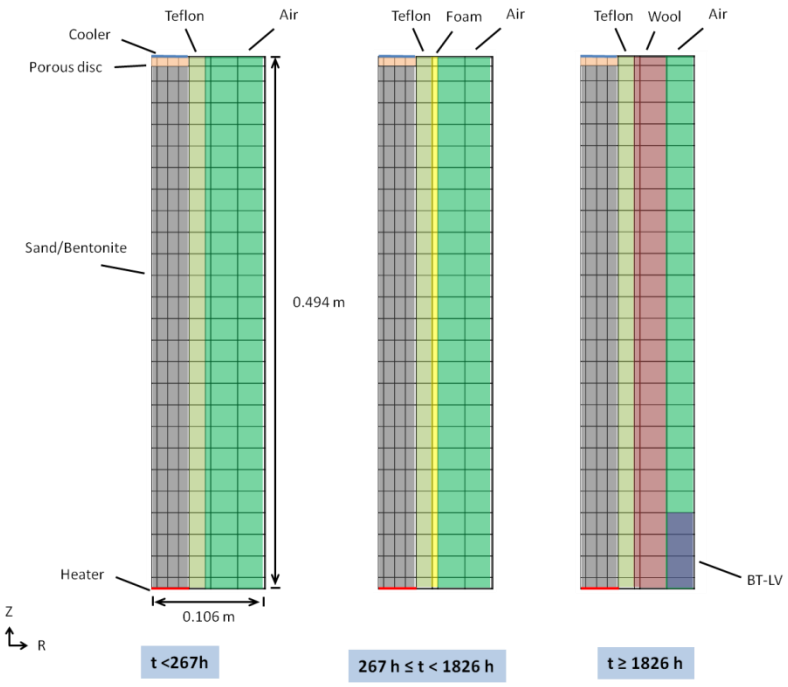

Figure 4.20. Model mesh and the materials represented in the model at different steps for column experiment A. The reference time (t = 0) is the start of heating.

The sand/bentonite mixture properties used in the model are as shown in Table 4.4. The sand/bentonite mixture has a solid grain density of 2700 kg/m^3. Its intrinsic permeability is 1.2×10^{-20} m^2, which is consistent with the measured permeability by Wieczorek et al. (2013). The porosity is 0.46. It has a wet thermal conductivity of 0.8 W/mºC and a dry thermal conductivity of 0.29 W/mºC. Thermal conductivity in between was interpolated linearly as a function of water saturation. The value of thermal conductivity is close to the measured values by Wieczorek et al. (2013), where the thermal conductivity of sand/bentonite mixture was measured to be 0.305 W/ mºC at a water saturation of 2.78%. The specific heat of the sand/bentonite mixture is 950 J/kgºC. Before the experiment started, the pores of the sand/bentonite mixture were initially saturated with 11% of water.

Table 4.4. Properties of sand/bentonite mixture used in the model.

Solid grain density	2700 kg/m^3
Porosity	0.46
Intrinsic permeability	1.2×10^{-20} m^2
Saturated thermal conductivity	0.8 W/ mºC
Unsaturated thermal conductivity	0.29 W/mºC
Specific heat	950 J/kgºC
Tortuosity	0.67

Similarly to the modeling of the granular bentonite, for the sand/bentonite mixture a diffusion coefficient of 2.13×10^{5} m^2/s was used for both vapor and air, and a tortuosity factor of 0.67 was

used in the model. A high Klinkenberg parameter of 2.5×10^{11} Pa was used to simulate high gas intrinsic permeability.

Transport of vapor in a tight formation is enhanced by diffusion and Klinkenberg effects. Olivella and Gens (2000) reported that the measured permeabilities of Full-scale Engineered Barrier Experiment (FEBEX) and Boom Clay samples to gas are about 6–7 orders of magnitude higher than those to liquid. To account for the increased gas permeability, we considered vapor and air diffusion and Klinkenberg effect in the model. A diffusion coefficient of 2.13×10^{5} m^2/s was used for both vapor and air, and a tortuosity factor of 0.67 was used in the model. A Klinkenberg parameter of 2.5×10^{11} Pa was used.

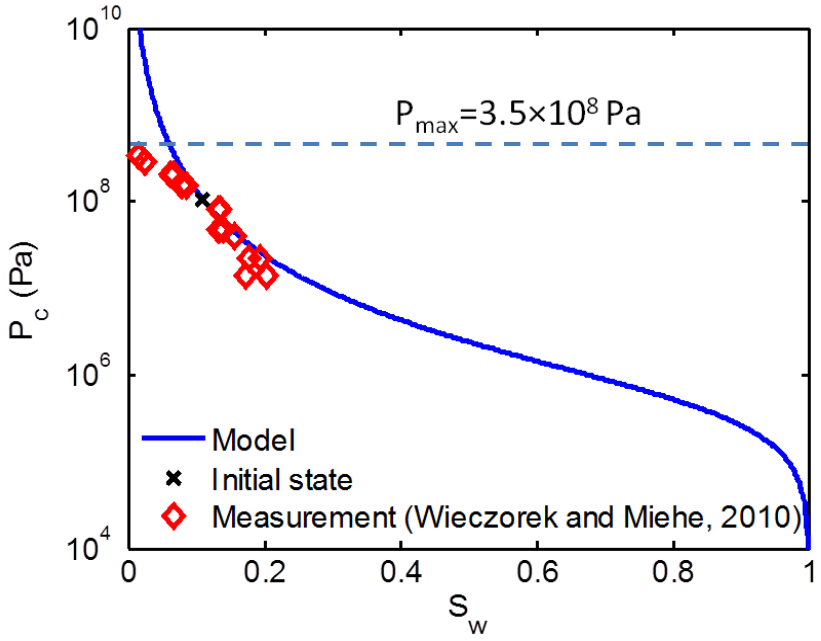

Figure 4.21. Capillary pressure curve used in the model and measured capillary pressures by Wieczorek and Miehe (2010) for sand/bentonite mixture.

Again, we used the van Genuchten formula (Equations (4.3) and (4.4)) to describe the water-retention curve (van Genuchten, 1980), where λ is the curve fitting parameter, P_0 is the entry pressure, and s_{ls} and s_{lr} are the full and residual water saturations, respectively. The variables λ and P_0 were adjusted to fit the capillary pressure curve over the capillary pressures measured with sand/bentonite mixture at varied water saturations (Wieczorek et al., 2013) and the measured initial state of the sand/bentonite mixture (Figure 4.21). The sand/bentonite mixture in column has an initial relative humidity of 46% (capillary pressure of 1.06×10^{8} Pa) at a water saturation of 11% (Figure 4.22). To better represent the capillary pressures at low water saturations, a cut-off upper limit of 3.5×10^{8} Pa was used for the capillary pressure curve in the model. Values for the parameters in the van Genuchten model are presented in Table 4.5. Temperature dependency of capillary pressure was considered using the simple square root function in Equation (4.5).

Table 4.5. Capillary pressure of the sand/bentonite mixture.

Parameters	Values
λ	0.29
s_{lr}	0
$1/P_0$ (1/Pa)	2.1×10^{-6}
P_{max} (Pa)	3.5×10^{8}
s_{ls}	1.0

The relative permeability used for liquid water is described as a power function of the degree of water saturation, and the gas phase was assumed to be perfectly mobile, with a relative permeability of 1 (Equations (4.1) and (4.2)).

Other materials in the model use values close to typical values of the materials and those measured by Villar (2012). The porous disc has a high permeability of 1.2×10^{-12} m^2. Teflon, heater, cooler, foam, wool, and BT-LV were assigned with an extremely low permeability (1.0×10^{-24} m^2). The thermal conductivities of other materials are shown in Table 4.6. The thermal conductivity values were close to the measured ones by Villar (2012) and typical thermal conductivity of the materials. Only slight adjustments were made to better match the temperature profile.

Table 4.6. Properties of other materials used in the model.

Materials	Permeability	Thermal conductivity
Porous disc	1.2×10^{-12} m^2	3.5 W/m^{o}C (wet), 0.5 W/m^{o}C (dry)
Teflon	1.0×10^{-24} m^2	0.4 W/m^{o}C (wet and dry)
Foam	1.0×10^{-24} m^2	0.08 W/m^{o}C (wet and dry)
Wool	1.0×10^{-24} m^2	0.06 W/m^{o}C (wet and dry)
BT-LV	1.0×10^{-24} m^2	0.054 W/m^{o}C (wet and dry)
Air	1.0×10^{-24} m^2	0.06 W/m^{o}C (wet and dry)

4.3.8 Sand/bentonite mixture simulation results and discussion

The simulated results agree with the experimental measurements well during the hydration (Figure 4.22). Relative humidity at 40 cm increased from 46% to 52%, during which the hydration valve was opened, while at other locations it remained unchanged. Temperature for all sensors remained at 22.5°C, because the heater has yet to be turned on.

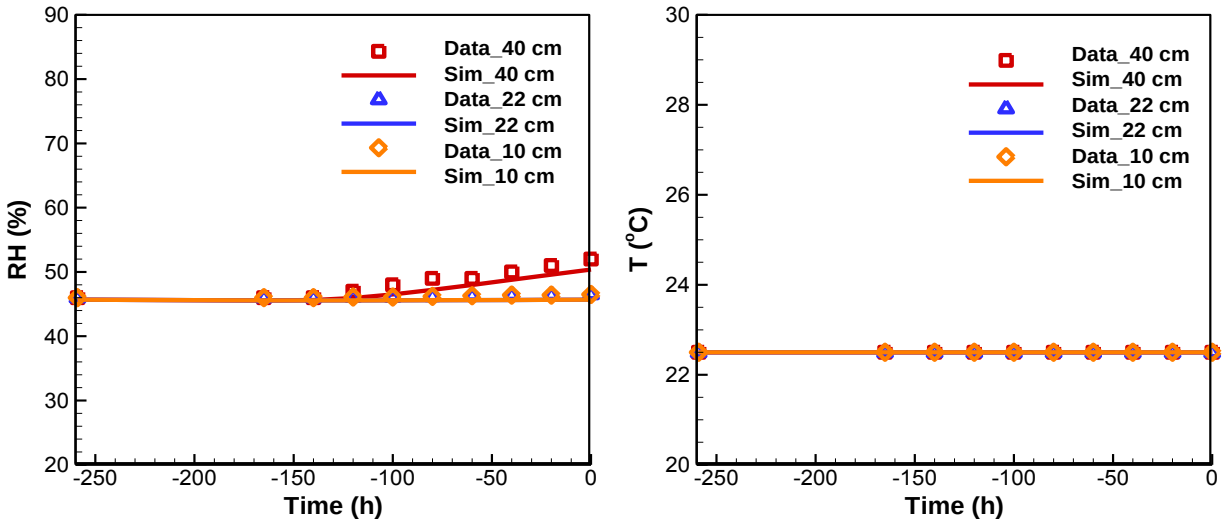

Figure 4.22. Simulated and measured relative humidity (RH) and temperature (T) during hydration.

After the heater was turned on, the simulated relative humidity increases rapidly at 10 cm (Figure 4.23), due to the increase in temperature and the vapor flowing up. When temperature increases at the 10 cm location, relative humidity increases as the capillary pressure drops, even if the water saturation remains unchanged. However, heating also causes the vapor pressure to increase near the heater, which drives vapor flowing up and contributes to the increased relative humidity at the 10 cm location during the early stage of heating. Over time, the relative humidity decreases at the 10 cm location. This is because further heating causes the drying at the 10 cm location with the vapor flowing further up. This upflow of vapor is evidenced by the continuous increases in relative humidity at the 22 cm and 40 cm locations. In addition to the upflow of vapor, the large increase in relative humidity at the 40 cm location is also contributed by the hydration process. As water flowed into the column before the start of heating, the water saturation at the 40 cm location gradually increases as a result of liquid water flowing downward via gravity and capillary forces. Overall, the simulated relative humidity at three locations is in a good agreement with the measured ones.

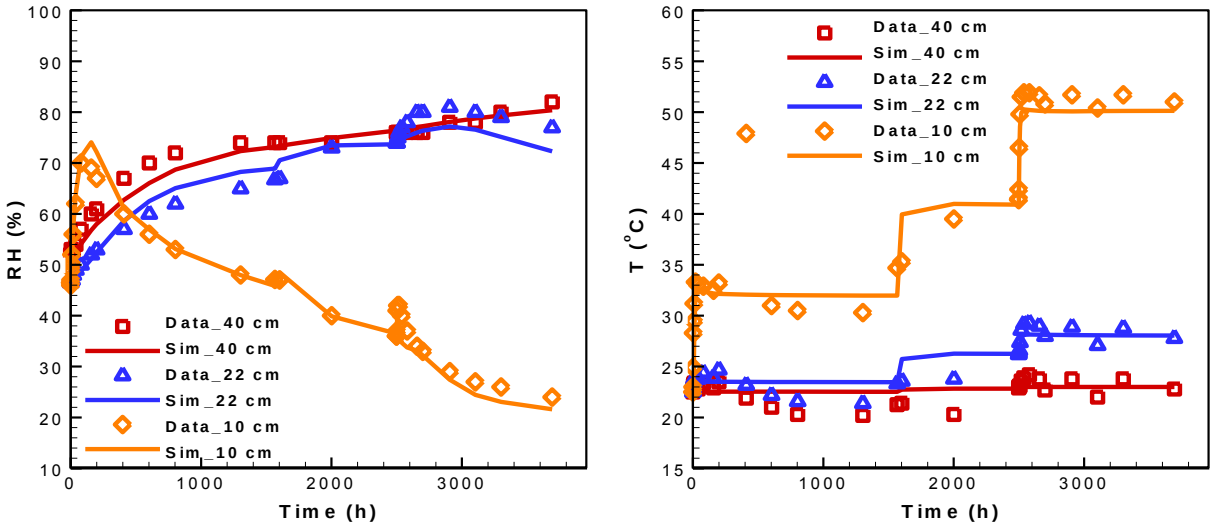

Figure 4.23. Simulated and measured relative humidity (RH) and temperature (T) after heater was turned on.

Simulated temperature profiles agree well with the measured data. As expected, the temperature at the 10 cm location increases rapidly to ~30°C after the start of heating. It then increases to 41°C when the heater temperature was increased to 140°C. Further increase to 50°C occurs as insulation was improved. The temperature at the 40 cm location only increases slightly, due to the heat loss along the column, suggesting that the increase in relative humidity at this location is primarily caused by the transport of vapor and liquid water.

4.3.9 Concluding remarks on CIEMAT column experiments

We have conducted very detailed model simulations of CIEMAT column experiments for the characterization of buffer properties used in the Mont Terri *in situ* heating experiments. The simulation of the CIEMAT turned out to be more cumbersome than expected, because of a substantial heat loss from the equipment that has to be considered in order to characterize the thermal properties of the buffer material. We learned that by looking at the transient temperature and moisture responses in addition to steady-state profiles, we could obtain a unique solution for back-calculating the thermal and hydraulic properties of the buffer material. Calibration against transient temperature data showed that the thermal conductivity of the granular bentonite is 0.4 W/mK at a water saturation of 22%, which is in agreement with other independent measurements on this type of bentonite. Moreover, we found that a gradual decrease in temperature during the first month could be used for validating the dependency of thermal conductivity on water saturation. The capillary-pressure curves for the buffer materials were adjusted to fit the measured data and initial state of the bentonite in the experiments. Temperature dependency of capillary pressure was considered using a square root function. By accounting for the enhanced permeability of gas and temperature dependency of the capillary pressure, the model can reasonably reproduce the evolution of relative humidity along the column in the experiments. Intrinsic permeability was calibrated against the water intake data when available. The calibrated model for the granular bentonite experiment showed that the heat flow entering the column was ~2.4 W, about 20% of the total power input.

4.4 Horonobe EBS Experiment (DECOVALEX)

This task focuses on coupled THMC modeling of a planned full-scale EBS experiment conducted by the Japan Atomic Energy Agency (JAEA) at the Horonobe URL, Hokkaido, Japan (Figure 4.24). The EBS experiment will be carried out at a depth of 350 m in a very porous and soft, siliceous mudstone with the following basic properties:

- Porosity 35-60%
- Permeability 10^{-20} – 10^{-18} m^2
- UCS (Strength) 5-25 MPa
- Young's Modulus 1-4 GPa
- Thermal Conductivity 1.34-1.53 W/mK

Figure 4.25 show the experimental layout with a vertical heater emplacement installed in a test pit at the bottom of an experimental drift. The experimental drift will be backfilled after the installation of the heater and bentonite buffer into the test pit. Backfill and buffer materials will be based on the Japanese Kunigel V1 bentonite. The experimental area will then be isolated by a concrete plug.

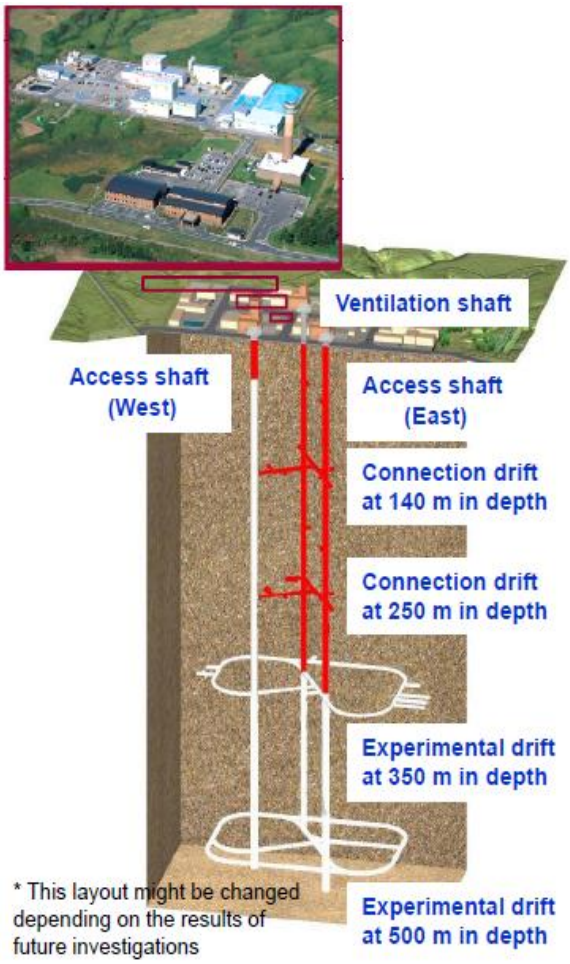

Figure 4.24. Layout of the Horonobe URL in Hokkaido, Japan.

(a)

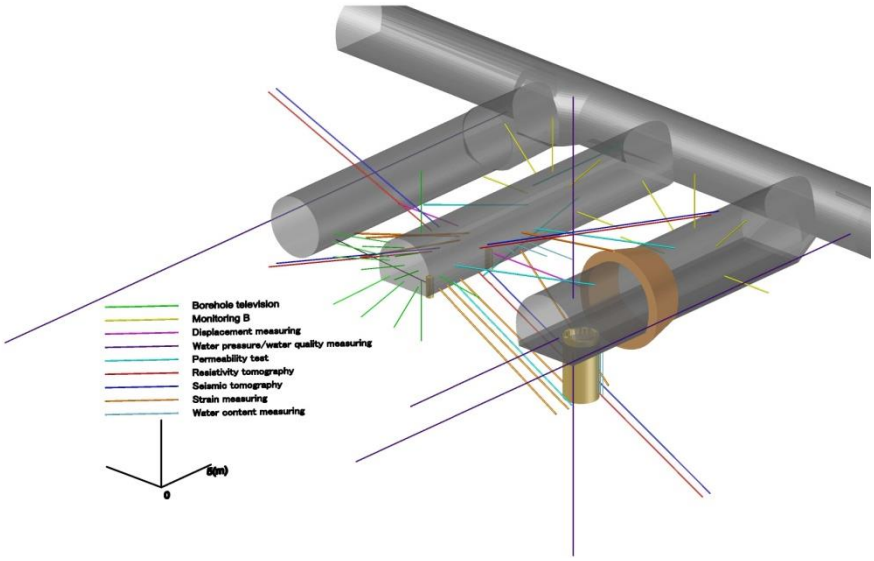

(b)

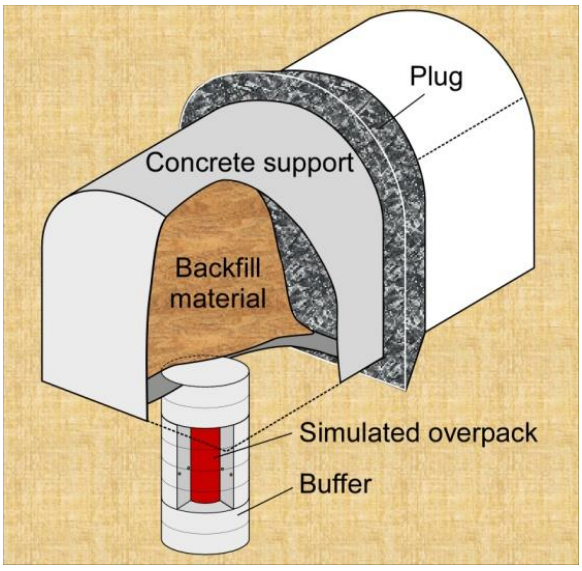

Figure 4.25. General description of the EBS experiment at the Horonobe URL Project in Japan.

Sensors will be installed in buffer, backfill, and rock to monitor temperature, stress, strain, pore pressure, humidity, displacement, pH, resistivity, electric potential, and seismic velocity. The detailed layout is not yet fixed and may be changed, depending on the initial modeling results.

The DECOVALEX Task B2 related to the Horonobe EBS experiment is divided into the following steps;

- Step 1 (1D benchmark test with comparison of numerical models)
- Step 2 (Prediction analysis and proposal of the sensors layout)
- Step 3 (Calibration analysis)

The 1D benchmark test (Step 1) was defined with exact properties and boundary conditions given by the JAEA. The benchmark test was conducted for the teams to familiarize themselves

with the problem and for precise comparison of computer codes before going into the more complex full-scale case. Thereafter, in Step 2, a model of the real experimental design should be constructed and a first predictive analysis should be performed for several years from the start of the heating. The results will then be used to guide the installation of sensors, which began in April 2014. The heating is planned to start in November 2014, and in April 2015, JAEA will provide the monitored data for the first six months of heating to the research teams. The research teams will calibrate their models against this first 6 months of field data and then carry out coupled numerical analysis for long-term predictions (100–1,000 years) using the test conditions of the EBS experiment.

JAEA provides reports from the investigations at the Horonobe URL for input parameters related to the mudstone host rock and buffer material properties for the Kunigel V1 bentonite from the previous H12 project, whereas properties for the backfill are being investigated along with this project.

Task B2 started in May 2013 with Step 1, which has been completed. In the next section, we present the final LBNL results and comparison to the simulation results of other research teams. Step 2 has begun and should be completed before the next DECOVALEX workshop, to be held in November 2014. In this report, we present the model setup and preliminary model prediction for this case.

4.4.1 Final 1D Benchmark Modeling and Comparison to Other Models

The initial modeling of the 1D benchmark modeling associated with the Horonobe EBS experiment was presented in the FY2013 milestone report entitled “THM and Reactive Transport Model Development and Evaluation: International Activities” (Rutqvist et al., 2013b). The results are to be presented at DECOVALEX-2015 workshops and compared with the results of other modeling teams. Here, we present the final results of this benchmark, as well as a comparison to the final results of other modeling teams. We used TOUGH-FLAC for modeling of this benchmark and comparison to the other modeling teams. We also used the ROCMAS code, which was beneficial for understanding input parameters given by the JAEA related to the diffusion properties of the bentonite. The material properties used for the overpack, buffer and rock used in the LBNL simulation are listed in Table 4.7.

Table 4.7. Material parameters for TOUGH-FLAC.

	Overpack	Buffer	Rock
Solids density (kg/m^3)	10,000.	2680.	2454.
Porosity	0.403	0.403	0.4482
Permeability (m^2)	5 x 10^{-51}	4 x 10^{-20}	1.33 x 10^{-15}
Thermal conductivity (saturated) (W/mºC)	20	1.986	1.231
Specific heat (solids) (J/kg°C)	10,000	341	626
Thermal conductivity (desaturated) (W/mºC)	20	0.444	0.579
Klinkenberg parameter (Pa)	8.47 x 10^{-10}	8.47 x 10^{-10}	8.47 x 10^{-10}
Water relative permeability parameter A, (Equation (4.7))	1.3	1.3	NA
Water relative permeability residual saturation, S_r (Equation (4.7))	0	0	NA
Water relative permeability maximum saturation, S_m (Equation (4.7))	1	1	NA
Water relative permeability parameter *m*, (Equation (4.8))	NA	NA	0.503
Water relative permeability residual saturation, S_r (Equation (4.8))	NA	NA	0
Water relative permeability maximum saturation, S_m (Equation (4.8))	NA	NA	1
Capillary pressure parameter, α (m^{-1}) (Equation (4.11))	8 x 10^{-3}	8 x 10^{-3}	9.928 x 10^{-3}
Capillary pressure parameter, *m*, (Equation (4.11))	0.375	0.375	0.503
Capillary pressure residual saturation, S_r (Equation (4.11))	0	0	0
Capillary pressure maximum saturation, S_r (Equation (4.11))	1	1	1
Vapor diffusion coefficients (m^2/s)	3.5 x 10^{-6}	3.5 x 10^{-6}	3.5 x 10^{-6}
Klinkenberg parameter (Equation (4.12))	-	2.5 x 10^{11}	-
Young's modulus E, (MPa)	200.000	37	1820.0
Poisson's ratio, ν (-)	0.3	0.3	0.21
Linear thermal expansion coefficient (C^{-1})	1 x 10^{-6}	1 x 10^{-6}	1.33 x 10^{-5}
Moisture swelling coefficient, β_{sw} (Equation (7.24))	0	0.0108	0

The water relative permeability in the buffer (and overpack) is a power-law relationship given by

$$k_{rw}(S_w) = \left(\frac{S_w - S_r}{S_m - S_r}\right)^A \tag{4.7}$$

The water relative permeability in the rock is given by the van Genuchten relationship:

$$k_{rw}(S_w) = \left(\frac{S_w - S_r}{S_m - S_r}\right)^{1/2} \left[1 - \left\{1 - \left(\frac{S_w - S_r}{S_m - S_r}\right)^{1/m}\right\}^m\right]^2 \tag{4.8}$$

In the buffer (and overpack), the gas relative permeability is represented by the Corey model,

$$k_{rg}(S_w) = \left\{1 - \left(\frac{S_w - S_r}{1 - S_r - S_{gr}}\right)^2\right\}\left\{1 - \left(\frac{S_w - S_r}{1 - S_r - S_{gr}}\right)\right\}^2 \tag{4.9}$$

In the rock, the gas relative permeability is:

$$k_{rg}(S_w) = 1 - k_{rw}(S_w) \tag{4.10}$$

Capillary pressure in the buffer (and overpack) and rock is given by the van Genuchten relationship:

$$\psi(S_w) = \frac{1}{\alpha}\left\{\left(\frac{S_w - S_r}{S_m - S_r}\right)^{-1/m} - 1\right\}^{1-m} \tag{4.11}$$

Variations in thermal conductivity and specific heat with water saturation are assumed to be linear between the defined end points. The vapor diffusion coefficient is constant; there is no temperature dependence.

For the multiphase flow simulation using TOUGH2 we found that gas permeability has an important effect. Indeed, laboratory data on bentonite and clay rocks have shown that the intrinsic permeability for air is up to six orders of magnitude higher than the intrinsic permeability for water flow (Olivella and Gens, 2000). A high value of gas permeability was also inferred by Xu et al. (unpublished) from modeling of a salt-imbibition experiment using a mixture of the Kunigel V1 bentonite. In order to match the saturation profile observed in the experiment, the gas permeability had to be increased to five-orders-of-magnitude larger than that of liquid. In TOUGH2, this was accomplished by specifying a large Klinkenberg parameter, which is used to account for the increase in gas-phase permeability at low pressures:

$$K_g = K_l\left(1 + b/P\right) \tag{4.12}$$

Xu et al. (unpublished) inverted the Klinkenberg parameter to 2.5×10^{11} Pa^{-1}. Using this parameter, the intrinsic permeability for air will be about 5 orders of magnitude higher than the intrinsic permeability for water.

In Figure 4.26, results are presented with and without high gas permeability. If the intrinsic permeability for the gas phase is similar to that of the liquid, the gas pressure will increase, and this will suppress the vapor diffusion. In such a case, no drying occurs near the heat source, and the evolution of saturation is completely different for that with high gas permeability.

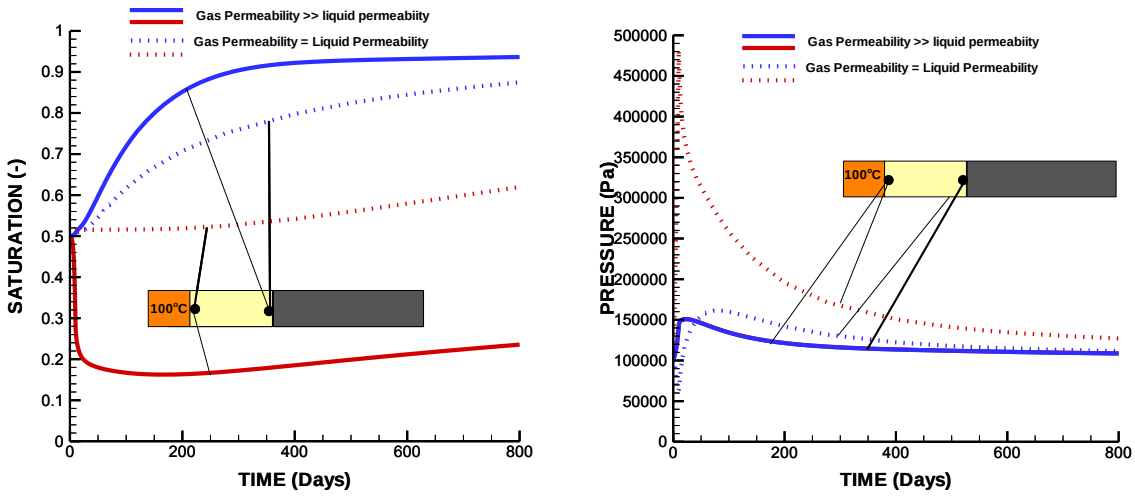

(a) (b)

Figure 4.26. Simulation results with and without high gas permeability: (a) saturation and (b) pressure evolution.

The selection of the diffusivity affecting the diffusive flux according to Equation (4.13) (Rutqvist et al. 2001a) has a pronounced impact on the simulation results. In the task definition, a constant thermal diffusivity is given as $D_T = 1.5\times10^{-11}$ m^2/sK (see Rutqvist et al. 2001a for explanation of thermal diffusivity). This is a parameter input to the THAMES code used by the JAEA. In TOUGH2, the basic diffusion coefficient should be given as an input, but it is not straightforward to know what basic diffusion coefficient would correspond to $D_T = 1.5\times10^{-11}$ m^2/sK. In this case, the basic diffusion coefficient was estimated using the ROCMAS code, in which either the basic diffusion coefficient or the thermal diffusivity can be given as an input. By model calibration using ROCMAS, it was found that a good value for the basic diffusion coefficient would be $D_{Vo} \approx 3.5\times10^{-6}$ m^2/s.

$$\mathbf{i}_{\psi}^{\kappa} = -\rho_{\psi} D_{v0} \phi S_g \mathbf{I} \nabla X_{\psi}^{\kappa} \tag{4.13}$$

Finally, a linear elastic swelling model was used to model the evolution of swelling stress, and the model input parameters can be determined analytically to achieve a desired maximum swelling stress of 0.5 MPa. In such a case, the bentonite is assumed to behave elastically, with a volumetric swelling and a swelling stress that depends on the changes in water saturation, ΔS_l, according to:

$$\Delta\sigma'_{sw} = 3K\Delta\varepsilon_{sw} = K\Delta S_l \beta_{sw} \tag{4.14}$$

where $\Delta\sigma'_{sw}$ is the induced swelling stress (an effective stress), K is the bulk modulus, and β_{sw} is a moisture swelling coefficient. For an average bulk modulus of 30.83 MPa, the appropriate moisture swelling coefficient can be calculated using Equation (4.14) as:

$$\beta_{sw} = \frac{\Delta\sigma'_{sw}}{3K\Delta S_l} = \frac{0.5 \cdot 10^6}{3 \cdot 30.83 \cdot 10^6 \cdot (1.0 - 0.5)} = 0.0108 \tag{4.15}$$

Thus a moisture swelling coefficient of β_{sw} = 0.0108 was applied in this case.

In Figure 4.27, results are presented for the thermal hydrological behavior using TOUGH2 and ROCMAS. In both simulations, a basic diffusion coefficient of 3.5×10^{-6} m^2/s was used. The results are almost identical, although it appears that the water infiltration from the rock is slightly faster in the TOUGH2 simulation.

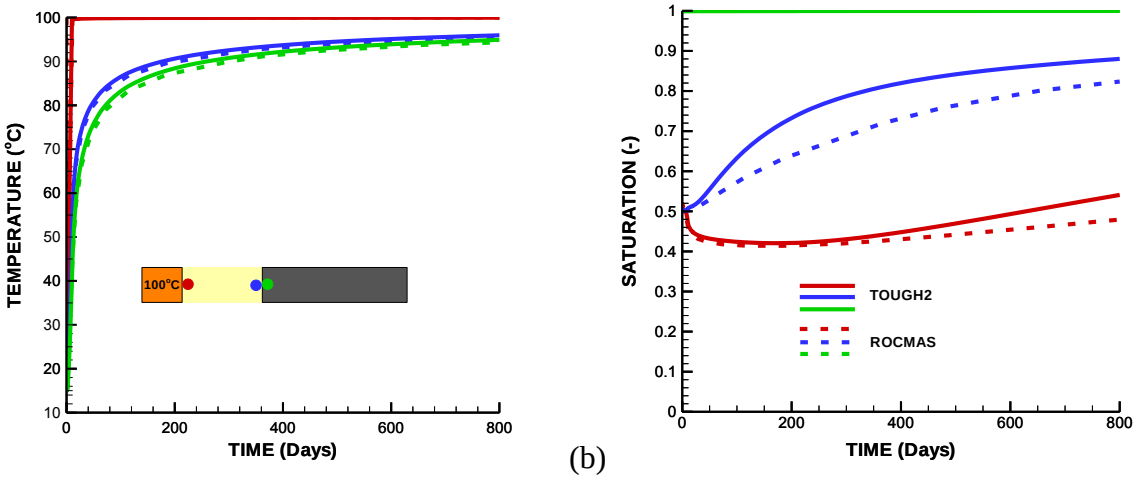

(a) (b)

Figure 4.27. (a) Temperature and (b) saturation evolution for simulations using TOUGH2 and ROCMAS.

Figure 4.28 shows the x-stress evolution in the buffer. The simulation results are shown for two simulations, with and without consideration of thermal expansion. The results show that over the 800 days, thermal stresses dominate. This is actually caused by thermal expansion of the rock, which in this 1D model expands inwards towards the bentonite buffer. The buffer is therefore compressed and compressive stress increases.

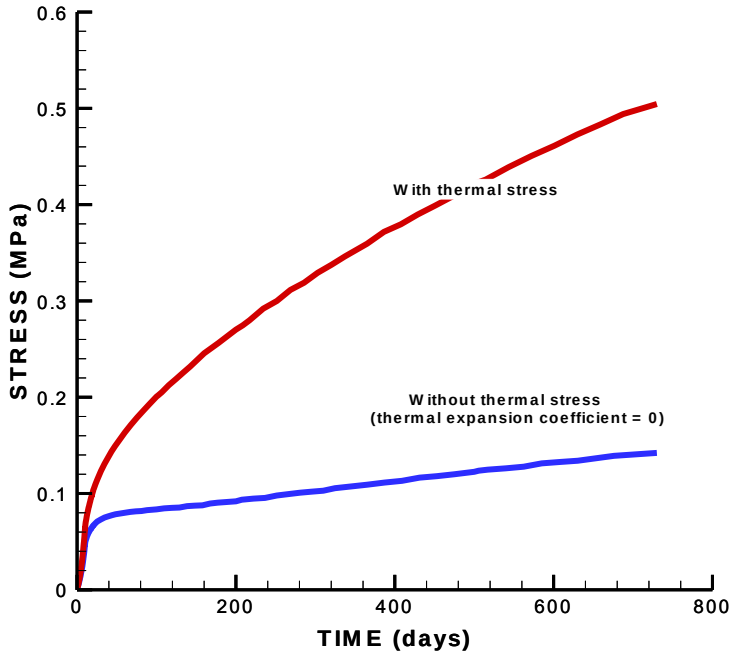

Figure 4.28. Buffer stress evolution with/without thermal expansion.

In DECOVALEX-2015, five research teams are participating in the modeling of the Horonobe EBS experiment with the models listed in Table 4.8. Some of the models listed in Table 4.10 have been extensively applied in previous DEOCOVALEX project phases, whereas some are new and being developed. Figures 4.29 to 4.33 show comparisons of the simulation results regarding temperature, saturation, and stress. A very good agreement between different models is achieved for temperature and saturation, whereas the results of stress show some differences. Heat conduction dominates the temperature evolution, though the buffer saturation can have a significant impact on thermal conductivity. There is good agreement in the wetting of the bentonite from the surrounding rock, whereas there is some difference in the saturation evolution near the heat source. At the point next to the heater, a slight drying occurs in the results of DOE, BGR and JAEA, whereas no drying occurs in the results of CAS and KAERI. This is most probably related to the modeling of diffusion of vapor in the gas phase, which was not considered by CAS and KAERI. The calculated stress evolution in the buffer is very similar for DOE, KAERI, and JAEA, whereas BGR and CAS obtained somewhat lower stress. However, considering all the complex THM processes that affect the stress evolution, the agreement between the different teams is acceptable.

Table 4.8. Research teams and numerical simulators applied in this study.

Research Team	Numerical Simulator	Brief Description of Numerical Simulator
DOE U.S. Department of Energy's Research Team: Lawrence Berkeley National Laboratory (LBNL)	TOUGH-FLAC	TOUGH-FLAC is a simulator for analysis of coupled THM processes under multiphase fluid flow conditions being developed at the LBNL (Rutqvist et al., 2002). The simulator is based on linking of the existing computer codes TOUGH2 and FLAC3D, and has been extended for modeling of coupled THM and THMC processes associated with nuclear waste disposal with backfilled emplacement tunnels in clay formations (Rutqvist et al., 2014).
	ROCMAS	ROCMAS is a finite element program for analysis of coupled THM processes in porous and fractured rock developed at LBNL (Rutqvist et al., 2001a). It can model unsaturated media with single-phase liquid flow and vapor diffusion in a static gas phase The code has been extensively applied in earlier phases of the DECOVALEX project for THM analysis in bentonite-rock systems (Rutqvist et al., 2001b; 2005).
BGR Bundesanstalt für Geowissenschaften und Rohstoffe's Research Team: University of Tübingen	GeoSys/ Rockflow	GeoSys/Rockflow is based on object-oriented programming (Kolditz et al., 2003). It was first applied in previous DECOVALEX phases for analysis of thermal-hydrological and thermal-mechanical processes and has been extended to THM (Wang et al., 2006). For the present study, an unsaturated single-phase liquid flow and vapor diffusion is considered.
CAS Chinese Academy of Sciences' Research Team	EPCA3D	The EPCA code (Elasto-Plastic Cellular Automata) uses the concept of cellular automata inspired by the self-organizing theory in biology. This code has been successfully used to simulate the failure process of heterogeneous rocks with and without consideration of hydro-mechanical coupling (Feng et al., 2006; Pan et al., 2008).
JAEA Japan Atomic Energy Agency's Research Team, including Hazama Cooperation	THAMES	THAMES is a finite element program for analyzing coupled THM processes in porous and fractured rock developed at the Kyoto University (Ohnishi and Kobayashi, 1996). The code has been extended to unsaturated media with single-phase liquid flow and vapor diffusion in a static gas phase (Chijimatsu et al., 2005).
KAERI Korean Atomic Energy Research Institute	FLAC/ FLAC3D/ Tough2	Simulation tools being developed along with the DECOVALEX-2015 project based on FLAC and FLAC3D linked with TOUGH2.

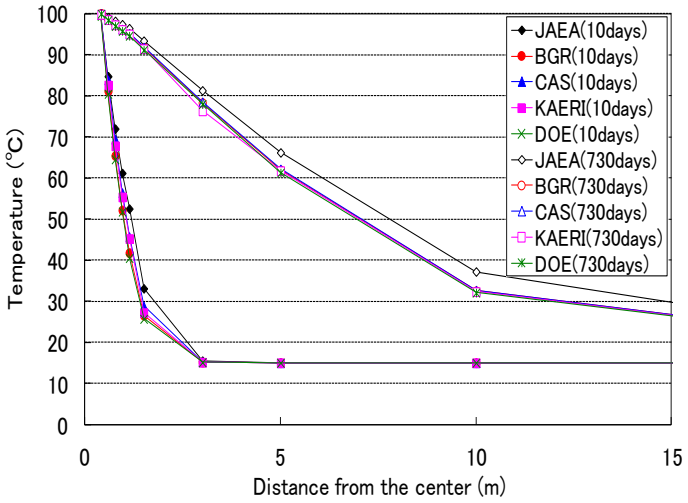

Figure 4.29. Comparison of the analytical results on distribution of temperature.

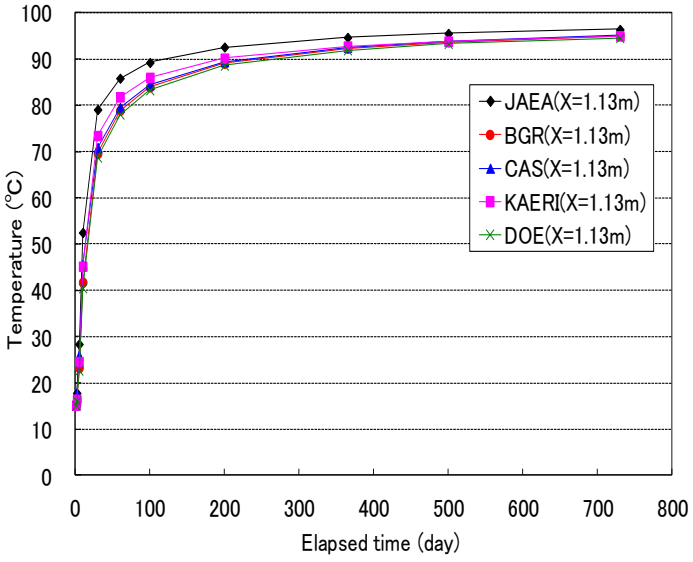

Figure 4.30. Comparison of the analytical results on variation of temperature at the output point (X=1.13m).

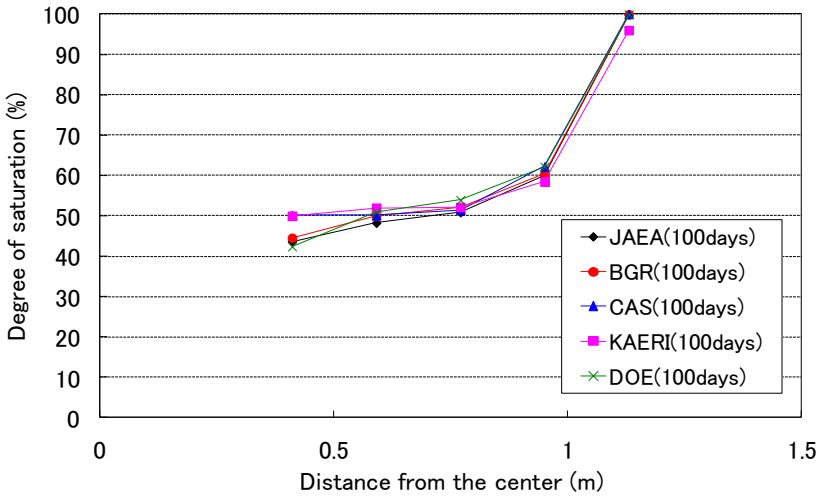

Figure 4.31. Comparison of the analytical results on degree of saturation in the buffer after 100 days.

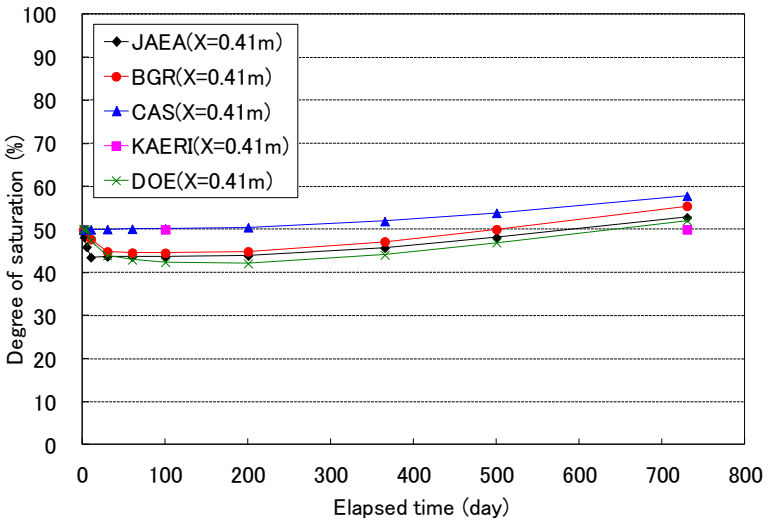

Figure 4.32. Comparison of the analytical results on variation of degree of saturation at the output point (X=0.41m).

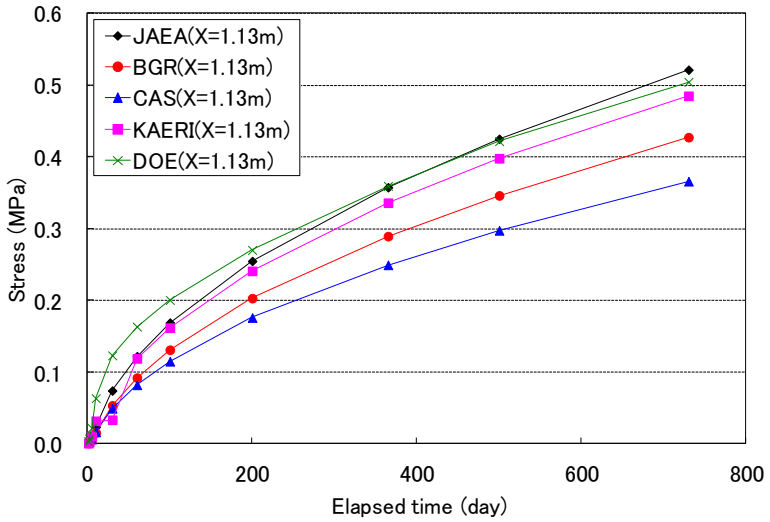

Figure 4.33. Comparison of the analytical results on vartiation of stress at the output point (X=1.13m).

4.4.2 Initial model prediction of the full scale Horonobe EBS experiment

We have recently developed a 3D model and made an initial prediction of the THM responses at the Horonobe EBS experiment. The model is half symmetric, including half of the tunnel and half of the deposition hole (Figure 4.34). It contains all relevant materials, including mudstone rock, buffer, backfill, a sand layer at the rock/buffer interface, concrete lining and plug. In this model prediction, we use the properties of the buffer and rock developed associated with the 1D benchmark calculation (Table 4.11). However, additional properties are needed for the backfill, sand layers, concrete lining and plug. At the moment, material properties for the backfill, which consists of bentonite mixed with sand and rocks, has not been completely characterized and provided to the DECOVALEX research teams.

The only parameters we currently have for the backfill is a dry density of 1300 kg/m^3, a porosity of 0.5, and an initial degree of liquid saturation of 0.7. Our approach is to use backfill properties determined in the Swedish nuclear waste program for a backfill consisting of a mixture of bentonite and crushed rock with a weight ratio of 30/70. The 30/70 backfill material was used in Rutqvist and Tsang (2008) for modeling of proposed Swedish nuclear waste disposal sites. Here we consider the 30/70 bentonite properties for estimating the properties of the backfill material to be used in the Horonobe EBS experiment. In general, the backfill will be emplaced at lower dry density having a higher porosity than the compacted bentonite buffer material. Therefore, we expect smaller stiffness (Young's modulus) and swelling stress, a higher intrinsic permeability, and a lower capillary pressure. The greatest difference is expected for the intrinsic permeability and water-retention curve. For estimating the intrinsic permeability, we used an empirical relation between dry density and intrinsic permeability provided by JAEA. According to this relation, for a backfill dry density of 1300 kg/m^3, the intrinsic permeability would be 0.64×10^{-19} m^2. We used the water-retention curve from the abovementioned 30/70 backfill material (Rutqvist and Tsang, 2008).

In addition, we have to assign properties for the concrete plug, concrete lining, and the sand layer at the rock-buffer interface. For the concrete material, we assigned typical properties including a

permeability of 1×10^{-19} m^2, Young's modulus of 23 GPa. For simplicity, we assumed a water-retention curve equivalent to that of the mudstone rock. For the sand layer, because of its expected high porosity and permeability, we used the same properties as for the surrounding mudstone rock.

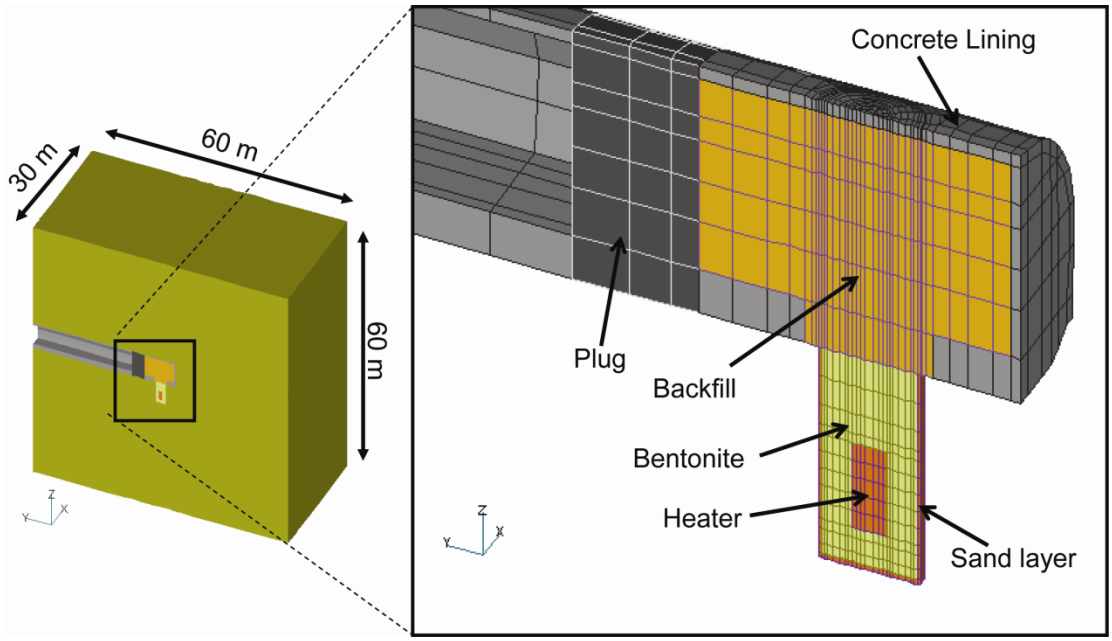

Figure 4.34. TOUGH-FLAC 3D numerical grid of the Horonobe EBS experiment.

We simulated the experiment in 3 steps:

1) Excavations are open for 3 months.

2) Excavations are filled with backfill and the heater, buffer and plug are all installed for 6 months.

3) Then heating starts.

In this preliminary study, we simulated heating for about 2 years. The results of temperature and saturation evolution for points located in the buffer and near-field rock are shown in Figures 4.36 and 4.37. When keeping the heater temperature constant at 100°C, the simulation shows that the temperature at the buffer-rock interface (P3, P4 in Figure 4.35) increases to about 60°C after 2 years. The liquid saturation in the buffer increases slowly by water infiltration from the surrounding rock (Figure 4.36). However, after 2 years, the liquid saturation at the inner parts of the buffer has not changed significantly (P1 in Figure 4.36). The calculated results in Figures 4.36 and 4.37 are sensible and show that we are able to use this full 3D TOUGH-FLAC model of the Horonobe EBS experiment for making a model prediction of the THM responses during the heating. Our next step will be to make a careful prediction of all the required output considering new material-property data for the backfill and concrete that will be distributed to the research teams by JAEA. The results will be presented at the next DECOVALEX-2015 workshop in November 2014 and then compared to initial monitoring results.

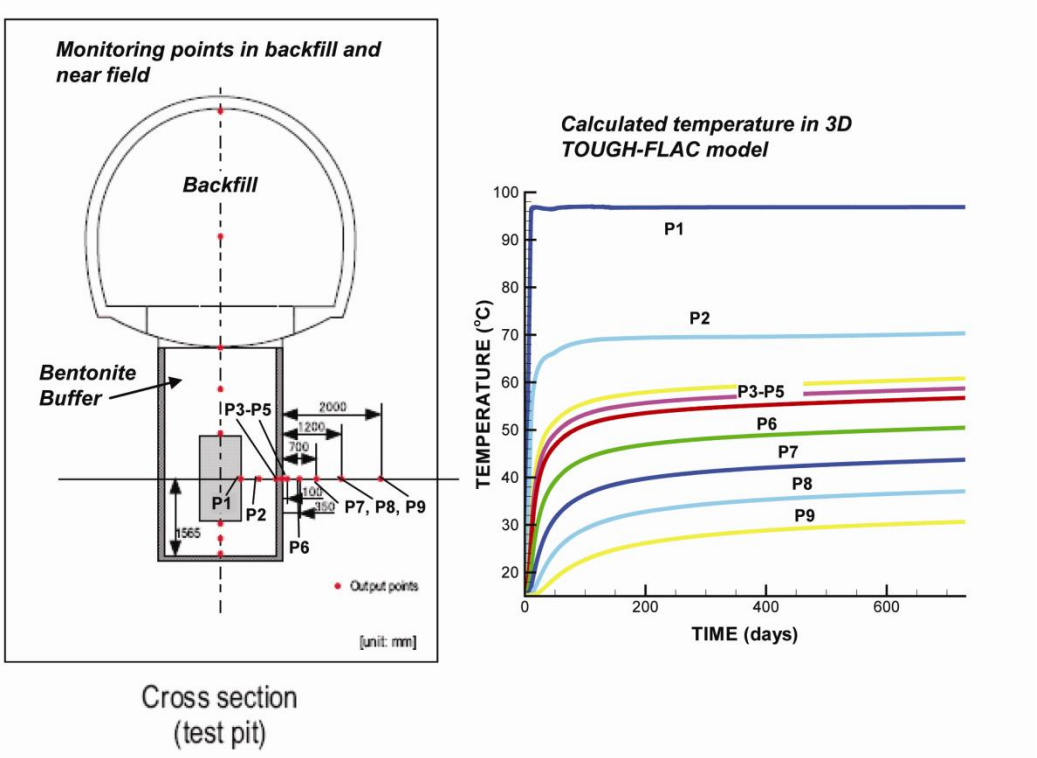

Figure 4.35. TOUGH-FLAC simulation results of temperature in the buffer and rock.

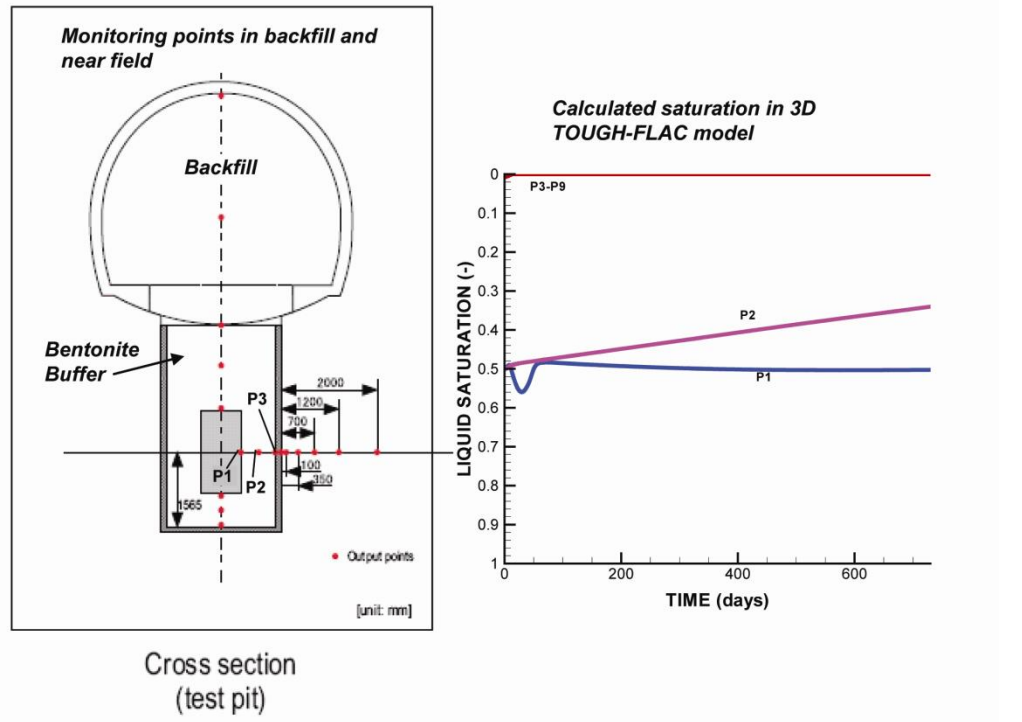

Figure 4.36. TOUGH-FLAC simulation results of liquid saturation in the buffer and rock.

4.5 FE Experiment at the Mont Terri Site

In this section, we present the FE Experiment and the current status of the modeling efforts, which are currently focused on the prediction of the temperature evolution as part of the experimental field test design. Moreover, we are actively working on defining the material properties for the granular bentonite and bentonite blocks that will be emplaced into the experimental tunnel. This includes the characterization of the bentonite in the CIEMAT column experiment, which was presented in Section 4.3 above.

As mentioned, the Mont Terri FE Experiment will be one of the largest and longest-duration heater tests worldwide, with focus on both the EBS components and the host-rock behavior. The FE experiment will be conducted in a side tunnel at Mont Terri, excavated along the claystone bedding planes for this purpose, extending 50 m in length and about 2.8 m in diameter (Figure 4.37). Heating from emplaced waste will be simulated by three heat-producing canisters of 1500 W maximum power. The temperature is expected to exceed 100°C, with a target temperature125 to 135°C at the inner parts of the buffer. A sophisticated monitoring program is planned, including dense pre-instrumentation of the site for *in situ* characterization, dense instrumentation of the bentonite buffer and host rock, and extensive geophysical monitoring (seismic and electric tomography).

The experiment will provide data useful for the validation of THM coupling effects regarding the processes in the host rock, while correctly accounting for (and examining) the conditions in the emplacement tunnel (temperature, saturation, and swelling pressure). Due to the 1:1 scale of the experiment, it will be possible to achieve realistic temperature, saturation, and stress gradients. It will also be possible to test backfilling technology with granular bentonite, as well as lining technology with shotcrete, anchors, and steel rips. Processes examined in the test cover many aspects of repository evolution, such as EDZ creation and desaturation of the EDZ during tunnel excavation and operation (including ventilation for about one year), as well as reconsolidation of the EDZ, resaturation, thermal stresses, and thermal pore-pressure increase after backfilling and heating (heating and monitoring period > 10 years).

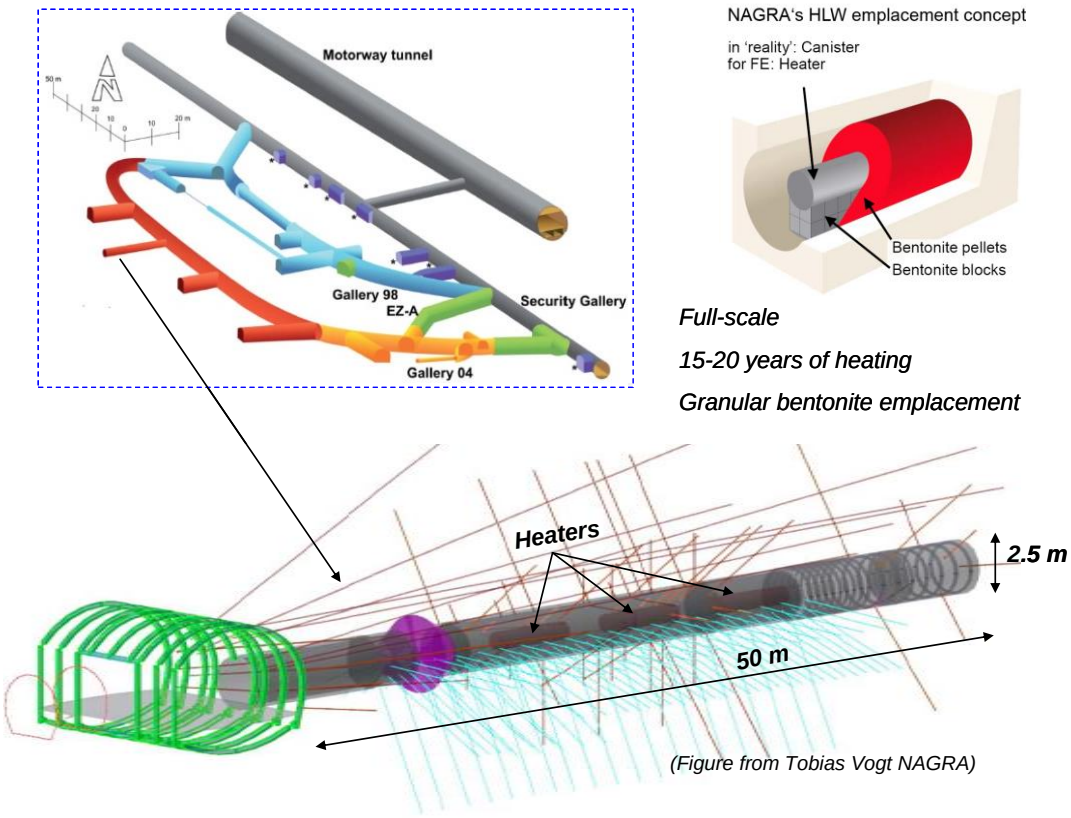

Figure 4.37. Plan view of experiment setup and borehole layout.

In 2011, a niche in front of the FE tunnel was constructed followed by a first phase of instrumentation of the rock mass surrounding the tunnel, using boreholes from the niche. The FE tunnel was then excavated by road-header in 2012; this was followed by another phase of instrumentation. The tunnel is currently open for a 1-year ventilation period. This will be followed by the emplacement of the heaters, bentonite buffer, and a concrete plug, after which the heating is expected to start at the end of 2014. The heating is then expected to go on for at least 15 years, with continuous monitoring of THM processes in both the bentonite buffer and surrounding rock.

DOE is one of the experimental partners for the FE heater experiment, and LBNL is one of the modeling teams. In addition to LBNL, there are currently six other modeling teams involved in the Mont Terri FE experiment from Germany (2 teams), U.K., Spain, Switzerland, and Canada.

The plans for the THM modeling program are discussed and updated at regular meetings and include three types of computations:

1) Scoping computations
2) Benchmarking
3) Predictive computations

The scoping computations include brainstorming on potential ongoing processes, evaluating their significance and parameter range, comparing simulation results and input parameters derived by

each team, and lessons learned (parameter range, importance, expected response). The benchmarking uses well-defined geometry problems with exact parameter values given to the teams, focusing on process modeling with precise comparison of codes. In the predictive calculations, likely parameters values and the as-built information of the experiment will be frozen.

The modeling will be used to predict the behavior of the system, and this should be reported prior to heating start (in 2014). Currently, each modeling team develops their conceptual models and material properties using available literature (papers and reports) on lab experiments and previous Mont Terri *in situ* tests, etc. Moreover, this is complemented with a restricted benchmark test for code comparison, in which properties and model geometry are set by NAGRA. In the FY2013 UFD milestone report entitled "Report on International Collaboration Involving the FE Heater and HG-A Tests at Mont Terri" (Houseworth et al., 2013), we presented results on the scoping calculations and the benchmarking which was completed in April 2014. We also made a first full THM 3D simulation of the FE heater test, including the BBM model for calculating the mechanical responses. These were scoping and preliminary predictions with the material properties available at the time, though in some cases including a different kind of bentonite.

In this report, we focus on the current task of predicting the temperature evolution and peak temperature, since this will be important for the design of the heat load of the experiment. Thus, in the following, we present the current LBNL model of the Mont Terri FE experiment, including numerical grid and thermal and hydraulic material properties. Finally, we present some simulation results related to the thermal evolution for different heat power schemes. This includes a staged heating during the first few months of the experiment, perhaps using only one of the three heaters. The staged heating schedule will be conducted to be able to make an early model calibration of the *in situ* thermal properties that can then be used to make a more reliable prediction of the peak temperature, once the full thermal power is applied. This will be done to assure that the temperature will not be so high that damage would happen to the monitoring system.

4.6 3D Model setup of the Mont Terri FE Experiment

For the modeling of the FE experiment, we have developed a conceptual model and modeling approach based on experience from previous design scoping calculations conducted by teams contracted by NAGRA, to help with the experimental design:

1) Pöyry (Engineering and Consulting): Modeling for excavation design using FLAC3D with ubiquitous joint model (anisotropic plasticity with different shear strength along bedding planes). This modeling approach was used to analyze the ground support design (Nater, 2012).

2) CINEMAT and UPC of Spain conducted scoping calculations for thermal and monitoring design using the CODE-Bright FEM code, and they used the BBM for modeling bentonite mechanical behavior (Garitte and Gens 2012).

3) The Interra Swiss Branch performed 3D TOUGH2 model simulations with anisotropic properties and inclined mesh. Their modeling was limited to thermal-hydrological processes (no mechanics) and done for thermal and monitoring design (Ewing and Senger, 2011).

LBNL's modeling approach contains important components from these three models. The host rock is modeled using TOUGH-FLAC with anisotropic properties considering bedding planes of the Opalinus Clay. The bedding planes across the FE tunnel are inclined, as can be seen in Figure 4.38. To accurately model anisotropic thermal and hydrological behavior, we created an inclined TOUGH2 mesh. Anisotropic mechanical material behavior is simulated using the FLAC3D ubiquitous joint model, with initial properties of those derived from the excavation design analysis by the Pöyry team (Nater 2012). In the ubiquitous joint model weak planes are assumed along the bedding planes of the Opalinus Clay in which the shear strength properties are different along bedding versus across bedding. The mechanical used for the Opalinus Clay were presented in Houseworth et al. (2013), but are not used in this study of peak temperature. For the bentonite, we started with the BBM model as applied by the CINEMAT and UPC (Garitte and Gens, 2012), and derived specific input material parameters for the MX-80 bentonite pellets that will be used as emplaced bentonite buffer around the heaters. With this modeling approach, we are able to simulate THM processes in both the bentonite and host rock, as well as their interactions.

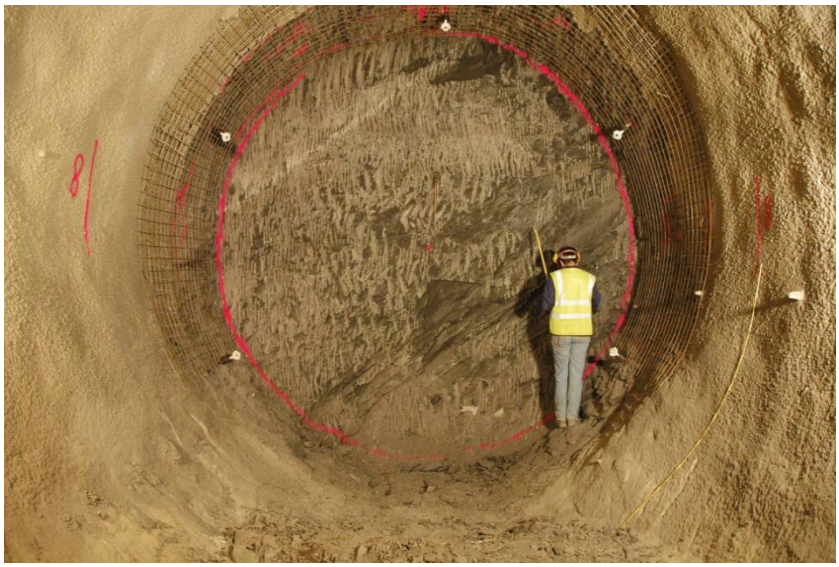

Figure 4.38. View of FE tunnel face from the FE niche showing beddings dipping 45° (Vietor, 2012).

Figure 4.39 presents the 3D TOUGH-FLAC numerical grid of the FE experiment. This model grid includes all vital material components for the modeling of the FE experiment, including layered Opalinus Clay host rock, excavation disturbed zone, tunnel, 3 heaters, bentonite buffer, concrete liner, and concrete plug. The initial conditions for the model simulation are 2 MPa in pore-fluid pressure and 15°C in temperature for the host rock. The 2 MPa of pore pressure is not under hydrostatic conditions, and the process is affected by the existing tunnel system at the site. In our simulations, we first run a simulation with an open tunnel at atmospheric pressure for 1 year, creating a pressure drop and hydraulic gradient around the tunnel. Thereafter, we assume instantaneous emplacement of the heater and buffer, and start our heating simulation.

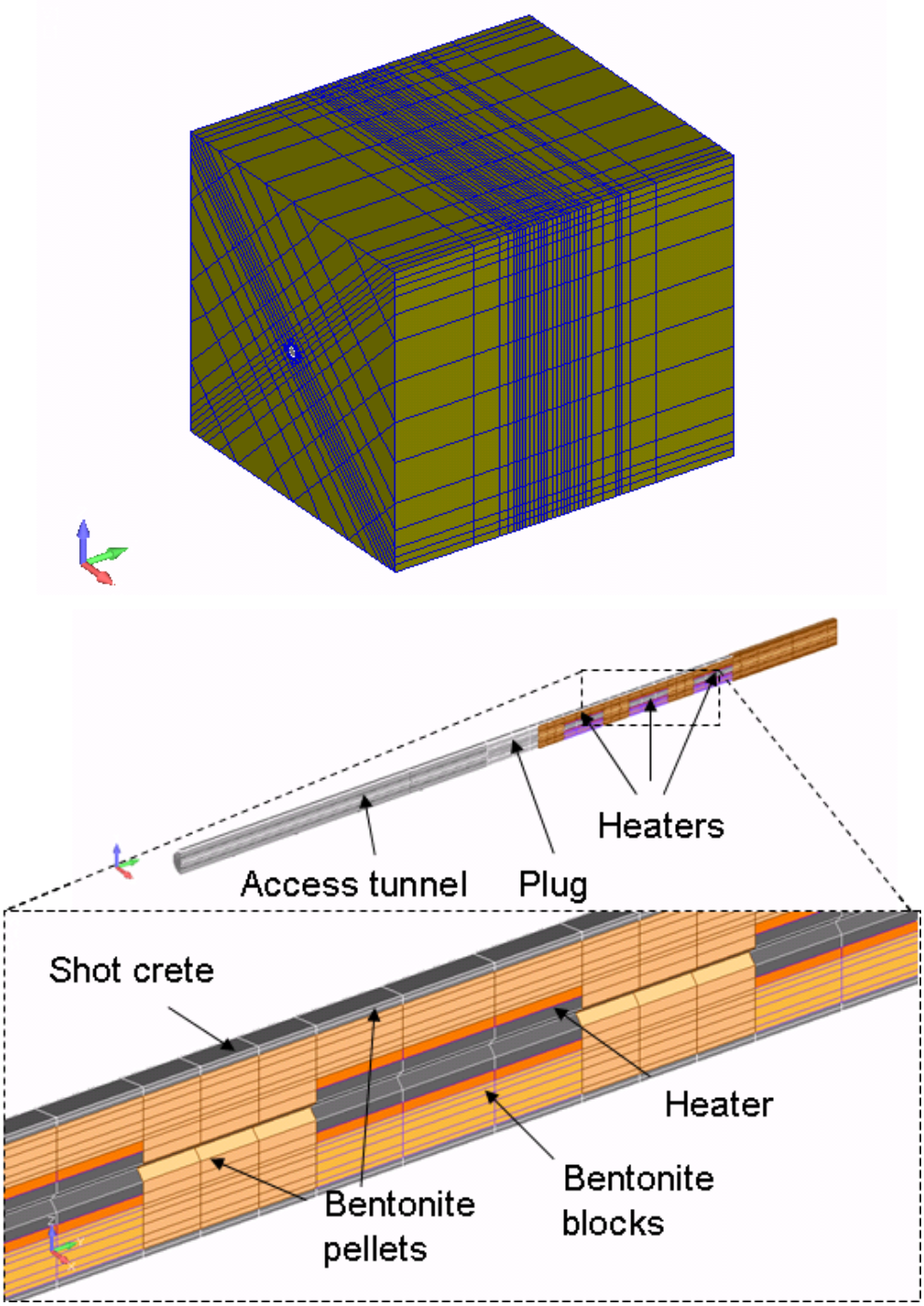

Figure 4.39. TOUGH-FLAC 3D numerical grid of the FE experiment.

The thermal and hydraulic material properties for modeling the FE experiment are given in Table 4.9. These include properties defined by NAGRA and used for the 1-D benchmarking exercise and reported in FY2013 milestone report "Report on International Collaboration Involving the FE Heater and HG-A Tests at Mont Terri" (Houseworth et al., 2013), and is considered the current best estimate of the properties.

Table 4.9. Parameters for the Opalinus and Bentonite clay used in the modeling of the FE experiment.

Properties	Parameters	Symbol	Opalinus Clay	Bentonite	Concrete (shotcrete and plug)	Unit
Physical	Grain density	ρ_g	2.7×10^{3}	2.7×10^{3}	2.7×10^{3}	kg/m^3
	Porosity	$Ø$	0.15	0.46	0.15	-
Hydraulic	Intrinsic permeability	K	5.0×10^{-20}	2.0×10^{-21}	3.5×10^{-21}	M^2
	Liquid relative permeability (Eq. 4.16)	A	-	5	-	-
	Liquid relative permeability (Eq. 4.17)	m	0.52	-	0.52	-
	Capillary curve (Eq. 4.18)	P_0	1.09×10^{7}	1.00×10^{7}	1.09×10^{7}	Pa
	Capillary curve (Eq. 4.18)	m	0.29	0.4	0.29	-
	Capillary curve (Eq. 4.18)	S_{ls}	1.0	1.0	1.0	-
	Capillary curve (Eq. 4.18)	S_{lr}	0.01	0.0	0.01	-
Thermal	Thermal conductivity (wet)	λ_{sat}	1.7	1.0	1.7	W/m/K
	Thermal conductivity (dry)	λ_{dry}	1.06	0.3	1.06	W/m/K
	Grain specific heat	C	800	950	800	J/kg/K

The water relative permeability in the buffer is a power-law relationship given by

$$k_{rw}(S_w) = \left(\frac{S_w - S_r}{S_m - S_r}\right)^A \tag{4.16}$$

The water relative permeability in the concrete and rock is given by the van Genuchten relationship,

$$k_{rw}(S_w) = \left(\frac{S_w - S_r}{S_m - S_r}\right)^{1/2} \left[1 - \left\{1 - \left(\frac{S_w - S_r}{S_m - S_r}\right)^{1/m}\right\}^m\right]^2$$

(4.17)

Capillary pressure in the buffer, concrete, and rock are given by the van Genuchten relationship:

$$\psi(S_w) = \frac{1}{\alpha}\left\{\left(\frac{S_w - S_r}{S_m - S_r}\right)^{-1/m} - 1\right\}^{1-m}$$

(4.18)

The relative permeability to gas for the buffer is set to a constant value of 1. The relative permeability to gas in the shotcrete and rock is

$$k_{rg}(S_w) = 1 - k_{rw}(S_w).$$

(4.19)

Variations in thermal conductivity and specific heat with water saturation are assumed to be linear between the defined end points. The vapor- and air-diffusion coefficients are a function of temperature and gas saturation defined by:

$$D_g^w = \tau S_g D \frac{P_{g0}(273.15+T)^n}{P_g(273.15)^n}$$

(4.20)

The problem was solved using TOUGH2 with the EOS4 equation of state module. We simulated high intrinsic gas permeability in the bentonite through the Klinkenberg parameter according to:

$$K_g = K_l\left(1 + b/P\right)$$

(4.21)

where K_g is intrinsic permeability for gas flow, K_l is intrinsic permeability of water flow, b is the Klinkenberg parameter, and P is pressure. In this case, we assigned a high value of the Klinkenberg parameter of 2.5×10^{11} Pa^{-1}, which means that the intrinsic permeability for gas flow would be about 6 orders of magnitude higher than the intrinsic permeability for water flow.

The simulation of the heating is conducted with the initial saturation in the bentonite equal to 20% in the bentonite. Although the bentonite pellets when emplaced will be very dry, with a saturation of a few percent, experience and monitoring in the Mont Terri HE-E experiment shows that moisture is quickly taken up by the pellets from the surrounding humid air. This means that an initial saturation of 20% is realistic. In our modeling, we assign an initial capillary pressure, which corresponds to an initial saturation of 20% (Figure 4.40).

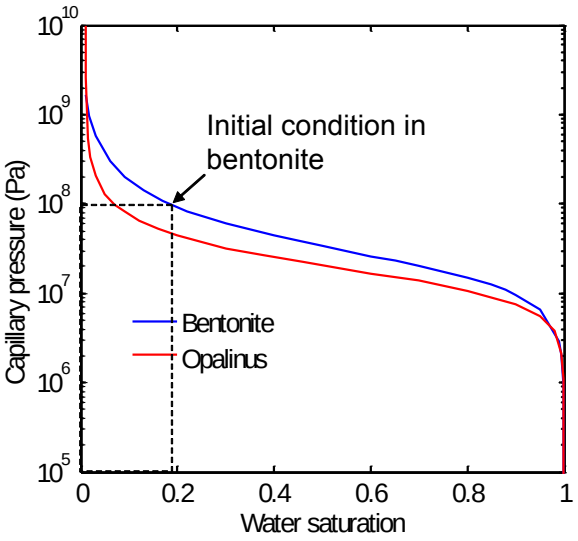

Figure 4.40. Capillary curves for Bentonite and Opalinus clays.

4.1 Model Prediction of Temperature and Saturation Evolution for Heat Power Design

Figure 4.41 shows our prediction of temperature and saturation evolution, assuming the full 1500 W power in each heater. In this case, the peak temperature at the buffer is as high as 160°C, i.e., considerably higher than the targeted 125 to 135°C. In the experiment, the temperature should not exceed 150°C, because this could be damaging for some of the monitoring sensors. The high peak temperature at the canister surface is caused by the combined effects of low thermal conductivity of the buffer and the rock, as well as the high diffusion coefficient that keeps the buffer dry around the heater. We consider these modeling results to be an initial predictive modeling, as there are still uncertainties related to the thermal conductivity and diffusion coefficient to be applied for this type of bentonite material.

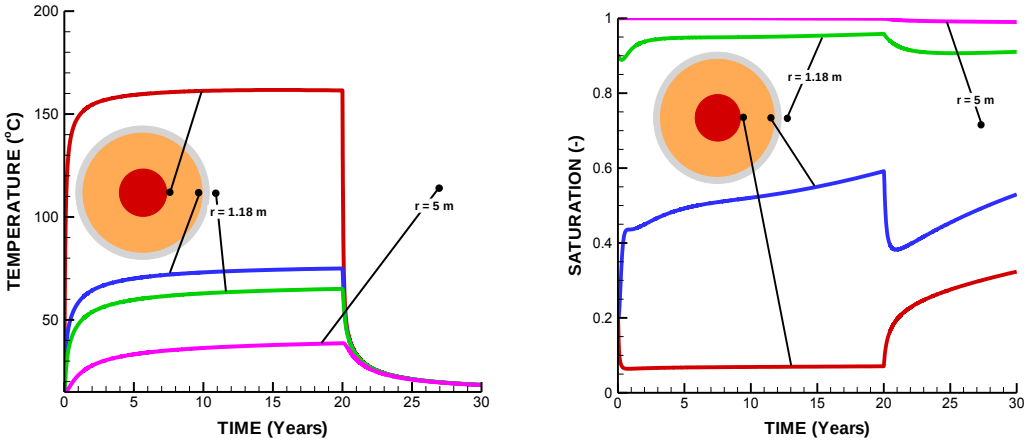

(a) (b)

Figure 4.41. Model prediction of (a) temperature and (b) liquid saturation for full power of 1500 W at each heater.

Figure 4.42 presents the results considering a staged heat power schedule the first few months. In this case, we assume that all 3 heaters are turned on and set at a constant power of 500 w for 30 days and then set to 1000 w for another 30 days. We then assume that full power of 1500 W is applied after 60 days. The simulation results in Figure 4.42 show that during the first 30 days, almost no drying occurs in the buffer. This means that a model calibration on this initial step can give a value of the initial thermal conductivity of the bentonite at 20% saturation (Figure 4.43c). During the next few months, there are some changes in saturation in the buffer, with some wetting from the rock and some drying near the heater. After turning on the full power at 60 days, the temperature increases and, finally at 1000 days, it has reached over 150°C at the heater surfaces. At this stage, the buffer has been substantially dried near the heater, and this drying has a significant impact on the peak temperature.

Figure 4.43 presents the results considering a staged heating only in the heater that is emplaced first, i.e., the one placed farthest into the tunnel. Included in Figure 4.43 are the temperature and saturation evolution at all three heaters, although heating is turned on only at one heater. By comparing Figures 4.43 and 4.42, we can conclude that during the first 100 days, the temperature and saturation evolution is identical at heaters that are turned on (solid lines). That is, the temperature and saturation evolution at one heater is not affected by the heating, temperature, saturation at the other two heaters. Figure 4.44 also shows the difference in temperature and saturation evolution between heaters that are turned on or off. At heaters that are turned off, there is no drying near the heater (red dashed line) and there is some slow infiltration from the rock, causing some slow increase in saturation (blue dashed line). The results indicate that for the heating design it is possible to first turn on only one heater with the staged heating test to calibrate the THM models. It might be possible to turn on the heater emplaced first and make this initial heating test before the entire test tunnel is completely backfilled.

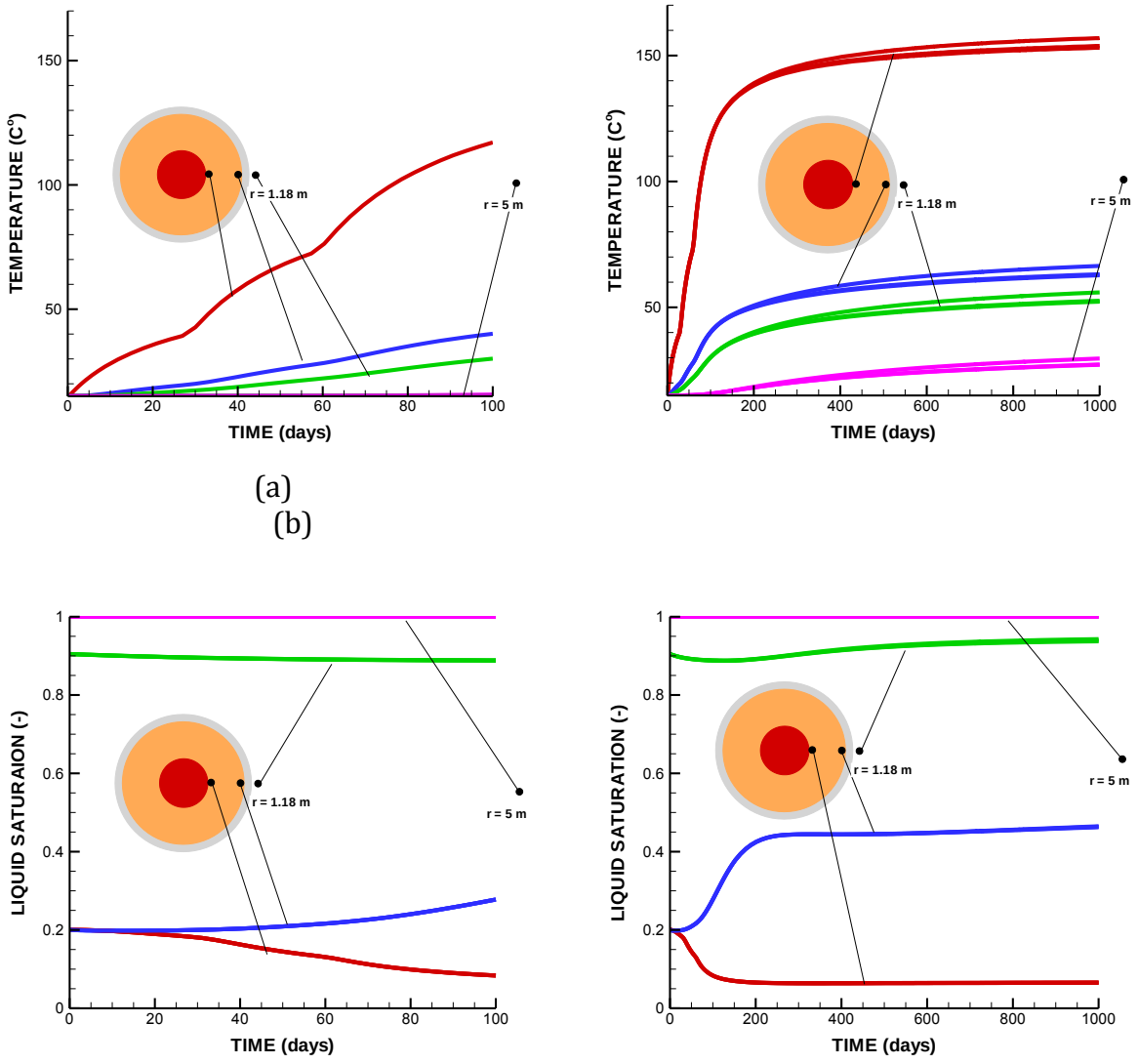

Figure 4.42. Model prediction of (a, b) temperature and (c, d) liquid saturation for staged power in 3 heaters.

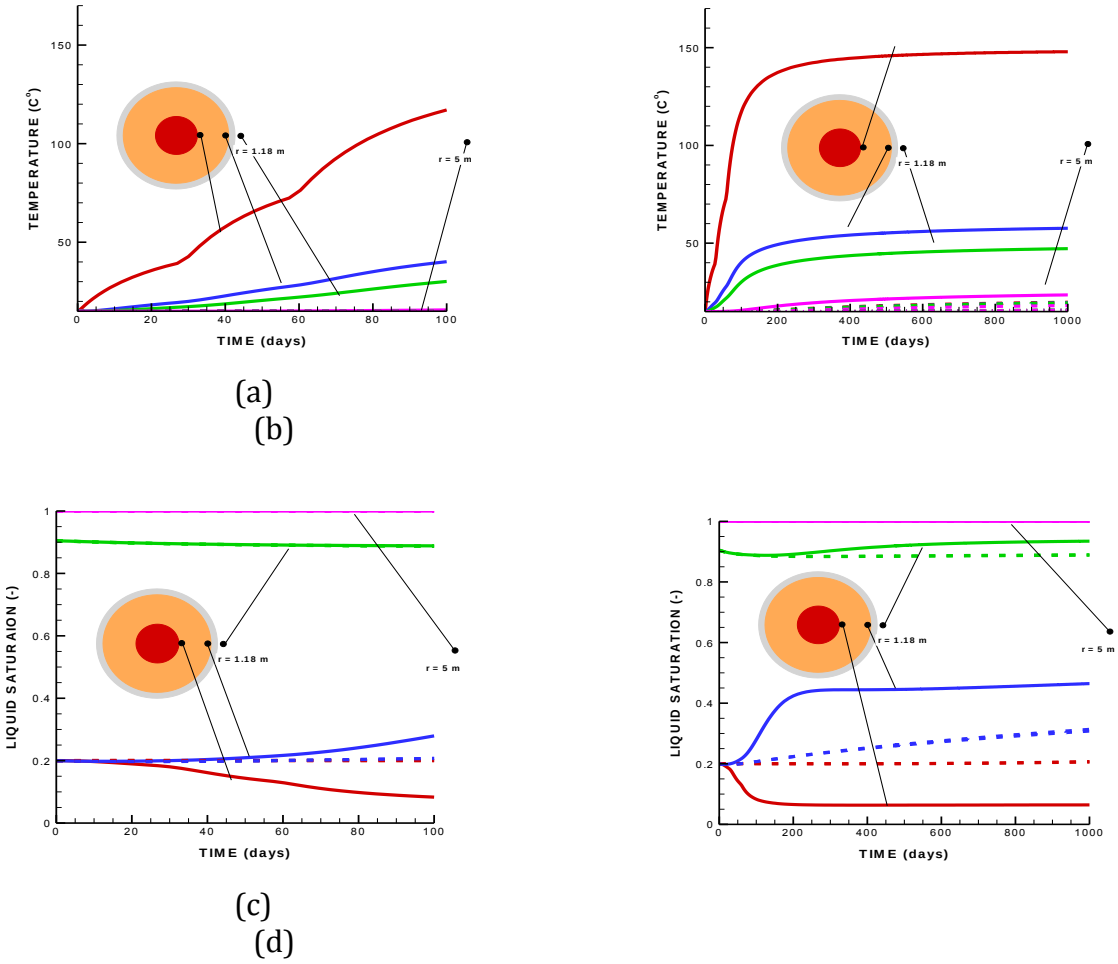

Figure 4.43. Model prediction of (a, b) temperature and (c, d) liquid saturation for staged power in first emplaced heater. Solid lines refers to evolution at the heater that is turned on, whereas dashed lines refers to evolution at heater that are turned off.

4.8 Status of THM Modeling of Heater Experiments and Plans

UFD and LBNL greatly benefit from participating in these international activities for developing expertise and testing advanced models for coupled THM processes. LBNL is leveraging on previous experience and existing models (TOUGH-FLAC and ROCMAS) that are extended to meet technical requirements for being able to predict the long-term THM and THMC evolution of a multibarrier nuclear waste repository system, involving backfilled emplacement tunnels in argillite host formations. FY2014 accomplishments include:

- Completed implementation of constitutive models for the coupled geomechanical behavior of bentonite-based buffer material, including most recently the advanced dual-structure model.
- Verification and testing of the implemented geomechanical constitutive models for bentonite-based buffer material by modeling laboratory experiments and long-term behavior of a generic repository.

- Validation of TOUGH-FLAC and characterization of THM properties for two types of bentonite-based buffer materials through modeling of CIEMAT laboratory column experiments.
- Development of full-scale 3D TOUGH-FLAC models of the Horonobe EBS experiment and Mont Terri FE experiment and initial model predictions of temperature and saturation evolutions.
- Benchmarking associated with the Horonobe EBS experiment achieving good agreement with the results of other international modeling teams, providing code-to-code verification of TOUGH-FLAC.
- Published one journal paper (Rutqvist et al., 2014) on THM modeling of nuclear waste disposal in argillite and submitted one journal paper on the use of the dual-structure model for modeling long-term behavior of a nuclear waste repository (Vilarrasa et al., 2014).

The implemented constitutive models have been verified and tested by modeling laboratory experiments and generic repository, but the dual-structure model has not yet been applied in the modeling of the large-scale field experiments. Although a number of features in the dual-structure model are important for evaluating the long-term performance of a buffer-rock system, there is still a lack of experimental data and experience to apply such a model. It is only LBNL's TOUGH-FLAC simulator and the Code-bright simulator at University of Catalonia (UPC) in Barcelona that have the full capabilities of such a dual-structure model in a THM simulator. In this context, participation as a modeling team in the FE Experiment will be particularly beneficial, as one of the other modeling teams participating is the UPC, who are planning to apply the dual-structure model in their modeling of the experiment. We note that UPC is one of the world leaders in unsaturated soil mechanics and the original developer of the dual-structure constitutive model for expansive clay that we have implemented into TOUGH-FLAC. Thus, participating in the Mont Terri FE experiment provides an important opportunity for collaboration and model comparison and comparison to field data using this advanced constitutive model. Likewise, the participation in the DECOVALEX-2015 provides the opportunity to gain experience and test our models for a range of different backfill materials (e.g., bentonite pellets and sand/bentonite mixture), as well as different host rocks (Opalinus Clay and mudstone).

Our work in the remaining months of FY2014 and beginning of FY2015 will be focused on the model predictions to be performed for the three *in situ* heater experiments; the Mont Terri HE-E experiment, the Horonobe EBS experiment, and the Mont Terri FE experiment. We have already developed full 3D models and made preliminary predictions for the Horonobe EBS Experiment and the Mont Terri FE experiment. Next, we will develop the 3D mesh for the Mont Terri HE-E experiment, with the prediction to be presented at the next DECOVALEX-2015 workshop in November 2014. By participating as a DECOVALEX research team for modeling the Mont Terri HE-E experiment, we will be able to compare the results with experimental data already at the November workshop— this will be an important model validation test and provide experience on modeling a buffer consisting of granular bentonite, which is also the buffer material that will be used at the Mont Terri FE experiment. Our work for FY2015 will then be very much focused on validation of our models against these field experiments, as well as characterization of parameters for BBM and dual-structure constitutive models from laboratory data that are now

becoming available in the various projects. In summary, proposed work for FY2015 related to these international activities include,

- Full-scale 3D model predictions for the three *in situ* heater experiments; the Mont Terri HE-E experiment, the Horonobe EBS experiment, and the Mont Terri FE experiment, and compare with data and with the results of other international modeling teams in the DECOVALEX and Mont Terri projects
- Collaborate with the UPC (Barcelona) modeling team in application of the BBM and dual-structure models to the Mont Terri FE experiment.
- Validation of models against these field experiments as well as characterization of parameters for BBM and dual-structure constitutive models from laboratory data that are now becoming available in the various projects.
- Review of THM properties of bentonite-based buffer and backfill materials in these field experiments (and in nuclear waste isolation in general) and identify critical parameters and experimental data needs.
- Participated and presenedt simulation results at DECOVALEX and Mont Terri workshops.

Finally, we note that by participating in these international activities we are making significant progress toward achieving UFD goals to fill data needs and confirm advanced modeling approaches (by 2015), and to have a robust modeling and experimental basis for evaluation of multiple disposal system options (by 2020).

5. Investigation of the Impacts of High Temperature Limits with THMC modeling

5.1 Introduction

Radioactive waste from spent fuel emanates a significant amount of thermal energy, due to decay processes, which cause temperature increases in the surrounding environment, particularly in the early stages of waste emplacement. The temperature to which the EBS and natural rock can be exposed is one of the most important design variables for a geological repository, because it determines waste package spacing, distance between disposal galleries, and therefore the overall size (and cost) of a repository for a given amount of heat-emanating waste (Horseman and McEwen, 1996). This is especially important for a clay repository, because argillaceous rocks have relatively small heat conductivity. A thermal limit of about 100°C is imposed unanimously in all disposal concepts throughout the world, despite their differences in design concepts (Hicks et al., 2009). Chemical alteration and the subsequent changes in mechanical properties are among the determining factors. A high temperature could result in chemical alteration of buffer and backfill materials (bentonite) within the EBS through illitization and cementation, which compromise the function of these EBS components by reducing their plasticity and capability to swell when wetting (Pusch and Karnland, 1996; Pusch et al., 2010; Wersin et al., 2007). The swelling capability of clay minerals within the bentonite is important for sealing gaps between bentonite blocks, between bentonite and other EBS components, and between the EBS and the surrounding host rock. Chemical alteration may also occur in the near-field host rock, which could reduce the clay capability for self-sealing within the excavation damaged zone (EDZ). As

a result of the low permeability of clay rock, a high temperature may induce significant pore-pressure buildup (through pore-water expansion and vaporization) in the near field, which could generate adverse mechanical deformation (such as fracturing), damaging the integrity of the host rock (Horseman and McEwen, 1996).

Regarding the concern of chemical alteration and the associated mechanical changes, Wersin et al. (2007), after reviewing a number of data sets, concluded that the criterion of 100°C for the maximum temperature within the bentonite buffer is overly conservative. Their conclusion was based on their findings that no significant changes in bentonite hydraulic properties occur at temperatures of at least 120°C under wet conditions and that bentonite is chemically stable to much higher temperatures under dry conditions. The impact of a high temperature on bentonite and clay host rock behavior, and the consequences on repository performance, are largely open questions for a clay repository system. While various studies shed light on certain aspects of this question, there is a lack of studies that integrate the relevant THMC processes and consider the interaction between the EBS and the host rock.

Since FY13, in UFDC, LBNL has used coupled THMC modeling to evaluate the chemical alteration and mechanical changes in EBS bentonite and the natural system (NS) clay formation under various scenarios, attempting to provide necessary information for decisions on temperature limits. In the FY13 report (Liu et al., 2013b), after an extensive review of the THMC alteration of EBS and clay formation (argillite) under various temperature conditions, fully coupled THMC simulations were developed for a nuclear waste repository in a clay formation with a bentonite-backfilled EBS. Two scenarios were simulated for comparison: a case in which the temperature in the bentonite near the waste canister can reach about 200°C, and a case in which the temperature in the bentonite near the waste canister peaks at about 100°C. In these simulations, it was assumed that the EBS bentonite was Kunigel-V1 bentonite (Ochs et al., 2004) and that the host rock properties were representative of Opalinus Clay (Bossart, 2011; Lauber et al., 2000). Simulations showed that the decrease in smectite volume fraction in bentonite ranges from 0.004 to a maximum of 0.085, or up to about 27% of the initial volume fraction of smectite for the 200°C scenario, and decrease in smectite volume fraction leads to a reduction in swelling stress around 16–27%, subject to a great deal of variation in terms of the decrease in smectite volume fraction and swelling pressure under different chemical conditions. In FY14, we first continued to analyze the sensitivity of calculated swelling pressure for Kunigel-V1 bentonite to critical parameters. Second, we replace Kunigel-V1 bentonite with FEBEX bentonite in the THMC model to evaluate potential chemical change in FEBEX bentonite and its effect on the swelling pressure. Kunigel-VI bentonite (Ochs et al., 2004) has low smectite content and relatively low swelling capacity, whereas FEBEX bentonite (ENRESA, 2000) has a high fraction of smectite and high swelling capacity. Modeling results showed that FEBEX bentonite undergoes less degree of illitization and smaller swelling pressure reduction that is very minimal comparing with the swelling capacity of FEBEX bentonite.

5.2 Modeling Study

5.2.1 Model Development

Because the model used in this report is the same as that of last year (Liu et al., 2013b), we only briefly describe each element of the THMC model here, referring the reader to Liu et al. (2013b) for details.

5.2.1.1 Simulator

Numerical simulations are conducted with TOUGHREACT-FLAC, which sequentially couples the multiphase fluid flow and reactive transport simulator, TOUGHREACT (Xu et al., 2011), with the finite-difference geomechanical code FLAC3D (Itasca, 2009). The coupling of TOUGHREACT and FLAC was initially developed in Zheng et al. (2011) to provide the necessary numerical framework for modeling fully coupled THMC processes. It was equipped with a linear elastic swelling model (Zheng et al., 2012; Rutqvist et al., 2013c) to account for swelling as a result of changes in saturation and pore-water composition and the abundance of swelling clay (Liu et al., 2013b).

5.2.1.2 Modeling scenario

The model is applied to a hypothetical bentonite-backfilled nuclear waste repository in clay rock, a repository example that involves a horizontal nuclear waste emplacement tunnel at 500 m depth (Figure 5.1) (Rutqvist et al., 2013c). The Z-axis is set as vertical in the model, while the horizontal Y- and X-axes are aligned parallel and perpendicular to the emplacement tunnel, respectively (Figure 5.1). An initial stress field is subjected to the self-weight of the rock mass. Zero normal displacements are prescribed on the lateral boundaries of the model. Vertical displacements are prevented at the bottom. The model simulation was conducted in a nonisothermal mode with a time-dependent heat power input (Rutqvist et al., 2013c), adopted from the heat load developed within the U.S. DOE's Used Fuel Disposition campaign as a generic disposal system environment for Pressurized Water Reactor (PWR) used nuclear fuel. This heat load is then scaled in the 2D model to represent a certain line load, which depends on the assumed spacing between individual waste packages along an emplacement tunnel. Initially, the EBS bentonite has a water saturation of 65% and the clay formation is fully saturated. From time zero, the EBS bentonite simultaneously undergoes resaturation, heating, chemical alteration, and stress changes.

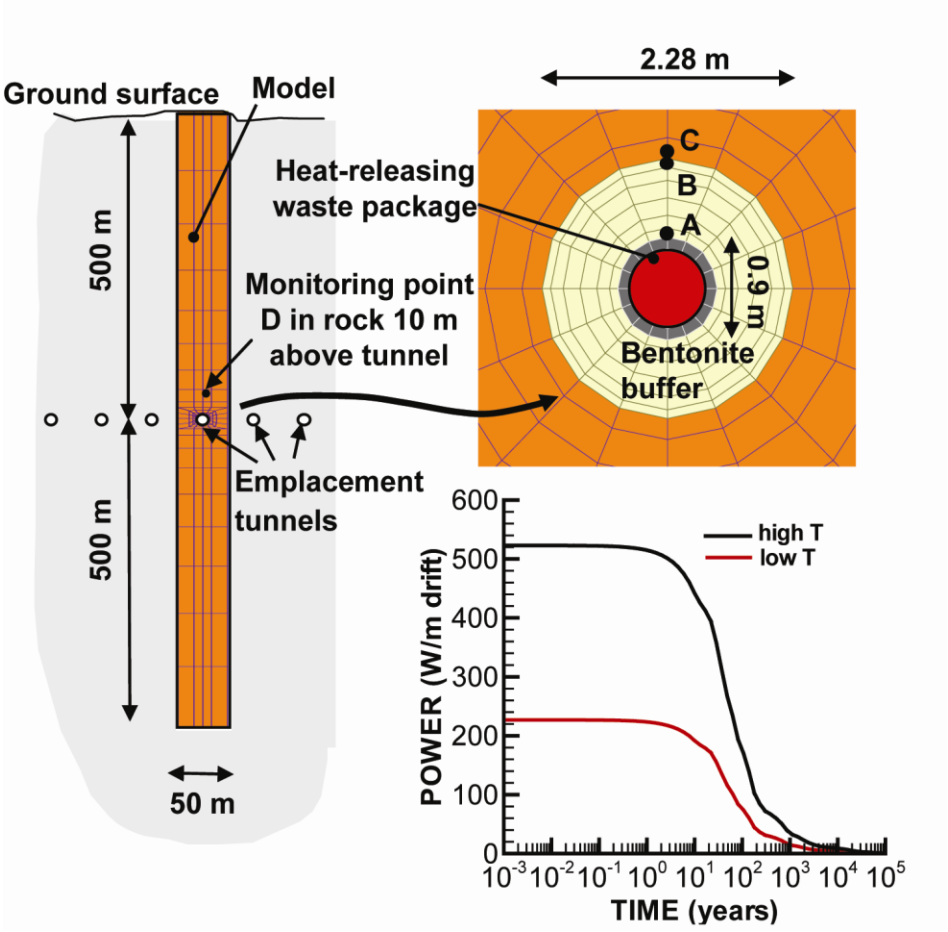

Figure 5.1. Domain for the test example of a bentonite back-filled horizontal emplacement drift at 500 m (Rutqvist et al., 2013c).

5.2.1.3 Mechanical Model

To consider the swelling due to both moisture and chemical concentration changes, we include the stress due to changes in chemical concentration and abundance of swelling clay:

$$d\sigma_s = 3K\beta_{sw}ds_l - A_n dC + A_{sc}dm_s \tag{5.1}$$

where K is the bulk modulus and β_{sw} is a moisture swelling coefficient. In this report, β_{sw} is 0.048, which is calibrated for the swelling pressure of 1 MPa (Börgesson et al., 2001) the swelling pressure measured for Kunigel-V1 bentonite (which was used in current models as the EBS material) under the condition that bentonite is saturated with dilute solution (e.g., deionized water), and K is 20 MPa (Rutqvist et al., 2011). A_n is a constant that linearly relates chemical concentration (C) variation and the corresponding stress change. A_n is typically calculated from swelling pressures measured using different solutions (e.g. deionized water versus 1 M NaCl solution) than are used to saturate the bentonite. Laredj et al. (2010) proposed the following expression for A_n:

$$A_n = \frac{(5.312 \ln C - 23.596)}{\sqrt{C}} - \frac{7.252 \times 10^{-4}}{C^2} \quad (5.2)$$

A_{sc} is a constant that relates the change in mass fraction of swelling clay, m_s, to change in stress. An empirical value is derived from measured swelling pressure for bentonite materials of different smectite mass fraction (Liu et al., 2013b), which is 2.5×10^6 Pa^{-1}.

5.2.1.4 Chemical Model

In these generic cases, it is assumed that the host-rock properties are representative of Opalinus Clay (Bossart, 2011; Lauber et al., 2000), and two cases for the EBS backfill, one composed of Kunigel-V1 bentonite (Ochs et al., 2004) and the other FEBEX bentonite (ENRESA, 2000). The mineral composition of the bentonite and clay formation is listed in Table 5.1. The pore-water composition of the Kunigel-V1 bentonite (Sonnenthal et al., 2008), FEBEX bentonite (Fernández et al., 2001) and the clay formation (Fernández et al., 2007) are listed in Table 5.2. Table 5.3 lists the thermal and hydrodynamic parameters used in the model. The majority of these parameters for the EBS bentonite are based on the properties of Kunigel-VI bentonite (Sonnenthal et al., 2008), and those for the NS clay formation are from Thury (2002). Permeability for the clay formation is from Soler (2001), and that for the bentonite is from Japan Nuclear Cycle Development Institute (JNC) (2000).

FEBEX and Kunigel-VI bentonite also have distinct hydrological and thermal parameters, with the most relevant ones being thermal conductivity and permeability. However, in this report, we keep them the same thermal conductivity and permeability, which are actually fairly similar for both bentonite — thermal conductivity for saturated Kunigel-VI bentonite is 1.5W/m°C (see Table 5.2)—and for FEBEX bentonite is 1.3 W/m^{o}C (Empresa Nacional de Residuos Radioactivos SA (ENRESA), 2000). Permeability for Kunigel-VI bentonite is 2E-21 m^2 and that for FEBEX ranges from 3.75E-21 to 1E-21 m^2 (ENRESA, 2000; Zheng et al., 2011; Chen et al., 2009). Moreover, by keeping thermal conductivity and permeability the same, we can isolate the effect of variation in chemical and CM coupling parameters on stress changes.

Table 5.1. Mineral volume fraction (dimensionless, ratio of the volume for a mineral to the total volume of medium) of the Kunigel-V1bentonite (Ochs et al., 2004), FEBEX bentonite (ENRESA, 2000; Fernández et al., 2004; Ramírez et al., 2002) and Opalinus Clay (Bossart 2011; Lauber et al., 2000).

Mineral	EBS Bentonite: Kunigel-V1	EBS Bentonite: FEBEX	Clay formation: Opalinus Clay
Calcite	0.016	0.0065	0.093
Dolomite	0.018	0.0	0.050
Illite	0.000	0.0	0.273
Kaolinite	0.000	0.0	0.186
Smectite	0.314	0.6	0.035
Chlorite	0.000	0.0	0.076
Quartz	0.228	0.026	0.111
K-Feldspar	0.029	0.0065	0.015
Siderite	0.000	0.0	0.020
Ankerite	0.000	0.0	0.045

Table 5.2. Pore-water composition of Kunigel-V1bentonite (Sonnenthal et al., 2008), FEBEX bentonite (Fernández et al., 2001) and Opalinus Clay (Fernández et al., 2007).

	EBS Bentonite: Kunigel-V1	**EBS Bentonite: FEBEX**	**Clay formation: Opalinus Clay**
pH	8.40	7.72	7.40
Cl	1.50E-05	1.60E-01	3.32E-01
SO_4^{-2}	1.10E-04	3.20E-02	1.86E-02
HCO_3^-	3.49E-03	4.1E-04	5.18E-03
Ca^{+2}	1.37E-04	2.2E-02	2.26E-02
Mg^{+2}	1.77E-05	2.3E-02	2.09E-02
Na^+	3.60E-03	1.3E-01	2.76E-01
K^+	6.14E-05	1.7E-03	2.16E-03
Fe^{+2}	2.06E-08	2.06E-08	3.46E-06
SiO_2(aq)	3.38E-04	1.1E-04	1.10E-04
AlO_2^-	1.91E-09	1.91E-09	3.89E-08

Table 5.3. Thermal and hydrodynamic parameters.

Parameter	**Clay formation : Opalinus Clay**	**EBS Bentonite**
Grain density [kg/m^3]	2700	2700
Porosity ϕ	0.162	0.33
Saturated permeability [m^2]	2.0×10^{-20}	2.0×10^{-21}
Relative permeability, k_{rl}	m = 0.6, S_{rl} = 0.01	$K_{rl} = S^3$
Van Genuchten α [1/Pa]	6.8×10^{-7}	3.3×10^{-8}
Van Genuchten m	0.6	0.3
Compressibility, β [1/Pa]	3.2×10^{-9}	5.0×10^{-8}
Thermal expansion coeff., [1/^{o}C]	1.0×10^{-5}	1.5×10^{-4}
Dry specific heat, [J/kg ^{o}C]	860	800
Thermal conductivity [W/m ^{o}C] dry/wet	1.48*/1.7$	1.1/1.5
Tortuosity for vapor phase	$\phi^{1/3}S_g^{10/3}$	$\phi^{1/3}S_g^{10/3}$
Bulk modulus, (GPa)	4.17	0.02
Shear modulus, (GPa)	1.92	0.0067

from http://www.mont-terri.ch/internet/mont-terri/en/home/geology/key_characteristics.html

The kinetic rates and surface areas for the minerals considered in current model are taken mostly from Xu et al. (2006). However, the illitization rate (the rate of illite precipitation and smectite dissolution) was calibrated (Liu et al., 2013) based on the measured illite percentage in an illite/smectite (I/S) mixed layer from Kinnekulle bentonite, Sweden (Pusch and Madsen, 1995). The thermodynamic data are from the data0.dat.YMPv4.0, a EQ3/6 (Wolery, 1993) database.

5.2.2 Model Results

5.2.2.1 Cases for Kunigel Bentonite

The model results for the base case, expressed as the evolution of temperature, pore pressure, water saturation, concentration, and stress, were discussed in detail in Liu et al. (2013b). In this report, the evolution of stress in EBS bentonite is further analyzed to study the contributions of different processes to total stress. We first briefly discuss the change in temperature, water saturation, and the volume fraction of smectite, because their changes essentially determine the evolution of stress. Then we discuss the changes in stress.

5.2.2.1.1 THC Evolution

The evolution of heat release from decaying waste is shown in Figure 5.1. The heat release rates have been adjusted to make two cases for comparison: a “high T” case, in which the temperature near the canister can reach 200°C; and a “low T” case, in which the temperature near the canister peaks at about 100°C. In this paper, the temporal evolution at four monitoring points (see Figure 5.1 for their positions) is used to present thermal, hydrological, chemical, and mechanical results: point A is inside the bentonite near the canister, point B is inside the bentonite and near the EBS-NS interface, point C is inside the clay formation and near the EBS-NS interface, and point D is inside the clay formation at a distance from canister of 10 m. The temperature evolution at the

four monitoring points A, B, C, and D is shown in Figure 5.3. Pore pressure increases as a result of resaturation and heating. The "high T" case exhibit much higher pore pressure than the "low T," with a difference of about 5 MPa after 1000 years (Figure 5.5). The clay formation near the EBS-NS interface goes through desaturation (Figure 5.4), which interestingly lasts much longer for the "low T" case than the "high T" case. The higher temperature leads to a higher pore pressure (Figure 5.5) in the EBS bentonite, which reduces desaturation in the clay formation because higher pore pressure in the EBS bentonite lowers the hydraulic pressure gradient and therefore the flow of water towards the EBS bentonite.

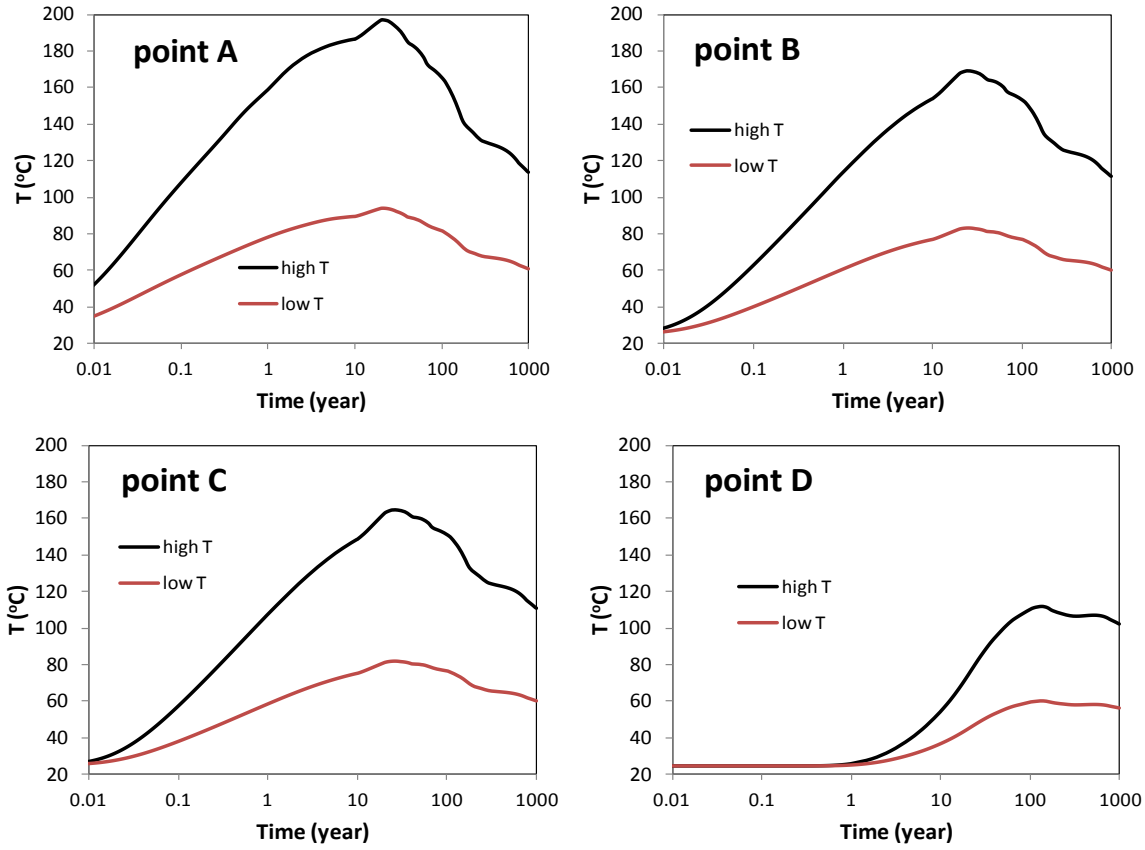

Figure 5.2. Temperature evolution at points A, B, C, and D.

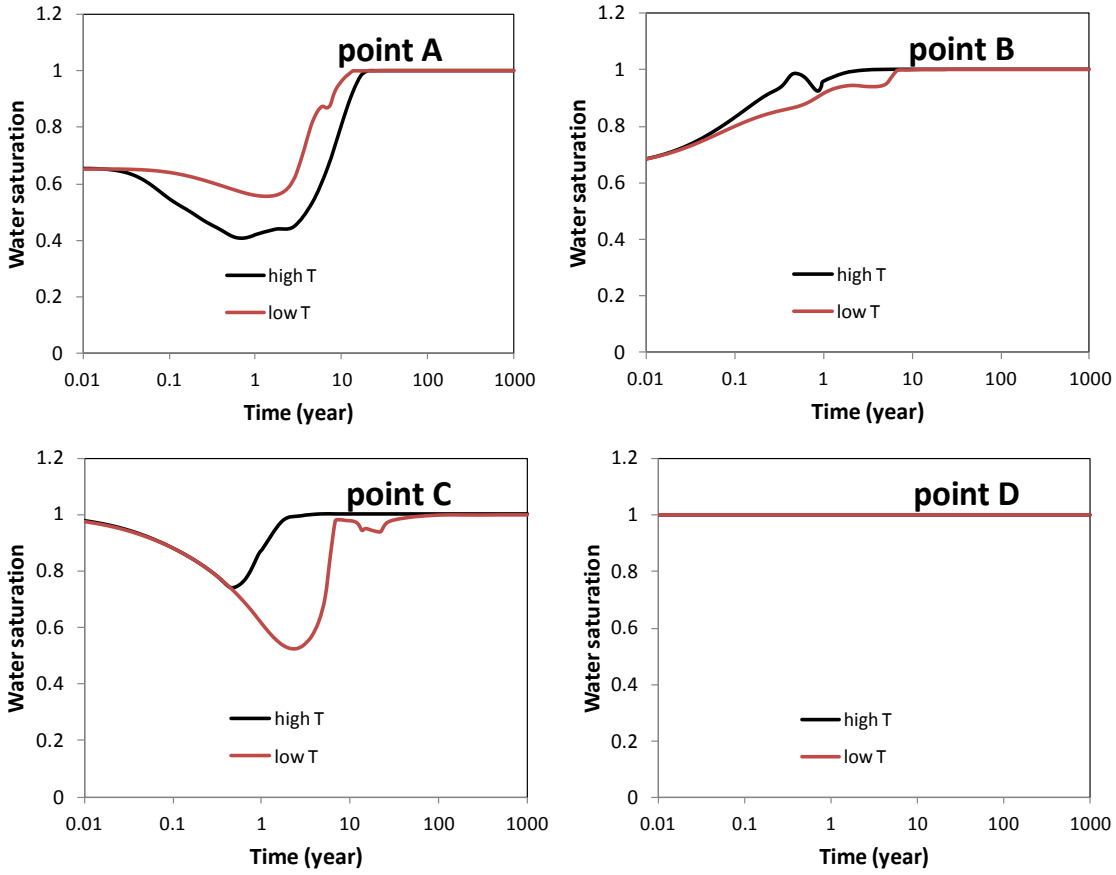

Figure 5.3. The temporal evolution of water saturation at points A, B, C, and D.

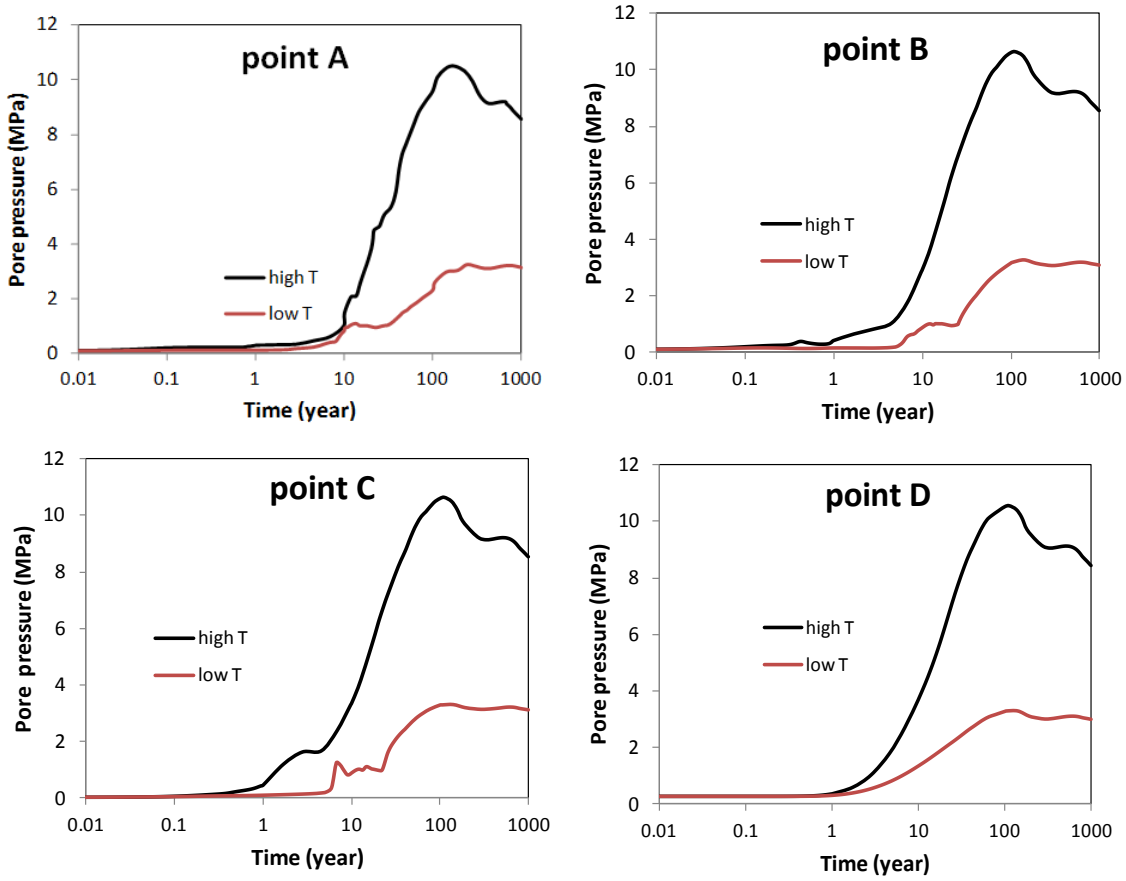

Figure 5.4. The temporal evolution of pore pressure at points A, B, C, and D.

Illitization is modeled as the dissolution of smectite and precipitation of illite. The overall reaction can be written as:

$$\text{Smectite} + 0.52H^{+} + 0.63AlO_2^{-} + 0.6K^{+} = \text{illite} + 0.26H_2O + 0.08Mg^{+2} + 0.33Na^{+} + 0.5SiO_2(aq) \quad (5.3)$$

Based on the database used in the model, this reaction yields a volume change of -4.9 ml/mol. Note that H_2O is not considered in the reaction.

Many factors can affect the chemical reactions, such as the initial water-mineral disequilibrium in bentonite (since the water used for making bentonite blocks is not necessarily in equilibrium with the mineral phase in bentonite, and it takes time to reach that equilibrium), as well as the thermal and hydrological disturbances in response to emplacement.

Results from the base case confirm that the clay host rock undergoes a small degree of illitization similar to the process widely observed in geological systems (e.g., Wersin et al., 2007; Pusch and Madsen 1995), as illustrated by the smectite dissolution at point C and D in Figure 5.5 and illite precipitation at point C and D in Figure 5.6. The volume fraction of smectite decreases by only about 0.002 (or 6% of the initial amount) in 1000 years. When the temperature is higher ("high T" case), illitization at point D in the clay rock is clearly accelerated, resulting in a decrease of 0.015 (or 43% of the initial amount) in the smectite volume fraction after 1,000 years. At point

C, located near the EBS-NS interface, more hydrological and chemical interactions take place between the bentonite and the clay formation. Subsequently, more smectite dissolves and more illite precipitates. For the “high T” case, the smectite volume fraction decreases by 0.035, a 100% loss of smectite.

Illitization also occurs in the EBS bentonite, as shown by the smectite and illite volume fraction changes at points A and B in Figures 5.5 and 5.6. In addition to temperature effects, illitization is affected by the initial disequilibrium between the pore-water solution and the mineral phase. Initially, the pore water in the bentonite buffer is oversaturated with respect to illite and undersaturated with respect to smectite. In addition, the pore water in the clay formation contains a much higher concentration of K and Al, and thus provides a source of Al and K for the EBS bentonite alteration through diffusion and advection. Note that the increase in Al and K concentrations in bentonite is caused not only by diffusion and advection, but also by the dissolution of other minerals, such as K-feldspar and quartz. The pore water in the clay formation also has a higher concentration of Mg and Na, which inhibits illitization. But it seems that the factors in favor of illitization outpace those against illitization. At the end of 1,000 years, the smectite volume fraction in the bentonite decreases by 0.035 (or 11%) for the “high T” case and 0.006 (or 2%) for the “low T” case, which corresponds to an illite volume fraction increase of similar magnitude. Clearly, the “high T” case demonstrates stronger illitization than the “low T” case. In “high T” case, at point A near the canister, bentonite undergoes desaturation in short term, the evaporation of pore water therefore results in the precipitation of smectite. The smectite start to dissolve (Figure 5.5) and illite starts to precipitate (Figure 5.6) after about 20-30 years. After that, the dissolution of smectite and precipitation of illite proceed rapidly.

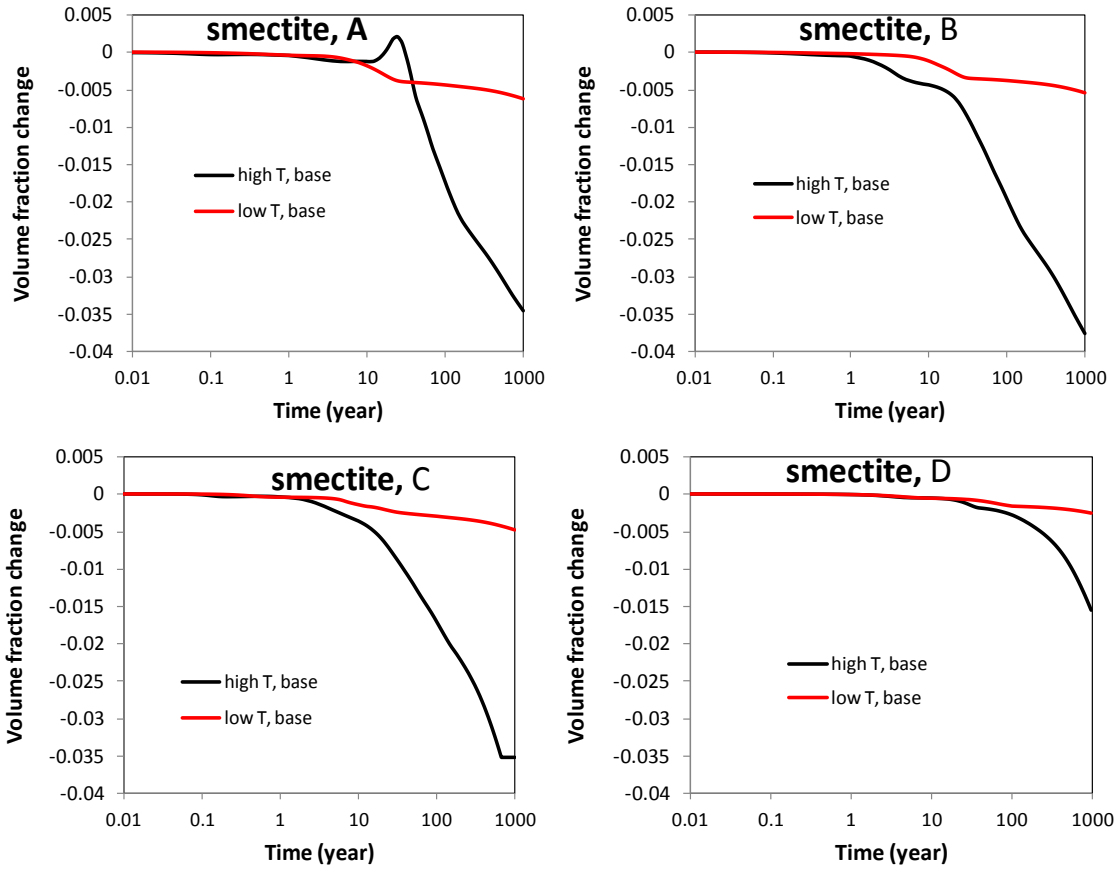

Figure 5.5. The temporal evolution of smectite volume fraction at points A, B, C, and D. Volume fraction change shown in the Y-axis is equal to the volume fraction of smectite at a given time minus the initial volume fraction (see Table 5.1), so negative value means dissolution.

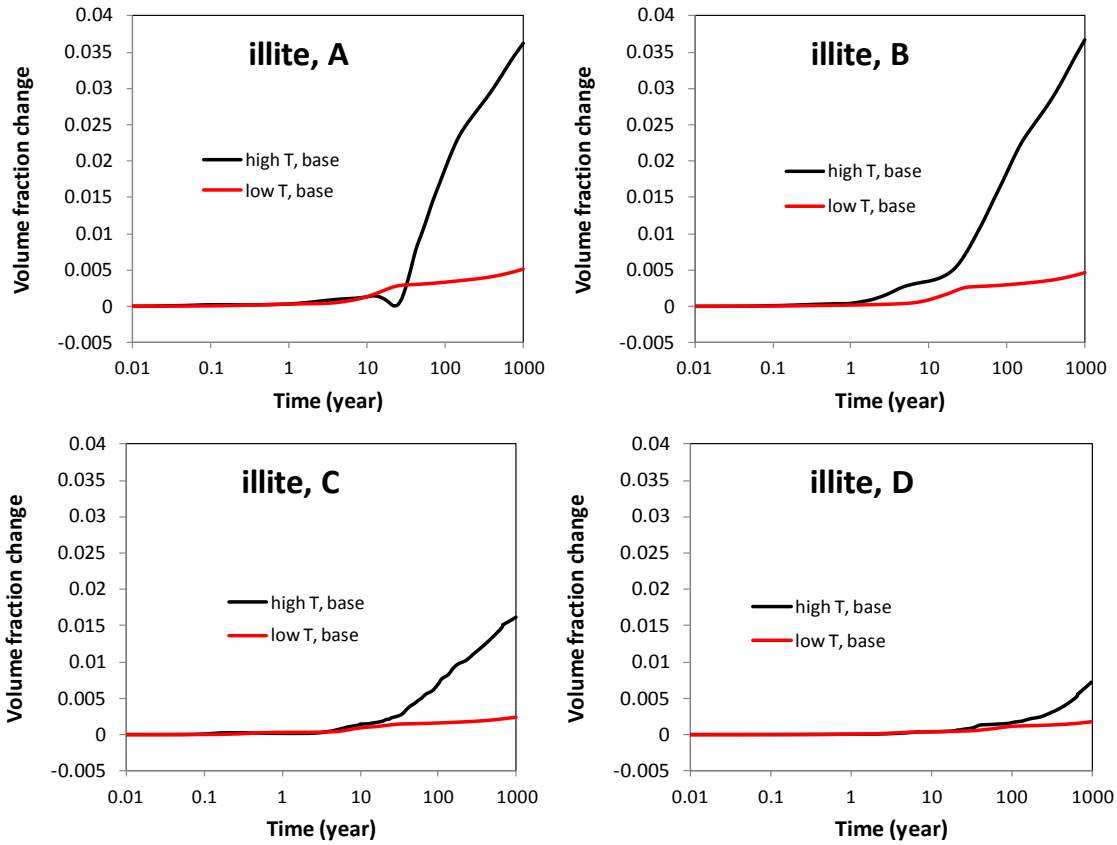

Figure 5.6. The temporal evolution of illite volume fraction at points A, B, C, and D. Volume fraction change shown in the Y-axis is equal to the volume fraction of smectite at a given time minus the initial volume fraction (see Table 5.1), so positive value means precipitation.

5.2.2.1.2 Stress Evolution

In this section, we estimate how the chemical changes observed above may affect the mechanical behavior of the EBS bentonite related to the evolution of swelling and total stress. We limit our analysis to the effects of ion concentration and illitization on swelling, and do not include other potential effects of chemical changes on mechanics, such as changes in mechanical properties due to cementation.

Figures 5.7 and 5.8 show the stress changes at points A and B for both "low T" and "high T" cases. Several processes combine to drive the stress in bentonite up to around 5.1 MPa for the "low T" and 11.5 MPa for the "high T" case after 1,000 years, including the increase in pore pressure due to hydration and thermal pressurization (a processes caused by the difference in thermal expansion of the fluid and solid host rock), bentonite swelling, and thermal expansion. In comparison with the "low T" case, clearly the stronger thermal pressurization in the "high T" case leads to much higher stress in the bentonite. For both the "high T" and "low T" case, the total stress within the buffer has the major contribution from pore pressure, with minor contributions from swelling and thermal stress.

The constitutive relationship described by Equation (5.1) provides an opportunity to evaluate the effect of chemical changes on swelling stress. The mechanical results presented in this section are based on the chemical results in the previous section. In order to isolate the contributions of

ion concentration changes versus smectite changes to swelling stress changes, we present three sets of calculated swelling stress. In the first set, denoted in Figures 5.9 and 5.10 as "S=f(Sl,C,Sc)", the swelling stress is calculated according to Equation (5.1) as a function of liquid saturation changes (Sl), ion concentration (C) changes, and smectite (Sc) changes. In the second set, denoted as "S=f(Sl,C)", the contribution from smectite changes in Equation (5.1) is disregarded, and the swelling stress is only a function of liquid saturation and ion concentration. In the third set, denoted as "S=f(Sl)", all chemical effects are neglected, and the swelling stress is only a function of liquid saturation changes.

At early time (< 20 years), the fact that results for "S=f(Sl,C,Sc)" and "S=f(Sl,C)" cases are indistinguishable (Figures 5.9 and 5.10) indicates that smectite changes have not yet contributed to the stress change, because the volume fraction of smectite shows significant changes only after about 20 years (see Figure 5.5). Ion concentration changes start to affect stress at early times (< 20 years) and maintain such effect afterwards. Initially, bentonite near the canister undergoes desaturation and therefore negative swelling stress (see Figure 5.9 for changes at point A). At point A, for the "low T" case, at the end of the 1,000-year simulation period, the ion concentration increase leads to a drop in swelling stress of about 0.14 MPa, and the dissolution of smectite reduces the swelling stress a little further, by about 0.003 MPa. For the "high T" case, after 1000 years, ion concentration changes cause about a 0.1 MPa decrease in swelling stress, and the loss of smectite due to dissolution results in about a 0.05 MPa reduction in swelling stress at the end of the 1000-year simulation (see Figure 5.9). In general, the chemical changes in bentonite have a fairly moderate effect on swelling stress, about 14% swelling stress reduction due to chemical change for the "low T" case and 15% swelling stress reduction for the "high T" case at point A (Figure 5.9). The stress changes near the EBS-NS (point B) interface behave similarly to those near the canister, except the stress starts to increase earlier; the stress after 1000 years is similar as well. The chemical changes in bentonite lead to about 15% swelling stress reduction for the "low T" case and 18% swelling stress reduction for the "high T" case (see Figure 5.10). In terms of the total stress, the decrease in swelling stress accounts for about a 1.4–1.7% reduction in the total stress.

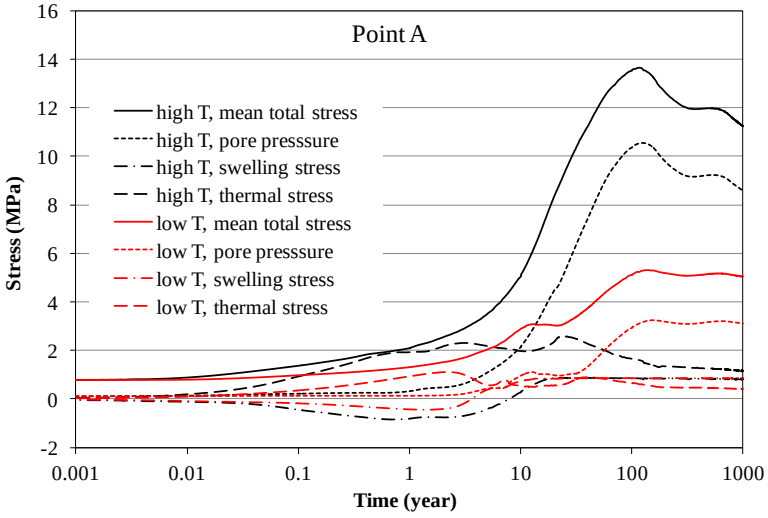

Figure 5.7. Simulation results of mean total stress, pore pressure, and thermal stress at point A for the "low T" and "high T" scenario, respectively.

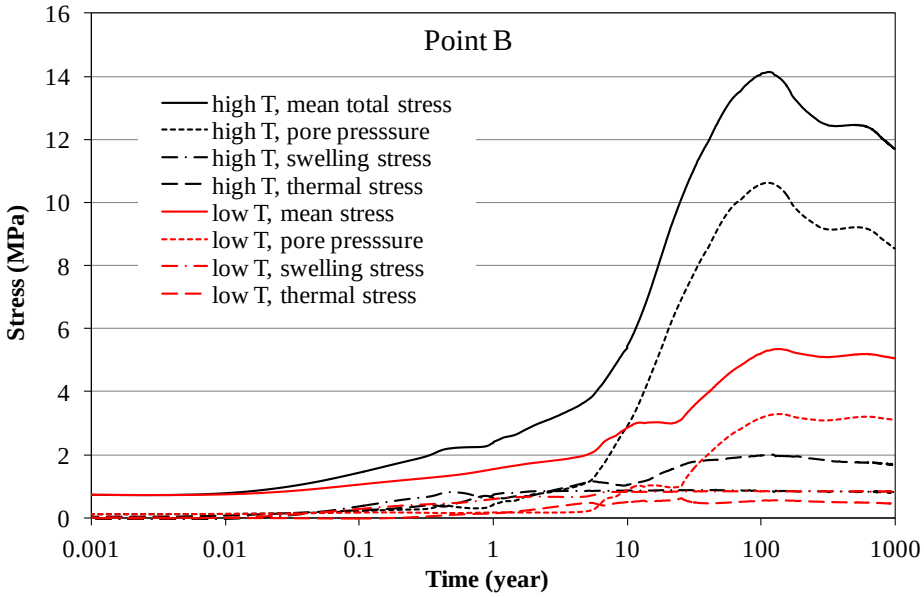

Figure 5.8. Simulation results of mean total stress, pore pressure, and thermal stress at point B for the "low T" and "high T" scenario, respectively.

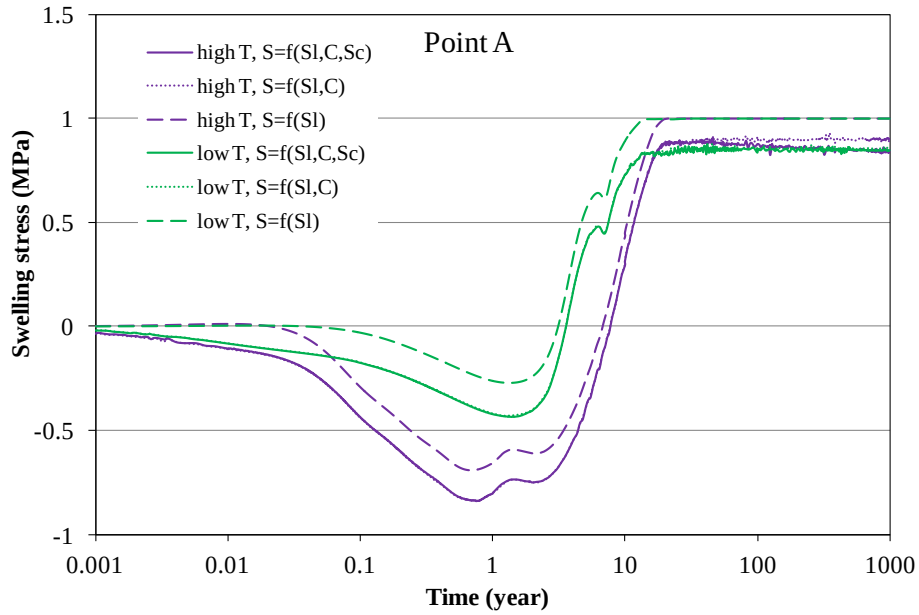

Figure 5.9. Simulation results of swelling stress at point A and B for the "low T" and "high T" scenarios, respectively.

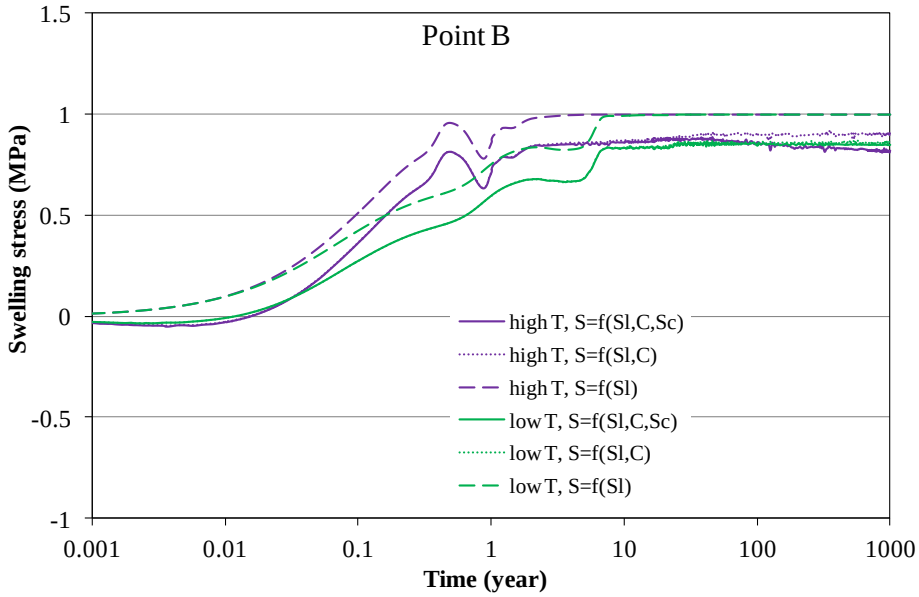

Figure 5.10. Simulation results of swelling stress at point A and B for the "low T" and "high T" scenarios, respectively.

5.2.2.1.3 The Effect of Mechanical Parameters

As shown by Equation (5.1), the reduction of swelling stress by the dissolution of smectite is dependent on the values of A_{sc}, an empirical constant that relates the swelling stress with the abundance of smectite. The value of A_{sc} is derived from measured swelling pressure for bentonite materials with different smectite mass fractions, as shown in Figure 5.11. However, probably because these bentonite materials differ not only in the mass fraction of smectite, but also in other properties, these data points are fairly scattered, which makes it hard to establish one linear correlation between swelling-pressure change and mass fraction change in smectite. We therefore chose a line through the measured swelling pressure for Kunigel VI bentonite and use the slope of this line as the value of A_{sc} which is 2.5×10^{6} Pa^{-1} for the base case. A sensitivity run with a A_{sc} of 9.3×10^{6} Pa^{-1} was also conducted to illustrate how the different behavior of other bentonites may affect the calculated swelling pressure, although an A_{sc} of 9.3×10^{6} Pa^{-1} is less likely for Kunigel VI bentonite.

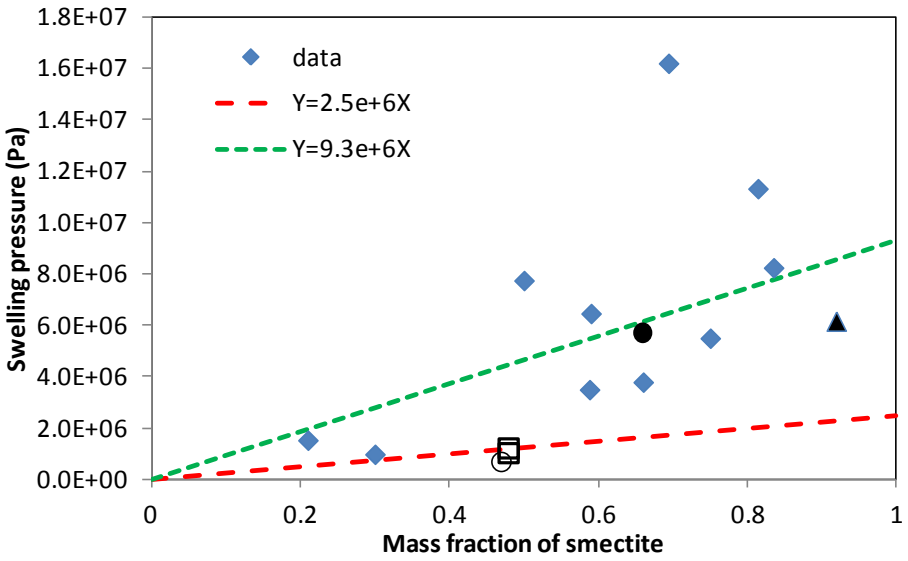

Figure 5.11. Swelling pressure versus mass fraction of smectite for various bentonites. ▲, FEBEX bentonite (ENRESA, 2000); ●, Montigel bentonite (Bucher and Muller-Vonmoos, 1989); □, Kunigel VI bentonite (JNC, 1999); ○, Kunigel bentonite (Konime and Ogata, 1996), ♦ are data for reference material from Czech, Danish, Friedland, Milos Deponit CA-N, Kutch (Indian) and Wyoming MX-80 (Karnland et al., 2006).

In the "high T" base case in which A_{sc} is 2.5×10^{6} Pa^{-1}, the calculated swelling pressure after 1000 years is around 1 MPa without considering any chemical effects. Ion concentration changes cause about a 0.1 MPa decrease in swelling stress, and the loss of smectite results in about an additional 0.05 MPa reduction of swelling stress. In contrast, an additional reduction in swelling pressure of about 0.21 MPa at point A (Figure 5.12) is observed in sensitivity runs with A_{sc} of 9.3×10^{6} Pa^{-1}. At point B, the swelling stress reduction caused by the dissolution of smectite in the sensitivity run is 0.31 MPa (Figure 5.13), which is higher than the 0.05 MPa in the base case. In total, chemical changes lead to about a 15–18% reduction in swelling stress (see Figures 5.10 and 5.11) in the base case, whereas chemical changes cause about a 32–40% decrease in swelling stress (see Figures 5.12 and 5.13). For the "low T" cases, because the dissolution of smectite is fairly moderate, the increase in A_{sc} has a less pronounced effect than that for "high T" cases.

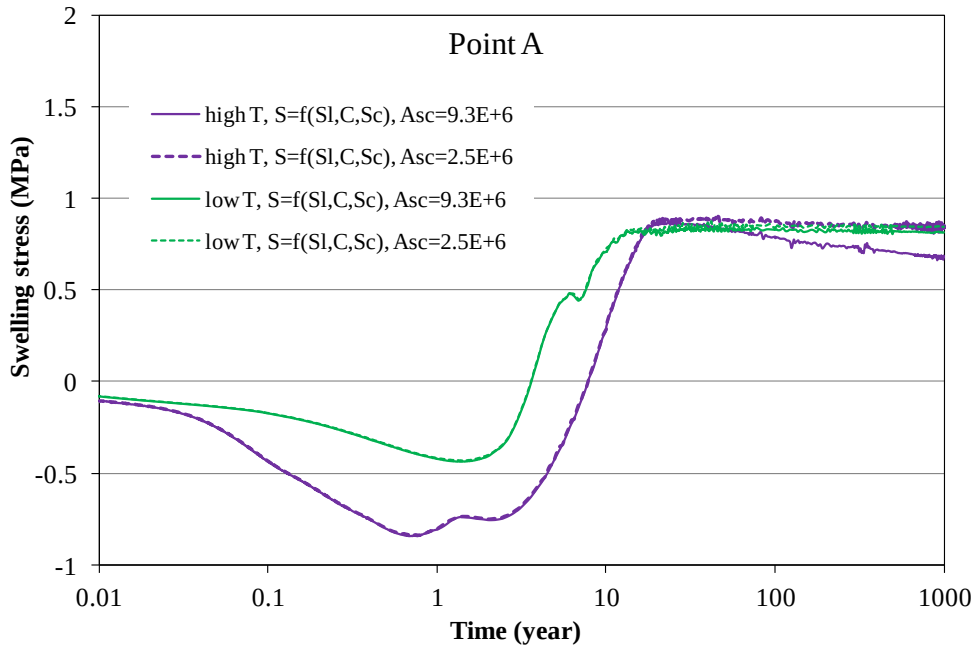

Figure 5.12. Simulation results of swelling stress at point A for the base case (A_{sc} is 2.5×10^{6} Pa^{-1}) and sensitivity cases with A_{sc} values of 9.3×10^{6} Pa^{-1}.

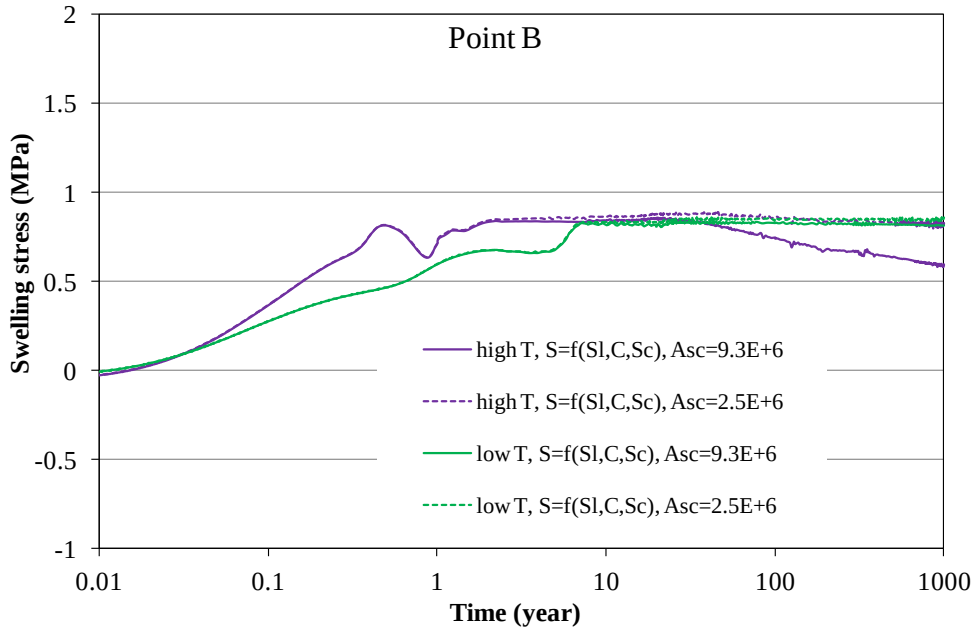

Figure 5.13. Simulation results of swelling stress at point B for the base case (A_{sc} is 2.5×10^{6} Pa^{-1}) and sensitivity cases with A_{sc} values of 9.3×10^{6} Pa^{-1}.

The more smectite dissolves, the larger the impact of A_{sc} values on the calculated swelling stress. Liu et al. (2013b) showed that among the many factors that affect the dissolution of smectite, the dissolution of K-feldspar plays a key role, and a maximum dissolution of smectite was observed if the dissolution of K-feldspar increased by two orders of magnitude. In Figures 5.15 and 5.16, we compare model results with A_{sc} values of 2.5×10^{6} Pa^{-1} to that with A_{sc} values of 9.3×10^{6} Pa^{-1}, for the case in which dissolution of K-feldspar increased by two orders of magnitude, the case "r(feldspar)*100". A further decrease in swelling stress of 0.26 MPa at point A and 0.44 MPa at point B is observed if A_{sc} values of 9.3×10^{6} Pa^{-1} are used in the model.

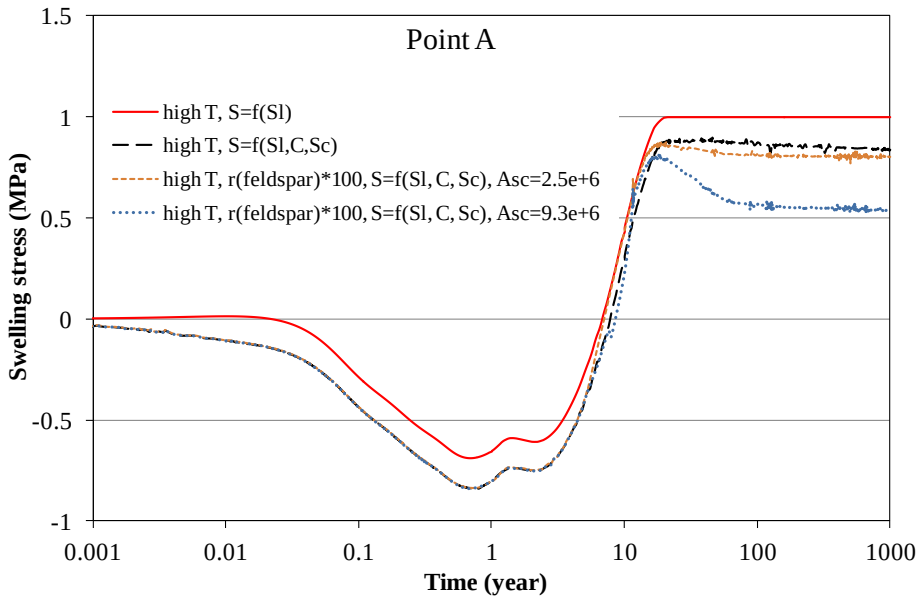

Figure 5.14. Simulation results of swelling stress at point A for the base case and two sensitivity cases for "r(feldspar)*100" with different A_{sc} values.

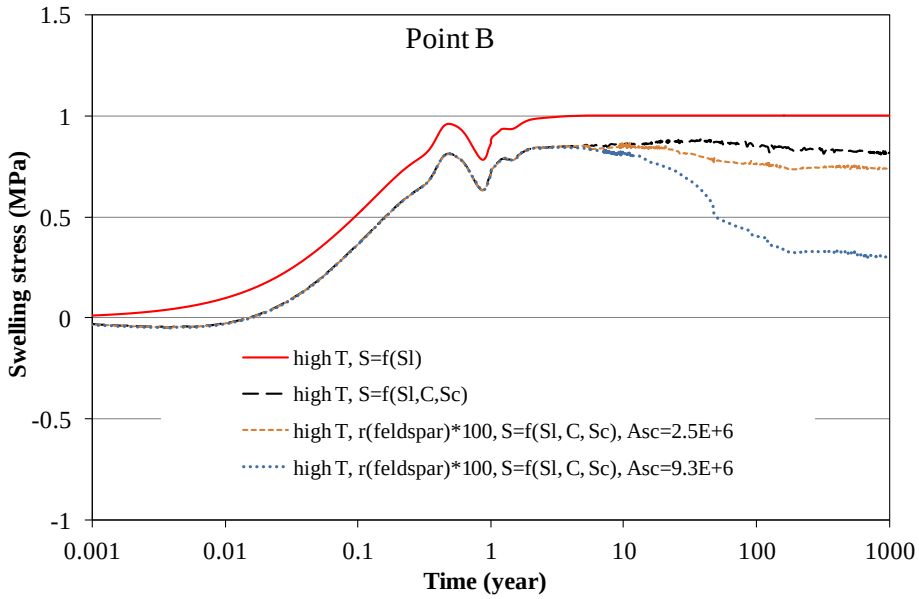

Figure 5.15. Simulation results of swelling stress at point B for the base case and two sensitivity cases for "r(feldspar)*100" with different A_{sc} values.

Our mechanical model for the clay formation is equivalent to that of Rutqvist et al. (2013c), and therefore the stress response in the clay formation is the same. Except for swelling, the mechanical model for the clay formation is not tied to chemical variables, which prevents further analysis of the effects of chemical changes on mechanical behavior in clay formations. In the future, a constitutive relation that incorporates the chemical component within the mechanical model for the clay formation will be implemented. Based on this development, we will be able to analyze the effects of chemical changes on mechanical behavior in a clay formation.

5.2.2.2 Cases for FEBEX Bentonite

A variety of type of bentonite has been studied as the EBS material throughout the world. Kunigel-VI bentonite (Ochs et al., 2004) is one of those that have low smectite content and relative low swelling capacity, whereas FEBEX bentonite (ENRESA, 2000) represents a type of bentonite that has high fraction of smectite and high swelling capacity. MX-80 bentonite (Herbert et al., 2008) is somewhere in between in term of the smectite content and swelling capacity. In the base case, the EBS bentonite is assumed to be Kunigel-VI bentonite (Ochs et al., 2004). In this section, we present model results using FEBEX bentonite as the EBS. Kunigel-VI bentonite differs from the FEBEX bentonite in the following aspects:

1. In terms of aqueous chemistry, FEBEX bentonite has higher ion concentration in pore water than Kunigel-VI bentonite, as shown in Table 5.2 in Section 5.2.1.4. The concentration of major cations, i.e., Ca, Mg, Na, K for FEBEX bentonite is about 2 orders of magnitude higher than that for Kunigel-VI bentonite, which could affect the illitization over the course of heating and hydration.
2. In terms of mineralogical composition, the most pronounced and relevant difference between FEBEX and Kunigel-VI bentonite is the content of smectite, with FEBEX bentonite containing about 60 vol% smectite and Kunigel-VI bentonite having only about

31 vol% smectite (see Table 5.1 in Section 5.2.1.4). FEBEX bentonite has also less K-feldspar, which could affect illitization. The published mineralogical compositions vary slightly, as shown in Table 5.4, and here we take the average. Note that Table 5.1 lists the volume fraction, whereas Table 5.4 lists the mass fraction; the numbers are therefore different.

3. FEBEX bentonite also has higher swelling pressure, ranging from 4.5 MPa (Castellanos et al., 2008) to 7 MPa (ENRESA 2000), than Kunigel-VI bentonite, which has swelling pressure of around 1 MPa (Börgesson et al., 2001; Konime and Ogata 1996) measured using distilled water. Therefore, the β_{SW} in Equation (5.1) for FEBEX bentonite is 0.238 (Rutqvist et al., 2011), which is higher than that used for Kunigel-VI bentonite (0.048).

4. Another difference between FEBEX and Kunigel-VI bentonite is the parameter A_{sc} that relates swelling stress to the abundance of smectite. For FEBEX bentonite, as shown in Figure 5.16, a linear regression curve is taken across the FEBEX bentonite, which give us a slope (A_{sc}) of 6.5E+6 Pa^{-1} that is higher than the 2.5E+6 Pa^{-1} used for Kunigel-VI bentonite.

Table 5.4. Mass fraction of minerals (%) for FEBEX bentonite from different publications.

Mineral	ENRESA (2000), Fernández et al. (2004)	Ramírez et al. (2002)
Calcite	trace	1 ± 0.7
Dolomite	0.0	0
Illite	0.0	0
Kaolinite	0.0	0
Smectite	92 ± 3	93 ± 3
Chlorite	0.8	-
Quartz	2 ± 1	2 ± 0.5
K-Feldspar	trace	2 ± 1
Siderite	0.0	0
Ankerite	0.0	0

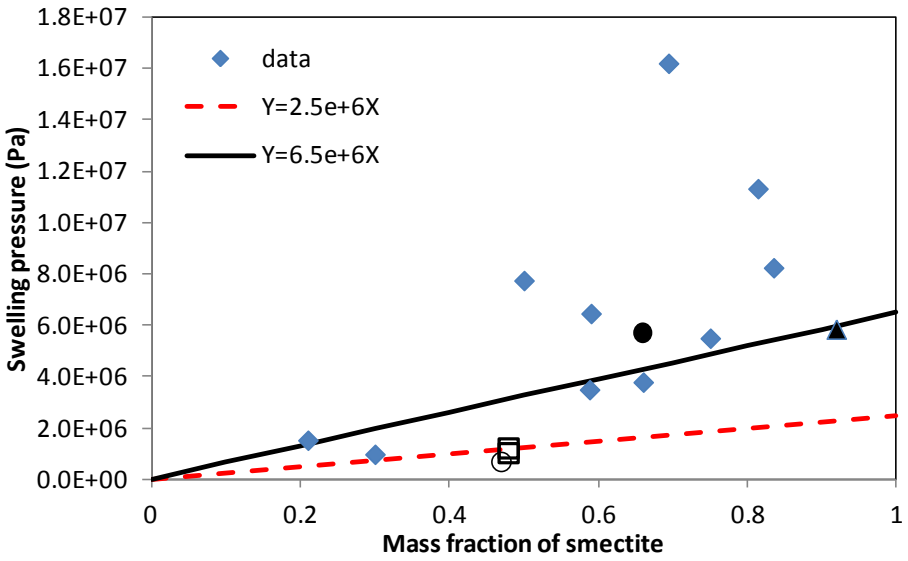

Figure 5.16. Swelling pressure versus mass fraction of smectite for various bentonites. ▲, FEBEX bentonite (ENRESA, 2000); ●, Montigel bentonite (Bucher and Muller-Vonmoos, 1989); □, Kunigel VI bentonite (JNC, 1999); ○, Kunigel bentonite (Konime and Ogata, 1996), ♦ are data for reference material from Czech, Danish, Friedland, Milos Deponit CA-N, Kutch (Indian) and Wyoming MX-80 (Karnland et al., 2006).

5.2.2.2.1 Chemical Evolution

As mentioned above, the thermal conductivity and permeability remain the same for the sensitivity run using FEBEX bentonite as the EBS. The temperature, water saturation, and pore pressure for the sensitivity run are therefore the same, as shown in Figures 5.2-5.4. Changes in smectite and illite volume fractions are shown in Figures 5.17 and 5.18. Model results from the sensitivity case confirm the occurrence of illitization (dissolution of smectite and precipitation of illite), and illitization is enhanced at higher temperature for FEBEX bentonite, just as what were observed for the base case for Kunigel bentonite. However, in comparison with the model results for the base case with Kunigel bentonite, several distinct features have been observed for the FEBEX bentonite. First, for the "high T" scenario, there is less smectite dissolution in the FEBEX bentonite. Smectite volume fraction decreases about 0.01 at point A and 0.018 at point B, about 1.6% and 3% of the initial smectite volume fraction, respectively, significantly lower than the decrease of 0.035 (11% of the initial amount) in Kunigel bentonite. Second, the enhancement of illitization (expressed as smectite dissolution and illite dissolution) is less pronounced for FEBEX, because while the amount of smectite dissolving for the "low T" scenario is similar for both FEBEX and Kunigel bentonite, the amount of smectite dissolving for the "high T" scenario is much less for FEBEX bentonite. The differences in dissolved smectite between "high T" and "low T" scenarios for FEBEX bentonite are smaller than that for Kunigel bentonite. Third, although different types of EBS bentonite have almost no impact on the chemical changes in the clay rock away from the EBS-NS interface (illustrated by the results at point D, Figures 5.17 and 5.18), such differences have a moderate impact on the clay rock near the interface. As shown by the results at point C in Figures 5.17 and 5.18, within the FEBEX bentonite, smectite dissolution occurs earlier. The reason for this earlier dissolution is that FEBEX bentonite has a higher K concentration (see Table 5.4), so that diffusion of K from clay

rock to bentonite occurs at a lower rate, and subsequently more K is available within the clay rock for illitization.

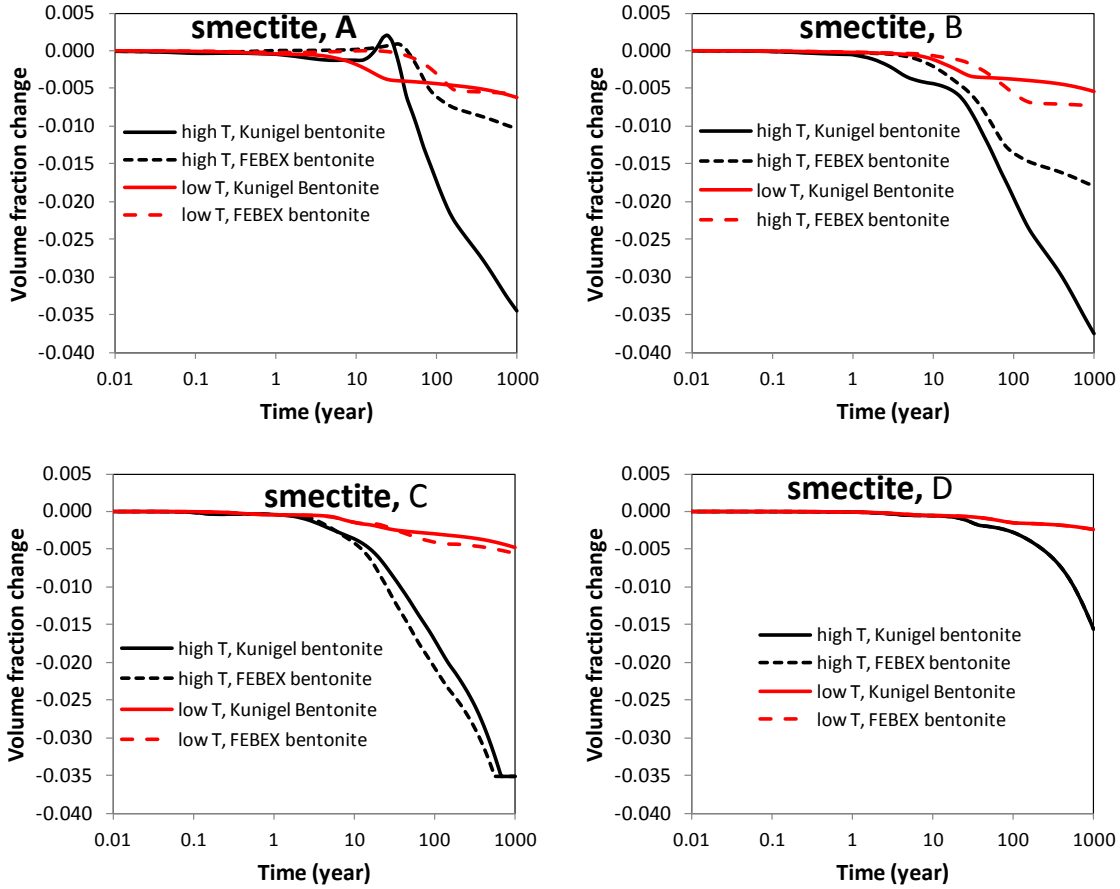

Figure 5.17. The temporal evolution of smectite volume fraction at points A, B, C, and D in the base case with Kunigel bentonite and a sensitivity case with FEBEX bentonite.

The sensitivity of illitization in EBS bentonite to key chemical parameters was investigated in Liu et al. (2013b), which confirmed the importance of available K as widely observed in geological formations (e.g., Cuadros 2006), but demonstrated that the source K is actually the dissolution of K-feldspar. When FEBEX bentonite is used as the EBS material, K-feldspar dissolves much less compared with the base case, which uses Kunigel bentonite, as illustrated in Figure 5.19. This is the reason why in Figure 5.17, smectite dissolves less in FEBEX bentonite than in Kunigel bentonite. Less dissolution of K-feldspar in FEBEX bentonite can be attributed to two factors: a lower volume of K-feldspar and a higher K concentration in pore water for FEBEX bentonite.

One of the byproducts of illitization is the precipitation of quartz, as shown in Equation 5.3. The cementation by quartz (or amorphous SiO_2 minerals) might lower the swelling of bentonite and increase the brittleness of the bentonite. In comparison with the base case using Kunigel bentonite, less quartz precipitates for the sensitivity case with FEBEX bentonite. For the "high T" scenario, the amount of quartz formed for FEBEX bentonite is only about 1/10 of that for kunigel bentonite.

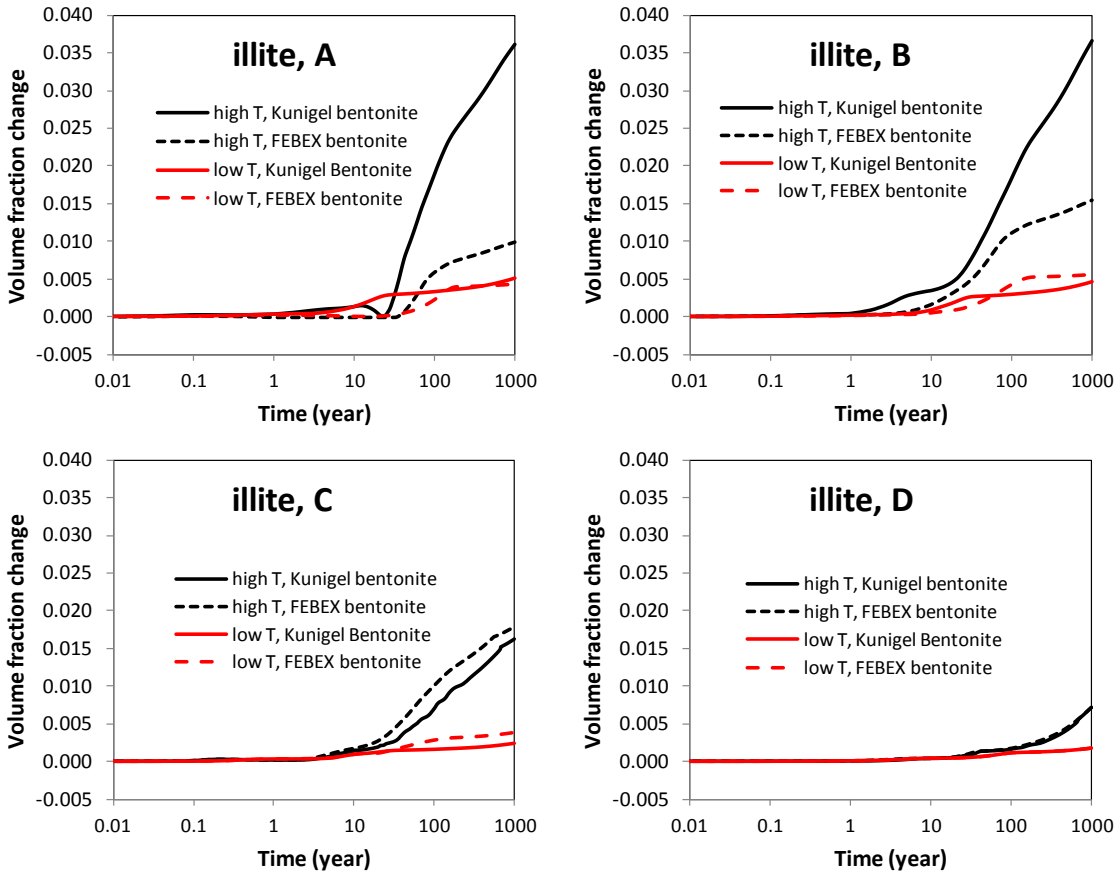

Figure 5.18. The temporal evolution of illite volume fraction at points A, B, C, and D in the base case with Kunigel bentonite and a sensitivity case with FEBEX bentonite.

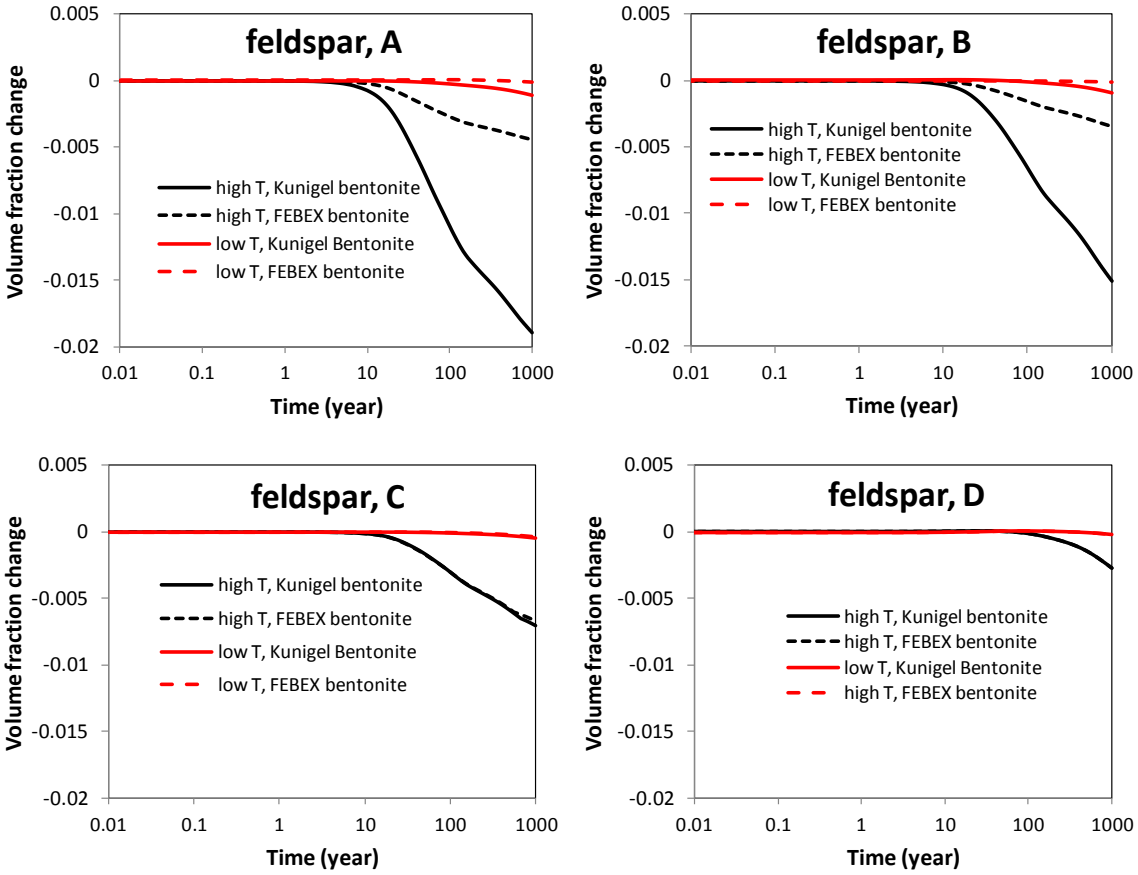

Figure 5.19. The temporal evolution of K-feldspar volume fraction at points A, B, C, and D in the base case with Kunigel bentonite and a sensitivity case with FEBEX bentonite.

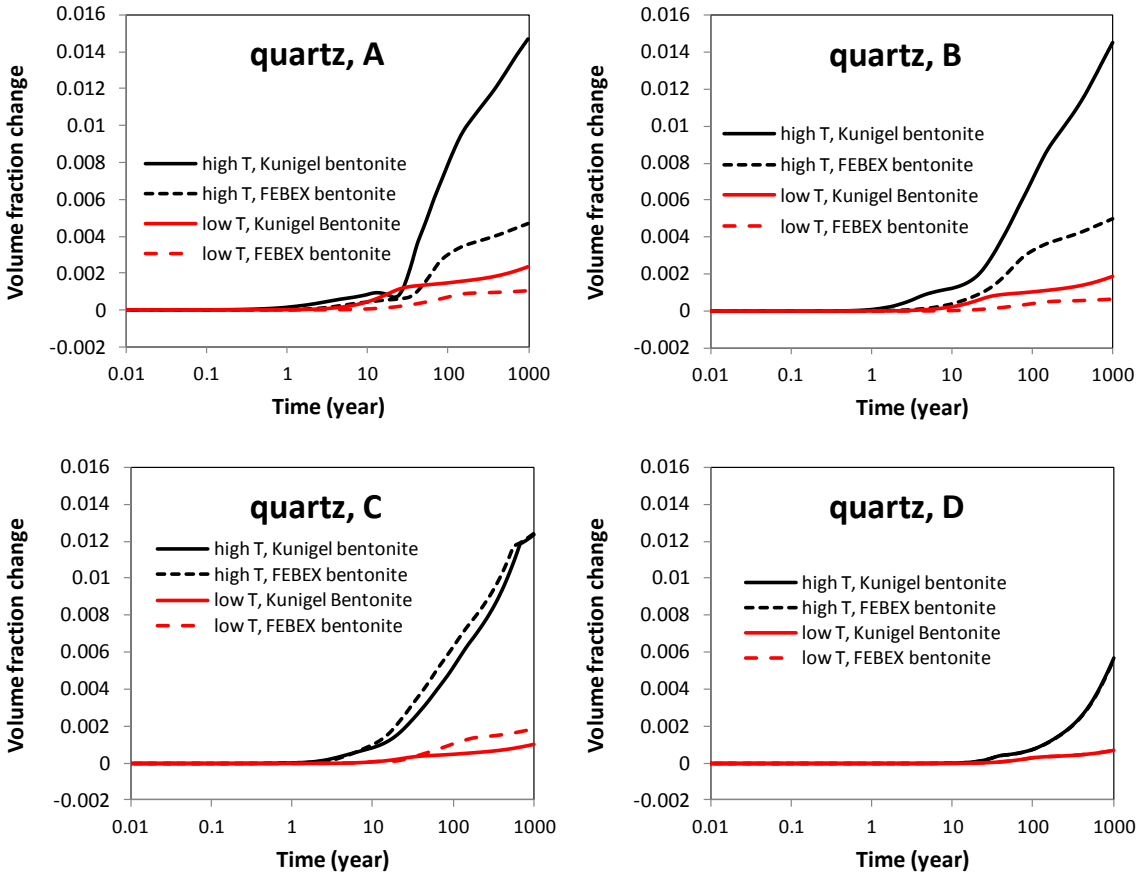

Figure 5.20. The temporal evolution of quartz volume fraction at points A, B, C, and D in the base case with Kunigel bentonite and a sensitivity case with FEBEX bentonite.

5.2.2.2.2 Stress Evolution

As discussed in Section 1.3.1, the increase in pore pressure due to hydration and thermal pressurization (processes caused by the difference in thermal expansion of the fluid and solid host rock), bentonite swelling, and thermal expansion are the main driving force for the increase in total stress in bentonite. In comparison with the "low T" case, clearly the stronger thermal pressurization in the "high T" case leads to much higher stress in the bentonite. For both the "high T" and "low T" case, the total stress within the buffer has the major contribution from pore pressure, with minor contributions from swelling and thermal stress.

Figures 5.21 and 5.22 compares the total stress calculated for the Kunigel (the base case) and FEBEX bentonite (the sensitivity case). Because FEBEX bentonite has higher swelling pressure, the total stress for FEBEX bentonite at point A and B are 3–4 MPa higher than that for Kunigel bentonite after 1000 years.

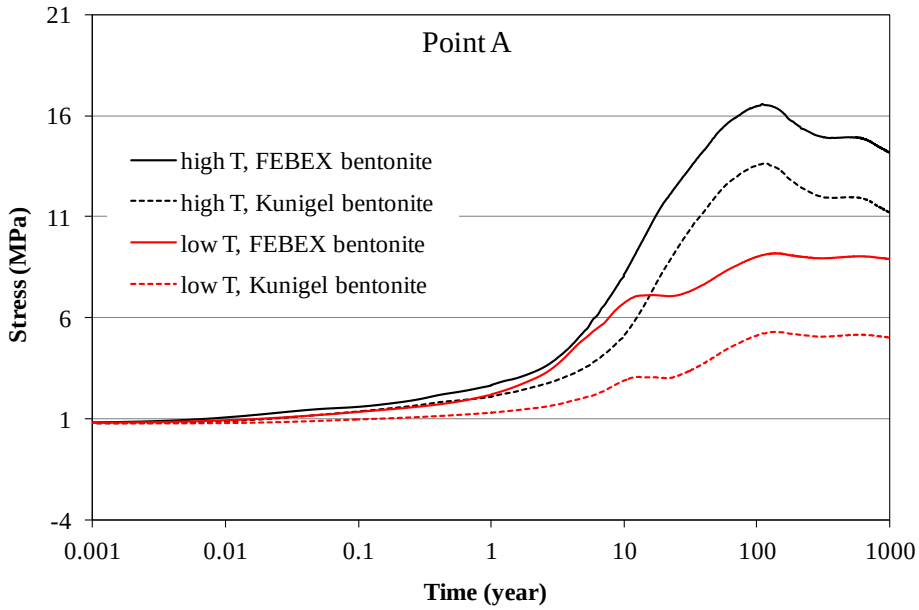

Figure 5.21. Simulation results for mean total stress at point A in the base case with Kunigel bentonite and the sensitivity case with FEBEX bentonite for the "low T" and "high T" scenarios, respectively.

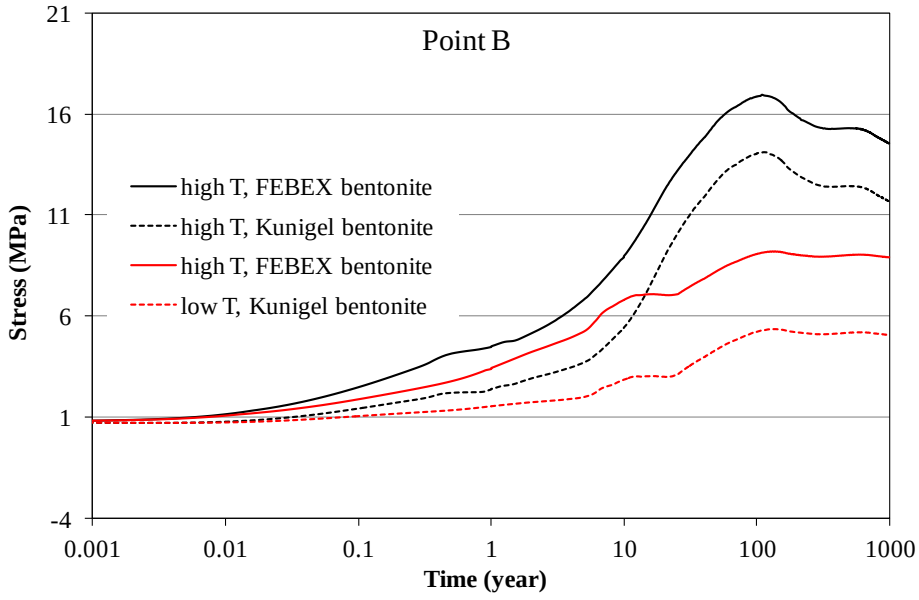

Figure 5.22. Simulation results of mean total stress at point B in the base case with Kunigel bentonite and the sensitivity case with FEBEX bentonite for the "low T" and "high T" scenarios, respectively.

The constitutive relationship described by Equation (5.1) shows that the swelling stress changes receive contributions from moisture, ion concentration, and smectite changes. Just as what has been done for the base case, we also present three sets of calculated swelling stresses for FEBEX bentonite to delineate the contribution from each process.

In the first set, denoted in Figures 5.23 to 5.26 as "S=f(Sl,C,Sc)", the swelling stress is calculated according to Equation (5.1) as a function of liquid saturation changes (Sl), ion concentration (C) changes, and smectite (Sc) changes. In the second set, denoted as "S=f(Sl,C)", the contribution from smectite changes in Equation (5.1) is disregarded, and the swelling stress is exclusively a function of liquid saturation and ion concentration. In the third set, denoted as "S=f(Sl)", all chemical effects are neglected, and the swelling stress is exclusively a function of liquid saturation changes. At point A near the canister, bentonite undergoes evaporation and liquid saturation decrease, which results in a decrease in swelling stress (shrinkage) for about 4 years for the "low T" scenario and about 8 years for the "high T" scenario (Figure 5.23). After that, the increase in liquid saturation induces swelling, and swelling stress keeps increasing, reaching the swelling capacity of 5 MPa. Figure 5.24 zooms in to the stress range from 4.5 to 5 MPa to illustrate the contribution from ion concentration and smectite changes.

Compared to the swelling stress for Kunigel bentonite presented in Section 5.2.2.1, the swelling stress for FEBEX bentonite has two distinct features. First, change in ion concentration has a minimal effect on the swelling stress, because the ion concentration of the pore water in FEBEX bentonite is fairly close to that for clay rock. Initially, pore water in clay rock, FEBEX bentonite, and Kunigel bentonite has an ionic strength of 0.38 M, 0.25 M, and 0.004 M, respectively. Clearly the concentration gradient between clay rock and FEBEX bentonite is smaller and therefore diffusion occurs at a lower rate. As a result, the ion concentration in pore water for FEBEX bentonite increases only moderately, which changes the swelling stress noticeably. Note that about 0.1 MPa swelling stress reduction due to ion concentration has been observed for Kunigel bentonite. Second, more stress reduction due to smectite dissolution has been observed for FEBEX bentonite. Despite the fact that less smectite dissolution has been observed for FEBEX bentonite (Figure 5.17), higher A_{sc} (a parameter that relates swelling stress to the abundance of smectite) for FEBEX bentonite leads to a slightly higher reduction in swelling stress.

Table 5.5 lists the stress reduction by ion concentration and smectite dissolution at point A for Kunigel and FEBEX bentonite. In total, chemical changes lead to about a 0.15 MPa stress change for Kunigel bentonite and 0.08 MPa for FEBEX bentonite. Relative to the swelling stress obtained with "S=f(Sl)", chemical change causes about a 15% reduction in swelling stress for Kunigel bentonite, but only 1.6% for FEBEX bentonite. Model results at point B (Figures 5.27 and 5.28) lead to the same observation in terms of the difference between Kunigel and FEBEX bentonite, although the specific values differ slightly from those at point A.

Table 5.5. The geochemically induced swelling stress for Kunigel and FEBEX bentonite at point A for "high T" scenario. Stress reduction by ion concentration is the difference between the swelling stress obtained with "S=f(Sl)" and "S=f(Sl,C)", and the stress reduction by smectite dissolution is the difference between the swelling stress obtained with "S=f(Sl,C)" and "S=f(Sl,C,Sc)" (see Figure 5.26), the relative amount (%) use the results from "S=f(Sl)" as the basis.

Kunigel bentonite				**FEBEX bentonite**			
Stress reduction by ion concentration, MPa	Stress reduction by ion concentration, (%)	Stress reduction by smectite dissolution MPa	Stress reduction by smectite dissolution (%)	Stress reduction by ion concentration, MPa	Stress reduction by ion concentration, (%)	Stress reduction by smectite dissolution, MPa	Stress reduction by smectite dissolution (%)
0.1	10%	0.05	5%	0.006	0.1%	0.076	1.5%

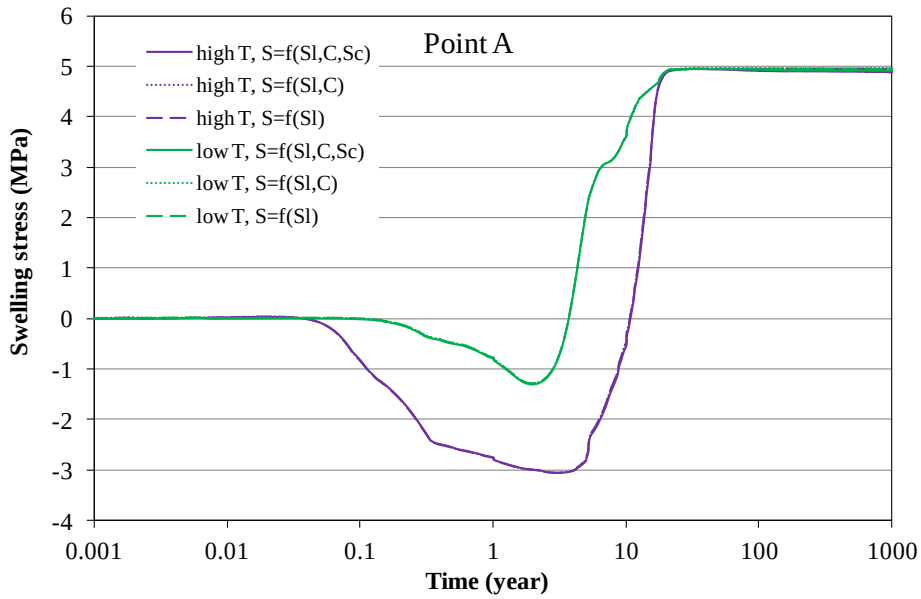

Figure 5.23. Simulation results of swelling stress at point A for the FEBEX bentonite for the "low T" and "high T" scenarios, respectively, focusing on the stress range from 4.5 to 5 MPa.

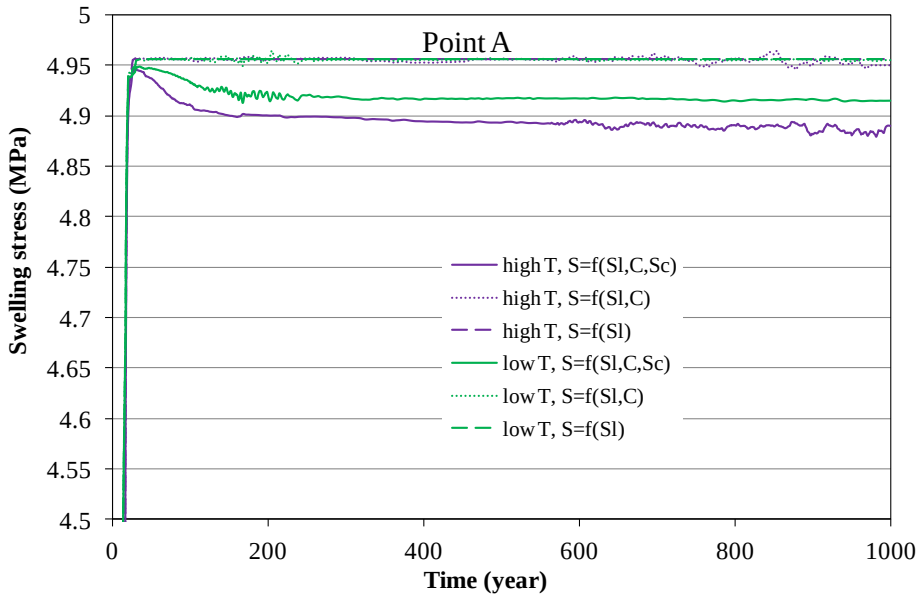

Figure 5.24. Simulation results of swelling stress at point A for the FEBEX bentonite for the "low T" and "high T" scenarios, respectively, focusing on the stress range from 4.5 to 5 MPa.

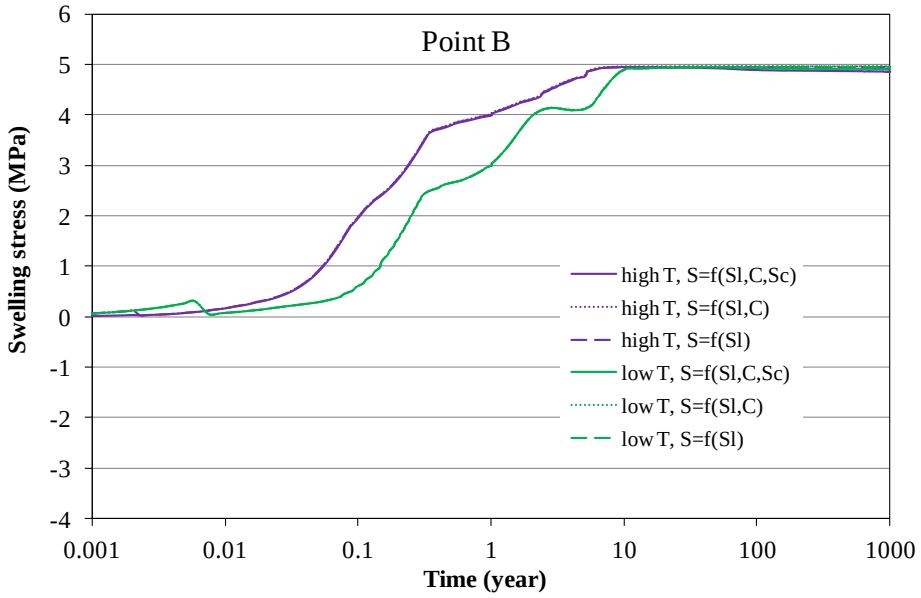

Figure 5.25. Simulation results of swelling stress at point B for the FEBEX bentonite for the "low T" and "high T" scenarios, respectively, focusing on the stress range from 4.5 to 5 MPa.

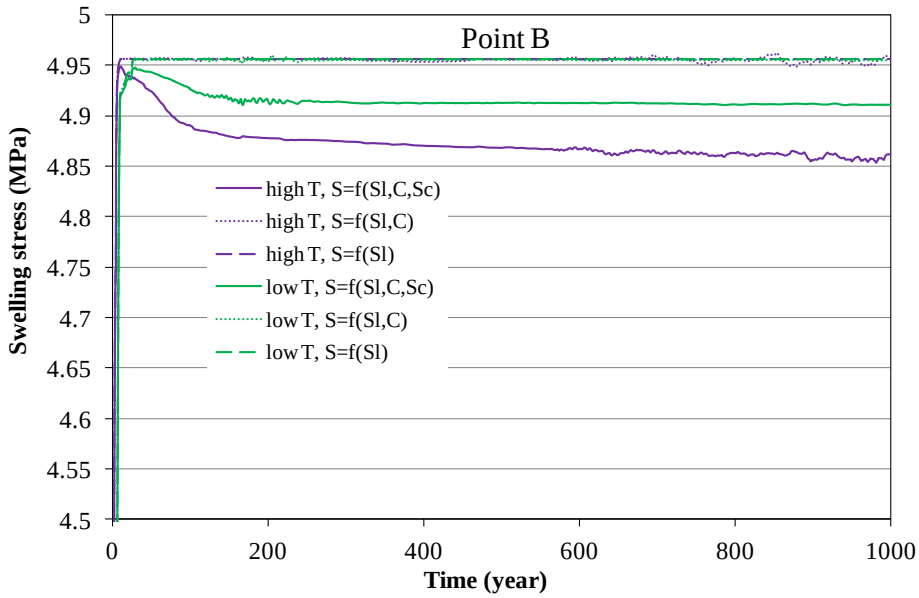

Figure 5.26. Simulation results of swelling stress at point B for the FEBEX bentonite for the "low T" and "high T" scenarios, respectively, focusing on the stress range from 4.5 to 5 MPa.

5.2.2.2.3 Effect of K-Feldspar Dissolution Rate on Illitization and Swelling Stress for FEBEX Bentonite

Sensitivity analyses conducted by Liu et al. (2013b) for the Kunigel bentonite showed that the pore-water concentration of K in the bentonite is critical for the illitization, with the dissolution of K-feldspar being the major source of K needed for illitization. The maximum dissolution of smectite for Kunigel bentonite is achieved in a run that has a K-feldspar dissolution rate two orders of magnitude higher than the base case. Here we conduct the same type of simulation for FEBEX bentonite, i.e. increasing the dissolution rate of K-feldspar by two orders of magnitude, to evaluate the quantity of smectite dissolution and the subsequent swelling stress reduction. As expected, a higher K-feldspar dissolution rate leads to more dissolution of feldspar (Figure 5.27) and eventually depletes the initially presented K-feldspar, so that the volume fraction of K-feldspar does not decrease any more after about 100 years. More smectite dissolves and illite precipitates when the dissolution rate of K-feldspar increases (Figures 5.28 and 5.29). Note that dissolution rate of K-feldspar in current model is taken from Xu et al. (2006) and it is know there is large uncertainty associated with this rate due to various reasons (e.g., Zhu 2005). At point A near the canister, because the dissolution of K-feldspar is the dominant source of K, no further dissolution of smectite is observed as K-feldspar is depleted; the smectite volume fraction decreases about 0.017 (about 3% of the initial amount) and remains at such a value from 100 to 1000 years. At point B near the EBS-NS interface, because the host clay can supply K through diffusion and advection, even local K-feldspar is depleted, dissolution of smectite continues, and at the end of 1000 years, the volume fraction decreases about 0.04 (about 7% of the initial amount).

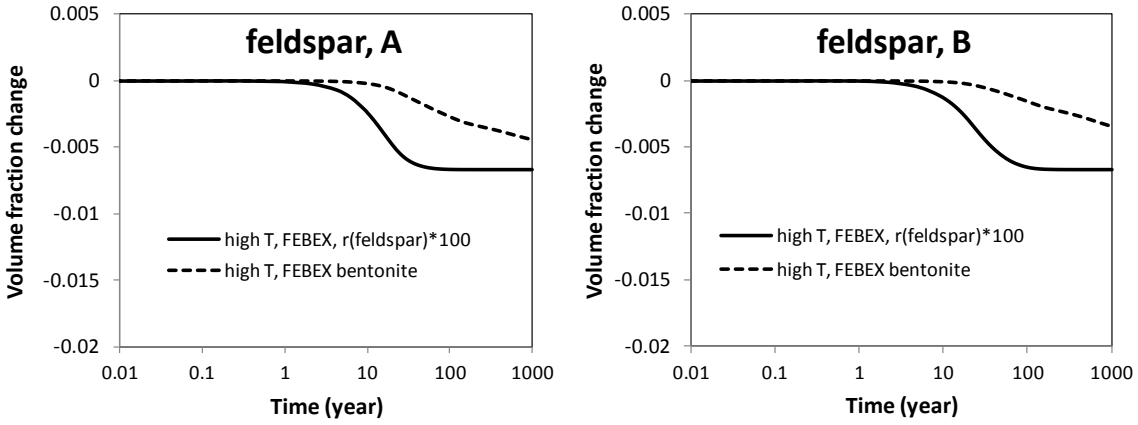

Figure 5.27. The temporal evolution of K-feldspar volume fraction at points A, B for the case with FEBEX bentonite with dissolution rate of K-feldspar being raised by two orders of magnitude.

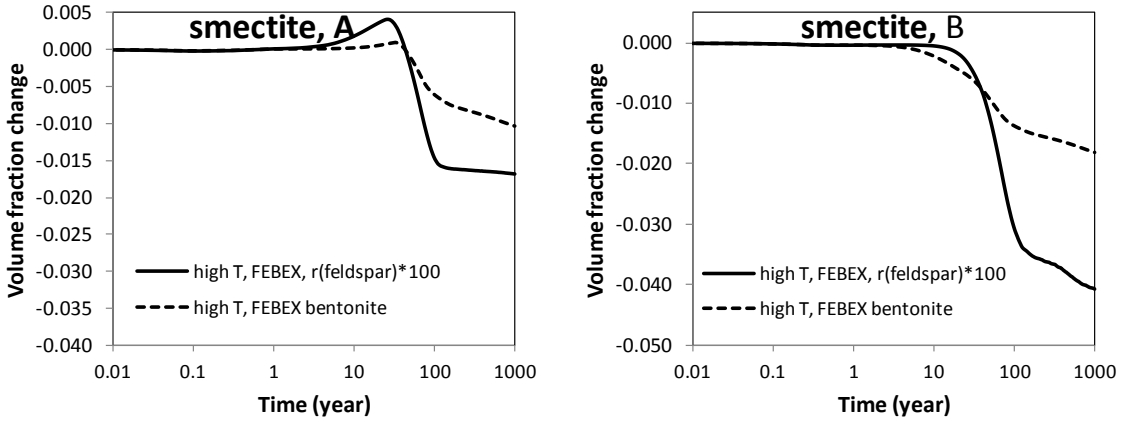

Figure 5.28. The temporal evolution of smectite volume fraction at points A, B for the case with FEBEX bentonite with dissolution rate of K-feldspar being raised by two orders of magnitude.

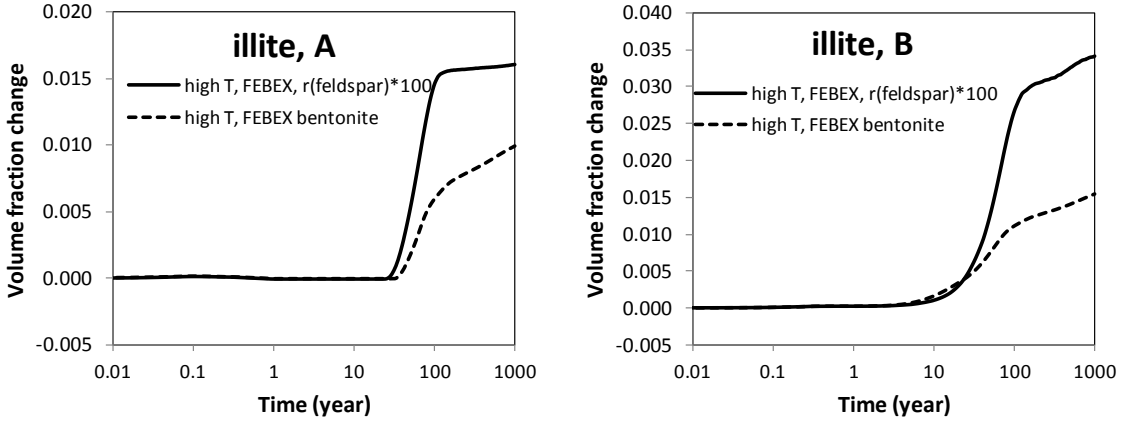

Figure 5.29. The temporal evolution of illite volume fraction at points A, B for the case with FEBEX bentonite with dissolution rate of K-feldspar being raised by two orders of magnitude.

The "high T" scenario with K-feldspar dissolution being increased by two orders of magnitude represents the worst scenario for FEBEX bentonite in terms of the swelling pressure reduction caused by chemical changes. However, even for this worst scenario, the swelling pressure reduction is still fairly moderate. As shown by the green line in Figures 5.30 and 5.31, in comparison with the swelling stress obtained by "s=f(Sl)," that swelling is the function of moisture change alone; when K-feldspar dissolution is increased by two orders of magnitude, the swelling stress decreases about 0.12 MPa, about 2.3%, at point A; and about 0.18 MPa, about 3.6%, at point B.

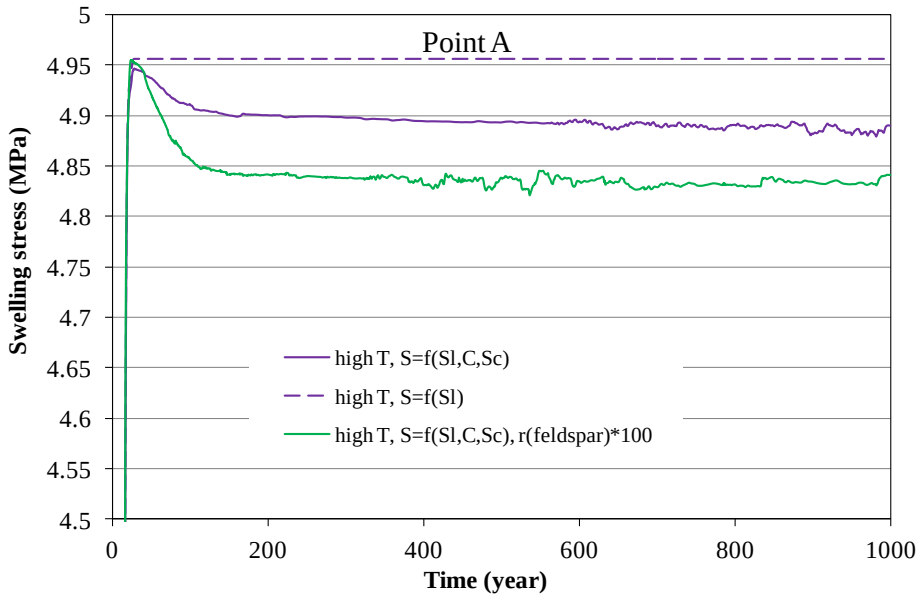

Figure 5.30. Simulation results of swelling stress at point A for the FEBEX bentonite "high T" scenario with K-feldspar dissolution being increased by two orders of magnitude, focusing on the stress range from 4.5 to 5 MPa.

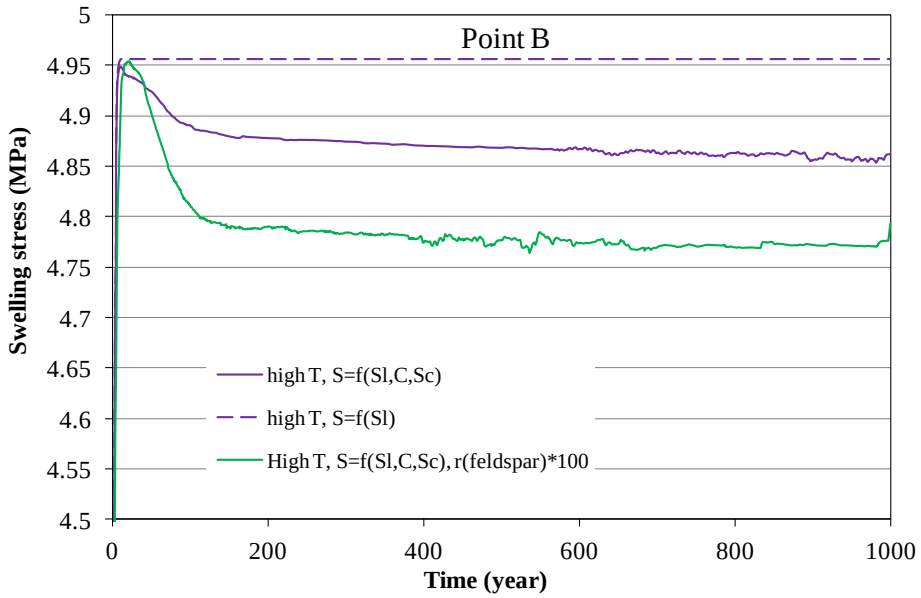

Figure 5.31. Simulation results of swelling stress at point A for the FEBEX bentonite "high T" scenario with K-feldspar dissolution being increased by two orders of magnitude, focusing on the stress range from 4.5 to 5 MPa.

5.1 High Temperature THM Experiments on Bentonite and Opalinus Clay

The primary objective of the laboratory experiments is to investigate the impact of high-T physical and chemical alterations of buffer and backfill materials (bentonite) and clay host rock on their geomechanical and hydrological properties, and on interaction between the EBS and the natural system. Our particular interest is the heat-induced chemical alteration—the illitization of smectite and cementation—within the buffer and backfill materials (bentonite) of the EBS.

Miniature core samples for the experiment were prepared from natural, untreated bentonite chips obtained from LANL and Opalinus Clay cores from Mont Terri URL through NAGRA. The bentonite containing either distilled water or aqueous KCl solution were made, which was introduced during compaction of ground bentonite powder. Both bentonite and Opalinus Clay cores were heated in sealed titanium containers over extended durations (1–3 months).

The heat-treated samples were tested for their triaxial compression strength and ultrasonic velocities. Also, a miniature indentation test setup was built to examine changes in the hardness and elastic moduli of the clay. However, the samples suffered progressive decreases in water content during heating, which indicated very slow leakage of water vapor from the pressure vessels. For this reason, the measured changes in the clay properties were strongly affected by desiccation-induced bulk volume decreases and increases in the strength. The details of the experimental results are described below.

5.3.1 Sample preparation

The Opalinus Clay cores previously obtained from Mon Terri were subcored to produce small, cylindrical core samples (Figure 5.32). Because of the strong bedding anisotropy of the clay and

preexisting microcracks and inclusions, slender, well-shaped cores were difficult to obtain, and only cores drilled along the bedding planes and microcracks were recovered successfully. The drilling was conducted using a custom-made core barrel (barrel inner diameter=0.56") which was designed to reduce seizing of the drill's cutting edge by the produced debris. No water or cryogen was used during the drilling, because we needed to avoid introduction of additional water into the clay (cryogen induces condensation of water from the air). This, however, resulted in heating of the rock cores from the drilling, which may have caused additional losses of the pore water from the cores already drying from long-term storage. The density and the water content of the cores used for the experiment were 2.3 g/cm^3 and 2.2 wt%, respectively.

The bentonite samples were obtained from LANL, sharing the same batch of the material (untreated *BARA-KADE*® brand bentonite chips, *Bentonite Performance* Minerals) with other experiments conducted by the LANL and LBNL teams. The chips were ground and pulverized to grain sizes smaller than 75 μm, which were dried in a convection oven at 60ºC for 24 hours. According to a previously published report (Caporuscio 2013, Table 3), similar bentonite chips contained 72%wt montmollironite, 13%wt clinoptilolite, 9%wt feldspar, and 2%wt biotite. Previously, Pusch (Pusch, R. [1992], Clay Minerals, 27, 353-361) used a similar commercial bentonite compacted at ~100 MPa (~14,490 psi) with 8–14%wt of water content. This resulted in compacted clay samples with a final density of ~2.1 g/cm^3 and water content ~60%. Based upon this knowledge, our samples were designed to have a water content of 15%wt and density 2.1 g/cm^3, compacted at 100 MPa in a sample mold (Figure 5.32). Also, to examine the effect of potassium in the pore water, either distilled water or 0.5 M KCl aqueous solution (reagent grade crystals obtained from BDH) was used as the pore fluid. Three types of cylindrical cores were prepared for the experiment: (1) permeability test cores [D(diameter)=0.56", H(height)=0.25"], compacted within a titanium-2 ring (PRM), (2) seismic and indentation test cores [D=0.56", H=0.25"] (S&I); and (3) geomechanical test cores [D=0.56", H=1.1"](GEO). The actual density of the cores varied from 1.92 g/cm^3 to 2.05 g/cm^3, depending upon the core types (GEO cores were less dense than other core types).

Both compacted bentonite and Mont Terri core samples were introduced in chemically passivated miniature titanium pressure vessels (High Pressure Company, titanium grade 5 miniature reactor C), and were heated at 200ºC over planned durations (Table 5.6). However, initial pressurization of the vessels with nitrogen gas indicated that the metal-to-metal contacts of the vessels did not form tight seals. Therefore, as an alternative, a 1/32"-thick, extreme-high-temperature silicone rubber (McMaster 8632K41, durometer 70A) was used as a gasket. A preliminary test using a wet Kaolin sample (15%wt water content) indicated no loss of fluid from the vessel over 7 days, while heated at 200ºC. Once each pressure vessel reached its "maturity," the vessel was removed from the oven and stored in a separate oven at 100ºC overnight, then stored at room temperature until the tests were conducted.

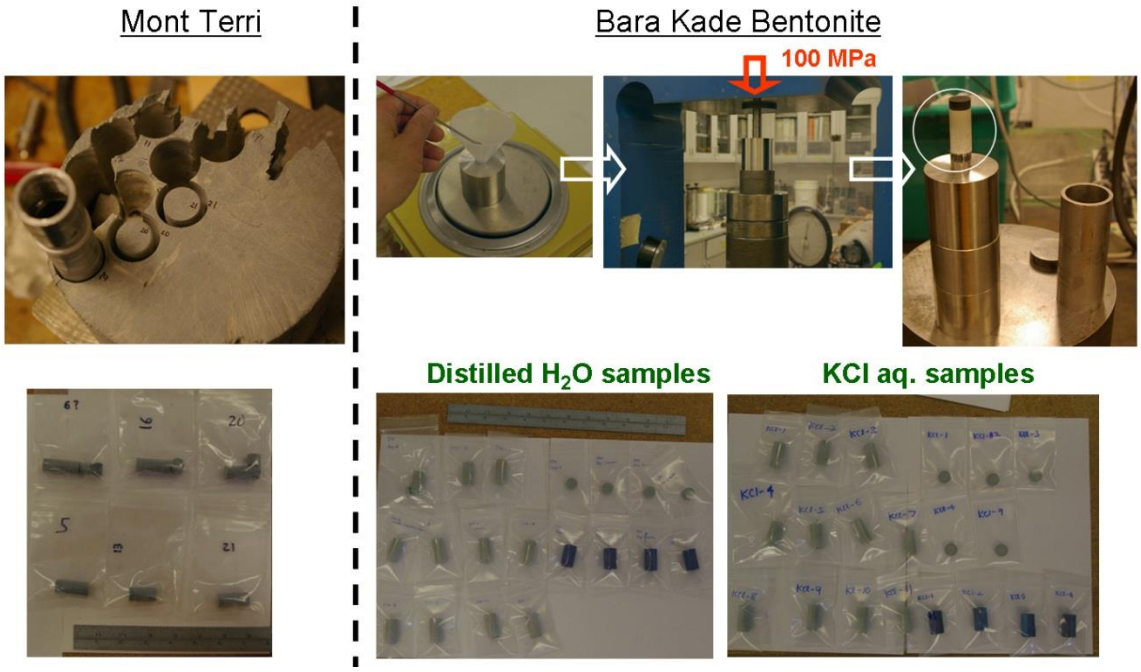

Figure 5.32. Preparation of clay cores used in the experiment. Opalinus Clay cores from Mont Terri (left) and bentonite cores (right).

Table 5.6. Core samples used for the experiments and heating durations.

		0 month	1 month	3 months	6 months (in progress)
Bentonite	Distilled Water	GEO-DW- 1, 3, 6 PRM-DW-1 S&I-DW-1	GEO-DW-2, 4, 5 PRM-DW-2 S&I-DW-2	GEO-DW-7, 8, 9 PRM-DW-3 S&I-DW-3	GEO-DW-10, 11 PRM-DW-4 S&I-DW-4
	0.5 M KCl aq.	GEO-KCL-1, 2, 3 PRM-KCL-1 S&I-KCL-1	GEO-KCL-4, 5, 6 PRM-KCL-2 S&I-KCL-2	GEO-KCL-7, 8, 9 PRM-KCL-3 S&I-KCL-3	GEO-KCL-10, 11 PRM-KCL-4 S&I-KCL-4
Mont Terri		GEO-MT-6, 13, 16 S&I-MT-16		GEO-MT-5, 20, 21 S&I-MT-20	

NOTE: DW and KCL cores indicate compacted bentonite cores. MT indicates Opalinus Clay (from Mont Terri) cores.

When the samples were examined after heating, however, slow, gradual decreases in the sample weight and water content were noticed (Table 5.7). This may be attributed to progressive degradation of the vessel seals, as indicated by accelerated loss of water in 3 months compared to 1 month (Figure 5.33).

Table 5.7. Sample weight, density, and water content changes in geomechanical test cores.

Sample	Heating Duration	Before-Heating weight and density	After-Heating weight	% lost weight
DW-2	1 month	9.23 g (1.92 g/cm^3)	9.16 g (1.91 g/cm^3)	0.68 %
DW-4		9.21 g (1.97 g/cm^3)	9.11 g (1.96 g/cm^3)	1.1 %
DW-5		9.22 g (1.92 g/cm^3)	9.13 g (1.92 g/cm^3)	1.1 %
DW-6	3 months	9.15 g (1.93 g/cm^3)	8.44 g (1.90 g/cm^3)	7.8 %
DW-7		9.20 g (1.95 g/cm^3)	8.41 g (1.91 g/cm^3)	8.6 %
DW-8		9.22 g (1.93 g/cm^3)	8.41 g (1.99 g/cm^3)	8.8 %
KCL-4	1 month	9.23 g (1.95 g/cm^3)	9.11 g (1.94 g/cm^3)	1.3 %
KCL-5		9.26 g (1.94 g/cm^3)	9.13 g (1.94 g/cm^3)	1.4 %
KCL-6		9.26 g (1.94 g/cm^3)	9.13 g (1.93 g/cm^3)	1.4 %
KCL-7	3 months	9.25 g (1.95 g/cm^3)	8.61 g (1.95 g/cm^3)	6.9 %
KCL-8		9.25 g (1.97 g/cm^3)	8.60 g (1.96 g/cm^3)	7.0 %
KCL-9		9.26 g (1.96 g/cm^3)	8.62 g (1.95 g/cm^3)	6.9 %

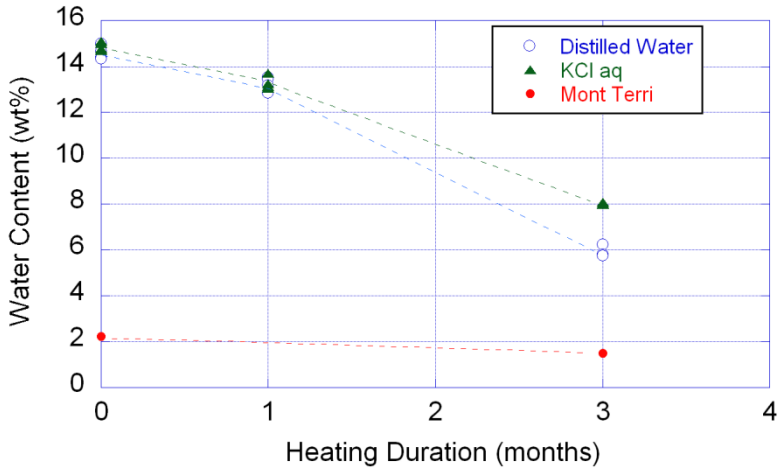

Figure 5.33. Decreases in the water content of the compacted bentonite core samples.

5.3.2 Ultrasonic velocity measurements

Ultrasonic velocity measurements were conducted on short, pill or "hockey-puck" shaped S&I samples (0.25"–0.5" in thickness). Both P-wave transducers (Panametrics, source central frequency 500 kHz) and S-wave transducers (1 MHz) were transmitted through the samples while a small load was applied through thin lead foils to improve mechanical coupling across the interfaces (Figure 5.34).

With increasing heating duration, both P and S-wave velocities of all the samples increased (Figure 5.35), as did the amplitude of the waves (Figure 5.35a). Considering the small changes in the density of the samples during heating, the observed velocity increases were mostly caused by increases in elastic moduli.

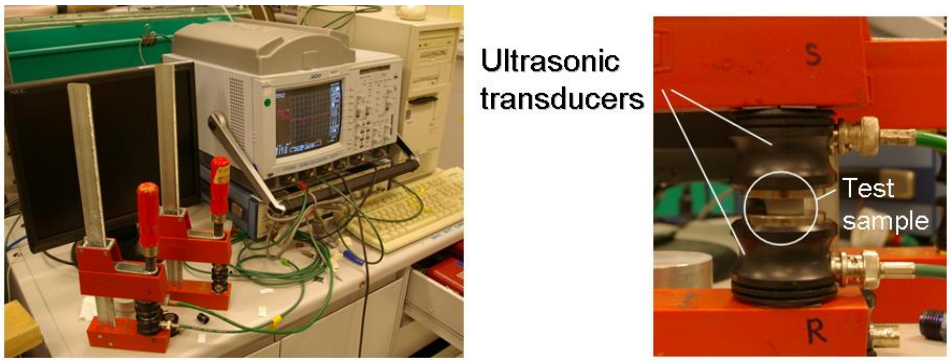

Figure 5.34. Ultrasonic velocity measurements on small clay cores. Minimal stress was applied to the surfaces through thin lead foils to establish good acoustic coupling.

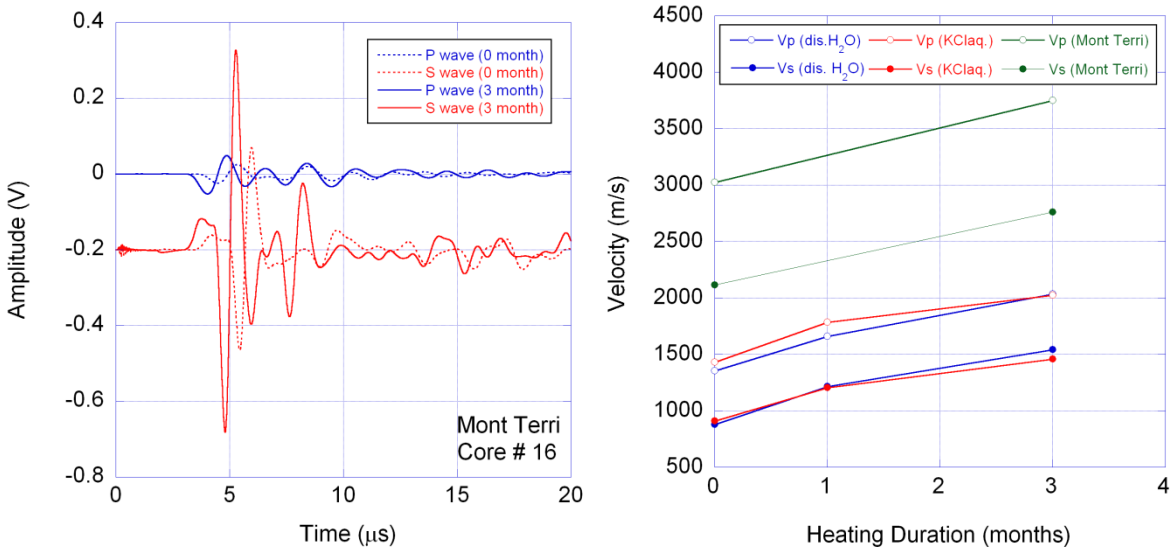

(a) (b)

Figure 5.35. An example of waveforms (a) and changes in the P and S-wave velocities (b) determined for the cores. Velocities of all the samples increased after heating.

5.3.3 Triaxial compression tests

Undrained triaxial compression tests were conducted on miniature cores with a diameter 0.56" and a length 1.1" (the length was slightly longer for the Mont Terri cores). A triaxial confining cell capable of quick exchanges of the samples between tests was built (Figure 5.36). Each sample was jacketed with a thick-walled latex tubing, and thin Teflon films were placed at the both ends of the sample to reduce the friction at the interfaces.

The tests were conducted at three different confining stresses of 10 psi, 100 psi, and 250 psi. Loading rate (strain rate) was ~3.0×10^{-5} s^{-1} for bentonite cores, and ~1.5×10^{-5} s^{-1} for Mont Terri cores. The reasons for the rather fast loading rates are the unsaturated condition of the samples and that our current focus is on the potential relative changes in the strength of heat-treated clays. The axial stress and displacement were monitored during the tests, and the dilation of the sample was determined from the volume of the fluid expelled from the confining cell and measured by a syringe pump (ISCO 500D pump).

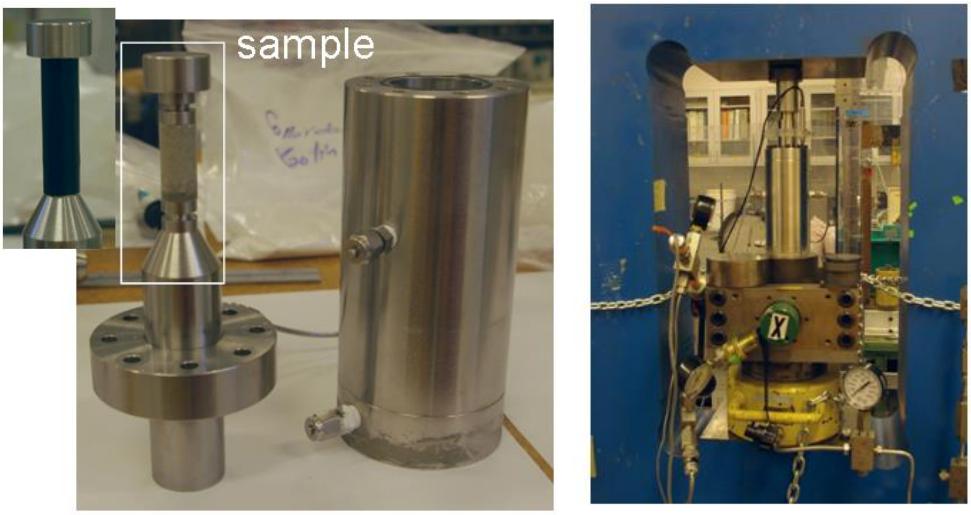

Figure 5.36. Triaxial compression tests on miniature core samples. The piston+jacketedsample assembly can be simply inserted in the confining cell through an o-ring, which does not require unbolting of the top vessel closure plate.

Both compacted bentonite and Mont Terri cores exhibited clear increases in the confined compressional strength (Table 5.8, Figures 5.37, 5.38). Brittleness of the samples also appeared to have increased somewhat, as seen from the more linear peak-failure load-displacement responses and the sudden drop in strength in the post-failure regime for the heated samples. Mohr's circles determined from the peak (failure) loads are also shown in Figure 5.39. Note that apart from the obvious increases in strength with increasing heating duration, the compacted bentonite samples showed no significant differences in strength (Figure 5.39a) or in the failure behavior (Figure 5.35) between the samples containing distilled-water and 0.5 M KCl solution.

Table 5.8. Undrained triaxial compression strength of clay samples.

Samples	Heating Duration	Confining Stress		
		10 psi	100 psi	250 psi
GEO-DW-6, 3, 1	0 month	1190.5 psi	1722.5 psi	2259.3 psi
GEO-KCL-1, 2, 3		1333.9 psi	1633.2 psi	2119.9 psi
GEO-DW-2, 4, 5	1 month	2278.9 psi	2898.7 psi	3392.0 psi
GEO-KCL-4, 5, 6		1994.4 psi	2956.8 psi	2967.0 psi
GEO-DW-7, 8, 9	3 months	3941.9 psi	5320.1 psi	5728.3 psi
GEO-KCL-7, 8, 9		4298.5 psi	5279.1 psi	5624.1 psi
MT-6, 13, 16	0 month	2213.1 psi	2957.9 psi	4093.6 psi
MT-5, 20, 21	3 months	6411.4 psi	7700.5 psi	8010.1 psi

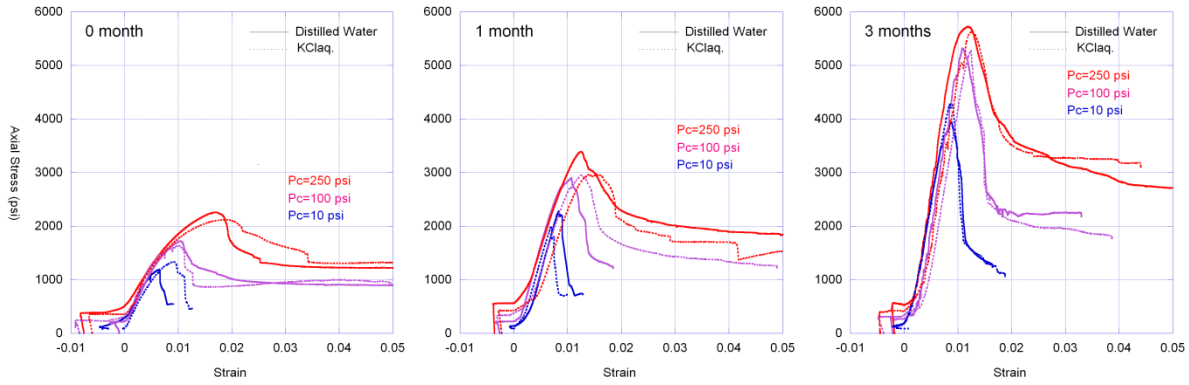

(a) No heating (b) Heated for 1 month (c) Heated for 3 months

Figure 5.37. Axial stress vs strain response of compacted bentonite samples. Solid lines indicate samples containing distilled water, and the broken lines indicate samples with 0.5 M KCl solution (Note that the concentration should have increased due to water loss). Increases in the heating duration resulted in higher compressional strength and more brittle behavior.

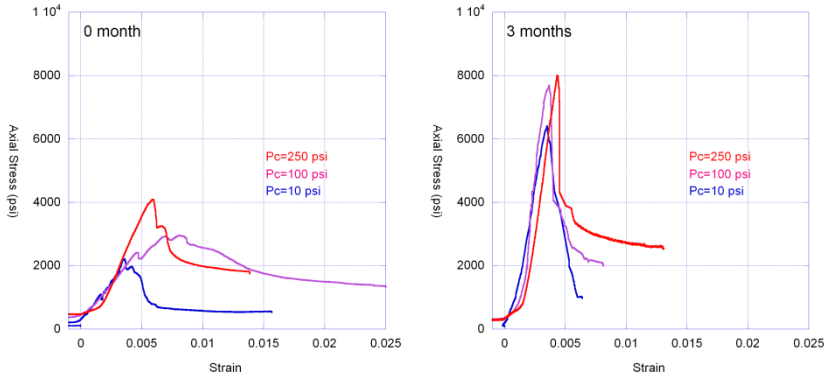

(a) No heating (b) Heated for 3 month

Figure 5.38. Axial stress vs strain response of Mont Terri core samples. Solid lines indicate samples containing distilled water, and the broken lines indicate samples with 0.5 M KCl solution (Note that the concentration should have increased due to water loss). Increases in the heating duration resulted in higher compressional strength and more brittle behavior.

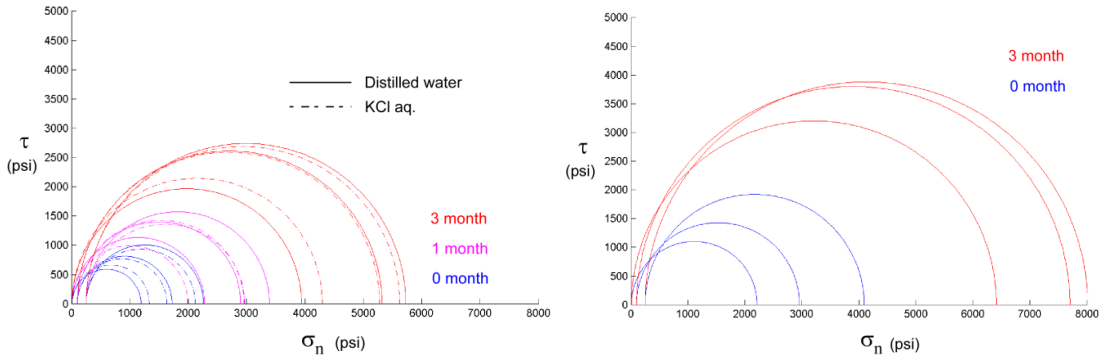

(a) Compacted bentonite cores (b) Mont Terri cores

Figure 5.39. Mohr's circles determined from the triaxial compression tests in Figures 5.37 and 5.38.

5.3.4 Development of a miniature indentation experiment setup and some preliminary results

Because only a limited number of samples can be produced for triaxial tests, the errors in the experimentally determined geomechanical parameters, such as the cohesion and friction angle of a Mohr-Coulomb envelope, can be significantly large. Although making direct links to such engineering parameters is not well established, as supplementary information, hardness and reduced Young's modulus determined from indentation tests can be used to investigate the effect of heating on the changes in the mechanical properties of clays.

We built a miniature/micro indentation test setup that applies controlled displacement to an indenter pushed onto the surface of clay samples to determine its hardness value (=force/area during indentation) and the reduced Young's modulus. Using this setup, a diamond-tipped conical indenter is driven using a piezo linear actuator (Polytech Nexline actuator N-216.2A) and an encoder (Polytech close-loop encoder E-755.1A1), and the resulting reaction force is recorded (Figure 5.40).

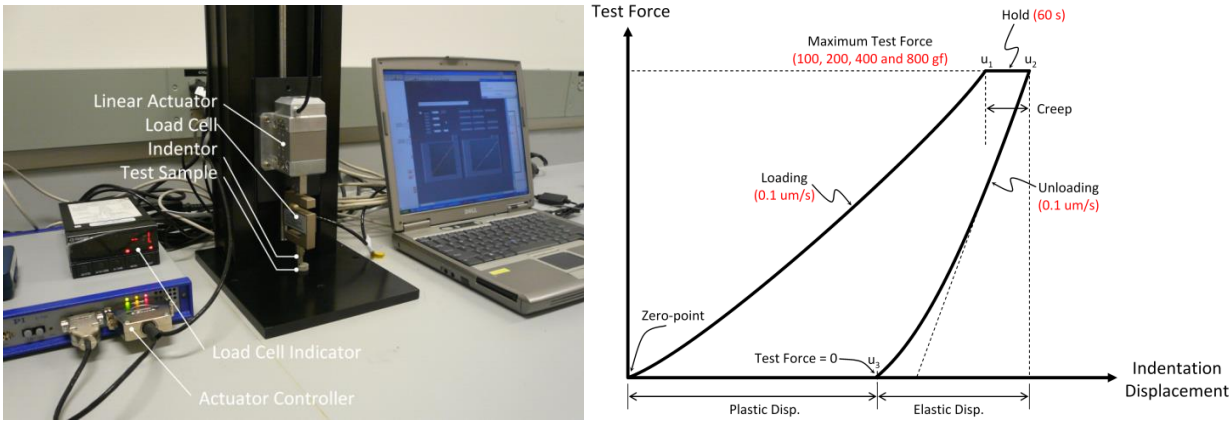

(a) Experimental setup (b) Loading protocol used in the experiment

Figure 5.40. Micro indentation experiment setup. Controlled displacement is applied to an indenter and the resulting force response is measured.

Once a series of indentations with a range of maximum forces are produced, the geometry of the depression ("crater") is determined using an optical surface profiler (Nanovea PS50) (Figure 5.41) and with image processing (Figure 5.42), which produces the area of depression used to compute the sample hardness.

Before the samples in the previous sections were made and the heating experiments were conducted, one sample of Mont Terri core was heated at 285ºC over 1 week, within one of the pressure vessels used in the experiments but without the silicon rubber gaskets. Although this resulted in severe desiccation of the sample, the result demonstrated promising performance of the new experimental system. Figure 5.43 shows a series of 2-D depression profiles (at the same gray scale for the depth) obtained from the same sample, before and after the heating experiment. The resulting hardness values are shown in Figure 5.44, as a function of the applied maximum loads. Although the results for the smallest load (250–500 gf) may not be reliable due to the noise, a series of measurements conducted over a range of loads can provide more consistent values as an average, indicating that heating increased the clay hardness to twice the original value.

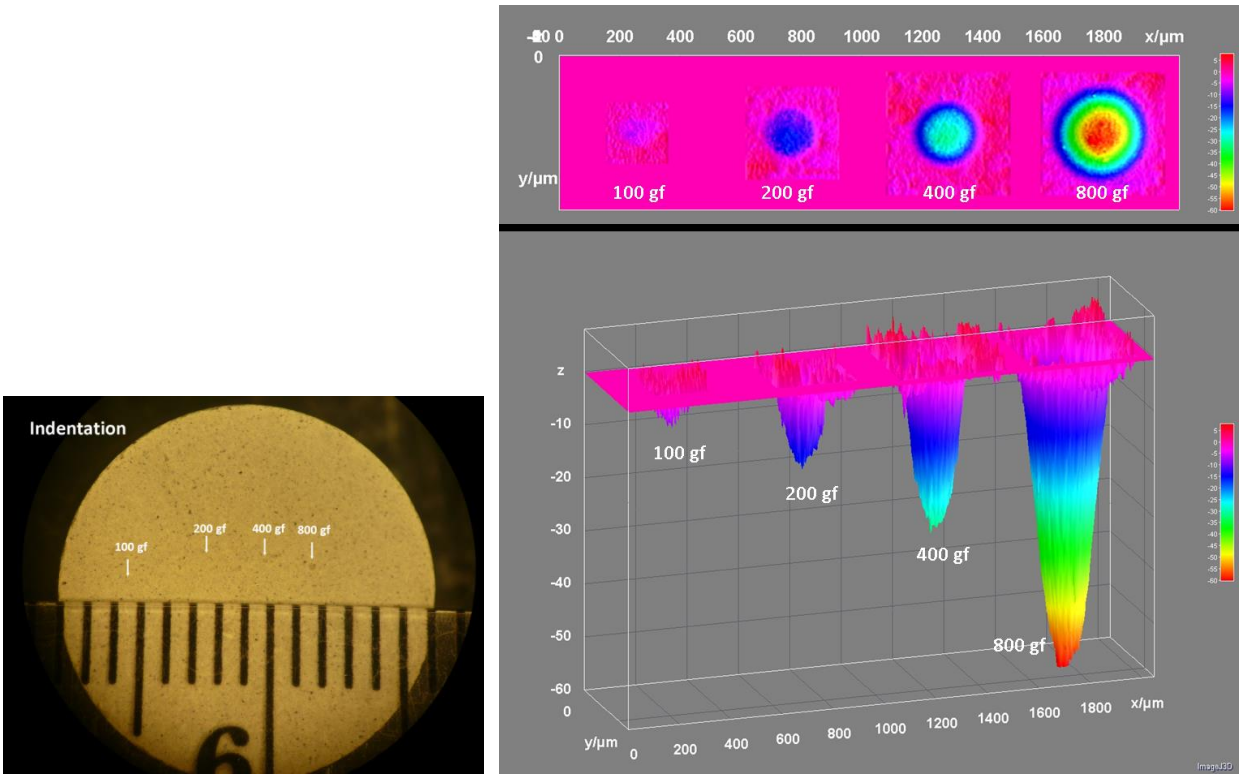

Figure 5.41. Indentations produced at different maximum forces on a compacted bentonite sample (contains distilled water. Density ~ 2.09 g/cm^3, water content ~15%wt).

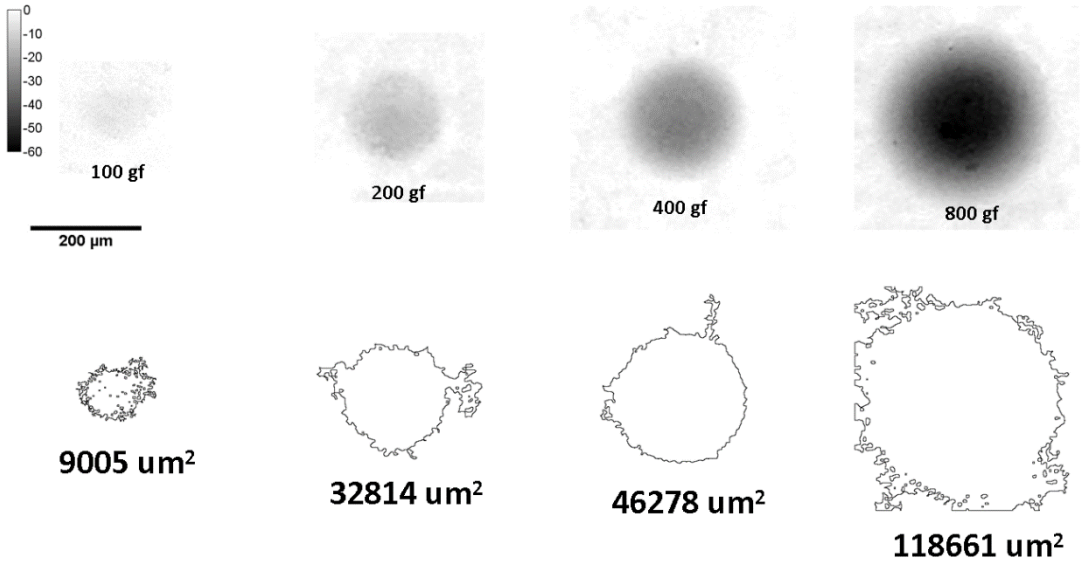

Figure 5.42. Indentations produced at different maximum forces on a compacted bentonite sample (contains distilled water. Density ~ 2.09 g/cm^3, water content ~15%wt).

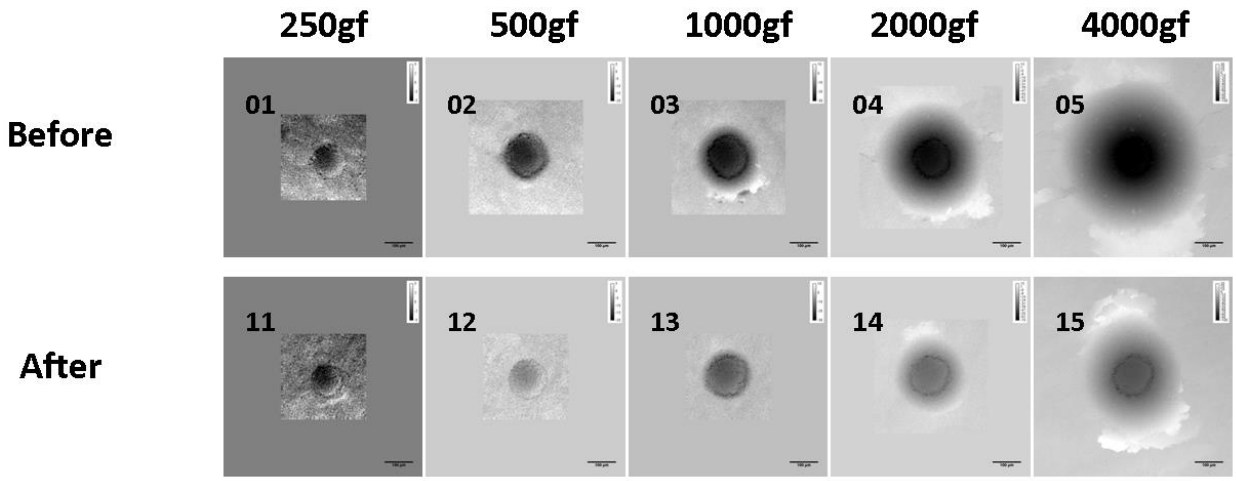

Figure 5.43. 2-D indentation profiles on a single sample of Mont Terri core before and after the sample was heated at 285ºC over 1 week.

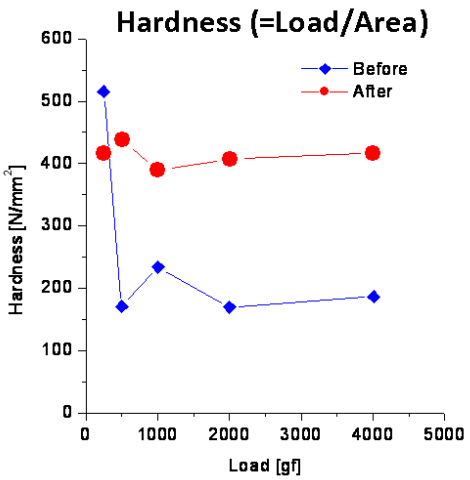

Figure 5.44. Hardness values determined from the area of indentation and the corresponding applied maximum force. The results indicate increases in the hardness of the sample due to the heating.

5.3.5 Summary and Future Work

It is highly likely that the observed heat-induced changes in the strength and failure behavior of the compacted bentonite and the Opalinus Clay from Mont Terri were caused by decreases of water content from the clay samples during heating. The effect, however, may also be superimposed by other effects such as redistribution (dissolution and re-precipitation) of quartz within the pore space and phase transformations of clay minerals. A summary of the accomplishments so far is as follows:

- Sample preparation procedures have been established and necessary tools developed.
- An efficient triaxial compression testing setup has been developed. The tests were conducted on compacted bentonite clay with different fluid chemistry and on Opalinus Clay cores from Mont Terri. However, the loss of fluid during heated resulted in ambiguities in the experimental results.
- A miniature indentation test setup has been developed. A sample hardness measurement procedure has been established and demonstrated.

Future work for the remaining months of FY14 and FY15 includes:

- Finding a solution for the slow leakage of water vapor from the pressure vessels used for heating of clay samples. Currently, use of soft metal foils (e.g., lead or tin [Sn] foils for unsaturated samples. Silver or gold if the sample is saturated.)
- Preparation of the clay samples and repeated experiments
- Chemical/mineralogical characterization of heat-treated samples. Interpretation of the results with the changes in the mechanical/hydrological properties.
- Improvement of mini indentation test setup. Currently, the reduced Young modulus of tested samples cannot be determined accurately because of large flexures in the loading column (particularly in the loadcell section). An additional displacement gage for determining the system deformation needs to be installed.

- Continued development of a gas permeability measurement setup for low-permeability clay samples. Current samples exhibit unusually high permeability which may be attributed to microcracks in the heated samples.

5.4 Discussion and Conclusions

5.4.1 Summary of current work

This study investigates the impact of strongly elevated temperature on the bentonite backfill and near-field clay host rock in a geologic repository for radioactive waste. We use coupled THMC modeling to evaluate the chemical alteration and associated mechanical changes in a generic repository and consider the interaction between EBS bentonite and the NS clay formation. Two main scenarios were developed for comparison: a "high T" case in which the temperature near the waste package reaches about 200°C, and a "low T" scenario in which the temperature peaks at about 100°C.

Our model results indicate the occurrence of some degree of illitization in the NS clay formation (as previously revealed by several earlier natural analogue studies), and also show that illitization occurs in the EBS bentonite. Other chemical alterations include the dissolution of K-feldspar and calcite, and the precipitation of quartz, chlorite, and kaolinite. In general, illitization in the bentonite and clay formation is enhanced at higher temperature. However, the quantity of illitization, expressed as the smectite volume fraction change, is affected by many chemical factors and subsequently varies a great deal, which could be the reason that illitization is not consistently observed in laboratory studies. The most important chemical factors are the concentration of K and dissolution rate of K-feldspar; less important are the concentration of Na and the quartz precipitation rate. Because of the differences in chemical properties, it is conceivable that the occurrence of illitization in different bentonite is different, which was manifested in current simulations for Kunigel-VI and FEBEX bentonite. For Kunigel bentonite, the decrease in smectite volume fraction in bentonite ranges from 0.004 to a maximum of 0.085, or up to about 27% of the initial volume fraction of smectite for the 200°C scenario. For FEBEX bentonite, the decrease in smectite volume fraction in bentonite ranges from 0.01 to a maximum of 0.04 (7% of the initial amount). The smectite volume fraction in the clay formation decreases moderately in some cases, but in other cases it decreases as much as 0.035, fully depleting the initial smectite.

Higher temperature leads to much higher stress in the near field, caused by thermal pressurization in the low-permeability rock surrounding and connected to the emplacement tunnel. During this period of strong thermal stresses, smectite dissolution causes only minimal changes in the simulated total stress. Chemical changes, including changes in pore water ion concentration and smectite volume fraction, lead to a reduction in swelling stress. But such reduction seems to be more pronounced for Kunigel-VI bentonite than for FEBEX bentonite. For Kunigel-VI bentonite, a reduction in swelling stress is up to 16–18% for the base case, and a reduction of swelling stress up to 70% could be observed in an extreme case in which key chemical and mechanical parameters are tuned to maximize the possible swelling stress reduction and to represent the worst scenario. The results for Kunigel-VI bentonite seem to suggest that the swelling stress reduction could compromise the ability of EBS bentonite to provide mechanical support to the tunnel walls and to seal any fractures in the disturbed rock zone. However, for FEBEX bentonite, the base case shows only about 1.5% reduction in swelling stress and 3.6% reduction in swelling stress in the worst scenario, which is much less

than that for Kunigel-VI bentonite. The reasons are (1) FEBEX bentonite undergoes less degree of illitization; (2) FEBEX bentonite has higher swelling capacity so that the relative reduction in swelling stress is fairly small.

Chemical alteration and the subsequent changes in mechanical properties are among the determining factors for establishing the thermal limit of a repository with a clay-based EBS. A thermal limit of about 100°C is imposed unanimously in all disposal concepts throughout the world—without rigorous studies to back up the choice. THMC simulations were conducted in FY13 (Liu et al., 2013b) and FY14 to answer the question whether an argillite repository with bentonite EBS can sustain higher than 100°C. While further refinement of the THMC models is needed and laboratory studies are recommended, the modeling work in FY13 and FY14 leads to a tentative conclusion that an argillite repository with bentonite EBS could sustain higher than 100°C as far as illitization concerns, with the following reasons:

1. Despite illitization in the bentonite and clay formation is enhanced at higher temperature, such enhancement is fairly limited even at 200 °C due to other constrains of illitization such as the supply of K and Al.
2. Illitization causes only moderate decrease of swelling pressure and thus compromise insignificantly the functionality of EBS such sealing the gap. Although for the bentonite having low swelling capacity (e.g., Kunigel-VI bentonite), chemical changes could results relatively large reduction in swelling pressure in the worst scenario, for bentonite with high swelling capacity (e.g., FEBEX bentonite) chemical changes could only lead to about a few percent reduction of swelling pressure. Using bentonite with high swelling capacity could diminish the undesirable consequence (if there is any) of illitization.
3. Illitization in EBS could be suppressed by relatively easy engineering method such as increasing the concentration of Na in the pore water of bentonite.

For the laboratory investigations, it is highly likely that the observed heat-induced changes in the strength and failure behavior of the compacted bentonite and the Opalinus Clay from Mont Terri were caused by decreases in water content from the clay samples during heating. The effect, however, may also be superimposed by other effects, such as redistribution (dissolution and re-precipitation) of quartz within the pore space and phase transformations of clay minerals.

5.4.2 Reconciliation of the apparent differences regarding illitization

Illitization is one of the major considerations for determining the thermal limit for a clay repository. It is widely observed in geological systems (e.g., Pusch and Madsen, 1995) and recent modeling work also showed the occurrence of illitization in EBS bentonite and clay rock. However, this process has not been conclusively confirmed for EBS bentonite in either small-scale laboratory experiments or large-scale mockup and field tests. There are seemingly contradictory conclusions reached by geological data and models versus laboratory and field tests. For example, our model in this report shows the occurrence of illitization in Kunigel or FEBEX bentonite, whereas experimental studies at LANL under UFDC (Cheshire et al., 2014) show no illitization for Wyoming bentonite. In this section, we discuss plausible factors that contribute to such seeming controversy.

First, the reaction rate of illitization is very low, and most laboratory and field tests did not run long enough to detect the change. The Pytte's model (Pytte, 1982) and similar types of models (Elliott and Matisoff 1996; Cuadros and Linares, 1996) have been widely used to calculate the

illitization rate in geological formations. In these models, the time derivative of smectite loss is related to the concentration of potassium (or the ratio of potassium to sodium concentration) and smectite mass fraction, via a rate constant that is a function of temperature. Because it is hard to know the concentration of potassium over the course of geological time or the inhibition effect from other cations, Cuadros (2006) used an "effective" potassium concentration within the following equation to match the illitization versus depth data for variety of geological formations in U.S.:

$$-dS/dt = kK^{0.25}S^n \tag{5.3}$$

where the proportion of smectite, S, is a fraction and has no units, t is expressed in days, and K is the effective potassium concentration in M, and k is a rate constant in $M^{-0.25}$ $days^{-1}$. Cuadros and Linares (1996) excrementally determined the rate constant, which is about 5E-6 $M^{-0.25}$ $days^{-1}$ at 100 ^oC and 3.3E-5 $M^{-0.25}$ $days^{-1}$ at 200°C. Cuadros (2006) used effective potassium concentration rather than the actual potassium concentration in the pore water to take into account the completion of other cations with potassium for the interlayer space and other possible inhibition effects. Effective potassium concentration, K, ranges from 10^{-10} M to 10^{-24} M, which is calibrated from illitization versus depth data. Taking the maximum K, i.e., 10^{-10} M, the smectite mass fraction decreases at a rate of 0.0006%/year at 100°C and 0.0038%/year at 200°C, which means an experiment needs to run at 200°C for around 300 years to realize about 1% changes in smectite (the detection limit of X-ray diffraction (XRD)). The models reported here show that for Kunigel bentonite, smectite dissolves about 3.5% in 1000 years, and for FEBEX bentonite, smectite dissolves only about 1% in 1000 years, which is largely aligned with those rates calibrated against geological data. The time needed to see detectable changes in smectite is probably the primary reason why most laboratory and field tests, which typically last for weeks to couple years, did not show any occurrence of illitization.

Second, illitization is a complex process and impacted by other factors, which might retard or even prevent the occurrence of illitization. This point is thoroughly discussed in Cheshire et al. (2014) when they explained the absence of illitization in their experiment. Although illitization during diagenesis is clearly evidenced by geological data, the reaction pathways are still a matter of debate (Wersin et al., 2007). In general, it is believed that the process starts with K-montmorillonite and then is followed by various stages of illite/smectite interlayer reaction**,** eventually ending up with discrete illite. The reaction mechanism could be via solid state transformation or dissolution-precipitation, depending on the water/rock ratio, fluid composition, redox state, or occurrence of microbial organism. Several factors could prevent the occurrence of illitization:

(1) The supply of K might be limited, which basically shuts down illitization. This is probably the reason why illitization was not observed in some field tests (Pacovsky et al., 2005; Pusch et al., 2010) in which K was not deliberately supplied.

(2) Illitization could be prevented by the presence of high contents of Na, Ca, and Mg, especially Na, in a water-bentonite system. It has been shown in several studies that a low supply of K with high Na activity significantly lowers the illitization rate (e.g. Roberson and Lahann 1981; Mosser-Ruck et al., 1999). As pointed out by Cheshire et al. (2014), in their system, even though high K concentration in aqueous solution is used in the experiment, the overall bentonite-water system is still Na-rich, which explains why in some experiments (Mosser-Ruck and Cathelineau 2004; Cheshire et al., 2014) using high

K solution does not necessary produce illite from Na-bentonite. Also, Liu et al. (2013b) showed that if bentonite blocks are fabricated with high Na solution, the illitization is dramatically inhibited.

(3) Over the course of transforming smectite to illite, excess silicate is produced and eventually precipitates out as quartz, which has two implications. One is that high silicate concentration in the system retards illitization, as shown by several studies (Eberl 1978; Abercrombie et al. 1994). Quartz has high solubility at high temperature, which allows more silicate to remain in the aqueous solution and therefore retard illitization. This is probably a negative effect of temperature on illitization. The other is that the precipitation rate of quartz becomes a bottleneck for illitization; the precipitation rate is known to be very low.

(4) The availability of Al also interferes with illitization. Illite and smectite are both dioctahedral phyllosilicates. What make them differ so much in physical properties is the interlayer charge and cation. Smectite has a low interlayer charge, such that Al is needed to substitute silicates in the tetrahedral layer to increase the interlayer charge as a precursor of forming illite. However, Al is involved in many minerals, and therefore the availability of Al for illitization faces competition from other minerals, which could inhibit the formation of illite.

5.5 Future Work

While the modeling exercise improves our understanding of the coupled processes contributing to chemical and mechanical alteration in EBS bentonite and NS argillite formation, our results should be taken cautiously, because of the limitations/assumptions in the model. These limitations and model refinements that could be conducted to overcome these limitations in the remaining month of FY14 and FY15 are as follows:

- First, illitization is simulated as a dissolution-precipitation process, i.e., the dissolution of smectite and neo-formation of illite, with the illitization rate calibrated against field data (Pusch and Madsen 1995). It is known that illitization could also occur through solid state transformation by substitution of intracrystal cations (e.g., Cuadros and Linares 1996), which is not considered in our model. Illitization through solid state transformation could be implemented in the model to evaluate the long-term illitization in the EBS bentonite and argillite.
- Second, since the mechanical-chemical coupling in bentonite is calculated via an extended linear elastic swelling model, a more rigorous approach to link chemistry to mechanics is needed for more accurate calculations. More comprehensive links between chemistry and mechanics taking advantage of the framework provided by a dual-structure model was implemented in TOUGHREACT-FLAC (Rutqvist et al., 2014), and could be used to simulate the chemical-mechanical coupling in EBS bentonite in the future.
- Third, the current mechanical model for the NS clay formation is not tied with chemical variables, i.e., mechanical-chemical coupling is only considered in the EBS bentonite. Constitutive relationship to link the chemistry with mechanics for clay formation needs to be developed and implemented in the THMC models.
- Fourth, in the current model, the canister serves only as a heat source; chemical changes on the surface of the canister are neglected for simplification. Further model analysis is

needed to consider chemical changes in the canister, specifically the release of Fe^{+2}, which might enhance the dissolution of smectite by forming chlorite.

For laboratory programs, future work needs to address the slow leakage of water vapor from the pressure vessels used for heating of clay samples. Currently, soft metal foils are used (e.g., lead or tin [Sn] foils for unsaturated samples; silver or gold if the sample is saturated). Better methods are needed for preparation of the clay samples, so that they can be reliably repeated. Chemical/mineralogical characterization of heat-treated samples is also needed for interpretation of the results regarding the changes in mechanical/hydrological properties. Regarding characterization, the mini-indentation test setup requires improvement. Currently, the reduced Young modulus of tested samples cannot be determined accurately because of large flexures in the loading column (particularly in the load cell section). An additional displacement gauge for determining the system deformation needs to be installed. Finally, development of a gas-permeability-measurement setup for low-permeability clay samples needs to be completed. Current samples exhibit unusually high permeability, which may be attributed to microcracks in the heated samples.

6. Transport in Clay and Clay Rock

6.1 Ion diffusion through clays

Clay minerals are high-surface-area lamellar aluminosilicates that possess a large capacity for retaining dissolved metal ions, which can be incorporated within interlayer spaces or adsorbed to external surfaces within the Electrical Double Layer (or EDL). However, metal ions associated with clay particles are not permanently sequestered, but may be mobile via diffusion. This task examines the role of the EDL in diffusion through clays, integrating microscopic characterization, molecular modeling, and mesoscale continuum models.

To date, we have developed two complementary approaches to modeling ion diffusion through clays, which are briefly summarized below. The first makes use of a Donnan Equilibrium or Mean Electrostatic Approach, in which a mean electrostatic potential is defined for the electrical double layer to balance the fixed negative charge of the clays. The volume of the EDL required for mass-balanced-based transport calculations is the product of the surface area of the clays and the width of the EDL, normally calculated as some multiple of the Debye length. Thus, the width of the EDL (and thus the volume) is a function of the ionic strength. The second approach involves the use of the Nernst-Planck and Poisson-Boltzmann equation (termed the Poisson-Nernst-Planck or PNP equation). In the PNP approach, the electrical potential as a function of distance from the charged clay surfaces is resolved. Both approaches predict that the electrical potential in the space between two clay layers does not decay to zero when the clay layers or interlamellae are closely spaced, and thus the water within the space does not have the same properties as "bulk water." The lack of electroneutrality in the clay interlamellae results in a swelling pressure that can now be quantified for the general multicomponent case (i.e., for systems that do not consist of a symmetric electrolyte).

6.2 Theoretical Background for Treatment of Electrostatic Effects

A rigorous model for the electrical double layer (EDL) can be derived from the combination of several equations, including the Poisson equation describing the distribution of electrical potential, ψ, in water:

$$\nabla^2\psi = -\frac{\rho_z}{\varepsilon}, \tag{6.1}$$

where ε is the permittivity and ρ_z is the volumetric charge density given by

$$\rho_z = e\sum_i z_i C_i. \tag{6.2}$$

In Equation (6.2), e is the elementary charge of the electron, z_i is the valence of the ion, and C_i is the concentration bulk solution. The Boltzmann distribution gives an expression for the concentration, $C_i^{EDL}(z)$, in the electrical double layer as a function of distance from the charge solid surface, z,

$$C_i^{EDL}(z) = C_i \exp\left(\frac{-z_i e\psi(z)}{k_B T}\right), \tag{6.3}$$

and where C_i is here the concentration in the bulk solution, k_B is the Boltzmann constant, and T is the absolute temperature. Combining Equation (6.3) with the Poisson equation (Equation 3.1) yields the Poisson-Boltzmann equation (Schoch et al., 2008):

$$\nabla^2\psi = \frac{-e}{\varepsilon}\sum_i z_i C_i \exp\left(\frac{-z_i e\psi(z)}{k_B T}\right) \tag{6.4}$$

which can be solved exactly for various simple formulations (e.g., the Gouy-Chapman model, which assumes a symmetric electrolyte).

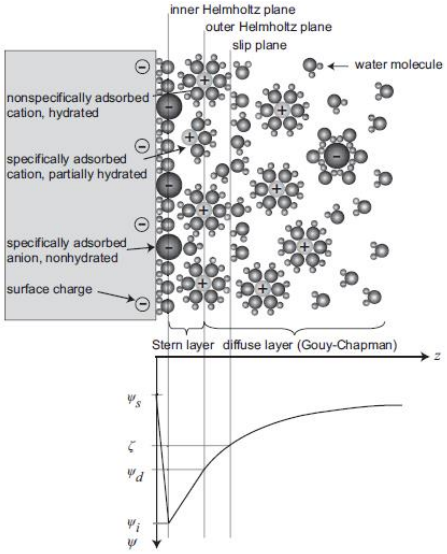

Figure 6.1. Schematic illustration of the Gouy-Chapman-Stern model of the solid-electrolyte interface, with the potential distribution $\psi(z)$ versus distance from the charged solid surface. The solid is illustrated with a negative surface potential ψ_s, described by three layers in solution. The inner Helmholtz plane layer ψ_i consists of nonhydrated co-ions and counterions (inner sphere complexes), whereas the outer Helmholtz plane layer ψ_d is built up of only hydrated counterions

(outer sphere complexes). The diffuse layer is defined beyond the outer Helmholtz plane (from Schoch et al., 2008).

6.2.1 Mean Electrostatic Approach

Integrating the Poisson-Boltzmann equation over nanometer length scales from charged mineral surfaces, however, was not practical in the present version of CrunchEDL, because of the desire to consider larger length scales. So an alternative approach is used, based on a Donnan Equilibrium model (Wersin et al., 2004; Leroy and Revil, 2004; Appelo and Wersin, 2007; Leroy et al., 2007; Appelo et al., 2008; Birgersson and Karnland, 2009; Tournassat and Appelo, 2011). The electrical double layer is conceptualized as consisting of two parallel layers of charge, one being the surface charge associated with direct sorption at the mineral surface (the Stern layer, typically divided into an inner and outer Helmholtz layer), and the other being the diffuse layer charge, a swarm of counterbalancing ions (Figure 6.1).

In the approach taken in CrunchEDL, the chemical potentials of the species in the diffuse layer and the bulk solution are equated. Writing equations for the chemical potentials of the species *i* in the bulk solution (or macroporosity) (superscript "B") and electrical double layer (superscript "EDL") respectively, we have

$$\begin{aligned} \mu_i^B &= \mu_i^{B,0} + k_B T \ln a_i^B \\ \mu_i^{EDL} &= \mu_i^{EDL,0} + k_B T \ln a_i^{EDL} + q_i \psi_m \end{aligned} \tag{6.5}$$

where the superscript *0* (first term on the right-hand side) refers to the chemical potential at the reference state, a_i are the species activities, q_i, is the charge of an ion (the elementary charge of a particle, *e*, multiplied by the valence of the ion, z_i), k_B is the Boltzmann constant, and ψ_m is the mean electrical potential in the electrical double layer. The condition of Donnan Equilibrium implies that

$$\begin{aligned} \mu_i^{EDL} &= \mu_i^B \\ \mu_i^{EDL,0} &= \mu_i^{B,0} \end{aligned} \tag{6.6}$$

Combining Equations (6.3), (6.5), and (6.6) and assuming that the activity coefficients for the diffuse layer and bulk solution are the same gives the Boltzmann distribution for the ion activities in the electrical double layer, C_i^{EDL}:

$$C_i^{EDL} = C_i^B \exp\left(\frac{-z_i e \psi_m}{k_B T} \right). \tag{6.7}$$

The diffuse layer charge balances the charge within the Stern layer, Q^{SL}, which may consist in CrunchEDL of either a fixed mineral charge due to vacancies in the mineral structure (as in the case of classical ion exchange), or of fixed mineral charge modified by inner sphere and outer sphere complexes developed within the Stern layer calculated with a surface complexation model:

$$\phi^{EDL} \sum_i z_i C_i^{EDL} = Q^{SL} \tag{6.8}$$

where ϕ^{DL} is the volume (or porosity) of the electrical double layer. The left-hand side of Equation (6.8) gives a volumetric charge density in units of charge equivalents per unit volume porous medium. The surface charge is given by

$$Q^{SL} = \sum_{k}^{Ns} z_k \Gamma_k \tag{6.9}$$

where Γ_k is the concentration in units of moles sorbed species per unit volume porous medium and z_k is the valence of the surface complex. In the CrunchEDL approach, therefore, one new equation is introduced (Equation 6.8), with one new unknown, the mean electrostatic potential of the diffuse layer, ψ_m. Note that in this formulation, the concentrations of the ions in the diffuse layer are dependent (or secondary) species that are calculated algebraically from the knowledge of the bulk solution composition and the mean electrostatic potential. A kinetic treatment of the diffuse layer ions would require that they be considered as primary unknowns.

Several approaches are available for calculating the fixed or Stern layer charge that is balanced by an electrical double layer. Even if the full Poisson-Boltzmann (PB) equation is used, special consideration needs to be given to the charge present in the Stern layer, a feature not always seen in the simpler implementations of the Poisson-Boltzmann equation. The starting point is the fixed mineral charge, which is normally given by the cation exchange capacity. If no Stern layer sorption occurred, the fixed mineral charge would provide a Dirichlet boundary condition for the electrostatic potential, ψ_f, at the solid surface:

$$\psi(0) = \psi_f \tag{6.10}$$

In the case of no Stern layer sorption, therefore, the PB equation can be integrated across the entire thickness *z* of the electrical double layer. In the case where the charged bentonite particles are bordered by bulk water, this would be the point in space where the local solution becomes electroneutral (where the electrostatic potential goes to zero). In the case of overlapping double layers, as considered by Goncalves et al. (2007) and Schoch et al. (2008), this would be the midpoint between the two charged clay (or solid) surfaces.

6.2.2 Dynamic Calculation of Electrical Double Layer Thickness

CrunchEDL also now includes a dynamic calculation of the electrical double layer porosity, ϕ^{EDL}, based on the diffuse layer thickness as a function of ionic strength according to

$$\phi^{EDL} = A_{clay} \lambda_{DL} D_L = A_{clay} \lambda_{DL} \frac{\beta_{DL}}{\sqrt{I}} \tag{6.11}$$

where D_L is the Debye length, λ_{DL} gives the multiples of the Debye length used in calculating the electrical double layer porosity (as in the approach of Tournassat and Appelo, 2011), β_{DL} is a temperature-dependent factor (= 2.15×10^{-10} meters at 25°C), I is the ionic strength of the bulk solution, and A_{clay} is the surface area of the charged mineral surfaces (normally clays). The Debye length provides an approximate measure of the width of the electrical double layer,

although in their Donnan or mean electrostatic model, Tournassat and Appelo (2011) included as many as five Debye lengths to describe the EDL porosity.

Previously, we have presented results in which the ionic strength is constant over the domain. It is also possible, however, to consider transient cases in which a salinity front propagates through the domain, changing the Debye length and thus the diffuse layer porosity dynamically. Note that in this case, the EDL thickness and thus the transport properties of the compacted bentonite are modified by the changing ionic strength. The effect is different from the swelling behavior described in Section 2, and may in fact work in the opposite way.

In the CrunchEDL approach in which solute mass is tracked in both the bulk porosity and the diffuse layer (EDL) porosity, this gives an accumulation term (neglecting liquid saturation) of

$$\frac{\partial\left[\phi^B C_i^B + \phi^{EDL} C_i^{EDL}\right]}{\partial t} = \frac{\partial\left[\phi^B C_i^B + \left(A_{clay}\lambda_{DL}\beta_{DL}\Big/\sqrt{I}\right) C_i^{EDL}\right]}{\partial t}. \tag{6.12}$$

In this case, the bulk porosity is treated as a constant, or at least as separately determined or fixed. Since the total porosity then can increase or decrease as the EDL thickness changes, special considerations need to be made to conserve mass in the system. Alternatively, it is preferred to treat the total porosity (bulk and EDL) as constant, in which case the bulk and EDL porosities would be updated according to:

$$\frac{\partial\left[\left(\phi^{Tot} - \phi^{EDL}\right) C_i^B + \phi^{EDL} C_i^{EDL}\right]}{\partial t} \tag{6.13}$$

where ϕ^{Tot} is the total porosity = $\phi^B + \phi^{EDL}$.

6.2.3 Modified Poisson-Nernst-Planck Equation for Ion Transport in Clays

The primary objective here is to develop improved models for the distribution of ions between the EDL and the Stern layer (inner and outer sphere sorption) on planar and edge sites in the clay. The novelty of the research is in the integration of a molecular modeling and characterization approach that quantifies the distribution and mobility of ions in the various domains (Stern layer, EDL, water film) and to use this, along with the transport experiments described below, to develop improved micro-continuum models for ion distributions and mobility in clays. The micro-continuum model will be based on a modified Poisson-Boltzmann description of the electrical double layer (EDL) within the context of a multicomponent reactive transport code that accounts for Nernst-Planck (electrochemical migration) effects. In the PNP equation, the Poisson-Boltzmann equation (Equation 6.4) is combined with the Nernst-Planck equation given by:

$$J_i = -D_i \nabla C_i - \frac{z_i F}{RT} D_i C_i \nabla \psi \tag{6.14}$$

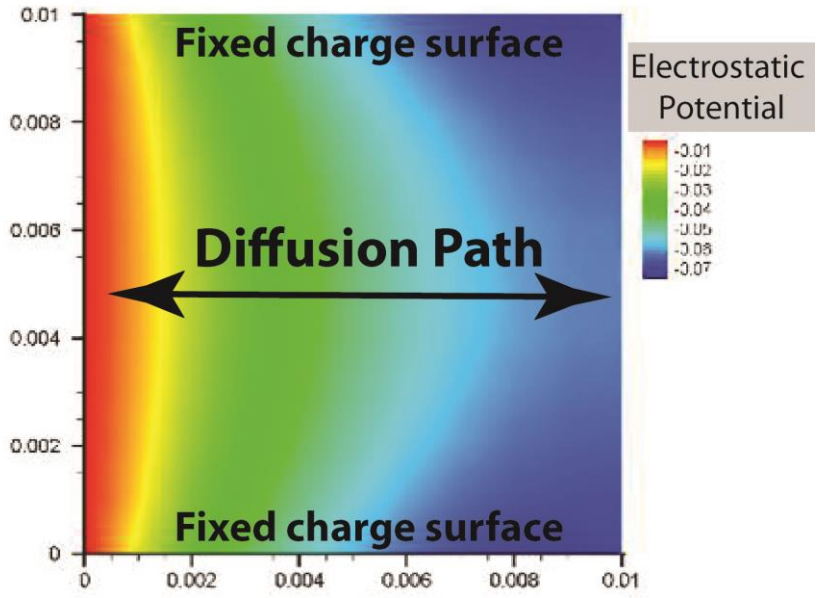

Figure 6.2. Calculation of the electrostatic potential by solving the Poisson-Nernst-Planck equation with fixed potential (Dirichlet) boundary conditions of fixed charge (0.001 mV) at the top and bottom. The gradient in potential in the diffusion direction is due to the different diffusion rates of the charged ions. The axis scales are microns and the electrostatic potential is dimensionless ($F\psi / RT$).

Classical Poisson-Boltzmann treatments perform reasonably adequately for monovalent ions, but they cannot handle as well the interactions between divalent ions (resulting in ion pairing) or the steric effects associated with the finite size of the ions (Lee et al.2012). Recently, however, modified Poisson-Nernst-Planck (PNP) models have been proposed that address the steric effects, as well as the interactions between multivalent ions in asymmetric electrolyte solutions (Grochowski and Trylska 2007; Wang et al. 2013). One possible formulation has been proposed by Wang et al. (2013) that accounts for steric and other thermodynamic (excess free energy) effects:

$$J_i = -D_i \nabla C_i - \frac{z_i F}{RT} D_i C_i \nabla \psi - D_i C_i \nabla \ln \gamma_i \tag{6.15}$$

where γ_i are the activity coefficients for the ith species. This is a general formulation that could be used to account for any excess free energy term, derived as it is from the chemical potential. Wang et al. (2013) proposed a form that accounted for steric (ion size) effects, suggesting an activity coefficient given by:

$$\gamma_i = \frac{1}{1 - \sum_i^N \frac{C_i}{C_{i,\max}}} \tag{6.16}$$

where $C_{i,max}$ is defined by the maximum concentration attainable with closest packing of the ions:

$$C_{i,\max} = \frac{1}{N_A a_i^3} \tag{6.17}$$

in which a_i is the diameter of the ion and N_A is Avogadro's number. Wang et al. (2013) have successfully compared their modified PNP model against results from cyclic voltammetry for a range of electrolyte compositions.

6.3 Benchmarking of CrunchEDL versus PHREEQC

In this section, we present the results of some preliminary benchmarking of CrunchEDL against PHREEQC, each using the Donnan or Mean Electrostatic approach. We have devised a simple test problem in which the system is comprised of both EDL and bulk water porosity (or macroporosity). The boundary conditions at both ends of this 1D system are no-flux, but diffusive transport can occur within the domain and between the two types of porosity. Two cases are considered: (1) Case 1, in which the properties of Porous Media 1 and 2 are the same; and (2) Case 2, in which the charge in EDL 1 is decreased relative to EDL 2 by a factor of 100. The total system length is 10 cm with porous media 1 and 2 having the same length (5 cm). Concentration profiles are monitored as a function of time for the numerical cells from both side of the interface and for the cells being centered on the positions at 4.5 cm and 5.5 cm.

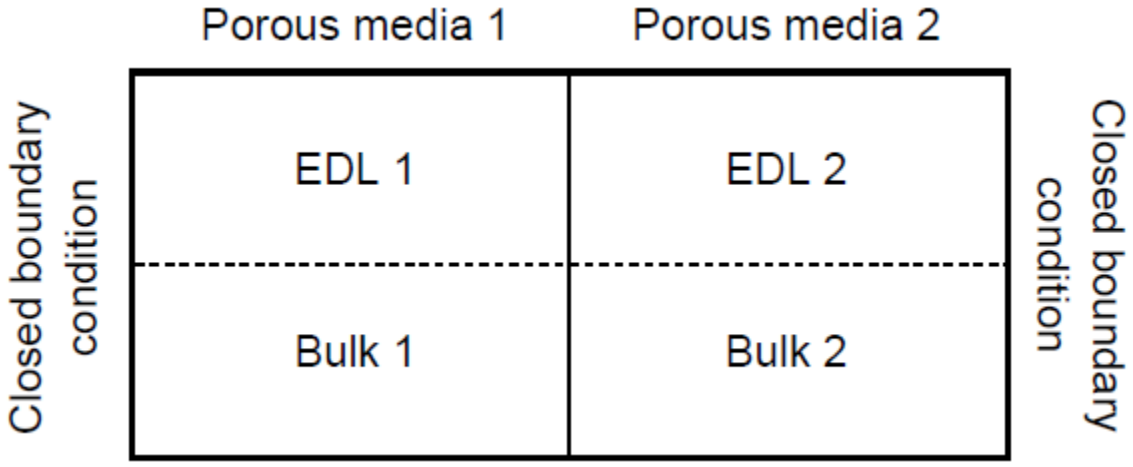

Figure 6.3. Schematic diagram of model system used for benchmark.

The volume (or porosity) of the EDL is the same as the volume of the bulk water. The initial solution composition in the bulk water is NaCl 0.01 mol kg-1 in porous media 1 and 2 (no salinity gradient, no activity coefficients gradient in bulk water), tracer A (Ac^+ and Aa^-) 10^{-6} mol kg^{-1} in bulk water of porous media 1 and 10^{-7} mol kg-1 in bulk water of porous media 2. The concentration gradient is opposite for tracer B (Bc^+ and Ba^-). Tracers Ac^+ and Bc^+ have the same chemical and transport parameters as Na^+. Tracers Aa- and Ba- have the same chemical and transport parameters as Cl^-.

6.3.1 Case 1: EDL charge the same in compartments 1 and 2

The EDL charge is -0.333 mol kg^{-1} in porous media 1 and 2. PHREEQC and CrunchEDL results are in perfect agreement (at least 3 digits) for the EDL mean composition (Table 6.1). Concentration gradients in the EDLs are in the same direction as in the bulk water. The diffusion coefficient was set to 10^{-9} m^2 s^{-1} for all species in bulk and in EDL water. PHREEQC and CrunchEDL results are consistent for a given grid refinement. A grid with 50 cells seems to be sufficient to ensure good calculation accuracy.

Table 6.1. Case 1. Comparison of mean concentrations in the EDL of the two porous media according to PHREEQC and CrunchEDL initial equilibrium calculations.

	Concentrations in EDL (mol kg^{-1}) Porous Media 1		Concentrations in EDL (mol kg^{-1}) Porous Media 2	
	PHREEQC	CRUNCH	PHREEQC	CRUNCH
Na^+	$3.336\ 10^{-1}$	$3.336\ 10^{-1}$	$3.336\ 10^{-1}$	$3.336\ 10^{-1}$
Cl^-	$2.998\ 10^{-4}$	$2.998\ 10^{-4}$	$2.998\ 10^{-4}$	$2.998\ 10^{-4}$
Ac^+	$3.336\ 10^{-5}$	$3.336\ 10^{-5}$	$3.336\ 10^{-6}$	$3.336\ 10^{-6}$
Ac^-	$2.998\ 10^{-8}$	$2.998\ 10^{-8}$	$2.998\ 10^{-9}$	$2.998\ 10^{-9}$
Bc^+	$3.336\ 10^{-6}$	$3.336\ 10^{-6}$	$3.336\ 10^{-5}$	$3.336\ 10^{-5}$
Bc^-	$2.998\ 10^{-9}$	$2.998\ 10^{-9}$	$2.998\ 10^{-8}$	$2.998\ 10^{-8}$

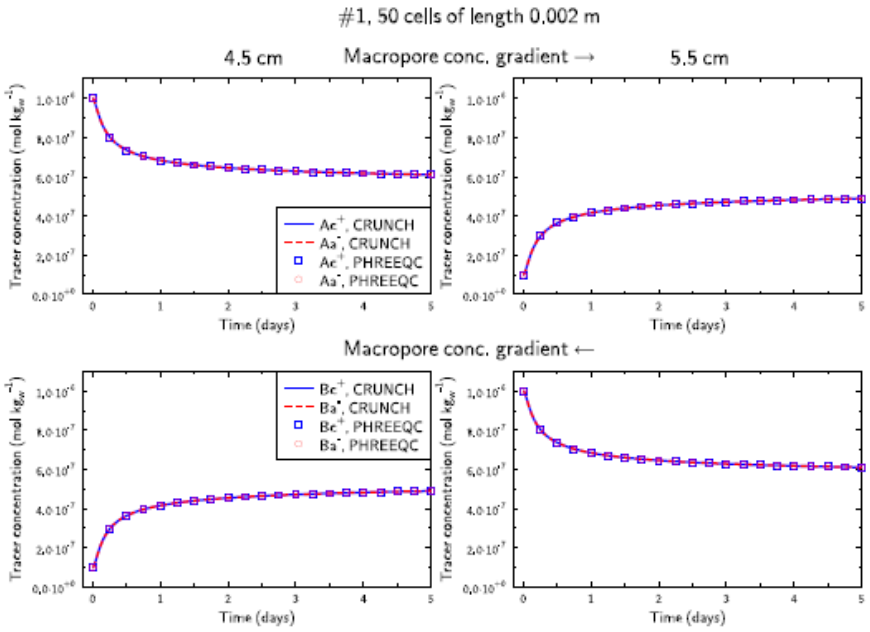

Figure 6.4. Comparison of bulk water (macropore) concentrations at 4.5 and 5.5 cm for Case 1 in which the two porous media have the same EDL charge of -0.333 equivalent moles/kgw.

6.3.2 Case 2: EDL charge different in porous media 1 and 2

This simulation is the same as the Case 1 simulation, except that the charge in the EDL of the porous media 1 is decreased by two orders of magnitude: -0.00333 mol kg-1. The agreement between CrunchEDL and PHREEQC for the initial calculation of the composition of the EDL is

perfect again (Table 6.2). In this configuration, we can see now that the concentration gradients in the EDL are different from the concentration gradients in the bulk solution: Ac+ is less enriched is the EDL of porous media 1 due to the decrease of the EDL electrostatic potential, and its concentration is now lower in the EDL of porous media 1 than in the EDL of porous media 2 despite the lower bulk concentration in porous media 2 (Table 6.2). In other words, the Ac+ concentration gradient in the EDL is opposite to the chemical potential gradient. All other tracers EDL concentration gradients remain of the same sign as their related chemical potential gradients.

PHREEQC and CrunchEDL predict the same trends of concentrations evolutions: tracer Ac+ is depleted more rapidly from porous media 1 than previously in case 1 where there were uniform EDL properties along the system. Anionic and cationic tracers now behave differently. With a 50-cell grid refinement, CrunchEDL and PHREEC results exhibit significant differences in concentration prediction as a function of time. Those discrepancies can be lowered by increasing the number of cells in the CrunchEDL calculation grid, but those discrepancies cannot be eliminated even by refining the grid to 0.1 mm cells. A grid where only the cells at the interface are refined (40 cells of 0.1 mm) provides results as good as the 1000-cell grid.

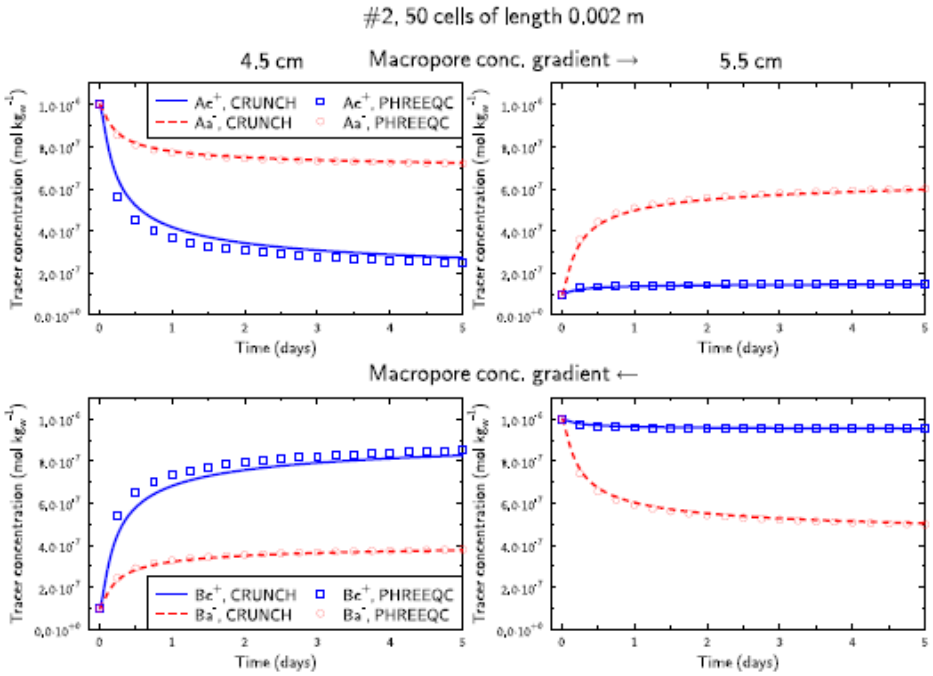

Figure 6.5. Comparison of bulk water (macropore) concentrations at 4.5 and 5.5 cm for Case 2 in which porous media 1 has an EDL charge 100 times lower than in porous media.

In addition, it can be shown that the mass balance is nearly exact in the case of PHREEQC, while CrunchEDL shows a mass imbalance in this case (unlike Case 1). The explanation is that CrunchEDL currently neglects the longitudinal gradient in the mean electrostatic potential, despite the fact that it contributes to the overall chemical potential. In the present implementation in CrunchEDL, the gradient in the electrostatic potential only accounts for the "diffusion potential" due to the diffusion of the charged ions at different rates, and not to any gradients in the electrostatic potential due to the clay charge concentration. In other words, all contributions

to the electrostatic potential need to be included in the Nernst-Planck equation (Equation (6.14)). The fix for this will be completed soon.

Table 6.2. Case 2 in which the charge in porous media 1 is 100 times lower than in 2.

	Concentrations in EDL (mol kg^{-1}) Porous Media 1		Concentrations in EDL (mol kg^{-1}) Porous Media 2	
	PHREEQC	CRUNCH	PHREEQC	CRUNCH
Na^+	$1.180\ 10^{-2}$	$1.180\ 10^{-2}$	$3.336\ 10^{-1}$	$3.336\ 10^{-1}$
Cl^-	$8.471\ 10^{-3}$	$8.472\ 10^{-3}$	$2.998\ 10^{-4}$	$2.998\ 10^{-4}$
Ac^+	$1.180\ 10^{-6}$	$1.180\ 10^{-6}$	$3.336\ 10^{-6}$	$3.336\ 10^{-6}$
Ac^-	$8.471\ 10^{-7}$	$8.471\ 10^{-7}$	$2.998\ 10^{-9}$	$2.998\ 10^{-9}$
Bc^+	$1.180\ 10^{-7}$	$1.180\ 10^{-7}$	$3.336\ 10^{-5}$	$3.336\ 10^{-5}$
Bc^-	$8.471\ 10^{-8}$	$8.471\ 10^{-8}$	$2.998\ 10^{-8}$	$2.998\ 10^{-8}$
	Concentrations in bulk water (mol kg^{-1})		Concentrations in bulk water (mol kg^{-1})	
Ac^+	10^{-6}	10^{-6}	10^{-7}	10^{-7}
Ac^-	10^{-6}	10^{-6}	10^{-7}	10^{-7}
Bc^+	10^{-7}	10^{-7}	10^{-6}	10^{-6}
Bc^-	10^{-7}	10^{-7}	10^{-6}	10^{-6}

6.4 Application to the DR-A Diffusion Test at Mont Terri, Switzerland

To test the EDL transport model developed and described here, we have used it to simulate nonreactive and reactive transport processes in the DR-A experiment at Mont Terri in Switzerland. The Mont Terri site consists of Opalinus Clay, a primarily marly claystone with differing proportions of sand and carbonates, and is about 180 million years old. The stratigraphic section in which the Mont Terri site is located is shown in Figure 6.6. The Opalinus Clay is characterized by very low permeability, which makes diffusion the dominant mode of solute transport (in this respect, similar to compacted bentonite under normal conditions).

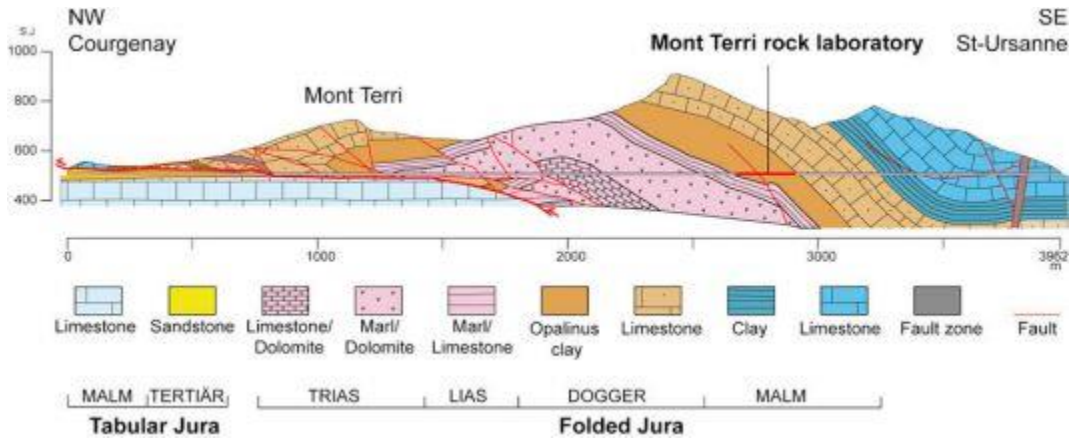

Figure 6.6. Stratigraphic section of the Jura Mountains in which the Mont Terri rock laboratory is located.

The DR-A test has consisted of a single borehole drilled in the Opalinus Clay that contains a constant ionic strength cocktail and anions, cations, and nonreactive tracers like tritium (HTO). Figure 6.7 shows the location of the DR-A niche in map view. Figure 6.8 shows the experimental

setup used for the earlier DI-A test at Mont Terri, similar in setup to what has been used for the DR-A test. A volume of cocktail in excess of the actual cylindrical volume of the borehole is used as reservoir. This is treated in CrunchEDL by defining a capacity factor, α (= 2.175), that represents the additional volume needed to accommodate the extra solution volume (11.2 L) available to the actual borehole volume (Figure 6.8). In the first stage through Day 189, the borehole cocktail is a 0.384 M ionic strength solution dominated by sodium (Table 6.4). At Day 189, a higher ionic strength solution (1.135M) was circulated in the borehole apparently without diluting the tracers (HTO, iodine, and bromine) in the cocktail. The higher ionic strength was made up of both Na^+ (0.50M) and K^+ (0.56M) and Cl^- (1.13M) and was allowed to diffuse out of the borehole through Day 412.

6.4.1 CrunchEDL Simulation of DR-A Test

6.4.1.1 DR-A Simulation Parameters

In the simulations, a total porosity of 0.15 was assumed for the Opalinus Clay. The total porosity was treated as fixed, with partitioning between the "bulk" and "EDL" porosities governed by the Debye length (determined by the ionic strength, and thus variable over the course of the 412 day experiment). The additional volume needed to accommodate the extra solution volume (11.2L) available to the actual borehole volume (Table 6.3) was treated in CrunchEDL by defining a capacity factor, α (= 2.175).

For the simulation, a preliminary estimate of the illite specific surface area (200 m^2/g) and volume fraction (0.25) was made for the Opalinus Clay, which is the material expected to provide most of the retardation. A fixed mineral charge of 200 μequivalents/g illite was assumed, all of which is compensated by the electrical double layer (i.e., no Stern Layer sorption was allowed). Cylindrical coordinates were used in the simulations, with the assumption that the system was axisymmetric—thus, the system is modeled in a 1D plane.

A high value for the diffusion coefficient of solutes in the filter has been used to avoid a limitation on the rate of loss from the borehole due to this material. A diffusion coefficient of 2.7×10^{-10} m^2/s was initially assumed for all of the species in the Opalinus Clay, with the exception of the anions, for which a value of 1.25×10^{-10} m^2/s was used. As an initial test, the same values for the diffusion coefficients were used in the bulk and EDL porosity, although this assumption will be relaxed in later simulations so as to optimize the fit to the ionic strength effect.

Table 6.3. Physical parameters for DR-A test.

Length of injection interval	104 cm
Length of filter screen	67 cm
Volume of circulation system	11.2 L
Borehole diameter	76 mm
Filter, outer diameter	70 mm
Filter, inner diameter	62 mm
Filter, porosity	45%
Gap between filter and borehole wall	3 mm
Central tube, outer diameter	61 mm
Dip of bedding	32.5º
Porosity of Opalinus Clay	15%

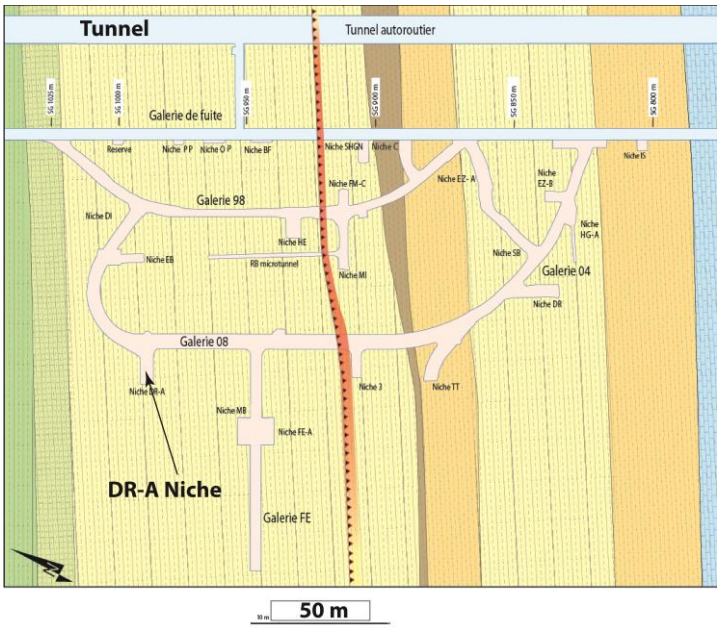

Figure 6.7. Plan view of the Mont Terri site showing location of DR-A niche.

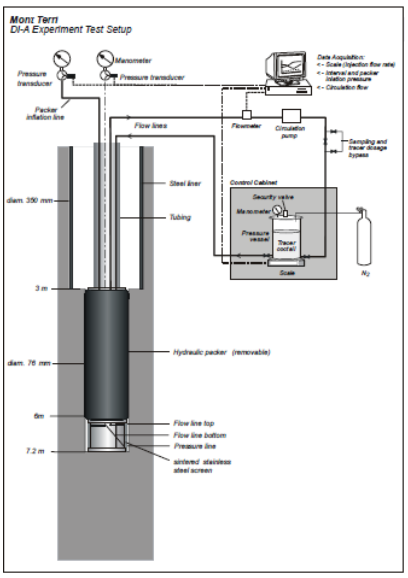

Figure 6.8. Schematic of the experimental setup from the DI-A test, similar in concept to the DR-A test.

Table 6.4. Geochemistry of borehole solution, with higher ionic strength used 189-413 days.

Species (Total)	0-189 Days	189-413 Days
	(M)	(M)
Ionic Strength	0.384	1.135
pH	4.16	7.60
Ca^{2+}	0.0188	0.0230
Mg^{2+}	0.0180	0.0147
Na^{+}	0.259	0.500
K^{+}	0.0016	0.560
Cl^{-}	0.300	1.113
SO_4^{2-}	0.0137	0.00024
HCO_3^{-}	0.00328	0.00050
Sr^{2+}	0.00051	0.00045
Cs^{+}	0.00027	0.0000062
I^{-}	0.0109	0.0109
Br^{-}	0.0109	0.0109
HTO	1.000	1.000

6.4.1.2 DR-A Simulation Results

Preliminary results from the simulations, including the increase in ionic strength in the borehole-reservoir system at Day 189, are shown in Figure 6.9. It should be noted that the anion (iodide and bromide) breakthrough data shows a slight increase in the rate of loss from the borehole starting about Day 189, the time when the ionic strength was increased. The simulation results show only a very small increase in the rate of loss from the borehole (solid line red for iodide), likely the result of the use of the same diffusion coefficients for the iodide and bromide in the EDL and bulk porosity. One expects that diffusion rates of anions in the EDL are smaller because of the greater tortuosity for the negatively ions versus the bulk fluid. Note that the data shows a stronger effect of the ionic strength, with the rate of loss from the hole increasing more dramatically for the anions at about Day 290. This effect is in keeping with a decrease in the thickness of the EDL, and thus an increase in bulk versus EDL porosity that follows from Equation (6.11). This is in contrast to some of the predictions based on swelling behavior alone that would have the effect of an increase in ionic strength reducing the bulk porosity. If the only effect of an increase in ionic strength were on the swelling behavior of the clays, then one would expect a less (not more) rapid loss of anions from the borehole. Here, the increase in diffusive loss of anions in particular from the borehole is attributed to the decrease in the EDL thickness, and thus to the increase in the proportion of bulk to EDL porosity. Properties of the Opalinus Clay considered in the simulation over time and predicted results are summarized in Table 6.5.

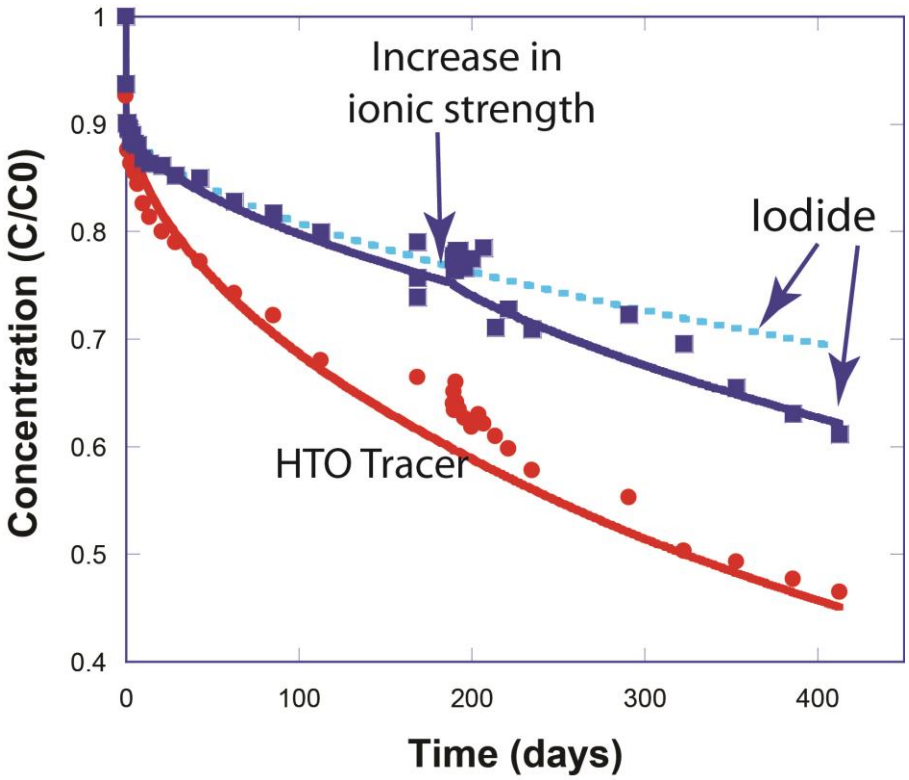

Figure 6.9. Data (symbols) versus simulation results (solid lines) for the DR-A test through Day 412. An increase in ionic strength (Na^+, K^+, and Cl^-) occurred at Day 189, which produces an increase in the rate of loss of the tracer anions iodide and bromide from the borehole. The pale blue dashed line represents the case for the anions where the EDL thickness and porosity is not affected by ionic strength.

Table 6.5. Opalinus Clay Properties and Simulation Results.

	0-189 Days	189-413 Days
Illite Specific Surface Area	200 m^2/g	200 m^2/g
Illite Volume Fraction	0.25	0.25
Fixed Charge of Illite	200 μeq/g	200 μeq/g
EDL Porosity (equilibrated w/ borehole)	0.076	0.049
Total charge in EDL (equivalents $/m^3$)	38.390	38.390
Na^+ Concentration in EDL (equilibrated)	0.253	0.661
K^+ Concentration in EDL (equilibrated)	0.0029	0.335
I^- Concentration in EDL (equilibrated)	0.0046	0.0049

7. Summary

(1) Development and validation of constitutive relationships for permeability, porosity and effective stress

The stress-dependent hydromechanical properties of low-permeability sedimentary rock are important for engineering. Accurate mathematical representations of stress-dependence of rock porosity and permeability are fundamental for studying the coupled hydromechanical processes of the underground rock, especially for understanding the evolution of permeability in EDZ for an argillite repository. In the work presented here, a new theoretical approach, a two-part Hooke's Model (TPHM), has been used. TPHM is based on the basic concept that the elastic deformation in a rock can be more accurately represented as a combination of two material types, a harder (or stiffer) material and a softer material. The small deformation approximation, used to linearize Hooke's law, is implemented exclusively for the harder (or stiffer) material type. Specific accomplishments are as follows:

- Existing stress-dependent formulations for porosity and permeability were reviewed, along with relationships between porosity and permeability.
- A series of rock stress-porosity and rock stress-permeability relationships based on the TPHM have been developed.
- Our preliminary evaluation of the model against published data produced encouraging results.

Recommended work for FY15 includes:

- Conduct testing of porosity and permeability as a function of effective stress to supplement the available published data.
- Use this data to perform additional validation analyses.
- Implement these constitutive relationships into our simulator TOUGHREACT-FLAC3D and conducted coupled processes simulation to evaluate the evolution of the hydromechanical properties in EDZ for an argillite repository.

(2) Discrete fracture network (DFN) approach for fractures in argillaceous rock

This study uses the RBSN approach to model geomechanical behavior including fracturing. The model provides a discrete representation of material elasticity and fracture development, and in that respect, it is considered to be suitable for the DFN approach to investigate fracturing processes. However, the original RBSN is limited to macroscopically modeling isotropic materials, or requires additional treatments in partitioning the domain (e.g., layering of individually isotropic materials) for introducing directivity of mechanical properties. Specific accomplishments are as follows:

- Linkage between TOUGH2 for simulating heat and mass transport and the RBSN method for simulating geomechanical responses, including the initiation and propagation of discrete fractures.
- Elastic spring coefficients and strength parameters have been systematically formulated for individual lattice elements, based on the principal bedding direction, which facilitate a straightforward representation of anisotropy.
- Uniaxial compression tests have been simulated for a transversely anisotropic material, the Opalinus Clay, to demonstrate the validity of the new modeling scheme.

- A simulation of fracture damage around the EDZ of the HG-A microtunnel has been conducted and has been found to qualitatively agree with the physical observations, in which nonuniform damage, due to the anisotropic mechanical characteristics, forms around the excavation wall.
- The capabilities of the TOUGH-RBSN simulator for strongly coupled hydro-mechanical processes have been shown through a simulation of hydraulic fracturing, which produces realistic hydromechanical behavior for the fracturing process.

Recommended work for FY15 includes:

- The original development of the RBSN model was mainly concerned with tensile failure. The model requires additional modifications to consider fracture surface forces that are important for compressive failure.
- Also, use of the Mohr-Coulomb fracture criterion involves brittle failure response. More realistic representation of failure response is needed for gradual degradation of strength parameters.
- Hydrological properties of discrete fractures will be estimated on the basis of the fracture geometry, so that quantitative simulations of flow and mass transport within discrete fracture networks can be conducted.
- Fracture nodes and the associated connections are defined for all the Voronoi cell boundaries from the beginning of simulations, which burdens the computational expense by increasing degrees of freedom to be calculated. The modeling scheme needs to be improved for dynamic introduction or event-based activation of the fracture components.
- A parallel version of TOUGH-RBSN is needed for computational efficiency to enable its use on larger field-scale 3-D problems.

(3) THM Modeling of Underground Heater Experiments:

The UFDC is utilizing previous experience and existing models (TOUGH-FLAC and ROCMAS) that are extended to predict the long-term THM and THMC evolution of a multibarrier nuclear waste repository system involving backfilled emplacement tunnels in argillite host formations. Specific accomplishments are as follows:

- Completed implementation of constitutive models for the coupled geomechanical behavior of bentonite-based buffer material, including most recently the advanced dual-structure model.
- Verification and testing of the implemented geomechanical constitutive models for bentonite-based buffer material by modeling laboratory experiments and long-term behavior of a generic repository.
- Validation of TOUGH-FLAC and characterization of THM properties for two types of bentonite-based buffer materials through modeling of CIEMAT laboratory column experiments.
- Development of full-scale 3D TOUGH-FLAC models of the Horonobe EBS experiment and Mont Terri FE experiment and initial model predictions of temperature and saturation evolutions.

- Benchmarking associated with the Horonobe EBS experiment achieving good agreement with the results of other international modeling teams, providing code-to-code verification of TOUGH-FLAC.

Published one journal paper (Rutqvist et al., 2014) on THM modeling of nuclear waste disposal in argillite and submitted one journal paper on the use of the dual-structure model for modeling long-term behavior of a nuclear waste repository (Vilarrasa et al., 2014). (((Recommended work for FY15 includes:

- Full-scale 3D model predictions for the three *in situ* heater experiments; the Mont Terri HE-E experiment, the Horonobe EBS experiment, and the Mont Terri FE experiment, and compare with data and with the results of other international modeling teams in the DECOVALEX and Mont Terri projects
- Collaborate with the UPC (Barcelona) modeling team in application of the BBM and dual-structure models to the Mont Terri FE experiment.
- Validation of models against these field experiments as well as characterization of parameters for BBM and dual-structure constitutive models from laboratory data that are now becoming available in the various projects.
- Review of THM properties of bentonite-based buffer and backfill materials in these field experiments (and in nuclear waste isolation in general) and identify critical parameters and experimental data needs.
- Participate and present simulation results at DECOVALEX and Mont Terri workshops.

(4) Investigation of the maximum allowable temperature and detailed impacts of a high temperature on repository performance:

Chemical alteration and the subsequent changes in mechanical properties are among the determining factors for establishing the thermal limit of a repository with a clay-based EBS. A thermal limit of about 100°C is imposed unanimously in all disposal concepts throughout the world—without rigorous studies to back up the choice. More rigorous studies are needed to answer the question whether an argillite repository with bentonite EBS can sustain higher than 100°C.We use coupled THMC modeling to evaluate the chemical alteration and associated mechanical changes in a generic repository and consider the interaction between EBS bentonite and the NS clay formation. Specific accomplishments are as follows:

- Coupled THMC models were developed, with properties of clay formation from Opalinus Clay, and two types of EBS bentonite—Kunigel-VI and FEBEX bentonites—are considered to understand the difference in chemical and mechanical changes in these two bentonites.
- Two main scenarios were developed for comparison: a “high T” case in which the temperature near the waste package can reach about 200°C and a “low T” scenario in which the temperature peaks at about 100°C.
- Sensitivity analyses to key parameters were conducted

For the laboratory investigations, it is highly likely that the observed heat-induced changes in the strength and failure behavior of the compacted bentonite and the Opalinus Clay from Mont Terri were caused by decreases of water content from the clay samples during heating. The effect, however, may also be superimposed by other effects such as redistribution (dissolution and re-

precipitation) of quartz within the pore space and phase transformations of clay minerals. A summary of the accomplishments so far is as follows:

- Sample preparation procedures have been established and necessary tools developed.
- An efficient triaxial compression testing setup has been developed. The tests were conducted on compacted bentonite clay with different fluid chemistry and on Opalinus Clay cores from Mont Terri. However, the loss of fluid during heating resulted in ambiguities in the experimental results.
- A miniature indentation test setup has been developed. A sample hardness measurement procedure has been established and demonstrated

Recommended work for FY15 includes:

- Conducting THMC simulations using more comprehensive links between chemistry and mechanics provided by a dual-structure model. In current models, the mechanical-chemical coupling in bentonite is calculated via an extended linear elastic swelling model, a more rigorous approach to link chemistry to mechanics is needed for more accurate calculations.
- Developing constitutive relationship to link the chemistry with mechanics for clay formation and considering it in the THMC models. The current mechanical model for the NS clay formation is not tied with chemical variables, i.e., mechanical-chemical coupling is only considered in the EBS bentonite.
- Considering chemical changes in the canister in the THMC model. In the current model, the canister serves only as a heat source; chemical changes on the surface of the canister are neglected for simplification.
- Integrating THMC modeling work with other laboratory studies (e.g. Cheshire et al. 2014) in UFDC. The finding from laboratory studies can be used to constrain the reaction paths and rate of key chemical reactions.
- Finding a solution for the slow leakage of water vapor from the pressure vessels used for heating of clay samples. Currently, use of soft metal foils (e.g., lead or tin [Sn] foils for unsaturated samples. Silver or gold if the sample is saturated) is considered.
- Preparation of the clay samples and repeated experiments.
- Chemical/mineralogical characterization of heat-treated samples. Interpretation of the results with the changes in the mechanical/hydrological properties.
- Improvement of mini-indentation test setup. Currently, the reduced Young modulus of tested samples cannot be determined accurately because of large flexures in the loading column (particularly in the loadcell section). An additional displacement gauge for determining the system deformation needs to be installed.
- Continued development of a gas permeability measurement setup for low-permeability clay samples. Current samples exhibit unusually high permeability, which may be attributed to microcracks in the heated samples.
- Illitization mechanisms in the current model need to be expanded to include solid state transformation by substitution of intracrystal cations (e.g., Cuadros and Linares 1996)
- The current mechanical model for the natural system clay formation needs to be coupled with chemical variables, i.e., mechanical-chemical coupling, as done for EBS bentonite.

- Mechanical-chemical coupling in bentonite is calculated via an extended linear elastic swelling model, therefore, a more rigorous approach to link chemistry to mechanics is needed for more accurate calculation.
- Chemical changes on the surface of the canister need to be considered, specifically the release of Fe^{+2}, which might enhance the dissolution of smectite by forming chlorite.
- Finding a solution for the slow leakage of water vapor from the pressure vessels used for heating of clay samples. Currently, use of soft metal foils (e.g., lead or tin [Sn] foils for unsaturated samples; silver or gold if the sample is saturated.) is considered.

For the laboratory investigations, it is highly likely that the observed heat-induced changes in the strength and failure behavior of the compacted bentonite and the Opalinus Clay from Mont Terri were caused by decreases of water content from the clay samples during heating. The effect, however, may also be superimposed by other effects such as redistribution (dissolution and re-precipitation) of quartz within the pore space and phase transformations of clay minerals. A summary of the accomplishments so far is as follows:

(5) Investigation of the maximum allowable temperature and detailed impacts of a high temperature on repository performance:

Modeling techniques based on electric double-layer theory have been developed and tested against experimental results from the DR-A test at Mont Terri. A summary of the accomplishments so far is as follows:

- Two complementary approaches to modeling ion diffusion through clays have been developed. The first makes use of a Donnan Equilibrium or Mean Electrostatic Approach, in which a mean electrostatic potential is defined for the electrical double layer to balance the fixed negative charge of the clays. The second approach involves the use of the Nernst-Planck and Poisson-Boltzmann equation (termed the PNP method).
- The Donnan Equilibrium or Mean Electrostatic Approach was tested in benchmark studies using the software codes CrunchEDL versus PHREEQC. Differences between the calculations in one of the benchmark studies were found to be a result of the neglect of the longitudinal gradient in the mean electrostatic potential in CrunchEDL.
- Comparisons between CrunchEDL calculations and DR-A test results provide evidence that the electric double layer influences anion diffusion rates in the Opalinus Clay.

Recommended work for FY15 includes:

- Modify CrunchEDL to account for the longitudinal gradient in the mean electrostatic potential.
- Conduct further analyses of the DR-A test results using the modeling techniques developed here.

8. References

Abercrombie, H. J., I. E. Hutcheon, J. D. Bloch and P. de Caritat 1994. Silica activity and the smectite-illite reaction. Geology 22(6): 539-542.

Alonso EE, Gens A, Josa A (1990) A constitutive model for partially saturated soils. Geotechnique. 40: 405-430.

Appelo, C.A.J. and Wersin, P., 2007. Multicomponent diffusion modeling in clay systems with application to the diffusion of tritium, iodide, and sodium in Opalinus Clay. Environmental Science and Technology 41, 5002-5007.

Appelo, C.A.J., Vinsot, A., Mettler, S. and Wechner, S., 2008. Obtaining the porewater composition of a clay rock by modeling the in- and out-diffusion of anions and cations from an in-situ experiment. Journal of Contaminant Hydrology 101, 67-76.

Arcos, D.; Fidel, G.; Domenech, C.; Fernández, A.M.; Villar, M.V.; Muurinen, A.; Carlsson, T.; Sellin, P.; Hernan, P. 2008. "Long-Term Geochemical Evolution of the Near Field Repository: Insights from Reactive Transport Modelling and Experimental Evidences," Journal of Contaminant Hydrology, 102, 196-209.

Armand, G., A. Noiret, J. Zghondi, and D.M. Seyedi. (2013). Short- and long-term behaviors of drifts in the Callovo-Oxfordian claystone at the Meuse/Haute-Marne Underground Research Laboratory. Journal of Rock Mechanics and Geotechnical Engineering 5, no. 3: 221-230.

Asahina, D., Landis, E.N. and Bolander, J.E. (2011). Modeling of phase interfaces during pre-critical crack growth in concrete. Cement & Concrete Composites, 33, 966-977.

Athy, L. F. (1930). "Density, porosity, and compaction of sedimentary rocks." AAPG Bulletin 14(1): 1-24.

Baechler, S., J.M. Lavanchy, G. Armand, M. Cruchaudet. (2011). Characterisation of the hydraulic properties within the EDZ around drifts at level -490 m of the Meuse/Haute-Marne URL: a methodology for consistent interpretation of hydraulic tests. Physics and Chemistry of the Earth, no. 17: 1922-1931

Barnichon, J.D. and Volckaert, G. (2003). Observations and Predictions of Hydromechanical Coupling Effects in the Boom Clay, Mol Underground Research Laboratory, Belgium. Hydrogeology Journal, 11(1), 193-202.

Bear, J. (1972). "Dynamics of Fluids in Porous Media," Elsevier, New York, New York.

Berton S. and Bolander, J.E. (2006). Crack band model of fracture in irregular lattices. Computer Methods in Applied Mechanics and Engineering, 195, 7171-7181.

Biot, M.A. and Willis, D.G. (1957). The elastic coefficients of the theory of consolidation. Journal of Applied Mechanics, 24, 594-601.

Birgersson M., Karnland, O., 2009. Ion equilibrium between montmorillonite interlayer space and an external solution - Consequences for diffusional transport. Geochimica et Cosmochimica Acta 73, 1908-1923.

Blümling, P., Bernier, F., Lebon, P. and Martin, C.D. (2007). The excavation damaged zone in clay formations time-dependent behaviour and influence on performance assessment. Physics and Chemistry of the Earth, 32, 588-599.

Bock, H. (2001). RA Experiment Rock Mechanics Analyses and Synthesis: Data Report on Rock Mechanics, Mont Terri Project, Technical Report 2000-02.

Bolander, J.E. and Saito, S. (1998). Fracture analyses using spring networks with random geometry. Eng Fract Mech, 61, 569-591.

Börgesson, L., Chijimatsu, M., Nguyen, T.S., Rutqvist, J., Jing L. (2001) Thermo-hydro-mechanical characterization of a bentonite-based buffer material by laboratory tests and numerical back analyses. Int. J. Rock Mech. & Min. Sci. 38, 105-127.

Bossart P. (2011) Characteristics of the Opalinus Clay at Mont Terri, http://www.mont-terri.ch/internet/mont-terri/en/home/geology/key_characteristics.html

Bossart, P. (2012). Characteristics of the Opalinus Clay at Mont Terri, http://www.montterri.ch/internet/montterri/en/home/geology/key_characteristics.parsys.49924.DownloadFile.tmp/characteristicsofopa.pdf

Bossart, P., Meier, P.M., Moeri, A., Trick, T. and Mayor, J.-C. (2004). Structural and hydrogeological characterisation of the excavation-disturbed zone in the Opalinus Clay (Mont Terri Project, Switzerland). Applied Clay Science, 26, 429- 448.

Brighenti, G. (1989). Effect of Confining Pressure On Gas Permeability of Tight Sandstones. ISRM International Symposium, International Society for Rock Mechanics.

Bucher, F., and Müller-Vonmoos, M. (1989) Bentonite as a containment barrier for the disposal of highly radioactive waste. Applied Clay Science, 4(2): 157–177.

Byrnes, A. (1996). "Reservoir characteristics of low-permeability sandstones in the Rocky Mountains."

Byrnes, A. P. (1997). "Reservoir characteristics of low-permeability sandstones in the Rocky Mountains." The Mountain Geologist.

Byrnes, A. P. and J. W. Castle (2000). Comparison of core petrophysical properties between low-permeability sandstone reservoirs: Eastern US Medina group and Western US Mesaverde group and Frontier formation. SPE Rocky Mountain Regional/Low-Permeability Reservoirs Symposium and Exhibition, Society of Petroleum Engineers.

Caporuscio, F. A. (2013) EBS Report - LANL Experimental update of buffer/backfill at elevated P,T. LA-UR-13-27015 2013-09-09.

Castellanos, E., M. V. Villar, E. Romero, A. Lloret and A. Gens 2008. Chemical impact on the hydro-mechanical behaviour of high-density FEBEX bentonite. Physics and Chemistry of the Earth, Parts A/B/C 33, Supplement 1(0): S516-S526.

Chen, Y., C. Zhou and L. Jing 2009. Modeling coupled THM processes of geological porous media with multiphase flow: Theory and validation against laboratory and field scale experiments. Computers and Geotechnics 36(8): 1308-1329.

Cheshire, M., F. Caporuscio, M. Rearick, C. Jove-colon and M. K. McCarney 2014. Bentonite evolution at elevated pressures and temperatures: an experimental study for generic nuclear repository designs. American Mineralogist: in press.

Chijimatsu M, Nguyen TS, Jing L, de Jonge J, Kohlmeier M, Millard A, Rejeb A, Rutqvist J, Souley M, Sugita Y (2005) Numerical study of the THM effects on the near-field safety of a hypothetical nuclear waste repository – BMT1 of the DECOVALEX III project. Part 1: Conceptualization and characterization of the problems and summary of results. Int. J Rock Mech & Min Sci 42:720–730.

Cosgrove, J.W. (2001). Hydraulic Fracturing during the Formation and Deformation of a Basin: A Factor in the Dewatering of Low-Permeability Sediments. AAPG Bulletin, 85(4), 737-748.

Cuadros, J. 2006. Modeling of smectite illitization in burial diagenesis environments. Geochimica et Cosmochimica Acta 70(16): 4181-4195.

Cuadros, J. and J. Linares 1996. Experimental kinetic study of the smectite-to-illite transformation. Geochimica et Cosmochimica Acta 60(3): 439-453.

Cui, X., et al. (2007). "Adsorption-induced coal swelling and stress: Implications for methane production and acid gas sequestration into coal seams." Journal of Geophysical Research: Solid Earth 112(B10): B10202.

David, C. and M. Darot (1989). Permeability And Conductivity of Sandstones. ISRM International Symposium, International Society for Rock Mechanics.

David, C., et al. (1994). "Laboratory measurement of compaction-induced permeability change in porous rocks: Implications for the generation and maintenance of pore pressure excess in the crust." Pure and Applied Geophysics 143(1-3): 425-456.

David, C., et al. (2001). "Mechanical compaction, microstructures and permeability evolution in sandstones." Physics and Chemistry of the Earth, Part A: Solid Earth and Geodesy 26(1): 45-51.

Davies, J. and D. Davies (2001). "Stress-dependent permeability: characterization and modeling." SPE Journal 6(02): 224-235.

Dewhurst, D. N., et al. (1998). "Compaction-driven evolution of porosity and permeability in natural mudstones: An experimental study." Journal of Geophysical Research-Solid Earth 103(B1): 651-661.

Dong, J.-J., et al. (2010). "Stress-dependence of the permeability and porosity of sandstone and shale from TCDP Hole-A." International Journal of Rock Mechanics and Mining Sciences 47(7): 1141-1157.

Eberl, D. 1978. Reaction series for dioctahedral smectites. Clays and Clay Minerals 26(5): 327-340.

Elliott, W. C. and G. Matisoff 1996. Evaluation of kinetic models for the smectite to illite transformation. Clays and Clay Minerals 44(1): 77-87.

ENRESA 2000. Full-scale engineered barriers experiment for a deep geological repository in crystalline host rock FEBEX Project, European Commission: 403.

Evans, J. P., et al. (1997). "Permeability of fault-related rocks, and implications for hydraulic structure of fault zones." Journal of Structural Geology 19(11): 1393-1404.

Ewing J. and Senger R. (2011) Evolution of Temperature, Pressure, and Saturation in the Bentonite Buffer: Scoping Calculations in Support of the Design of the Full-Scale Emplacement Experiment at the Mont Terri URL. NAGRA NAB 10-38, September 2011.

Feng Xia-Ting, Pan Peng-zhi, Zhou Hui (2006) Simulation of rock microfracturing process under uniaxial compression using elasto-plastic cellular automata. Int J Rock Mech & Min Sci 43: 1091–1108.

Fernández, A. M., B. Baeyens, M. Bradbury and P. Rivas (2004). Analysis of the porewater chemical composition of a Spanish compacted bentonite used in an engineered barrier. Physics and Chemistry of the Earth, Parts A/B/C 29(1): 105-118.

Fernández, A. M., Turrero, M. J., Sánchez, D. M., Yllera, A., Melón, A. M., Sánchez, M., Peña, J., Garralón, A., Rivas, P., Bossart, P. and Hernán, P. (2007) On site measurements of the redox and carbonate system parameters in the low-permeability Opalinus Clay formation at the Mont Terri Rock Laboratory. Physics and Chemistry of the Earth, Parts A/B/C 32(1-7): 181-195.

Fernández, A., Cuevas, J., Rivas, P., 2001. Pore water chemistry of the FEBEX bentonite. Mat. Res. Soc. Symp. Proc. 663, 573–588.

Fouche, O., Wright, H., Cleach, J.L. and Pellenard, P. (2004). Fabric Control on Strain and Rupture of Heterogeneous Shale Samples by Using a Non-Conventional Mechanical Test. Applied Clay Science, 26, 367-387.

Gangi, A. F. (1978). Variation of whole and fractured porous rock permeability with confining pressure. International Journal of Rock Mechanics and Mining Sciences & Geomechanics Abstracts, Elsevier.

Garitte B. and Gens A. (2012) TH and THM Scoping computations for the definition of an optimal instrumentation layout in the Full-scale Emplacement (FE) experiment NAGRA NIB 10-34, March 2012.

Garitte, B. (2012) HE-E experiment - In situ Heater Test, Presentation given at 1th DECOVALEX 2015 workshop, April 2012, Berkeley.

Gens A, Sánchez, M Sheng, D (2006) On constitutive modelling of unsaturated soils. Acta Geotechnica. 1, 137-147

Gens, A, Alonso, E. A framework for the behaviour of unsaturated expansive clays. Can. Geotech. J. 29, 1013–1032 (1992).

Gens, A., Sánchez, M., Guimaraes, L.D.N., Alonso, E.E., Lloret, A., Olivella, S., Villar, M.V., Huertas, F. (2009) A full-scale in situ heating test for high-level nuclear waste disposal: observations, analysis and interpretation. Geotechnique 59, 377–399.

Ghabezloo, S., et al. (2009a). "Effective stress law for the permeability of a limestone." International Journal of Rock Mechanics and Mining Sciences 46(2): 297-306.

Ghabezloo, S., et al. (2009b). "Evaluation of a permeability–porosity relationship in a low-permeability creeping material using a single transient test." International Journal of Rock Mechanics and Mining Sciences 46(4): 761-768.

Gonçalvès J., Rousseau-Gueutin P., Revil A. Introducing interacting diffuse layers in TLM calculations: A reappraisal of the influence of the pore size on the swelling pressure and the osmotic efficiency of compacted bentonites. J. Colloid Interface Sci., 316, 92-99 (2007).

Grochowski, P. and J. Trylska, 2007 Continuum molecular electrostatics, salt effects, and counterion binding—A review of the Poisson-Boltzmann theory and its modifications. Biopolymers 89: 93-113.

Hama, K., Kunimaru, T., Metcalfe, R., Martin, A.J. 2007. The Hydrogeochemistry of Argillaceous Rock Formations at the Horonobe URL Site, Japan, Physics and Chemistry of the Earth, 32, 170–180.

Herbert, H.-J., J. Kasbohm, H. Sprenger, A. M. Fernández and C. Reichelt 2008. Swelling pressures of MX-80 bentonite in solutions of different ionic strength. Physics and Chemistry of the Earth, Parts A/B/C 33, Supplement 1(0): S327-S342.

Hicks, T.W., White, M.J. and Hooker, P.J. (2009) Role of Bentonite in Determination of Thermal Limits on Geological Disposal Facility Design, Report 0883-1, Version 2, Falson Sciences Ltd., Rutland, UK, Sept. 2009.

Hoholick, J. D., et al. (1984). "Regional variations of porosity and cement: St. Peter and Mount Simon sandstones in Illinois Basin." AAPG Bulletin 68(6): 753-764.

Holditch, S. A. (2006). "Tight gas sands." Journal of Petroleum Technology 58(6): 86-93.

Horseman S.T. and McEwen, T. J. (1996) Thermal constrains on disposal of heat-emitting waste in argillaceous rocks, Engineering Geology 41, 5-16.

Houseworth J., Rutqvist J., Asahina D., Chen F., Vilarrasa V., Liu H.H., Birkholzer J. Report on International Collaboration Involving the FE Heater and HG-A Tests at Mont Terri. Prepared for U.S. Department of Energy, Used Fuel Disposition Campaign, FCRD-UFD-2014-000002, Lawrence Berkeley National Laboratory (2013).

Itasca, 2009. FLAC3D, Fast Lagrangian Analysis of Continua in 3 Dimensions, Version 4.0, Minneapolis, Minnesota, Itasca Consulting Group.

Itasca, FLAC3D V5.0, Fast Lagrangian Analysis of Continua in 3 Dimensions, User's Guide. Itasca Consulting Group, Minneapolis, Minnesota (2011).

Jaeger, J.C. (1960). Shear failure of anisotropic rocks. Geologic Magazine, 97, 65-72.

Jasinge, D., et al. (2011). "Effects of effective stress changes on permeability of Latrobe Valley brown coal." Fuel 90(3): 1292-1300.

JNC, Japan Nuclear Cycle Development Institute. (2000) H12: project to establish the scientific and technical basis for HLW disposal in Japan: supporting report 2 (respiratory design and engineering Technology). Japan Nuclear Cycle Development Institute, Tokyo.

Jones, F. O. and W. W. Owens (1980). "A Laboratory Study of Low-Permeability Gas Sands." Journal of Petroleum Technology 32(9): 1631-1640.

Jones, S. C. (2013). "Two-Point Determinations of Permeability and PV vs. Net Confining Stress." SPE Formation Evaluation 3(01): 235-241.

Karnland, O., Olsson, S. and Nilsson, U. (2006) Mineralogy and sealing properties of various bentonites and smectite-rich clay materials, SKB Technical Report TR-06-30.

Kawai, T. (1978). New Discrete Models and their Application to Seismic Response Analysis of Structures. Nuclear Engineering and Design, 48, 207-229.

Kilmer, N. H., et al. (1987). "Pressure sensitivity of low permeability sandstones." Journal of Petroleum Science and Engineering 1(1): 65-81.

Kirsch, G. (1898). Die Theorie der Elastizität und die Bedürfnisse der Festigkeitslehre. Zeitschrift des Vereines deutscher Ingenieure, 42, 797-807.

Klinkenberg, L. (1941). "The permeability of porous media to liquids and gases." Drilling and production practice.

Kolditz O, Bauer S, Beinhorn M, de Jonge J, Kalbacher T, McDermott C, Wang W, Xie M, Kaiser R, Kohlmeier M (2003) ROCKFLOW - Theory and Users Manual, Release 3.9, Groundwater Group, Center for Applied Geosciences, University of Tübingen, and Institute of Fluid Mechanics, University of Hannover.

Komine, H., and Ogata, N. (1996) Prediction for swelling characteristics of compacted bentonite. Canadian Geotechnical Journal, 33: 11–22.

Konecny, P. and A. Kozusnikova (2011). "Influence of stress on the permeability of coal and sedimentary rocks of the Upper Silesian basin." International Journal of Rock Mechanics and Mining Sciences 48(2): 347-352.

Kristensson O, Åkesson M (2008) Mechanical modeling of MX-80 – Quick tools for BBM parameter analysis. Phys Chem Earth, Parts A/B/C. 33, Supplement 1: S508-S515.

Kwaśniewski, M.A. and Mogi, K. (2000). Faulting in an anisotropic, schistose rock under general triaxial compression. 4th North American Rock Mechanics Symposium, Seattle, WA.

Kwon, O., et al. (2001). "Permeability of Wilcox shale and its effective pressure law." Journal of Geophysical Research-Solid Earth 106(B9): 19339-19353.

Lanyon, G.W., Marschall, P., Trick, T., de La Vaissière, R., Shao, H. and Leung, H. (2009). Hydromechanical Evolution and Self-Sealing of Damage Zones around a Microtunnel in a Claystone Formation of the Swiss Jura Mountains. American Rock Mechanics Association, ARMA 09-333.

Laredj, N., Missoum, H. and Bendani, K. (2010) Modeling the effect of osmotic potential changes on deformation behavior of swelling clays. Journal of Porous Media 13(8): 743-748.

Lauber, M., B. Baeyens and Bradbury, M. H. (2000) Physico-Chemical Characterisation and Sorption Measurements of Cs, Sr, Ni, Eu, Th, Sn and Se on Opalinus Clay from Mont Terri. PSI Bericht Nr. 00-10 December 2000 ISSN 1019-0643.

Lee, J.W., R.H. Nilson, J.A. Templeton, S.K. Griffiths, A. Kung, B.M. Wong, 2012, Comparison of molecular dynamics with classical density functional and Poisson-Boltzmann theories of the electrical double layer in nanochannels. Journal of Chemical Theory and Computation 8: 2012-2012.

Lei, Q., et al. (2008). Analysis of stress sensitivity and its influence on oil production from tight reservoirs, Lawrence Berkeley National Laboratory.

Leroy P., Revil, A., Altmann, S., Tournassat, C., 2007. Modeling the composition of a pore water in a clay-rock geological formation (Callovo-Oxfordian, France). Geochimica et Cosmochimica Acta 71, 1087-1097.

Leroy, P., Revil, A., 2004. A triple-layer model of the surface electrochemical properties of clay minerals. Journal of Colloid and Interface Science 270, 371-380.

Li, L., et al. (2014). "The use of two-part Hooke's Model (TPHM) to model the mine-by test at Mont Terri Site, Switzerland." Computers and Geotechnics 58(0): 28-46.

Li, X., et al. (2008). Multi-stage fracturing stimulations improve well performance in tight oil reservoirs of the Changqing Oilfield. International Petroleum Technology Conference.

Liu, H. H., et al. (2011). "Constitutive Relationships for Elastic Deformation of Clay Rock: Data Analysis." Rock mechanics and rock engineering 44(4): 463-468.

Liu, H.-H., et al. (2009). "On the relationship between stress and elastic strain for porous and fractured rock." International Journal of Rock Mechanics and Mining Sciences 46(2): 289-296.

Liu, H.-H., et al. (2013a). "Normal-stress dependence of fracture hydraulic properties including two-phase flow properties." Hydrogeology Journal 21(2): 371-382.

Liu, H.H., Houseworth, J., Rutqvist, J., Zheng, L., Asahina, D., Li, L., Vilarrasa, V., Chen, F., Nakagawa, S., Finsterle, S., Doughty, C., Kneafsey, T. and Birkholzer, J. (2013b). Report on THMC modeling of the near field evolution of a generic clay repository: Model validation and demonstration. (FCRD-UFD-2013-000244), U.S. DOE Used Fuel Disposition Campaign.

Louis, L., et al. (2005). "Microstructural control on the anisotropy of elastic and transport properties in undeformed sandstones." International Journal of Rock Mechanics and Mining Sciences 42(7–8): 911-923.

Marschall, P., Distinguin, M., Shao, H., Bossart, P., Enachescu, C. and Trick, T. (2006). Creation and Evolution of Damage Zones Around a Microtunnel in a Claystone Formation of the Swiss Jura Mountains. Society of Petroleum Engineers, SPE-98537-PP.

Marschall, P., Trick, T., Lanyon, G.W., Delay, J. and Shao, H. (2008). Hydro-Mechanical Evolution of Damaged Zones around a Microtunnel in a Claystone Formation of the Swiss Jura Mountains. American Rock Mechanics Association, ARMA 08-193.

Martin, C.D. and Lanyon, G.W. (2003). Measurement of In-Situ Stress in Weak Rocks at Mont Terri Rock Laboratory, Switzerland. International Journal of Rock Mechanics & Mining Sciences, 40, 1077-1088.

Mazurek, M., Pearson, F.J., Volckaert, G., and Bock, H. 2003. Features, Events and Processes Evaluation Catalogue for Argillaceous Media. ISBN 92-64-02148-5. Nuclear Energy Agency.

McGuire, W. and Gallagher, R.H. (1979). “Matrix Structural Analysis,” John Wiley & Sons, New York.

McKee, C. R., et al. (1988). "Stress-dependent permeability and porosity of coal."

McLamore, R. and Gray, K.E. (1967). The mechanical behavior of anisotropic sedimentary rocks. J Manuf Sci Eng, Trans ASME, 89(1), 62-73.

McLatchie, A., et al. (1958). "The effective compressibility of reservoir rock and its effects on permeability." Journal of Petroleum Technology 10(06): 49-51.

Meier, P., Trick, T., Blumling, P. and Volckaert, G. (2000). Self-Healing of Fractures within the EDZ at the Mont Terri Rock Laboratory: Results after One Year of Experimental Work. In: Proceedings of the International Workshop on Geomechanics, hydromechanical and Thermomechanical Behavior of deep argillaceous Rocks: Theory and Experiments, Paris, October11-12, 2000.

Metwally, Y. M. and C. H. Sondergeld (2011). "Measuring low permeabilities of gas-sands and shales using a pressure transmission technique." International Journal of Rock Mechanics and Mining Sciences 48(7): 1135-1144.

Mohiuddin, M., et al. (2000). Stress-dependent porosity and permeability of a suite of samples from Saudi Arabian sandstone and limestone reservoirs. SCA2033, 2000 Symposium of Core Analysts, Abu Dhabi, UAE.

Morrow, C. A., et al. (1984). "Permeability of fault gouge under confining pressure and shear stress." Journal of Geophysical Research: Solid Earth 89(B5): 3193-3200.

Mosser-Ruck, R. and M. Cathelineau 2004. Experimental transformation of Na, Ca-smectite under basic conditions at 150 C. Applied Clay Science 26(1): 259-273.

Mosser-Ruck, R., M. Cathelineau, A. Baronnet and A. Trouiller 1999. Hydrothermal reactivity of K-smectite at 300 C and 100 bar: dissolution-crystallization process and non-expandable dehydrated smectite formation. Clay Minerals 34(2): 275-290.

Nater P. (2012) Mont Terri / FE-Experiment Geomechanische Modellierung des Vortriebs. NAGRA AN 12-184.

Nutt, M. (2011). Used Fuel Disposition Campaign Disposal Research and Development Roadmap (FCR&D-USED-2011-000065 REV0), U.S. DOE Used Fuel Disposition Campaign.

Ochs, M., Lothenbach, B., Shibata, M. and Yui, M. (2004) Thermodynamic modeling and sensitivity analysis of porewater chemistry in compacted bentonite. Physics and Chemistry of the Earth, Parts A/B/C 29(1): 129-136.

Ohnishi Y, Kobayashi A (1996) THAMES. In O. Stephansson, L. Jing, and C.-F. Tsang, editors, Coupled Thermo-hydro-mechanical Processes of Fractured Media, Developments in Geotechnical Engineering, Elsevier, 79:545–549.

Okabe, A., Boots, B., Sugihara, K. and Chiu, S.N. (2000). Spatial tessellations: Concepts and applications of Voronoi diagrams, 2nd ed. Probability and Statistics. Wiley, NYC. 671 pages.

Olivella S., Gens A. Vapour transport in low permeability unsaturated soils with capillary effects. Transport in Porous Media 40: 219–241, 2000.

Ostensen, R. (1983). "Microcrack permeability in tight gas sandstone." Society of Petroleum Engineers Journal 23(6): 919-927.

Pacovsky, J., Svoboda, J. and Zapletal, L. (2005) Saturation development in the bentonite barrier of the mock-up CZ geotechnical experiment. Clay in Natural and Engineered Barriers for Radioactive Waste Confinement—Part 2. Physics and Chemistry of the Earth, 32(8–14). Elsevier, Amsterdam, pp. 767–779.

Pan Peng-zhi, Feng Xia-Ting, Huang Xiao-Hua, Cui Qiang, Zhou Hui (2008) Study of coupled THMC processes in crystalline rock in the EDZ using an ECPA code. Environmental Geology.

Pariseau, W.G. (2006). “Design Analysis in Rock Mechanics,” Taylor & Francis, London, UK.

Patriarche, D., Ledoux, E., Simon-Coincon, R., Michelot, J. and Cabrera, J. (2004). Characterization and Modeling of Diffusive Process for Mass Transport through the Tournemire Argillites Aveyron, France. Applied Clay Science, 26, 109-122.

Perry, F.V., Kelley, R.E., Dobson, P.F., Houseworth, J.E. 2014. Regional Geology: A GIS Database for Alternative Host Rocks and Potential Siting Guidelines (FCRD-UFD-2014-000068), U.S. DOE Used Fuel Disposition Campaign.

Pietruszczak, S. and Mroz, Z. (2001). On failure criteria for anisotropic cohesive-frictional materials. Int J Numer Anal Meth Geomech, 25, 509-524.

Pusch, R. (1992) Use of Bentonite for Isolation of Radioactive Waste Products. Clay Minerals, 27: 353-361.

Pruess, K., Oldenburg, C.M., Moridis, G. (2011) TOUGH2 User's Guide, Version 2.1, LBNL-43134(revised), Lawrence Berkeley National Laboratory, Berkeley, California.

Pusch R. and Karnland, O. (1996) Physico/chemical stability of smectite clays, Engineering Geology 41: 73-85.

Pusch, R. and Madsen, F. t. (1995) Aspects on the illitization of the kinnekulle bentonites. Clays and Clay Minerals 43(3): 261-270.

Pusch, R., Kasbohm, J. and Thao, H. T. M. (2010) Chemical stability of montmorillonite buffer clay under repository-like conditions—A synthesis of relevant experimental data. Applied Clay Science 47(1–2): 113-119.

Pytte A. 1982. The kinetics of the smectite to illite reaction in contact metamorphic shales [M.A. Thesis]. Dartmouth College: Hanover, N.H. 78p.

Ramírez, S., J. Cuevas, R. Vigil and S. Leguey 2002. Hydrothermal alteration of "La Serrata" bentonite (Almeria, Spain) by alkaline solutions. Applied Clay Science 21(5–6): 257-269.

Rizzi, M., A. Seiphoori, A. Ferrari, D. Ceresetti, and L. Laloui. 2011. Analysis of the behaviour of the granular MX-80 bentonite in THM-processes. Lausanne: Swiss Federal Institute of Technology, Orders No 7'928 and 5'160.

Roberson, Herman E., and Richard W. Lahann. "Smectite to illite conversion rates: effects of solution chemistry." Clays and Clay Minerals 29.2 (1981): 129-135.

Rutqvist, J., Börgesson, L., Chijimatsu, M., Kobayashi, A., Nguyen, T.S., Jing, L., Noorishad, J., Tsang, C.-F. (2001a) Thermohydromechanics of partially saturated geological media – Governing equations and formulation of four finite element models. Int. J. Rock Mech. & Min. Sci. 38, 105-127.

Rutqvist J., Börgesson L., Chijimatsu M., Nguyen T. S., Jing L., Noorishad J., Tsang C.-F. (2001b) Coupled Thermo-hydro-mechanical Analysis of a Heater Test in Fractured Rock and Bentonite at Kamaishi Mine – Comparison of Field Results to Predictions of Four Finite Element Codes. Int. J. Rock Mech. & Min. Sci. 38, 129-142.

Rutqvist J. and Tsang C.-F. (2002). A study of caprock hydromechanical changes associated with CO2-injection into a brine formation. Environmental Geology, 42, 296-305.

Rutqvist, J., Wu, Y.-S., Tsang, C.-F. and Bodvarsson, G. (2002). A modeling approach for analysis of coupled multiphase fluid flow, heat transfer and deformation in fractured porous rock. International Journal of Rock Mechanics & Mining Sciences, 39, 429-442.

Rutqvist J., Chijimatsu M., Jing L., De Jonge J., Kohlmeier M., Millard A., Nguyen T.S., Rejeb A., Souley M., Sugita Y. and Tsang C.F. Numerical study of the THM effects on the near-field safety of a hypothetical nuclear waste repository – BMT1 of the DECOVALEX III project. Part 3: Effects of THM coupling in fractured rock Int. J. Rock Mech. & Min. Sci, 42, 745-755 (2005).

Rutqvist J. and Tsang C.-F. Review of SKB's Work on Coupled THM Processes Within SR-Can: External review contribution in support of SKI's and SSI's review of SR-Can. Swedish Nuclear Power Inspectorate (SKI) Technical Report 2008:08 (2008).

Rutqvist J., Barr D., Birkholzer J.T., Fujisaki K., Kolditz O., Liu Q.-S., Fujita T., Wang W. and Zhang C.-Y. A comparative simulation study of coupled THM processes and their effect on fractured rock permeability around nuclear waste repositories. Environ Geol, 57, 1347–1360 (2009)

Rutqvist J. Status of the TOUGH-FLAC simulator and recent applications related to coupled fluid flow and crustal deformations. Computers & Geosciences, 37, 739–750 (2011).

Rutqvist, J., Ijiri, Y. and Yamamoto, H. (2011). Implementation of the Barcelona Basic Model into TOUGH-FLAC for simulations of the geomechanical behavior of unsaturated soils. Computers &Geosciences, 37, 751-762.

Rutqvist, J., Leung, C., Hoch, A., Wang, Y. and Wang, Z. (2013a). Linked multicontinuum and crack tensor approach for modeling of coupled geomechanics, fluid flow and transport in fractured rock. J Rock Mech Geotech Eng, 5, 18-31.

Rutqvist J., Steefel C., Chen F., Houseworth J., Vilarrasa V., Liu H.-H., Birkholzer J. THM and Reactive Transport Model Development and Evaluation: International Activities. Prepared for U.S. Department of Energy, Used Fuel Disposition Campaign, FCRD-UFD-2013-000372, Lawrence Berkeley National Laboratory (2013b).

Rutqvist, J., Zheng, L., Chen, F., Liu, H.-H. and Birkholzer, J. (2013c) Modeling of Coupled Thermo-Hydro-Mechanical Processes with Links to Geochemistry Associated with Bentonite-Backfilled Repository Tunnels in Clay Formations. Rock Mechanics and Rock Engineering: 1-20.

Rutqvist J., Zheng L., Chen F, Liu H.-H, and Birkholzer J. Modeling of Coupled Thermo-Hydro-Mechanical Processes with Links to Geochemistry Associated with Bentonite-Backfilled Repository Tunnels in Clay Formations. Rock Mechanics and Rock Engineering, 47, 167–186 (2014).

Sadhukhan, S., et al. (2012). "Porosity and permeability changes in sedimentary rocks induced by injection of reactive fluid: A simulation model." Journal of Hydrology 450–451(0): 134-139.

Sánchez, M., Gens, A., Guimarães, L. do N., Olivella, S. A double structure generalized plasticity model for expansive materials. Int. J. Numer. Anal. Meth. Geomech., 29, 751–787 (2005).

Schoch, R.B., Han, J., Renaud, P., 2008. Transport phenomena in nanofluidics. Reviews of Modern Physics 80, 840-883.

Shanley, K. W., et al. (2004). "Factors controlling prolific gas production from low-permeability sandstone reservoirs: Implications for resource assessment, prospect development, and risk analysis." AAPG Bulletin 88(8): 1083-1121.

Shi, Y. and C. Y. Wang (1986). "Pore pressure generation in sedimentary basins: overloading versus aquathermal." Journal of Geophysical Research: Solid Earth (1978–2012) 91(B2): 2153-2162.

Soeder, D. J. and P. L. Randolph (2013). "Porosity, Permeability, and Pore Structure of the Tight Mesaverde Sandstone, Piceance Basin, Colorado." SPE Formation Evaluation 2(02): 129-136.

Somerton, W. H., et al. (1975). "Effect of stress on permeability of coal." International Journal of Rock Mechanics and Mining Sciences & Geomechanics Abstracts 12(5–6): 129-145.

Sonnenthal, E. Chapter 5 in: Birkholzer, J. Rutqvist, E. Sonnenthal, and D. Barr, Long-Term Permeability/Porosity Changes in the EDZ and Near Field due to THM and THC Processes in Volcanic and Crystalline-Bentonite Systems, DECOVALEX-THMC Project Task D Final Report, 2008.

Spencer, C. W. (1989). "Review of characteristics of low-permeability gas reservoirs in western United States." AAPG Bulletin 73(5): 613-629.

Tanikawa, W. and T. Shimamoto (2009). "Comparison of Klinkenberg-corrected gas permeability and water permeability in sedimentary rocks." International Journal of Rock Mechanics and Mining Sciences 46(2): 229-238.

Thomas, R. D. and D. C. Ward (1972). "Effect of overburden pressure and water saturation on gas permeability of tight sandstone cores." Journal of Petroleum Technology 24(02): 120-124.

Tournassat, C., Appelo, C.A.J., 2011. Modelling approaches for anion-exclusion in compacted Na-bentonite. Geochimica et Cosmochimica Acta 75, 3698-3710.

Tsang, C.-F., et al. (2005). "Geohydromechanical processes in the Excavation Damaged Zone in crystalline rock, rock salt, and indurated and plastic clays—in the context of radioactive waste disposal." International Journal of Rock Mechanics and Mining Sciences 42(1): 109-125.

Tsang, C.-F., J.D. Barnichon, J.T. Birkholzer, , X.L. Li, H.H. Liu, X. Sillen, and T. Vietor. (2012). Coupled Thermo-Hydro-Mechanical Processes in the Near-Field of a High-Level Radioactive Waste Repository in Clay Formations. International Journal of Rock Mechanics and Mining Sciences 49: 31-44

Vairogs, J., et al. (1971). "Effect of rock stress on gas production from low-permeability reservoirs." Journal of Petroleum Technology 23(09): 1,161-161,167.

van Genuchten, M.T. 1980. A closed-form equation for predicting the hydraulic conductivity of unsaturated soils. Soil Science Society of America Journal 44, : 892-898.

Vietor T. (2012).Mont Terri Project - FE Experiment Modelling Kick-off Meeting. February 9, 2012, Mont Terri, Switzerland. NAGRA Technical Discussion TD-217

Vilarrasa, V., Bolster, D., Olivella, S. and Carrera, J. (2010). Coupled hydromechanical modeling of CO2 sequestration in deep saline aquifers. Int J Greenhouse Gas Control, 4, 910-919.

Villar, M.V. (2012) THM Cells for the HE-E Test: Setup and First Results; PEBS Report D2.2.7a. CIEMAT Technical Report CIEMAT/DMA/2G210/03/2012; Euratom 7th Framework Programme Project: PEBS: Madrid, Spain.

Villar, M.V., P.L. Martín, and F.J. Romero. 2014. Long-term THM tests reports: THM cells for the HE-E test: Update of results until February 2014. CIEMAT Technical Report, CIEMAT/DMA/2G210/2014.

Volckaert, G., Bernier, F., Sillen, X., Van Geet, M., Mayor, J.-C., Göbel, I., Blümling, P., Frieg, B. and Su, K. (2004). Similarities and Differences in the Behaviour of Plastic and Indurated Clays, The Sixth European Commission Conference on 'The Management and Disposal of Radioactive Waste: Euradwaste '04', held on 29-31 March 2004 in Luxembourg.

Walls, J. D., et al. (1982). "Effects of pressure and partial water saturation on gas permeability in tight sands: experimental results." Journal of Petroleum Technology 34(04): 930-936.

Walsh, J. and W. Brace (1984). "The effect of pressure on porosity and the transport properties of rock." Journal of Geophysical Research: Solid Earth (1978–2012) 89(B11): 9425-9431.

Wang W, Xie M, Nowak T, Kunz H, Shao H, Kolditz O (2006) Modeling THM coupled problem of Task D of the DECOVALEX project. Proc. GEOPROC2006 International symposium: 2nd International Conference on Coupled Thermo-hydro-mechanical-chemical processes in Geosystems and Engineering, HoHai University, Nanjing, China, May 22-25, 2006, 226–232, HoHai University.

Wang, H., A. Thiele, L. Pilon, 2013, Simulations of cyclic voltammetry for electric double layers in asymmetric electrolytes: A generalized modified Poisson-Nernst-Planck model. Journal of Physical Chemistry 117: 18286-18297.

Wang, Y. (2011). Research & Development (R&D). Plan for Used Fuel Disposition Campaign (UFDC). Natural System Evaluation and Tool Development, U.S. DOE Used Fuel Disposition Campaign.

Wei, K., et al. (1986). "Effect of Fluid Confining Pressure and Temperature on Absolute Permeabilities of Low-Permeability Sandstones." SPE Formation Evaluation 1(04): 413-423.

Wersin P., Johnson, L.H. and McKinley, I.G. (2007) Performance of the bentonite barrier at temperature beyond 100oC: A critical review, Physics and Chemistry of the Earth 32: 780-788.

Wersin, P., Curti, E. and Appelo, C.A.J., 2004. Modelling bentonite-water interactions at high solid/liquid ratios: swelling and diffuse double layer effects. Applied Clay Science 26, 249-257.

Wibberley, C. A. and T. Shimamoto (2005). "Earthquake slip weakening and asperities explained by thermal pressurization." Nature 436(7051): 689-692.

Wieczorek, K., Miehe, R. (2010): Measurement of Thermal Parameters of the HE-E Buffer Materials, Deliverable D2.2-5 of the PEBS project.

Wieczorek, K., R. Miehe, and B. Garitte. 2013. Thermal characterisation of HE-E buffer. PEBS, FP7 24968.

Witherspoon, P., et al. (1980). "Validity of cubic law for fluid flow in a deformable rock fracture." Water Resources Research 16(6): 1016-1024.

Wolery, T. J., 1993. EQ3/6, A software package for geochemical modelling of aqueous systems, Version 7.2. Lawrence Livermore National Laboratory, USA.

Wu, W.-J. and J.-J. Dong (2012). "Determining the maximum overburden along thrust faults using a porosity versus effective confining pressure curve." Tectonophysics 578(0): 63-75.

Wyble, D. (1958). "Effect of Applied Pressure on the Conductivity Porosity and Permeability of Sandstones." Journal of Petroleum Technology 10(11): 57-59.

Xu, T., Sonnenthal, E. Spycher, N., Pruess, K., 2006. TOUGHREACT, A simulation program for non-isothermal multiphase reactive geochemical transport in variably saturated geologic media. Computers and Geosciences 32, 145-165.

Xu, T., Spycher, N., Sonnenthal, E., Zhang, G., Zheng, L. and Pruess, K. (2011) TOUGHREACT Version 2.0: A simulator for subsurface reactive transport under non-isothermal multiphase flow conditions. Computers & Geosciences 37(6): 763-774.

Yale, D. P. and A. Nur (1985). Network modeling of flow storage and deformation in porous rocks. 1985 SEG Annual Meeting, Society of Exploration Geophysicists.

Zhang, K., Wu, Y.S., Bodvarsson, G.S. and Liu, H.H. (2004). Flow focusing in unsaturated fracture networks: a numerical investigation. Vadose Zone Journal, 3, 624-633.

Zhao, Y. and H.-H. Liu (2012). "An Elastic Stress–Strain Relationship for Porous Rock Under Anisotropic Stress Conditions." Rock mechanics and rock engineering 45(3): 389-399.

Zheng, L., J. Samper and L. Montenegro 2011. A coupled THC model of the FEBEX in situ test with bentonite swelling and chemical and thermal osmosis. Journal of Contaminant Hydrology 126(1–2): 45-60.

Zheng, L., Li, L., Rutqvist, J., Liu, H. and Birkholzer, J.T., (2012). Modeling Radionuclide Transport in Clays. Lawrence Berkeley National Laboratory. FCRD-URD-2012-000128

Zimmerman, R. and G. Bodvarsson (1996). "Hydraulic conductivity of rock fractures." Transport in Porous Media 23(1): 1-30.

Zhu, C., 2005. Feldspar dissolution in saturated aquifers, in situ rates. Geochimica et Cosmochimica Acta 69(6), 1435-1453.

Update on Experimental Activities on Buffer/Backfill Interactions at elevated Pressure and Temperature

(PART III)

1. Introduction

The United States has initiated the Used Fuel Disposition Campaign to evaluate various generic geological repositories for the permanent disposal of used nuclear fuel. The development and evaluation of engineered barrier system (EBS) design concepts and their potential interactions with the natural barrier or with other EBS interfaces are inherently important to the long-term (i.e., tens of thousands of years) safety and performance of geological repositories (Jove Colon et al. 2011; Nutt et al. 2011). One of the more commonly proposed ideas for high-level nuclear waste repository is to surround waste canisters with bentonite in an underground repository (Pusch 1979; Meunier et al. 1998). There have been numerous investigations on the stability of bentonites under various repository conditions and in contact with various metals replicating possible canister compositions (Pusch 1979; Madsen 1998; Meunier et al. 1998; Guillaume et al. 2003; Wersin et al. 2007; Mosser-Ruck et al. 2010; Ferrage et al. 2011). However, there remain uncertainties regarding the long-term stability of bentonite EBS and corrosion products under potential repository conditions. The focus of this experimental work is to expand our understanding of the stability of bentonite barriers under different geochemical, mineralogical, and engineering conditions than what has been previously investigated. Alteration of smectite to other minerals (i.e., illite, illite/smectite, chlorite), steam-induced swelling loss, and interaction of smectite with metal waste canisters are some of the more prevalent concerns (Couture 1985; Wersin et al. 2007; Mosser-Ruck et al. 2010).

The exact barrier concept has yet to be determined, but the U.S. has considered the possible use of dual purpose canisters for storage and subsequent disposal (Greenberg and Wen 2013). At present, dual purpose canister designs vary greatly, but, in most cases, canisters will be constructed from steel or stainless steel with a steel reinforced concrete overpack (IAEA 2000). In some designs, copper cladding can be added on to the steel canister (Pusch 2008). These canisters can have up to 32 spent fuel assemblies (32 pressurized water reactors or 32-PWR), while many of the European concepts are limited to four spent fuel assemblies (4-PWR) (Pusch 2008; Greenburg and Wen 2013). This increased number of spent fuel assemblies will generate a greater amount of heat radiating into the host rock. High-level modeling suggests a 32-PWR waste package (at 60 gigawatt-days per metric ton burnup) disposed in a clay/shale host rock, has the potential to reach 299°C after 85 years within 1 meter from the waste package (25 years ventilation; 15 m package spacing; Greenberg and Wen 2013). These results are just one of many models or designs for a U.S. nuclear repository, but, this particular model provides one possible high temperature scenario (Figure 1).

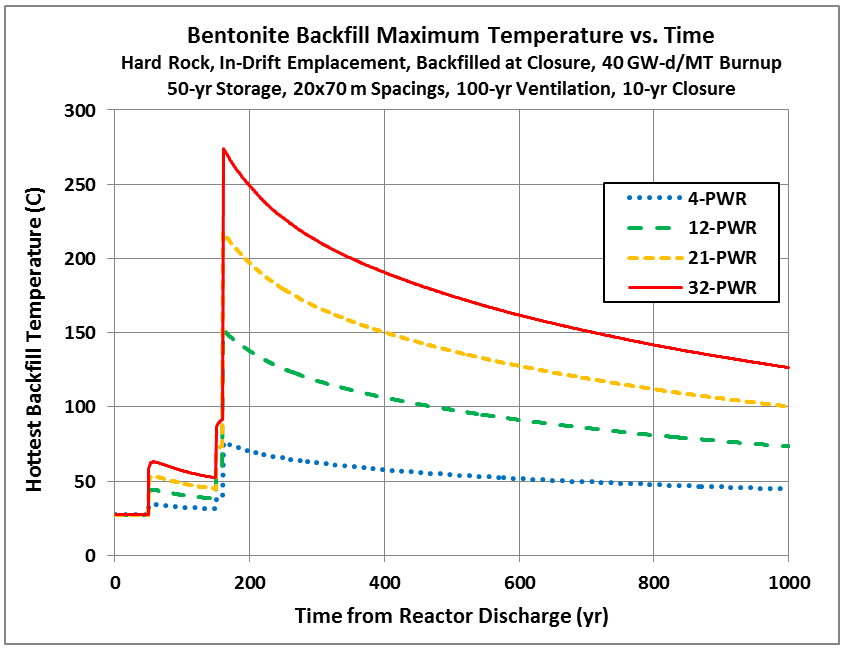

Figure 1. Bounding backfill temperature histories at the waste package surface, for in-drift emplacement in crystalline rock (2.5 W/m-K) with a compacted bentonite backfill (0.6 W/m-K). Backfill rehydration is neglected as a bounding approximation. Waste packages with various capacities are plotted, for fuel with 40 GW-d/MT burnup. For this comparative calculation all packages would be stored at the surface 50 years, then ventilated in the repository 100 years, and finally backfilled over a period of 10 years before permanent closure (personal communication from Ernest Hardin).

One of the more commonly proposed ideas for permanent high-level nuclear waste disposal is to emplace the steel waste canister in a geological repository with a bentonite barrier between the canister and host rock (Pusch 1979; Meunier et al. 1998). Bentonite is used to provide a physical barrier to prevent fluid seeping in from natural surroundings and interacting with the waste package, while acting as a chemical barrier by attenuating actinide migration if a release occurs. Additionally, the bentonite's swelling capacity has the capability of self-sealing if cracks develop within the bentonite due to shrink-swell phenomena. However, there remain uncertainties regarding the long-term stability of bentonite under potential repository conditions, particularly, under prolonged periods of high thermal loads. There have been numerous investigations on the stability of bentonites under various repository conditions and in contact with various metals replicating possible canister compositions (Pusch 1979; Madsen 1998; Meunier et al. 1998; Guillaume et al. 2003; Wersin et al. 2007; Mosser-Ruck et al. 2010; Ferrage et al. 2011).

This report addresses the various authigenic minerals occurring within unprocessed Wyoming bentonite, clay/metal interface, clay/host rock reactions during hydrothermal investigations replicating a high temperature repository-like environment. Much of the characterization and discussion on the early EBS (1-12) results have been published in Cheshire et al. (2013; 2014a). Further analyses on EBS-1 through -12 have been included to better describe the processes that progress during the hydrothermal reactions. In addition to expanded analyses of the earlier reactions, experiments on host-rock interaction and post-heat cooling were conducted to further our understanding of this complex system.

2. Methods

2.1 Experimental setup

The bentonite used in this experimental work is mined from a reducing horizon in Colony, Wyoming. The bentonite was pulverized and sieved to < 3 mm and used with a free moisture of ~15.5 wt. %. The synthetic groundwater solution was chosen to replicate a deep groundwater composition (Table 1, Stripa sample V2 (69-4), Frape et al. 2003). The groundwater solution was prepared using reagent grade materials dissolved in double deionised water. NaOH and HCl were added to adjust the initial solution pH. This solution was then filtered through a 0.45 μm filter and sparged with He before each experiment. The salt solution was added at 9:1 water: bentonite ratio. Initial components for all experiments have been summarized in Table 3.

A second series of experiments were performed to examine the bentonite system with host rock inclusion. Host-rock experiments focused on Opalinus Clay from the Swiss Underground Research Laboratory located at Mont Terri. The core was collected from BFE-A10 drillcore (interval from 11 to 12 m and interval from 33 to 34 m from the borehole head). A portion of the Opalinus Clay was crushed and sieved with 10 mesh (~2 mm). Opalinus Clay to be used in experiments was reconstituted at 80 wt.% -10 mesh and 20 wt.% +10 mesh. Synthetic groundwater was chosen to replicate the groundwater composition that represents Opalinus Clay porewater (Table 2, Pearson et al., 2003). The salt solution was added at 9:1 water: rock ratio.

Table 1. Synthetic groundwater chemistries used in the hydrothermal experiments. All values were measured at 25°C.

Species	Stripa V2.1 mg/L	Stripa V2.2 mg/L	Stripa V2.3 mg/L	Stripa V2.4 mg/L
Ca^{2+}	93	95	43	61
Cl^{-}	931	455	686	882
K^{+}	583	9	299	559
Na^{+}	171	166	162	201
Si	1	2	2	1
SO_4^{2-}	46	48	31	53
Sr^{2+}	0.05	<0.05	<0.05	0.06
TDS	1863	773	1226	1759
pH	7.35	9.48	6.93	11.2
Experiment Used	EBS 1-5	EBS 6-9	EBS 10-12	EBS 13, 16

Table 2. Synthetic groundwater chemistry used in the Opalinus Clay experiments. All values were measured at 25°C. n.m. = not measured

	Type Solution	**Actual Solution**
Species	mg/L	mg/L
Ca^{2+}	421	426
Cl^{-}	5672	6470
CO_3^{2-}	162	n.m.
K^{+}	221	225
Na^{+}	3885	3846
Si	5	1
SO_4^{2-}	2305	998
Sr^{2+}	27	0.16
TDS	11502	12153
pH	7.24	7.50
Experiment Used		EBS 14, 15, 17

The redox conditions for each system were buffered using a 1:1 mixture (by mass) of Fe_3O_4 and Fe° added at 0.07 wt. % of the bentonite mass. Approximately 7 wt. % (of total solids mass) 304 stainless steel (NIST SRM 101g), 316 stainless steel (NIST SRM 160b), Cu-foil, and low-carbon steel (provided by Sandia National Laboratory) were added to the experiments to mimic the presence of a waste canister.

Reactants were loaded into either a flexible gold or titanium bag and fixed into a 500 mL Gasket Confined Closure reactor (Seyfried et al. 1987). Experiments were pressurized to 150 - 160 bar and were heated following three different temperature profiles: 1) 120°C for 2 weeks, 210°C for 2 weeks, and then 300°C for 1 week, 2) isothermal at 300 °C for 6 weeks and 3) 300°C for 4 months, 210°C for 1 month, and 120°C for 1 month. Reaction liquids were extracted during the experiments and analyzed to investigate the aqueous geochemical evolution in relationship to mineralogical alterations. The sampled reaction liquids were split three-ways producing aliquots for unfiltered anion, unfiltered cation, and filtered (0.45 μm syringe filter) cation determination. All aliquots were stored in a refrigerator at 1°C until analysis.

2.2 Capsule Experiment Setup

A series of small reactions were run within the pressure media of the major reaction vessels. These reaction series are designed as controls and bounding conditions on the bentonite stability. An advantage of these experiments is that many different geochemical parameters may be tested under the same parent EBS reaction conditions. Reactants listed in Table 4 and 5 were loaded in gold tubes, crimped, and welded shut. Each gold capsule was heated to 105°C for about 1 hour to

determine if mass loss occurred. If mass loss was observed, the capsules were not sealed and the setup was repeated until the system was sealed. The sealed capsules were included into the surrounding pressure media for each EBS experiment. Following experiment shut down, each capsule was washed and weighed to determine if they leaked during the experiment. Capsules that did not leak were then cut open and their contents were dispersed in deionized (DI) H_2O and washed 2 – 3 times to remove any soluble salts. Washed samples were then redispersed in DI H_2O and pipetted onto a zero-background quartz plate for X-ray diffraction (XRD) analyses. XRD methods and data interpretations are described below in the XRD methods section below.

	Clay, g	Brine, g	pH	Fe°, g	Fe_3O_4, g	Accessory, g	EBS Component	Run temp, °C	Run time
EBS-1	7.4	79.0	8.59	0.257	0.252	na	na	25/100/200/300/25	4 weeks
EBS-2	7.2	62.0	8.59	0.251	0.253	4.980	304SS	25/100/200/300/25	4 weeks
EBS-3	6.790	59.4	7.56	0.255	0.261	4.245	316SS	25/100/200/300/25	5 weeks
EBS-4	16.207	145.0	7.56	0.574	0.579	9.753	Cu	25/100/200/300/25	5 weeks
EBS-5	15.770	135.9	6.73	0.505	0.505	11.189	304SS	300	6 weeks
EBS-6	12.109	104.2	9.48	0.424	0.424	8.375	Low-C Steel	25/100/200/300/25	5 weeks
EBS-7	14.627	157.9	6.69	0.589	0.586	3.656	Graphite	25/100/200/300/25	5 weeks
EBS-8	15.284	131.9	7.72	0.489	0.489	10.816	Cu	300	6 weeks
EBS-9	15.516	167.6	7.16	0.625	0.625	3.878	Quartz sand	25/100/200/300/25	5 weeks
EBS-10	21.105	182.3	6.36	0.675	0.675	14.937	316SS	300	6 weeks
EBS-11	15.039	129.8	6.74	0.481	0.481	10.643	Cu	300	6 weeks
EBS-12	208.5	41.7	6.74	na	na	na	none	300	7 weeks

	Clay, g	Brine, g	pH	Fe°, g	Fe_3O_4, g	Accessory, g	EBS Component	Run temp, °C	Run time
EBS-13	29.621	245.3	11.0	0.950	0.951	13.304	316 SS	300 to 120	6 months
EBS-16	29.620	248.3	11.2	0.948	0.945	20.936	Cu	300 to 120	6 months

	Clay, g	Brine, g	pH	Fe°, g	Fe_3O_4, g	Accessory, g	EBS Component	Run temp, °C	Run time
EBS-14	14.858	128.1	7.5	0.476	0.476	na	na	300	6 weeks
EBS-15	14.715	158.5	7.6	0.588	0.589	3.679/12.633	Opalinus Clay/316SS	300	6 weeks
EBS-17	14.437	155.2	7.5	0.578	0.575	3.608/12.205	Opalinus Clay/Cu	300	6 weeks

Table 3. Initial components and reaction conditions for EBS experiments. EBS-8 developed a leak during experiment. This experiment was discarded and was repeated as EBS-11.

	Clay,	Clay Type	Accessory Type	Brine,	Solution Type	Run temp,	Run	Rxn
CAP-1	0.020	-2 µm, K-		0.185	Stripa V2.3 Low-	300	6 weeks	EBS-
CAP-2	0.020	-2 µm, K-		0.220	K-sat Brines	300	6 weeks	EBS-
CAP-3	0.021	-2 µm, K-		0.271	Ca-sat Brines	300	6 weeks	EBS-
CAP-4	0.019	WY Bentonite		0.186	Stripa V2.3 Low-	300	6 weeks	EBS-
CAP-5	0.019	WY Bentonite		0.222	K-sat Brines	300	6 weeks	EBS-
CAP-6	0.018	WY Bentonite		0.276	Ca-sat Brines	300	6 weeks	EBS-
CAP-	0.019	-2 µm, K-		0.197	K-Al brine	300	6 weeks	EBS-
CAP-	0.021	-2 µm, K-		0.198	Ca-Al brine	300	6 weeks	EBS-
CAP-	0.020	-2 µm, K-		0.265	Ca-sat Brines	300	6 weeks	EBS-
CAP-	0.018	WY Bentonite		0.199	K-Al brine	300	6 weeks	EBS-
CAP-	0.020	WY Bentonite		0.199	Ca-Al brine	300	6 weeks	EBS-
CAP-	0.020	WY Bentonite		0.251	K-Al Citric	300	6 weeks	EBS-
CAP-	0.020	WY Bentonite		0.254	Ca-Al Citric	300	6 weeks	EBS-
CAP-	0.022	-2 µm, K-		0.199	Ca-Al brine	300	6 weeks	EBS-
CAP-	0.020	WY Bentonite	5% IMt-2 Illite	0.184	Stripa V2.3 Low-	300	6 weeks	EBS-
CAP-	0.020	WY Bentonite	15% IMt-2 Illite	0.185	Stripa V2.3 Low-	300	6 weeks	EBS-
CAP-	0.020	WY Bentonite	25% IMt-2 Illite	0.185	Stripa V2.3 Low-	300	6 weeks	EBS-
CAP-	0.020	WY Bentonite	5% Montana I/S	0.185	Stripa V2.3 Low-	300	6 weeks	EBS-
CAP-	0.021	WY Bentonite	15% Montana I/S	0.185	Stripa V2.3 Low-	300	6 weeks	EBS-
CAP-	0.020	WY Bentonite	25% Montana I/S	0.215	Stripa V2.3 Low-	300	6 weeks	EBS-

Table 4. Initial components and reaction conditions for capsule experiments.

	Clay,	Clay Type	Accessory Type	Brine,	Solution Type	Run temp,	Run	Rxn
CAP-	0.020	-2 µm, K-		0.234	K-sat Brines	300 to 120	6 months	EBS-
CAP-	0.020	-2 µm, K-		0.233	K-sat Brines + DI	300 to 120	6 months	EBS-
CAP-	0.020	-2 µm, K-		0.227	Ca-sat Brines	300 to 120	6 months	EBS-
CAP-	0.020	-2 µm, K-		0.243	Ca-sat Brines + DI	300 to 120	6 months	EBS-
CAP-	0.020	WY Bentonite		0.233	K-sat Brines	300 to 120	6 months	EBS-
CAP-	0.021	WY Bentonite		0.233	K-sat Brines + DI	300 to 120	6 months	EBS-
CAP-	0.021	WY Bentonite		0.282	Ca-sat Brines	300 to 120	6 months	EBS-
CAP-	0.021	WY Bentonite		0.212	Ca-sat Brines + DI	300 to 120	6 months	EBS-
CAP-	0.021	-2 µm, Ca-		0.232	K-sat Brines	300 to 120	6 months	EBS-
CAP-	0.021	-2 µm, Ca-		0.234	K-sat Brines + DI	300 to 120	6 months	EBS-
CAP-	0.021	-2 µm, Ca-		0.275	Ca-sat Brines	300 to 120	6 months	EBS-
CAP-	0.021	-2 µm, Ca-		0.229	Ca-sat Brines + DI	300 to 120	6 months	EBS-
CAP-	0.020	-2 µm, Bentonite	10% K-feldspar	0.185	Stripa V2.4 Low-	300	6 weeks	EBS-
CAP-	0.020	-2 µm, Bentonite	20% K-feldspar	0.187	Stripa V2.4 Low-	300	6 weeks	EBS-
CAP-	0.019	-2 µm, Bentonite	10% albite	0.186	Stripa V2.4 Low-	300	6 weeks	EBS-
CAP-	0.020	-2 µm, Bentonite	20% albite	0.187	Stripa V2.4 Low-	300	6 weeks	EBS-
CAP-	0.021	-2 µm, Bentonite	10% muscovite	0.189	Stripa V2.4 Low-	300	6 weeks	EBS-
CAP-	0.020	-2 µm, Bentonite	20% muscovite	0.188	Stripa V2.4 Low-	300	6 weeks	EBS-
CAP-	0.020	-2 µm, Bentonite	10% Grimsel granite	0.189	Stripa V2.4 Low-	300	6 weeks	EBS-
CAP-	0.021	-2 µm, Bentonite	20% Grimsel granite	0.189	Stripa V2.4 Low-	300	6 weeks	EBS-
CAP-	0.022	-2 µm, Bentonite	30% Grimsel granite	0.188	Stripa V2.4 Low-	300	6 weeks	EBS-

Table 5. Initial components and reaction conditions for capsule experiments

2.3 Mineral analyses

X-ray diffraction (XRD) analyses of experimental materials determined mineral compositions. Each sample was ground with 20 wt. % corundum (Al_2O_3) for quantitative XRD analysis of the bulk rock (Chung 1974). XRD measurements were conducted with a Siemens D500 diffractometer using Cu-Kα radiation. Data were collected from 2 to 70 °2θ with a 0.02 º2θ step-size and count times of 8 to 12 seconds per step. To better analyze the non-clay and clay fractions, the < 2 μm particles were separated via sedimentation in DI H_2O. An aliquot of the < 2 μm suspension was dropped on a zero-background quartz plate and dried. This oriented mount was X-rayed from 2 to 40 °2θ at 8 to 12 s per step. The oriented mount was then saturated with ethylene glycol in a 60 °C oven for 24 hours and XRD analysis was repeated. A portion of the > 2 μm particles was ground with a mortar/pestle, deposited on a zero-background quartz plate, and X-rayed under the same parameters as the bulk powder material. The remaining > 2 μm portion was used for electron microscopy. Mineral identification and unit-cell parameters analysis was performed using Jade© 9.5 X-ray data evaluation program with ICDD PDF-4 database. Quantitative phase analysis was performed using FULLPAT (Chipera and Bish 2002). Illite-smectite composition of higher-ordered (R1-3) illite-smectites were modeled via ClayStrat+ (developed by Hongji Yuan and David Bish). Expandable component abundances for the disordered illite-smectites were calculated via the Δ°2Θ method (Środoń 1980; Eberl et al. 1993; Moore and Reynolds 1997). A regression from calculated data were used to calculate the % expandable (%Exp) component in each untreated and reacted bentonite. The equations are:

$$\%Exp = 973.76 - 323.45\Delta + 38.43\Delta^2 - 1.62\Delta^3$$ (Eberl et al. 1993, Eq. 3, R^2=0.99),

with Δ corresponding to Δ°2Θ between the 002 and 003 peak positions for the oriented, ethylene glycol saturated samples.

X-ray florescence (XRF) analysis of the experimental materials was performed using a Rigaku ZSX Primus II. Samples were mixed with Li-metaborate at 36:1 and fluxed at 1100° C for 45 minutes. All reported values exceed three times the reported detection limits. Loss on ignition (LOI) was determined by heating the sample to 1000°C for 30 minutes.

Analytical electron microscopy was performed using a FEI™ Inspect F scanning electron microscope (SEM). All samples were Au/Pd-coated prior to SEM analysis. Imaging with the SEM was performed using a 5.0 kV accelerating voltage and 1.5 spot size. Energy dispersive X-ray spectroscopy (EDX) was performed at 30 kV and a 3.0 spot size.

Electron microprobe (EMP) analyses were performed at the University of Oklahoma using a Cameca SX50 electron microprobe equipped with five wavelength-dispersive spectrometers and PGT PRISM 2000 energy-dispersive X-ray detector. Petrographic characterization was performed by backscattered electron imaging coupled with energy-dispersive X-ray analysis, using beam conditions of 20 kV acceleration and 20 nA sample current. Quantitative analysis was performed by wavelength-dispersive spectrometry using 20 kV accelerating voltage, 20 nA beam current, and 2 μm spot size. Matrix corrections employed the PAP algorithm (Pouchou and Pichoir 1985), with oxygen content calculated by stoichiometry. Counting times were 30 seconds

on peak for all elements, yielding minimum levels of detection (calculated at 3-σ above mean background) in the range of 0.01 to 0.03 wt. % of the oxides for all components except F (0.16 wt. %). All standards for elements in the silicates were analyzed using 30 second count times on peak, using K-alpha emissions. The standards and oxide detection limits are presented in Appendix A, with analytical data presented in Appendix B.

Cation exchange capacity (CEC) determinations followed methods described by Busenberg and Clemency (1973). The < 2 µm fraction used in the XRD analyses was saturated with 1N ammonium acetate overnight. After which, samples were then washed with a 1N NH_4Cl solution followed with multiple DI H_2O/methanol rinses until chloride was not detected with a few drops of a 1N $AgNO_3$ solution. Each sample was air-dried and powered for CEC analyses. Prior to CEC measurements, an ammonia-mV calibration curve was developed for the ammonia probe with 10^{-2}, 10^{-3}, 10^{-4} and 10^{-5} M standard NH_4^+ solutions (Figure 2).

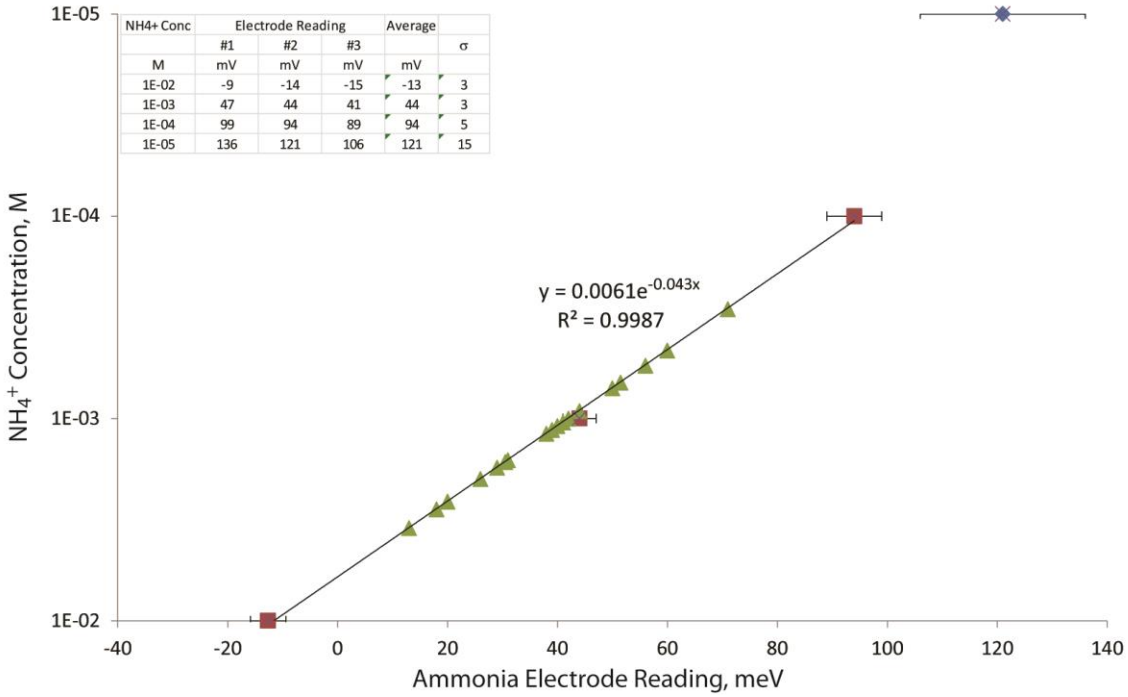

Figure 2. Ammonia-mV calibration curved of an ammonia electrode used for the CEC calculations. Red square data points were used to develop the calibration curve for each sample analysis (green triangles). All sample data points fall within the calibration boundaries.

20 – 200 mg of each NH_4-exchanged sample was dispersed in 50 ml DDI H_2O and constantly stirred with the ammonia electrode inserted into the suspension. Exactly 0.5 ml of 10M NaOH was added to the stirring suspension. Electrode readings were collected upon stabilization of the mV reading. CEC values were then calculated from the following equation:

$$CEC = \frac{(c)(v)}{(w)(f)}$$

where, CEC is cation exchange capacity of sample in mEq/100g of clay, c is concentration of ammonia in M, v is volume of water added, w is mass of sample (mg), f is a conversion factor of 10^{-5}.

To better determine the expandability of the post-reacted montmorillonites, the < 2 µm fractions were separately cation exchanged with Li^+, K^+, and Ca^{2+}. Each of these cations has differing hydration energies and charge densities. These exchanges should show subtle changes to the layer charge of the montmorillonite upon expansion with ethylene glycol due to the Coulombic interaction between the competing cation-layer attractive forces and interlayer cation hydration energies. About 0.5 g of < 2 µm fraction from starting bentonite and the post reacted bentonite were repetitively washed in 250 ml of 2 M LiCl, 2M KCl, and 1M $CaCl_2$. Following the salt washed, the cation exchanged materials were then washed in DI H_2O/ethanol until chloride was no longer detected with a few drops of a 1N $AgNO_3$ solution. Each sample was then redispersed in DI H_2O and pipetted onto a zero-background quartz plate for XRD analyses. Each cation-exchanged samples was then ethylene glycol saturated to expand the expandable layers and X-rayed. Expandability of each sample was then calculated via ClayStrat+.

2.4 Aqueous geochemical analyses

Major cations and trace metals were analyzed via inductively coupled plasma-optical emission spectrometry (Perkin Elmer Optima 2100 DV) and inductively coupled plasma-mass spectrometry (Elan 6100) utilizing EPA methods 200.7 and 200.8. Ultra-high purity nitric acid was used in sample and calibration preparation prior to sample analysis. Internal standards (Sc, Ge, Bi, and In) were added to samples and standards to correct for matrix effects. Standard Reference Material (SRM) 1643e Trace Elements in Water was used to check the accuracy of the multi-element calibrations. Inorganic anion samples were analyzed by ion chromatography (IC) following EPA method 300 on a Dionex DX-600 system. Aqueous geochemical results are presented in Appendix C.

3. Results

3.1 Analyses performed on samples from FY'12-FY'13

Electron microprobe chemical analyses for silicate constituents from EBS experiments are presented in Appendix B; Tables B1 to B7.

Cation exchange capacity determination was performed on the < 2 µm fraction of EBS-1 through EBS-11, in addition to the starting bentonite. The < 2 µm fraction was determined to be predominantly montmorillonite with minor amounts of opal-CT. Results are summarized in Table 6. There appears to be no significant CEC alteration of treated clays compared to the starting montmorillonite. This is a key parameter in understanding changes in layer charge associated with montmorillonite alteration. Increases in layer charge typically are associated with an increase in CEC to the point when Coulombic attraction dominates over swelling pressure and irreversible collapse occurs lowering the CEC values (based on these methods).

A select number of samples were chosen for cation exchange to quantify post-reacted montmorillonite's expandability. Results are summarized in Table 7. Samples labeled as a Na-exchanged montmorillonite are reaction products without further exchange treatments. Reaction

products typically are Na-based montmorillonite, but can have non-trivial amounts of K^+ and Ca^{2+} in the interlayer. Expandability data are consistent with reaction products' CEC values showing no significant alteration to the starting montmorillonite's layer charge.

Table 6. Expandability from cation-exchanged starting and post-reacted montmorillonite. Hydration energies were from Burgess (1978).

Interlayer Cation	$\Delta G_{hydration}$ kJ mol^{-1}	% Expandable			
		Bentonite	Ramped	Isothermal	"Dry"
K^+	-337	93	94	96	~*93*
Na^+	-411	100	100	100	100
Li^+	-511	n.d.	98	100	100
Ca^{2+}	-1593	98	96	98	n.d.

Table 7. CEC from the < 2 μm fraction of the starting bentonite and EBS reaction products. Some samples were run in duplicate.

	#1				#2				Average CEC	σ
	Mass *Mg*	**Reading** *eV*	**NH_4^+ conc** *M*	**CEC** *meq/100g*	**Mass** *mg*	**Reading** *eV*	**NH_4^+ conc** *M*	**CEC** *meq/100g*	**Average CEC** *meq/100g*	σ
Bentonite	78	40	0.0011	**70**	168	20	0.002581	**77**	**73**	5
EBS-1	21	71	0.0003	**69**					**69**	
EBS-2	52	51.5	0.0007	**64**					**64**	
EBS-3	145	26	0.0020	**69**	111	30.5	0.0016	**74**	**71**	4
EBS-4	79	41	0.0010	**66**	223	13	0.0035	**78**	**72**	8
EBS-6	127	31	0.0016	**63**	180	20	0.0026	**72**	**68**	6
EBS-7	88	38	0.0012	**68**	70	42	0.0010	**72**	**70**	3
EBS-9	71	44	0.0009	**65**	75	39	0.0011	**76**	**70**	8
EBS-5	129	29	0.0018	**68**	189	18	0.0028	**74**	**71**	5
EBS-10	53	50	0.0007	**67**	37	56	0.0006	**74**	**71**	5
EBS-11	33	60	0.0005	**70**					**70**	

3.2 "Dry" Bentonite Experiment – EBS-12

Various mineral alterations and textural developments occurred during the water limited experiment of EBS-12 that is significantly different from the fluid dominated experiments.

Bentonite compaction produced significant foliation of the montmorillonite particles (Figure 3A). Montmorillonite developed rough edges during the long-term cooling experiments due to what appears to be a partial dissolution, but maintained the typical foily smectite morphology (Figure 3A and B). Additionally, glycol saturated samples yielded d_{001} of 17 Å with higher order $d_{00\ell}$ consistent with integer values of the d_{001} values, suggesting the montmorillonite did not undergo extensive illitization.

Analcime and cristobalite were produced as a result of a partial dissolution/alteration of clinoptilolite and remnant volcanic glass. Clinoptilolite did not undergo complete dissolution yielding clinoptilolite with dissolution features (Figure 3C). Analcime occurs as 5 to 10 μm deformed spheres and cubes primarily from the agglomeration of nanometer-sized analcime particles (Figure 3D and E). Analcime morphology does indicate impeded growth due to the solids-dominated system forcing deformed crystal growth. Previous EBS experiments (i.e., w/r 9:1) displayed analcime with subhedral to euhedral trapezohedrons (Cheshire et al. 2013; 2014a). Growth of analcime appears to have been stopped due to the quenching of the reaction preserving the various stages of analcime ripening.

Silica precipitation was observed primarily as opal-CT or cristobalite forming spherical aggregates along the edges of the montmorillonite particles (Figure 3F). It is difficult to determine if the silica precipitation occurred during the heating phase or the quenching phase as solution chemistry was not able to be monitored during the experiment.

Pyrite did not appear to undergo decomposition or dissolution, with original cubic morphology was (Figure 3B). Much of the pyrite preservation might be due to the water limited environment, thereby restricting pyrite solubility. There is no evidence of other sulfide or sulfate formation.

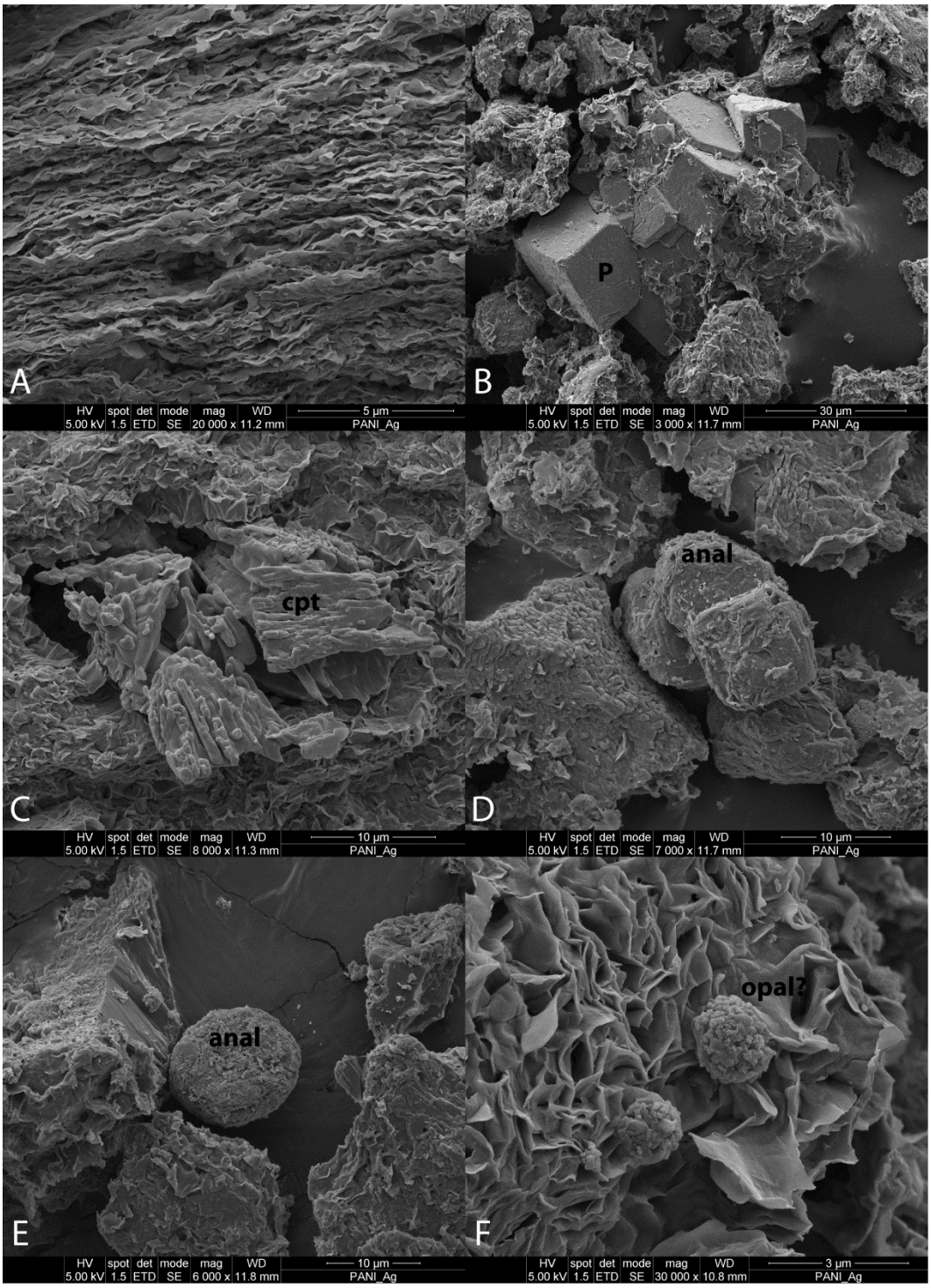

Figure 3. SEM images of reaction products from EBS-12. A) Bedding associated with the montmorillonite foils developed during pressurization in a fluid poor environment. B) Unaltered, cubic pyrite. C) Partially altered clinoptilolite showing dissolution features. D) Poorly formed analcime aggregates next to a partially altered clinoptilolite (lower left). E) Deformed analcime particle. F) Possible opaline nodule precipitated on montmorillonite edges.

3.3 Six-Month Cooling – EBS-13

3.3.1 Mineralogy. Mineral reactions observed in the six-month, cooling experiments are consistent mineral reactions in the ramped and isothermal experiments. Partial dissolution of the montmorillonite developed rough edges during the long-term cooling experiments, but maintained the typical foily smectite morphology (Figure 4A and B). However, the glycol saturated samples yielded d_{001} of 17 Å with higher order $d_{00\ell}$ consistent with integer values of the d_{001} values (Figure 5), suggesting the montmorillonite did not undergoes extensive illitization.

Analcime and cristobalite formation appears to be as a result of clinoptilolite dissolution and silica saturation with respect to cristobalite. 5 to 10 μm analcime particles (Figure 4D) have an average structural composition of $(Na_{0.64},Ca_{0.05})(Si_{2.23},Al_{0.76})O_6{\cdot}nH_2O$. Analcime growth appears to have been stopped due to the quenching of the reaction preserving the various stages of analcime ripening.

Odor of the aqueous samples and loss of pyrite in post-experiment samples suggests pyrite decomposition occurred during the experiments yielding $H_2S_{(aq,g)}$. Experiments containing stainless steel evolved $H_2S_{(g)}$ more readily, limiting sulfide-induced corrosion. Experiments with Cu° plates did not evolve substantial $H_2S_{(g)}$ due to chalcocite (Cu_2S) formation on Cu surfaces.

SEM examination of the bulk material and > 2 μm fraction indicates minor amounts of an authigenic fibrous mineral. These fibers occur as bundles or isolated fibers (Figure 4C). Fiber lengths span from 1.5 μm to 17.4 μm with widths ranging from 0.10 μm to 0.51 μm, producing aspect ratios (l/w) from 15.5 to 55.5. Chemical analyses of the discrete fibers were not collected due to the fiber thicknesses and the chemical contribution from the underlying montmorillonite.

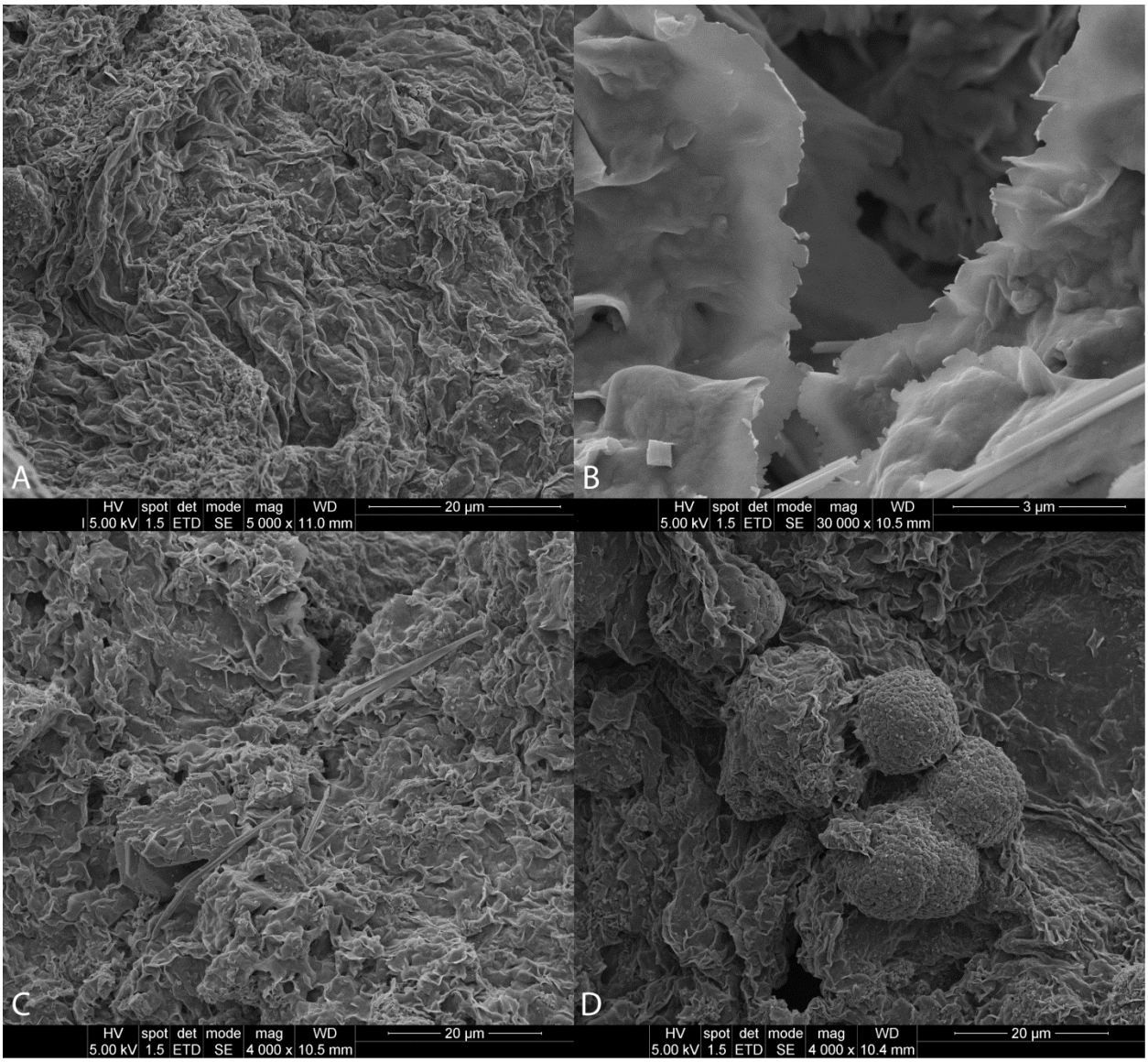

Figure 4. SEM images from EBS-13 bulk samples. A) Typical smectite foily morphology. B) Smectite edges with increased roughness possibly from partial dissolution during experiment. C) Foily smectite with fibrous/acicular minerals. Fiber identity is currently unknown but might be a zeolite or illite. D) Agglomerated nanometer-sized high-silica analcime particles showing spherical morphology.

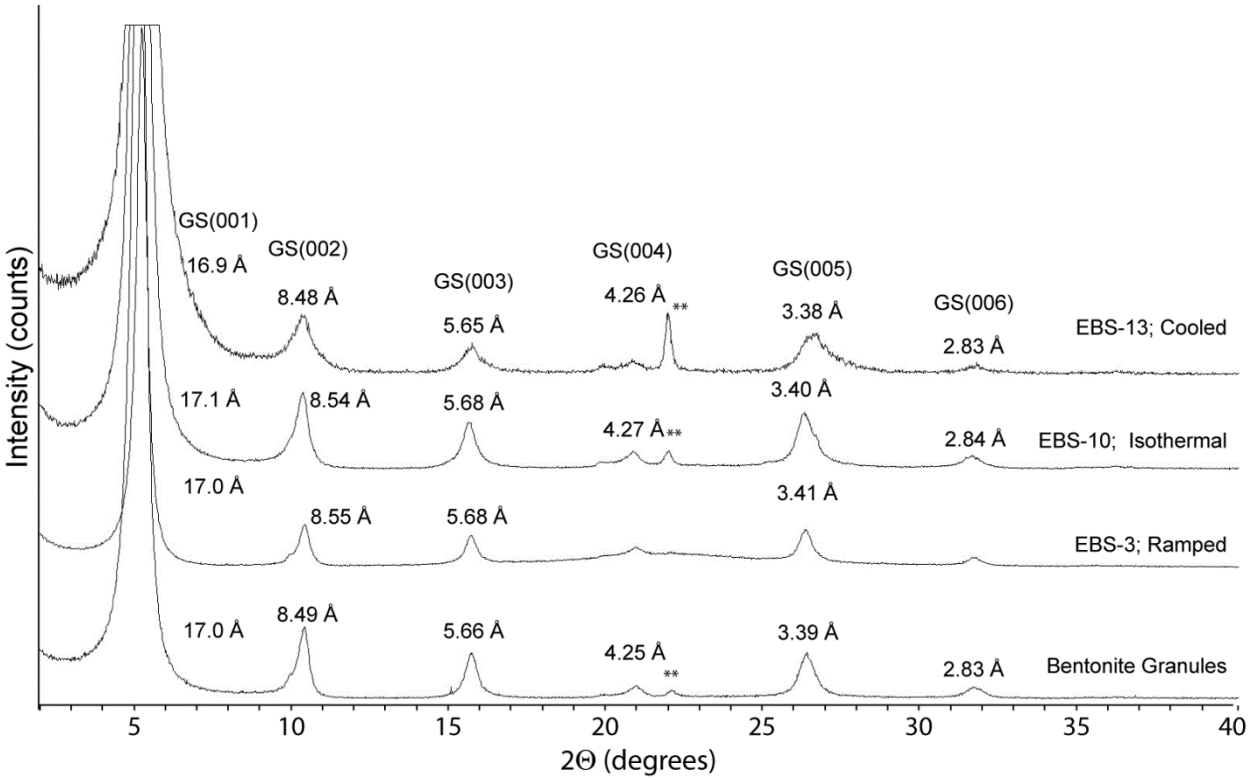

Figure 5. XRD patterns from the ethylene glycol saturated, oriented -2 µm fractions showing the effects of differing heating profile and duration on the montmorillonite fraction. ** represents opal-CT or cristobalite.

3.3.2 Solution Chemistry. Solution chemistry for the six-month (EBS-13) experiment is presented in Appendix C; Table C1 to C2. Changes to the solution chemistry are fairly consistent between the different EBS experiments. There is a Na^+ for K^+ exchange in the solution most likely controlled by the cation exchange capacity of both the Na-montmorillonite and clinoptilolite (Figure 6A). This cation exchange yielded a 274 - 470 mg/L Na^+ enrichment and 491 - 514 mg/L K^+ depletion in solution producing a K^+ enriched montmorillonite. However, this does not replace all Na^+ in the montmorillonite interlayer, thereby maintaining a Na-rich montmorillonite. Additionally, a 55.3 - 59.7 mg/L decline in the Ca^{2+} aqueous concentrations was observed during experiments mostly due to montmorillonite exchange.

Silica activity remained low during the 300°C stage of the six-month long experiment (Figures 6B). However, it is believed that silica precipitation occurred during storage at 1°C forcing an artificially low silica concentration. This is supported by the transparent solids at the bottom of the aqueous samples. Additionally, silica concentrations jumped up to 600 to 700 mg/L upon lowering reaction temperature to 220°C. Based on the other two experiments (EBS-3 and EBS-10); silica concentrations should have and probably reached 1,000 to 1,200 mg/L at 300°C (Figure 6B). Silica concentrations decreased incrementally following the temperature profile during the cooling stages of EBS-13. Partial smectite dissolution and clinoptilolite alteration are likely controls on silica activity.

Sulfur evolution is complicated by the occurrence of multiple redox states and interaction with metal plates (Figure 7). These probably contributed to the mixed results regarding sulfur concentrations. Past experiments showed in ramped experiments sulfur (as sulfate) increased from ~47 mg/L to ~125 mg/L until reactions temperatures reached 300°C, when sulfur values dropped to ~46 mg/L. However, during the 300°C experiments, sulfur concentrations steadily climbed to a ~191 mg/L. In the current experiments, sulfur ranged from 60 – 81 mg/L at 300°C, increased to 142 – 156 mg/L at 210°C, and slightly decreased to 123 - 129 mg/L at 120°C.

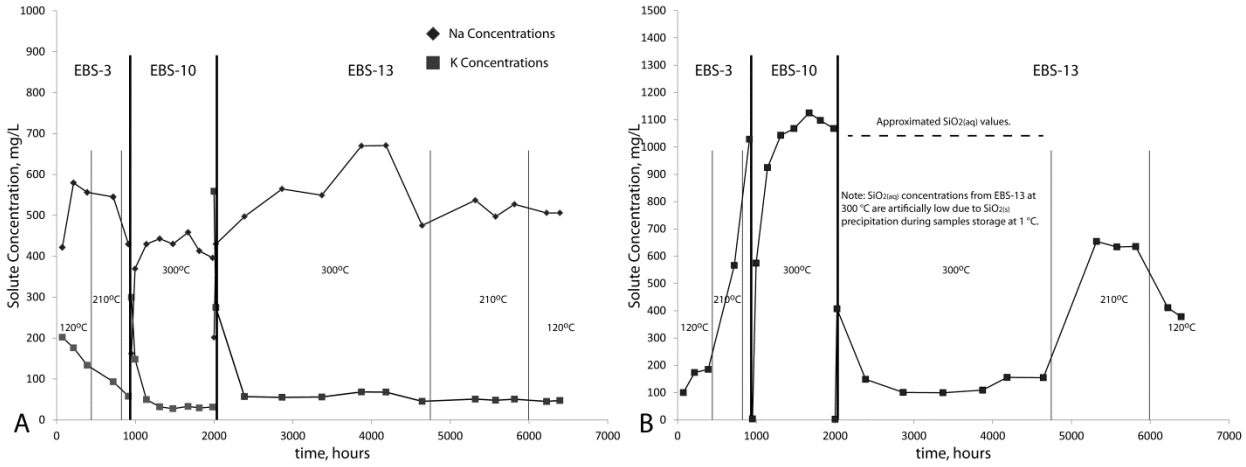

Figure 6. Solution chemistry evolution combining EBS-3, EBS-10, and EBS-13 showing full experimental heating profiles. Each experiment started with a fresh solution therefore slight discrepancies exist between each experimental solution profile. $SiO_{2(aq)}$ concentrations from EBS-13 at 300 °C are artificially low due to $SiO_{2(s)}$ precipitation during sample storage at 1 °C.

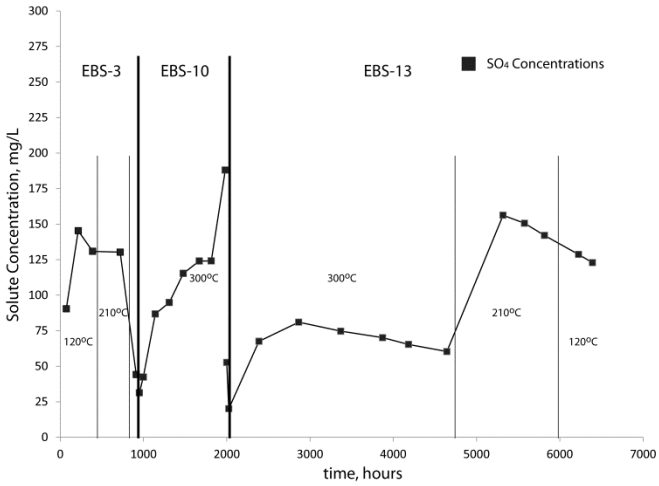

Figure 7. Sulfur (presented as sulfate) evolution combining EBS-3, EBS-10, and EBS-13 showing full experimental heating profiles. Each experiment started with a fresh solution therefore slight discrepancies exist between each experimental solution profile.

3.3.3 316 SS Corrosion. Chemical analyses for steel (EBS-5 and EBS-10) and copper (EBS-4 and EBS-11) corrosion products are presented in Appendix B; Tables B8 to B19. The initial 316 SS (NIST SRM 160b) is an iron alloy primarily with 18.37 wt. % Cr, 12.35 wt. % Ni, 2.26 wt. % Mo, 1.619 wt. % Mn, 0.5093 wt. % Si, and 0.175 wt. % Cu.

All systems containing stainless steel (304SS or 316SS) seem to behave similarly. Results from the six-month, 316SS experiment are indistinguishable from the previous two 316SS experiments (EBS-3 and EBS-10). Corrosion products associated with 316 SS were primarily smectite with minor occurrences of pentlandite ($(Ni, Fe)_9S_8$) (Figure 8). Smectite expands to 16.8 Å (with 002 at 8.44 Å) upon ethylene glycol saturation suggesting no significant amount of mixed-layering is present. XRD data (06l diffraction bands) and chemical analysis suggest that the smectite associated with 316SS corrosion is a Fe-saponite (Figures 9 and 11). The smectite morphology tends to be fairly consistent producing a bladed to micaceous habit with a rose-like texture (Figure 10). Chemical analyses of post-reaction 316SS and corrosion products indicates there was significant Fe and Ni leaching from the 316SS forming a chromite-like film on the stainless steel surface (Figure 11). Nickel leached from the stainless steel is partitioned into the sulfide phase. Fe-saponites were precipitated most likely from the iron leached from the 316 SS and the silica-rich fluid from the bentonite system. Fe-rich phyllosilicates that formed on steel plates in the ramped experiments have 06ℓ diffraction bands 1.535 Å (9.210 Å b-parameters), corresponding to a Fe-saponite (Figure 9; Kohyama et al. 1973; Moore and Reynolds 1997).

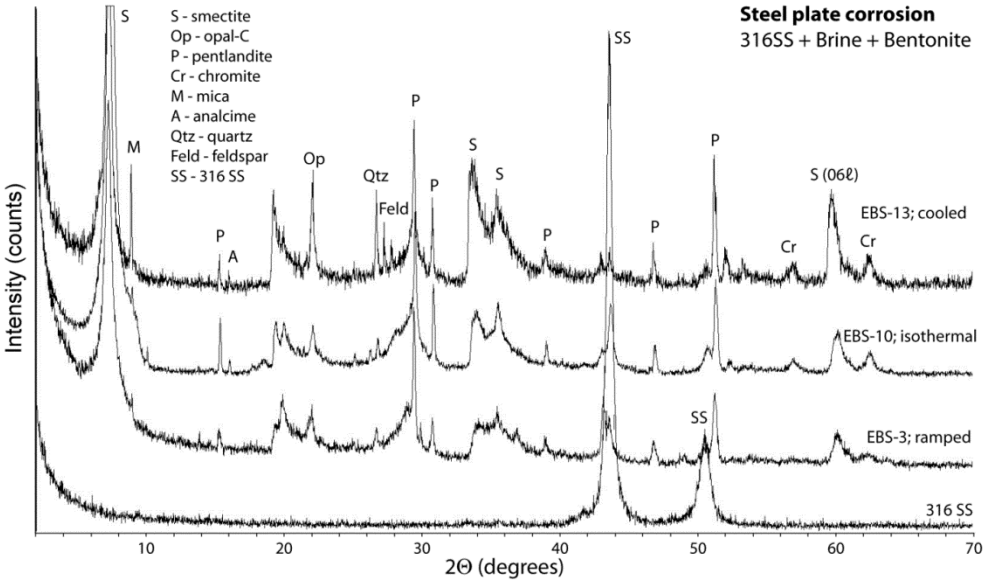

Figure 8. XRD patterns of the starting 316SS and corroded 316SS plates from EBS-3; -10; and -13. Fe-saponite is the dominate corrosion product associated with steel. Sulfide is the primary sink for leached Ni forming both pentlandite and millerite. Mica, analcime, quartz, and feldspars are from residual bentonite coating the steel plates.

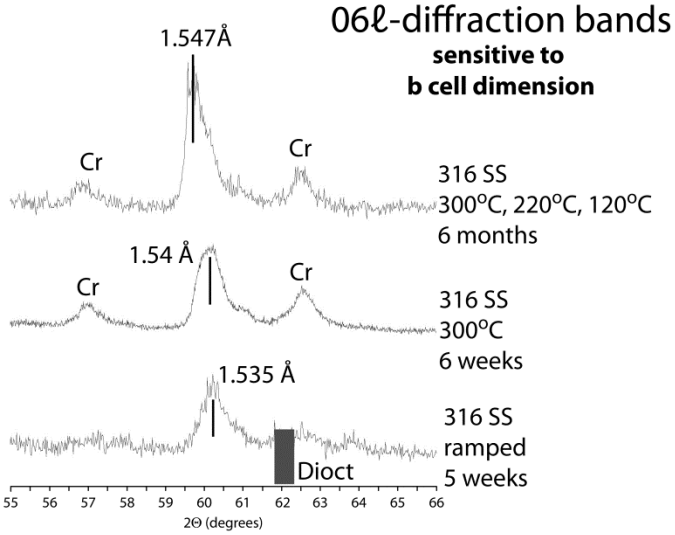

Figure 9. XRD plots of the showing the 06ℓ diffraction bands or Fe-rich smectite formed during EBS-3, EBS-10, and EBS-13. d-spacings ranging from 1.535 – 1.547 Å (9.210 - 9.282 Å *b* unit cell dimension) corresponding to trioctahedral phyllosilicates. Montmorillonite (dioctahedral) typically has a 1.492 – 1.504 Å (8.952 – 9.024 Å *b* unit cell dimension) 06ℓ band (red box). The smectite principally is a Fe-saponite with varying amounts of Ni and Cr substitutions. Chromite (Cr) signal is derived from the passivation layer developed on the 316SS surface from preferential Fe and Ni leaching.

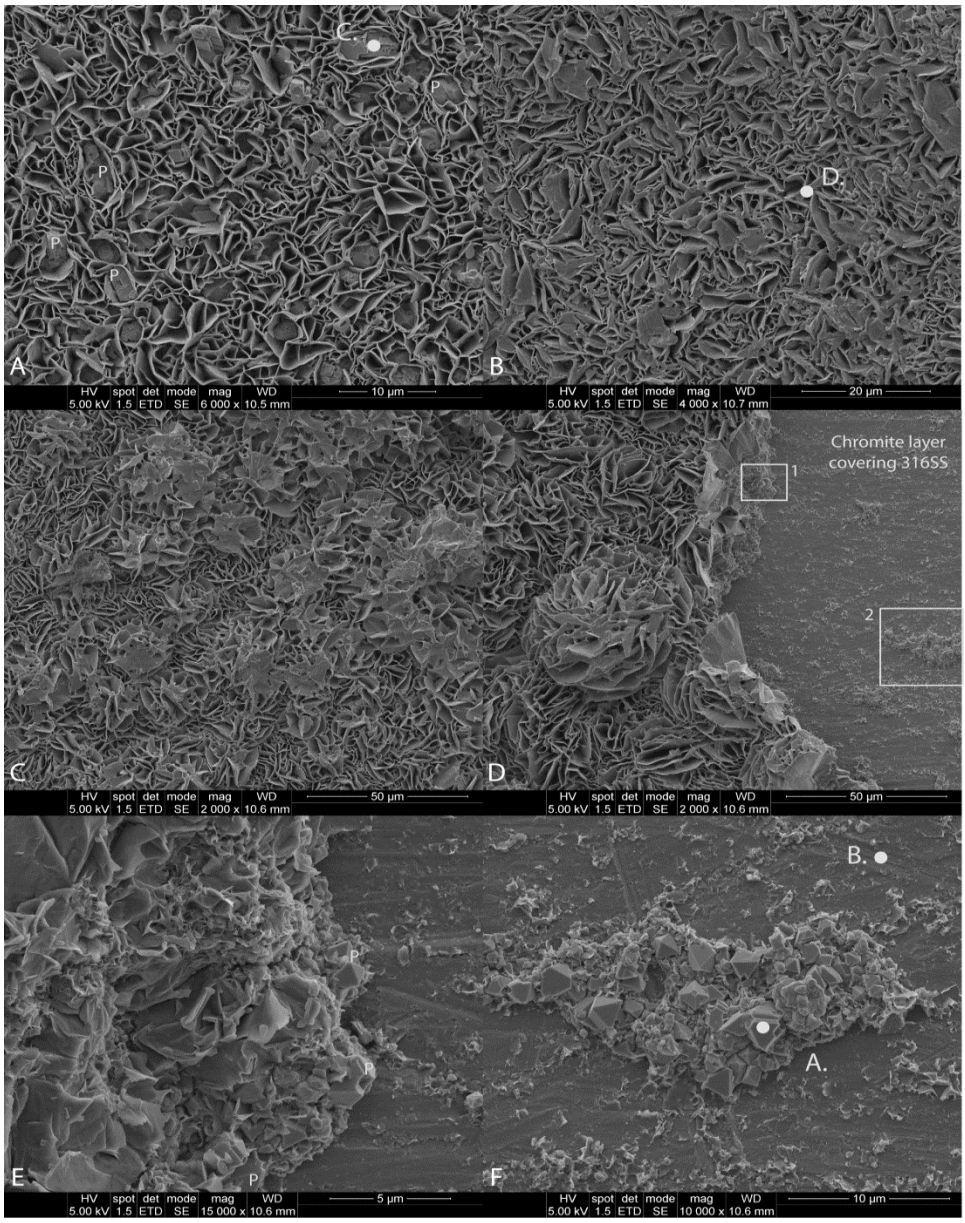

Figure 10. SEM image of corrosion products from 316 SS in EBS-13. A) Typical Fe-saponite morphology associated with 316SS surfaces with intergrowths of pentlandite (P) and without pentlandite intergrowths (B). Energy dispersive X-ray (EDX) analyses at points C. and D. are presented in Figure 11 C and D. C) Start of the two-layer corrosion layers previously seen in 316SS corrosion. First-layer characteristics are represented in A and B, but the second-layer has a rose-like and botryoidal texture. Change in textures might be due to changing substrates for Fe-saponite growth. D) Interface between Fe-saponite and the chromite surface associated with 316SS. E) Close up of the Fe-saponite-chromite interface (Box #1) with extensive pentlandite growths at the interface. F) Pentlandite cluster (from Box #2) directly in contact with the chromite surface associated with the 316SS. EDX analyses at points A. and B. are presented in Figure 11 A and B.

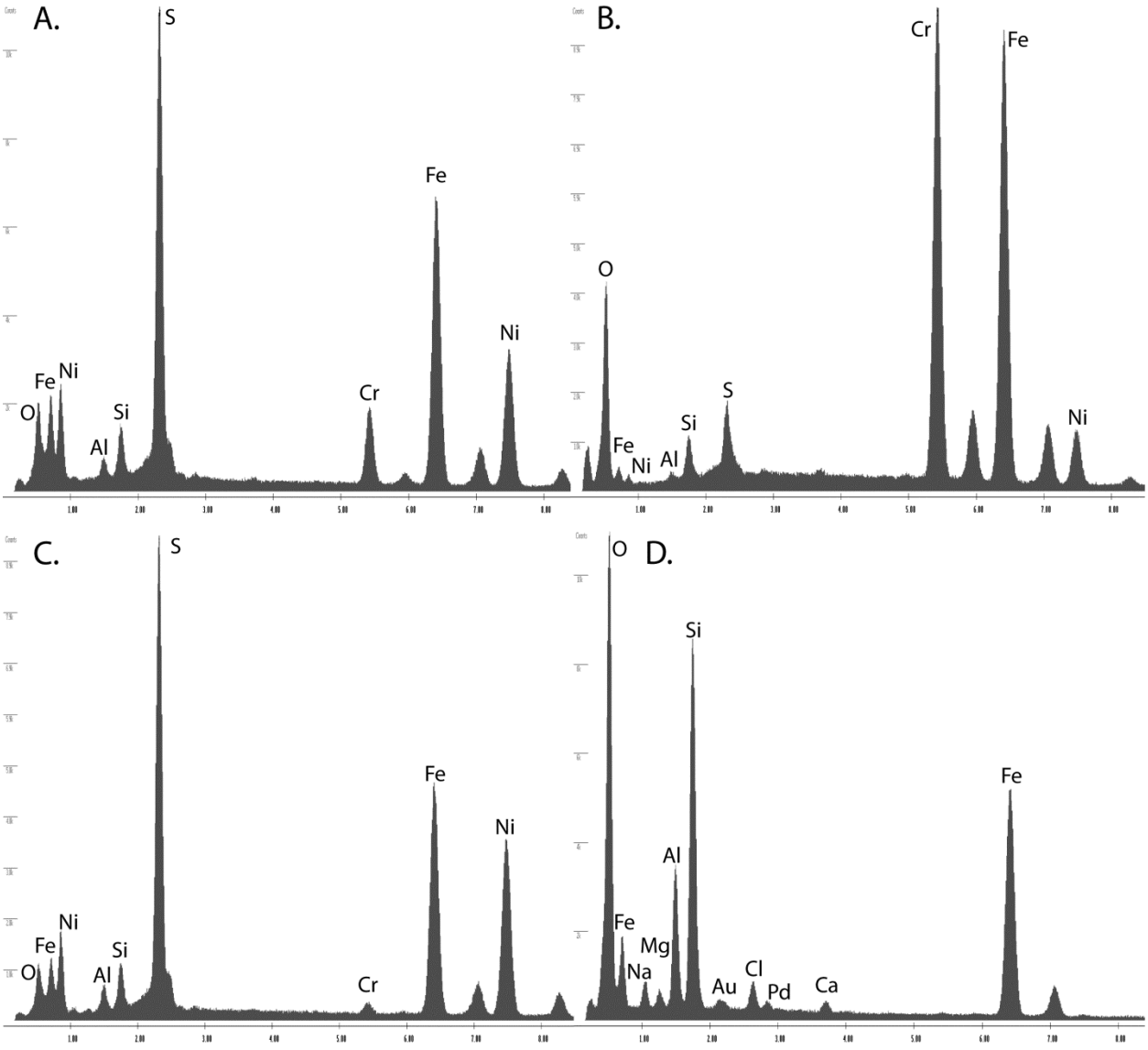

Figure 11. EDX analyses of 316SS corrosion products associated with EBS-13 in Figure 10. Letters correspond to locations described in Figure 10. A) Octahedral pentlandite immediately in contact with the chromite passivation layer. B) Clean surface of the 316SS indicating much of the surface corresponds to the chromite passivation layer. C) Pentlandite surrounded by saponite foils. D) Fe-saponite on edge to minimize underlying contamination. Chloride is primarily from NaCl formation upon drying.

3.4 Chemical Mapping from EBS-10.

Figure 12 is an EDX chemical map from a cross-section of a 316SS plate from EBS-10. It is evident from the mapping Ni and S are strongly associated with little correlation to Fe. Based on the fibrous morphologies in the previous report (Caporuscio et al., 2013) and a Ni-S correlation, it is evident that millerite (NiS) also is a corrosion product not previously identified. Sulfide minerals appear to form early in the corrosion process, most likely due to very low Fe and Ni

solubility in the presence of sulfide. Fe-saponite growth seems to become the primary corrosion product as sulfide crystallization tapers off, either from sulfide or Ni depletion. However, there appears to be a second pulse of sulfide formation developing a secondary layer of sulfide-saponite products. The oxide passivation layer (chromite) is evident by the bright green zone at the 316SS surface in the O-K chemical map.

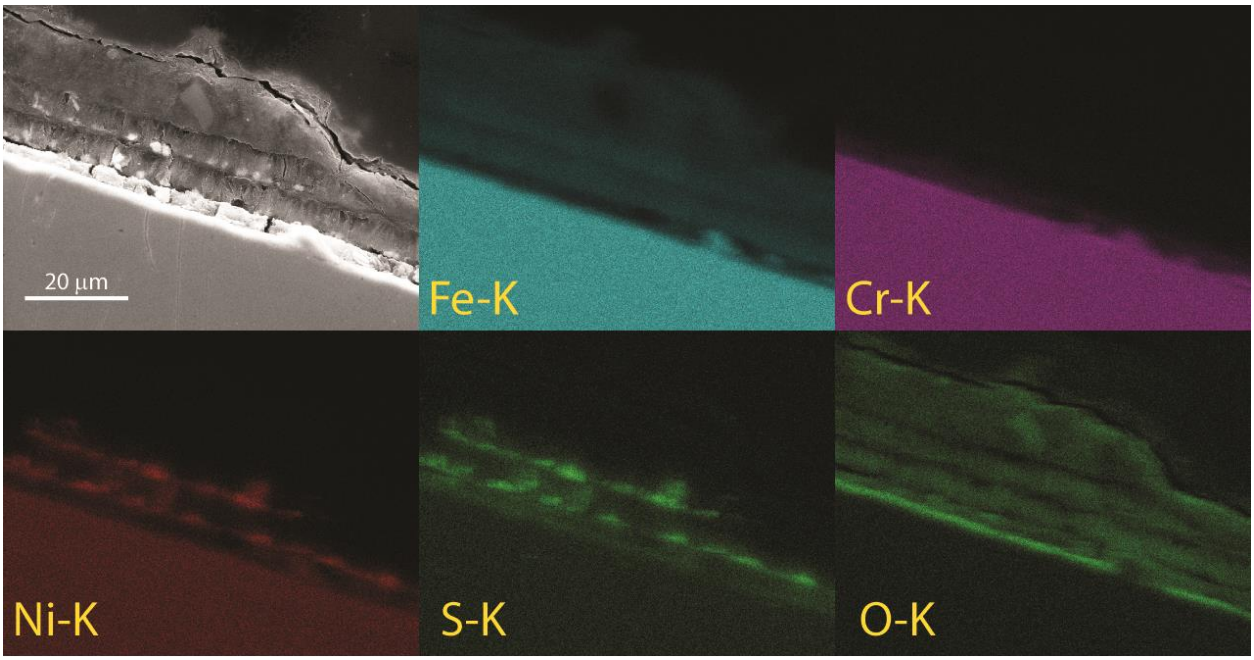

Figure 12. Chemical mapping of the 316SS from EBS-10 showing the distribution of Fe, Cr, Ni, S, and O at the metal-bentonite boundary dominated by corrosion products.

3.5 Opalinus Clay Experiments

3.5.1 Original Opalinus Clay. Opalinus Clay is thinly-laminated, dark grey shale with dry density of 2.2–2.4 g/cm^3 and water content of 6.5–8.0% (Pearson et al., 2003). This shale is dominated with 69 wt. % illite, illite-smectite mixed layers, and discrete smectite (Table 8, Figure 13). These phases were quantification together due to difficulty of quantifying these mineral phases when they are mixed. The illite-smectite appears to be a low expandable with a R3 illite (0.92)-smectite composition. Other clay minerals present in significant quantities include kaolinite (12 wt. %) and chlorite (1 wt. %) (Table 8, Figure 13). These clay minerals are intimately mixed making them indistinguishable in the SEM investigation (Figure 14A and B). The exchangeable cations present within the clay fraction are listed in Table 9 (Pearson et al., 2003). Na^+ is the dominant exchangeable cation in the Opalinus Clay followed by Ca^{2+}, Mg^{2+}, K^+, and Sr^{2+}, however, the bulk composition is dominated with CaO (7.96 wt. %), K_2O (3.05 wt.%), MgO (2.38 wt. %), and Na_2O (0.481 wt. %). These exchangeable cations should be in equilibrium with the pore water described above (Table 2). Other minerals present include calcite, ankerite, dolomite, quartz, and biotite. Well-preserved pyrite occurs primarily as < 2 µm octahedral crystals, filling fractures and/or along bedding planes. Calcite primarily occurs as

pocket filling agglomerates showing layered structures with alternating calcite and clay layers (Figure 14E and F). Ankerite and dolomite were not observed in SEM analyses.

Table 8. Mineralogical composition of starting Opalinus Clay, Wyoming Bentonite, and reaction products from EBS-14 and EBS-15. + represents material detectable but below 0.5 wt. %. b.d.l. represents material below detection limits. Illite, illite-smectite, and smectite were combined in the analyses due to difficulty quantifying each phase when a physical mixture of two or three are present.

	Opalinus Clay	**Bentonite**	**EBS-14**	**EBS-15**
	Switzerland	**Wyoming**	**Opalinus**	**Bent-Opalinus**
Illite, I-S, S	69		78	72
Smectite		72		
Chlorite	1	b.d.l.	3	+
Kaolinite	12	b.d.l.	b.d.l.	b.d.l.
Clinoptilolite	b.d.l.	13	b.d.l.	14
Analcime/Wairakite	b.d.l.	b.d.l.	3	1
Quartz	8	1	8	4
Cristobalite/Opal-C	b.d.l.	2	b.d.l.	b.d.l.
Biotite	0.5	3	0.8	0.5
Pyrite	+	0.4	0.7	b.d.l.
Plagioclase	b.d.l.	9	b.d.l.	8
K-feldspar	b.d.l.	b.d.l.	b.d.l.	+
Calcite	6	b.d.l.	5	b.d.l.
Dolomite	+	b.d.l.	b.d.l.	b.d.l.
Ankerite	2	b.d.l.	b.d.l.	b.d.l.

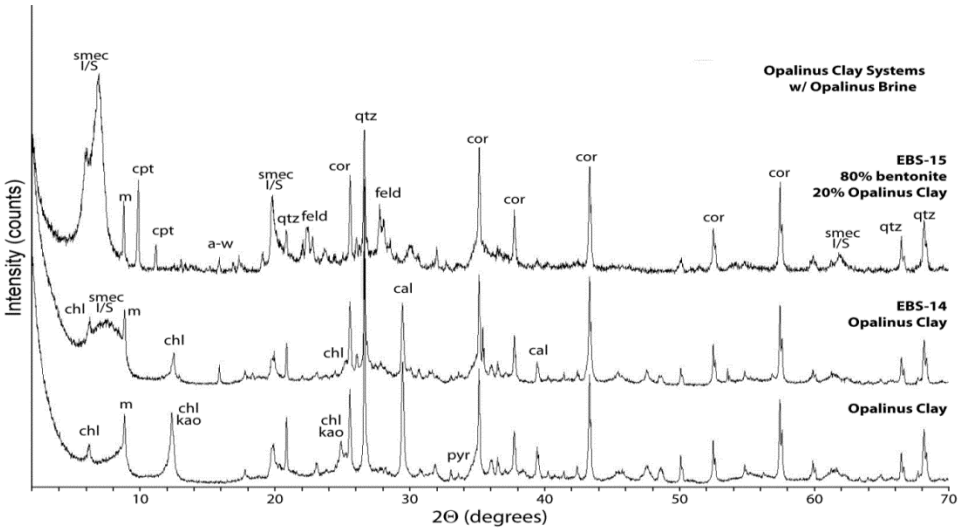

Figure 13. XRD patterns of bulk samples from starting Opalinus Clay and EBS-14 and EBS-15 reaction products.

Table 9. Exchangeable cation populations for the Opalinus Clay associated with the Mont Terri Rock Laboratory (modified from Pearson et al., 2003).

Sample	Laboratory	Na	K	NH_4	Mg	Ca	Sr	Sum	Na	K	NH4	Mg	Ca	Sr
		meq/Kg_{rock}							% cation occupancy					
E2-Ni	Uni Bern	27.8	9.3		21.3	29.1	3.6	91.1	30.5	10.2	0.0	23.4	31.9	4.0
E3-Ni	Uni Bern	27	8.6		22	22.5	3.5	83.6	32.3	10.3	0.0	26.3	26.9	4.2
A4	CIEMAT	31.3	8.8		25.4	59.1	0.8	125.4	25.0	7.0	0.0	20.3	47.1	0.6
A5	CIEMAT	26	7.9		23.3	53.3	0.7	111.2	23.4	7.1	0.0	21.0	47.9	0.6
A5-Ni	Uni Bern	50.1	6.9		18.9	26.7	1	103.6	48.4	6.7	0.0	18.2	25.8	1.0
A1-C12	PSI case I	48.1	5.4		15.6	25.4		94.5	50.9	5.7	0.0	16.5	26.9	0.0
A1-C12	PSI case II	44.4	5.4		15.6	29.1		94.5	47.0	5.7	0.0	16.5	30.8	0.0
A6-Ni	Uni Bern	63.7	9		23.9	35.9	1.2	133.7	47.6	6.7	0.0	17.9	26.9	0.9
A6/MIN1	BRGM	58.2	15.2	23.7	28.9	36.6		162.6	35.8	9.3	14.6	17.8	22.5	0.0
A6/TEM1	BRGM	54.9	15.7	46	25.9	33.2		175.7	31.2	8.9	26.2	14.7	18.9	0.0

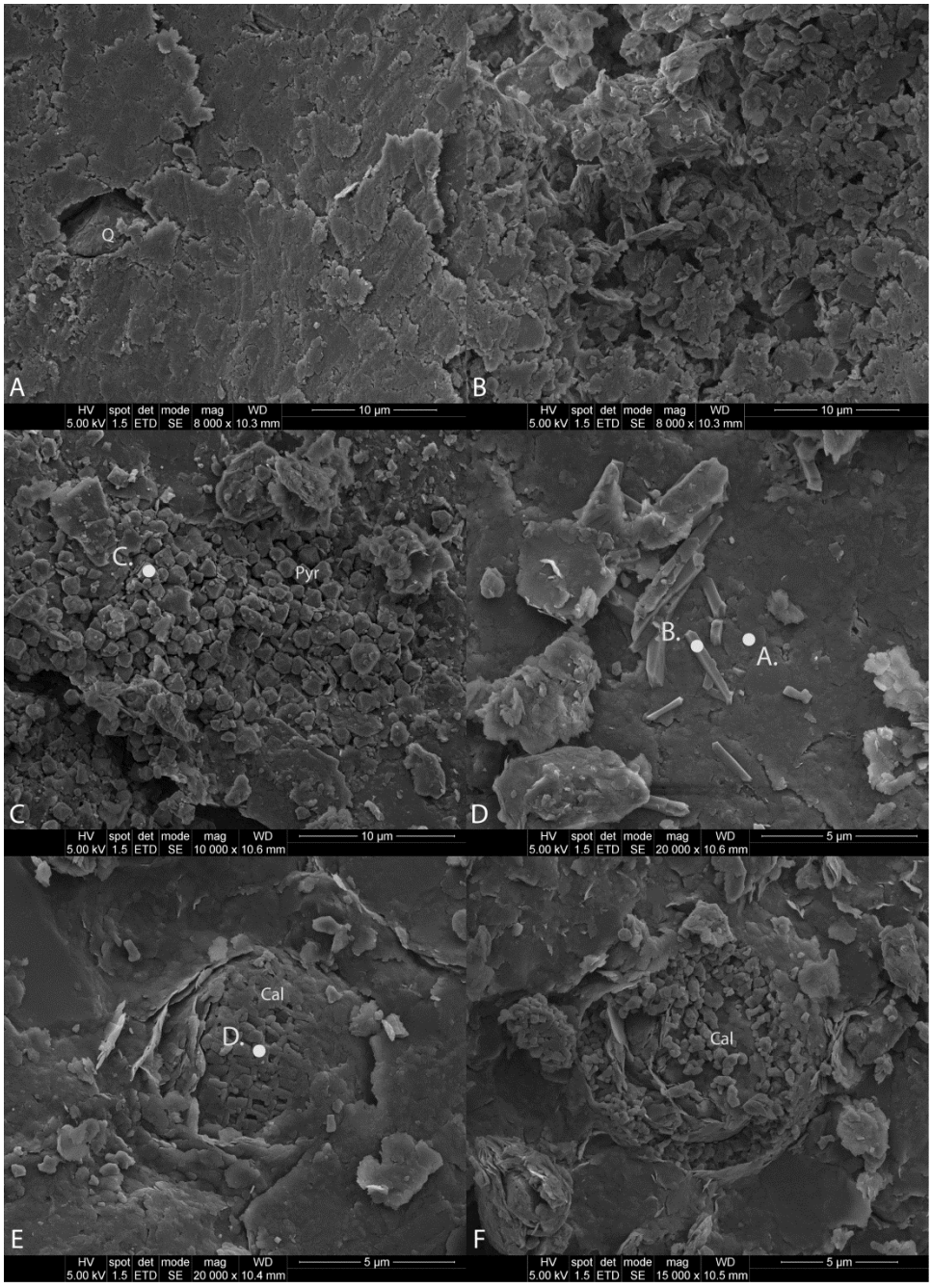

Figure 14. SEM images from Opalinus Clay. A) Opalinus Clay bedding planes formed from the aggregation of smaller particles. Quartz (Q) particle is imbedded in the matrix. B) Pore spaces within Opalinus Clay. C) Cluster of < 2 µm octahedral pyrite (Pyr) fill void spaces or are disseminated throughout samples. EDX analyses at point C. are presented in Figure 15C. D) Opalinus Clay bedding plane with platy-bladed mineral embedded in illite, illite-smectite, and chlorite matrix. EDX analyses at points A. and B. are presented in Figure 15A and B. E) Biogenic calcite (Cal) filling a pocket with in the Opalinus Clay matrix. EDX analysis at point D. is presented in Figure 15D. F) Disturbed pocket-filling calcite showing layered structure with alternating calcite and clay layers.

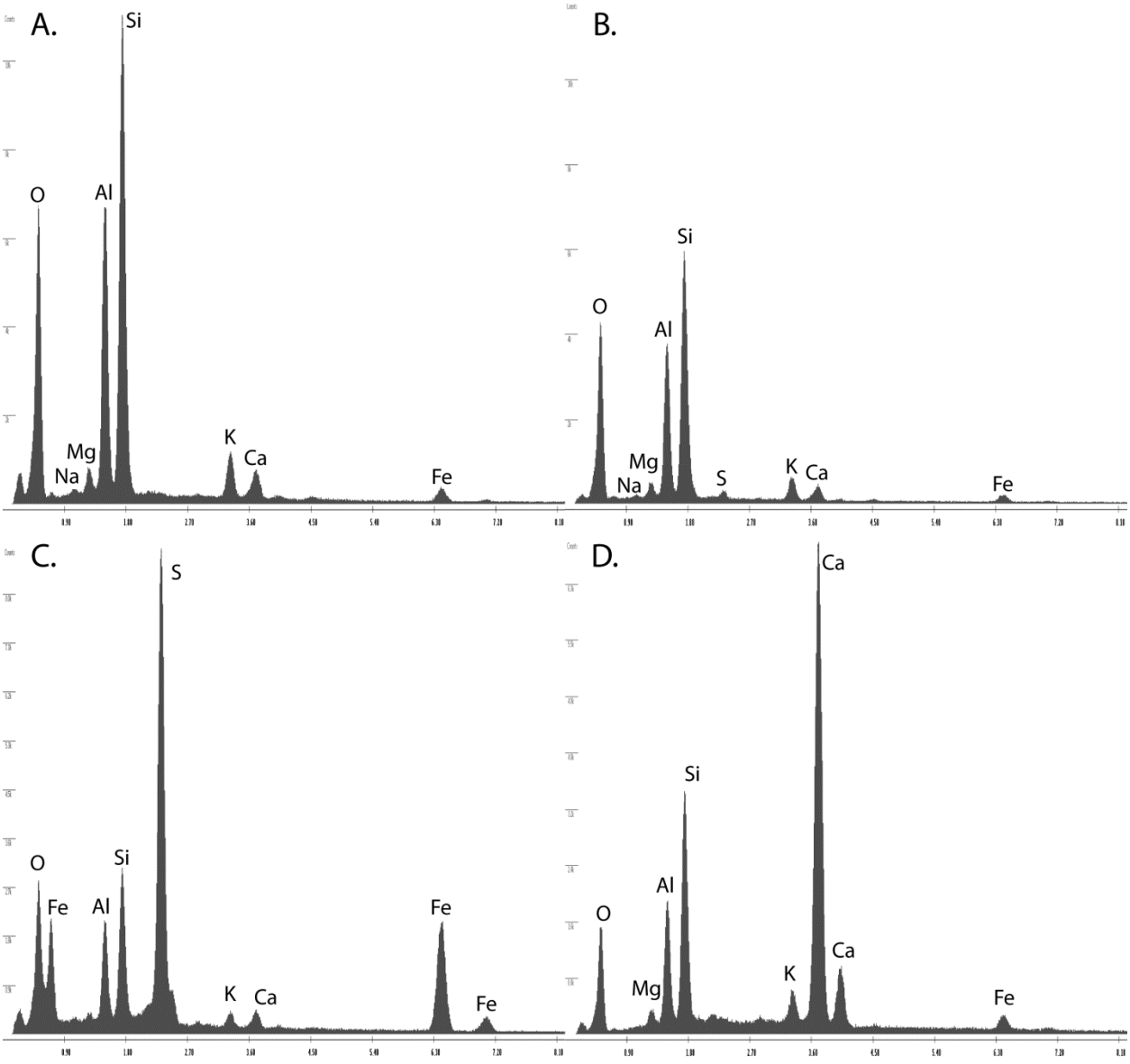

Figure 15. EDX analyses from Opalinus Clay starting material in Figure 14. A) Bulk compositions from the illite, chlorite, and illite-smectite matrix. B) Composition from the bladed structure. Composition is essentially indistinguishable from the clay matrix possible due to the zone of interaction during analysis gain strong influence from clay matrix. C) Composition from the octahedral pyrite clusters. Other non-pyrite elements are present from the clay matrix or clay mixing between pyrite particles. D) Elemental composition from the biogenic calcite filled pockets. Clay matrix is intimately mixed within the calcite crystals.

3.5.2 Post-reacted Opalinus.

Clay mineral evolution in the Opalinus experiments is more diverse compared to the EBS experiments with bentonite as the only geomaterial due to the clay diversity in the Opalinus Clay. The starting Opalinus Clay is dominated with illite-smectite (I-S) mixed-layers and discrete illite with minor amounts of smectite. Reaction product from EBS-14 shows three different major clay fractions: two different I-S mixed layers and one illite fraction (Figure 16). It would appear that the two I-S fractions are an R3 illite (0.9)-smectite and a R1 illite (0.7)-smectite. Exact quantification is not possible, but it appears that the R3 I-S is the dominant phase in the EBS-14 reaction products.

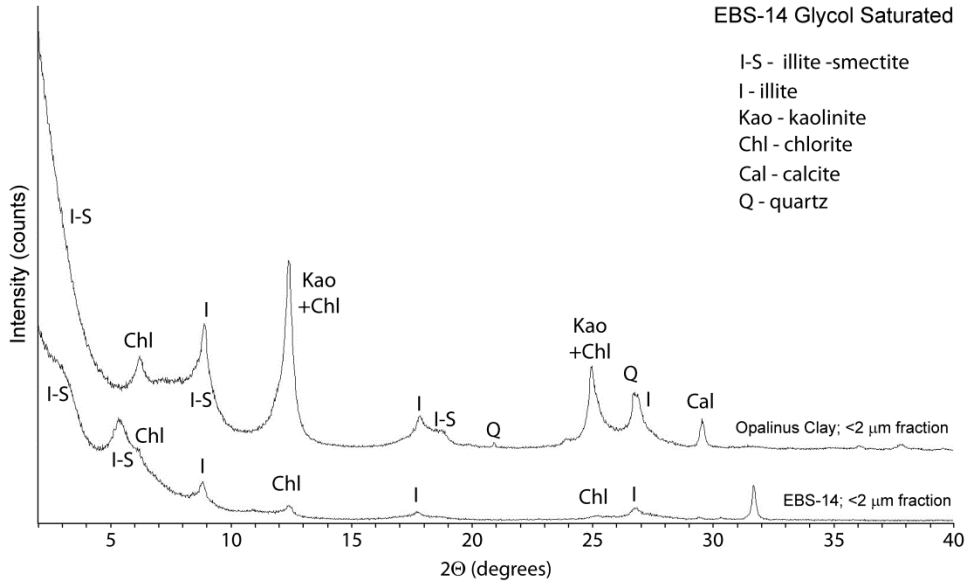

Figure 16. XRD patterns from the ethylene glycol saturated, oriented < 2 μm fractions from original Opalinus Clay and EBS-14 reactions products showing the effects of heating Opalinus Clay to 300°C for six weeks.

EBS-15 reaction products vary depending on the various < 2 μm fractions examined. In the bulk < 2 μm size fraction, all clay products show 100% expandability with minor occurrences of illite (Figure 17). It is evident from the bulk < 2 μm fraction, that (1) it is montmorillonite from the bentonite component that dominates this fraction and (2) this montmorillonite has not experienced significant illitization (i.e., > illite (0.05)/smectite). Montmorillonite expands to 16.8 – 16.9 Å with a Δ2θ (002/003) values of 5.25 – 5.25°, corresponding to 100% expandability (Figure 17). Post-reacted Opalinus Clay fragments from EBS-15 showed a composition more characteristic of the starting Opalinus Clay. It was dominated with illite (possibly two), I-S, chlorite, and quartz. Illite could potentially be deconvoluted into a well-crystalline illite and a poorly-crystalline illite displaying a low, broad reflection superimposed on a sharp 10 Å illite reflection. The I-S appears to be a R0 illite (0.1)/smectite and expands to 16.8 Å with a Δ2θ (002/003) values of 5.44°, corresponding to 91% expandability. R1-3 ordered I-S were not detected.

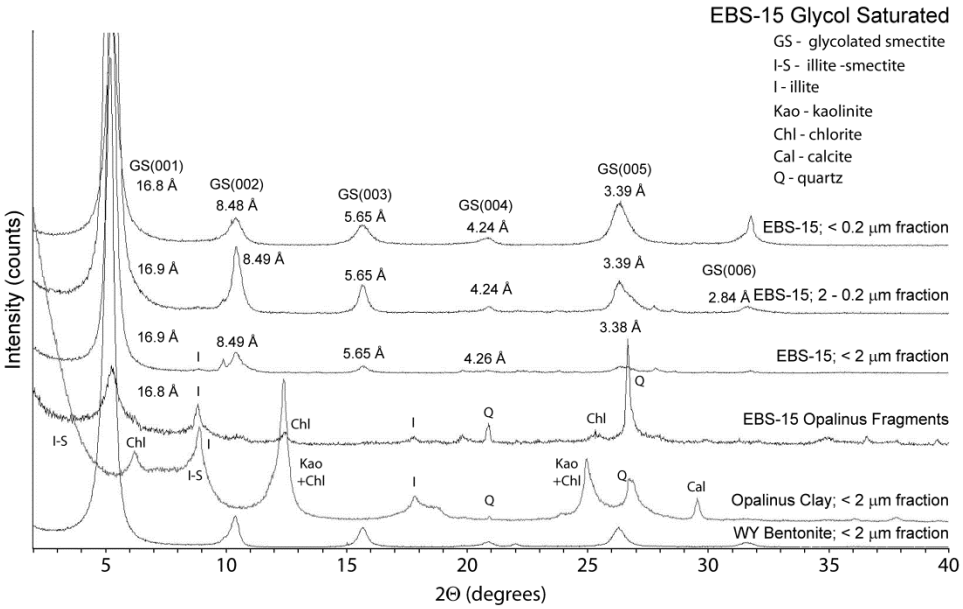

Figure 17. XRD patterns from the ethylene glycol saturated, oriented fraction from original Opalinus Clay, WY bentonite, EBS-15 Opalinus fragments, and various size fractions from EBS-15 reaction products.

There was significant analcime-wairakite formation with the addition of Opalinus Clay and brine. EBS-14 produced 22 – 53 µm analcime-wairakite particles (Figure 18B and C). Compositionally, these particles resemble wairakite with a high Ca/Na ratio (1.52 – 2.91) and a relatively low Si/Al (2.16), compared to the high-silicon analcime from the EBS experiments with Stripa solution and no Opalinus material (Figure 19A). EBS-15 produced spherical 10 - 20 µm analcime-wairakite particles with terraced surfaces from crystallization (Figures 19C and D; 21A and B). Compositionally, these analcime-wairakite particles have an intermediate composition with a Ca/Na ratio (0.206) and a relatively higher Si/Al ratio (2.70) compared to EBS-14, but lower Si/Al ratio compared to bentonite EBS experiments (Figure 21A). The analcime-wairakite material formed even though clinoptilolite was not present in EBS-14 and was preserved during EBS-15 (Table 8, Figure 13).

Other than the analcime-wairakite formation, it appears that a series of other zeolite were produced during EBS-14 and EBS-15. EBS-14 produced 2 – 5 µm fibers and a couple of 12 – 40 µm fibers throughout the samples (Figure 18A). Positive identification of these fibrous materials was not completed, but it would appear that the short prismatic fibers with a Si/Al (2.09) and Ca/Na ratio (0.472) are consistent with Na-rich laumontite ($CaAl_2Si_4O_{10}{\cdot}4H_2O$) (Figure 18C). The long fibers have 3.89 Si/Al and 0.371 Ca/Na ratios, along with a fibrous morphology suggests that these are either mordenite ($(Ca,Na_2,K_2)Al_2Si_{10}O_{24}{\cdot}7H_2O$) or erionite ($(K_2,Na_2,Ca,Mg)_4Al_8Si_{28}O_{72}{\cdot}28H_2O$) (Figures 20; 21C and D; and 22). These same bimodal fibrous populations were also present in EBS-15, with a greater concentration of the long fibers. There are no new XRD peaks that provide clues as to what the new phases are, but, morphology and composition suggests the long fibers are either mordenite or erionite and the short fibers are laumontite.

Kaolinite is the only mineral to undergo complete decomposition. The starting Opalinus Clay had 12 wt. % kaolinite, but EBS-14 and EBS-15 reaction products do not appear to have

kaolinite (Table 8, Figure 13). EBS-15 kaolinite may have been diluted below detection limits with the addition of 80 wt. % bentonite (which does not have kaolinite). However, kaolinite if preserved should be around 2-3 wt. %, which is above detection limits for XRD.

It would appear from SEM data that pyrite was unaltered during the reactions. The octahedral pyrite still occupies fractures and/or between bedding planes and displays not signs of corrosion (Figure 18F). Also, there appears to be a partial calcite loss from 6 wt. % to 5 wt. % (EBS-14) to below detection limits (EBS-15), but SEM analyses show several pore-filling calcite nodules present throughout EBS-14 and EBS-15 reaction products (Table 8; Figure 18C). However, dolomite and ankerite does appear to have completely decomposed. Even though these carbonates were not observed in SEM, XRD data shows dolomite's and ankerite's complete removal. These carbonate mineral losses corresponds with excess gas evolution during fluid sampling. In most cases, 50 vol. % of the sampled volume was a mixed gas phase (most probably CO_2 and H_2S).

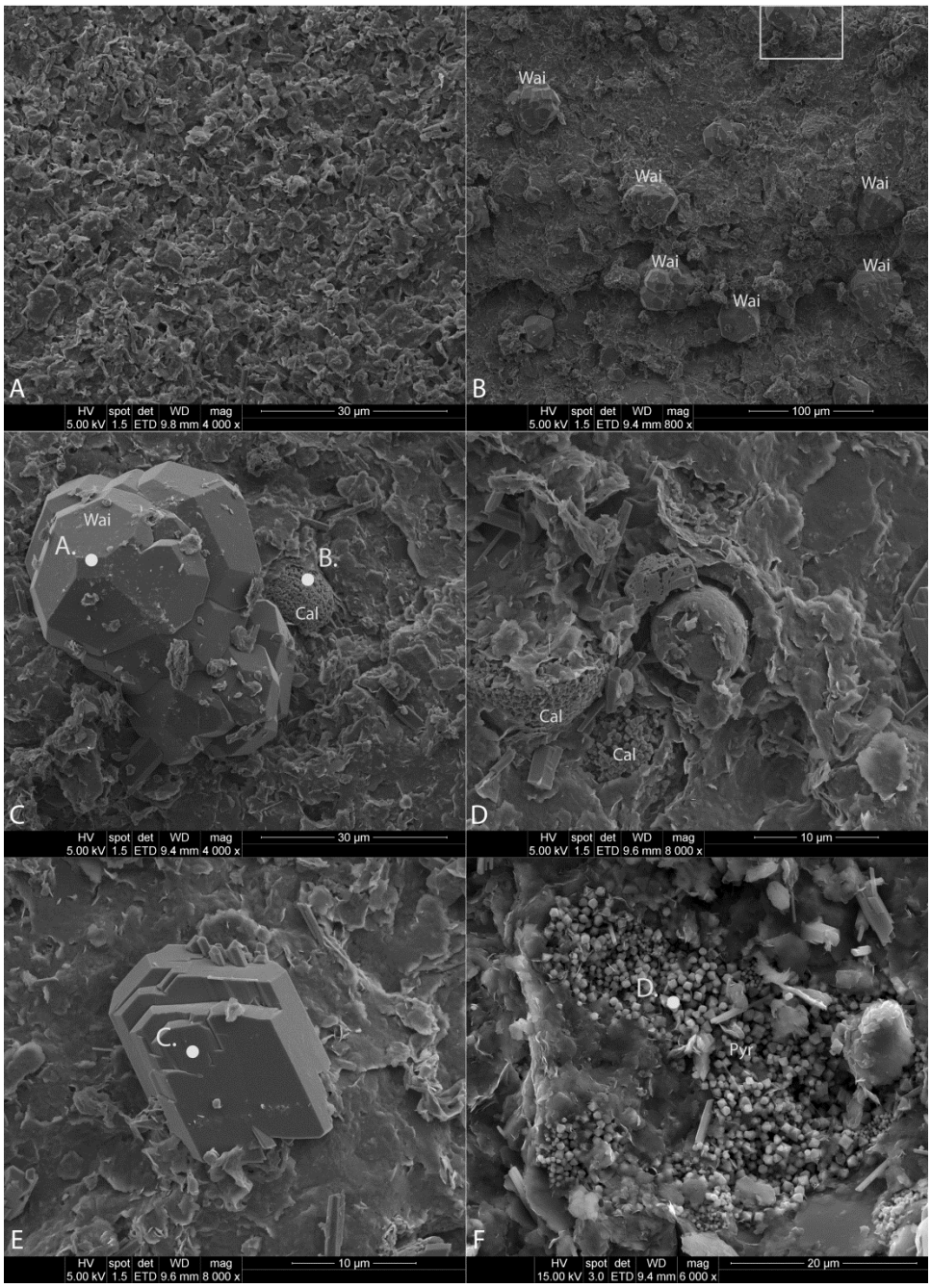

Figure 18. SEM images from EBS-14 Opalinus Clay. A) Fine grained illite, illite-smectite, chlorite matrix associated with post-reacted Opalinus Clay granules. 2 - 5 µm zeolite (?) fibers are dispersed throughout Opalinus Clay granules. B) 22 – 53 µm Na-bearing wairakite (wai). C) Close up of a euhedral wairakite crystal from Figure 18B boxed area. EDX analyses at points A. and B. are presented in Figure 19A and B. D) Remnant clay matrix associated with a nodule that underwent dissolution during EBS-14. Pockets typically have a clay rind preserved. Calcite (cal) is still preserved in this granule. E) Particle that might be associated with the 2 - 5 µm fibers. EDX analysis at point C is presented in Figure 19C. Composition suggests this particle is either a zeolite or feldspar. F) Cluster of 1-2 µm octahedral pyrite (Pyr) fill void spaces or are disseminated throughout samples. EDX analysis at point D. is presented in Figure 19D.

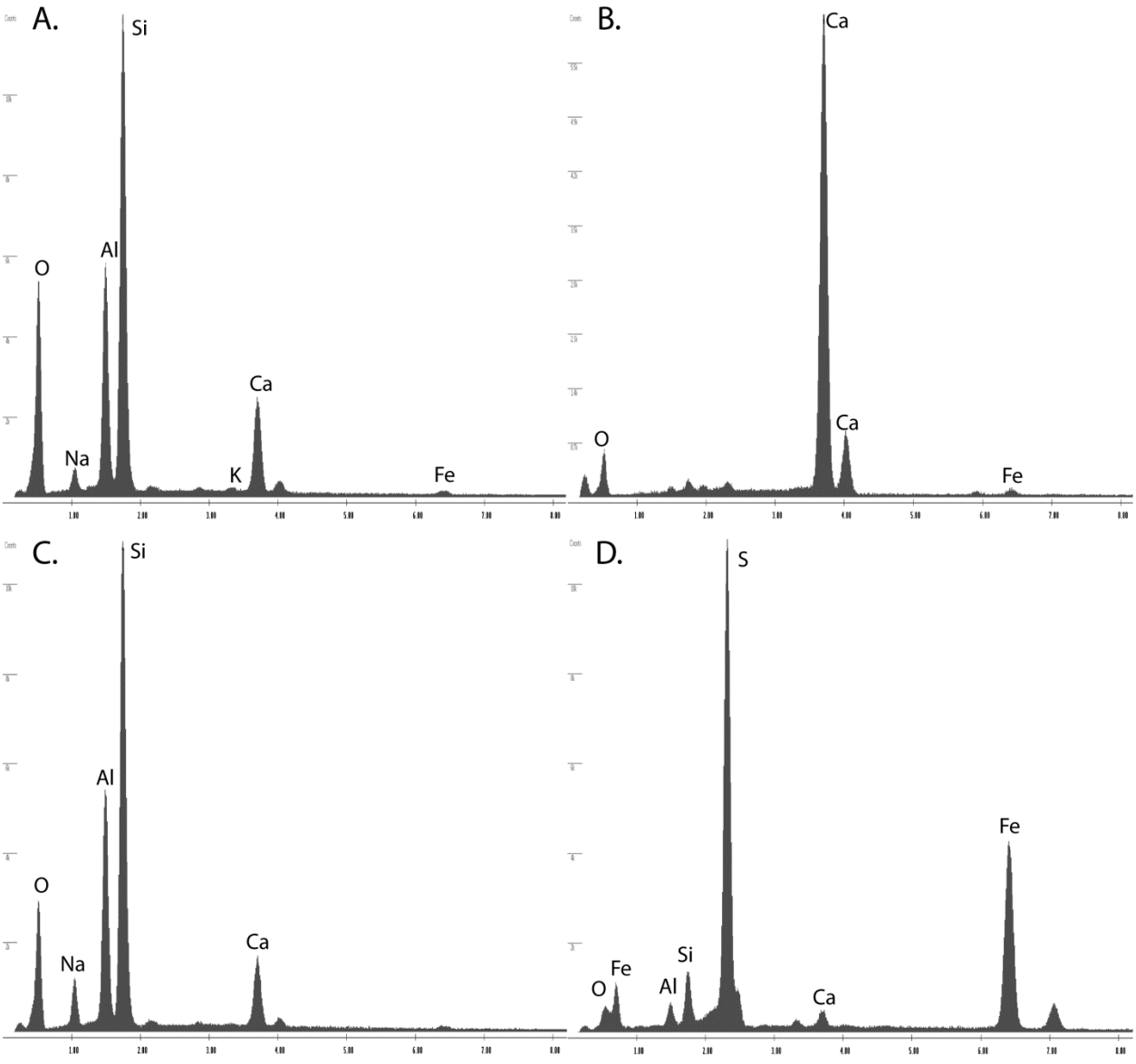

Figure 19. EDX analyses from EBS-14 reaction products in Figure 18. A) Composition of the Na-bearing wairakite particle (Si/Al = 2.16). B) Fine grained pocket filling calcite. C) Particle with a composition (Si/Al = 2.09) and morphology similar to laumontite or mesolite. However, positive identification of laumontite is not complete. D) Composition from the octahedral pyrite clusters. Other non-pyrite elements are present from the clay matrix or clay mixing between pyrite particles.

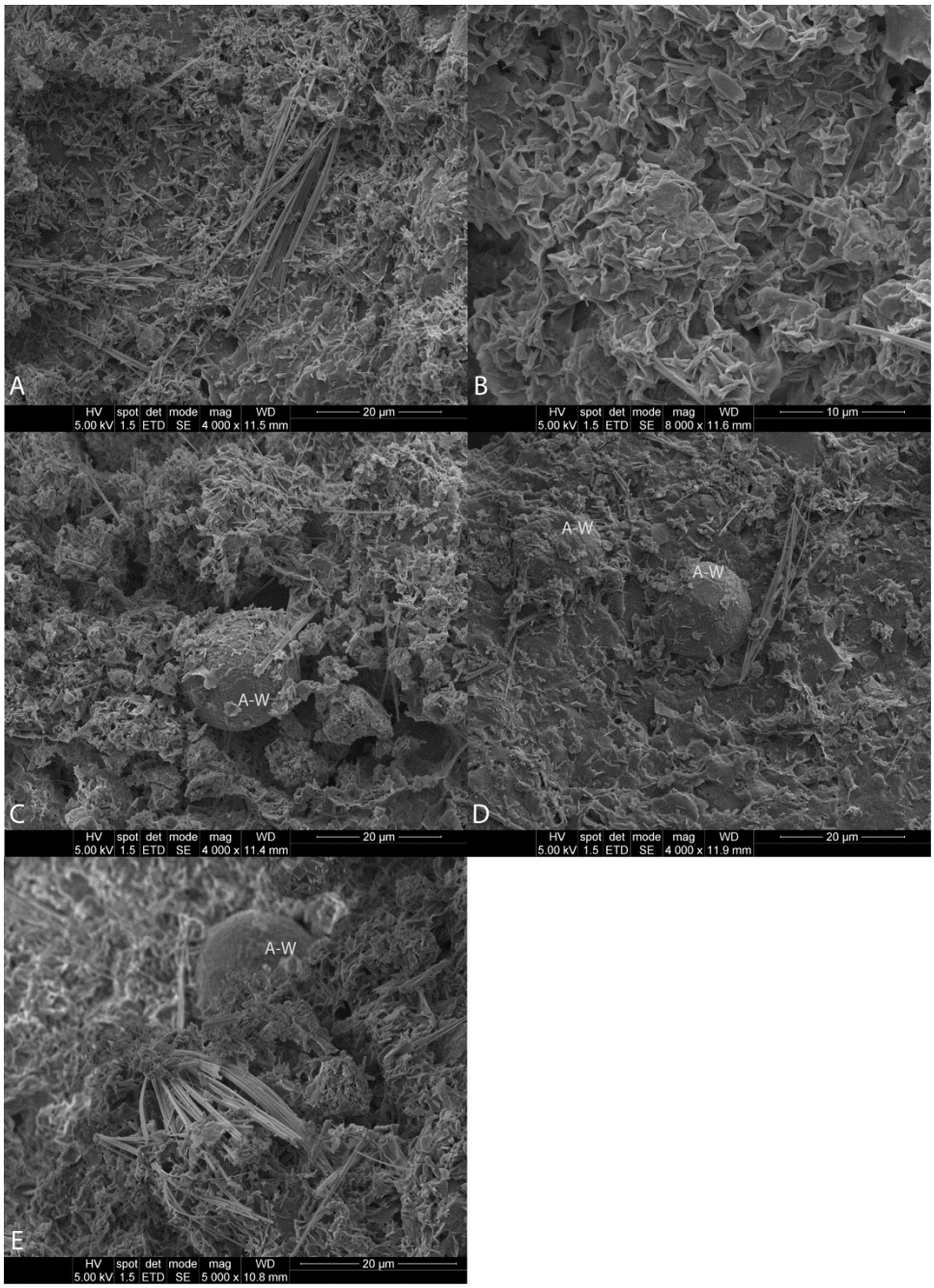

Figure 20. SEM images from EBS-15 bulk reaction products. A) A bimodal population of fibers ranging from 2 - 5 µm and 12 – 40 µm in length are dispersed throughout EBS-15 reaction products. EDX analyses on other fibrous material from EBS-15 suggest these fibers are either mordenite or erionite. B) Typical smectite foily morphology associated with WY bentonite mixed with fibers. C) Analcime-wairakite (A-W) crystal mixed within the clay matrix showing well developed growth terraces on the particle surfaces. EDX composition from separated analcime-wairakite is presented in Figure 21A. D) Analcime-wairakite crystal imbedded within the low porous clay matrix indicating analcime-wairakite grew within the clay matrix. Clay matrix in this image appears to be the Opalinus Clay. E) Fibers growing from a central substrate.

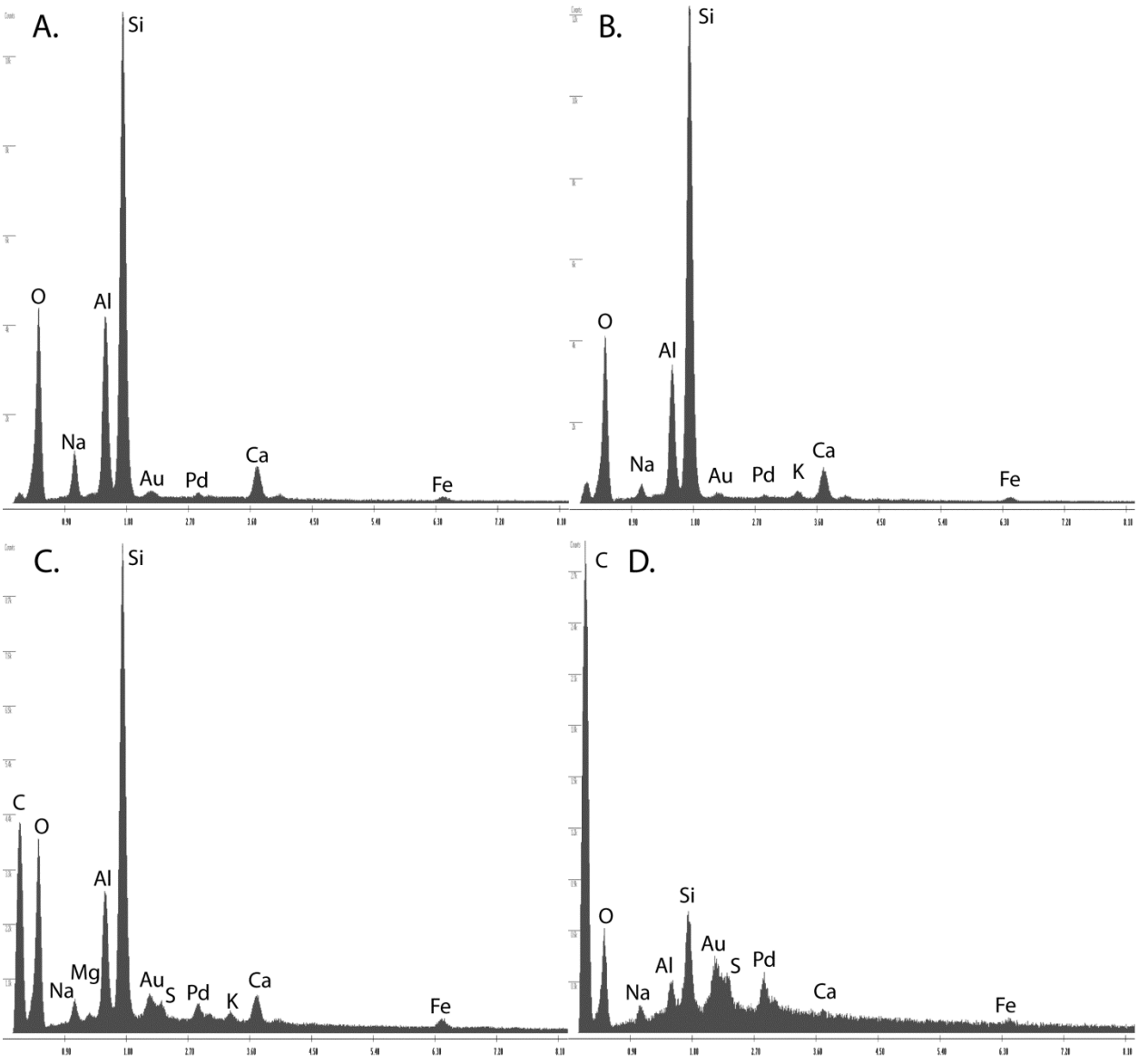

Figure 21. EDX analyses from > 2 µm grain mounts of EBS-15 reaction products. A) Analcime-wairakite product with an intermediate analcime-wairakite composition. Si/Al ratio is 2.70 is typical for a high-silica analcime-wairakite. B) Bladed material with a feldspar composition. C and D) Composition of the fibrous materials observed throughout the EBS-15 reaction products. Si/Al ratio is 3.85 suggesting the fibrous material could be either mordenite or erionite. Carbon peak is from the carbon tape in which the fibrous/acicular particles are affixed.

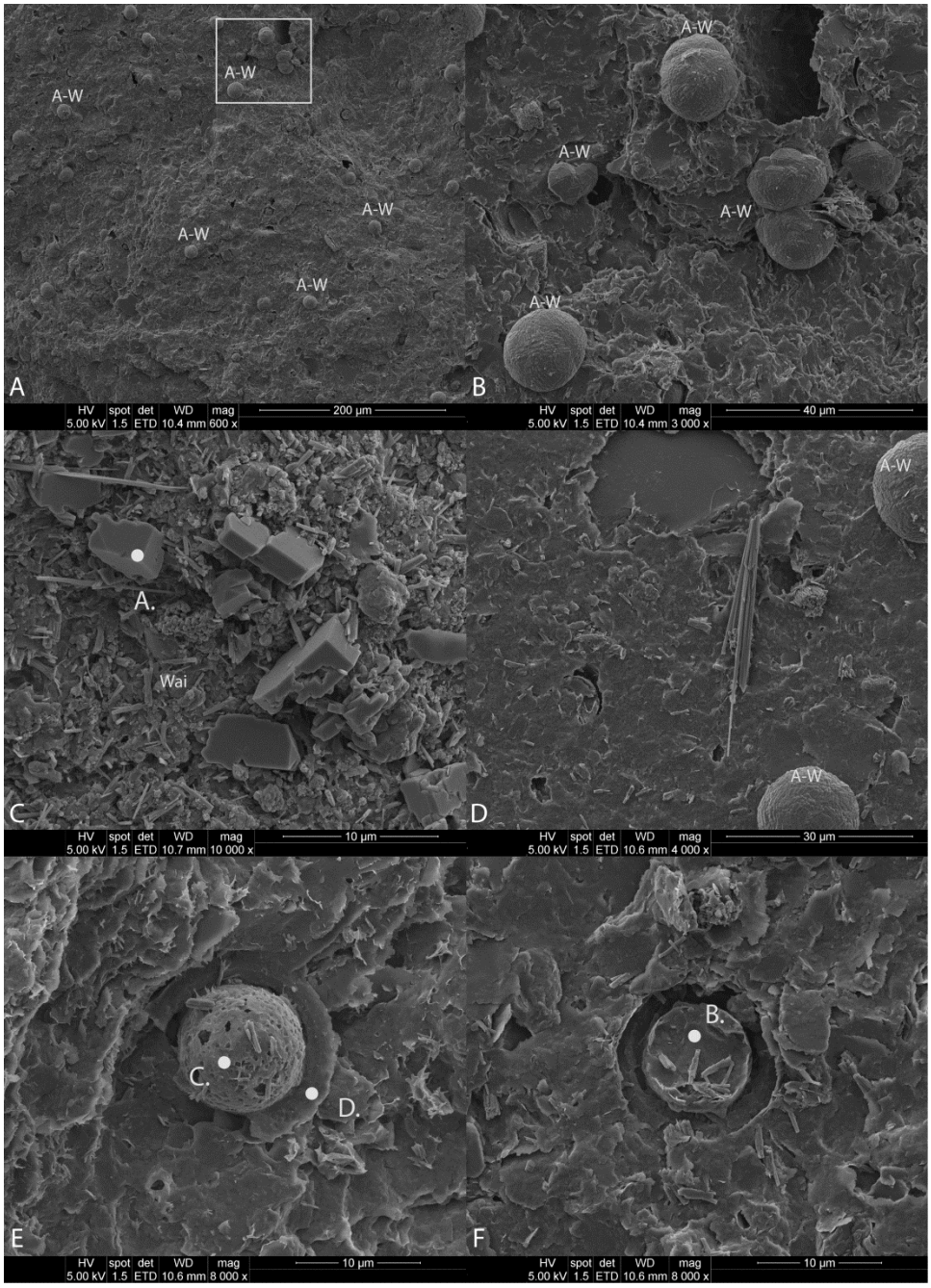

Figure 22. SEM images from EBS-15 Opalinus Clay fragments. A) 10 – 20 µm analcime-wairakite (a-w). B) Spherical analcime-wairakite crystal from Figure 22A boxed area. C) Possible feldspar crystals. EDX analysis at point A. is presented in Figure 23A. D) Possible mordenite or erionite fibers. E) Remnant clay matrix associated with a nodule that underwent dissolution during EBS-15. It is unclear what the original material in the pocket. Pockets typically have a clay rind preserved with a similar composition to the clay matrix, but enriched in Ti. EDX analyses at points C. and D. are presented in Figure 23C and D. F) Cleaved remnant clay matrix associated with a nodule that underwent dissolution during EBS-15. It is unclear what the original material in the pocket. Pockets typically have a clay rind preserved. EDX analysis at point B. is presented in Figure 23B.

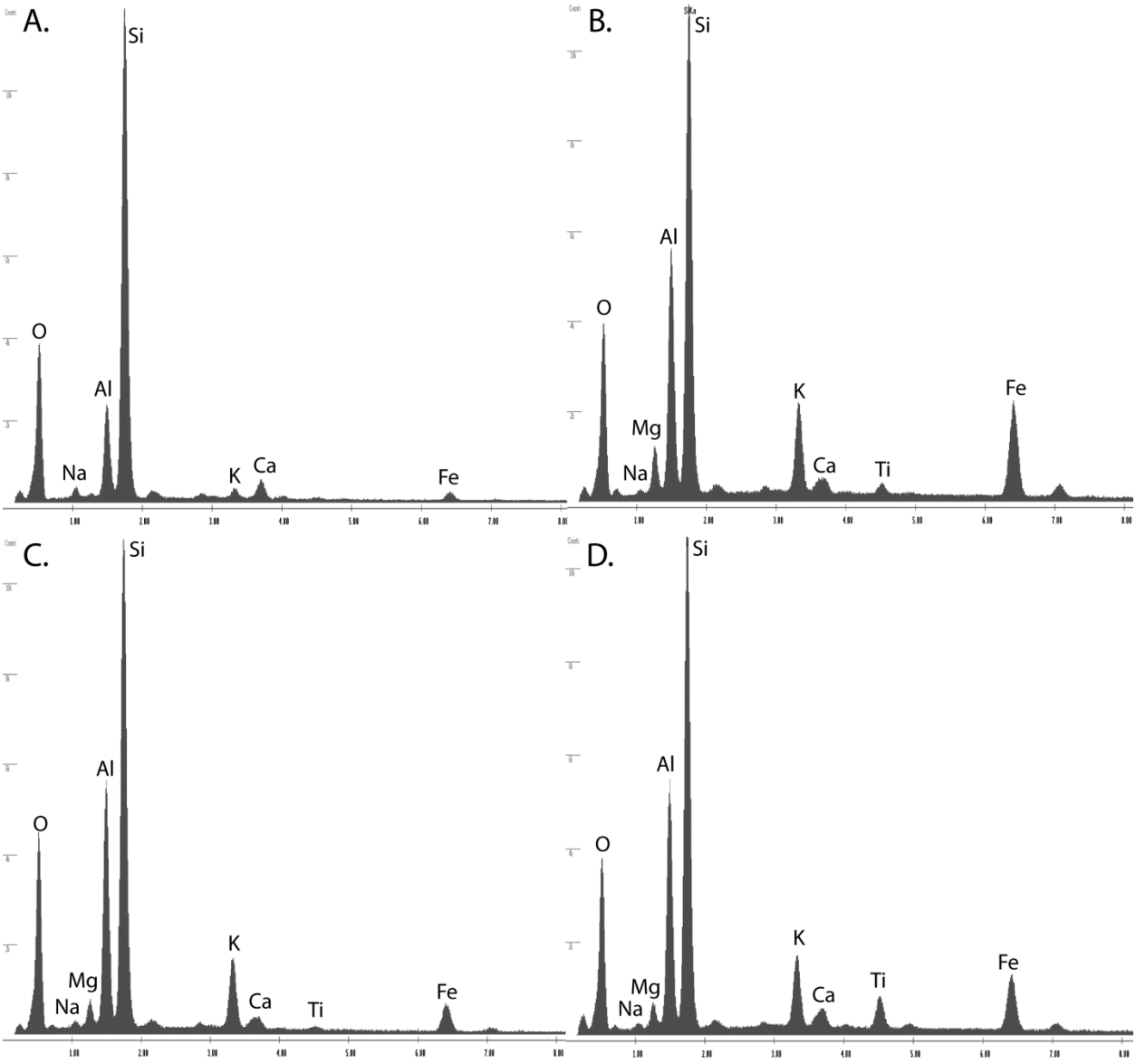

Figure 23. EDX analyses from EBS-15 Opalinus Clay fragments in Figure 22. A) Unknown, high-silicon material (Si/Al = 5.52) that displays dissolution. B) Cleaved spherical cavity filling clay material. This is probably the averaged composition between the illite, illite-smectite, and chlorite matrix. C) Spherical cavity filling clay material which probably is residual from the dissolution of the primary cavity filling mineral(s). D) Composition from the clay rind around the cavity. These Ti-enriched rinds are consistently associated with these spherical cavities. Composition from C and D are probably an average between the illite, illite-smectite, and chlorite matrix.

3.5.3 Solution Chemistry. Solution chemistry associated with the Opalinus Clay experiments are significantly different compared to solutions use in traditional EBS experiments (1-13). The fluid composition used in the experiment was derived from reported Opalinus Clay pore fluids. It is unknown whether the reported fluid composition is in equilibrium with the solid phases associated with the Opalinus Clay. Unlike experiments with Na-montmorillonite, there was not a major shift in the solution chemistry upon contact with solids during heating. Na, Ca, and K concentrations show fairly consistent concentrations during the experiment duration (Figure 23A). Sodium concentration ranged from 3400 to 4000 mg/L, calcium ranged from 300 to 600 mg/L, and potassium ranged from 100 to 250 mg/L. Silica also remained fairly constant even though there was a slight decline upon reaching 180 mg/L $SiO_{2(aq)}$ (Figure 24B). Chloride concentrations (Figure 24B) did not change significantly suggesting the experiment system remained sealed and no mass loss/gain developed. Sulfate concentrations dropped from 988 mg/L to below detection limits (1 mg/L; Appendix C; Table C3). Magnesium concentrations also experienced a drop from 197 mg/L to ~ 1 mg/L (Appendix C; Tables C3 and C4). Original solution pH (7.8) dropped immediately to 4.6 to 5.4 (Appendix C; Tables C3 and C4).

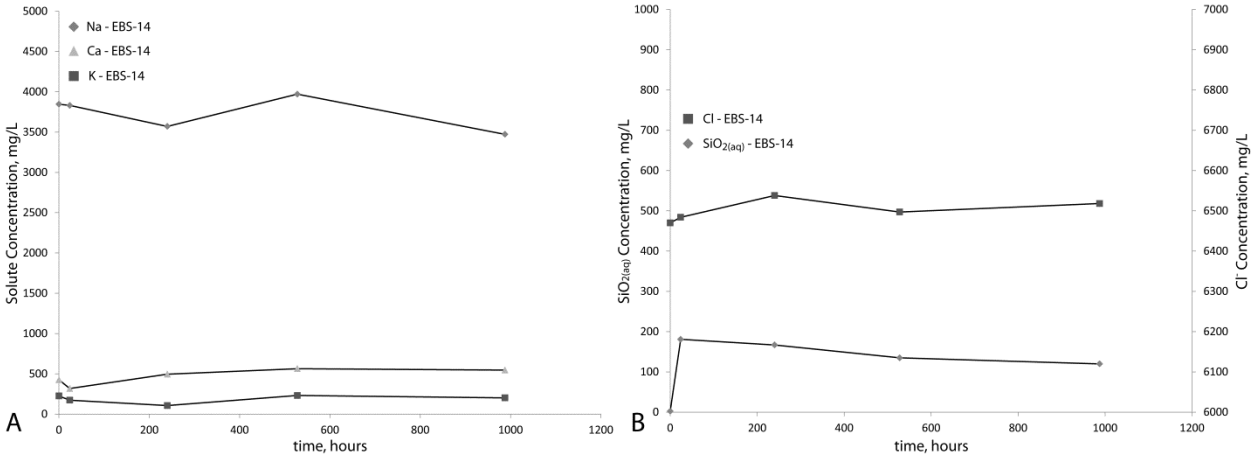

Figure 24. Solution chemistry associated with EBS-14. This reaction setup is Opalinus Clay with Opalinus brine. A) There appears to be no significant Na, K, and Ca exchange as each remains fairly constant during the experiment lifetime. B) Silica concentrations rapidly increase at the start of the experiment and stabilize around 150 mg/L. Chloride concentration does not change indicating no mass gain/loss during experiments.

3.5.4 Corrosion under Opalinus Clay conditions. Initial 316 SS (NIST SRM 160b) is an iron alloy primarily with 18.37 wt. % Cr, 12.35 wt. % Ni, 2.26 wt. % Mo, 1.619 wt. % Mn, 0.5093 wt. % Si, and 0.175 wt. % Cu. 316SS underwent uniform corrosion during the 80% bentonite/20% Opalinus Clay isothermal, 300 °C experiments. Post-reaction 316SS formed a smectite dominated interface product (Figure 25). The primary type smectite associated with the steel surface appears to be an Fe-saponite. Smectite expands to 16.8 Å (with 002 at 8.44 Å) upon ethylene glycol saturation suggesting no significant amount of mixed-layering is present. Pentlandite ($(Ni,Fe)_9S_8$) also formed concurrently with the smectite phase (Figure 25). The smectite morphology tends to be fairly consistent producing a bladed to micaceous habit with a rose-like texture (Figure 26). Chemical analyses of post-reaction 316SS and corrosion products

indicate there was significant Fe leaching from the 316SS forming a Cr-enriched steel outer layer. Smectite coatings were enriched in iron most likely from the iron leached from the 316SS (Figure 27). Fe-rich phyllosilicates that formed on steel plates in the ramped experiments have 06ℓ diffraction bands 1.535 (9.210 Å b-parameters), corresponding to a trioctahedral phyllosilicate (Figure 25; Kohyama et al. 1973; Moore and Reynolds 1997). Ni is preferentially sequestered into the sulfide phase. There was no Ni observed in any of the silicate fractions.

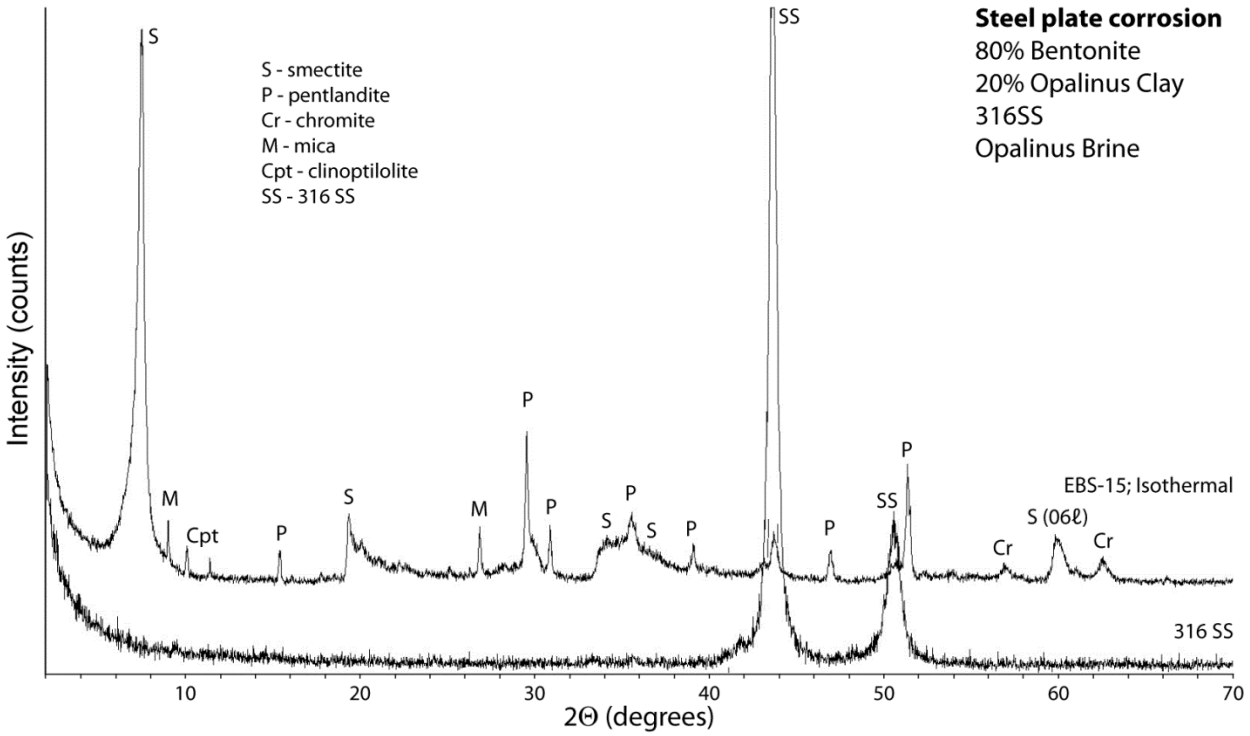

Figure 25. XRD patterns of starting 316SS and corroded 316SS associated with EBS-15. Fe-saponite is the dominate corrosion product associated with steel. Sulfide is the primary sink for leached Ni forming pentlandite. Mica and clinoptilolite are from residual bentonite coating the steel plates.

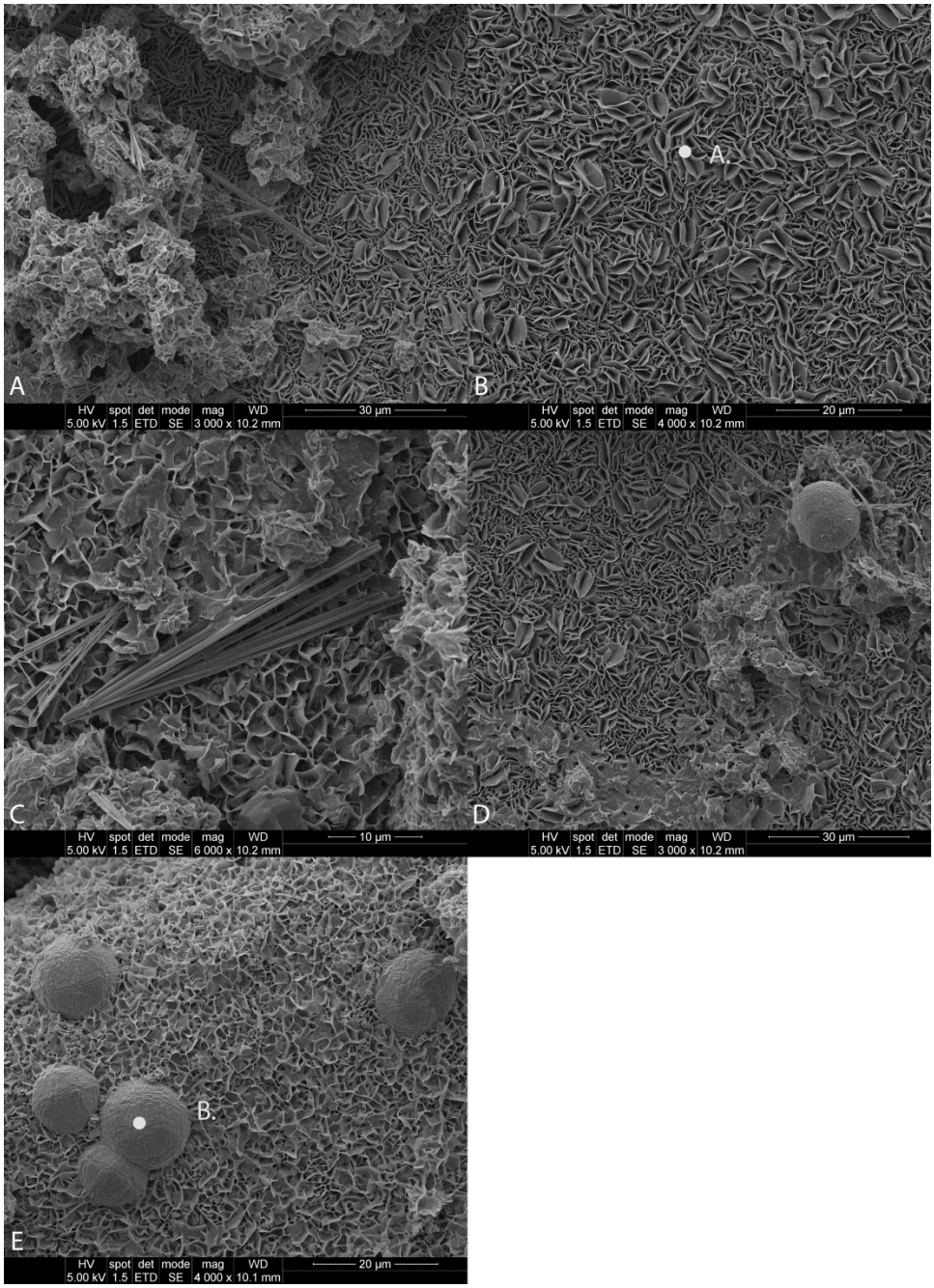

Figure 26. SEM image of 316SS corrosion products associated with Opalinus Clay in EBS-15. A) Fe-saponite corrosion product associated with the 316SS surface partially covered with clay matrix from the bulk system. B) Fe-saponite corrosion product showing typical morphology associated with this type of corrosion. EDX analysis at point A. is presented in Figure 27 A. C) Possible zeolite fibers from the bulk system laying on Fe-saponite. D) Analcime-wairakite particle lying on top of Fe-saponite. E) Analcime-wairakite grown within the Fe-saponite corrosion products suggesting they utilized the 316SS surface as a growth substrate. EDX analysis at point B. is presented in Figure 27 B.

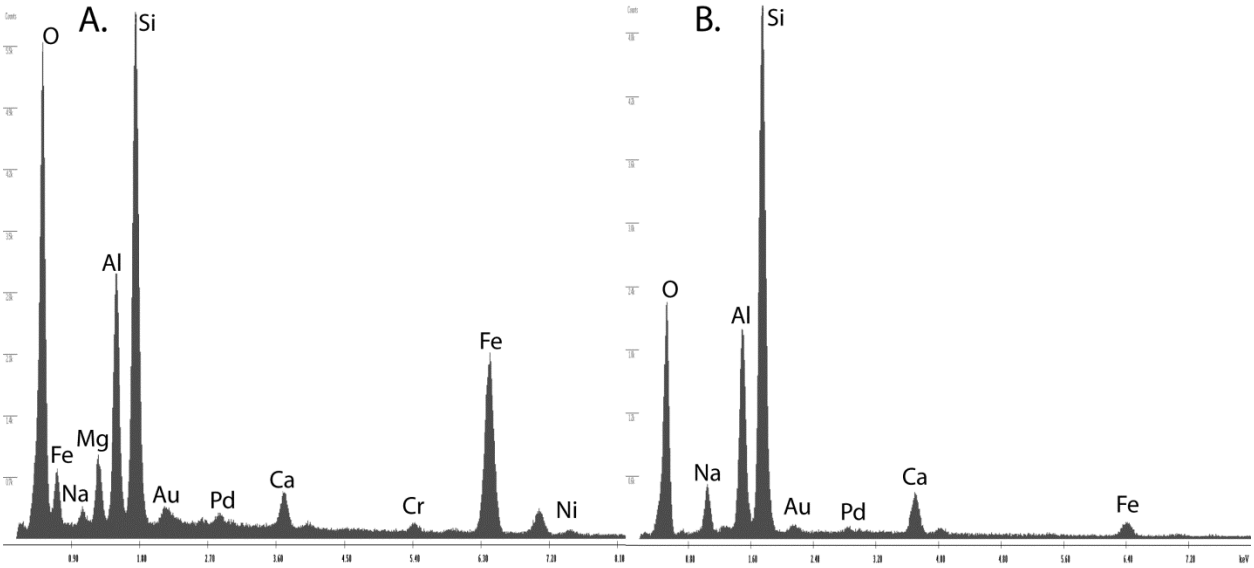

Figure 27. EDX analyses of 316SS corrosion products associated with EBS-15 in Figure 25. A) Fe-saponite on edge to minimize underlying contamination. B) Analcime-wairakite particle imbedded within the Fe-saponite corrosion coating. Many analcime-wairakite particles utilized the 316SS as a growth substrate.

3.6 Capsule Experiments

Mineralogical results from the various capsule experiments are summarized in Tables 10 and 11.

Initial experiments were setup to have an excess of potassium as the primary interlayer cation and a KCl solution to force montmorillonite illitization under the same EBS thermal conditions. Under these conditions a poorly-crystalline R3 illite (0.90-0.95)-smectite was produced with no R0-1 I-S observed. Decreasing potassium to 300 - 559 mg/L (Stripa solution) yielded similar results to the all K system by producing a R3 illite (0.90-0.95)-smectite. Interestingly, none of the K-dominated experiments yielded pure illite even with excess K and experimental times up to 6 months at temperature above 120°C.

Adding a K-saturated montmorillonite to a saturated $CaCl_2$ solution significantly slowed the illitization process. After 6 weeks at 300°C, no smectite illitization was observed, but after six months an R0 illite (0.36)-smectite was produced. Lowering the $CaCl_2$ concentration, does little to the illitization rates, but does produce mordenite in addition to the R0 illite (0.37)-smectite.

Alternatively, adding a Ca-saturated montmorillonite to a saturated KCl solution does not significantly alter the illitization rates compared to the K-dominated system by producing a R3 illite (0.95)-smectite. Diluting the $CaCl_2$ concentration by a third produced a less ordered illitized product (R1 illite (0.72)-smectite).

Experiments with WY bentonite without any processing yielded similar results to the other EBS experiments. WY bentonite in contact with Stripa or $CaCl_2$ solutions yielded no illitization

producing 100% expandability. However, using a KCl solution, R3 illite (0.95)-smectite is produced.

$AlCl_3$ and citric acid additions to the KCl and $CaCl_2$ solutions completely dissolved the montmorillonite fractions and precipitated kaolinite, halloysite, and amorphous materials. Adding various types of host rock components (i.e., Montana illite, Montana illite-smectite, Grimsel granodiorite, K-feldspar (orthoclase), albite, and muscovite) had a negligible effect on smectite illitization.

	Clay Type	Solution Type	Run temp, °C	Run time	°2θ				Δ°2θ	Expandable	Mineralogy
					001	002	003	005	002/003	%	
CAP-1	-2 µm, K-Bentonite	Stripa V2.3	300	6 weeks	ClayStrat+						R3 illite(0.95)-smectite
CAP-2	-2 µm, K-Bentonite	3,550 mg/L KCl	300	6 weeks	ClayStrat+						R3 illite(0.95)-smectite
CAP-3	-2 µm, K-Bentonite	8,130 mg/L $CaCl_2$	300	6 weeks	5.20	10.31	15.62	26.15	**5.31**	97	R0 illite(0.03)-smectite R0 illite(0.16)-smectite
CAP-4	WY Bentonite	Stripa V2.3	300	6 weeks	5.20	10.39	15.70	26.30	**5.31**	97	R0 illite(0.03)-smectite
CAP-5	WY Bentonite	3,550 mg/L KCl	300	6 weeks	ClayStrat+						R3 illite(0.95)-smectite
CAP-6	WY Bentonite	8,130 mg/L $CaCl_2$	300	6 weeks	5.19	10.37	15.61	26.08	**5.24**	101	smectite
CAP-11	-2 µm, K-Bentonite	K-Al brine	300	6 weeks							kao, halloy, amph
CAP-12	-2 µm, K-Bentonite	Ca-Al brine	300	6 weeks							kao, halloy, amph
CAP-13	-2 µm, K-Bentonite	8,130 mg/L $CaCl_2$	300	6 weeks							kao, halloy, amph
CAP-14	WY Bentonite	K-Al brine	300	6 weeks							kao, halloy, amph
CAP	WY Bentonite	Ca-Al brine	300	6							kao, halloy,

-15				weeks							amph
CAP -16	WY Bentonite	K-Al Citric	300	6 weeks							kao, halloy, amph
CAP -17	WY Bentonite	Ca-Al Citric	300	6 weeks							kao, halloy, amph
CAP -18	-2 µm, K-Bentonite	Ca-Al brine	300	6 weeks							kao, halloy, amph
CAP -19	WY Bentonite; 5% IMt-2	Stripa V2.3	300	6 weeks	5.16	10.33	15.59	26.2	**5.26**	100	smectite
CAP -20	WY Bentonite; 15% IMt-2	Stripa V2.3	300	6 weeks	5.15	10.32	15.60	26.16	**5.28**	99	smectite
CAP -22	WY Bentonite; 5% ISMT	Stripa V2.3	300	6 weeks	5.21	10.38	15.7		**5.32**	97	R0 illite(0.03)-smectite
CAP -23	WY Bentonite; 15% ISMT	Stripa V2.3	300	6 weeks							n.d.
CAP -24	WY Bentonite; 25% ISMT	Stripa V2.3	300	6 weeks							n.d.

Table 10. Mineralogical results from capsule experiments with a brief reaction condition summary. Expandability was determine by the Δ°2θ method, but more complicated illite-smectite was model using ClayStrat+.

	Clay Type	Solution Type	Run temp, °C	Run time	°2θ				Δ°2θ	Expand	Mineralogy
					001	002	003	005	002/003	%	
CAP-26	-2 µm, K-Bentonite	3,550 mg/L KCl	300 to 120	6 months	ClayStrat+						R3 illite(0.95)-smectite
CAP-27	-2 µm, K-Bentonite	1,183 mg/L KCl	300 to 120	6 months	ClayStrat+						R3 illite(0.95)-smectite
CAP-28	-2 µm, K-Bentonite	8,130 mg/L $CaCl_2$	300 to 120	6 months	5.32	10.11	16.19		**6.08**	64	R0 illite(0.36)-smectite
CAP-29	-2 µm, K-Bentonite	2,710 mg/L $CaCl_2$	300 to 120	6 months	5.32	10.14	16.12	26.66	**5.98**	67	R0 illite (0.37)-smectite; mord
CAP-31	WY Bentonite	3,550 mg/L KCl	300 to 120	6 months	ClayStrat+						R3 illite(0.95)-smectite
CAP-32	WY Bentonite	1,183 mg/L KCl	300 to 120	6 months	ClayStrat+						R3 illite(0.95)-smectite
CAP-33	WY Bentonite	8,130 mg/L $CaCl_2$	300 to 120	6 months	5.25	10.55	15.89	26.7	**5.34**	96	R0 illite(0.04)-smectite
CAP-34	WY Bentonite	2,710 mg/L $CaCl_2$	300 to 120	6 months	5.27	10.56	15.91	26.69	**5.35**	95	R0 illite(0.05)-smectite; mord
CAP-36	-2 µm, Ca-Bentonite	3,550 mg/L KCl	300 to 120	6 months	ClayStrat+						R3 illite(0.95)-smectite
CAP-37	-2 µm, Ca-Bentonite	1,183 mg/L KCl	300 to 120	6 months	7.08	9.53	16.96	26.98	**7.43**	28	R1 illite(0.72)-smectite
CAP-39	-2 µm, Ca-Bentonite	2,710 mg/L $CaCl_2$	300 to 120	6 months	5.26	10.53	15.89	26.69	**5.36**	95	R0 illite(0.05)-smectite; mord
CAP-40	-2 µm, Bentonite;10% Kspar	Stripa V2.4	300	6 weeks	5.20	10.37	15.60	26.42	**5.23**	102	smectite
CAP-41	-2 µm, Bentonite20% Kspar	Stripa V2.4	300	6 weeks	5.21	10.40	15.65	26.29	**5.25**	100	smectite

CAP-42	-2 µm, Bentonite;10% alb	Stripa V2.4	300	6 weeks	5.21	10.39	15.62	26.27	**5.23**	102	smectite
CAP-43	-2 µm, Bentonite; 20% alb	Stripa V2.4	300	6 weeks	5.19	10.37	15.62	26.24	**5.25**	100	smectite
CAP-44	-2 µm, Bentonite; 10% musc	Stripa V2.4	300	6 weeks	5.21	10.39	15.66		**5.27**	99	smectite
CAP-45	-2 µm, Bentonite; 20% musc	Stripa V2.4	300	6 weeks	5.22	10.39	15.68		**5.29**	98	smectite
CAP-46	-2 µm, Bentonite; 10% Grimsel	Stripa V2.4	300	6 weeks	5.21	10.40	15.69	26.27	**5.29**	98	smectite
CAP-47	-2 µm, Bentonite; 20% Grimsel	Stripa V2.4	300	6 weeks	5.23	10.38	15.74		**5.36**	95	R0 illite(0.05)-smectite
CAP-48	-2 µm, Bentonite; 30% Grimsel	Stripa V2.4	300	6 weeks	5.19	10.36	15.65	26.34	**5.29**	98	smectite

Table 11. Mineralogical results from capsule experiments with a brief reaction condition summary. . Expandability was determine by the Δ°2θ method, but more complicated illite-smectite was model using ClayStrat+.

4. Discussion

4.1 Bentonite Experiments

4.1.1 Layer Charge. To better determine if any layer charge increase took place during the EBS experiments, a series of cation exchanges was performed followed by ethylene glycol saturation. Smectite swelling is the competing effects between the interlayer cation hydration energy (hydration-repulsion) and the Coulombic attractive forces between negatively-charged 2:1 layers and positively-charged interlayer cations (Laird, 1996; 2006). When Coulombic attractive forces dominate over hydration-repulsion collapse of the interlayer spaces occurs. Collapse can be cause by several possible scenarios, increased layer charge (i.e., illitization), increased interlayer cation charges (i.e., interlayer exchange reactions), or decreased interlayer cation hydration energy (i.e., interlayer exchange reactions). Alternatively, swelling occurs when the hydration-repulsion dominates over the Coulombic attractive forces.

The purpose of these cation exchanges was to exchange in different cations with differing hydration energies. If there was an increase in layer charge, but the Coulombic attraction is not enough to overcome the hydration energy of the dominant interlayer cation (Na^+ @ -411 kJ mol^{-1}), then the material should fully expand upon ethylene glycol saturation. However, performing exchanges with the same reaction material with cations that have lower hydration energies (i.e., K^+ @ -337 kJ mol^{-1}) or with cations that have a higher valence charge (i.e., Ca^{2+} -1,593 kJ mol^{-1}) and the interlayers do not fully expand upon ethylene glycol saturation, then there was an increase in the 2:1 layer charge.

Upon saturation with K^+, the montmorillonite peaks broadened and lost about 4 – 7 % expandability. Compared to the starting K-exchanged montmorillonite, there was no significant difference in expandable material. This suggests that the starting montmorillonite has about 7% of the interlayer spaces with a high-layer charge. This same trend is observed with the Ca^{2+} and Li^+ saturated reaction products. It is evident that there is variation in the layer charge within the starting montmorillonite, but the current EBS reaction conditions do not significantly alter the layer charges or charge distribution. This is also confirmed by the CEC measurement showing no change in CEC values between all reaction products and the starting montmorillonite.

4.1.2 Mineral Evolution. There was no evidence of illite-smectite mixed-layering during the six-month cooling experiment where montmorillonite was heated to 300°C for four months. This is consistent with the other EBS experiments in our Na-dominated hydrothermal systems. Much of the illitization concepts related to a Na-rich systems have been previously discussed (Caporuscio et al., 2013; Cheshire et al., 2014a; 2014b), but is repeated here as it applies to the six-month system.

Smectite-to-illite transformation is not well understood and probably follows several different reaction pathways, i.e. solid-state transformation and dissolution-precipitation (Güven 2001; Dong 2005; Zhang et al. 2007). These different reaction mechanisms may be due to different geological or experimental conditions, including variables such as water/rock ratio, fluid composition, redox state, occurrence of microbial organisms, and presence or absence of organic matter (Small et al. 1992; Small 1993; Güven 2001; Dong

2005; Zhang et al. 2007). Solid-state transformation may be operative in closed systems with a low water/rock ratio, whereas, dissolution-precipitation may be the dominant mechanism in open systems with high water/rock ratios (Zhang et al. 2007). In the current experiments, it appears that two major parameters are preventing smectite-to-illite alteration: alkali and silica solution compositions.

Current experimental results are consistent with other experimental data showing that a limited supply of K^+ along with a relatively high Na^+ activity significantly decreases dioctahedral smectite illitization rates (Eberl and Hower 1977; Eberl 1978, Eberl et al. 1978; Roberson and Lahann 1981; Mosser-Ruck et al. 1999). Their studies also show that, in general, dioctahedral smectites with low hydration-energy interlayer-cations (e.g., K^+, Rb^+, Cs^+) are more susceptible to smectite-to-illite alteration reaction compared to dioctahedral smectites with higher hydration-energy interlayer-cations (e.g., Na^+, Ca^{2+}, Mg^{2+}). These results are consistent with capsule experiments from the current work. However, the presence of a Na-rich system does not preclude smectite illitization. There have been numerous occurrences of illite and illite/smectite occurring in natural or experimental systems that are Na-dominated (Bannister 1943; Frey 1969; Eberl and Hower 1977; Eberl et al. 1978; Whitney and Velde 1993; Mosser-Ruck et al. 1999; Środoń 1999). But, in all these cases, either the temperatures exceeded 300°C or there was a significant potassium source from groundwater or coexisting minerals. Temperatures beyond 300°C exceed the upper temperature limits expected for a repository environment and the experimental temperature from this investigation (Greenburg and Wen 2013). Additionally, Na-bentonites are currently the bentonite of choice for a repository backfill, thereby, providing a K-depleted and Na-enrich system. Even though the aqueous solutions in the current experiments were K-rich, the overall system (bentonite + water) was Na^+ dominant (~ 2,400 mg Na/L) and K^+ poor (~ 1,000 mg K/L). Include Ca^{2+} (~750 mg/L, bentonite + water) in the discussion, the overall (Na^+ + Ca^{2+})/K^+ ratio is greater than 3.0. It is evident that the dominance of Na^+ and Ca^{2+} along with the low abundance of K^+ does not facilitate illite-smectite formation after 45 days at 300°C.

Silica activities in these experiments appear to be controlled partially by silicate mineral dissolution and precipitation, in addition to clinoptilolite to analcime alteration. Solutions saturated with respect to cristobalite probably contributed to illitization retardation in these current experiments. Systems with silica concentrations higher than quartz saturation have been shown to significantly retard illitization rates (Eberl et al. 1978; Lahann and Roberson 1980; Abercrombie et al. 1994). Abercrombie et al. (1994) has shown that a K-smectite to be the stable phase, potentially up to 200°C, provided silica activity is higher than ~10^{-2}. It was noted by Abercrombie et al. (1994) that as silica levels decreased, due to quartz precipitation, illitization progressed within the system. Therefore, an environment with silica concentrations saturated with respect to cristobalite at temperatures less than 300°C, such as the current experiments, smectite-to-illite alteration should further be inhibited. However, it is important to consider differences between closed, experimental systems versus geological or repository environments that open to the surrounding environment. Many processes that are observed in a closed, experimental system might be mitigated in an open system where solutes can freely move in and out of the environment.

We have shown that at higher silica activities (i.e., cristobalite saturation) clinoptilolite is altered to a high-silicon analcime under the current experimental conditions. Again, these reactions were observed in the other EBS experiments with extended periods at 300°C. Previous studies (Smyth 1982; Wilkin and Barnes 1998; 2000; Cheshire et al., 2013; 2014a) have linked changes in Na, Al, and Si activities with the alteration of clinoptilolite by analcime. However, experimental work (T < 300°C) from Wilkin and Barnes (1998) indicate silica activity influences clinoptilolite alteration by affecting the reaction affinity rather than controlling the reaction equilibrium. Wilkin and Barnes (1998) also show that analcime can form in an environment saturated with respect to cristobalite provided there is a sufficient change in the Na and/or Al activities.

The effect on the repository due the changes in the system's silica phases and concentrations appears to be a significant issue regarding the repository stability and physical properties. Cementation via silica precipitation is believed to pose the greatest risks to the repository stability and isolation capability compared other mineral reaction (Pusch et al. 1998). Silica precipitation has the potential to weld the smectite lamellae together and reduce the smectite expandability (Pusch et al. 1998; Pusch 2001). The primary mechanism for silica liberation includes smectite illitization, silica/silicate dissolution/saturation, and zeolite alteration.

Production of $H_2S_{(aq,g)}$ is most likely related to pyrite solubility in a chloride-bearing solution (Crerar et al. 1978; Ohmoto et al. 1994). The highly reducing nature of the experimental system easily preserves the $H_2S_{(aq,g)}$ species. Sulfide-induced corrosion of the waste canisters is the primary concern in repository systems (Börjesson et al. 2010). The Swedish Nuclear Fuel and Waste Management Company (SKB) have emplaced fairly strict sulfur specifications (sulfide content < 0.5 wt. %; total sulfur < 1 wt. %) for the bentonite buffer used in their repositories (Börjesson et al. 2010).

4.1.3 Wet vs. Dry Experiments. Dry system kinetics and mineral solubility are highly restricted. Many of the chemical reactions observed in the wet system (9:1 water: rock systems) either do not take place or are restricted in the dry (~ 15 wt. %) system. Pyrite does not undergo decomposition and clinoptilolite undergoes limited dissolution with limited analcime formation. These conditions are more realistic to a repository at 300 °C, because bentonite blocks or pellets typically have ~10 – 20 wt. % H_2O and would be compressed during the repository lifetime. It is evident that reaction kinetics are accelerated under water saturation due to increased ion mobility and minerals' saturation limits.

4.1.4 Heating profile. As stated above mineral evolution and geochemical processes are consistent between all three reactions with differing heating profiles. These profiles were designed to mimic the maximum heating profile during a repository's lifetime, with exception to the duration of each stage: (1) heating from 120°C (2 weeks); 220°C (2 weeks); 300°C (1 week); (2) isothermal, 300°C (6 weeks); (3) cooling from 300°C (16 weeks), 220°C (4 weeks); 120°C (4 weeks). There were no retrograde reactions observed during the cooling phase. Essentially EBS-10 and EBS-13 show no significant differences between the two reaction products.

It would be expected during the early emplacement of the waste canister that silica saturation, exchange reaction will take place under limited conditions. The relatively dry environment of the early bentonite would significantly restrict the mineral reactions due to the limited ion mobility and early saturation. It is possible that sulfide gas could be generated, but as shown in the 15 wt. % free moisture experiment (EBS-12) pyrite decomposition was not readily observed due to the restricted solubility. As temperatures increase to peak temperature (currently unknown and will be determine during repository design), various possible zeolite reactions (mordenite, laumontite, analcime, wairakite formation) will occur due to the precursor clinoptilolite and volcanic glasses. These zeolite reactions, along with silica saturation reactions, will control the porewater solution chemistry and determine any further mineral alteration. Illite formation can still progress, if a K-source is available, but, K-source stability with respect to the repository conditions will determine the illitization rates. As shown in the capsule experiments, adding K-bearing minerals does not necessarily force illitization; dissolution of those mineral phases has to take place. Illitization thermodynamics and kinetics are strongly tied to the alkali, alkaline earth, silica, and hydrogen (pH) activities; therefore, it is difficult to predict whether illitization will occur in a repository. After the high temperature pulse passes and temperatures begin to decrease, retrograde reaction have the potential to further change the high temperature mineralogy. As observed in current work, no significant retrograde reactions took place, but as with any experimental work slow kinetics of such reactions make them difficult to show experimentally. It would be expected silica saturation is maintained at continuing lower temperatures by releasing silica from solution. This in turn should partially cement and fill pores in the bentonite. Retrograde zeolite reactions are expected, but currently the extent of such reaction and types are unknown.

4.1.5 Corrosion in bentonite. Results from these experiments have shown the more dynamic environment associated with this system is at the bentonite-metal interface. Trioctahedral, Fe-rich saponite are crystallized on steel surfaces forming a reactive substrate with a high surface area compared to the original steel surfaces. Partial dissolution of the steel plates contributing ferrous iron into a fluid phase with silica and aluminum facilitates Fe-saponite (smectite) crystallization (Figure 28). Liberated Ni is preferentially is crystallized in the sulfide phases forming pentlandite ($(Fe,Ni)_9S_8$) and millerite (NiS). Oxidative leaching of Fe and Ni forms a chromite $(Cr_{1.04},Fe_{0.96})(Fe_{0.69},Ni_{0.31})O_4$ passivation layer on the outer surface of the 316SS plates, restricting corrosion rates (0.1 $\mu m \cdot d^{-1}$ stainless steel) compared to non-alloyed metals (0.6 $\mu m \cdot d^{-1}$ low-carbon steel and 0.8 $\mu m \cdot d^{-1}$ copper). Formation mechanism for Fe-saponite is not completely understood for this system. There are two possible scenarios for Fe-saponite formation: 1) direct crystallization in a Fe- and Si-rich solution as a result from bulk mineralogy influences or 2) Fe + montmorillonite interactions breaking down montmorillonite and producing Fe-saponite. The latter mechanism would be a deleterious reaction to the overall repository as montmorillonite is primary mineral in the barrier.

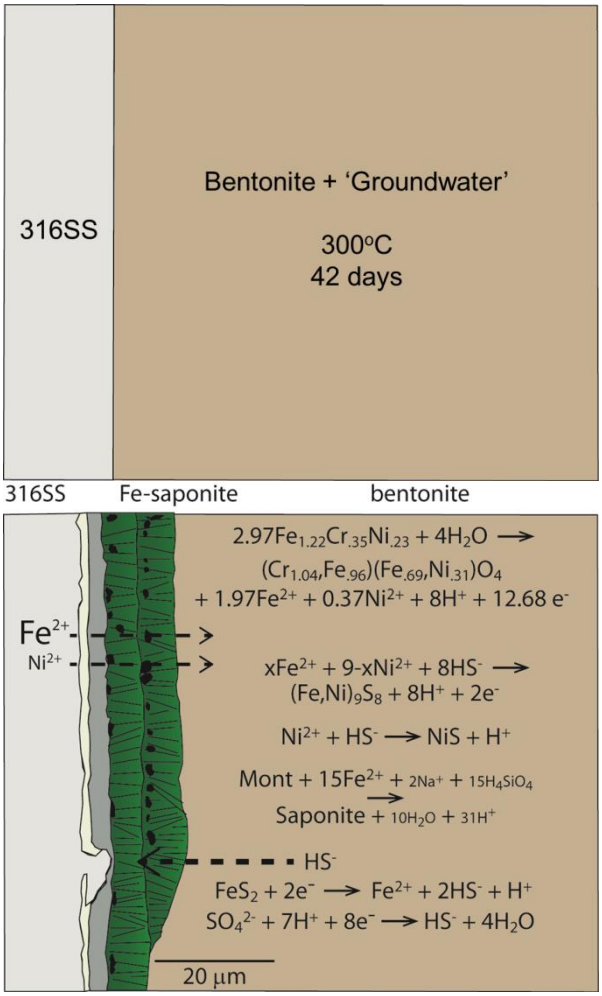

Figure 28. Cartoon of corrosion processes related to EBS experiments containing 316SS.

Fe-phyllosilicates tend to have strong sorption properties towards actinides and other radioactive materials; therefore, they have the potential to provide added barrier properties for actinide containment. The dynamics and reactivity of actinide adsorption need to be incorporated into the long term repository performance evaluation models. However, this work has never been addressed in repository studies. Inclusion of a reactive, high surface-area canister into used-fuel repositories performance assessments should help provide a viable repository evaluation.

4.2 Opalinus Clay

There are very limited cation exchange reactions associated with the Opalinus Clay and solution chemistry due to no significant amount of smectite. Opalinus Clay is dominated with clay phases (i.e., illite, I-S, kaolinite, and chlorite) that typically do not freely exchange cations.

4.2.1 Zeolite formation. The primary authigenic zeolite in experiments with Opalinus Clay alone differs from the Opalinus Clay experiments with bentonite. These differences appear to be strongly related to the solution chemistry. Bentonite-barring experiments most likely exchanged Ca into the montmorillonite interlayer producing a Ca depleted solution compared to the Opalinus Clay experiments. Solution chemistry associated with the Opalinus clay will remain fairly unchanged unless mineral alteration occurs. The changing of solution chemistry as function of the types of clays in the system appears to indirectly control zeolite stability.

The analcime-wairakite series typically forms through dissolution-precipitation mechanisms through an intermediate mineral or glass phase. In the other EBS experiments, it appears that analcime formed from a direct dissolution-precipitation at the expense of precursor clinoptilolite and volcanic glass. This paragenetic sequence has been previously observed by many other researchers (Smyth, 1982; Masuda et al., 1996; Wilkin and Barnes, 1998). Natural paragenetic sequences suggest that clinoptilolite to analcime may progress at temperatures as low as 75 - 90° C (Smyth 1982; Masuda et al. 1996). Alternatively, work from Wilkin and Barnes (1998; 2000) shows analcime formation kinetics are significantly increased at alkaline pH's (9 - 10), whereas, experiments with circum-neutral pH's showed limited to no analcime formation even at with temperatures > 100° C lasting up to 26 days. It is evident that onset temperatures associated with mineral alterations that pH, along with many other solution chemistry parameters, are important to understand.

Wairakite primarily forms when excess silica is present and typically crystallizes through either an intermediate Ca-mordenite ($CaAl_2Si_{10}O_{24}\cdot 7H_2O$) or laumontite ($CaAl_2Si_4O_{12}\cdot 4H_2O$) phase (Ames and Sands, 1958; Jové and Hacker, 1997). In their experimental works, wairakite lower limit of formation is around 315°C, with an upper limit of 450°C. However, the inclusion of small amount of Na-substitution lowers the formational conditions for wairakite. Additionally, there are limited isomorphous substitutions between analcime and wairakite making Na- or Ca-enriched end members, as opposed of a true intermediate analcime-wairakite (Steiner, 1955; Coombs, 1955; Ames and Sands, 1958). Na-mordenite has an experimental stability range between 190 to 300°C, whereas, Ca-mordenite ranges from 340 to 380°C (Ames and Sand, 1958).

The possible presence of mordenite and laumontite combined with information from Ames and Sand (1958) and Jové and Hacker (1997) strongly suggests that wairakite in this system is probably from the decomposition of mordenite and/or laumontite. Mordenite and laumontite, therefore, appears to have crystallized from the decomposition of kaolinite in the silica and Na/Ca-rich fluids. This reaction would have progressed either until the reaction was quenched or when one of the reactants was depleted and in this case, kaolinite appears to be the limiting resource as it has been completely removed. The presence of Na in our system appears to have lowered the formation temperatures to below 300°C for Na-enriched wairakite.

However, when bentonite is included into Opalinus Clay experiments, the solution chemistry changes significantly forcing the formation of a high-silicon, Ca-enriched analcime. The analcime composition from this experiment is similar to analcime from

EBS experiments with bentonite as the only clay. However, it is evident that the reaction mechanisms are very different. In bentonite only reactions, high-silicon analcime crystallized from clinoptilolite and unaltered glass with in the high Na and $SiO_{2(aq)}$ fluids. EBS experiments with 20 wt. % Opalinus Clay much of the original clinoptilolite is preserved, but kaolinite is completely removed. When kaolinite and clinoptilolite are present in a Na/Ca-rich fluid, kaolinite is preferentially recrystallized into either Na/Ca-mordenite and laumontite or analcime.

4.2.2 Clay mineralogy. Following the clay mineral evolution within Opalinus materials is complicated due to the variety of clay minerals present in the Opalinus experimental systems. Two systems were tested: (1) Opalinus Clay and (2) bentonite with 20 wt. % Opalinus Clay. The latter experiment was setup to represent mixing between a repository host rock with a bentonite backfill to determine what effects (if any) the host rock has on the backfill material. After thermal processing in brine, the Opalinus Clay appears to have an increase in the I-S distribution. The original Opalinus material appeared to have an R3 illite (0.8-0.9)-smectite, but after 300°C for 6 week in an Opalinus brine an R3 illite (0.9)/smectite and a R1 illite (0.7)/smectite was produced. However, illitization in the host rock may not be a major concern as Opalinus Clay is primarily a low-permeable barrier with very limited swelling capacity due to the low amounts of swelling smectite within the Opalinus Clay. The major concern is the reactivity of Opalinus Clay with the bentonite causing alteration to the bentonite constituents. There was negligible illitization within the bentonite fraction in the mixed reaction (EBS-15). This is consistent with the capsule experiments containing a bentonite with a secondary rock phase. It is important to note that these experiments do not preclude the possibility of host rock – bentonite interaction at these temperatures because kinetics may not allow the observation of mineral alterations under the current experimental duration. With any of these experiments representing repository system, kinetics is always an issue that has to be taken into account when interpreting data.

4.2.3 *pH effects*. Many of the reactions described above are strongly influence by the pH of the system. Most mineral reaction rates that are of concern to a repository are increased under high pH systems. Chermak (1992) showed that under pH conditions of 11-13, Na-rectorite was formed at 150 – 200°C within 17 days. Fully formed Na-mica (paragonite) developed after 32 days. Work from Eberl and Hower (1977) and Eberl (1978) do not show illitization until 260 – 400°C at quenched pH's ranging from 4 – 5. These observations are consistent with the current research. The Opalinus Clay experiment starts with a 7.5 – 7.8 solution pH, but during the reaction the pH drops to 4 – 5. The reactions experience significant zeolite reactions, but it appears illitization does not occur under the Na-dominated environment. These high pH dependent reactions will play a major factor within the bentonite backfill near the concrete liners, especially if the concrete used contains significant K^+ concentrations. However, these same reactions should have a minor impact on the bentonite backfill near the waste package because steel and copper corrosion tend to lower the pH.

5. Conclusions

There have been a large number of investigations on bentonite stability under various repository conditions (Madsen 1998; Meunier et al. 1998; Guillaume et al. 2003; Guillaume et al. 2004; Mosser-Ruck et al. 2010; Ferrage et al. 2011). Yet, there remain questions regarding bentonite's overall stability and more importantly whether montmorillonite will remain relatively unaltered through the repository life-time. After initial used-fuel emplacement there will be a pulse of heat flowing into the bentonite buffer producing an environment in which montmorillonite is typically not stable. It would be expected during the early stages of canister emplacement that silica saturation and exchange reactions will take place. However, the relatively dry environment would significantly restrict the mineral reactions due to the limited ion mobility and early saturation. As temperatures increase to peak temperature (currently unknown and will be determine during repository design), various possible zeolite reactions (mordenite, laumontite, analcime, wairakite formation) have the potential to occur if repository conditions shift to the zeolite metamorphic facies (typically starts at 50 - 150 °C; 100 – 500 bars). These zeolite reactions, along with silica saturation reactions, will control the porewater solution chemistry and determine any further mineral alteration. Illite formation can still progress, if a K-source is available, but, K-source stability with respect to the repository conditions will determine the illitization rates. It is expected that the initial heat pulse should start to decay after about 100 to 1,000 years (Wersin et al. 2007). After the high temperature pulse passes and temperatures begin to decrease, retrograde reaction have the potential to further change the high temperature mineralogy. As observed in current work, no significant retrograde reactions took place, but as with any experimental work slow kinetics of such reactions make them difficult to show experimentally. It would be expected silica saturation is maintained at continuing lower temperatures by releasing silica from solution, cementing the bentonite. Retrograde zeolite reactions are expected, but currently the extent of such reaction and types are unknown.

The repository is expected to remain "dry" during the initial 100 to 1,000 years (Wersin et al. 2007). Dry system kinetics and mineral solubility are highly restricted. Many of the chemical reactions observed in the wet system either do not take place or are restricted in the dry system. These conditions are more realistic to a repository at 300°C, because bentonite blocks or pellets typically have 10 – 20 wt. % H_2O and would be compressed during the repository lifetime. It is evident that reaction kinetics are accelerated under water saturation due to increased ion mobility and minerals' saturation limits.

There have been a number of similar investigations on bentonite stability under various repository conditions and in contact with various metals replicating possible canister compositions (Guillaume et al. 2003; Guillaume et al. 2004; Wilson et al. 2006; Mosser-Ruck et al. 2010; Ferrage et al. 2011). Partial dissolution of the steel plates contributing ferrous iron into a fluid phase with silica and aluminum facilitates Fe-saponite (smectite) crystallization. Liberated Ni is preferentially is crystallized in the sulfide phases forming pentlandite ($(Fe,Ni)_9S_8$) and millerite (NiS). Oxidative leaching of Fe and Ni forms a chromite $(Cr_{1.04},Fe_{0.96})(Fe_{0.69},Ni_{0.31})O_4$ passivation layer on the outer surface of the 316SS plates, restricting corrosion rates (0.1 μm d^{-1} stainless steel) compared to non-alloyed metals (0.6 μm d^{-1} low-carbon steel and 0.8 μm d^{-1} copper). Bentonite not in contact with

the steel waste container does not show the formation of these Fe-rich phyllosilicates. The occurrence of Fe-rich phyllosilicates most likely will not form in the bentonite away from the waste container because there is a low abundance of iron in the system. Formation mechanism for Fe-saponite is not completely understood for this system. There are two possible scenarios for Fe-saponite formation: 1) direct crystallization in a Fe- and Si-rich solution as a result from bulk mineralogy influences or 2) Fe + montmorillonite interactions breaking down montmorillonite and producing Fe-saponite. The latter mechanism would be a deleterious reaction to the overall repository as montmorillonite is primary mineral in the barrier.

In this work, we start to consider the impact host rock (i.e., Opalinus Clay from Switzerland) will have on the bentonite barrier. Several mineral alterations were observed in the heating of Opalinus clay. The primary mineral reactions are associated with zeolite formation (i.e., analcime-wairakite, laumontite, and mordenite) at the expense of kaolinite in the host rock. When bentonite is included into Opalinus Clay experiments, the solution chemistry changes significantly forcing the formation of a high-silicon, Ca-enriched analcime. Interpreting clay mineral evolution within Opalinus materials is complicated due to the variety of clay minerals present in the Opalinus experimental systems. However, it does appear that illitization does not occur within the bentonite fraction in the mixed reactions at the current experimental conditions. It is important to note that these experiments do not preclude the possibility of host rock – bentonite interaction at these temperatures because kinetics may not allow the observation of mineral alterations under the current experimental duration. With any of these experiments representing repository system, kinetics is always an issue that has to be taken into account when interpreting data.

6. FY14 – FY15 Experimental program

Research objectives for the upcoming year will be a natural progression of experimental results obtained in FY13-FY14. For the remainder of FY14, an emphasis will be put on performing detailed geochemical modeling of the bentonite and Opalinus systems. Focus on reactive modeling between the three barrier segments (bentonite-metal, bentonite, and bentonite-host rock) will provide further information on our experimental systems. Additional work for FY14 will be to complete and submit two peer-reviewed publications on 1) the corrosion behavior of steel and copper in contact with bentonite and 2) alteration processes associated with Opalinus Clay at elevated temperatures.

For FY15 we expect to develop three research thrusts. First, we will run a series of high pressure, temperature experiments containing brine – bentonite – metal – host rock at the isothermal, 300°C and six-month cooling heating profiles. Completing our six-month experiments with different types of metals will provide valuable data on the long-term corrosion effects associated with bentonite. We will continue to examine the Opalinus Clay, but would also investigate granitic (i.e., Grimsel granodiorite) and mafic (e.g., basalt or amphibolite) materials if funding is appropriated from Granite EBS studies. Critical information would be gleaned from geochemical and petrographic information, which would allow us to trace mineral transitions through pressure, temperature, time (P, T, t) space. These experiments would be the first to duplicate the events occurring during

a thermal pulse and will provide date on irreversible mineral transformations in correlation with various host rock compositions.

Our secondary approach will be to focus on the expanding the experimental geochemical parameters. First evaluating the possible interaction between the radiological elements and bentonite will provide data on the possible retention of radionuclides if a release is to occur. We will use non-radiological proxies as a substitute for possible alkali earths (i.e., not radioactive Cs^{+}) and actinides present in the waste form (actinide proxies, e.g., Nd^{3+}, Tb^{3+}, or Eu^{3+} for Am^{3+}; Nd^{3+} or Hf^{4+} for Pu^{4+}). Expanding the solution chemistry properties to probe the conditions for illitization and other mineral reactions will provide reaction dynamics that were not considered and can provide kinetic data on important reactions (i.e., SiO_2 concentrations, H_2O content, series of more dilute systems or reactant limited series as to not saturate the system forcing illitization).

A third focus for FY14 – FY15 is the preparation for expected research on the FEBEX-DP international project. We will focus our efforts on designing our experimental program to investigate chemical and physical characteristics of bentonite blocks from the 18 years at 100°C full-scale heater test. We will perform routine mineralogical and geochemical characterizations, but will further test the thermal limits of the system. Sub-cores from each sample provided will be placed in Au-capsules for further heating to temperature ranging from 150 to 300°C to examine the thermal reactivity of the 18 year bentonite. We will examine bentonite-metal, bentonite, and bentonite-cement reactivities. Results from these heating experiments will provide valuable data associated increasing thermal repository limits and diffusional data related to cementitious materials and metals.

Other research that will be ongoing include: (1) further investigation of Fe-saponite and chalcocite reaction surfaces on steel and copper, respectively, as potential passivating agents, (2) transmission electron microscopy (TEM) examination of the pre- and post-reaction montmorillonite particles to quantify if localized chemical zonation is present within discrete particles, and (3) perform solution calorimetry and differential scanning calorimetry of purified reaction products to produce accurate thermodynamic properties for our experimental system and thereby providing the most accurate thermodynamic and kinetic models.

The proposed lines of study are presented in bullet form below for easy reference.

- Provide information on complete repository thermal pulse event, using long term (6 month) experiments with and without host rocks.
- Performed detailed geochemical modeling of F13-FY15 experimental reaction
- International FEBEX-DP – hydrothermal treatment of FEBEX samples expanding the thermal range in addition to routine mineral/geochemical interrogations.
- Capsule experiments with Cs and proposed non-radioactive actinide proxies (e.g., Nd^{3+}, Tb^{3+}, or Eu^{3+} for Am^{3+}; Nd^{3+} or Hf^{4+} for Pu^{4+}) and expanded parameters (SiO_2 concentrations, longer reaction times, H2O content, series of more dilute systems or reactant limited series (not flood the system forcing illitization) .

- Perform transmission electron microscope (TEM) investigation looking at very local chemical changes in a single montmorillonite particle.
- Purify mineral phases for thermodynamic investigations using solution calorimetry

7. Acknowledgements

We would like to thank Emily Kluk and Diana Brown for XRF analyses. Scanning electron microscopy facilities were provided by Materials Science and Technology group at Los Alamos National Laboratory. Dr. George Mason at the University of Oklahoma was instrumental in the obtaining of EMP analyses. Funding was through the Department of Energy's Used Fuel Disposition Campaign.

8. References

Abercrombie, H.J., Hutcheon, I.E., Bloch, J.D., and de Caritat, P. (1994) Silica activity and the smectite-illite reaction. Geology, 22, 539-542.

Ames, L.L. and Sand, L.B. (1958) Hydrothermal synthesis of wairakite and calcium-mordentite. *The American Mineralogist*, 43, 476-480.

Bannister, R.A. (1943) Brammalite (sodium-illite) a new mineral from Llandebie, South Wales. Mineralogical Magazine, 26, 304-307.

Börjesson, L., Gunnarsson, D., Johannesson, L-E., and Jonsson, E. (2010) Design, production and initial state of the buffer. Svensk Kärnbränslehantering Technical Report, TR-10-15, pp. 89.

Burgess, J. (1978) Metal Ions in Solution. John Wiley & Sons, Inc. pp. 481.

Busenberg, E. and Clemency, C.V. (1973) Determination of the cation exchange capacity of clays and soils using an ammonia electrode. *Clays and Clay Minerals*, 21, 213-217.

Caporuscio, F.A., Cheshire, M.C., Rearick, M.S., Jove-Colon, C., and McCarney, M.K. (2013). EBS Report - LANL Experimental update of buffer/backfill at elevated P,T. FCRD-USED-2013-000207.

Chermak, J.A. (1992) Low temperature experimental investigation of the effect of high pH NaOH solutions on the Opalinus Shale, Switzerland. *Clays and Clay Minerals*, 40, 650-658.

Cheshire, M.C., Caporuscio, F.A., Jové-Colón, C., and McCarney, M.K. (2013) Alteration of clinoptilolite into high-silica analcime within a bentonite barrier system under used nuclear fuel repository conditions. *Proceeding from the 14th International High-Level Radioactive Waste Management Conference,* 410-415.

Cheshire, M.C., Caporuscio, F.A., Jove-Colon, C., and McCarney, M.K. (2014a) Bentonite Clay Evolution at Elevated Pressures and Temperatures: An experimental study for generic nuclear repositories. *In Press, American Mineralogist*.

Cheshire, M.C., Hardin, E., Caporuscio, F.A., Jove-Colon, C., and McCarney, M.K. (2014b) Geochemical Investigation in an Effort to Increase Bentonite Barrier's

Thermal Load Capacity to Accommodate 32-PWR Dual Purpose Canisters. *Proceedings from the International Conference on the Performance of Engineered Barriers*, 185-190.

Chipera, S.J. and Bish, D.L. (2002) FULLPAT: a full-pattern quantitative analysis program for X-ray powder diffraction using measured and calculated patterns. *Journal of Applied Crystallography*, 35, 744–749.

Chung, F.H. (1974) Quantitative interpretations of X-ray diffraction patterns of mixtures. I. Matrix flushing method for quantitative multicomponent analysis. *Journal of Applied Crystallography*, 7, 519-525.

Coombs, D.S. (1955) X-ray observations on wairakite and non-cubic analcime. *Mineralogical Magazine*, 30, 699-708.

Couture, R.A. (1985) Steam rapidly reduces the swelling capacity of bentonite. *Nature*, 318, 50-52.

Crerar, D.A., Susak, N.J., Borcsik, M., and Schwartz, S. (1978) Solubility of the buffer assemblage pyrite + pyrrhotite + magnetite in NaCl solution from 200 to 350°C. Geochimica et Cosmochimica Acta, 42, 1427-1437.

Dong, H. (2005) Interstratified illite-smectite: A review of contributions of TEM data to crystal chemical relation and reaction mechanisms. Clay Science, 12, Supplement 1, 6-12.

Eberl, D. and Hower, J. (1977) The hydrothermal transformation of sodium and potassium smectite into mixed-layer clay. *Clays and Clay Minerals*, 25, 215-227.

Eberl, D. (1978) Reaction series for dioctahedral smectites. *Clays and Clay Minerals*, 26, 327-340.

Eberl, D., Whitney, G., and Khourym, H. (1978) Hydrothermal reactivity of smectite. *American Mineralogist*, 63, 401-409.

Eberl, D.D., Velde, B., and McCormick, T. (1993) Synthesis of illite-smecite from smectite at Earth surface temperatures and high pH. *Clay Minerals*, 28, 49-60.

Ferrage, E., Vidal, O., Mosser-Ruck, R., Cathelineau, M., and Cuadros, J. (2011) A reinvestigation of smectite illitization in experimental hydrothermal conditions: Results from X-ray diffraction and transmission electron microscopy. *American Mineralogist*, 96, 207-223.

Frape, S.K., Blyth, A., Blomqvist, R., McNutt, R.H., and Gascoyne, M. (2003) Deep Fluids in the Continents: II. Crystalline Rocks, Treatise on Geochemistry, 5, J. I. Drever, ed., 541-580.

Frey, M. (1969) A mixed-layer paragonite/phengite of low-grade metamorphic origin. Contribution to Mineralogy and Petrology, 24, 63-65.

Greenberg, H.R. and Wen, J. (2013) Repository layout and host rock thermal gradient trade study for large waste packages in clay/shale: Using the DSEF thermal analytical model. LLNL-TR-639869-DRAFT, pp. 38.

Guillaume, D., Neaman, A., Cathelineau, M., Mosser-Ruck, R., Peiffert, C., Abdelmoula, M., Dubessy, J., Villieras, F., Baronnet, A., and Michau, N., (2003) Experimental synthesis of chlorite from smectite at 300 °C in the presence of metallic Fe. *Clay Minerals*, 38, 281-302.

Guillaume, D., Neaman, A., Cathelineau, M., Mosser-Ruck, R., Peiffert, C., Abdelmoula, M., Dubessy, J., Villieras, F., and Michau, N., (2004) Experimental study of the transformation of smectite at 80 to 300 ^{o}C in the presence of Fe oxides. *Clay Minerals*, 39, 17-34.

Güven, N. (2001) Mica structure and fibrous growth of illite. Clays and Clay Minerals, 49, 189-196.

International Atomic Energy Agency (IAEA) (2000) Multi-purpose container technologies for spent fuel management. IAEA Technical Document, IAEA-TECDOC-1192, pp. 56.

Jové, C. and Hacker, B.R. (1997) Experimental investigation of laumontite → wairakite + H2O: A model diagenetic reaction. *American Mineralogist*, 82, 781-789.

Jové-Colón, C. F., Caporuscio, F. A., Levy, S. S., Sutton, M., Blink, J., Greenberg, H. R., Fratoni, M., Halsey, W. G., Wolery, T. J., Rutqvist, J., et al. (2011) Disposal Systems Evaluations and Tool Development - Engineered Barrier System (EBS) Evaluation (Fuel Cycle Research and Development). Sandia National Laboratory, FCRD-USED-2011-000132, 1-192.

Kohyama, N., Shimoda, S., and Sudo, T. (1973) Iron-rich saponite (ferrous and ferric forms). Clays and Clay Minerals, 21, 229-237.

Lahann, R.W. and Roberson, H.E. (1980) Dissolution of silica from montmorillonite: effect of solution chemistry. Geochimica et Cosmochimica Acta, 44, 1937-1943.

Laird, D.A. (1996) Model for crystalline swelling of 2:1 phyllosilicates. *Clays and Clay Minerals*, 44, 553-559.

Laird, D.A. (2006) Influence of layer charge on swelling of smectites. *Applied Clay Science*, 34, 74-87.

Madsen, F.T. (1998) Clay mineralogical investigations related to nuclear waste disposal. *Clay Minerals*, 33, 109-129.

Masuda, H., O'Neil, J.R., Jiang, W-T, and Peacor, D.R. (1996) Relation between interlayer composition of authigenic smectite, mineral assemblages, I/S reaction rate and fluid composition in silicic ash of the Nankai Trough. *Clays and Clay Minerals*, **44**, 443-459.

Meunier, A., Velde, B., and Griffault, L. (1998) The Reactivity of Bentonites: a Review. An Application to Clay Barrier Stability for Nuclear Waste Storage. *Clay Minerals*, 33, 187-196.

Moore, D. M. and Reynolds, R.C. (1997) X-ray Diffraction and the Identification and Analysis of Clay Minerals. Oxford University Press, New York, New York, pp. 377.

Mosser-Ruck, R., Cathelineau, M., Baronnet, A., and Trouiller, A. (1999) Hydrothermal reactivity of K-smectite at 300 °C and 100 bar: dissolution-crystallization process and non-expandable dehydrated smectite formation. *Clay Minerals*, 34, 275-290.

Mosser-Ruck, R., Cathelineau, M., Guillaume, D., Charpentier, D., Rousset, D., Barres, O., and Michau, N. (2010) Effects of Temperature, pH, and Iron/Clay and Liquid/Clay Ratios on Experimental Conversion of Dioctahedral Smectite to Berthierine, Chlorite, Vermiculite, or Saponite. *Clays and Clay Minerals*, 58, 280-291

Nutt, M. Voegele, M., Jové-Colón, C.F., Wang, Y., Howard, R., Blink, J., Liu, H.H., Hardin, E., and Jenni, K. (2011) Used fuel disposition campaign disposal research and development road map (Fuel cycle research and development). Sandia National Laboratory, FCRD-USED-2011-000065, 1-121.

Ohmoto, H., Hayashi, K-I, and Kajisa, Y. (1994) Experimental study of the solubilities of pyrite in NaCl-bearing aqueous solutions at 250-350°C. Geochimica et Cosmochimica Acta, 58, 2169-2185.

Pearson, F.J., Arcos, D., Bath, A., Boisson, J.-Y., Fernandez, A.M., Gabler, H.-E., Gaucher, E., Gautschi, A., Griffault, L., Hernan, P., and Waber, H.N. (2003) Mont Terri Project-Geochemistry of water in the Opalinus Clay Formation at the Mont Terri Rock Laboratory. – Reports of the Federal Office for Water and Geology (FOWG), Geology Series No. 5.

Pouchou, J.L. and Pichoir, F. (1985) "PAP" $\phi(\rho z)$ correction procedure for improved quantitative microanalysis. Microbeam Analysis. Ed. Armstrong, J.T. San Francisco Press, pp. 104-106.

Pusch, R. (1979) Highly compacted sodium bentonite for isolating rock-deposited radioactive waste products. Nuclear Technology, 45, 153-157.

Pusch, R (2008) Geological Storage of Radioactive Waste. Springer-Verlag, Berlin, Germany, pp. 379.

Roberson, H.E. and Lahann, R.W (1981) Smectite to illite conversion rates: Effects of solution chemistry. Clays and Clay Minerals, 29, 129-135.

Seyfried, J.R., Janecky, D.R., and Berndt, M.E. (1987) Rocking autoclaves for hydrothermal experiments II. The flexible reaction-cell system. Hydrothermal Experimental Techniques. Eds. Ulmer, G.C. and Barnes, H.L. John Wiley & Sons, pp. 216 – 239.

Small, J.S., Hamilton, D.L., and Habesch, S. (1992) Experimental simulation of clay precipitation within reservoir sandstones 2: Mechanism of illite formation and controls on morphology. Journal of Sedimentary Petrology, 62, 520-529.

Small, J.S. (1993) Experimental determination of the rates of precipitation of authigenic illite and kaolinite in the presence of aqueous oxalate and comparison to the K/Ar ages of authigenic illite in reservoir sandstones. Clays and Clay Minerals, 41, 191-208.

Smyth, J.R. (1982) Zeolite stability constraints on radioactive waste isolation in zeolite-bearing volcanic rocks. *Journal of Geology*, 90, 195-201.

Środoń, J. (1980) Precise identification of illite/smectite interstratifications by X-ray powder diffraction. *Clays and Clay Minerals*, 28, 401-411.

Środoń, J. (1999) Nature of mixed-layer clays and mechanisms of their formation and alteration. Annual Review of Earth and Planetary Sciences, 27, 19-53.

Steiner, A. (1955) Wairakite, the calcium analogue of analcime, a new zeolite mineral. *Mineralogical Magazine*, 30, 691-698.

Wersin, P., Johnson, L.H., and McKinley, I.G. (2007) Performance of the bentonite barrier at temperatures beyond 100°C: A critical review. *Physics and Chemistry of the Earth*, 32, 780-788.

Whitney, G. and Velde, B. (1993) Changes in particle morphology during illitization: An experimental study. Clays and Clay Minerals, 41, 209-218.

Wilkin, R.T. and Barnes, H.L. (1998) Solubility and stability of zeolites in aqueous solution: I. Analcime, Na-, and K-clinoptilolite. *American Mineralogist*, 83, 746-761.

Wilkin, R.T. and Barnes, H.L. (2000) Nucleation and growth kinetics of analcime from precursor Na-clinoptilolite. *American Mineralogist*, 85, 1329-1341.

Zhang G., Kim, J., Dong, H., and Sommer, A. (2007) Microbial effects in promoting the smectite to illite reaction: Role of organic matter intercalated in the interlayer. American Mineralogist, 92, 1401-1410.

Thermodynamic Database Development: Evaluation Strategy, Modeling Tools, First-Principles Modeling of Clay, and Sorption Database Assessment

(Part IV)

1. Introduction

In the previous report (Jove Colon et al. 2013), emphasis was given to progress in the development of thermodynamic databases (TDBs) relevant to geochemical processes, their key sources of data, and the needs for data corrections based on new estimates of thermodynamic properties of various complex clays and related sheet silicates. The latter groups of minerals are important to nuclear waste disposal since these are both the main components of the engineered barrier system (EBS) (including seals) and also the natural barrier in the case of disposal concepts in shale/argillite. As expected, this sort of correction would affect the computed equilibrium relations between clay minerals and related sheet silicates, including the illites and chlorite, and with other silicates and aluminosilicates (e.g., zeolites). Assessing the needed corrections leads to the necessary reevaluation of the widely-used Helgeson et al. (1978) dataset along with data retrieval methodologies with a similar but the more modern one of Holland and Powell (2011). The resolution of key data issues and inconsistencies are therefore necessary for applications to the UFDC, particularly on the accurate prediction of mineral solubilities and phase relations at elevated temperatures. Currently, there is a strong consideration for the use of large UNF waste packages (e.g., dual purpose canisters (DPCs) with 32 PWR UNF assemblies) generating thermal loads with temperatures of up to 299°C (see Part III of this report). Such high temperatures on bentonite backfill material can exert large effects on mineral-fluid interactions, mineral phase transformation, and thus solution-mineral equilibria. Part III of this report documents results of hydrothermal experiments in this thermal regime and the ensuing effects of such high temperature interactions with bentonite clay. Further, processes affected by the equilibrium states of the system like sorption, kinetics, diffusion, and thus reactive-transport may be also impacted by thermodynamic data.

Jove Colon et al. (2013) advanced recommendations for future TDB development based on the NEA TDB review program. That report advanced the need for benchmarking in TDB development to assess gaps on high temperatures extrapolation and formalization of retrieval methods that are tractable, traceable, and transparent. This part IV of the report describes the following:

- Progress on the assessment and retrieval strategies of thermodynamic data for mineral and aqueous species
- Analysis of thermodynamic data and mineral phase stability relations of clays and zeolites at elevated temperatures with the CHNOSZ software
- Comprehensive approaches to developing ion exchange and surface complexation models for nuclear waste repository conditions
- Application of first-principles computational approaches in the retrieval of thermodynamic properties for kaolinite clay ($Al_2Si_2O_5(OH)_4$) and bischofite salt plus its dehydrated phases [$MgCl_2 \cdot nH_2O$ (n=6, 4, 2, 1)]

These efforts encompass the use of various tools and approaches towards the common goal of evaluating and retrieving thermodynamic properties of phases of interest to the EBS in deep subsurface disposal concepts.

Following the efforts of international TDB development is an important aspect of leveraging and bridging progress towards common objectives in the UFDC disposal R&D. For example, the most recent NEA-TDB publication is the first of two volumes summarizing the thermodynamics of iron (Lemire et al., 2013). It should be noted the participation of Cynthia Atkins-Duffin (LLNL) in the NEA Thermodynamic Database (TDB) program. We have also been following the progress of the Thereda database effort. The most recent 9th data release included parameter files for the system Na, K, Mg-Ca-Cl-SO4-HCO_3/CO_2(g)-Si-U(IV)/U(VI)-H_2O. More importantly, the Thereda effort is focused on a Pitzer model which is most relevant to high ionic strengths prevalent in repositories hosted in salt and other disposal scenarios. The Thereda database project continues to support the LLNL EQ3/6 modeling code input database format. In addition, international activities on sorption databases in support of ion exchange models and surface adsorption phenomena have gotten considerable attention for applications to contaminant transport and disposition of nuclear waste. Development of surface complexation modeling databases was supported through discussions with the RES^{3}T development group. This task involves a collaboration with Dr. V. Brendler (Dresden-Rossendorf) focused on the development of thermodynamic databases for high ionic strength conditions as well as surface complexation modeling. Another task to report is a recently completed study of Np interaction with clay, looking at the effect of solution chemistry on ion exchange processes.

1.1 Thermodynamic Data for Minerals and Aqueous Species: Consistency "Links"

We have previously focused on key thermodynamic data, their development over approximately the past century, and historical and present differences and discrepancies. Generally speaking, key data (also referred to as "reference" data or "anchor" data) are those data from which a substantial body of other data are derived from analysis of equilibrium and calorimetric data. The derived data typically include standard Gibbs energies and enthalpies of formation from the elements at the usual reference temperature and pressure (presently 298.15K and 1 bar). Key data include atomic weights, the standard entropies of the chemical elements in their reference forms at the reference temperature and pressure, and the standard Gibbs energies and enthalpies of formation and absolute standard entropies of key species at the reference temperature and pressure (the standard formation properties of the elemental reference forms are necessarily zero). Other thermodynamic properties of key species necessary to account for the temperature and pressure dependence of the corresponding Gibbs energy and enthalpy functions may also be considered as key data. However, these are generally less problematic.

Key species apart from the elemental reference forms are generally simple in chemical composition, placing them "close" to the elemental reference forms. One can think of MgO as closer to the elemental reference forms Mg and O_2 than something more complex such as talc ($Mg_3Si_4O_{10}(OH)_2$. In theory, one might derive say the Gibbs energy of formation of talc from that of MgO by analyzing data linking the former directly or indirectly to the latter. Alternatively, one might use the aqueous ion Mg^{2+} in such a key role, especially if one were analyzing solubility or acid dissolution calorimetry data for talc. For constructing a thermodynamic dataset, the formation property data for say MgO and Mg^{2+} should be consistent, in that some data set could be used to establish closure.

Thus, consistent results might be obtained using either (although in many instances the form of the experimental data being analyzed might force the use of one or the other). Consistency of alternative key species such as MgO and Mg^{2+} would be most likely if the data for one were derived from that for the other. Different determinations of the Gibbs energy (or enthalpy) of formation of some species such as talc could arise from the use of non-equivalent (and therefore inconsistent) links back to one or more of the chemical elements.

We consider it likely that the most notable discrepancies in formation property data for more complex species such as talc are due to the use of inconsistent links back to the elemental forms. We will define such a *link* as consisting of two parts. The *path* includes the set of reactions involved (commonly one or more) and the associated *data*, including the primary measured data and any necessary corrections to derive data for the reference temperature and pressure and to correct solution data to standard states (unit activities). Potential links are not equivalent if the path is the same but the data are not, although if the data are close enough, they may be functionally equivalent. Links may be equivalent or functionally equivalent if the paths are different but the data are such that closure or near-closure can be demonstrated.

In deriving thermodynamic data for a species, it is essential to understand the links to the chemical elements in their reference forms. In building a thermodynamic database, it is necessary to use only a minimal set of well-defined and established links in order to assure consistency. Unfortunately, this links-oriented concept seems to be not widely understood or appreciated, possibly because the burden it imposes is considerable and because it has not, to our knowledge, been formally developed. For example, Engi (1992) wrote an entire article on thermodynamic database assessment but never directly touched on this.

Thermodynamic data may be obtained experimentally using either calorimetry or measurement of equilibrium. In some instances they may also be estimated from theory. Tabulated thermodynamic data generally consist of pairs of values for the Gibbs energy of formation from the elements and the enthalpy of formation from the elements. Generally one is calculated from the other, using entropy values for the species in question and the relevant entropies of the elements in their reference forms according to the well-known relation $\Delta G°_f = \Delta H°_f - T\Delta S°_f$. In assessing such data, one must first ask, which is primary, the Gibbs energy or the enthalpy? Then one must establish the links to the chemical elements, which in either case are likely to involve a combination of calorimetric and equilibrium results. The information required to establish the links is often not directly tabulated, requiring the investigator to chase a sometimes complex trail of references. We note that without understanding the links and the uncertainties associated with the steps in the links, it is not possible to do anything in a meaningful way with uncertainties assigned to a high level result, such as the Gibbs energy of most minerals. For example, in calculating the equilibrium constant for a reaction involving Al(III) species, it is necessary to remove the uncertainty associated with transforming Al(metal) to Al(III).

The 1989 CODATA recommendations for key thermodynamic values (Cox et al., 1989) represent the last major set of key data recommendations from this “standards” organization. It is useful in that it contains many useful consistent paired links consisting

of a simple oxide and a corresponding aqueous ion. In particular, it gives a brief but detailed summary of how the recommended values tie back to the chemical elements. However, this data set is rather limited in scope. It is now a quarter-century old, so it does not incorporate the results of more recent investigations. The NEA thermodynamic databases (starting with Grenthe et al., 1992) build on the CODATA 89 dataset, providing extensions for numerous radionuclide elements.

Older datasets differ in the key data values presented, as we have previously shown. However, many thermodynamic data values still extant are based on them. In general, there has been no automatic updating process in the production of various thermodynamic databases and data compilations as the best key data have changed. This can be demonstrated by pointing to some of the errors that can be found. For example, Barin and Platzki (1995) give a Gibbs energy for CsCl that was miscalculated from the enthalpy. The thermodynamic relation here is $\Delta G°_f = \Delta H°_f - T\Delta S°_f$, as discussed previously. Unfortunately the sign of the $T\Delta S°_f$ term was reversed. Barin and Platzki took the CsCl data from JANAF 2 (Stull and Prophet, 1971), which presented an original calculation. The error is repeated in JANAF 3 (Chase et al., 1985) and JANAF 4 (Chase et al., 1998). We have previously pointed out that Robie and Hemingway (1995) give the same thermodynamic data for PO_4^{3-} (within precision) as the earlier USGS compilation of Robie et al. (1978). However, the earlier work uses red phosphorus as the reference form for P (entropy of 22.85 J/mol-K), while the later one follows the modern practice of using the white form (41.09 J/mol/K). The point of these examples is not that errors may occur somewhere in a compilation. The point is that such errors demonstrate that no process was in place to assure consistency with key data, in these instances the entropies of the elements in their reference forms. Such a process would have led to detection and correction. Many of the data in these and other works may be affected by lesser errors associated with changes in values for the key data, or with the use of different but functionally fairly equivalent key data, without obvious indication.

Thermodynamic Data "Deconstruction"

This year we have deconstructed the mineral thermodynamic data set of Helgeson et al. (1978) onto a spreadsheet for analyzing the effect of key data choices and to facilitate an ongoing reconstruction using more modern and reliable key data drawn in particular from CODATA 89 (Cox et al., 1989). This mineral dataset is a major part of the SUPCRT92 (Johnson et al., 1992) database as represented by the data file slop98.dat and other data files based on it, such as the speq06.dat file (see BSC, 2007). It has not had a significant update since changes in March 1990 to resolve a problem related to Ca. The strength of the SUPCRT92 database has been its inclusion of the HKF "equation of state" treatment for aqueous species (see Oelkers et al., 2009). Therefore, an effort to resolve the issues with the mineral part of the database seems worthwhile, as the knowledge gained would be useful even if a decision were made to switch to mineral data from another source, such as Berman (1988) or Holland and Powell (2011). This is because only a careful consideration of key data including that for key aqueous species can result in a database that correctly deals with both mineral solubilities and mineral-mineral phase equilibria.

The Helgeson et al. (1978) mineral data include as a strength the use of phase equilibrium data for a number of reactions including aqueous species, including besides H_2O, the ions Na^+, K^+, Mg^{2+}, and Ca^{2+}, and the neutral species $SiO_{2(aq)}$. We consider this a necessary

feature if accurate representation of solubilities is a goal. We also note that Helgeson et al. used some acid dissolution calorimetry data, which also provides a tie to aqueous species.

Helgeson et al. (1978) intended their work to be an example of an "internally consistent" data set for minerals. Unfortunately they did not adopt the key data concept as a guide to their work, nor did they specifically address the demands of using a consistent (preferably minimal) set of links to the elemental reference forms. The actual links that we identified are shown in Table 1. The data for $SiO_{2(aq)}$ (from Walther and Helgeson, 1977) are consistent with the data for quartz. There appear to be no really significant issues with the data for H_2O, $H_2O_{(g)}$, and CO_2, nor that for H^+ (for which the values are defined by convention) or $O_{2(g)}$, although the data they used for this were for 1.013 bar, not 1 bar.

A link to Mg was established using periclase (MgO), based on enthalpy and entropy data from JANAF 2 (Stull and Prophet, 1971), with the Gibbs energy being calculated from them and elemental entropy data from Wagman et al. (1968) and Parker et al. (1971). Another link to Mg was established using Mg^{2+}, with data taken from Parker et al. (1971). The consistency of these two links was not evaluated by Helgeson et al. A third link to Mg of some kind (but not documented) was also established in obtaining data for six magnesium silicates: enstatite, forsterite, talc, anthophyllite, chrysotile, and antigorite. Talc, which represents a possibility in that a value for its Gibbs energy may have been assumed, is shown in the table, primarily as a placeholder. The Gibbs energy value they obtained is very close to some averages of data they cited in comparison. However, they might well have done something else.

Table 1. Key data used by Helgeson et al. (1978), in order of appearance.

Species	$\Delta G°_f$ cal/mol	$\Delta H°_f$ cal/mol	S° cal/mol-K	V° cm^3/mol	Formula
Quartz	-204,646	-217,650	9.88	22.688	SiO2
SiO_2(aq) (WH77)	-199,190	-210,726	14.8		SiO_2(aq)
Periclase	-136,086	-143,800	6.44	11.248	MgO
H_2O (H78)	-56,687	-68,315	16.71	18.068	H_2O
H_2O(g) (H78)	-54,634	-57,796	45.1	24465	H2O
CO_2 (H78)	-94,262	-94,054	51.072	24465	CO_2
Ca^{++} (P71)	-132,300	-129,740	-12.7		Ca^{++}
CO_3^{--} (W68)	-126,170	-161,840	-13.6		CO_3^{--}
Talc*	-1,320,188	-1,410,920	62.34	136.25	$Mg_3Si_4O_{10}(OH)_2$
H^+	0	0	0		H^+
Mg^{++} (P71)**	-108,700	-111,580	-33		Mg^{++}
Gibbsite	-276,168	-309,065	16.75	31.956	$Al(OH)_3$
Kaolinite***	-905,614	-982,221	48.53	99.52	$Al_2Si_2O_5(OH)_4$
Sanidine_high****	-893,738	-946,538	54.53	109.008	$K(AlSi_3)O_8$
K^+ (C75)*****	-67,510	-60,270	24.15		K^+
Na^+ (C75)	-62,591	-57,433	13.96		Na^+
Magnetite	-242,574	-267,250	34.83	44.524	Fe_3O_4
O_2 (H78)******	0	0	49.003		O_2

*Talc may have been used and if so represents a second link to elemental Mg (Periclase is the first).

The origin of the data, if used, is not clear. If talc was not used, something else was.

**Mg++ (P71) appears to represent a third link to elemental Mg.

***Kaollinite is linked to Gibbsite, but through a poorly-supported assumption of equilbrium among these two minerals and bauxitic groundwaters. Kaolinite is treated here as an independent link to elemental Al.

****Though used as a link to elemental K, it is also another link to elemental Al.

*****K+ appears to represent another link to elemental K after Sanidine_high.

******The entropy value for O_2 is for 1 atm., not 1 bar. See CODATA (1989).

A link to Ca was established using data from Parker et al. (1971) along with data for CO_3^{2-} from Wagman et al. (1968) to obtain a Gibbs energy for calcite ($CaCO_3$) from solubility data. The calcite data were then used in subsequent phase equilibrium analyses to obtain Gibbs energies for various calcium silicates and aluminosilicates. We note that CO_3^{2-} represents a second link to elemental C, but any inconsistency there is likely insignificant.

To obtain a link to Al, Helgeson et al. (1978) adopted the enthalpy of gibbsite ($Al(OH)_3$) from Hemingway and Robie (1977a), which was subsequently used to derive a value for the Gibbs energy of kaolinite ($Al_2Si_2O_5(OH)_4$) through a groundwater chemisty equilibrium assumption that is poorly supported (see for example Tutolo et al., 2014) and which was controversial from the start as noted by many prominent investigators (such as Robie and Hemingway, 1995) having ignored this result. Unfortunately, the kaolinite data were used in many of the phase equilibrium analyses and affected most of the results obtained for aluminosilicate minerals. For reasons documented in their paper, Helgeson et al. were unwilling to accept extant thermodynamic data for corundum (Al_2O_3) as a basis for their effort. To make matters more complicated, they introduced high sanidine ($KAlSI_3O_8$) with data from Robie and Waldbaum (1968) as another link to elemental Al.

Links to elemental Na and K, respectively, were established using CODATA (1975) data for Na^+ and K^+. In the case of K^+, this represents a second link to elemental K, the first being that involving sanidine. A link to Fe was established by assuming data for magnetite (Fe_3O_4), based on privately communicated data to Helgeson et al. (see p. 181 of their paper) and the data of Chou (1978) for the hematite-magnetite buffer, along with data for O_2 from Wagman et al. (1968).

Our deconstruction reveals the use of multiple links to the chemical elements, some of which are likely inconsistent. Many of these links are also obsolete, as better associated key data values are now available. In our deconstruction, we have determined that Helgeson et al. (1978) had some alternative choices available at the time of their study. For example, they adopted the Hemingway and Robie (1977a) Gibbs energy for gibbsite, while rejecting the same source's Gibbs energy for albite ($NaAlSi_3O_8$) (obtained using the same experimental approach), which could have provided an alternative to the use of their kaolinite value.

Other potential improvements relate to newer link data. For example, CODATA 89 (Cox et al., 1989) has recommended data for corundum (Al_2O_3), which also could be used as an alternative to the Helgeson et al. (1978) kaolinite data. CODATA 89 data for other species (notably Mg^{2+} and Ca^{2+}) can also be used in an update-reconstruction. More recently, the data Helgeson et al. used for $SiO_{2(aq)}$ have been supplanted with other data consistent with a notably higher solubility of quartz (see BSC, 2007 and Tutolo et al., 2014, and references cited in these works). Most recently, Sverjensky et al. (2014) have proposed a new model for aqueous silica in which the dimer $Si_2O_{4(aq)}$ is important (especially at high pressure and temperature) in addition to the monomer $SiO_{2(aq)}$. The consequences of this development require further investigation.

We do not mean to overly criticize the work of Helgeson et al. (1978). It was a groundbreaking piece of work in its time, and spawned the development of later "internally consistent" mineral databases (such as those of Berman, 1988, and Holland

and Powell, 2011). Apart from an unfortunate choice regarding kaolinite and aluminum, it has basically been overtaken by newer results, some of which were appearing even as the work was being done.

For future work, we plan on preparing a manuscript on the links-to-the-chemical elements concept (including some of the results included here). We will also reconstruct the Helgeson et al. (1978) mineral set using newer or otherwise appropriate links, evaluating various alternatives and hopefully generating something more consistent with CODATA 89. An important result of such a reconstruction is to provide a better set of sheet silicate data to use in estimating the thermodynamic properties of complex clay minerals. The results of the reconstruction will also provide a basis for establishing how to proceed using mineral data from other sources, such as Berman (1988) and Holland and Powell (2011).

2. Analysis of thermodynamic data and mineral phase stability of clays and zeolites at elevated temperatures with the CHNOSZ software

Jove Colon et al. (2013b) described the use of CHNOSZ in the evaluation of thermodynamic data and equilibrium phase relations for cement-fluid systems. CHNOSZ (Dick, 2008) is a software package (in R language) that includes multiple functions and data to conduct chemical thermodynamic modeling covering large sets of chemical species for biochemistry and geochemistry. A description of CHNOSZ is given in Jove Colon et al. (2013b) but for completeness it will be summarized here. CHNOSZ is developed in R (http://www.r-project.org/) which is an open-source language and computational environment for statistical analysis with a wide variety of graphical resources. The advantages of R as a language platform lie in its rich set of integrated capabilities for graphics, statistical computations, and data manipulation. A key capability of the CHNOSZ package is the generation of activity phase diagrams as a function of temperature, pressure, and species activities. It also has the ability to calculate thermodynamic properties of aqueous species using the Helgeson-Kirkham-Flowers (HKF) EoS. Further, it accepts inputs of standard thermodynamic data for solids and gases similar to the supcrt92code. However, CHNOSZ is more flexible for heat capacity extrapolating expressions since polynomial terms are reported in various forms beyond the "traditional" Maier-Kelley expression in supcrt92.

The CHNOSZ OBIGT database has been expanded to include some of the aqueous and solid species based partially on the analysis of the previous section. Updates to existing data we deem necessary was mainly based on recent assessments of thermodynamic data and overall internal consistency. Updates to existing data include the minerals kaolinite, diaspore, quartz, and corundum. The sources for these thermodynamic data are the THERMODDEM database (Blanc et al. 2006; Blanc et al. 2012), Tutolo et al. (2014), Rimstidt (1997), and Holland and Powell (2011), respectively. The updates to existing aqueous species are for SiO_2(aq), Al^{+++}, and AlO_2^- with thermodynamic data from Rimstidt (1997) for SiO_2(aq) (i.e., consistent with updated quartz solubility), and Tagirov and Schott (2001) for the Al aqueous species. New clay data added to the CHNOSZ database are the clays smectite MX-80 (Gailhanou et al., 2012), Na-saponite (Gailhanou et al., 2013). Thermodynamic data for the Si-rich analcime is from Neuhoff et al. (2004).

An example of how a potential inconsistency in the thermodynamic data for a given clay system can affect fluid-mineral equilibrium calculations is depicted in Figure 1. The traditional activity phase diagram for the system K-Al-Si-H_2O is generated with CHNOSZ using 'old' supcrt92 data and with 'new' updates from the sources given above.

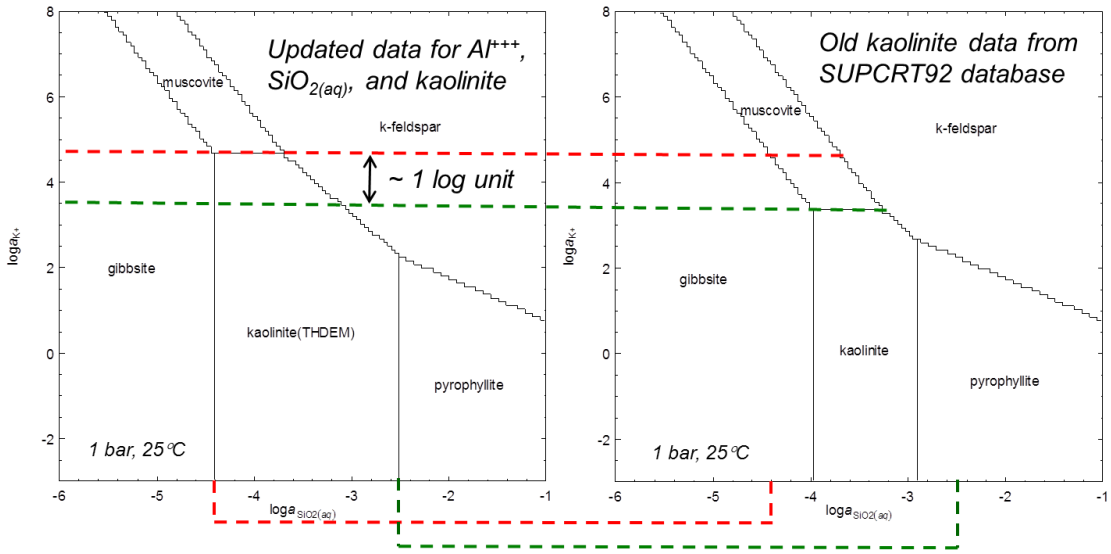

Figure 1. Activity phase diagram (25°C, 1 bar) generated for the K-Al-Si-H_2O system generated with CHNOSZ using 'old' and new thermodynamic data. Notice the shifts (marked by the red and green dashed lines) in the stability field for kaolinite (see text).

The shifts in the stability field of kaolinite are rather significant, in the order of about one log unit with respect to the activity of K^+ and about two log units with respect to the activity of SiO_2(aq). Such differences could translate in relatively large discrepancies in predicted solubilities. As expected, the overall extent of the enlargement of the kaolinite field also shifts the invariant points of the phase diagram with respect to other aluminosilicates.

The evaluation of thermal limits in the EBS and natural barrier involves the analysis of potential interactions of clay and zeolites phases at elevated temperatures. A key component in these interactions is aqueous silica which controls the equilibria with respect to zeolites, clays, and silica cementation. Thermodynamic data for clays at high temperatures is scarce and evaluation of fluid-mineral interactions of these phases is largely dependent on estimates and extrapolations. Recently, thermodynamic data for smectite (MX-80; $K_{0.026}Na_{0.435}Ca_{0.010}(Si_{3.612}Al_{0.388})(Al_{1.593}Fe^{3+}_{0.184}Mg_{0.228}Fe^{2+}_{0.038}Ti_{0.011})O_{10}(OH)_2$), illite (IMt-2; $K_{0.762}Na_{0.044}(Si_{3.387}Al_{0.613})(Al_{1.427}Fe^{3+}_{0.292}Mg_{0.241}Fe^{2+}_{0.084})O_{10}(OH)_2$), and Na-saponite (Sap-Ca-1; $Na_{0.394}K_{0.021}Ca_{0.038}(Si_{3.569}Al_{0.397}Fe^{3+}_{0.034})(Mg_{2.948}Fe^{2+}_{0.021}Mn_{0.001})O_{10}(OH)_2$) were obtained through calorimetric methods (Gailhanou et al., 2012, 2013). In addition to standard thermodynamic data at the reference state, these studies also obtained heat capacity data that allows for extrapolations to elevated temperatures. Incorporation of all these data into the CHNOSZ database allows for the construction of activity phase diagrams representing a mineral assemblage relevant to engineered and natural barrier materials (smectite, illite, and possibly zeolite). The diagrams are generated using the updated data for kaolinite(THDEM), SiO_2(aq), and

Al aqueous species as described above. The construction of activity phase diagrams with aqueous silica as a function of temperature provides a useful mapping of equilibrium phase relations whose topologies can change with solution composition and temperature. Figure 2 shows the equilibrium phase relations for the system Na-Ca-Mg-K-Si-Al-H_2O as a function silica activity and temperature. Experimental data from LANL hydrothermal experiments (Cheshire et al. 2014) on bentonite-metal interactions is overlaid for comparison. The diagram was constructed using fixed activities of aqueous species based on average solution compositions sampled at the temperature range of the experiments after Cheshire et al. (2014). The range of SiO_2(aq) activities from experimental data depicted as vertical rectangles in the figure represents samples taken throughout the duration of the experiment at a given temperature. Notice that these experimental SiO_2(aq) are well within the stability field of smectite MX-80, consistent with observations by Cheshire et al. (2014) on the overall stability of bulk smectite phase away from the bentonite-metal interface. Also overlaid in the figure is the quartz saturation line which is consistent with the range of SiO_2(aq) activities obtained from the experimental data. This close correspondence may be indicative of quartz saturation but characterization of the experimental run products only confirmed the formation of silica and silicate phases (Cheshire et al. 2014). These authors also emphasized the importance of silica precipitation on the performance of engineered barrier materials due to effects on bentonite plasticity and permeability.

The experiments in Cheshire et al. (2014) observed the lack if illite or mixed-layer illite-smectite in the run products. Instead, a K-bearing montmorillonite was produced where Na^+ from the initial smectite was to some extent exchanged by K^+. The process of illitizaton not only requires elevated temperatures but also the presence of K^+ and possibly unsaturated silica conditions. Cheshire et al. (2014) discusses the controls for silica activity through heterogeneous reactions (dissolution/precipitation) for silicates. It also alludes to studies suggesting that silica-saturated conditions are conducive to retardation of illitization. To investigate the clay phase equilibrium topology for illite as a function of temperature, the activity of K^+ and Fe^{++} were increased substantially in CHNOSZ to resolve the stability field of this phase. Figure 3 also shows preliminary results on the equilibrium phase relations for the system Na-Ca-Mg-K-Si-Al-H_2O similar to the previous Figure 2 but with the appearance of illite(IMt-2). Notice that the illite stability field appears below that of smectite(MX-80), at a lower activity of silica relative to quartz saturation. Such phase topological relation is consistent with the literature observations noted in Cheshire et al. (2014) where lower silica concentrations may favor illitization. Such phase equilibria analysis demonstrates the importance of the aqueous solution composition when constructing this type of diagrams. If the K^+ and Fe^{++} activities were increased further, the enlargement of the illite stability field would result shifting phase equilibria boundaries closer to quartz saturation. This analysis is still work in progress.

The use of CHNOSZ tool to construct activity phase diagrams with temperature as a variable is very useful for mapping phase equilibria boundaries multicomponent clay system.

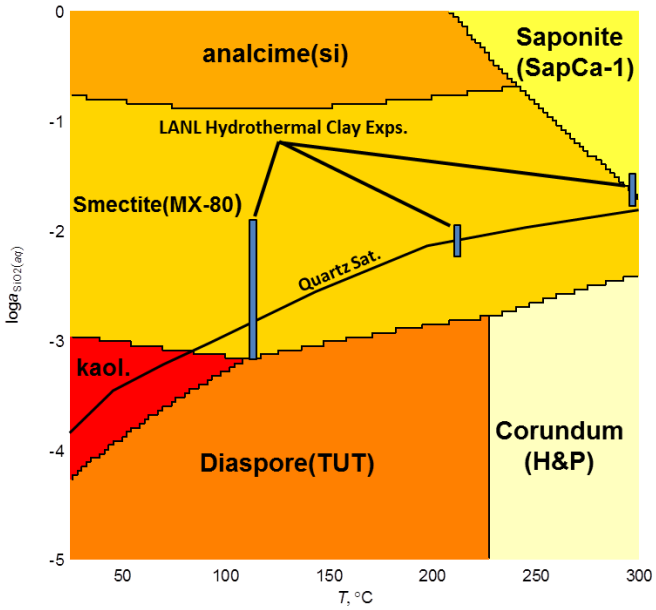

Figure 2. Log activity SiO_2(aq) vs. temperature phase diagram for the system Ca-Na-Al-Si-Fe-H_2O generated using CHNOSZ. Thermodynamic input data for smectite(MX-80), saponite, and illite are from Gailhanou et al. (2012, 2013). Data for diaspore(TUT) and corundum(H&P) are from Tutolo et al. (2014) and Holland and Powell (2011), respectively. Analcime(Si) and "kaol." (i.e., kaolinite(THDEM)) data are from Neuhoff et al. (2004) and Blanc et al. (2006), respectively (see text).

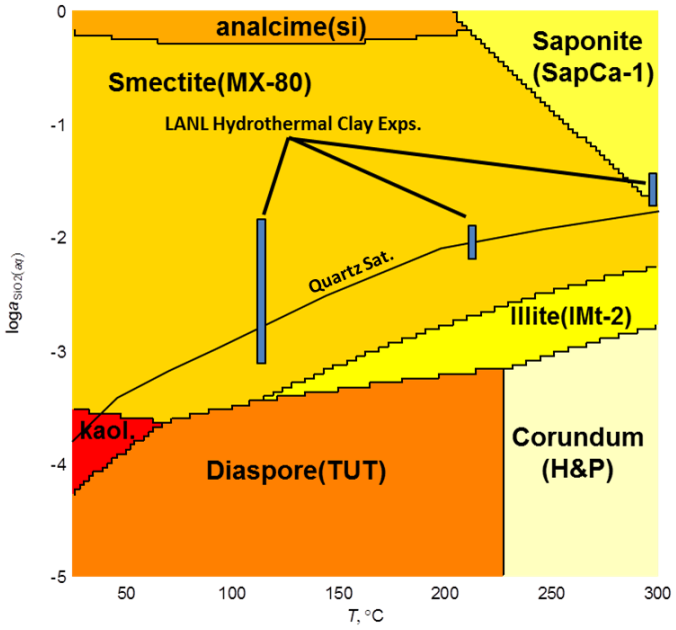

Figure 3. Log activity SiO_2(aq) vs. temperature phase diagram for the system Ca-Na-Al-Si-Fe-H_2O generated using CHNOSZ. Sources of data as in Figure 2. "kaol" stands for "kaolinite(THDEM)".

Update on the Thermodynamic Analysis of Smectite Ion Exchange

The application of the Cantera code implementation to model ion exchange using the Margules representation for solid solutions was introduced in Jove Colon et al. (2013). Following is a brief update on the thermodynamic modeling of ion exchange in the development of an object-oriented integrated tool for multiphase multicomponent equilibria. An attempt to use the Margules approach to model solid solutions was partially successful due to the limitation of fitting Margules parameters in incremental steps which resulted in a satisfactory fit to the data but with somewhat limited success on the predicted solution compositions. Fortunately, refinements in the Cantera code and the use of a more recent and extensive set of ion exchange data for monovalent and divalent ions (Gaucher et al. 2006) resulted in a better model representation of this approach. The code can now be used in a titration mode which facilitates the fitting of data in a single run producing results that are within the scatter of the Na-Ca exchange data. This work is still ongoing and further tests will be developed for mono- and di-valent ions.

Concluding Remarks

Progress has been made on the assessment and retrieval strategies of thermodynamic data for mineral and aqueous species. The thermodynamic data "deconstruction" to key reference data permits the analysis of potential inconsistencies in TDBs. Subsequent 'reconstruction' of data allows for more confidence in database consistency and the inclusion newer data, particularly Al-silicates that are of concern to EBS materials and shale host-rock. By combining thermodynamic data inputs from the calorimetric experiments, revised thermodynamic datasets, and superimposing aqueous solution chemistry from hydrothermal experiment facilitates a synergistic analysis of thermal limits through barrier material stability in response to temperature. The use of chemographic approaches with CHNOSZ and thermodynamic calculations allows for a comprehensive evaluation of thermodynamic data in the integrated and consistent assembly of TDBs.

Planned TDB Development Work for FY15

FY15 work on TDB development as described in Sections 1 and 2 will include the following:

- Conduct thermodynamic data "deconstruction" to establish consistency links with key reference data. This approach facilitates the evaluation of thermodynamic data from the "ground up" maintaining consistency in a manner that is tractable, traceable, and transparent.
- Integration of the above thermodynamic data "deconstruction" with CHNOSZ tool. Expand CHNOSZ OBIGT database for the analysis of thermodynamic data for other clays such as nontronite, illite-smectite, and vermicullite. This effort will be integrated with that described in the previous bullet.
- Perform chemographic/thermodynamic analysis with CHNOSZ to examine sensitivities to redox state, aqueous component activities, and temperature on the stability of smectite-illite phase equilibria.

3. Comprehensive Approaches to Developing Ion Exchange and Surface Complexation Models for Nuclear Waste Repository Conditions

The need to develop self-consistent surface complexation/ion exchange models, in concert with thermodynamic models, for nuclear waste repository performance assessment was identified many years ago (Bradbury and Baeyens, 1993). However, significant progress on this issue has been made only recently in various international nuclear waste repository programs (e.g. (Bradbury and Baeyens, 2009), (Dresden-Rossendorf, 2013), (Geckeis et al., 2013)). Hybrid approaches have also been attempted (Bradbury et al., 2010). The best path forward for developing such databases remains an open question (Geckeis et al., 2013), particularly in cases where generic repositories are being investigated resulting in a need to model radionuclide behavior over a very broad range of solution and mineralogic conditions.

One promising effort underway in Germany is the development of an open source database of surface complexation constants reported in the open literature (Dresden-Rossendorf, 2013). RES³T is a digital open source thermodynamic sorption database. It is mineral-specific and can therefore also be used for additive models of more complex solid phases such as rocks or soils. The database includes an integrated user interface to access selected mineral and sorption data and export data into formats suitable for other modeling software. Data records comprise mineral properties, specific surface areas, characteristics of surface binding sites and their protolysis, sorption ligand information, and surface complexation reactions. The database includes the following surface complexation models: Non-Electrostatic, Diffuse Double Layer, Constant Capacitance, Triple Layer, Basic Stern, and the 1-pK Model as extended to CD-MUSIC. The concept of strong and weak binding sites is also included. An extensive bibliography is included in the database, providing links to the original publications, but also to background information concerning surface complexation model theories, related software for data processing and modeling, and sorption experiment techniques. The intent of the database is to substitute the present Kd approach in risk assessment studies to the more realistic description of sorption phenomena with SCM. The RES³T approach represents the first international attempt to produce a digital thermodynamic database for surface complexation equilibria from the vast amount of data available in the literature. Recent improvement include automated conversion of reaction constants to zero ionic strength for use in surface complexation models. In addition, all database records are identified with a Digital Object Identifier (DOI) that provides a direct link to the original reference. An example database output for U(VI) sorption to quartz is reported in Table 1.

One significant difficulty in directly utilizing reaction constants supplied in the RES^{3}T database is that reported constants are dependent on the specific surface complexation model used in the referenced manuscript and the associated protonation/deprotonation constants, surface areas, site densities, and associated aqueous speciation constants and activity correction methods (e.g. Table 2). For example, reaction constants reported for U(VI) sorption to quartz are based on three different models (Diffuse Double Layer, Non-electrostatic, and Triple Layer models). A present, there is no mechanisms by which these three models can be reconciled. Moreover, within the DDL model constants, five unique surface protonation/deprotonation models are used for the quartz surface and three different surface site densities. Lastly, the choice of surface species used to fit sorption

data varies; a total of seven different surface species were identified in the DDL models alone (Table 2). An additional underlying issue associated with the application of these reaction constants is that they were developed in conjunction with aqueous speciation databases available at the time of model development. As aqueous speciation databases have changed and hopefully improved with time, a mechanism by which the surface complexation constants can be updated to provide consistency with the latest aqueous speciation databases does not exist. As a result, integration of the different surface complexation models, different parameter choices, and different surface species is not straightforward. The inconsistent application of surface complexation models in the literature limits our ability to develop self-consistent databases that would be directly applicable to reactive transport modeling efforts.

One potential remedy to this situation would be for the RES^{3}T database to be expanded and store raw sorption data from which one could develop surface complexation reaction constants based on preferred SCM modeling approaches and most up to date aqueous speciation databases. UFD program at LLNL is actively engaged with the RES^{3}T group to evaluate options for a next generation RES^{3}T database that would include such raw data. A demonstration project is underway at HZDR and will be presented in a special session on Environmental Radiochemistry at the 248th ACS National Meeting, San Francisco, California, August 10-14, 2014. This session is being organized by Don Reed, Ralph Sudowe, Brian Powell, and Mavrik Zavarin.

As a test case, we recently extracted and digitized all uranium sorption data for quartz that were reported in the RES^{3}T database (see Appendix A of Zavarin et al. 2014). The dataset amounts to approximately 500 individual sorption data points. Digitization of data allowed for simultaneous modeling off all available sorption data and the formulation of a consistent set of reactions. Furthermore, the data were fitted using the most up-to-date aqueous speciation data documents in the NEA database and accounted for the estimated uncertainty of individual data points. A statistical comparison of the data to the resulting model is presented in Figure 4. The model was developed based on the simplest one-site non-electrostatic surface complexation model. Remarkably, the data were fit using only four fitting parameters: the reaction constants, K, for the species $>SiO^-$, $>SiOUO_3H$, $SiOUO_3^-$, and $SiOUO_2CO_3$. While additional evaluation of these results is still in progress, particularly with respect to testing other surface complexation modeling approached (DLM, CCM, TLM, GEM, etc.), the results show promise in our ability to develop comprehensive and self-consistent models to predict metal sorption to mineral surfaces. Figure 5 presents a comparison of measured and predicted U concentrations in each batch experiment. Again, the modeling approach used here shows remarkable promise in being able to simulated U(VI) concentrations across a very wide range of pH, ionic strength, and major ion composition. This test case provides confidence that the approach undertaken here can lead to an effective and self-consistent database of reaction constant for use in performance assessment and other nuclear waste repository risk assessments. Importantly, when compiled in a digital format, the reaction constants can be updated as aqueous speciation models evolve and our numerical models for interfacial reactions improve.

Table 2. Data extracted from RES3T database for uranium sorption to quartz.

SCM Type	Mineral	Area m2/g	Site Density nm-1	pK_1	pK_2	logK	Chemical Equation	Literature Reference
DDL	Quartz	0.2	4.81		5.62	-5.72	»Si-(OH)2 + UO2<2+> = »Si-O2-UO2 + 2 H<1+>	AZBN00a
DDL	Quartz	0.2	4.81		5.62	-5.51	»Si-(OH)2 + UO2<2+> = »Si-O2-UO2 + 2 H<1+>	AZZBN01
DDL	Quartz	10	10	-1.6	7.6	-7.259	»X-OH + UO2<2+> + H2O = »X-O-UO2(OH) + 2 H<1+>	JHLCH99
DDL	Quartz	10	10	-1.6	7.6	9.529	»X-OH + UO2<2+> + CO3<2-> = »X-O-UO2CO3<1-> + H<1+>	JHLCH99
DDL	Quartz	10	10	-1.6	7.6	-1.978	»X-OH + UO2<2+> = »X-O-UO2<1+> + H<1+>	JHLCH99
DDL	Quartz	0.05			-7.2	-16.75	»SiOH + 3 UO2<2+> + 5 H2O = »SiO-(UO2)3(OH)5 + 6 H<1+>	NB10
DDL	Quartz	0.05			-7.2	0.3	»SiOH + UO2<2+> = »SiO-UO2<1+> + H<1+>	NB10
DDL	Quartz	0.05			-7.2	-5.65	»SiOH + UO2<2+> + H2O = »SiO-UO2(OH) + 2 H<1+>	NB10
DDL	Quartz	0.31	2.3	-1.24	7.06	-0.3	»Si-OH + UO2<2+> = »Si-O-UO2<1+> + H<1+>	PJTP01
DDL	Quartz	0.31	2.3	-1.24	7.06	-18.7	»Si-OH + UO2<2+> + 3 H2O = »Si-O-UO2(OH)3<2->+ 4 H<1+>	PJTP01
DDL	Quartz	0.03	2.3		7.2	0.3	»Si-OH + UO2<2+> = »Si-O-UO2<1+> + H<1+>	PTBP98
DDL	Quartz	0.03	2.3		7.2	-16.75	»Si-OH + 3 UO2<2+> + 5 H2O = »Si-O-(UO2)3(OH)5 + 6 H<1+>	PTBP98
DDL	Quartz	0.03	2.3		7.2	-5.65	»Si-OH + UO2<2+> + H2O = »Si-O-UO2(OH) + 2 H<1+>	PTBP98
DDL	Quartz	0.1	2.31		7.2	-8.45	»Si-OH + UO2<2+> + 2 H2O = »Si-O-UO2(OH)2<1-> + 3 H<1+>	VT98
NE	Quartz	0.33	0			-4.95	»Si(w)-OH + UO2<2+> + H2O = »Si(w)-O-UO2(OH) + 2 H<1+>	DK01
NE	Quartz	0.33	0			1.06	»Si(s)-OH + UO2<2+> = »Si(s)-O-UO2<1+> + H<1+>	DK01
NE	Quartz	0.33	0			-3.19	»Si(s)-OH + UO2<2+> + H2O = »Si(s)-O-UO2(OH) + 2 H<1+>	DK01

SCM Type	Mineral	Area m2/g	Site Density nm-1	pK_1	pK_2	logK	Chemical Equation	Literature Reference
NE	Quartz	0.33	0			-2.56	»Si(s)-OH + UO2<2+> + H2O = »Si(s)-O-UO2(OH) + 2 H<1+>	DK01
NE	Quartz	0.33	0			-4.98	»Si(w)-OH + UO2<2+> + H2O = »Si(w)-O-UO2(OH) + 2 H<1+>	DK01
NE	Quartz	0.33	0			1.2	»Si(s)-OH + UO2<2+> = »Si(s)-O-UO2<1+> + H<1+>	DK01
NE	Quartz	0.33	0			-4.64	»Si(w)-OH + UO2<2+> + H2O = »Si(w)-O-UO2(OH) + 2 H<1+>	DK01
NE	Quartz	0.33	0			-0.03	»Si(w)-OH + UO2<2+> = »Si(w)-O-UO2<1+> + H<1+>	DK01
NE	Quartz	0.33	0			-5.28	»Si(w)-OH + UO2<2+> + H2O = »Si(w)-O-UO2(OH) + 2 H<1+>	DK01
NE	Quartz	0.33	0			10.183	»Si(w)-OH + UO2<2+> + CO3<2-> = »Si(w)-O-UO2CO3<1-> + H<1+>	DK01
NE	Quartz	0.33	0			-3.28	»Si(s)-OH + UO2<2+> + H2O = »Si(s)-O-UO2(OH) + 2 H<1+>	DK01
NE	Quartz	0.33	0			-4.73	»Si-OH + UO2<2+> = »Si-O-UO2(OH) + 2 H<1+>	KCKD96
NE	Quartz	0.33	0			-5.32	»Si(w)-OH + UO2<2+> + H2O = »Si(w)-O-UO2(OH) + 2 H<1+>	KCKD96
NE	Quartz	0.33	0			-2.65	»Si(s)-OH + UO2<2+> + H2O = »Si(s)-O-UO2(OH) + 2 H<1+>	KCKD96
NE	Quartz	0.33	0			-2.56	»Si(s)-O(0.5)H + UO2<2+> + H2O = »Si(s)-O(0.5)-UO2(OH) + 2 H<1+>	K02b
NE	Quartz	0.33	0			-7.78	»Si(w)-O(0.5)H + UO2<2+> + CO2 + H2O = »Si(w)-O(0.5)-UO2CO3(OH)<2-> + 3 H<1+>	K02b
NE	Quartz	0.33	0			-6.56	»Si(w)-O(0.5)H + UO2<2+> + H2O = »Si(w)-O(0.5)-UO2(OH) + 2 H<1+>	K02b
NE	Quartz	0.33	0			-5.57	»Si(s)-O(0.5)H + UO2<2+> + H2O = »Si(s)-O(0.5)-UO2(OH) + 2 H<1+>	K02b

SCM Type	Mineral	Area m2/g	Site Density nm-1	pK_1	pK_2	logK	Chemical Equation	Literature Reference
NE	Quartz	0.33	0			-6.5	»Si(w)-O(0.5)H + UO2<2+> + CO2 + H2O = »Si(w)-O(0.5)-UO2CO3(OH)<2-> + 3 H<1+>	K02b
NE	Quartz	0.33	0			-5.28	»Si(w)-O(0.5)H + UO2<2+> + H2O = »Si(w)-O(0.5)-UO2(OH) + 2 H<1+>	K02b
TL	Quartz	0.32	0.00184		8.4	1.98	»Si(s)-OH + UO2<2+> = »Si(s)-O-UO2<1+> + H<1+>	FDZ06
TL	Quartz	0.32	0.00184		8.4	-1.88	»Si(s)-OH + UO2<2+> + H2O = »Si(s)-O-UO2(OH) + H<1+>	FDZ06

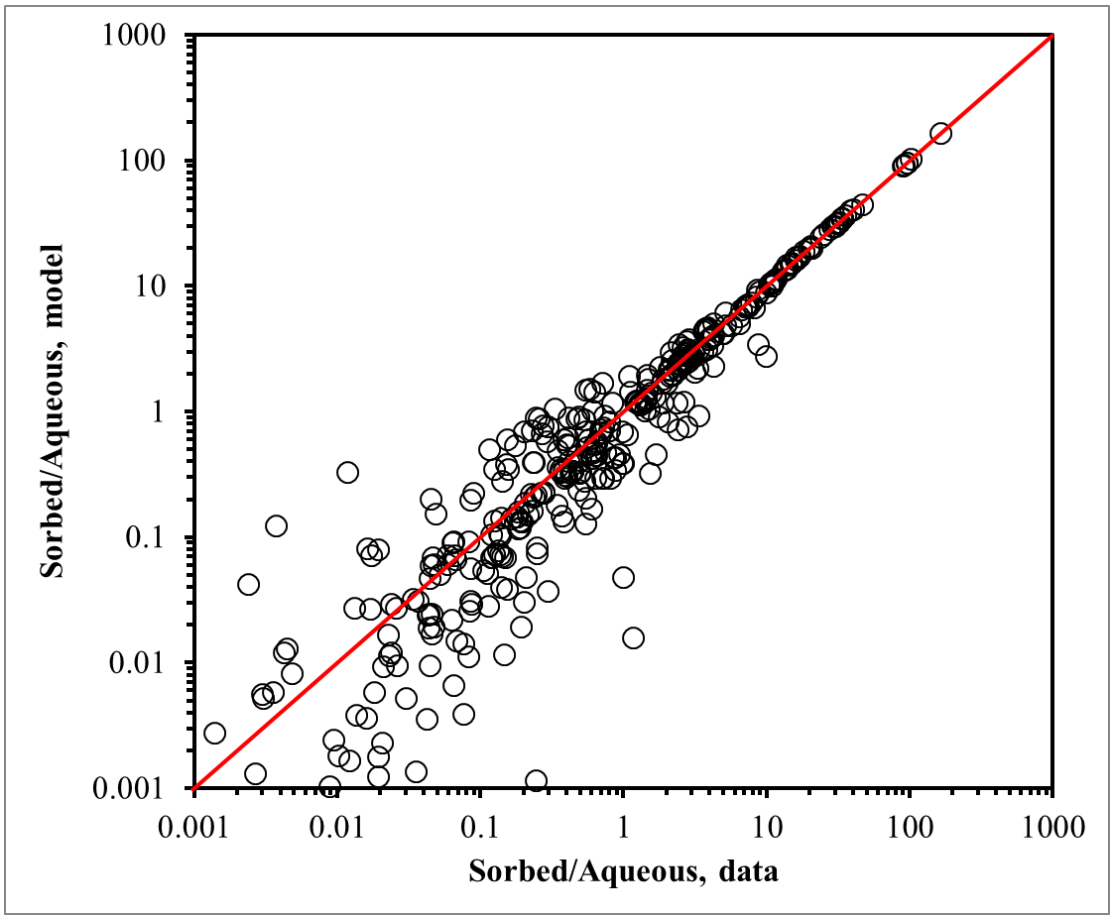

Figure 4. Comparison of data and model fits of the ratio of sorbed to aqueous concentrations for all batch sorption data contained in references identified by the RES^{3}T database for U(VI) sorption to quartz. Increasing scatter at low Sorbed/Aqueous ratios is a result of inherent uncertainties associated with samples with little to no U(VI) sorption.

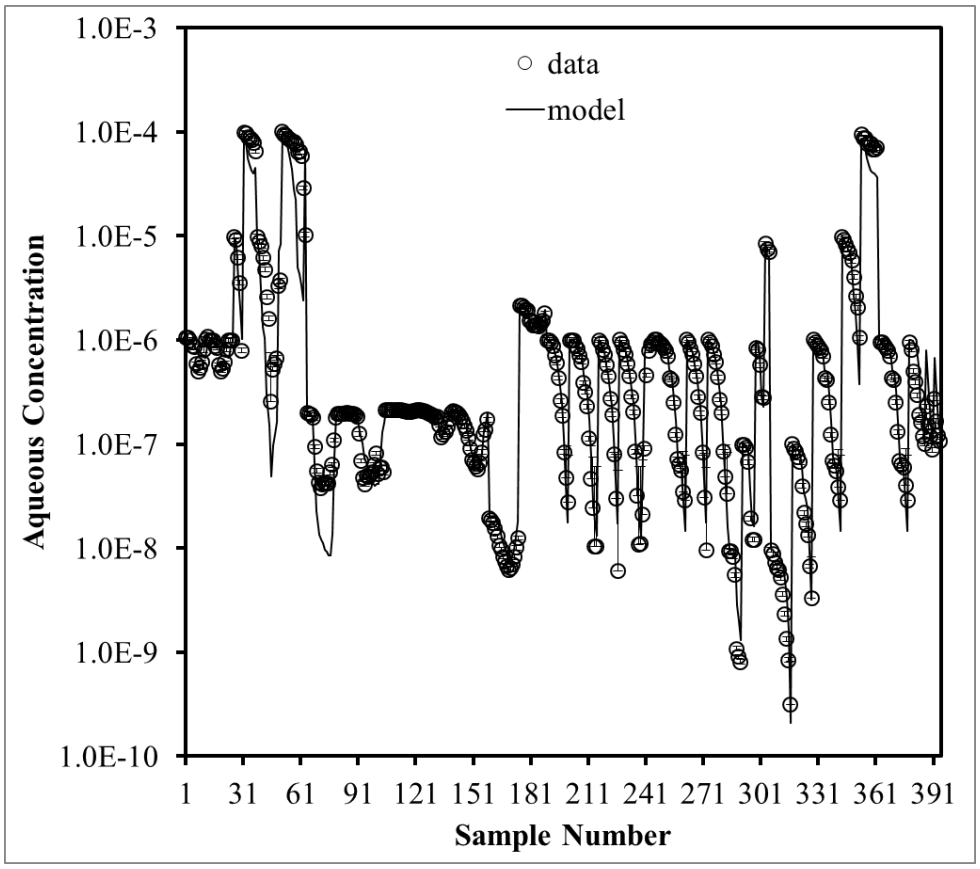

Figure 5. Comparison of measured and predicted U(VI) concentration in ~400 batch sorption data points digitized from the literature based on references contained in the RES^{3}T database for U(VI) sorption to quartz.

3.1 Development of a Np(V) Ion Exchange Model

The aim of the ion exchange study was to isolate the ion exchange mechanism of Np(V) sorption to montmorillonite. Np(V) exchange on homoionic Na, K, Ca and Mg-montmorillonite was determined experimentally at pH 4.5 using Na^+, K^+, Ca^{++} and Mg^{++} as electrolyte cations at ionic strengths ranging from 0.001 to 0.1 M. This experimental data was then modeled to estimate selectivity coefficients for the exchange reactions. These coefficients are essential for accurate prediction of Np mobility in reactive transport models. The experimental work described herein was extracted from a manuscript recently published in Applied Geochemistry (Benedicto et al., 2014).

The experimental data obtained in this study indicate that Np ionic exchange depends on the major cation composition of the aqueous system, being especially limited by the presence of divalent cations such as Ca^{2+} and Mg^{2+} in solution. At basic conditions, ionic exchange becomes less significant and surface complexation of Np(V) will dominate. An ion exchange model was developed on the basis of the experimental data, which is consistent with selectivity coefficients reported in the literature for the exchange between major cations and NpO_2^+ on montmorillonite. The recommended selectivity coefficients for Np(V) ionic exchange on montmorillonite,

according to the Vanselow convention, are as follows: $\log\left({}^{NpO_2^+}_{Na^+}K_V\right) = -0.26$, $\log\left({}^{NpO_2^+}_{K^+}K_V\right) = -0.52$, $\log\left({}^{NpO_2^+}_{Ca^{2+}}K_V\right) = -0.69$, $\log\left({}^{NpO_2^+}_{Mg^{2+}}K_V\right) = -0.69$.

3.2 Planned FY15 Efforts

In FY15, we plan to continue our interaction with national and international partners in the development of thermodynamic models and databases. In particular, there is growing interest in expanding the capabilities of the RES^{3}T surface complexation development to capture raw sorption data and associated meta-data contained in published documents. A proof of principal effort will be used to test the robustness of data digitization software and optimal data storage and formatting structures that are compatible with the RES^{3}T database framework. One test case dataset (i.e. U(VI) binary sorption to silica) was digitized in FY14. More detailed evaluation of various surface complexation modeling approaches is planned for FY15.

4. Structural and Thermal-Mechanical Data of Clay Minerals and Crystalline Disposal Systems: A First-Principles Approach

4.1 Background

Thermodynamic parameters for the corrosion phases of spent nuclear fuel (SNF), engineered barrier systems (EBS) materials and natural (barrier) system (NS) minerals are critical to assess their stability and behavior in geologic disposal environments for safety assessments. Among the thermodynamic data gaps and research needs, the thermal properties of NS minerals surrounding the waste package (e.g. clays, complex salts, granite…) are of particular importance to determine phase stability of materials and interfacial processes leading to the degradation of the waste package.

The main objectives of the present study using first-principles methods are to:

- Calculate missing thermodynamic data needed for SNF and barrier materials degradation models, as a fast, systematic approach, to circumvent expensive and time-consuming experiments on real materials. Note that this approach is not a substitute but a complementary aspect of experimental activities.
- Provide an independent assessment of existing experimental thermodynamic data and to evaluate inconsistencies in existing calorimetric data. It also provides missing data such as entropy and heat capacities which is key to high temperature extrapolations.
- Validate our computational approach using high-quality calorimetric data.

In order to assess our first-principles computational approach, structural optimization of kaolinite clay (i.e. $Al_2Si_2O_5(OH)_4$) and bischofite salt and its dehydrated phases [$MgCl_2 \cdot nH_2O$ (n=6, 4, 2, 1)] were carried out using density functional theory (DFT), followed by density functional perturbation theory (DF-PT) calculations to determine their phonon and thermal properties.

Details of our computational approach are given in the next section, followed by a complete analysis and discussion of our results.

4.1.1 Computational Methods

A schematic representation of the three-step computational approach used in this report is displayed in Figure 6. The first step consists of a crystal structure optimization using density functional theory (DFT), followed by a calculation of phonon frequencies using density functional perturbation theory (DFPT), and, finally, a phonon analysis is carried out to derive the thermodynamic properties of the crystalline system investigated.

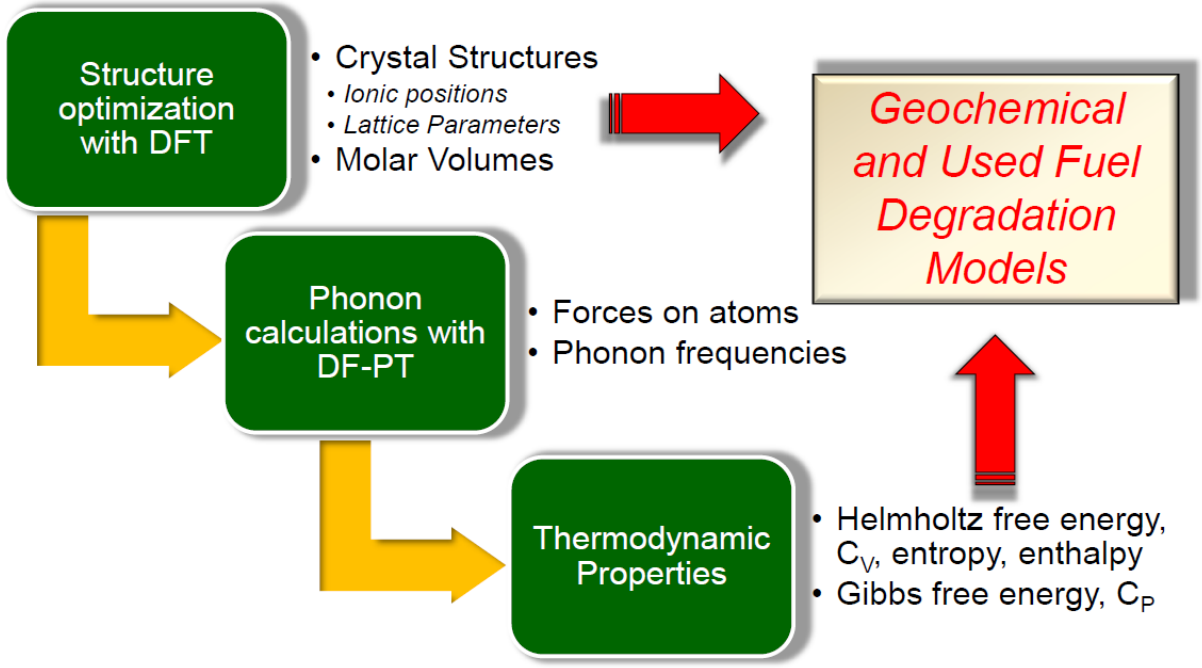

Figure 6. Schematic representation of the three-step computational approach used to calculate the thermal properties of crystalline systems using first-principles methods.

The equilibrium structures of kaolinite and bischofite and its dehydrated phases were optimized using the standard density functional theory (DFT) implemented in the Vienna Ab initio Simulation Package (VASP) (Kresse & Furthmüller, 1996). Details of standard geometry optimization calculations have been reported previously in Weck et al. (2012). The exchange-correlation energy was calculated within the generalized gradient approximation (GGA) (Perdew, et al., 1992), with the parameterization of Perdew, Burke, and Ernzerhof (PBE) (Perdew, Burke, and Ernzerhof, 1996).

For bischofite and its dehydrated phases, standard DFT was used. The structure of kaolinite consists of stacked layers linked by weak interatomic forces, therefore it can be inferred that van der Waals dispersion interactions may play a role in the structure of this compound. However, popular density functionals are unable to describe correctly the van der Waals interactions resulting from dynamical correlations between fluctuating charge distributions. A pragmatic method to work around this problem has been given by density functional theory corrected for dispersion (DFT-D) (Wu et al., 2001), which consists in adding a semi-empirical dispersion potential to the conventional Kohn-Sham GGA total-energy functional, E_{GGA} , i.e.,

$$E_{\mathrm{GGA-DFT-D}} = E_{\mathrm{GGA}} + E_{\mathrm{disp}}.$$

In the DFT-D2 method of Grimme (Grimme, 2006) utilized in this study, the van der Waals interactions are described via a simple pair-wise force field, which is optimized for DFT functionals. The dispersion energy for periodic systems is defined as:

$$E_{\text{disp}} = -\frac{s_6}{2} \sum_{i=1}^{N} \sum_{j=1}^{N} \sum_{L}' \frac{C_6^{ij}}{|\vec{r}^{i,0} - \vec{r}^{j,L}|^6} f\left(|\vec{r}^{i,0} - \vec{r}^{j,L}|\right),$$

where the summation are over all atoms N and all translations of the unit cell $L = (l_1, l_2, l_3)$, with the prime sign indicating that cell $i \neq j$ for $L = 0$, s_6 is a global scaling factor, C_6^{ij} is the dispersion coefficient for the atom pair ij, $\vec{r}^{j,L}$ is a position vector of atom j after performing L translations of the unit cell along lattice vectors. In practice, terms corresponding to interactions over distances longer than a certain suitably chosen cutoff radius contribute only negligibly to the dispersion energy and can be ignored. The term $f\left(r^{i,j}\right)$ is a damping function:

$$f\left(r^{i,j}\right) = \frac{1}{1+e^{-d\left(r^{i,j}/R_0^{ij}-1\right)}},$$

whose role is to scale the force field such as to minimize contributions from interactions within typical bonding distances. Combination rules for dispersion coefficients C_6^{ij} and van der Waals radii R_0^{ij} are:

$$C_6^{ij} = \sqrt{C_6^i C_6^j},$$

and

$$R_0^{ij} = R_0^i + R_0^j.$$

The global scaling parameter s_6 has been optimized for several different DFT functionals and corresponds to a value of $s_6 = 0.75$ for the PBE functional used in this study. The R_0 and C_6 parameters defined in the empirical force-field of Grimme (Grimme, 2006) were systematically used.

Once the equilibrium structures of kaolinite and bischofite and its dehydrated phases were obtained, the forces exerted on atoms of the set of crystal supercells were calculated using density functional perturbation theory (DFPT) with VASP at the same level of theory and phonon frequencies were computed. Phonon analysis was performed at constant equilibrium volume in order to derive isochoric thermal properties (e.g., the phonon (Helmholtz) free energy, the entropy and the isochoric heat capacity).

The Helmholtz free energy was calculated using the following formula:

$$F = \frac{1}{2}\sum \hbar\omega + k_B T \sum \ln\left[1 - e^{-\hbar\omega/k_B T}\right].$$

The entropy was computed using the expression:

$$S = -k_B \sum \ln\left[1 - e^{-\hbar\omega/k_B T}\right] - \frac{1}{\mathrm{T}}\sum \frac{\hbar\omega}{e^{\hbar\omega/k_B T} - 1}.$$

The heat capacity at constant volume was calculated using the formula:

$$C_V = \sum k_B \left[\frac{\hbar\omega}{k_B T}\right]^2 \frac{e^{\hbar\omega/k_B T}}{[e^{\hbar\omega/k_B T} - 1]^2}.$$

Further analysis from a set of phonon calculations in the vicinity of each computed equilibrium crystal structure was carried out to obtain thermal properties at constant pressure (e.g., the Gibbs free energy and the isobaric heat capacity) within a quasi-harmonic approximation (QHA). The QHA mentioned here introduces volume dependence of phonon frequencies as a part of anharmonic effect. A part of temperature effect can be included into the total energy of electronic structure through the phonon (Helmholtz) free energy at constant volume, but thermal properties at constant pressure are what we want to know. Therefore, some transformation from a function of volume *V* to a function of pressure *p* is needed. The Gibbs free energy is defined at a constant pressure by the transformation:

$$G(T, p) = \min_V \left[U(V) + F_{phonon}(T; V) + pV\right],$$

where $\min_V[\text{ function of } V]$ means to find unique minimum value in the brackets by changing volume. Since volume dependencies of energies in electronic and phonon structures are different, volume giving the minimum value of the energy function in the square brackets shifts from the value calculated only from electronic structure even at $T = 0$ K. By increasing temperature, the volume dependence of phonon free energy changes, then the equilibrium volume at temperatures changes.

The heat capacity at constant pressure versus temperature was also derived as the second derivative of the Gibbs free energy with respect to *T*, i.e.:

$$C_P = -T\frac{\partial^2 G}{\partial T^2}.$$

The thermal evolutions of the isobaric heat capacity calculated from first-principles were first fitted using a nonlinear least-squares regression to a Haas-Fisher-type polynomial, i.e,

$$C_P(T) = a + bT + cT^{-2} + dT^{-0.5} + eT^2.$$

4.1.2 Results and Discussion

4.1.2.1 Structure and thermal-mechanical properties of kaolinite:

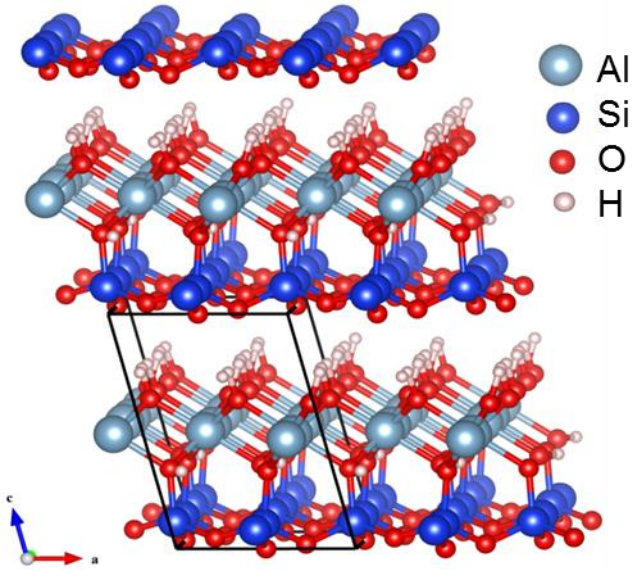

Figure 7. Crystal unit cell of kaolinite ($Al_2Si_2O_5(OH)_4$) relaxed with DFT-D at the GGA/PBE level of theory.

A schematic representation of the kaolinite crystal unit cell and extended structure relaxed at the GGA/PBE level of theory is shown in Figure 7. The crystal parameters computed using standard DFT are: a = 5.21 Å, b = 9.05 Å, c = 7.48 Å; α = 91.8°, β = 105.1°, γ = 89.7°; V = 340.11 Å^3. Using DFT-D to account for van der Waals interactions, the computed lattice parameters are: a = 5.18 Å, b = 8.99 Å, c = 7.33 Å; α = 91.6°, β = 105.1°, γ = 89.8°; V = 329.03 Å^3. These results are in excellent agreement with the experimental values: a = 5.153 Å, b = 8.942 Å, c = 7.391 Å; α = 91.93°, β = 105.05°, γ = 89.80°; V = 328.708 Å^3 (Bish, 1993). The volume calculated with DFT-D overestimates experiment by less than 1%, while standard DFT overestimates expt. by ca. 3.5 %. This clearly shows the importance of using DFT corrected for dispersion interaction for layered systems such as clays, therefore all the calculations reported hereafter have been carried out using DFT-D.

Starting from the equilibrium structure of kaolinite relaxed with DFT-D, two types of cell deformation were investigated, namely hydrostatic deformation and uniaxial deformation along the z-axis normal of the layers. Both deformation modes and the corresponding calculated total energies are shown in Figure 8.

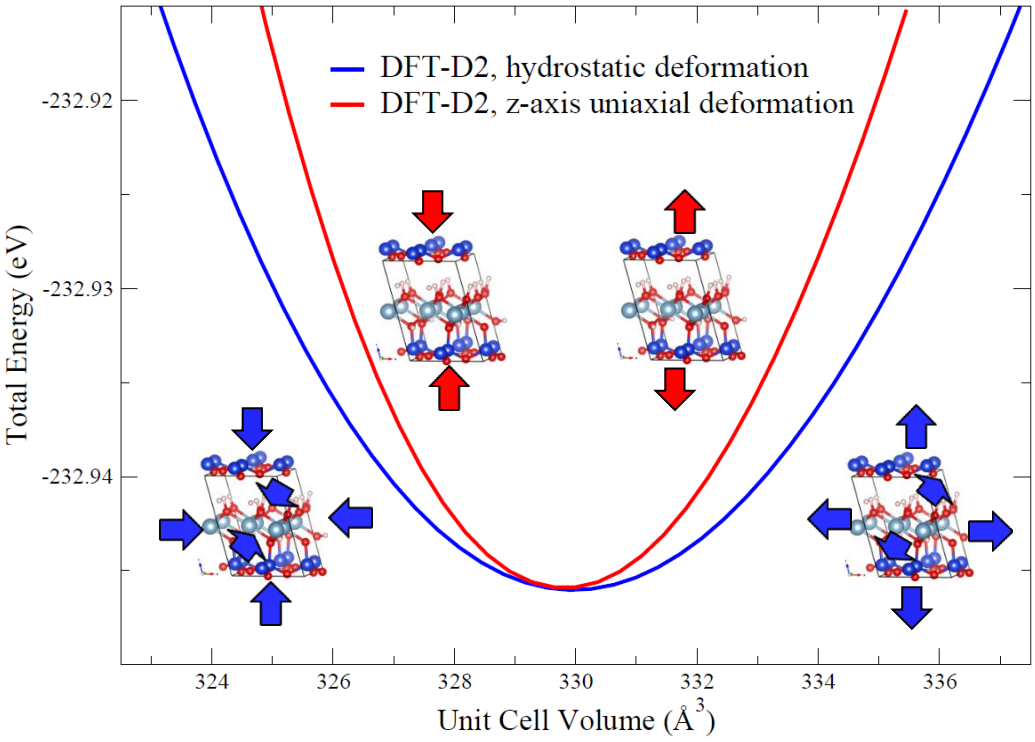

Figure 8. Energetics of the hydrostatic and uniaxial (z-axis) deformations of the kaolinite ($Al_2Si_2O_5(OH)_4$) unit cell calculated with DFT-D at the GGA/PBE level of theory.

As shown in Figure 8, significant differences exist between hydrostatic and uniaxial deformations of kaolinite, i.e. uniaxial deformation resulting in a stiffer material than when deformed hydrostatically.

As a standard measure of the compression of kaolinite, the bulk modulus was calculated with DFT-D for both hydrostatic and uniaxial compression using the Birch-Murnaghan 3rd-order equation of state:

$$P(V) = \frac{3B_0}{2}\left[\left(\frac{V_0}{V}\right)^{\frac{7}{3}} - \left(\frac{V_0}{V}\right)^{\frac{5}{3}}\right]\left\{1 + \frac{3}{4}(B_0' - 4)\left[\left(\frac{V_0}{V}\right)^{\frac{2}{3}} - 1\right]\right\},$$

where P is the pressure, V_0 is the reference volume, V is the deformed volume and

$$B_0 = -V\left(\frac{\partial P}{\partial V}\right)_{P=0} \text{ and } B_0' = \left(\frac{\partial B}{\partial P}\right)_{P=0}.$$

The computed bulk moduli for hydrostatic and uniaxial compression are: B_0 = 54 and 116 GPa, respectively. The value for hydrostatic compression is in close agreement with the experimental values in the range B_0 = 44-56 GPa (Wang et al., 2001). The large difference between bulk moduli for hydrostatic and uniaxial compression show the strong impact of the system anisotropy on the mechanical-elastic properties of layered materials such as clays.

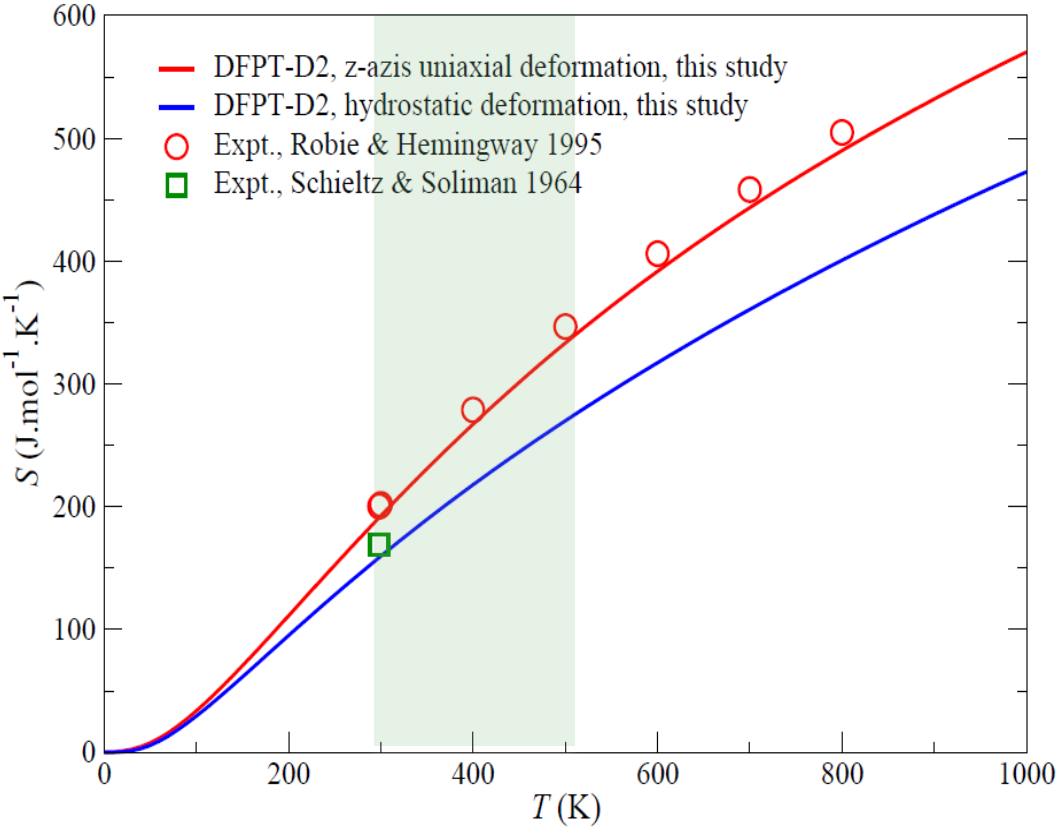

Figure 9. Entropy of kaolinite computed with DFT-D at the GGA/PBE level along with the experimental values of Robie and Hemingway (1995) and Schieltz and Soliman (1964).

As shown in Figure 9, the calculated entropy using uniaxial deformation along the z-axis of the unit cell is in excellent agreement with experimental values of Robie and Hemingway (1995). However, the entropy calculated using hydrostatic deformation consistently underestimates data derived from calorimetry. This shows that uniaxial deformation of the cell maximizes the entropy compared to hydrostatic deformation. Maximizing the entropy appears to be the thermodynamic driving force for the formation of layered structures. Potential thermal conditions of interest for nuclear waste disposal in geological repositories are indicated as a green shaded area in Figure 9.

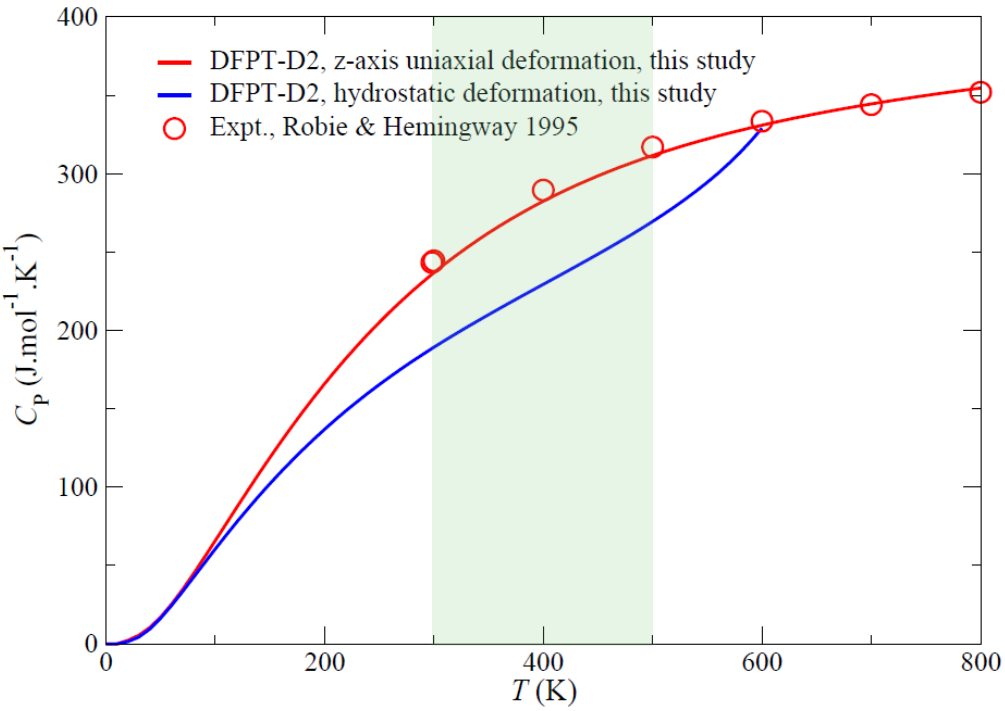

Figure 10. Isobaric heat capacity of kaolinite calculated at constant atmospheric pressure at the DFT-D/PBE level of theory for uniaxial and hydrostatic deformations. The experimental values of Robie and Heningway (1995) are also depicted for the sake of comparison. Potential thermal conditions of interest nuclear waste disposal in geological repositories are indicated as a shaded area.

Calculations of the isobaric heat capacity of kaolinite calculated within the quasi-harmonic approximation (QHA) at constant atmospheric pressure at the DFT-D/PBE level of theory for uniaxial and hydrostatic deformations are shown in Figure 10. The computed isobaric heat capacity using uniaxial deformation of the cell reproduces the calorimetric data of Robie and Heningway (1995), while the values calculated with hydrostatic deformation underestimates calorimetric data for temperatures < 600 K.

4.1.2.2 Structures and thermal properties of bischofite and its dehydrated phases

Bichofite, $MgCl_2 \cdot 6H_2O$, thermally decomposes according to the successive reactions (Sugimoto et al., 2007):

$$MgCl_2.6H_2O \rightarrow MgCl_2.4H_2O + 2H_2O$$
$$MgCl_2.4H_2O \rightarrow MgCl_2.2H_2O + 2H_2O$$
$$MgCl_2.2H_2O \rightarrow MgCl_2.H_2O + H_2O$$

where the crystallization temperatures are *ca.* 107 and 153 °C for $MgCl_2.4H_2O$ and $MgCl_2.2H_2O$, respectively. The crystal unit cells of $MgCl_2 \cdot nH_2O$ (n = 6, 4, 2, 1) optimized at the GGA/PBE level of theory are shown in Figure 11, and their computed and measured crystallographic parameters are summarized in Table 3.

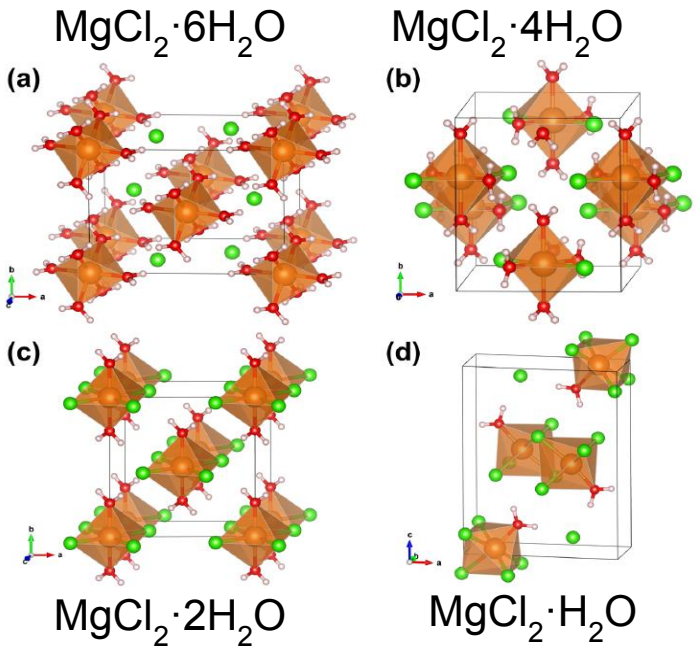

Figure 11. Crystal structures of (a) $MgCl_2 \cdot 6H_2O$ (space group *C*2/*m*; *Z* = 2), (b) $MgCl_2 \cdot 4H_2O$ (space group *Pbcn*; *Z* = 4), (c) $MgCl_2 \cdot 2H_2O$ (space group *C*2/*m*; *Z* = 2), and (d) $MgCl_2 \cdot H_2O$ (space group *Pnma*; *Z* = 4), optimized at the DFT/PBE level of theory. Color legend: Mg, orange; O, red; Cl, green; H, white.

In Figure 12, the experimental values of the entropy from the FactSage FACTPS (Bale et al., 2002) database are displayed for the sake of comparison; these reference data are based on the early calorimetric measurements of Kelley and Moore (Kelley, 1960; Kelley & Moore, 1943). The entropy predicted from first-principles is in very good agreement with experimental data for $MgCl_2 \cdot nH_2O$ (*n* = 4, 2, 1): the computed entropy underestimates experimental data by *ca.* 5% and *ca.* 3% for $MgCl_2 \cdot 4H_2O$ and $MgCl_2 \cdot 2H_2O$, respectively, and overestimates experiment by *ca.* 2% for $MgCl_2 \cdot H_2O$. However, for $MgCl_2 \cdot 6H_2O$, the predicted entropy is 14−17% lower than calorimetric data. As shown in Figure 12, the entropy increases steadily with temperature and decreases, for a fixed temperature, as the molar volume contracts with successive dehydration reactions from $MgCl_2 \cdot 6H_2O$ to $MgCl_2 \cdot H_2O$. This is consistent with the fact that a temperature increase (a molar volume decrease and the loss of water molecules) results in a larger (smaller) number of microstates in the system, *W*, which in turn increases (decreases) logarithmically the entropy according to Boltzmann's entropy formula, $S = k_B.\log(W)$, where k_B is the Boltzmann constant.

Table 3. Crystallographic data of $MgCl_2 \cdot nH_2O$ (n = 6, 4, 2, 1) calculated at the GGA/PBE level of theory (experimental data are given in parentheses).

formula	$MgCl_2 \cdot 6H_2O$	$MgCl_2 \cdot 4H_2O$	$MgCl_2 \cdot 2H_2O$	$MgCl_2 \cdot H_2O$
space group	$C2/m$	$Pbcn$	$C2/m$	$Pnma$
Z	2	4	2	4
a (Å)	9.91	7.38	7.90	8.98
	(9.8607)[a]	(7.2557)[b]	(7.4279)[c]	(8.9171)[c]
b (Å)	7.16	8.42	8.50	3.69
	(7.1071)[a]	(8.4285)[b]	(8.5736)[c]	(3.6342)[c]
c (Å)	6.12	11.00	3.70	11.58
	(6.0737)[a]	(11.0412)[b]	(3.6506)[c]	(11.4775)[c]
α (deg)	90	90	90	90
	(90)[a]	(90)[b]	(90)[c]	(90)[c]
β (deg)	94.25	90	104.0	90
	(93.758)[a]	(90)[b]	(98.580)[c]	(90)[c]
γ (deg)	90	90	90	90
	(90)[a]	(90)[b]	(90)[c]	(90)[c]
V (Å^3)	433.18	683.63	241.06	383.65
	(424.736)[a]	(675.226)[b]	(229.886)[c]	(371.954)[c]

[a] Agron and Busing, 1985. [b] Schmidt, Hennings, and Voigt, 2012. [c] Sugimoto, Dinnebier, and Hanson, 2007.

For $MgCl_2 \cdot 6H_2O$, large discrepancies are observed among the experimental estimates of $C_P(T)$ (cf. Figure 13a). For example, the isobaric molar heat capacity value reported by Yaws (Yaws, 2009) is 243.31 J.mol^{-1}.K^{-1} at 298.15 K and atmospheric pressure, significantly lower than the values of 315.02 and 337.03 J.mol^{-1}.K^{-1} measured at the same temperature by Kelley (Kelley, 1960) and Pilar et al. (Pilar et al., 2012), respectively. Such large differences were tentatively ascribed to the varying amount of crystallographic water in the $MgCl_2 \cdot 6H_2O$ samples characterized by calorimetry (Pilar et al., 2012). The calorimetric data reported by Kelley and Moore (Kelley and Moore, 1943) between 54.1 and 295.8 K are also displayed in Figure 13. In the 298−385 K range, a simplified Maier−Kelley polynomial fit, $C_P = a + bT + cT^{-2}$ with $c = 0$, was used by Wagman et al. (Wagman et al., 1982) based on the measurements of Kelley (Kelley, 1960) and Pilar et al. (Pilar et al., 2012) recently reported Maier−Kelley fits to their experimental data in the 298.15−387.15 K range with a declared uncertainty of ca. 3%. As shown in Figure 8, the computed C_P systematically underestimates the calorimetric measurements of Kelley and Moore and Pilar et al., while overestimating by ca. 9% the value reported by Yaws at 298.15 K. Surprisingly, the agreement between computed and empirical C_P values of Kelley improves as the temperature ramps up from 298 to 385 K, although one would expect a slight deterioration of this agreement due to the breakdown of the QHA. Large discrepancies are observed between the recent data of Pilar et al. and both the experimental data of Kelley (Kelley, 1960) and the calculations in the vicinity of 390 K, corresponding to the zone of phase transition between $MgCl_2 \cdot 6H_2O$ and $MgCl_2 \cdot 4H_2O$.

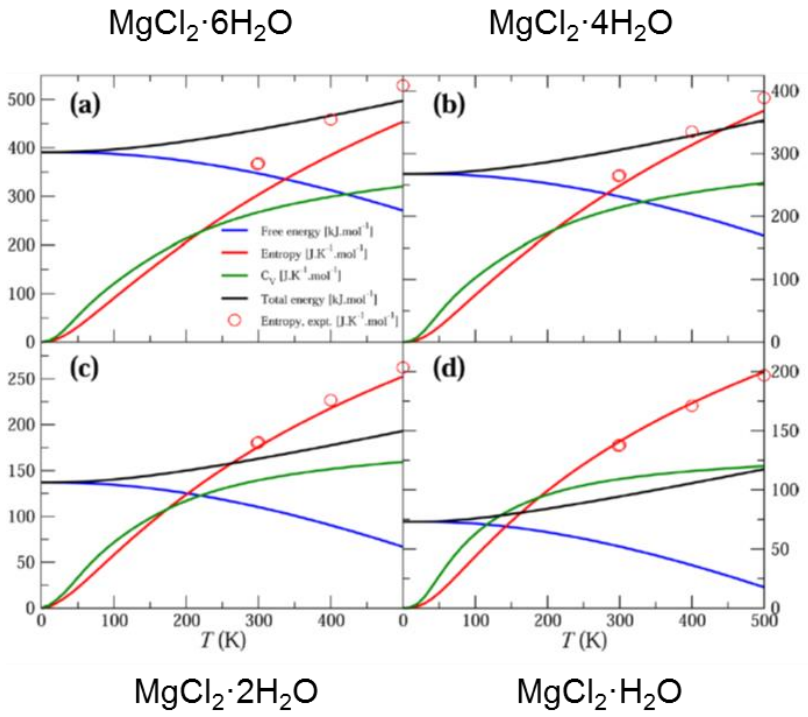

Figure 12. Thermal properties of (a) bischofite and ((b) to (d)) its dehydrated phases calculated at constant equilibrium volume at the DFT/PBE level of theory. Experimental data for the entropy (red circles) are from the FactSage FACTPS database.

The experimental isobaric molar heat capacity data for $MgCl_2 \cdot nH_2O$ (n = 4, 2, 1) from Wagman et al. (Wagman et al., 1982), with thermal extrapolation by Pabalan and Pitzer (Pabalan and Pitzer, 1987), are depicted along with the present predictions in Figures 13(b) to 13(d). Similar to $MgCl_2 \cdot 6H_2O$ discussed above, the experimental estimates of C_P for those compounds consist merely of linear extrapolations as functions of the temperature of data collected near room temperature (Wagman et al., 1982; Pabalan & Pitzer, 1987). The ranges of validity claimed for those linear fits are 298−450 K for $MgCl_2 \cdot 4H_2O$, 298−500 K for $MgCl_2 \cdot 2H_2O$, and 298−650 K for $MgCl_2 \cdot H_2O$. Within those temperature ranges, the heat capacity values computed in this study systematically underestimate experimental estimates by ca. 6−7% for $MgCl_2 \cdot 4H_2O$, ca. 11−13% for $MgCl_2 \cdot 2H_2O$, and ca. 5−8% for $MgCl_2 \cdot H_2O$. Further experimental work is needed to improve upon those existing linear fits to the isobaric heat capacities.

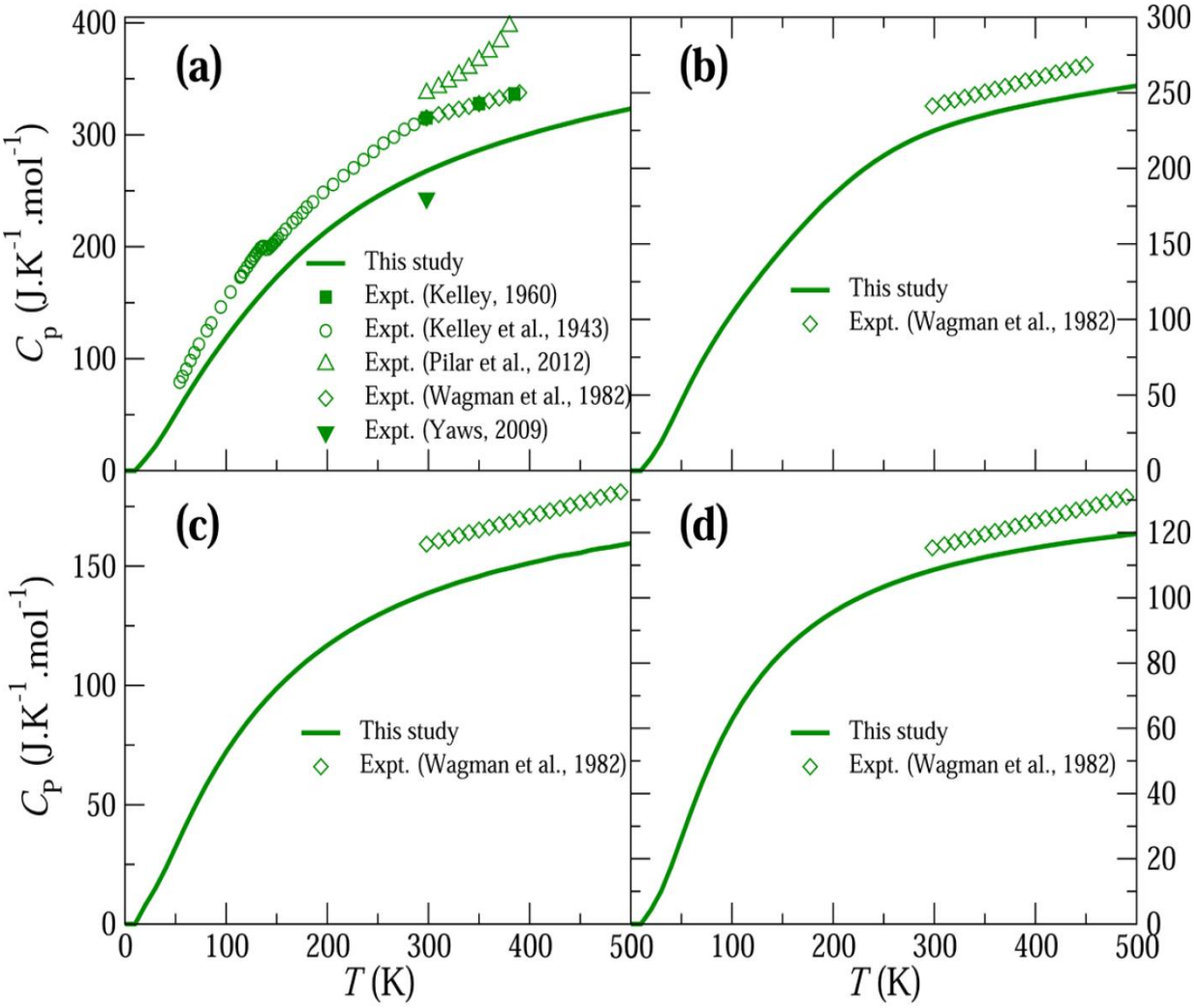

Figure 13. Molar heat capacities of (a) $MgCl_2 \cdot 6H_2O$, (b) $MgCl_2 \cdot 4H_2O$, (c) $MgCl_2 \cdot 2H_2O$, and (d) $MgCl_2 \cdot H_2O$, per formula unit, calculated at standard atmospheric pressure at the DFT/PBE level of theory.

Toward the higher end of the their thermal stability range, the computed heat capacity values for these compounds are still well below their respective Dulong−Petit asymptotic value, i.e., $C_P = 3NR$, where N is the number of atoms per formula unit and $R = 8.314426$ J.K^{-1}.mol^{-1} is the Regnault molar gas constant. The calculated Dulong-Petit limits are 523.8 J.K^{-1}.mol^{-1} for $MgCl_2 \cdot 6H_2O$, 374.1 J.K^{-1}.mol^{-1} for $MgCl_2 \cdot 4H_2O$, 224.5 J.K^{-1}.mol^{-1} for $MgCl_2 \cdot 2H_2O$, and 149.7 J.K^{-1}.mol^{-1} for $MgCl_2 \cdot H_2O$.

The thermal evolutions of the isobaric heat capacity calculated from first-principles for $MgCl_2 \cdot nH_2O$ (n = 6, 4, 2, 1) were fitted over the 290−500 K range using a nonlinear least-squares regression to a Haas−Fisher type polynomial, i.e.

$$C_P(T) = a + bT + cT^{-2} + dT^{-0.5} + eT^2,$$

with the resulting optimized coefficients given in Table 4.

Table 4. Coefficients of the Haas-Fisher heat capacity polynomial $C_p(T)$ for $MgCl_2{\cdot}nH_2O$ (n = 6, 4, 2, 1)[a].

compound	$a \times 10^2$ (T^0)	$b \times 10^{-2}$ (T^1)	$c \times 10^5$ (T^{-2})	$d \times 10^3$ ($T^{-0.5}$)	$e \times 10^{-5}$ (T^2)	SSD[b]
$MgCl_2{\cdot}6H_2O$	5.7643	−8.674	4.521784	−5.066334	5.97	0.004
$MgCl_2{\cdot}4H_2O$	−2.3567	52.839	−72.422160	6.983317	−22.90	0.006
$MgCl_2{\cdot}2H_2O$	2.0589	1.284	−5.574830	−1.118995	−0.21	0.124
$MgCl_2{\cdot}H_2O$	1.5498	−0.858	−3.357095	−0.704519	0.71	0.001

[a]The range of validity of the fits is 290−500 K. [b]Sum of squared differences between calculated and fitted data.

The amount of molar latent heat stored when the material is heated, at constant atmospheric pressure, from an initial temperature T_0 to its phase change temperature T_{pc} can be calculated as (Pilar et al., 2012):

$$Q_P = \int_{T_0}^{T_{pc}} C_P(T)dT + \Delta_{pc}H,$$

where $\Delta_{pc}H$ is the molar phase change enthalpy at the phase change temperature T_{pc} and C_P is the isobaric molar heat capacity of the solid phase. The recent experimental value of phase change enthalpy obtained by Pilar and co-workers (Pilar et al., 2012) using differential scanning calorimetry, i.e., $\Delta_{pc}H$ = 34.6 ± 0.5 kJ.mol^{-1} (170.1 ± 2.5 J.g^{-1}) at T_{pc} = 390.3 ± 0.2 K, was used in this study to calculate the amount of heat accumulated in $MgCl_2{\cdot}6H_2O$ from T_0 = 298.15 K to T_{pc}. This value is in line with previous estimates (Farid et al., 2004; Pilar et al., 2012; Lorsch et al., 1975; Guion et al, 1983) in the range $\Delta_{pc}H$ = 33.5−35.0 kJ.mol^{-1} (165−172 J.g^{-1}). The Haas−Fisher polynomial fit to the computed $C_P(T)$ was also used in the equation above. The molar latent heat obtained from first-principles calculations is Q_P = 60.8 kJ.mol^{-1}, i.e., slightly underestimating the experimental value of 68.2 kJ.mol^{-1} (335 J.g^{-1}) (Pilar et al., 2012).

A similar assessment of the amount of molar latent heat stored when $MgCl_2{\cdot}nH_2O$ (n = 4, 2, 1) crystals are heated to their respective phase change temperature can be made based on first-principles thermodynamic calculations. However, to the best of our knowledge, no consistent and reliable values of the phase change temperatures and enthalpies exist for these materials. Additional calorimetric studies and molecular dynamics simulations are needed to better characterize the thermochemical properties of the $MgCl_2{\cdot}nH_2O$ (n = 4, 2, 1) dehydrated phases.

4.2 Conclusions

Density functional theory (DFT) calculations of the thermodynamic properties of crystalline kaolinite clay (i.e. $Al_2Si_2O_5(OH)_4$) and bischofite salt and its dehydrated phases [$MgCl_2{\cdot}nH_2O$ (n=6, 4, 2, 1)] were carried out within the generalized gradient approximation. Specifically, phonon analysis using density functional perturbation theory was carried out in order to derive both their isochoric and isobaric thermal properties. Further experimental work is needed to assess our theoretical predictions for the dehydrated phases of bischofite salt [$MgCl_2{\cdot}nH_2O$ (n = 4, 2, 1. This methodology will be applied in a systematic way to other clays (e.g. montmorillonite clays,…) to expand the applicability of this data set to realistic systems. Such an expanded data set will facilitate investigation of NS, EBS, and SNF thermal-mechanical evolution in geological repositories.

Planned DFT Work on Clays for FY15

Expansion of this work is proposed given the above-mentioned successes in modeling clay systems using first-principles:

- Expand the adopted DFT-D methodology applied on kaolinite to montmorillonite clays.
- Evaluate expansive clay behavior using first-principles.

5. References

Agron, P. A., and W. R. Busing (1985). Magnesium Dichloride Hexahydrate, $MgCl_2 \bullet 6H_2O$, by Neutron Diffraction. Acta Crystallogr., Sect. C: Cryst. Struct. Commun., 41, 8−10.

Bale, C. W., P. Chartrand, S. A. Decterov, G. Eriksson, K. Hack, R. Ben Mahfoud, J. Melancon, A. D. Pelton, S. Petersen (2002). FactSage Thermochemical Software and Databases. CALPHAD: Comput. Coupling Phase Diagrams Thermochem., 26, 189−228.

Benedicto, A., Begg, J. D., Zhao, P., Kersting, A. B., Missana, T., and Zavarin, M. (2014) Effect of major cation water composition on the ion exchange on Np(V) on montmorillonite: NpO_2^+-Na^+-K^+-Ca^{2+}-Mg^{2+} selectivity coefficients. Applied Geochemistry 47, 177-185.

Bale, C. W., P. Chartrand, S. A. Decterov, G. Eriksson, K. Hack, R. Ben Mahfoud, J. Melancon, A. D. Pelton, S. Petersen (2002) FactSage Thermochemical Software and Databases. CALPHAD: Comput. Coupling Phase Diagrams Thermochem., 26, 189−228.

Barin, I. and Platzki, G. (1995) Thermochemical Data of Pure Substances. 3rd Edition. Two volumes. New York, New York: VCH Publishers.

Berman, R.G. (1988) Internally-Consistent Thermodynamic Data for Minerals in the System Na_2O-K_2O-CaO-MgO-FeO-Fe_2O_3-Al_2O_3-SiO_2-TiO_2-CO_2, Journal of Petrology, 29, 445-522.

Blanc, P., P. Piantone, A. Lassin, and A. Burnol (2006) Thermochimie : Sélection de constantes thermodynamiques pour les éléments majeurs, le plomb et le cadmium, Rapport final BRGM/RP-54902-FR, BRGM: France. 157 p.

Blanc, P., A. Lassin, P. Piantone, M. Azaroual, N. Jacquemet, A. Fabbri, and A. Gaucher (2012). Thermoddem: A geochemical database focused on low temperature water/rock interactions and waste materials. Applied Geochemistry, 27, 2107-2116.

Bradbury, M. H. and Baeyens, B. (1993) A general application of surface complexation modeling radionuclide sorption in natural systems. J. Colloid Interface Sci. 158, 364-371.

Bradbury, M. H. and Baeyens, B. (2009) Sorption modelling on illite. Part II: Actinide sorption and linear free energy relationships. Geochim. Cosmochim. Acta 73, 1004-1013.

Bradbury, M. H., Baeyens, B., and Thoenen, T. (2010) Sorption Data Bases for Generic Swiss Argillaceous Rock Systems. Nagra, Wettingen, Switzerland.

BSC (Bechtel SAIC Company) (2007). Qualification of Thermodynamic Data for Geochemical Modeling of Mineral–Water Interactions in Dilute Systems. ANL-WIS-GS-000003 REV 01. Las Vegas, Nevada: Bechtel SAIC Company. DOC.20070619.0007.01. Las Vegas, Nevada: Bechtel SAIC Company. DOC.20070619.0007.

Chase, M.W., Jr., Davies, C.A., Downey, J.R., Jr., Frurip, D.J., McDonald, R.A., and Syverud, A.N. (1985) JANAF Thermochemical Tables Third Edition, Journal of Physical and Chemical Reference Data 14, Supplement No. 1. American Chemical Society, Washington, DC and American Institute of Physics, New York, for the National Bureau of Standards. 1856 p.

Chase, M.W., Jr., editor. (1998) NIST-JANAF Thermochemical Tables, Fourth Edition. Journal of Physical and Chemical Reference Data, Monograph No. 9. The American Institute of Physics, Woodbury, New York. 1963 p. ISBN 1-56396-831-2.

Cheshire, M., F.A. Caporuscio, M.S. Rearick, C.F. Jové Colón, and M.K. McCarney (2014). Bentonite evolution at elevated pressures and temperatures: An experimental study for generic nuclear repository designs, American Mineralogist, 99, 1662-1675.

Chou, I. (1978) Calibration of oxygen buffers at elevated P and T by the hydrogen fugacity sensor. American Mineralogist, 63, p. 690-703.

CODATA. (1975) CODATA Recommended Key Values for Thermodynamics. Report of the CODATA Task Group on Key Values for Thermodynamics, November, 1973. Journal of Chemical Thermodynamics 7, 1-3.

Cox, J.D.; Wagman, D.D.; and Medvedev, V.A., eds. (1989) CODATA Key Values for Thermodynamics. CODATA Series on Thermodynamic Values. New York, New York: Hemisphere Publishing Company.

Dick, J.M., (2008). Calculation of the relative metastabilities of proteins using the CHNOSZ software package. Geochemical Transactions, Vol. 9, No 10.

Dresden-Rossendorf, H.-Z. (2013) RES³T - Rossendorf Expert System for Surface and Sorption Thermodynamics. RES³T - Rossendorf Expert System for Surface and Sorption Thermodynamics, Dresden, Germany.

Engi, M. (1992) Thermodynamic data for minerals: a critical assessment, In Price, G.D., and Ross, N.L., editors, The Stability of Minerals. Chapman & Hall, New York.

Farid, M. M.; A. M. Khudhair, S. A. K. Razack, S. A. Al-Hallaj (2004). Review of Phase Change Energy Storage: Materials and Applications. Energy Convers. Manage., 45, 1597−1615.Geckeis, H., Lützenkirchen, J., Polly, R., Rabung, T., and Schmidt, M. (2013) Mineral–Water Interface Reactions of Actinides. Chemical Reviews 113, 1016-1062.

Gailhanou, H., P. Blanc, J. Rogez, G. Mikaelian, H. Kawaji, J. Olives, M. Amouric, R. Denoyel, S. Bourrelly, V. Montouillout, P. Vieillard, C.I. Fialips, N. Michau, and E.C. Gaucher, (2012). Thermodynamic properties of illite, smectite and beidellite by calorimetric methods: Enthalpies of formation, heat capacities, entropies and Gibbs free energies of formation. Geochimica et Cosmochimica Acta, 89, 279-301.

Gailhanou, H., P. Blanc, J. Rogez, G. Mikaelian, K. Horiuchi, Y. Yamamura, K. Saito, H. Kawaji, F. Warmont, J.M. Greneche, P. Vieillard, C.I. Fialips, E. Giffaut, and E.C. Gaucher, (2013). Thermodynamic properties of saponite, nontronite, and vermiculite derived from calorimetric measurements. American Mineralogist, 98(10), 1834-1847.

Gaucher, E., P. Blanc, F. Bardot, G. Braibant, S. Buschaert, C. Crouzet, A. Gautier, J.P. Girard, E. Jacquot, A. Lassin, G. Negrel, C. Tournassat, A. Vinsot, and S. Altmann (2006).

Modelling the porewater of the Callovo-Oxfordian formation at a regional scale. Comptes Rendus Geoscience, 338, p. 917-930.

Grenthe, I.; Fuger, J.; Konings, R.J.M.; Lemire, R.J.; Muller, A.B.; Nguyen-Trung, C.; and Wanner, H. (1992) Chemical Thermodynamics of Uranium. Chemical Thermodynamics. Volume 1. Amsterdam, The Netherlands: North-Holland Publishing Company.

Grimme, S. (2006). Semiempirical GGA-type density functional constructed with a long-range dispersion correction , J. Comp. Chem., 27, 1787.

Guion, J.; J. D. Sauzade, and M. Laügt (1983). Critical Examination and Experimental Determination of Melting Enthalpies and Entropies of Salt Hydrates. Thermochim. Acta, 67, 167−179.Helgeson, H.C.; Delany, J.M.; Nesbitt, H.W.; and Bird, D.K. (1978) Summary and Critique of the Thermodynamic Properties of Rock Forming Minerals, American Journal of Science, 278-A. New Haven, Connecticut: Yale University, Kline Geology Laboratory.

Holland, T. J. B. and Powell, R. (1985) An internally consistent thermodynamic dataset with uncertainties and correlations.2. Data and Results, Journal of Metamorphic Geology 3, 343-370.

Holland, T. J. B. and Powell, R. (2011) An improved and extended internally consistent thermodynamic dataset for phases of petrological interest, involving a new equation of state for solids. Journal of Metamorphic Geology 29, 333-383.

Johnson, J.W.; Oelkers, E.H.; and Helgeson, H.C. (1992) SUPCRT92: A Software Package for Calculating the Standard Molal Thermodynamic Properties of Minerals, Gases, Aqueous Species, and Reactions from 1 to 5000 Bar and 0 to 1000°C. Computers & Geosciences, 18, (7), 899-947.

Kelley, K. K., and Moore, G. E. (1943). Specific Heats at Low Temperatures of Hydrates of Magnesium Chloride. J. Am. Chem. Soc., 65, 2340−2342.

Kelley, K. K. (1960). Contributions to the Data on Theoretical Metallurgy. 13. High Temperature Heat-Content, Heat-Capacity, and Entropy Data for the Elements and Inorganic Compounds. Bull. - U.S., Bur. Mines, 584, 232.

Kresse, G., and J. Furthmüller (1996). Efficient iterative schemes for ab initio total-energy calculations using a plane-wave basis set. Physical Review B, 54(16), 11169–11186.Lemire, R. J., Berner, U., Musikas, C., Palmer, D. A., Taylor, P., and Tochiyama, O., 2013. Chemical Thermodynamics of Iron: Part I. OECD Nuclear Energy Agency, Issy-les-Moulineaux, France.

Lemire, R. J., Berner, U., Musikas, C., Palmer, D. A., Taylor, P., and Tochiyama, O., 2013. Chemical Thermodynamics of Iron: Part I. OECD Nuclear Energy Agency, Issy-les-Moulineaux, France.

Lorsch, H. G. W. K. Kauffman, W. Kenneth, C. J. Dentons (1975). Thermal Energy Storage for Solar heating and Off-Peak Air Conditioning. Energy Convers., 15, 1−8.Oelkers, E.H., Bénézeth, P., and Pokrovski, G.S. (2009) Thermodynamic databases for water-rock interaction, Reviews in Mineralogy & Geochemistry, 70, 1-46.

Neuhoff, P.S., G.L. Hovis, G. Balassone, and J.F. Stebbins, (2004). Thermodynamic properties of analcime solid solutions. American Journal of Science, 304(1), p. 21-66.

Pabalan, R. T., and K. S. Pitzer (1987). Thermodynamics of Concentrated Electrolyte Mixtures and the Prediction of Mineral Solublities to High Temperatures for Mixtures in the System Na-K-Mg-Cl-SO_4-OH-H_2O. Geochim. Cosmochim. Acta, 51, 2429−2443.

Parker, V.B., Wagman, D.D., and Evans (1971) Selected Values of Chemical Thermodynamic Properties. Tables for the Alkaline Earth Elements (Elements 92 Through 97 in the Standard Order of Arrangement. National Bureau of Standards Technical Note 270-6. United States Government Printing Office, Washington, DC. 106 p.

Perdew, J., J. Chevary, S. Vosko, K. Jackson, M. Pederson, D. Singh, et al. (1992). Atoms, Molecules, Solids, and Surfaces - Applications of the Generalized Gradient Approximation for Exchange and Correlation. Physical Review B, 46(11), 6671–6687.

Perdew, J. P., K. Burke, and M. Ernzerhof (1996). Generalized gradient approximation made simple. Physical Review Letters, 77, 3865.

Pilar, R.; L. Svoboda, P. Honcova, and L. Oravova, L. (2012). Study of Magnesium Chloride Hexahydrates as Heat Storage Material. Thermochim. Acta, 546, 81−86.Powell, R. and Holland, T. J. B. (1985) An internally consistent thermodynamic dataset with uncertainties and correlations.1. Methods and a worked example, Journal of Metamorphic Geology 3, 327-342.

Robie, R.A., Hemingway, B.S., and Fischer, J.R. (1978) Thermodynamic Properties of Minerals and Related Substances at 298.15K and 1 Bar (105 Pascals) Pressure and at Higher Temperatures. U.S. Geological Survey Bulletin 1452, United States Government Printing Office, Washington, DC. 456 p. [Reprinted with corrections, 1979]

Robie, R. A. and Hemingway, B. S. (1995) Thermodynamic properties of minerals and related substances at 298.15K and 1 bar (10^5 pascals) pressure and at higher temperatures. U.S. Geological Survey, Reston, Virginia.

Robie, R.A. and Waldbaum, D.R. (1968) Thermodynamic Properties of Minerals and Related Substances at 298.15K (25.0°C) and One Atmosphere (1.013 Bars) Pressure and at Higher Temperatures. U.S. Geological Survey Bulletin 1259, United States Government Printing Office, Washington, DC. 256 p.

Schieltz, N. C., and M. R. Soliman (1964). Thermodynamics of the Various High Temperature Transformations of Kaolinite. Clays and Clay Minerals, 13, 419-428.

Schmidt, H., E. Hennings, and W. Voigt (2012). Magnesium chloride tetrahydrate, $MgCl_2$•$4H_2O$. Acta Crystallogr., Sect. C: Cryst. Struct. Commun., 68, i4−i6

Stull, D.R., and Prophet, H. (1971) JANAF Thermochemical Tables, Second Edition. United States Department of Commerce, National Bureau of Standards. NSRDS-NBS 37. United States Government Printing Office, Washington, DC. 1141 p.

Sverjensky, D.A., Harrison, B., and Azzolini, D. 2014. Water in the deep Earth: The dielectric constant and the solubilities of quartz and corundum to 60 kb and 1200C. Geochimica et Cosmochimica Acta 129, 125-145.

Sugimoto, K., R. E. Dinnebier and J. C. Hanson, (2007). Structures of Three Dehydration Products of Bischofite from In-Situ Synchrotron Powder Diffraction Data ($MgCl_2$•nH_2O; n = 1,2,4) . Acta Crystallogr., Sect. B: Struct. Sci., B63, 235−242.

Tagirov, B. and J. Schott, Aluminum speciation in crustal fluids revisited (2001). Geochimica et Cosmochimica Acta, 65(21), p. 3965-3992.

Tutolo, B.M., Kong, X.-Z., Seyfried, W.E., Jr., and Saar, M.O. 2014. Internal consistency in aqueous geochemical data revisited: Applications to the aluminum system. Geochimica et Cosmochimica Acta 133, 216-234.

Wagman, D.D., Evans, W.H., Parker, V.B., Halow, I, Bailey, S.M., and Schumm, R.H. 1968. Selected Values of Chemical Thermodynamic Properties. Tables for the First Thirty-Four Elements in the Standard Order of Arrangement. National Bureau of Standards Technical Note 270-3. United States Government Printing Office, Washington, DC. 264 p.

Wagman, D. D., W. H. Evans, V. B. Parker, R. H. Schumm, I. Halow, S. M. Bailey, K. L. Chrurney, and R. L. Nuttall (1982). The NBS Tables of Chemical Thermodynamic Properties: Selected Values for Inorganic and C-1 and C-2 Organic-Substances in SI Units. J. Phys. Chem. Ref. Data, 11 (Suppl. No. 2), 1−392.

Wang, Z. Z., H. Wang, and M. E. Cates (2001). Effective Elastic Properties of Solid Clays. Geophysics, 66, 428-440.

Walter, J.V., and Helgeson, H.C. (1977) Calculation of the thermodynamic properties of aqueous silica and the solubility of quartz and its polymorphs at high pressures and temperatures. American Journal of Science 277, 1315-1351.

Weck, P. F., E. Kim, C. F. Jové-Colón, and D. C. Sassani (2012). Structures of uranyl peroxide hydrates: a first-principles study of studtite and metastudtite. Dalton Transactions, 41(32), 9748–9752.

Wolery, T. J. and Sutton, M. (2013) Evaluation of Thermodynamic Data. Lawrence Livermore National Laboratory, Livermore, California.

Wu, X., M. C. Vargas, S. Nayak, V. Lotrich, and G. Scoles (2001). Towards extending the applicability of density functional theory to weakly bound systems. Journal of Chemical Physics, 115, 8748.

Yaws, C. L. Handbook of Thermodynamic Properties for Hydrocarbons and Chemicals. Knovel: New York, NY, 2009.

Zavarin, M., Benedicto, A., Kersting, A. B., and M. Sutton (2014), Thermodynamic Evaluations Progress Report M4FT-14LL0806039, Washington, D.C., U.S. Department of Energy, Office of Nuclear Energy, Used Fuel Disposition Campaign, 24 p.

ANL Mixed Potential Model for Used Fuel Degradation: Application to Argillite and Crystalline Rock Environments

(Part V)

1. Introduction and Objectives

The high-level objective for this work is to develop a used fuel degradation model that:

- Calculates the dissolution rate of used fuel based on the corrosion potential and redox reaction currents of electrochemical reactions (most importantly the anodic reaction releasing UO_2^{2+} into solution, which is the fuel dissolution rate) that are established at the fuel/solution interface.
- Produces surface area-scalable results that can be used to define a fractional fuel degradation rate for performance assessment models.
- Accounts for interfacial redox reaction kinetics, radiolytic oxidants (H_2O_2), and the catalytic behavior of the noble metal particles (NMP) present within the fuel.
- Accounts for the evolution of fuel burnup and the related temperature and dose histories of the exposed fuel.

The objectives specifically addressed in FY2014 are shown in the context of previous and future work in Figure 1. Briefly, MPM V.1 represents the implementation of the model developed in Canada with modifications to facilitate including additional processes affecting fuel dissolution. Specifically, MPM V.2 includes separate UO_2 and NMP phases to model catalytic effects, a more sophisticated radiolysis model, and a modified diffusion model that facilitates calculations over long times. Other planned modifications include adding a steel corrosion module to quantify hydrogen generation, modifying the catalytic efficiency of NMP to account for the effects of catalytic poisons in the groundwater (e.g., bromide) and corrosion, and evolving the reactive surface area of the corroding fuel. This report focuses on the progress made during FY 2014 in the following areas:

- Integrating the MPM with the Radiolysis Model (RM) developed at PNNL (e.g., Buck et al., 2013).
- Updating the MPM parameter database based on an ongoing literature review.
- Performing sensitivity runs with the updated MPM.
- Translating MPM (with RM subroutine) to Fortran 2003 to facilitate integration with performance assessment models.

A generalization of the envisioned relationships between the MPM and the generic performance assessment models for the argillite and crystalline rock disposal concepts is shown in Figure 2. Updates to the parameter database and the information exchange between the MPM and PA models summarized in Figure 2 are discussed in this report.

Part of the proposed scope of FY2015 will be to begin the process of actually integrating the MPM into the generic performance assessment models for argillite and crystalline repositories. Specifically the MPM will be used to calculate the dissolution rate or fractional degradation rate of used fuel to provide source terms for radionuclides released from a breached waste package. Work to extend the MPM to include the chemical and redox effects of canister corrosion (primarily the hydrogen source term in the waste package) will be coordinated with container breaching models being developed in other UFD activities. The extensive parameter database used by the MPM V2 (presented below) makes it applicable to a wide range of geochemical settings (e.g., Tables 1 and 2); however, more experimental data are required to reduce uncertainties in key functionalities such as the pH and temperature dependencies of rate constants.

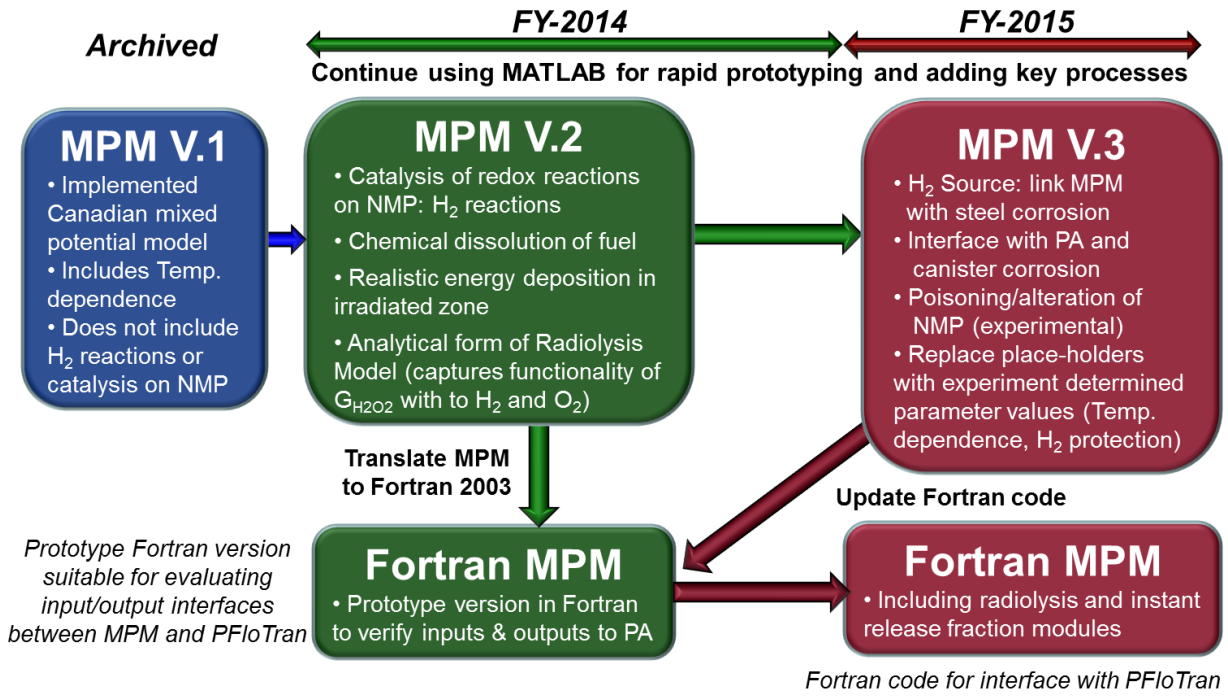

Figure 1. Schematic flow diagram highlighting progress made in the development of the MPM and future priorities based on sensitivity results from MPM V.2.

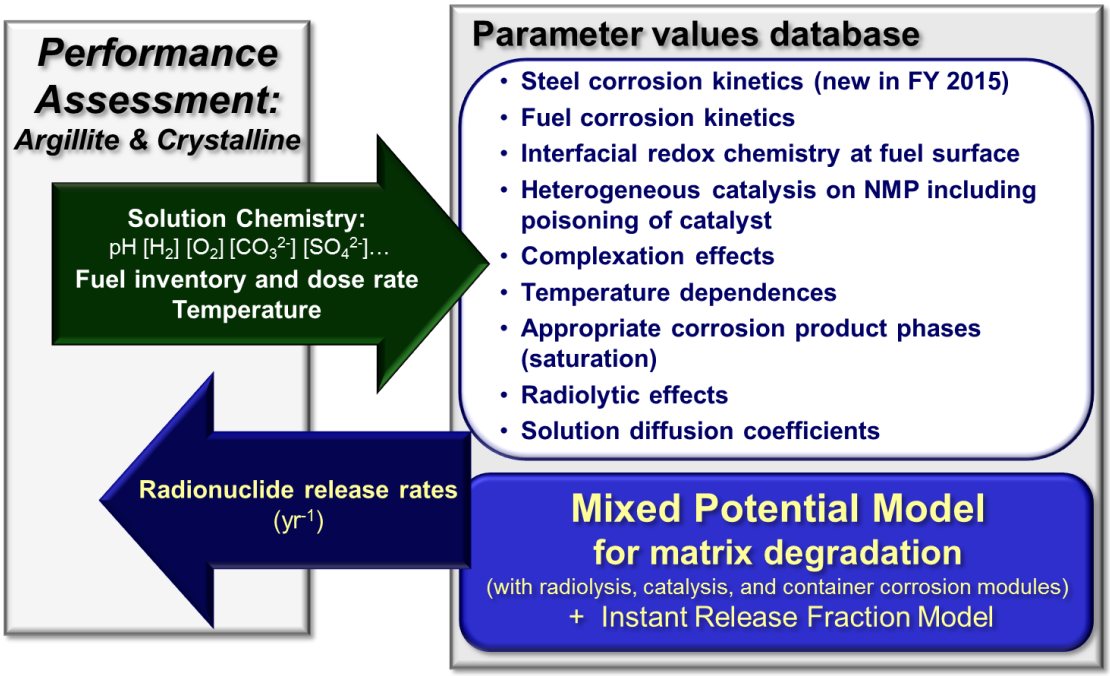

Figure 2. Schematic flow diagram showing relationships between the MPM and the generic performance assessment models.

1.1 Summary of Argillite and Crystalline Rock Repository Concepts

Clayrock/shale (here synonymous with argillite) bedrock formations are recognized as promising repository host rocks. For example, Callovo-Oxfordian formations at Bure France, the Boom Clay at Mol Belgium, the Boda formations at Mecsek Hungary, the Opalinus Clay at Mont Terri Switzerland, the Oxford Clay in the UK and the Queenston formation in Canada (list from Gaucher et al., 2009). Due to their low permeability, it is difficult to extract undisturbed water samples from clayrock formations; therefore, modeling techniques base on equilibrium with dominant mineral assemblages have been developed (e.g., Gaucher et al., 2009).

Table 1 shows a typical modeled clayrock/shale pore water composition and a measured pore water composition from The Callovo-Oxfordian in France (Vinsot et al., 2008).

Table 1. Measured and modeled pore water compositions from a clayrock or argillite formation. The model assumes that the water is in equilibrium with the mineral assemblage illite-calcite-dolomite-iron chlorite-quartz-pyrite–celestite. The measured composition is from the Callovo-Oxfordian formations in France.

	Model (Gaucher et al., 2009)	Measured (Vinsot et al., 2008)
pH	7.1	7.2
Eh_{SHE} (mV)	-163	-199
	(moles/kg)	(moles/kg)
Inorganic C	2.19E-3	4.2E-3
Cl	3.01E-2	4.1E-2
S	3.39E-2	1.9E-2
Na	3.21E-2	5.6E-2
K	7.09E-3	9.0E-4
Ca	1.49E-2	7.6E-3
Mg	1.41E-2	5.9E-3
Sr	1.12E-3	2.5E-4
Si	9.41E-5	1.4E-4
Al	7.39E-9	----
Fe	2.14E-4	1.5E-5

These values can be used to place the MPM V2 model runs within the contexts of the geologic environments in question. Crystalline shield sites that have been identified as promising as repository settings include rock units in Canada, Finland and Sweden. Examples of crystalline rock groundwater chemistries are shown in Table 2.

Table 2. Modeled and measured pore water compositions from crystalline rock units (compiled by Guimera et al., 2006). The model is for a fracture hosted groundwater after 5,000 years of a deglaciation period at repository depth (for discussion see Guimerà et al., 2006).

Components	Forsmark groundwater	Grimsel groundwater	5,000 year old Forsmark water (modeled)
pH	7.0	9.6	9.8
Eh_{SHE} (mV)	-143	-200	-240
	(moles/L)	(moles/L)	(moles/L)
HCO_3^-	1.77E-3	4.50E-4	9.28E-5
Cl	1.53E-1	1.60E-4	4.04E-4
S	6.80E-3	6.10E-5	----
Na	8.88E-2	6.90E-4	6.90E-4
K	8.75E-5	5.00E-6	3.18E-4
Ca	2.33E-2	1.40E-4	2.17E-4
Mg	9.30E-3	6.20E-7	6.20E-7
Si	1.85E-4	2.50E-4	5.60E-4
Br	2.98E-4	3.80E-7	3.80E-7
Fe	3.31E-5	3.00E-9	2.91E-7

As will be discussed below, the chemical properties of the groundwater examples shown in Tables 1 and 2 that will influence the MPM fuel dissolution rate calculations are the pH, Eh, dissolved carbonate and dissolved iron. Chloride and bromide are also important species because they are radiolytically active. It is expected that future versions of the MPM will account for radiolytically active halides after planned experiments to quantify their effects on the fuel dissolution rate.

The MPM V2 sensitivity runs discussed in Section 3 below account for the full ranges of groundwater compositions expected from different argillaceous and crystalline repository environments.

1.2 Mixed Potential Model Process Overview

As shown in Figure 1, the Argonne MPM was developed based on the Canadian-mixed potential model for UO_2 fuel dissolution of King and Kolar, 2003 and was implemented using the numerical computing environment and programming language MATLAB (Jerden et al., 2013). The MPM is a 1-dimensional reaction-diffusion model that accounts for the following processes:

- Rate of oxidative dissolution of the fuel matrix U(VI) as determined by interfacial redox reaction kinetics (quantified as a function of the corrosion potential) occurring at the multiphase fuel surface (phases include UO_2 and the noble metal fission product alloy phase (NMP), often referred to as the epsilon phase).
- Chemical (solubility-based) dissolution of the fuel matrix U(IV).
- Complexation of dissolved uranium by carbonate near the fuel surface and in the bulk solution.
- Production of hydrogen peroxide (which is the dominant fuel oxidant in anoxic repository environments) by alpha-radiolysis.
- Diffusion of reactants and products in the groundwater towards and away from the reacting fuel surface.
- Precipitation and dissolution of a U–bearing corrosion product layer on the fuel surface.
- Diffusion of reactants and products through the porous and tortuous corrosion product layer covering the reacting fuel surface.
- Arrhenius-type temperature dependence for all interfacial and bulk reactions.

In the MPM, the fuel degradation rate is calculated using mixed potential theory to account for all relevant redox reactions at the fuel surface, including those involving oxidants produced by solution radiolysis. Because the MPM is based on fundamental chemical and electrochemical principles, it is flexible enough to be applied to the full range of repository environments and conditions.

Of particular interest is the surface chemical properties of the NMP, which have been shown to catalyze redox reactions at the fuel/solution interface (e.g., Broczkowski et al., 2005, Shoesmith, 2008, Trummer, et al., 2009, Cui et al., 2010). These studies show that the degradation rate of the used fuel may be dramatically affected if dissolved hydrogen is present. Therefore, this process was incorporated into the MPM V2 using user-input hydrogen concentrations (Jerden et al., 2013).

In FY2014, the MPM V2 with the catalytic NMP domain was run for a number of conditions to determine the relative effects of key variables such as temperature, dose rate, and solution chemistry. As discussed below, the most important process in terms of fuel dissolution rate is the reaction of hydrogen at the NMP domains. The main source of hydrogen in the repository near field and waste package will be as a by-product of the anoxic corrosion of steel. This process and its relationships to the MPM calculated used fuel degradation rate are shown in Figure 3. Figure 3a illustrates the abundance of steel surrounding the fuel in a generic waste package. Figure 3b shows the chemical and redox couples between the fuel dissolution (i.e., the reaction releasing UO_2^{2+} into the solution between corroding steel and the fuel). The reaction releasing UO_2^{2+} into solution is the key reaction modeled by the MPM and is defined as the fuel dissolution rate

$$UO_2 + H_2O_2 = UO_2^{2+} + 2\ OH^- . \quad (1)$$

The MPM is designed to quantify the effects of other reactions and processes on the kinetics of that reaction through chemical and electrochemical couples. The diagram in Figure 3c shows the

catalyzed oxidation of hydrogen on the NMP surface and the transfer of electrons from NMP sites to the fuel matrix are coupled chemically through the dissolved hydrogen concentration. The electrical coupling between NMP and fuel grains establishes a galvanic link that effectively protects the fuel from oxidative dissolution by mitigating the reaction in Equation 1. The poisoning of NMP shown on the right side represents catalytic deactivation due to the formation of surface coatings and corrosion. The kinetics of the steel oxidation to release H_2 and the effects of poisoning of NMP remain to be included in the MPM; this is planned for FY 2015.

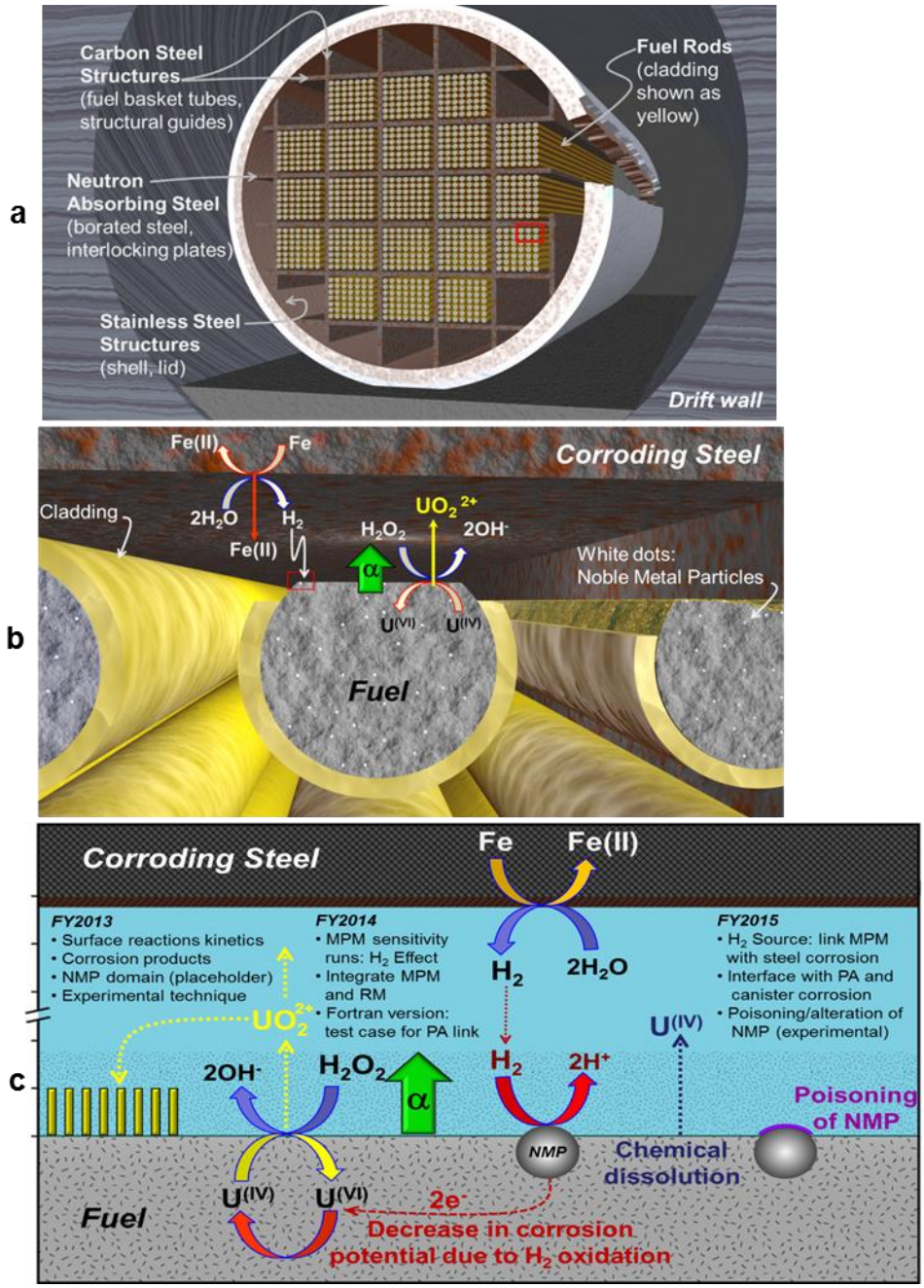

Figure 3. Conceptual diagrams of a used fuel waste package (a), exposed fuel (b), and a summary of the key interfacial processes that determine the overall degradation rate highlighting when each process was/will be incorporated into the MPM (c).

2. Updated MPM Parameter Database for Argillite and Crystalline Repository Environments

Tables 3 – 7 show the MPM parameter database that has been updated based on recent literature and used in sensitivity runs discussed in below. Although there remain quite a few estimated values that require experimental evaluation to quantify model uncertainties, the sensitivity runs yield important information about the relative (order of magnitude) effects that different variables have on the predicted fuel dissolution rate. The results can be used to prioritize which parameters are experimentally verified.

The extensiveness of the MPM parameter database makes it possible to use the model to calculate used fuel dissolution rates over a wide range of geochemical and electrochemical conditions. For example, the model accounts for the range of temperature, pH and carbonate concentrations anticipated in both argillite and crystalline rock repositories (e.g., Tables 1 and 2).

Table 3. Parameter and variable inputs used for in sensitivity runs with MPM V2.

Variables set by user (these will ultimately be inputs from other PA models)	**Range of values used in Sensitivity runs**	**Notes**
Temperature	25 ^{o}C to 200 ^{o}C	The evolution of the waste form temperature will be the output of other models accounting for burnup, fuel age, repository design, etc.
Dose rate	1 – 500 rad/s	Dose evolution will also be the output of other models accounting for fuel burnup and age.
Environmental concentration of dissolved oxygen	Zero to millimolar	This key variable will be determined by a number of interdependent kinetic processes within the waste package and near-field, but the dominant buffer may be the geologic environment: Argillite vs. Crystalline Rock.
Environmental concentration of dissolved carbonate	Zero to millimolar	This is a key variable determined by specifics of the geologic environment: Argillite vs. Crystalline Rock.
Environmental concentration of dissolved ferrous iron	Zero to millimolar	This key variable will be determined by a number of interdependent kinetic processes within the waste package and near-field, but the dominant source will be corroding steel components.
Environmental concentration of dissolved hydrogen	Zero to millimolar	This key variable (the most important for the present work) will also be determined by a number of interdependent kinetic processes within the waste package and near-field, but the dominant source will be anoxic corrosion of steel components.

pH	4 to 9.5	The effect of pH is incorporated into the MPM V2 by modifying the rate constants for fuel dissolution (Table 4) based on the experimental results of Torrero et al., 1997 which yield: r (mol/m^2s) = 3.5E-8[H^+]$^{0.37}$ for pH 3.0 to 6.7 and r (mol/m^2s) = 3.5E-8ror pH values greater than 6.7. *Note*: groundwaters in Argillite and Crystalline environments are anticipated to have pH > 6.7 (e.g., Tables 1 and 2).
Space and Time Parameters		
Length of diffusion grid in model	3 mm	Arbitrary, can be changed by user to represent system of interest.
Number of calculation nodes (points) in diffusion grid	200	Arbitrary, can be changed by user to optimize calculation efficiency.
Duration of simulation	100,000 years	Arbitrary, can be changed by user to represent duration of interest.
Radiolysis Parameters		
Alpha-particle penetration depth	35 micrometers	The basis for this value was re-examined in FY 2014, but remains unchanged (confirmed).See section 2.1 for discussion.
Generation value for H_2O_2	Calculated by new Radiolysis Model subroutine	In MPM V2, this value varies depending on the dose rate and dissolved concentrations of O_2 and H_2 within the irradiation zone (see Section 2.2 below)
Physical Interfacial Parameters		
Surface coverage of NMP	Zero to 1%	Based on qualitative examination of photomicrographs of spent fuels of different burnups e.g., Tsai, 2003.
Resistance between UO_2 and NMP domains	Constant 1.0E-3 V/Amp	Assumed that fuel and NMP are electrically well-coupled
Porosity of schoepite corrosion layer	50%	Reasonable assumption based on qualitative assessment of photomicrographs of schoepite layers e.g., Finch and Ewing, 1992.
Tortuosity factor of schoepite corrosion layer	0.1	Reasonable assumption based on analogy of schoepite layer with compacted clay (King and Kolar, 2003)

Table 4. Rate constants for all relevant reactions and their associated activation energies used in MPM V2. The far right column provides notes on recent updates based on our on-going literature survey.

Reaction	**Rate Constant** (mol/m^2 s)	**Activation energy** (J/mole)	**Updates based on literature review**
Fuel Dissolution Reaction			
$UO_2^{fuel} \rightarrow UO_2^{2+} + 2e^-$	5.00E-08	6.00E+04	Zeroth-order electrochemical rate constant for the irreversible oxidation of UO_2 from King and Kolar, 2003.
$UO_2^{fuel} + 2CO_3^{2-} \rightarrow UO_2(CO_3)_2^{2-} + 2e^-$	1.30E-08	6.00E+04	Electrochemical rate constant for the irreversible oxidation of UO_2 in carbonate solution from King and Kolar, 2003. (the reaction order with respect to carbonate is m = 0.66).
$UO_2^{fuel} \rightarrow UO_2(aq)$	8.60E-12	6.00E+04	Based on solubility of UO_2 in reducing conditions. Calculated using GWB and YMP data0 R5 thermodynamic database.
Reactions at Fuel Surface	(m/s)	(J/mole)	
$H_2O_2 \rightarrow O_2 + 2H^+ + 2e^-$	7.40E-08	6.00E+04	1^{st}-order electrochemical rate constant for irreversible oxidation of H_2O_2 on UO_2 estimated based on assumption that, at a potential of 0.08 VSCE, the oxidation and reduction rates of H_2O_2 on UO_2 are equal and that the Tafel slopes are identical: from King and Kolar, 2003.
$H_2O_2 + 2e^- \rightarrow 2OH^-$	1.20E-12	6.00E+04	1^{st}-order electrochemical rate constant for irreversible reduction of H_2O_2 on UO_2: from King and Kolar, 2003.
$O_2 + 2H_2O + 4e^- \rightarrow 4OH^-$	1.40E-12	6.00E+04	1^{st}-order electrochemical rate constant for irreversible reduction of O_2 on UO_2: from King and Kolar, 2003.
Reaction at NMP surface	(m/s)	(J/mole)	
$H_2O_2 \rightarrow O_2 + 2H^+ + 2e^-$	7.40E-07	6.00E+04	1^{st}-order electrochemical rate constant for irreversible oxidation of H_2O_2 on NMP catalyst, assumed to be one order of magnitude faster than on oxide - needs experimental evaluation.

$H_2O_2 + 2e^- \rightarrow 2OH^-$	1.20E-11	6.00E+04	1st-order electrochemical rate constant for irreversible reduction of H_2O_2 on NMP catalyst: assumed to be one order of magnitude faster than on oxide - needs experimental evaluation.
$O_2 + 2H_2O + 4e^- \rightarrow 4OH^-$	1.40E-11	6.00E+04	1st-order electrochemical rate constant for irreversible reduction of O_2 on NMP catalyst: assumed to be one order of magnitude faster than on oxide - needs experimental evaluation.
$H_2 \rightarrow 2H^+ + 2e^-$	5.00E-04	6.00E+04	1st-order electrochemical rate constant for irreversible oxidation of H_2 on NMP catalyst: based on data for Pt-Ru catalyst (Uchida et al., 2009) - needs experimental evaluation.
Corrosion Layer Reactions	(/s)	(J/mole)	
$UO_2^{2+} + 2H_2O \rightarrow UO_3{:}2H_2O + 2H$	1.00E-03	6.00E+04	Estimate based on residence time of UO_2^{2+} in supersaturated solution - needs experimental/literature evaluation. Rate law from King and Kolar, 2003: $1.0E\text{-}3*\exp(6.0E4*dT)/(2.4*[UO_2^{2+}]_{saturation})^4$.
$UO_2(CO_3)_2^{2-} + 2H_2O \rightarrow UO_3{:}H_2O + 2CO_3^{2-} + 2H^+$	1.00E-04	6.00E+04	Estimate based on residence time of UO_2^{2+} in supersaturated solution containing carbonate - needs experimental/literature evaluation. Rate law from King and Kolar, 2003: $1.0E\text{-}4*\exp(6.0E4*dT)/(2.4*[UO_2(CO_3)_2^{2-}]_{saturation})^4$.
$UO_3{:}H_2O + 2CO_3^{2-} + 2H^+ \rightarrow UO_2(CO_3)_2^{2-} + 2H_2O$	6.30E-12	6.00E+04	Based on data for dissolution of soddyite in carbonate solution: from King et al., 2001.
Key Bulk Reactions	(/s)	(J/mole)	
$H_2O_2 \rightarrow H_2O + 0.5O_2$	4.50E-07	6.00E+04	Personal communication with Rick Wittman of PNNL on 3/12/2014, the overall reaction rate constant comes from runs using the PNNL Radiolysis model which uses rate constants from Pastina and Laverne, 2001.
	(m/mol s)	(J/mole)	
$O_2 + 4Fe^{2+} + 8OH^- \rightarrow 4H_2O + 2Fe_2O_3$	5.90E-01	6.00E+04	Rate is highly pH dependent below 8.0. Derived from experimental data at pH = 8.7 by King and Kolar, 2003.
$H_2O_2 + 2Fe^{2+} + 4OH^- \rightarrow 3H_2O + Fe_2O_3$	6.90E-01	4.20E+04	From King and Kolar, 2003, notes that pH dependence unknown - needs experimental evaluation.

$UO_2^{2+} + 2Fe^{2+} + 6OH^- \rightarrow UO_2 + 3H_2O + Fe_2O_3$	1.00E-02	6.00E+04	Assumed value based on similar redox reactions, from King and Kolar, 2003.
$UO_2(CO_3)_2^{2-} + 2Fe^{2+} + 6OH^- \rightarrow UO_2 + 2CO_3^{2-} + 3H_2O + Fe_2O_3$	1.00E-03	6.00E+04	Assumed value based on similar redox reactions, from From King and Kolar, 2003.

Table 5. Electrochemical parameters for all relevant reactions and their associated temperature dependence used in MPM V2. The far right column provides notes on recent updates based on our on-going literature survey.

Reactions	**Charge Transfer Coefficient**	**Standard Potential ($Volts_{SCE}$)**	**Temperature Dependence ($Volts_{SCE}/K$)**	**Updates based on literature review**
Fuel Dissolution				
$UO_2^{fuel} \rightarrow UO_2^{2+} + 2e^-$	9.60E-01	0.169	-2.48E-04	From King and Kolar, 2003
$UO_2^{fuel} + 2CO_3^{2-} \rightarrow UO_2(CO_3)_2^{2-} + 2e^-$	8.20E-01	-0.173	2.10E-03	From King and Kolar, 2003
Reactions at Fuel Surface				
$H_2O_2 \rightarrow O_2 + 2H^+ + 2e^-$	4.10E-01	-0.121	-9.93E-04	From King and Kolar, 2003
$H_2O_2 + 2e^- \rightarrow 2OH^-$	4.10E-01	-0.973	-6.98E-04	From King and Kolar, 2003
$O_2 + 2H_2O + 4e^- \rightarrow 4OH^-$	5.00E-01	-0.426	-1.23E-04	From King and Kolar, 2003
Reaction at NMP surface				
$H_2O_2 \rightarrow O_2 + 2H^+ + 2e^-$	4.10E-01	-0.121	-9.93E-04	Assumed to be equal to values on UO_2 surface - needs experimental evaluation.
$H_2O_2 + 2e^- \rightarrow 2OH^-$	4.10E-01	-0.973	-6.98E-04	Assumed to be equal to values on UO_2 surface - needs experimental evaluation.
$O_2 + 2H_2O + 4e^- \rightarrow 4OH^-$	5.00E-01	-0.426	-1.23E-04	Assumed to be equal to values on UO_2 surface - needs experimental evaluation.
$H_2 \rightarrow 2H^+ + 2e^-$	1	-0.421	0	Standard potential from Lide, R.D. (Ed.), 1999. Handbook of Chemistry and Physics, 80th ed. Charge transfer coefficient and temperature dependence need experimental evaluation.

Table 6. Diffusion coefficients and associated temperature dependence used in MPM V2. The far right column provides notes on recent updates based on our on-going literature survey.

Species	**Diffusion coefficient** (cm^2/s)	**Activation energy** (J/mole)	**Updates based on literature review**
UO_2^{2+}	7.66E-10	1.50E+04	Changed from 5.0E-10 (estimate King et al., 2001) based on Kerisit and Liu, 2010.
$UO_2(CO_3)_2^{2-}$	6.67E-10	1.50E+04	Changed from 5.0E-10 (estimate King et al., 2001) based on Kerisit and Liu, 2010.
$U(IV)O_2(aq)$	5.52E-10	1.50E+04	Assumed to be neutral species and set equal to neutral $UO_2CO_3(aq)$ from Kerisit and Liu, 2010.
CO_3^{2-}	8.12E-10	1.50E+04	Changed from 5.0E-10 (estimate King et al., 2001) based on Kerisit and Liu, 2010.
O_2	1.70E-09	1.50E+04	No change: from From King and Kolar, 2003.
H_2O_2	1.70E-09	1.50E+04	No change: from From King and Kolar, 2003.
Fe^{2+}	7.19E-10	1.50E+04	Added from Lide, R.D. (Ed.), 1999. Handbook of Chemistry and Physics, 80th ed.
H_2	5.00E-09	1.50E+04	Added from Macpherson and Unwin, 1997.

Table 7. Saturation concentrations and associated temperature dependence used in MPM V2. The far right column provides notes on recent updates based on our on-going literature survey.

Species	**Saturation Concentration** ($mole/m^3$)	**Activation energy** (J/mole)	**Updates based on literature review**
UO_2^{2+}	3.00E-02	-6.00E+04	Changed from 3.2E-2 $mole/m^3$ based on GWB runs using YMP data0 R5 equilibrium constant database. The negative activation energy reflects the observations of Murphy and Codell (1999) that common uranyl minerals exhibit retrograde solubility.
$UO_2(CO_3)_2^{2-}$	9.00E-02	-6.00E+04	Changed from $5.12(mol/cm^3)^{0.34}$ $mole/m^3$ based on GWB runs using YMP data0 R5 equilibrium constant database. The negative activation energy reflects the observations of Murphy and Codell (1999) that common uranyl minerals exhibit retrograde solubility
Fe^{++}	5.00E-02	6.00E+04	Changed from 3.2E-2 $mole/m^3$ based on GWB runs using YMP data0 R5 equilibrium constant database.

2.1 Alpha Particle Penetration Depth and Dose Rate Profile Used in MPM V2.

In the MPM, the primary oxidant driving the oxidative dissolution of the fuel is H_2O_2 formed by radiolysis and the width of the irradiated zone in which H_2O_2 is produced is of fundamental importance. (This was shown conceptually as the length of the green arrow labeled α in Figure 3c). Thus far, the Argonne MPM has used the value of 35 micrometers from the fuel surface as the width of the irradiated zone (also referred to as the alpha particle penetration depth), which is the value used in the Canadian mixed potential model of King and Kolar 2003. The basis for this value and its applicability was reexamined because the Canadian work assumed only CANDU fuel assemblies.

The width of the alpha penetration depth is determined by the energy of the alpha particles emitted from the fuel surface. The 2013 version of the well-established and validated code "The Stopping and Range of Ions in Matter" (SRIM, 2013) was used to determine the relationship between alpha particle energy and penetration depth in water (Figure 4). The results show that the alpha penetration depth can vary from between 35 μm for and alpha energy of around 5 MeV up to 55 μm for and alpha energy of 6.5 MeV. 5 – 6.5 MeV is the reasonable range of alpha energies emitted from used fuel.

Based on the used fuel energy spectra shown in Radulescu (2011), a reasonable argument can be made for using an energy value of 5 MeV for used fuel alpha particles. Furthermore, Radulescu (2011) show that the alpha energy spectra does not change dramatically with time; therefore it is also reasonable to use a constant alpha penetration depth of 35 μm throughout the duration of MPM simulations.

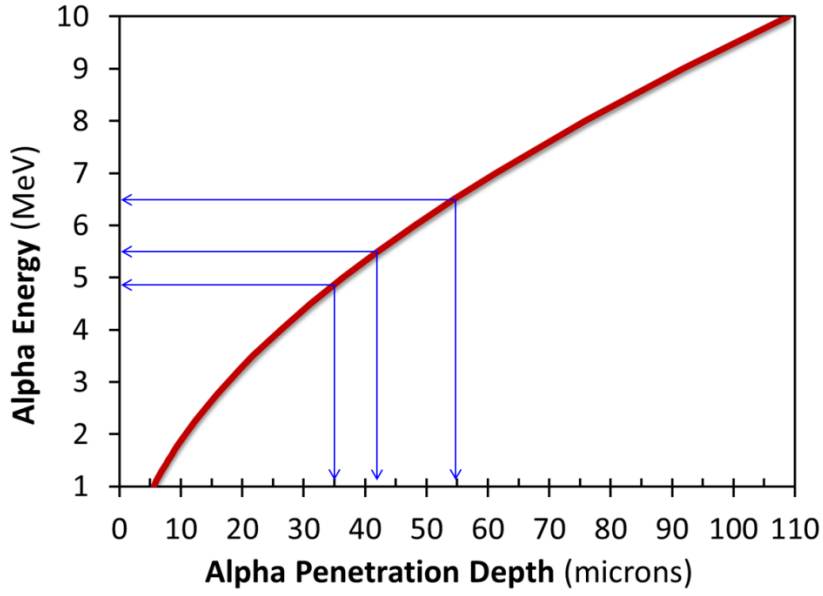

Figure 4. Alpha particle penetration depths vs. the alpha particle energy based on the stopping power of water, calculated using SRIM, 2013.

Another key physical quantity that determines the amount of radiolytic oxidants, and thus the local solution oxidative potential, is the dose rate within the alpha penetration zone. The earlier version of the MPM used a constant dose rate (step-function) across the entire 35 μm alpha irradiation zone. This assumption was conservative (produced the maximum amount of radiolytic oxidants) but was also physically unrealistic. This step function has been replaced in MPM V2 with an exponentially decreasing alpha dose rate within the alpha penetration zone (Figure 5). The analytical function shown the curve in Figure 5 was fit to the dependence measured by Nielsen and Jonsson, 2006 (blue circles).

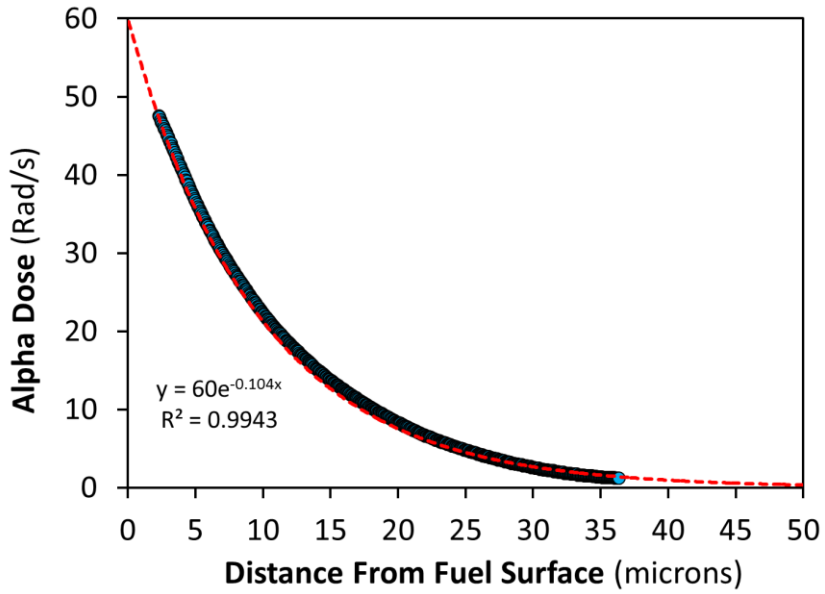

Figure 5. Alpha dose rate profile used in the MPM V2 (red line, $Y=60e^{-0.104x}$), which is a fit to the data points of Nielsen and Jonsson, 2006.

2.2 Incorporation of Radiolysis Model Analytical Function into MPM V2.

In January 2014, Rick Wittman and Edgar Buck of PNNL produced a straight forward analytical function that captures the functional dependence of the effective or conditional generation value of H_2O_2 (G_{H2O2}) on the local dissolved concentrations of H_2 and O_2. A description of the PNNL Radiolysis Model and the quantitative definition of the conditional G_{H2O2} can be found in Buck et al, 2013 and a forthcoming FY2014 PNNL report.

The function provided by PNNL was converted from Fortran to MATLAB and incorporated as a subroutine into the MPM V2 (Appendix D). The radiolysis model function essentially replaces the constant G_{H2O2} value that had been used in MPM V1. The following relationship describes the basic equation for H_2O_2 production as a function of space and time used in MPM V2:

Molar yield of H_2O_2 (x,t) = $[G_{H2O2}](H_2,O_2)$ * [Dose Rate](x,t) * g(x)

The amount of H_2O_2 produced is determined as the product of G_{H2O2}, which is a function of local solution chemistry (radiolysis model subroutine), the dose rate, which varies in both time (as fuel decays) and space (see Figure 5), and a geometrical factor g(x). The geometrical factor accounts for how the diffusion of aqueous species is modified by the tortuosity of the uranyl corrosion layer (schoepite). The subroutine written in MATLAB code is shown in Appendix D.

The topology of the radiolysis model function that determines G_{H2O2} in the MPM V2 is shown in Figure 6. The striking feature of this function is the precipitous decrease in the value of G_{H2O2} from around 1.0 (the value used in the previous MPM version) down to less than 0.1 for conditions of low dissolved O_2 and moderate to high concentrations of H_2. This feature is strongly dependent on the dose rate, as shown in the plots at the bottom Figure 6. The impact this G_{H2O2} "cliff" on the dissolution rate of used fuel calculated by the MPM V2 has been explored as part of the sensitivity runs (discussed in Section 3.0 below).

Sensitivity runs show that even at a low starting $[O_2]$ = 1.0E-9 moles/L, the dissolved concentration of O_2 rarely drops below 1.0E-7 moles/L. This is due to the production of O_2 as H_2O_2 decomposes at the fuel surface by the reaction $H_2O_2 \rightarrow O_2 + 2H^+ + 2e^-$.

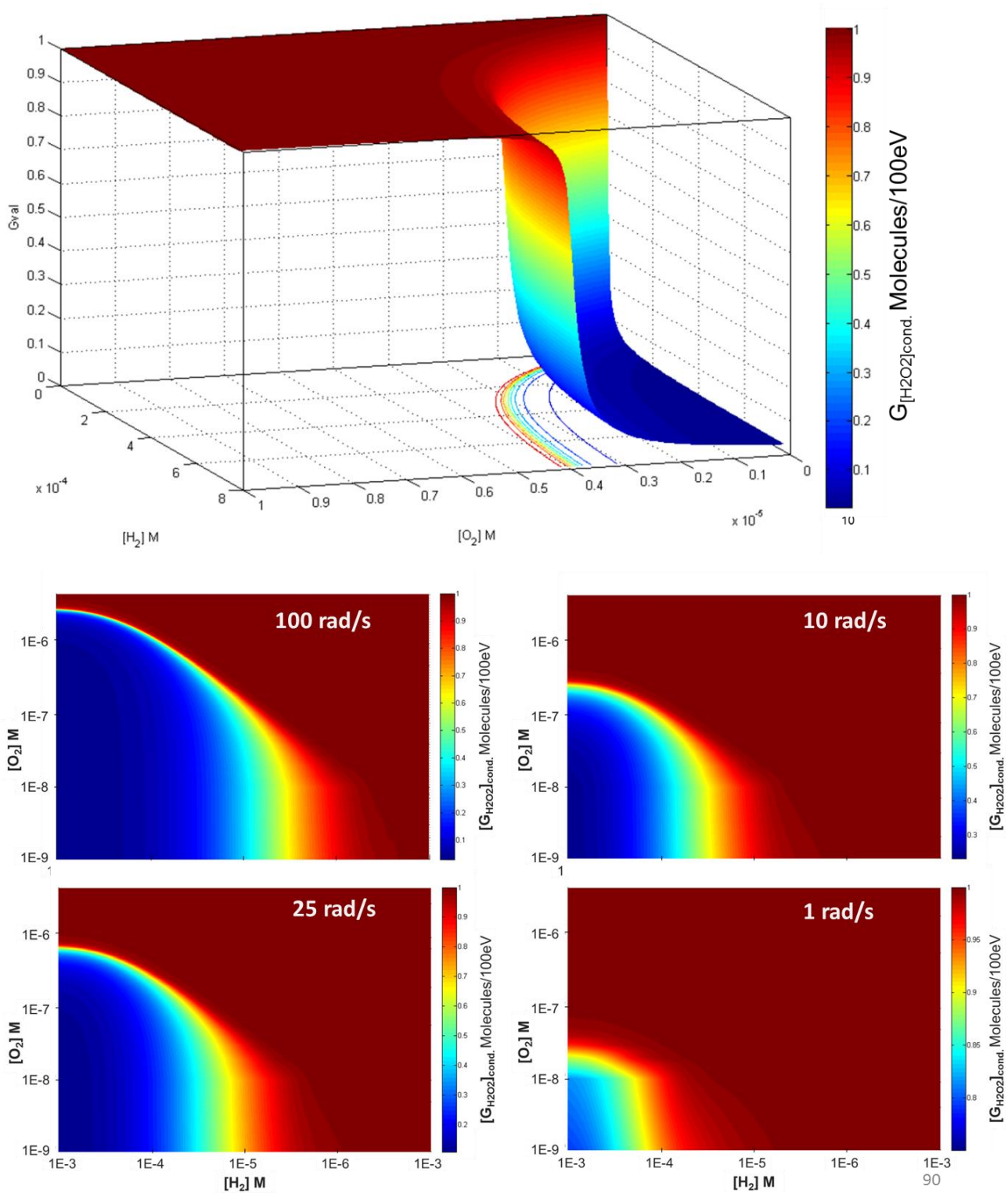

Figure 6. Topology of the analytical function that comprises the Radiolysis Model subroutine within the MPM V2.

3. Sensitivity Results Mixed Potential Model V2.

For anoxic to low oxygen conditions (nano- to micromolar), the fuel dissolution rate predicted by the MPM V2 will depend directly on the concentration of H_2O_2 at the fuel surface. A number of competing processes determine this concentration:

- H_2O_2 is continuously produced within the first 35 μm of the fuel surface. The H_2O_2 concentration depends on dose rate and the generation value G_{H2O2}, which is determined by the Radiolysis Model subroutine based on local $[O_2]$ and $[H_2]$ for a given dose rate.
- H_2O_2 diffuses towards or away from the fuel surface depending on the concentration; the diffusion rates near the surface will be moderated by the corrosion layer.
- H_2O_2 concentration at environmental boundary (3 mm from fuel) is defined to be zero.
- H_2O_2 is consumed (dominantly) at the fuel surface by the following coupled half-reactions:

$$H_2O_2 + 2e^- \rightarrow 2OH^- \qquad (2)$$

$$UO_2 \rightarrow UO_2^{2+} + 2e^- \qquad (3)$$

- H_2O_2 consumption rate at the fuel surface increases significantly when the NMP-catalyzed hydrogen oxidation reaction is taken into account and $[H_2] \geq$ 1.0E-5 mole/L (Figure 8):

The increase in the rate of H_2O_2 consumption at the fuel surface when NMP-catalyzed hydrogen oxidation is occurring is caused by the kinetic balance of reactions 1, 2 and 3:

$$H_2 + 2OH^- \rightarrow 2H_2O + 2e^- \qquad (4)$$

Specifically, the large anodic current associated with the hydrogen oxidation reactions increases the rate of the dominant cathodic reaction involving hydrogen peroxide reduction. This process is shown schematically in Figure 3c. Therefore, hydrogen peroxide is rapidly depleted when enough hydrogen is present at a fuel surface bearing active NMP sites, thereby decreasing the rate of oxidative dissolution (Equation 1). The relative importance of these processes and other chemical and physical effects on the fuel dissolution rate were studied through a series of model sensitivity runs.

Approximately 300 model runs were performed with MPM V2 to determine the relative impacts that different processes, variables and parameters have on the used fuel dissolution rate calculated by the code. Each model run produces an output file consisting of a 100x2000 cell matrix that includes corrosion potentials, reaction current densities, component fluxes, and

concentrations of all components at every point in time at every point in space for the specified conditions. These results have been tabulated and key trends identified.

The detailed model output files are important for understanding interactions between the radiolytic, chemical and physical processes included in the code; however, our ultimate interest (what will be provided to the performance assessment model) is the dissolution rate. Therefore, the output of the MPM V2 sensitivity runs has been synthesized and is represented here in terms of grams of fuel dissolved per surface area per time (Figure 7).

Figure 7 does not explicitly show the time evolution of the variables; however, the direction of the dose rate and temperature arrows are used to indicate that these variables will be decreasing with time as the fuel decays. The pH and temperature effects on the fuel dissolution rate are of about the same magnitude and are indicated by the same arrow.

It is important to note that there are still relatively large uncertainties in the quantification of how the temperature and pH will affect the fuel dissolution rate. For example, the temperature dependence of most reactions in the parameter database (specifically Table 4) is quantified using a reasonable (based on geochemical literature) place holder value of 60,000 J/mole for the activation energy. This, as well as terms accounting for pH dependence and complexation, need to be evaluated experimentally to reduce uncertainties.

Consistent with the experimental literature, the model indicates that decreasing dose rates and temperature decrease the rate of fuel dissolution by almost two orders of magnitude. The main chemical effects included in the model are due to pH and dissolved carbonate, which complexes uranium to increase its dissolved concentration limit. As acidity and carbonate concentrations increase, the fuel dissolution rate increases. The light blue arrows show that fuel dissolution rate decreases with decreasing G_{H2O2} values (due to increasing $[H_2]$ and decreasing $[O_2]$), increasing schoepite corrosion layer thickness, and increasing concentrations of ferrous iron.

All of these effects, however, are minor relative to the fuel-protecting process that involves the oxidation of H_2 at the fuel surface (dark blue arrow in Figure 7). As shown in Figure 3, H_2 is included in the MPM V2 in a catalytic reaction occurring on the NMP surfaces. The amount of hydrogen reacted depends on its concentration and the surface area of the NMP. For the sensitivity runs summarized in Figure 7, a surface coverage of 1% NMP on the fuel surface was used to quantify the H_2 effect for various H_2 concentrations. Results show that presence of 100 bar H_2, which may be expected in repositories at 500 meters depth with steel waste package materials, can essentially shut off the oxidative dissolution of the fuel (SKB, 2011). Radiolytic production of H_2 is sufficient to cause a small decrease in the fuel dissolution rate on the same order as the effects of G_{H2O2} and surface layers, but the anodic corrosion of steel can have a much greater effect.

Figure 8 shows plots from the MPM V2 sensitivity runs that quantify the H_2 effect at two dose rates. The identical shapes indicate that it is the decrease in the fuel corrosion potential caused by the coupling of the H_2 oxidation to the U(IV)/U(VI) couple that is responsible for the dramatic decrease in the fuel dissolution rate with increasing H_2 concentrations (through the reactions shown conceptually in Figure 3). The dissolution rates calculated for H_2 generated from radiolysis and by steel corrosion (values of 1 bar and 10 bars provided to show sensitivity) are indicated in Figure 8a. Figure 8b shows the corrosion potentials from the electrochemical experiments of Broczkowski et al, 2005 for SIMFUELs made with and without added NMP. Those results suggest that the presence of NMP at the fuel surface is largely responsible for the

observed H_2 effect, although the effect does occur to a lesser extent in the absence of NMP. An experimental approach has been designed at ANL to quantify that effect in a future version of the MPM.

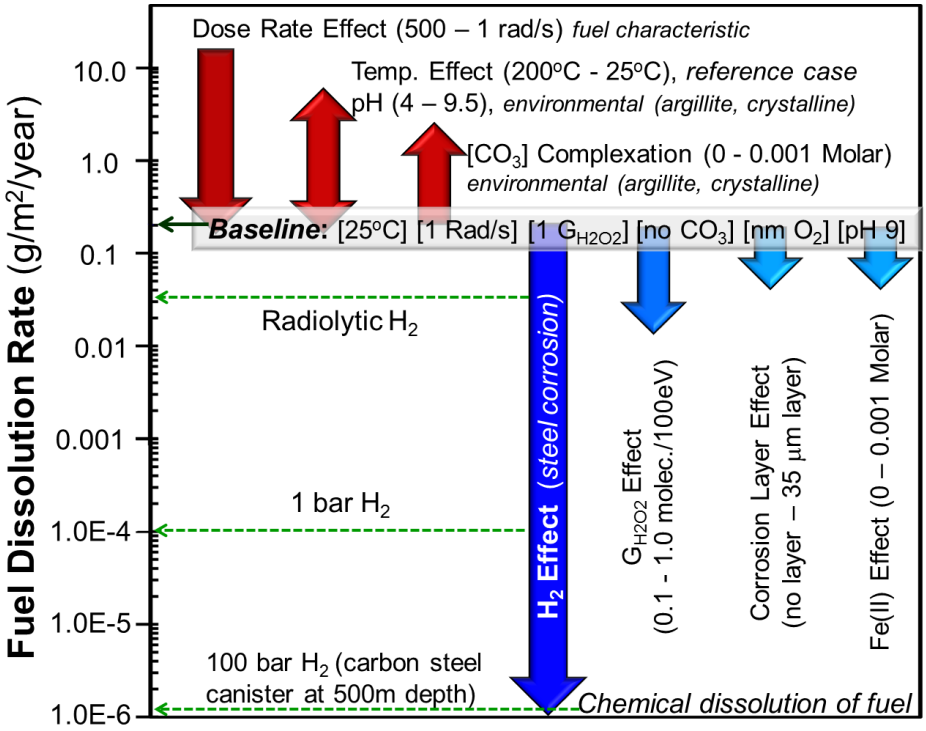

Figure 7. Summary of compiled results from FY2014 MPM V2 sensitivity runs.

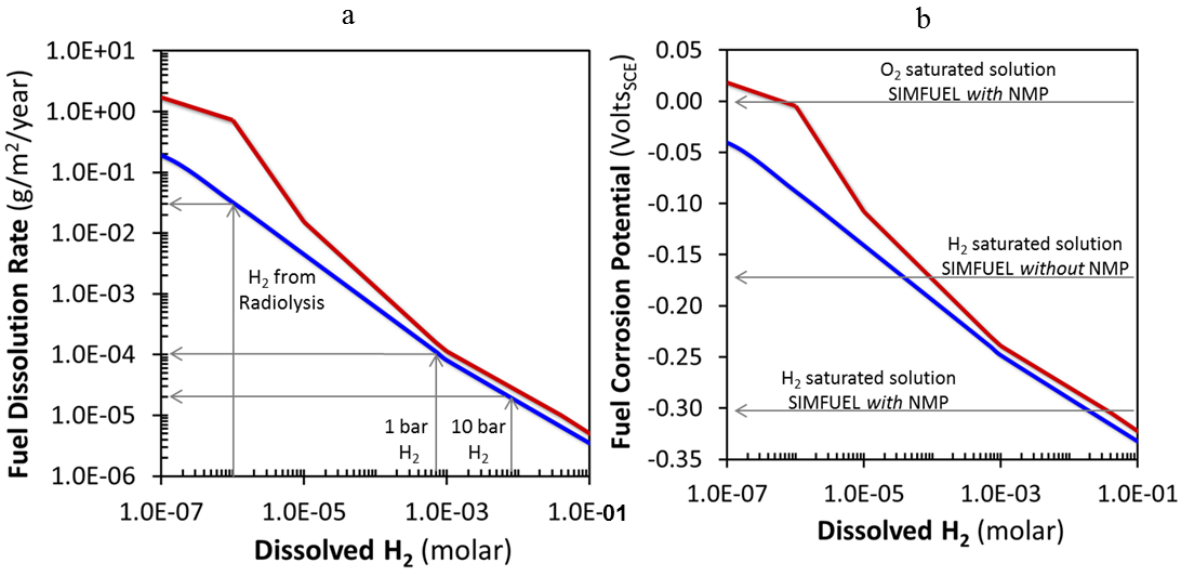

Figure 8. Details of (a) fuel dissolution rate and (b) corrosion potential calculated using MPM V2 for two dose rates (100 rad/s, red and 25 rad/s, blue).

4. Conversion of MPM V2 from MATLAB to Fortran

The MPM was written in MATLAB to utilize available functions (e.g., to solve ordinary differential equations for mass transport) to facilitate the development of additional process modules, such as including catalytic reactions on NMP and a more detailed radiolysis model. The purpose of the language conversion is to facilitate incorporation of the MPM directly into the performance assessment models for argillite and crystalline rock environments. The initial Fortran version of the Argonne MPM will be issued in early FY2015 to serve as a prototype to develop input and output communication links with PA and other process models. Continued development of the MPM, such as including modules for steel corrosion and the degraded NMP catalysis efficiency due to corrosion and poisoning, will be done using MATLAB to quickly evaluate optional approaches and interactions with the rest of the code. The finalized modules will then be translated to Fortran. This development plan is summarized schematically in Figure 1.

The specifics on the conversion are as follows:

- Programming language: Intel(R) Visual Fortran Compiler XE 14
- Additional libraries: LAPACK 3.5.0 Windows 32-bit static library (from http://icl.cs.utk.edu/lapack-for-windows/lapack/#libraries)
- Development environment: Visual Studio 2008

To date, a significant amount of the MPM Fortran code has been written and some internal checks (convergence of individual modules) have been done. Initial meetings with personnel developing the PA model have been scheduled for August and November 2014 to discuss the conceptual approach being taken and the interfaces and information exchanges between the Fortran MPM and PA process models. The following provides an annotated list of issues being addressed in the development of the Fortran MPM to support those discussions.

Inputs to MPM:

- There will be two entry points, one for interaction with the PA model and one for a stand-alone run.
- The input to the MPM is the environmental solution chemistry, temperature and dose rate
    - Currently, the environmental solution information that needs to be passed into the MPM includes the pH and concentrations of dissolved oxygen, hydrogen, iron, and carbonate.
    - It is anticipated that reactions with sulfate, chloride and bromide will be added to the MPM in future versions, so the codes are being set up to allow for expanding the number of components (chemical species).
- There are two types of parameters:
    - System parameters that are used in the PA model and other process models
    - MPM parameters that define characteristics of the mixed potential model only.
- The interface is under development, but it is envisioned that the system parameters will be passed into the MPM while an auxiliary function will read the MPM parameters from a data file.

The MPM parameters will be contained in a user-modifiable text file.

Outputs from MPM:

- There will be two exit points, one for interaction with the PA model and one for a stand-alone run.
    - Output to the PA model will be the fuel dissolution rate (mass/surface area/time) and the final concentrations of all components.
    - Output for the stand-alone model will generate a text data file containing the fuel dissolution rate, the concentrations of components, and calculated electrochemical quantities used to determine the fuel dissolution rate, namely, corrosion potential and reaction current densities.

5. Conclusions and Future Work

The major accomplishments for Argonne's FY2014 work on the Mixed Potential Model (MPM) development project were as follows:

- Added a working noble metal particle (epsilon phase) domain on fuel surface to account for the protective hydrogen effect.
- Incorporated the radiolysis model subroutine in MPM (using an analytical function provided by PNNL)
- Performed systematic sensitivity runs that identify and quantify the processes that affect the fuel dissolution rate.
- Compared sensitivity results with available experimental data (ongoing)
- Developed a research priority list based on results from sensitivity study and comparison with experimental results

The key observation to come out of the MPM sensitivity studies was that the set of coupled electrochemical reactions that comprise the model can be used to quantify the effectiveness of hydrogen within a breached canister to effectively shut down the radiolytic oxidative dissolution of the fuel. At sufficiently high hydrogen concentrations, fuel dissolution will only occur through the much slower chemical dissolution mechanism. This is consistent with experimental results from a number of repository programs (e.g., Shoesmith, 2008; Grambow and others, 2010) and with results from initial electrochemical tests performed in FY2013 as part of this study. The capacity to quantify the hydrogen effect in the used fuel degradation model will provide more realistic radionuclide source terms for use in PA.

The relative effects of temperature, dose rate (burnup), radiolysis, pH, carbonate complexation, ferrous iron and corrosion layer formation were also evaluated in the FY2014 sensitivity runs. All of these variables will influence the fuel degradation rate in distinct ways within argillite and crystalline rock, and other potential disposal environments. However, our sensitivity runs show that the hydrogen effect could be by far (up to four orders of magnitude greater, depending on the hydrogen concentration) the most dominant.

The MPM is uniquely suited to quantify the hydrogen effect on used fuel degradation because it explicitly accounts for all relevant interfacial redox reaction kinetics using fundamental electrochemical principles. This includes the impacts of phases present in the fuel, such as the catalytic effects of noble metal particles and the fuel surface itself, and other materials present in the disposal system that supply reactants or affect key redox reactions. The anoxic corrosion of steels present in the waste package is the main source of hydrogen in the waste package. The MPM was developed with the initial focus on reactions at the fuel surface, and the dissolved hydrogen concentration is currently a user-input value. To account for the hydrogen effect in

long-term model runs, corrosion kinetics of steel components leading to hydrogen generation needs to be incorporated into the model and coupled with fuel dissolution kinetics through the dissolved hydrogen concentration.

The current version of the MPM has proven effective for quantifying key processes affecting the rate of used fuel degradation; however, the implementation of MPM within a performance assessment model requires further model development and focused experimental work to provide data and quantify uncertainties in the existing database used to determine model parameter values representing disposal environments of interest. In order to take advantage of the work that has been done so far on the MPM, a number of needs have been identified:

- Incorporate the kinetics for hydrogen generation during the anoxic corrosion of steels into MPM as the source term for hydrogen.
- Perform focused electrochemical experiments with noble metal particle and lanthanide-doped UO_2 electrodes to determine parameter values needed to accurately model the effects of hydrogen, potential catalytic poisons such as bromide, and the pH and reaction temperature dependencies of fuel dissolution.
- Convert the MPM from MATLAB to Fortran to facilitate integration with PA codes (PFLOTRAN) (ongoing)
- Complete sensitivity runs to identify and assess inputs and outputs for integrating Fortran MPM into PA

6. References

Broczkowski, M. E., Noël, J. J., Shoesmith, D. W., (2005). The inhibiting effects of hydrogen on the corrosion of uranium dioxide under nuclear waste disposal conditions. Journal of Nuclear Materials 346, 16-.

Buck E., Jerden, J., Ebert, W., Wittman, R, (2013). Coupling the Mixed Potential and Radiolysis Models for Used Fuel Degradation. FCRD-UFD-2013-000290.

Christensen, H., Sunder, S. (1996). An evaluation of water layer thickness effective in oxidation of UO_2 fuel due to radiolysis of water. Journal of Nuclear Materials, 238, 70-77.

Ebert, W. L., Cruse, T. A., and Jerden J., (2012). Electrochemical Experiments Supporting Oxide Fuel Corrosion Model. FCRD-UFD-2012-000201.

R.J. Finch, R.C. Ewing (1992) The corrosion of uraninite under oxidizing conditions. Journal of Nuclear Materials, 190, 133-156.

B. Grambow, J. Bruno, L. Duro, J. Merino, A. Tamayo, C. Martin, G. Pepin, S. Schumacher, O. Smidt, C. Ferry, C. Jegou, J. Quiñones, E. Iglesias, N. Rodriguez Villagra, J. M. Nieto, A. Martínez-Esparza, A. Loida, V. Metz, B. Kienzler, G. Bracke, D. Pellegrini, G. Mathieu, V. Wasselin-Trupin, C. Serres, D. Wegen, M. Jonsson, L. Johnson, K. Lemmens, J. Liu, K. Spahiu, E. Ekeroth, I. Casas, J. de Pablo, C. Watson, P. Robinson, D. Hodgkinson, (2010). Model Uncertainty for the Mechanism of Dissolution of Spent Fuel in Nuclear Waste Repository, 2010 Euratom EUR 24597 EN EUROPEAN COMMISSION, Final Report for MICADO project.

E.C. Gaucher, C. Tournassat, F.J. Pearson, P. Blanc, C. Crouzet, C. Lerouge, S. Altmann, 2009, A Robust Model for Pore-water Chemistry of Clayrock. Geochimica et Cosmochimica Acta, 73 6470–6487

Guimerà, J., Duro, L., Delos, A. (2006). Changes in Groundwater Composition as a Consequence of Deglaciation Implications for performance Assessment, R-06-105, Swedish Nuclear Fuel and Waste Management Co, SKB, November 2006.

Jerden, J., Frey, K., Cruse, T., and Ebert, W. (2012). Waste Form Degradation Model Status Report: ANL Mixed Potential Model, Version 1. Archive. FCRD-UFD-2013-000057.

Jerden, J., Frey, K., Cruse, T., and Ebert, W. (2013). ANL Mixed Potential Model with Experimental Results: Implementation of Noble Metal Particle Catalysis Module. FCRD-UFD-2013-000305.

Kerisit, S., Liu, C. (2010). Molecular simulation of the Diffusion of Uranyl Carbonate Species in Aqueous Solution. Geochimica et Cosmochimica Acta, 74, 4937-4952.

King, F. and Kolar, M. (1999) Mathematical Implementation of the Mixed-Potential Model of Fuel Dissolution Model Version MPM-V1.0, Ontario Hydro, Nuclear Waste Management Division Report No. 06819-REP-01200-10005 R00.

King, F. and Kolar, M. (2002). Validation of the Mixed-Potential Model for Used Fuel Dissolution Against Experimental Data., Ontario Hydro, Nuclear Waste Management Division Report No. 06819-REP-01200-10077-R00.

King, F. and Kolar, M. (2003). The Mixed-Potential Model for UO2 Dissolution MPM Versions V1.3 and V1.4., Ontario Hydro, Nuclear Waste Management Division Report No. 06819-REP-01200-10104 R00.

Macpherson, J.V., and Unwin, P.R. (1997). Determination of the Diffusion Coefficient of Hydrogen in Aqueous Solution Using Single and Double Potential Step Chronoamperometry at a Disk Ultramicroelectrode. Analytical Chemistry, 69, 2063-2069.

Murphy, W.M. and Codell, R.C. (1999). Sci. Basis Nuclear Waste Mgt. XXII, Materials Research Society, 551-558.

Nielsen and Jonsson, (2006). Geometrical Alpha- and Beta-dose Distributions and Production Rates of Radiolysis Products in Water in Contact with Spent Nuclear Fuel. Journal of Nuclear Materials, 359, 1-7.

Pastina, B. and LaVerne, J. A. (2001). Effect of Molecular Hydrogen on Hydrogen Peroxide in Water Radiolysis. Journal of Physical Chemistry A105, 9316-9322.

Radulescu, (2011), LETTER REPORT, Reactor and Nuclear Systems Division, Repository Science/Criticality Analysis FTOR11UF0334, August, 2011

Shoesmith, D.W., M. Kolar, and F. King (2003). A Mixed-Potential Model to Predict Fuel (Uranium Dioxide) Corrosion Within a Failed Nuclear Waste Container Corrosion, 59, 802-816.

Shoesmith, D. W. (2008). The Role of Dissolved Hydrogen on the Corrosion/Dissolution of Spent Nuclear Fuel, NWMO TR-2008-19, November 2008 Nuclear Waste Management Organization, 22 St. Clair Avenue East, 6th Floor, Toronto, Ontario M4T 2S3, Canada

SKB (Svensk Kämbränslehantering AB [Swedish Nuclear Fuel and Waste Management Company]) (2011). Long-Term Safety for the Final Repository for Spent Nuclear Fuel at Forsmark, Technical Report TR-11-01. Three volumes. Stockholm, Sweden: Svensk Kärnbränslehantering AB.

Torrero, M.E., E. Baraj, J. De Pablo, J. Gimenez, and I. Casas (1997). Kinetics of Corrosion and Dissolution of Uranium Dioxide as a Function of pH. International Journal of Chemical Kinetics, 29, 261-267.

Trummer, M., Roth, O., and M. Jonsson, M. (2009). H_2 Inhibition of Radiation Induced Dissolution of Spent Nuclear Fuel. Journal of Nuclear Materials, 383, 226-230

Tsai, H. (2003). NRC Review of ANL High-Burnup Cladding Performance Program, July 16, (2003).

Uchida, H., Izumi, K., Aoki, K., Watanabe, M., (2009). Temperature-Dependence of Hydrogen Oxidation Reaction Rates and CO-Tolerance at Carbon-Supported Pt, Pt-Co, and Pt-Ru Catalysts. Phys. Chem. Chem. Phys., 11, 1771-1779

Vinsot A., Mettler S. and Wechner S. (2008). In situ characterization of the Callovo-Oxfordian pore water composition. Phys.Chem. Earth, 33, S75–S86.

Appendices

Appendix A

EMP standards and oxide detection limits for silicate analyses

Phlogopite (Synthetic): MgO = 0.02 wt.% , F = 0.11 wt.%

Albite (Amelia, NC, U.S.A, Rutherford mine): Na_2O = 0.02 wt.%

Labrodorite (Chihuahua, Mexico): Al_2O_3 = 0.02 wt.%, SiO_2 = 0.02 wt.%, CaO = 0.01 wt.%

Tugtupite (Greenland): Cl = 0.01 wt.%

Adularia (St. Gotthard, Switzerland): K_2O = 0.01 wt.%

Titanite glass (Penn State): TiO_2 = 0.02 wt.%

MagnesioChromite (Synthetic): Cr_2O_3 = 0.04 wt.%

Rhodonite (unknown locality): MnO = 0.02 wt.%

Augite (unknown locality): FeO = 0.02 wt.%

Liebenbergite (synthetic): NiO = 0.06 wt.%

Gahnite: ZnO = 0.05 wt.%

Appendix B:
Electron Microprobe Mineral Data

All data are presented as wt. % of the oxide.

Table B1. Clinoptilolite, unknown phases, and glasses EMP data.

	SiO_2	TiO_2	Al_2O_3	Cr_2O_3	FeO*	MnO	MgO	NiO	ZnO	CaO	Na_2O	K_2O	F	Cl	Total
Clinoptilolite															
EBS4-Cpt1-1	69.54	0.06	14.91	0.02	2.68	0.00	0.85	0.00	0.00	0.68	1.60	0.84	0.00	0.04	91.21
EBS4-Cpt2-1	74.50	0.00	13.08	0.00	0.16	0.00	0.13	0.00	0.00	1.55	0.32	0.48	0.00	0.01	90.24
AVE	**72.02**	**0.03**	**13.99**	**0.01**	1.42	**0.00**	**0.49**	**0.00**	**0.00**	**1.12**	**0.96**	**0.66**	**0.00**	**0.03**	**90.73**
EBS9-Cpt1-1	70.04	0.05	15.11	0.00	0.99	0.01	0.57	0.00	0.01	1.94	1.11	0.31	0.00	0.03	90.17
Unknown Species															
EBS4-Anl1-1	54.03	0.04	13.53	0.00	2.21	0.01	0.81	0.01	0.00	11.41	1.47	0.66	0.26	0.02	84.34
EBS4-unk1-1	37.85	0.05	10.63	0.00	2.02	0.00	0.91	0.00	0.00	24.04	0.62	0.52	0.00	0.40	76.98
EBS7-Cpt1-1	59.65	0.11	15.71	0.00	3.52	0.03	1.58	0.02	0.01	4.26	1.54	0.17	0.13	0.03	86.68
Glass (altered)															
EBS9-gls1-1	75.05	0.01	12.30	0.00	0.15	0.01	0.16	0.00	0.00	1.38	1.89	0.01	0.00	0.02	90.98
EBS11-gls1	72.53	0.00	11.99	0.00	0.19	0.01	0.10	0.00	0.02	1.70	2.29	0.22	0.00	0.00	89.05
EBS12-Gls-1	73.04	0.02	12.58	0.00	0.11	0.00	0.13	0.01	0.00	1.29	2.84	0.15	0.00	0.01	90.16

EBS12-Gls-2	74.83	0.02	12.23	0.00	0.10	0.00	0.15	0.00	0.00	1.31	2.90	0.14	0.00	0.00	91.66
EBS12-Gls-2	72.88	0.01	10.19	0.00	0.08	0.00	0.18	0.00	0.02	1.76	2.12	0.07	0.02	0.01	87.32
EBS12-Gls-3	73.58	0.02	12.40	0.00	0.08	0.00	0.15	0.01	0.04	1.73	3.16	0.17	0.09	0.00	91.39
AVE	**73.58**	**0.02**	**11.85**	**0.00**	0.09	**0.00**	**0.15**	**0.01**	**0.01**	**1.52**	**2.75**	**0.13**	**0.03**	**0.01**	**90.13**

Table B2. Biotite samples from EBS reaction products.

	SiO_2	TiO_2	Al_2O_3	Cr_2O_3	FeO*	MnO	MgO	NiO	ZnO	CaO	Na_2O	K_2O	F	Cl	Total
EBS4-Bt1-1	35.21	5.25	12.93	0.00	28.20	0.21	6.41	0.02	0.09	0.00	0.45	8.48	0.63	0.30	97.84
EBS4-Bt1-2	34.88	5.15	12.91	0.00	28.21	0.20	6.42	0.01	0.08	0.03	0.55	8.39	0.71	0.26	97.46
Ave.	**35.05**	**5.20**	**12.92**	**0.00**	**28.21**	**0.20**	**6.41**	**0.02**	**0.08**	**0.02**	**0.50**	**8.44**	**0.67**	**0.28**	**97.65**
EBS7-Bt1-1	35.36	5.10	13.26	0.00	27.84	0.19	6.38	0.02	0.02	0.03	0.57	8.40	0.82	0.27	97.85
EBS7-Bt1-2	36.03	4.89	13.21	0.01	27.31	0.20	6.24	0.00	0.06	0.02	0.65	8.16	0.82	0.27	97.47
Ave.	**35.69**	**4.99**	**13.23**	**0.00**	**27.58**	**0.20**	**6.31**	**0.01**	**0.04**	**0.03**	**0.61**	**8.28**	**0.82**	**0.27**	**97.66**
EBS9-Bt1-1	38.58	3.92	14.64	0.00	22.65	0.19	7.50	0.00	0.04	0.07	0.59	7.12	0.49	0.23	95.77
EBS9-Bt1-2	37.07	4.22	13.78	0.01	23.81	0.22	7.44	0.01	0.10	0.13	0.38	7.54	0.45	0.23	95.15
Ave.	**37.82**	**4.07**	**14.21**	**0.00**	**23.23**	**0.21**	**7.47**	**0.00**	**0.07**	**0.10**	**0.49**	**7.33**	**0.47**	**0.23**	**95.46**
EBS10-Bt-1	34.81	5.20	12.85	0.00	28.07	0.20	6.46	0.00	0.07	0.03	0.57	8.47	0.68	0.26	97.33
EBS10-Bt-2	34.99	5.06	12.97	0.00	28.08	0.21	6.51	0.00	0.05	0.03	0.61	8.43	0.60	0.27	97.49
EBS10-Bt2-1	35.60	5.03	12.92	0.00	27.56	0.21	6.48	0.01	0.07	0.01	0.48	8.47	0.61	0.25	97.38

EBS10-Bt2-2	34.69	4.93	12.82	0.01	27.01	0.18	6.43	0.00	0.07	0.04	0.57	8.08	0.60	0.25	95.36
Ave.	**35.02**	**5.05**	**12.89**	**0.00**	**27.68**	**0.20**	**6.47**	**0.00**	**0.06**	**0.03**	**0.56**	**8.36**	**0.62**	**0.26**	**96.89**
EBS11-Bt-1	36.65	4.17	13.43	0.00	25.16	0.22	7.36	0.01	0.10	0.04	0.49	8.17	0.70	0.23	96.38
EBS11-Bt-2	36.52	4.24	13.52	0.00	25.63	0.26	7.40	0.01	0.05	0.03	0.56	8.25	0.60	0.24	97.01
Ave.	**36.59**	**4.20**	**13.47**	**0.00**	**25.39**	**0.24**	**7.38**	**0.01**	**0.07**	**0.04**	**0.52**	**8.21**	**0.65**	**0.23**	**96.70**
EBS12-Bt1-1	35.65	4.44	12.72	0.01	25.85	0.29	7.99	0.00	0.06	0.04	0.39	8.57	0.71	0.22	96.58
EBS12-Bt1-2	35.56	4.38	13.12	0.00	25.35	0.28	8.14	0.00	0.07	0.06	0.38	8.29	0.74	0.24	96.24
Ave.	**35.61**	**4.41**	**12.92**	**0.01**	**25.60**	**0.28**	**8.06**	**0.00**	**0.07**	**0.05**	**0.38**	**8.43**	**0.72**	**0.23**	**96.41**

Table B3. EMP analyses from analcime.

	SiO_2	TiO_2	Al_2O_3	Cr_2O_3	FeO*	MnO	MgO	NiO	ZnO	CaO	Na_2O	K_2O	F	Cl	Total
EBS10-Anl1-1	69.67	0.00	19.12	0.00	0.18	0.00	0.03	0.02	0.00	1.53	4.44	0.06	0.00	0.00	95.05
EBS10-Anl-2	69.83	0.03	18.98	0.00	0.21	0.01	0.05	0.01	0.02	1.13	4.04	0.02	0.03	0.00	94.34
EBS10-Anl-3	69.08	0.01	18.98	0.01	0.23	0.02	0.10	0.00	0.00	1.37	4.37	0.06	0.00	0.00	94.22
EBS10-Anl-4	68.65	0.01	18.89	0.00	0.18	0.03	0.04	0.00	0.01	1.14	5.29	0.01	0.09	0.00	94.28
EBS10-Anl-5	69.37	0.00	18.92	0.00	0.23	0.00	0.05	0.00	0.00	1.15	3.17	0.01	0.00	0.00	92.91
EBS10-Anl-7	69.74	0.00	18.54	0.00	0.16	0.00	0.04	0.00	0.00	1.44	4.56	0.02	0.08	0.02	94.58
EBS10-Anl-8	69.81	0.01	19.96	0.00	0.20	0.00	0.05	0.01	0.00	1.06	3.57	0.02	0.00	0.01	94.69
EBS10-Anl-9	70.03	0.00	19.77	0.00	0.20	0.00	0.04	0.00	0.00	1.35	4.04	0.02	0.12	0.00	95.52
EBS10-Anl-10	71.44	0.13	19.86	0.00	0.60	0.02	0.22	0.01	0.01	0.88	4.42	0.20	0.03	0.01	97.83
EBS10-Anl-11	68.93	0.00	18.98	0.00	0.20	0.00	0.04	0.00	0.00	1.55	3.58	0.05	0.00	0.01	93.34
AVE	**69.66**	**0.02**	**19.20**	**0.00**	**0.24**	**0.01**	**0.06**	**0.01**	**0.00**	**1.26**	**4.15**	**0.05**	**0.03**	**0.01**	**94.68**
Std Dev	**0.77**	**0.04**	**0.48**	**0.00**	**0.13**	**0.01**	**0.06**	**0.01**	**0.01**	**0.22**	**0.61**	**0.06**	**0.05**	**0.01**	**1.34**
EBS11-Anl-1	68.03	0.02	18.52	0.00	0.14	0.00	0.04	0.00	0.01	1.37	4.68	0.04	0.00	0.01	92.85
EBS11-Anl-2	68.06	0.00	18.23	0.02	0.12	0.02	0.04	0.00	0.00	1.34	4.46	0.05	0.00	0.02	92.35
EBS11-Anl-3	68.82	0.00	18.44	0.00	0.16	0.01	0.04	0.00	0.01	1.52	4.49	0.09	0.00	0.00	93.60
EBS11-Anl-4	69.10	0.02	18.79	0.01	0.17	0.00	0.04	0.00	0.00	1.38	3.79	0.04	0.00	0.02	93.35
EBS11-Anl-5	69.10	0.02	18.33	0.00	0.19	0.00	0.06	0.01	0.02	1.33	3.72	0.04	0.05	0.02	92.87
EBS11-Anl-6	70.07	0.03	18.50	0.00	0.17	0.01	0.04	0.01	0.02	1.53	4.28	0.08	0.00	0.01	94.73

EBS11-Anl-7	69.71	0.00	18.86	0.00	0.18	0.01	0.04	0.01	0.02	1.33	4.29	0.04	0.09	0.01	94.56
EBS11-Anl-10	70.21	0.00	18.40	0.00	0.15	0.00	0.02	0.01	0.00	1.55	3.77	0.08	0.00	0.00	94.21
EBS11-Anl-11	68.95	0.04	19.53	0.00	0.43	0.00	0.23	0.00	0.00	0.81	3.74	0.08	0.01	0.02	93.84
EBS11-Anl-13	67.06	0.07	19.47	0.00	0.47	0.01	0.26	0.00	0.02	0.93	3.79	0.13	0.07	0.01	92.26
AVE	**68.91**	**0.02**	**18.71**	**0.00**	**0.22**	**0.01**	**0.08**	**0.00**	**0.01**	**1.31**	**4.10**	**0.07**	**0.02**	**0.01**	**93.46**
Std Dev	**0.98**	**0.02**	**0.46**	**0.01**	**0.12**	**0.01**	**0.09**	**0.00**	**0.01**	**0.25**	**0.38**	**0.03**	**0.03**	**0.01**	**0.88**

Table B4. EMP analyses from analcime.

	SiO_2	TiO_2	Al_2O_3	Cr_2O_3	FeO*	MnO	MgO	NiO	ZnO	CaO	Na_2O	K_2O	F	Cl	Total
EBS11-Anl-8 20u	64.05	0.00	17.76	0.00	0.10	0.00	0.02	0.01	0.00	1.51	8.50	0.10	0.10	0.00	92.11
EBS11-Anl-9 20u	64.70	0.00	17.76	0.00	0.08	0.01	0.01	0.01	0.00	1.46	7.64	0.09	0.00	0.01	91.76
AVE	**64.37**	**0.00**	**17.76**	**0.00**	**0.09**	**0.00**	**0.02**	**0.01**	**0.00**	**1.49**	**8.07**	**0.09**	**0.05**	**0.00**	**91.93**
EBS12-Anl?-1	71.17	0.00	18.61	0.00	0.33	0.01	0.20	0.00	0.00	0.55	1.83	0.05	0.02	0.01	92.76
EBS12-Anl?-2	70.45	0.03	18.66	0.00	0.27	0.01	0.14	0.00	0.00	0.45	4.02	0.04	0.00	0.01	94.08
EBS12-Anl?-3	70.62	0.01	18.97	0.02	0.38	0.02	0.17	0.01	0.00	0.50	3.90	0.02	0.06	0.01	94.66
EBS12-Anl?-4	70.39	0.04	18.69	0.00	0.33	0.01	0.23	0.00	0.03	0.43	3.91	0.12	0.03	0.02	94.21
AVE	**70.66**	**0.02**	**18.73**	**0.01**	**0.33**	**0.01**	**0.18**	**0.00**	**0.01**	**0.48**	**3.41**	**0.06**	**0.03**	**0.01**	**93.93**
Std Dev	**0.35**	**0.02**	**0.16**	**0.01**	**0.04**	**0.00**	**0.04**	**0.01**	**0.01**	**0.05**	**1.06**	**0.05**	**0.03**	**0.01**	**0.82**

Table B5. EMP analyses from K-feldspars. Samples with low totals probably had significant Ba contributions.

	SiO_2	TiO_2	Al_2O_3	Cr_2O_3	FeO*	MnO	MgO	NiO	ZnO	CaO	Na_2O	K_2O	F	Cl	Total
EBS7-Afs1-1	65.63	0.01	18.84	0.01	0.16	0.00	0.00	0.02	0.05	0.16	3.39	11.58	0.10	0.00	99.90
EBS9-Afs1-1	65.39	0.01	18.74	0.00	0.18	0.02	0.01	0.01	0.00	0.17	3.46	11.56	0.12	0.00	99.62
EBS10-Afs-1	63.28	0.02	18.43	0.00	0.17	0.00	0.02	0.01	0.00	0.25	2.99	11.19	0.06	0.00	96.40
EBS10-Afs-2	63.71	0.00	18.58	0.00	0.19	0.00	0.00	0.00	0.00	0.27	3.68	10.38	0.00	0.00	96.80
EBS10-Afs3-1	64.91	0.02	18.82	0.01	0.15	0.00	0.00	0.01	0.00	0.19	3.22	11.39	0.03	0.00	98.74
EBS10-Afs-4	65.49	0.00	18.99	0.00	0.18	0.00	0.00	0.03	0.02	0.19	3.24	11.22	0.07	0.00	99.40
AVE	**64.35**	**0.01**	**18.70**	**0.00**	**0.17**	**0.00**	**0.00**	**0.01**	**0.01**	**0.23**	**3.28**	**11.04**	**0.04**	**0.00**	**97.83**
STD DEV	**1.03**	**0.01**	**0.25**	**0.00**	**0.02**	**0.00**	**0.00**	**0.01**	**0.01**	**0.04**	**0.29**	**0.45**	**0.03**	**0.00**	**1.46**
EBS11-Afs-1	65.58	0.01	18.37	0.00	0.14	0.00	0.00	0.00	0.01	0.24	3.71	10.40	0.20	0.00	98.58
EBS11-Afs-2	65.36	0.00	18.52	0.01	0.11	0.01	0.01	0.00	0.00	0.17	3.41	11.39	0.00	0.00	98.97
EBS11-Afs-4	66.72	0.00	18.76	0.00	0.18	0.00	0.01	0.00	0.01	0.17	4.18	10.34	0.03	0.00	100.39
AVE	**65.89**	**0.00**	**18.55**	**0.00**	**0.14**	**0.00**	**0.00**	**0.00**	**0.01**	**0.20**	**3.77**	**10.71**	**0.08**	**0.00**	**99.31**
STD DEV	**0.73**	**0.01**	**0.20**	**0.00**	**0.04**	**0.00**	**0.00**	**0.00**	**0.01**	**0.04**	**0.39**	**0.59**	**0.11**	**0.00**	**0.95**

EBS12-Afs-1	62.89	0.02	18.55	0.02	0.17	0.00	0.00	0.00	0.00	0.17	3.28	11.07	0.00	0.00	96.17
EBS12-Afs-1	63.58	0.01	18.66	0.00	0.19	0.00	0.00	0.00	0.00	0.18	3.26	10.96	0.00	0.01	96.87
EBS12-Afs-2	61.36	0.00	18.67	0.00	0.18	0.00	0.00	0.02	0.00	0.20	3.19	10.03	0.00	0.00	93.64
EBS12-Afs-3	64.53	0.03	18.48	0.01	0.11	0.00	0.00	0.00	0.00	0.15	3.27	11.42	0.00	0.00	98.01
AVE	**63.09**	**0.01**	**18.59**	**0.01**	**0.16**	**0.00**	**0.00**	**0.00**	**0.00**	**0.18**	**3.25**	**10.87**	**0.00**	**0.00**	**96.17**
STD DEV	**1.34**	**0.01**	**0.09**	**0.01**	**0.04**	**0.00**	**0.00**	**0.01**	**0.00**	**0.02**	**0.04**	**0.59**	**0.00**	**0.00**	**1.85**

Table B6. EMP analyses from plagioclase.

	SiO_2	TiO_2	Al_2O_3	Cr_2O_3	FeO*	MnO	MgO	NiO	ZnO	CaO	Na_2O	K_2O	F	Cl	Total
EBS4-AltPlag1-1	68.44	0.22	19.26	0.00	1.22	0.02	0.35	0.02	0.00	1.64	3.98	6.92	0.02	0.02	102.10
EBS4-AltPlag1-2	61.37	0.34	24.68	0.00	1.18	0.01	0.40	0.00	0.02	3.49	4.31	3.94	0.00	0.03	99.78
AVE	**64.90**	**0.28**	**21.97**	**0.00**	**1.20**	**0.01**	**0.37**	**0.01**	**0.01**	**2.57**	**4.15**	**5.43**	**0.01**	**0.03**	**100.94**
EBS9-Ab1 (vfg)	68.43	0.05	20.33	0.00	0.36	0.00	0.06	0.00	0.00	0.11	11.19	0.11	0.06	0.01	100.68
EBS9-Pl1-1	61.98	0.00	23.57	0.00	0.28	0.00	0.01	0.00	0.00	5.27	8.01	0.99	0.00	0.00	100.12
AVE	**65.20**	**0.03**	**21.95**	**0.00**	**0.32**	**0.00**	**0.04**	**0.00**	**0.00**	**2.69**	**9.60**	**0.55**	**0.03**	**0.01**	**100.40**
EBS10-Pl-1	63.53	0.02	22.85	0.00	0.26	0.02	0.00	0.00	0.01	4.46	8.36	1.00	0.00	0.00	100.51
EBS10-Pl-2	60.50	0.00	24.31	0.00	0.30	0.02	0.00	0.00	0.00	6.22	7.41	0.77	0.00	0.00	99.53
EBS10-Pl2-1	60.52	0.03	24.57	0.01	0.26	0.00	0.01	0.02	0.02	6.00	7.44	0.86	0.00	0.00	99.74
EBS10-Pl-4	64.03	0.00	22.66	0.01	0.27	0.02	0.00	0.00	0.00	3.53	7.95	1.17	0.09	0.00	99.70
AVE	**62.15**	**0.01**	**23.60**	**0.00**	**0.27**	**0.02**	**0.01**	**0.00**	**0.01**	**5.05**	**7.79**	**0.95**	**0.02**	**0.00**	**99.87**
STD DEV	**1.90**	**0.01**	**0.98**	**0.01**	**0.02**	**0.01**	**0.00**	**0.01**	**0.01**	**1.28**	**0.46**	**0.18**	**0.04**	**0.00**	**0.44**
EBS11-Pl-1	60.70	0.02	24.40	0.00	0.23	0.00	0.01	0.00	0.02	6.79	7.44	0.74	0.00	0.00	100.35
EBS11-Pl-2	62.65	0.02	22.87	0.00	0.22	0.01	0.00	0.01	0.02	4.45	8.37	1.00	0.00	0.00	99.62
AVE	**61.68**	**0.02**	**23.63**	**0.00**	**0.23**	**0.00**	**0.01**	**0.01**	**0.02**	**5.62**	**7.90**	**0.87**	**0.00**	**0.00**	**99.98**
STD DEV	**1.38**	**0.00**	**1.08**	**0.00**	**0.01**	**0.00**	**0.00**	**0.01**	**0.01**	**1.65**	**0.66**	**0.18**	**0.00**	**0.00**	**0.51**

EBS12-PI-1	59.53	0.00	26.09	0.00	0.24	0.00	0.00	0.00	0.03	8.05	6.90	0.57	0.01	0.00	101.42
EBS12-PI-1	60.59	0.00	26.57	0.00	0.27	0.00	0.01	0.02	0.00	7.92	7.16	0.59	0.07	0.01	103.18
EBS12-PI-2	62.17	0.00	23.18	0.02	0.23	0.00	0.00	0.01	0.01	4.88	8.04	1.01	0.02	0.01	99.57
AVE	**60.76**	**0.00**	**25.28**	**0.01**	**0.25**	**0.00**	**0.00**	**0.01**	**0.01**	**6.95**	**7.37**	**0.72**	**0.03**	**0.00**	**101.39**
STD DEV	**1.33**	**0.00**	**1.83**	**0.01**	**0.02**	**0.00**	**0.00**	**0.01**	**0.02**	**1.79**	**0.60**	**0.25**	**0.03**	**0.00**	**1.80**

Table B7. EMP data on chlorite associated with ZVI from redox buffer.

	SiO_2	TiO_2	Al_2O_3	Cr_2O_3	FeO*	MnO	MgO	NiO	ZnO	CaO	Na_2O	K_2O	F	Cl	Total
EBS7-Chl1-1	34.88	0.05	15.55	0.00	33.78	0.12	1.62	0.01	0.05	0.08	0.82	0.02	0.00	0.06	87.02
EBS7-Chl1-2	34.32	0.07	15.08	0.02	33.58	0.11	1.64	0.00	0.00	0.07	0.50	0.01	0.00	0.11	85.48
EBS7-Chl1-3	32.39	0.05	14.80	0.00	37.47	0.13	1.60	0.00	0.01	0.07	1.01	0.04	0.00	0.05	87.60
AVE	**33.86**	**0.05**	**15.14**	**0.01**	**34.94**	**0.12**	**1.62**	**0.01**	**0.02**	**0.07**	**0.77**	**0.02**	**0.00**	**0.07**	**86.70**
STD DEV	**1.30**	**0.01**	**0.38**	**0.01**	**2.19**	**0.01**	**0.02**	**0.01**	**0.03**	**0.00**	**0.26**	**0.02**	**0.00**	**0.03**	**1.09**
EBS9-Chl1-1	35.06	0.05	14.06	0.00	32.78	0.08	1.73	0.00	0.00	0.55	3.14	0.09	0.00	0.01	87.56
EBS9-Chl2-1	37.02	0.06	15.10	0.00	33.26	0.13	1.78	0.00	0.01	0.64	1.50	0.13	0.00	0.00	89.62
EBS9-Chl2-2	36.83	0.02	15.08	0.00	33.31	0.10	1.84	0.00	0.06	0.69	0.98	0.08	0.04	0.00	89.01
AVE	**36.30**	**0.04**	**14.75**	**0.00**	**33.11**	**0.10**	**1.78**	**0.00**	**0.02**	**0.63**	**1.87**	**0.10**	**0.01**	**0.01**	**88.73**
STD DEV	**1.08**	**0.02**	**0.59**	**0.00**	**0.29**	**0.02**	**0.05**	**0.00**	**0.03**	**0.07**	**1.12**	**0.03**	**0.02**	**0.00**	**1.06**
EBS11-Chl1	38.39	0.08	13.56	0.01	31.34	0.11	3.40	0.02	0.01	1.18	2.30	0.13	0.00	0.01	90.55
EBS11-Chl2	36.96	0.02	12.60	0.00	30.04	0.06	3.35	0.02	0.03	1.07	2.22	0.14	0.00	0.09	86.58
AVE	**37.68**	**0.05**	**13.08**	**0.01**	**30.69**	**0.09**	**3.37**	**0.02**	**0.02**	**1.13**	**2.26**	**0.13**	**0.00**	**0.05**	**88.57**

Table B8. EMP data from 316SS associated with EBS-10.

Wt. %	Si	P	V	Cr	Mn	Fe	Co	Ni	Cu	Mo	Total
Transect 1a, inward from upper edge: 20 mm spacing											
EBS10-T1-1	0.36	0.05	0.05	16.37	1.81	65.30	0.18	11.17	0.57	2.26	98.13
EBS10-T1-2	0.37	0.04	0.08	16.97	1.81	65.45	0.17	11.29	0.50	2.23	98.90
EBS10-T1-3	0.38	0.04	0.08	16.96	1.81	65.34	0.18	11.73	0.58	2.17	99.26
EBS10-T1-4	0.38	0.04	0.07	16.82	1.75	65.40	0.20	11.72	0.61	2.20	99.18
EBS10-T1-5	0.37	0.03	0.05	16.89	1.69	65.24	0.18	11.39	0.53	2.13	98.49
AVE	**0.37**	**0.04**	**0.07**	**16.80**	**1.77**	**65.34**	**0.18**	**11.46**	**0.56**	**2.20**	**98.79**
STD DEV	**0.01**	**0.01**	**0.01**	**0.25**	**0.05**	**0.08**	**0.01**	**0.25**	**0.05**	**0.05**	**0.48**
Transect 1b, inward from lower edge: 20 mm spacing											
EBS10-T1b-1	0.36	0.04	0.07	16.85	1.81	65.69	0.17	11.32	0.57	2.23	99.11
EBS10-T1b-2	0.37	0.06	0.08	16.87	1.71	66.15	0.15	11.34	0.55	2.08	99.35
EBS10-T1b-3	0.37	0.06	0.10	17.00	1.82	65.87	0.17	11.36	0.54	1.98	99.26
EBS10-T1b-4	0.35	0.03	0.09	16.98	1.76	66.07	0.20	11.39	0.55	2.07	99.49
EBS10-T1b-5	0.35	0.04	0.06	16.83	1.73	65.82	0.21	11.51	0.54	2.13	99.23
AVE	**0.36**	**0.05**	**0.08**	**16.90**	**1.77**	**65.92**	**0.18**	**11.38**	**0.55**	**2.10**	**99.29**
Std Dev	**0.01**	**0.01**	**0.02**	**0.08**	**0.05**	**0.19**	**0.02**	**0.07**	**0.01**	**0.09**	**0.14**

Table B9. EMP data from 316SS associated with EBS-10.

	Si	P	V	Cr	Mn	Fe	Co	Ni	Cu	Mo	Total
Transect 2a, inward from upper edge: 20 mm spacing											
EBS10-T2-1	0.38	0.02	0.10	16.69	1.69	65.66	0.17	11.51	0.55	2.24	99.00
EBS10-T2-2	0.36	0.01	0.10	17.19	1.79	66.63	0.21	11.25	0.53	1.95	100.02
EBS10-T2-3	0.37	0.06	0.07	16.97	1.67	66.18	0.19	11.75	0.52	2.03	99.82
EBS10-T2-4	0.38	0.07	0.08	17.08	1.91	65.61	0.21	11.37	0.62	2.00	99.32
EBS10-T2-5	0.39	0.04	0.05	17.40	1.77	66.33	0.22	11.48	0.48	2.04	100.21
AVE	**0.38**	**0.04**	**0.08**	**17.07**	**1.77**	**66.08**	**0.20**	**11.47**	**0.54**	**2.05**	**99.67**
Std Dev	**0.01**	**0.03**	**0.02**	**0.27**	**0.09**	**0.44**	**0.02**	**0.18**	**0.05**	**0.11**	**0.50**
Transect 2b, inward from lower edge: 20 mm spacing											
EBS10-T2b-1	0.37	0.02	0.06	17.25	2.11	65.79	0.21	11.53	0.52	2.04	99.90
EBS10-T2b-2	0.37	0.02	0.06	17.22	1.72	65.87	0.20	11.72	0.58	1.97	99.73
EBS10-T2b-3	0.39	0.04	0.07	17.22	1.84	66.07	0.18	11.53	0.55	2.29	100.18
EBS10-T2b-4	0.38	0.02	0.10	17.59	1.79	66.33	0.19	11.27	0.53	2.29	100.49
EBS10-T2b-5	0.36	0.03	0.07	17.13	1.85	65.94	0.20	11.43	0.50	2.11	99.60
AVE	**0.37**	**0.03**	**0.07**	**17.28**	**1.86**	**66.00**	**0.20**	**11.50**	**0.54**	**2.14**	**99.98**
Std Dev	**0.01**	**0.01**	**0.02**	**0.18**	**0.15**	**0.21**	**0.01**	**0.16**	**0.03**	**0.14**	**0.36**

Table B10. EMP data from 316SS associated with EBS-10.

	Si	P	V	Cr	Mn	Fe	Co	Ni	Cu	Mo	Total
Transect 3a, inward from upper edge: 20 mm spacing											
EBS10-T3-1	0.43	0.05	0.09	17.34	1.70	63.24	0.21	11.26	0.52	2.26	97.11
EBS10-T3-2	0.38	0.05	0.09	17.86	1.87	65.62	0.20	11.45	0.47	2.24	100.24
EBS10-T3-3	0.37	0.03	0.08	17.96	1.95	66.06	0.21	11.28	0.50	2.11	100.55
EBS10-T3-4	0.38	0.04	0.06	17.70	1.81	65.69	0.19	11.59	0.52	2.17	100.14
EBS10-T3-5	0.37	0.03	0.08	17.68	1.81	65.74	0.17	11.79	0.59	2.10	100.37
EBS10-T3-6	0.37	0.03	0.06	17.73	1.76	66.33	0.21	11.51	0.56	2.16	100.73
EBS10-T3-7	0.39	0.05	0.08	17.96	1.86	65.71	0.24	11.30	0.52	2.21	100.31
EBS10-T3-8	0.37	0.02	0.09	17.65	1.82	66.20	0.18	11.69	0.58	2.09	100.70
EBS10-T3-9	0.37	0.03	0.05	18.30	1.76	66.27	0.19	11.04	0.45	2.28	100.76
EBS10-T3-10	0.39	0.01	0.11	17.86	1.86	66.14	0.20	11.76	0.54	2.26	101.13
AVE	**0.38**	**0.04**	**0.08**	**17.80**	**1.82**	**65.70**	**0.20**	**11.47**	**0.53**	**2.19**	**100.20**
Std Dev	**0.02**	**0.01**	**0.02**	**0.25**	**0.07**	**0.91**	**0.02**	**0.25**	**0.04**	**0.07**	**1.13**
Transect 3b, inward from lower edge: 20 mm spacing											

EBS10-T3b-1	0.37	0.04	0.09	18.36	1.83	66.33	0.19	11.21	0.59	2.23	101.24
EBS10-T3b-2	0.37	0.02	0.11	18.14	1.78	66.12	0.14	11.59	0.62	1.97	100.85
EBS10-T3b-3	0.37	0.03	0.09	18.08	1.82	66.06	0.20	11.61	0.56	2.23	101.06
EBS10-T3b-4	0.37	0.04	0.08	17.97	1.83	65.46	0.19	11.92	0.50	2.21	100.57
EBS10-T3b-5	0.37	0.05	0.09	18.03	1.88	65.76	0.18	11.89	0.56	2.15	100.95
EBS10-T3b-6	0.37	0.03	0.07	17.82	1.79	65.69	0.19	11.75	0.52	2.15	100.37
EBS10-T3b-7	0.37	0.02	0.06	18.20	1.77	66.14	0.21	11.32	0.62	2.06	100.77
EBS10-T3b-8	0.38	0.03	0.07	18.04	1.83	66.13	0.18	11.64	0.54	2.17	101.02
EBS10-T3b-9	0.39	0.05	0.10	17.95	1.75	65.60	0.22	11.83	0.57	2.19	100.66
EBS10-T3b-10	0.37	0.03	0.06	17.93	1.64	65.87	0.20	11.54	0.58	2.26	100.48
AVE	**0.37**	**0.03**	**0.08**	**18.05**	**1.79**	**65.92**	**0.19**	**11.63**	**0.57**	**2.16**	**100.80**
Std Dev	**0.01**	**0.01**	**0.02**	**0.15**	**0.07**	**0.28**	**0.02**	**0.23**	**0.04**	**0.09**	**0.28**

Table B11. EMP data from 316SS associated with EBS-10.

	Si	P	V	Cr	Mn	Fe	Co	Ni	Cu	Mo	Total
Points along center line of metals											
EBS10-Cent1-1	0.34	0.04	0.04	16.63	1.67	66.44	0.18	11.11	0.56	2.09	99.09
EBS10-Cent1-2	0.34	0.05	0.07	16.75	1.68	66.74	0.20	11.00	0.52	2.13	99.49
EBS10-Cent1-3	0.35	0.02	0.05	16.81	1.63	66.59	0.25	11.02	0.50	1.99	99.22
EBS10-Cent1-4	0.35	0.04	0.11	17.23	1.63	66.91	0.22	10.57	0.48	2.25	99.78
EBS10-Cent1-5	0.35	0.05	0.08	17.00	1.62	66.75	0.15	10.59	0.49	2.17	99.24
EBS10-Cent2-1	0.35	0.05	0.10	17.08	1.74	66.28	0.19	11.26	0.49	1.88	99.42
EBS10-Cent2-2	0.35	0.05	0.06	17.70	1.70	66.19	0.20	10.48	0.47	2.23	99.42
EBS10-Cent2-3	0.36	0.06	0.09	16.90	1.86	66.19	0.20	11.14	0.44	1.93	99.17
EBS10-Cent2-4	0.38	0.06	0.11	17.37	1.82	65.80	0.19	11.82	0.61	2.09	100.24
EBS10-Cent2-5	0.36	0.03	0.08	17.28	1.89	65.67	0.20	11.68	0.55	2.10	99.84
EBS10-Cent3-1	0.41	0.05	0.08	18.14	1.99	63.88	0.22	12.61	0.54	2.46	100.38
EBS10-Cent3-2	0.42	0.04	0.09	18.46	2.02	64.02	0.20	12.16	0.65	2.40	100.46
EBS10-	0.38	0.03	0.08	18.15	1.82	64.87	0.24	11.94	0.61	2.08	100.20

Cent3-3											
EBS10-Cent3-4	0.97	0.05	0.10	17.71	2.31	64.23	0.16	12.13	0.59	2.34	100.60
EBS10-Cent3-5	0.41	0.06	0.05	18.21	1.81	65.40	0.20	12.00	0.59	2.39	101.12
Average	**0.41**	**0.04**	**0.08**	**17.43**	**1.81**	**65.73**	**0.20**	**11.43**	**0.54**	**2.17**	**99.84**
Std Dev	**0.16**	**0.01**	**0.02**	**0.60**	**0.19**	**1.03**	**0.03**	**0.66**	**0.06**	**0.17**	**0.62**

Table B12. EMP data from 304SS associated with EBS-5.

	Si	P	V	Cr	Mn	Fe	Co	Ni	Cu	Mo	Total
Transect 1a, inward from upper edge: 20 mm spacing											
EBS5-T1-1	0.49	0.02	0.02	18.80	1.79	69.89	0.16	8.76	0.21	0.16	100.32
EBS5-T1-2	0.50	0.02	0.04	19.28	1.86	69.86	0.13	8.48	0.24	0.14	100.55
EBS5-T1-3	0.50	0.02	0.07	19.19	1.82	69.92	0.11	8.40	0.26	0.11	100.39
EBS5-T1-4	0.51	0.02	0.07	19.16	1.79	69.97	0.11	8.61	0.23	0.05	100.52
EBS5-T1-5	0.49	0.04	0.07	19.32	1.88	70.26	0.10	8.46	0.20	0.19	101.00
AVE	**0.50**	**0.02**	**0.05**	**19.15**	**1.83**	**69.98**	**0.12**	**8.54**	**0.23**	**0.13**	**100.56**
Std Dev	**0.01**	**0.01**	**0.02**	**0.21**	**0.04**	**0.16**	**0.02**	**0.14**	**0.02**	**0.05**	**0.27**
Transect 1b, inward from lower edge: 20 mm spacing											
EBS5-T1b-1	0.49	0.04	0.05	19.33	1.98	69.96	0.11	8.60	0.24	0.12	100.92
EBS5-T1b-2	0.50	0.03	0.03	19.27	1.90	70.28	0.17	8.57	0.24	0.12	101.11
EBS5-T1b-3	0.50	0.04	0.05	19.25	1.80	70.45	0.13	8.26	0.27	0.12	100.89
EBS5-T1b-4	0.51	0.04	0.07	19.24	1.84	70.13	0.12	8.74	0.26	0.12	101.07
EBS5-T1b-5	0.51	0.02	0.04	18.99	1.89	70.00	0.12	8.54	0.26	0.12	100.49

AVE	**0.50**	**0.03**	**0.05**	**19.22**	**1.88**	**70.16**	**0.13**	**8.54**	**0.25**	**0.12**	**100.90**
Std Dev	**0.01**	**0.01**	**0.02**	**0.13**	**0.07**	**0.20**	**0.02**	**0.17**	**0.02**	**0.00**	**0.25**

Table B13. EMP data from 304SS associated with EBS-5.

	Si	P	V	Cr	Mn	Fe	Co	Ni	Cu	Mo	Total
Transect 2a, inward from upper edge: 20 mm spacing											
EBS5-T2-1	0.51	0.04	0.06	19.27	1.84	70.17	0.12	8.26	0.24	0.07	100.56
EBS5-T2-2	0.50	0.01	0.07	19.61	2.06	69.63	0.17	8.80	0.24	0.15	101.23
EBS5-T2-3	0.51	0.02	0.03	19.24	1.80	70.77	0.13	8.57	0.22	0.17	101.47
EBS5-T2-4	0.52	0.02	0.04	19.45	1.94	70.51	0.13	8.35	0.25	0.17	101.37
EBS5-T2-5	0.51	0.04	0.07	19.34	1.87	70.45	0.11	8.68	0.25	0.12	101.43
AVE	**0.51**	**0.03**	**0.05**	**19.38**	**1.90**	**70.30**	**0.13**	**8.53**	**0.24**	**0.13**	**101.21**
Std Dev	**0.01**	**0.01**	**0.02**	**0.15**	**0.10**	**0.44**	**0.02**	**0.23**	**0.01**	**0.04**	**0.38**
Transect 2b, inward from lower edge: 20 mm spacing											
EBS10-T3-1	0.43	0.05	0.09	17.34	1.70	63.24	0.21	11.26	0.52	2.26	97.11
EBS10-T3-2	0.38	0.05	0.09	17.86	1.87	65.62	0.20	11.45	0.47	2.24	100.24
EBS10-T3-3	0.37	0.03	0.08	17.96	1.95	66.06	0.21	11.28	0.50	2.11	100.55
EBS10-	0.38	0.04	0.06	17.70	1.81	65.69	0.19	11.59	0.52	2.17	100.14

T3-4											
EBS10-T3-5	0.37	0.03	0.08	17.68	1.81	65.74	0.17	11.79	0.59	2.10	100.37
EBS10-T3-6	0.37	0.03	0.06	17.73	1.76	66.33	0.21	11.51	0.56	2.16	100.73
EBS10-T3-7	0.39	0.05	0.08	17.96	1.86	65.71	0.24	11.30	0.52	2.21	100.31
EBS10-T3-8	0.37	0.02	0.09	17.65	1.82	66.20	0.18	11.69	0.58	2.09	100.70
EBS10-T3-9	0.37	0.03	0.05	18.30	1.76	66.27	0.19	11.04	0.45	2.28	100.76
EBS10-T3-10	0.39	0.01	0.11	17.86	1.86	66.14	0.20	11.76	0.54	2.26	101.13
AVE	**0.38**	**0.04**	**0.08**	**17.80**	**1.82**	**65.70**	**0.20**	**11.47**	**0.53**	**2.19**	**100.20**
Std Dev	**0.02**	**0.01**	**0.02**	**0.25**	**0.07**	**0.91**	**0.02**	**0.25**	**0.04**	**0.07**	**1.13**

Table B14. EMP data from 304SS associated with EBS-5.

	Si	P	V	Cr	Mn	Fe	Co	Ni	Cu	Mo	Total
Transect 3a, inward from upper edge: 20 mm spacing											
EBS5-T3-1	0.46	0.05	0.02	18.43	1.79	68.49	0.12	8.38	0.26	0.17	98.17
EBS5-T3-2	0.50	0.02	0.05	19.05	1.85	69.04	0.12	8.65	0.21	0.23	99.71
EBS5-T3-3	0.50	0.01	0.03	18.92	1.90	68.87	0.11	8.33	0.24	0.20	99.11
EBS5-T3-4	0.49	0.02	0.02	18.97	1.84	69.16	0.12	8.50	0.21	0.24	99.57
EBS5-T3-5	0.49	0.04	0.01	19.12	1.77	69.07	0.15	8.32	0.22	0.11	99.30
EBS5-T3-6	0.51	0.02	0.05	19.21	1.95	69.81	0.15	8.45	0.23	0.21	100.59
EBS5-T3-7	0.50	0.02	0.07	18.80	1.84	69.16	0.13	8.60	0.25	0.11	99.48
EBS5-T3-8	0.49	0.02	0.06	18.63	1.82	69.11	0.13	8.42	0.22	0.20	99.09
EBS5-T3-9	0.49	0.03	0.07	18.83	1.79	68.78	0.15	8.43	0.23	0.12	98.92
EBS5-T3-10	0.49	0.02	0.00	18.83	1.86	68.65	0.13	8.53	0.26	0.22	99.00
AVE	**0.49**	**0.03**	**0.04**	**18.88**	**1.84**	**69.01**	**0.13**	**8.46**	**0.23**	**0.18**	**99.30**
Std Dev	**0.01**	**0.01**	**0.02**	**0.23**	**0.05**	**0.36**	**0.01**	**0.11**	**0.02**	**0.05**	**0.63**
Transect 3b, inward from lower edge: 20 mm spacing											
EBS5-T3b-1	0.50	0.02	0.04	19.14	1.82	69.66	0.13	8.33	0.26	0.19	100.09

EBS5-T3b-2	0.50	0.02	0.04	19.14	1.89	69.01	0.16	8.52	0.28	0.11	99.67
EBS5-T3b-3	0.49	0.03	0.04	19.25	1.89	68.82	0.13	8.23	0.23	0.13	99.23
EBS5-T3b-4	0.49	0.02	0.07	18.89	2.02	68.90	0.09	8.32	0.20	0.10	99.11
EBS5-T3b-5	0.50	0.02	0.02	18.84	1.87	69.28	0.13	8.49	0.21	0.12	99.47
EBS5-T3b-6	0.49	0.03	0.04	19.01	1.86	69.40	0.09	8.49	0.26	0.15	99.81
EBS5-T3b-7	0.48	0.01	0.03	18.98	1.81	69.47	0.11	8.39	0.23	0.17	99.68
EBS5-T3b-8	0.49	0.03	0.05	18.88	1.81	69.04	0.17	8.67	0.24	0.08	99.46
EBS5-T3b-9	0.49	0.04	0.06	18.76	1.96	69.55	0.07	8.47	0.18	0.11	99.69
EBS5-T3b-10	0.51	0.00	0.04	18.89	1.88	69.82	0.14	8.60	0.28	0.11	100.26
AVE	**0.49**	**0.02**	**0.04**	**18.98**	**1.88**	**69.29**	**0.12**	**8.45**	**0.24**	**0.13**	**99.65**
Std Dev	**0.01**	**0.01**	**0.02**	**0.16**	**0.07**	**0.34**	**0.03**	**0.13**	**0.03**	**0.04**	**0.35**

Table B15. EMP data from 304SS associated with EBS-5.

	Si	P	V	Cr	Mn	Fe	Co	Ni	Cu	Mo	Total
Points along center line of metals											
EBS5-Cent1-1	0.50	0.04	0.07	19.31	1.84	70.08	0.09	8.50	0.21	0.16	100.82
EBS5-Cent1-2	0. 50	0.04	0.04	19.23	1.83	70.22	0.11	8.50	0.27	0.08	100.82
EBS5-Cent1-3	0.54	0.01	0.03	19.11	1.90	69.24	0.13	9.25	0.26	0.10	100.59
EBS5-Cent1-4	0.50	0.04	0.05	19.35	1.80	70.03	0.13	8.57	0.26	0.17	100.90
EBS5-Cent1-5	0.52	0.01	0.05	19.26	1.86	69.59	0.07	8.84	0.24	0.07	100.52
EBS5-Cent2-1	0.52	0.03	0.05	19.46	2.05	69.49	0.11	8.92	0.24	0.16	101.03
EBS5-Cent2-2	0.52	0.01	0.04	19.37	2.00	69.89	0.10	9.05	0.28	0.16	101.41
EBS5-Cent2-3	0.54	0.04	0.07	19.32	1.86	70.42	0.11	8.98	0.30	0.13	101.75
EBS5-Cent2-4	0.53	0.03	0.05	19.37	1.97	69.86	0.09	9.30	0.29	0.13	101.62
EBS5-Cent2-5	0.53	0.06	0.05	19.30	1.98	70.39	0.12	8.98	0.25	0.16	101.83
EBS5-Cent3-1	0.49	0.02	0.06	19.04	1.74	68.96	0.13	8.57	0.26	0.10	99.37
EBS5-Cent3-2	0.51	0.00	0.07	18.91	1.81	68.45	0.10	8.90	0.23	0.22	99.20
EBS5-	0.50	0.03	0.05	19.25	1.94	70.58	0.16	8.65	0.24	0.23	101.62

Cent3-3											
EBS5-Cent3-4	0.49	0.01	0.02	18.75	1.85	68.61	0.11	8.64	0.23	0.15	98.86
EBS5-Cent3-5	0.51	0.04	0.05	19.00	1.85	68.43	0.14	8.61	0.20	0.17	99.00
Average	**0.51**	**0.03**	**0.05**	**19.20**	**1.88**	**69.62**	**0.11**	**8.82**	**0.25**	**0.15**	**100.62**
Std Dev	0.02	0.02	0.01	0.20	0.08	0.73	0.02	0.26	0.03	0.05	1.04

Table B16. Fine-grained coatings on 316SS associated with EBS-10. Starting montmorillonite is residual from the surrounding bentonite material. Saponite is the corrosion product associated with the 316SS.

	SiO_2	TiO_2	Al_2O_3	Cr_2O_3	FeO*	MnO	MgO	NiO	ZnO	CaO	Na_2O	K_2O	F	Cl	O=F	O=Cl	Total
Low-Iron Phase (Montmorillonite)																	
EBS10-Sil-29	50.80	0.08	19.64	0.11	4.21	0.04	1.17	0.05	0.00	0.60	0.36	0.52	0.09	0.18	-0.04	-0.04	77.78
EBS10-Sil-30	45.77	0.12	17.38	0.14	4.67	0.06	1.04	0.05	0.00	0.69	0.47	0.51	0.12	0.22	-0.05	-0.05	71.14
EBS10-Sil-32	61.29	0.01	11.76	0.35	3.26	0.05	0.46	0.03	0.00	1.89	0.63	0.22	0.06	0.13	-0.03	-0.03	80.08
EBS10-Sil-33	64.44	0.00	17.54	0.30	2.29	0.04	0.24	0.01	0.00	1.05	3.23	0.01	0.12	0.06	-0.05	-0.01	89.28
Average	**55.57**	**0.05**	**16.58**	**0.23**	**3.61**	**0.05**	**0.73**	**0.04**	**0.00**	**1.06**	**1.17**	**0.31**	**0.10**	**0.15**	**-0.04**	**-0.03**	**79.57**
Std Dev	**8.76**	**0.06**	**3.37**	**0.12**	**1.05**	**0.01**	**0.45**	**0.02**	**0.00**	**0.59**	**1.38**	**0.25**	**0.03**	**0.07**	**0.01**	**0.02**	**7.50**
High-Iron Phase (Saponite)																	
EBS10-Sil-7	28.30	0.07	17.74	1.08	28.06	0.37	3.45	0.38	0.02	1.08	0.70	0.04	0.12	0.27	-0.05	-0.06	81.57
EBS10-Sil-8	22.52	0.08	18.01	1.20	26.78	0.35	3.18	1.42	0.00	0.84	0.47	0.06	0.11	0.22	-0.05	-0.05	75.14
EBS10-Sil-9	28.14	0.08	17.39	1.06	27.03	0.40	3.22	0.37	0.02	1.17	0.82	0.06	0.23	0.32	-0.10	-0.07	80.12
EBS10-Sil-10	28.50	0.07	17.73	0.98	27.89	0.38	3.18	1.25	0.00	1.17	0.85	0.05	0.08	0.25	-0.03	-0.06	82.31
EBS10-Sil-11	27.97	0.08	15.26	0.94	27.38	0.35	2.67	0.99	0.00	1.11	0.92	0.07	0.00	0.29	0.00	-0.06	77.97
EBS10-Sil-12	27.07	0.06	17.20	1.24	28.48	0.41	3.09	0.66	0.01	1.01	0.69	0.04	0.15	0.19	-0.06	-0.04	80.20
EBS10-Sil-13	31.92	0.09	16.29	1.15	28.96	0.37	3.20	0.61	0.00	1.24	1.05	0.06	0.08	0.27	-0.03	-0.06	85.20
EBS10-Sil-14	29.67	0.07	16.67	0.73	27.98	0.39	3.18	0.31	0.00	1.04	0.92	0.07	0.00	0.25	0.00	-0.06	81.23
EBS10-Sil-15	26.88	0.07	16.79	1.06	28.35	0.37	3.15	0.66	0.00	0.83	0.85	0.06	0.00	0.17	0.00	-0.04	79.20

EBS10-Sil-17	28.70	0.06	16.82	1.17	28.65	0.40	3.09	0.40	0.01	1.08	0.77	0.06	0.01	0.20	0.00	-0.04	81.38
EBS10-Sil-18	28.75	0.09	16.84	0.92	28.76	0.40	3.20	2.80	0.02	1.34	0.72	0.06	0.10	0.28	-0.04	-0.06	84.18
EBS10-Sil-19	29.98	0.08	17.63	0.92	27.90	0.43	3.03	0.70	0.02	1.03	0.90	0.06	0.07	0.26	-0.03	-0.06	82.92
EBS10-Sil-20	29.53	0.08	16.24	0.73	28.06	0.43	2.82	0.58	0.00	1.21	0.88	0.08	0.15	0.28	-0.06	-0.06	80.95
EBS10-Sil-25	32.89	0.09	15.65	0.38	23.31	0.30	3.23	0.23	0.00	1.28	1.10	0.23	0.14	0.40	-0.06	-0.09	79.10
EBS10-Sil-26	38.06	0.08	15.69	0.22	22.63	0.34	2.66	0.25	0.00	1.29	0.59	0.66	0.06	0.15	-0.02	-0.03	82.64
Average	**29.26**	**0.08**	**16.80**	**0.92**	**27.35**	**0.38**	**3.09**	**0.77**	**0.01**	**1.12**	**0.81**	**0.11**	**0.09**	**0.25**	**-0.04**	**-0.06**	**80.94**
Std Dev	**3.37**	**0.01**	**0.84**	**0.30**	**1.88**	**0.03**	**0.22**	**0.66**	**0.01**	**0.15**	**0.17**	**0.16**	**0.07**	**0.06**	**0.03**	**0.01**	**2.51**

Table B17. Fine-grained coatings on 304SS associated with EBS-5. Starting montmorillonite is residual from the surrounding bentonite material. Saponite is the corrosion product associated with the 304SS.

Label	SiO_2	TiO_2	Al_2O_3	Cr_2O_3	FeO*	MnO	MgO	NiO	ZnO	CaO	Na_2O	K_2O	F	Cl	O=F	O=Cl	Total
Low-Iron Phase (starting montmorillonite)																	
EBS5-Sil-1	53.24	0.12	16.53	0.09	5.64	0.04	2.00	0.14	0.01	1.11	0.34	0.59	0.13	0.04	-0.06	-0.01	79.95
EBS5-Sil-2	52.91	0.13	17.43	0.07	3.66	0.04	1.62	0.15	0.00	0.77	0.29	0.59	0.27	0.04	-0.11	-0.01	77.83
EBS5-Sil-3	54.33	0.08	17.14	0.09	3.63	0.03	1.68	0.15	0.03	0.68	0.36	0.61	0.02	0.04	-0.01	-0.01	78.85
EBS5-Sil-4	57.69	0.13	16.16	0.13	4.12	0.01	1.62	0.06	0.01	0.62	0.63	0.63	0.18	0.05	-0.08	-0.01	81.96
EBS5-Sil-5	60.13	0.12	14.90	0.12	3.25	0.02	1.45	0.06	0.00	0.69	0.71	0.82	0.05	0.05	-0.02	-0.01	82.32
EBS5-Sil-7	58.44	0.11	13.70	0.13	3.67	0.05	1.49	0.14	0.00	0.65	0.56	0.68	0.26	0.04	-0.11	-0.01	79.80
EBS5-Sil-8	63.84	0.00	7.32	0.54	7.70	0.12	1.48	0.33	0.02	0.66	0.33	0.15	0.19	0.03	-0.08	-0.01	82.63
EBS5-Sil-12	52.70	0.08	14.94	0.09	5.38	0.06	2.19	0.10	0.00	0.96	0.40	0.33	0.24	0.10	-0.10	-0.02	77.44
EBS5-Sil-14	62.14	0.08	14.63	0.38	5.85	0.03	2.11	0.12	0.00	0.84	0.63	0.40	0.25	0.14	-0.10	-0.03	87.46
EBS5-Sil-18	59.26	0.06	14.23	0.13	4.44	0.03	1.88	0.10	0.01	0.84	0.49	0.35	0.12	0.11	-0.05	-0.02	81.95
EBS5-Sil-19	62.40	0.06	12.58	0.16	3.19	0.02	1.39	0.10	0.03	0.71	0.42	0.42	0.08	0.08	-0.03	-0.02	81.61
EBS5-Sil-20	58.20	0.08	15.70	0.13	4.21	0.02	1.87	0.07	0.03	0.81	0.49	0.35	0.13	0.07	-0.06	-0.02	82.10
EBS5-Sil-22	63.02	0.05	14.42	0.20	4.75	0.04	1.35	0.11	0.00	0.64	0.76	1.21	0.12	0.03	-0.05	-0.01	86.66
EBS5-Sil-26	57.53	0.08	19.43	0.24	5.29	0.02	1.92	0.16	0.00	0.97	0.51	0.44	0.24	0.06	-0.10	-0.01	86.76
EBS5-Sil-	65.94	0.05	10.02	0.07	2.34	0.00	1.21	0.05	0.00	0.54	0.53	0.33	0.19	0.11	-	-0.02	81.26

30															0.08		
Average	**59.16**	**0.08**	**13.98**	**0.15**	**4.23**	**0.03**	**1.63**	**0.11**	**0.01**	**0.72**	**0.51**	**0.49**	**0.15**	**0.07**	**-0.06**	**-0.02**	**81.25**
Std Dev	3.71	0.03	2.78	0.12	1.42	0.03	0.28	0.06	0.01	0.16	0.15	0.23	0.09	0.03	0.04	0.01	2.93
High-Iron Phase: Saponite																	
EBS5-Sil-23	46.02	0.08	12.59	0.08	18.93	0.20	2.87	0.23	0.00	1.14	0.90	0.15	0.10	0.04	-0.04	-0.01	83.26
EBS5-Sil-28	32.53	0.08	12.45	0.84	26.74	0.22	4.33	0.48	0.01	0.46	0.18	0.02	0.00	0.00	0.00	0.00	78.34
Average	**39.27**	**0.08**	**12.52**	**0.46**	**22.83**	**0.21**	**3.60**	**0.35**	**0.00**	**0.80**	**0.54**	**0.08**	**0.05**	**0.02**	**-0.02**	**0.00**	**80.80**

Table B18. EMP data from Cu corrosion products associated with EBS-4. Oxides are mostly likely related to oxidation of primary sulfide corrosion products between experiment end and analyses.

	O	S	Cu	Total
High-Density Oxides				
EBS4-Ox1	10.02	0.00	89.63	99.65
EBS4-Ox2	10.25	0.01	89.75	100.01
EBS4-Ox3	10.07	0.00	89.70	99.77
EBS4-Ox4	10.30	0.02	89.87	100.19
EBS4-Ox5	10.16	0.00	89.51	99.67
EBS4-Ox6	11.21	0.00	90.21	101.42
EBS4-Ox11	11.24	0.01	89.61	100.86
EBS4-Ox12	10.47	0.00	90.22	100.69
EBS4-Ox13	10.51	0.00	90.41	100.92
Average	**10.47**	**0.01**	**89.88**	**100.35**
Std Dev	**0.46**	**0.01**	**0.32**	**0.64**
Low-Density Oxides				
EBS4-Ox7	22.57	0.03	69.61	92.21
EBS4-Ox8	21.63	0.02	70.62	92.27
EBS4-Ox9	19.54	0.08	72.34	91.95
EBS4-Ox10	19.01	0.09	73.89	92.99
Average	**20.69**	**0.05**	**71.62**	**92.36**
Std Dev	**1.69**	**0.03**	**1.89**	**0.45**
Sulfides				
EBS4-Sulf1	0.01	20.96	79.70	100.67
EBS4-Sulf2	0.00	20.49	80.02	100.51
EBS4-Sulf3	0.03	20.53	79.93	100.48
EBS4-Sulf4	0.01	20.76	79.61	100.38
EBS4-Sulf5	0.05	21.25	79.35	100.65
EBS4-Sulf6	0.08	22.47	77.44	99.99
EBS4-Sulf7	0.00	21.87	77.72	99.59
EBS4-Sulf8	0.00	21.41	78.75	100.16
EBS4-Sulf9	0.00	21.32	78.32	99.64
EBS4-Sulf10	0.00	22.59	76.98	99.57
Average	**0.02**	**21.36**	**78.78**	**100.16**
Std Dev	**0.03**	**0.74**	**1.11**	**0.44**

Table B19. EMP data from Cu corrosion products associated with EBS-11.

	O	S	Cu	Total
EBS11-sulf1	0.06	20.88	81.06	102.00
EBS11-sulf2	0.00	20.68	81.37	102.05
EBS11-sulf3	0.02	20.68	81.05	101.75
EBS11-sulf4	0.02	20.49	80.15	100.66
EBS11-sulf5	0.04	20.47	80.44	100.96
EBS11-sulf6	0.00	20.68	80.90	101.58
EBS11-sulf7	0.05	20.63	80.51	101.19
EBS11-sulf8	0.00	20.74	80.60	101.34
EBS11-sulf9	0.00	20.80	80.22	101.02
EBS11-sulf10	0.09	20.94	80.56	101.58
EBS11-sulf11	0.05	20.69	79.81	100.54
EBS11-sulf12	0.03	20.81	80.54	101.38
EBS11-sulf13	0.06	20.79	81.38	102.23
EBS11-sulf14	0.00	20.70	80.73	101.42
EBS11-sulf15	0.10	20.32	80.64	101.06
EBS11-sulf16	0.00	20.86	80.63	101.49
EBS11-sulf17	0.00	20.68	80.86	101.54
EBS11-sulf18	0.06	20.71	80.91	101.68
EBS11-sulf19	0.07	20.74	80.89	101.69
EBS11-sulf20	0.07	20.78	81.13	101.98
Average	**0.04**	**20.70**	**80.72**	**101.46**
Std Dev	**0.03**	**0.15**	**0.40**	**0.45**

Appendix C:
Solution Chemistry

All data are presented as mg/L, unless otherwise as noted.

Lab ID	13/00 UF	13/01 UF	13/02 UF	13/03 UF	13/04 UF	13/05 UF	13/06 UF	13/07 UF	13/08 UF	13/09 UF	13/10 UF	13/11 UF	13/12 UF
Date Sampled	9/17/2013	9/18/2013	10/3/2013	10/24/2013	11/14/2013	12/5/2013	12/18/2013	1/6/2014	2/3/2014	2/14/2014	2/24/2014	3/13/2014	3/20/2014
Time, hours	0	24	386	864	1369	1872	2184	2644	3319	3576	3816	4224	4392
Temperature, °C	25	300	299	300	300	300	300	300	221	221	221	114	114
pH	11	6.06	5.91	5.97	5.83	5.90	5.75	5.78	5.99	5.92	5.96	6.48	6.56
Al	<0.02	0.51(0)	0.27(1)	0.78(1)	0.41(0)	0.02(0)	0.02(0)	0.09(0)	0.29(0)	0.36(0)	0.33(0)	0.08(0)	0.07(0)
B	0.28(1)	4(0)	7(0)	7(0)	7(0)	10(0)	10(0)	7(0)	7(0)	7(0)	7(0)	6(0)	6(0)
Ba	0.04(0)	<0.02	0.04(0)	0.03(0)	0.06(0)	<0.02	<0.02	<0.02	0.02(0)	0.03(0)	0.03(0)	0.06(0)	0.06(0)
Ca	61(1)	0.8(1)	2.1(1)	2.6(1)	2.5(1)	5.7(1)	2.6(1)	1.3(1)	4.6(1)	4.3(1)	4.0(1)	3.4(2)	3.6(2)
Cl	882	895	867	905	859	851	840	830	717	702	682	605	612
Cr	<0.02	<0.02	<0.02	<0.02	<0.02	<0.02	<0.02	<0.02	<0.02	<0.02	<0.02	<0.02	<0.02
Fe	<0.2	<0.2	<0.2	<0.2	<0.2	<0.2	<0.2	<0.2	<0.2	<0.2	<0.2	<0.2	<0.2
K	559(8)	275(3)	57(1)	55(1)	56(1)	68(1)	68(0)	45(0)	51(0)	48(0)	51(0)	45(0)	47(1)
Li	<0.02	0.13(0)	0.24(2)	0.28(1)	0.32(1)	0.37(2)	0.39(1)	0.28(0)	0.44(1)	0.46(1)	0.48(1)	0.45(0)	0.50(2)
Mg	<0.2	<0.2	<0.2	<0.2	0.25(2)	<0.2	<0.2	<0.2	<0.2	0.39(4)	0.39(3)	<0.2	0.43(4)
Mn	<0.02	<0.02	<0.02	<0.02	<0.02	<0.02	<0.02	<0.02	<0.02	<0.02	<0.02	0.02	0.02
Na	201(4)	430(4)	497(9)	564(6)	549(5)	670(6)	671(3)	475(4)	537(5)	497(2)	527(1)	506(2)	506(5)
Si	1(0)	190(2)	69(2)	47(1)	46(1)	51(0)	73(0)	72(1)	306(3)	296(5)	297(4)	192(1)	177(1)
SiO2	3(0)	407(4)	149(4)	101(2)	99(1)	109(1)	156(1)	155(2)	654(6)	634(11)	635(8)	411(2)	378(2)
SO4	53	20	68	81	75	70	65	60	156	151	142	129	123
Sr	0.06(0)	<0.02	<0.02	<0.02	0.02(0)	0.03(0)	0.02(0)	<0.02	0.06(0)	0.07(0)	0.07(0)	0.08(0)	0.08(0)
Ti	<0.04	<0.04	<0.04	<0.04	<0.04	<0.04	<0.04	<0.04	<0.04	<0.04	<0.04	<0.04	<0.04
Zn	<0.02	<0.02	0.03(1)	0.06(0)	0.10(0)	0.03(1)	0.03(1)	<0.02	<0.02	<0.02	<0.02	<0.02	<0.02
TDS	1759	2032	1647	1717	1649	1784	1813	1574	2128	2044	2049	1706	1677
Cation	26	26	23	26	26	31	31	22	25	23	25	23	23
Anion	26	26	26	28	26	26	25	25	24	23	22	20	20
Balance	0.00	0.00	-0.06	-0.02	-0.01	0.09	0.10	-0.06	0.02	0.00	0.04	0.08	0.08

Table C1. Unfiltered solution chemistry from EBS-13.

Table C2. Filtered solution chemistry from EBS-13.

Lab ID	13/00 F	13/01 F	13/02 F	13/03 F	13/04 F	13/05 F	13/06 F	13/07 F	13/08 F	13/09 F	13/10 F	13/11 F	13/12 F
Date Sampled	9/18/2013	9/18/2013	10/3/2013	10/24/2013	11/14/2013	12/5/2013	12/18/2013	1/6/2014	2/3/2014	2/14/2014	2/24/2014	3/13/2014	3/20/2014
Time, hours	0	24	386	864	1369	1872	2184	2644	3319	3576	3816	4224	4392
Temperature, °C	25	300	299	300	300	300	300	300	221	221	221	114	114
pH	11	6.06	5.91	5.97	5.83	5.90	5.75	5.78	5.99	5.92	5.96	6.48	6.56
Al	<0.02	0.18(0)	<0.02	0.42(0)	0.45(1)	0.03(0)	0.42(0)	0.39(1)	0.28(0)	0.35(1)	0.34(0)	0.05(2)	0.04(0)
B	<0.04	4(0)	8(0)	7(0)	8(0)	11(0)	10(0)	7(0)	7(0)	7(0)	6(0)	6(0)	6(0)
Ba	<0.02	0.03(0)	0.05(0)	0.03(0)	<0.02	0.04(0)	0.04(0)	<0.02	0.02(0)	0.03(0)	0.03(0)	0.06(0)	0.07(0)
Ca	62(1)	2.0(1)	4.1(2)	2.5(1)	2.4(2)	3.7(1)	2.9(2)	1.8(0)	4.6(1)	4.2(1)	4.0(1)	3.9(2)	3.6(2)
Cr	<0.02	<0.02	<0.02	<0.02	<0.02	<0.02	<0.02	<0.02	<0.02	<0.02	<0.02	<0.02	<0.02
Fe	<0.2	<0.2	<0.2	<0.2	<0.2	<0.2	<0.2	<0.2	<0.2	<0.2	<0.2	<0.2	<0.2
K	926(3)	281(6)	66(0)	56(0)	56(0)	75(1)	69(0)	81(1)	67(1)	48(1)	49(0)	44(0)	46(0)
Li	0.04(0)	0.16(1)	0.28(1)	0.28(1)	0.30(1)	0.41(1)	0.40(0)	0.59(1)	0.61(2)	0.44(0)	0.44(1)	0.44(1)	0.47(0)
Mg	<0.2	0.32(1)	<0.2	<0.2	<0.2	<0.2	<0.2	<0.2	<0.2	<0.2	<0.2	<0.2	<0.2
Mn	<0.02	<0.02	<0.02	<0.02	<0.02	<0.02	<0.02	<0.02	<0.02	<0.02	<0.02	0.02	0.02
Na	234(3)	451(6)	578(2)	552(7)	555(6)	721(6)	666(3)	638(3)	598(5)	494(7)	531(2)	504(5)	510(0)
Si	<0.2	110(2)	32(0)	38(1)	33(0)	55(0)	68(0)	78(2)	382(3)	303(3)	308(2)	191(1)	179(1)
SiO2	<0.4	235(4)	68(0)	80(2)	70(0)	118(1)	145(1)	166(4)	818(7)	649(7)	659(5)	409(3)	383(3)
Sr	0.08(0)	0.02(0)	0.02(0)	<0.02	<0.02	0.04(0)	0.02(0)	0.03(0)	0.08(0)	0.06(0)	0.06(0)	0.08(0)	0.08(0)
Ti	<0.04	<0.04	<0.04	<0.04	<0.04	<0.04	<0.04	<0.04	<0.04	<0.04	<0.04	<0.04	<0.04
Zn	<0.02	<0.02	0.03(2)	0.07(0)	<0.02	0.02(0)	0.06(1)	<0.02	<0.02	<0.02	<0.02	<0.02	<0.02
TDS	1222	974	724	698	692	929	894	895	1495	1203	1251	967	949
Cation	37	27	27	26	26	34	31	30	28	23	25	23	24
Anion	0	0	0	0	0	0	0	0	0	0	0	0	0
Balance	1.00	0.99	0.97	0.97	0.97	0.97	0.97	0.98	0.98	0.97	0.98	0.98	0.98

Table C3. Unfiltered solution chemistry from EBS-14.

Lab ID	14/00 UF	14/01 UF	14/02 UF	14/03 UF	14/04 UF
Date Sampled	11/26/2013	11/27/2013	12/6/2013	12/18/2013	1/6/2014
Time, hours	0	24	240	528	988
Temperature, °C	25	299	299	300	300
pH	7.50	4.59	5.39	4.88	4.96
Al	<0.05	<0.05	<0.05	<0.05	<0.05
B	0.1(0)	5(0)	6(0)	6(0)	7(0)
Ba	<0.05	0.18(0)	0.17(2)	0.16(0)	0.28(1)
Ca	426(6)	317(4)	496(6)	564(8)	546(4)
Cl	6470	6484	6538	6497	6518
Cr	<0.05	<0.05	<0.05	<0.05	<0.05
Fe	<0.5	<0.5	<0.5	<0.5	<0.5
K	225(3)	174(2)	106(1)	232(6)	202(1)
Li	<0.05	2(0)	6(0)	12(0)	7(0)
Mg	194(2)	8(0)	1(0)	1(0)	0.9(0)
Mn	<0.05	0.09(0)	0.17(0)	0.23(0)	0.29(0)
Na	3846(32)	3831(40)	3571(54)	3971(39)	3473(8)
Si	1(0)	84(2)	78(1)	63(2)	56(1)
SiO2	2(0)	181(5)	167(3)	135(4)	120(1)
SO4	988	<1	<1	<1	<1
Sr	0.16(0)	2.5(0)	1.5(0)	2.3(0)	2.1(0)
Ti	<0.1	<0.1	<0.1	<0.1	<0.1
Zn	<0.05	0.06(1)	0.08(0)	0.09(1)	0.09(1)
TDS	12153	11006	10892	11420	10877
Cation	208	186	182	206	183
Anion	201	181	183	181	182
Balance	0.02	0.01	0.00	0.06	0.00

Table C4. Filtered solution chemistry from EBS-14.

Lab ID	14/00 F	14/01 F	14/02 F	14/03 F	14/04 F
Date Sampled	11/27/2013	11/27/2013	12/6/2013	12/18/2013	1/6/2014
Reaction time, hours	17	24	233	521	977
Temperature	25	300	300	300	300
pH	7.50	4.59	5.39	4.88	4.96
Al	<0.05	<0.05	<0.05	<0.05	<0.05
B	0.2(0)	5(0)	6(0)	6(0)	6(0)
Ba	<0.05	0.21(2)	0.12(0)	0.23(1)	0.29(1)
Ca	441(4)	319(3)	507(7)	573(5)	590(17)
Cr	<0.05	<0.05	<0.05	<0.05	<0.05
Fe	<0.5	<0.5	<0.5	<0.5	<0.5
K	223(2)	176(0)	106(1)	225(4)	334(6)
Li	<0.05	2(0)	6(0)	11(0)	13(0)
Mg	193(3)	8(0)	1(0)	1(0)	1.3(1)
Mn	<0.05	0.09(0)	0.16(0)	0.22(0)	0.24(0)
Na	3781(17)	3835(11)	3581(36)	4056(19)	4065(28)
Si	1(0)	36(0)	41(1)	51(1)	47(1)
SiO2	1(0)	78(0)	87(1)	108(2)	100(3)
Sr	0.17(0)	2.5(0)	1.5(0)	2.4(0)	2.8(1)
Ti	<0.1	<0.1	<0.1	<0.1	<0.1
Zn	<0.05	0.11(1)	0.06(1)	0.08(1)	0.15(1)
TDS	4640	4426	4296	4984	5113
Cation	207	187	184	212	216
Anion	0	0	0	0	0
Balance	1.00	1.00	1.00	1.00	1.00

Appendix D:

MATLAB Code for The Radiolysis Mode Subroutine

MATLAB Code for The Radiolysis Mode Subroutine

The analytical function on which this code is based was supplied by Rick Wittman and Edgar Buck of PNNL in early 2014.

```
%*********************************************************************
*****
%
% Inputs:
%   rad    = (J/kg)/s
%   cO2    = mol/m^3
%   cH2    = mol/m^3
% Outputs:
%   Gval   =  mol/(J/kg)/m^3
%   dcO2    = (mol/(J/kg)/m^3)/(mol/m^3)
%   dcH2    = (mol/(J/kg)/m^3)/(mol/m^3)
%
%*********************************************************************
*****

function [Gval,dcO2,dcH2] = PNNL_gval(rad,cO2,cH2)

  % Constants
  Na      = 6.022e23;      % 1/mol            (Avogadro's constant)
  eV      = 1.602e-19;     % J/eV             (Elementary charge)
  mwH2O   = 0.018;         % kg/mol           (Molecular weight of water)

  % Parameters
  hH2      = 7.8e-1;        % mol/bar/m^3     (Henry's law constant: H2)
  penD     = 3.5e-5;        % m               (Alpha penetration depth)
 % DO2      = 1.7e-9;
  DO2     = 2.5e-9;        % m^2/s            (Diffusivity: O2)
 % DH2O2    = 1.7e-9;
  DH2O2   = 1.9e-9;        % m^2/s            (Diffusivity: H2O2)
  rhoH2O   = 1e3;           % kg/m^3          (Groundwater density)
```

```
  % Rate constants
  rk27 = 2.1e7;          % m^3/mol/s
  rk23 = 1.1e-2/56;      % m^3/mol/s
  rk26 = 9.0e4;          % m^3/mol/s

  % Equilibrium constants
  ratk1 = rk26/rk27;
  ratk2 = rk27/rk23;

  % Intermediate quantities
  presH2  = cH2/hH2;         % bar
  concH2O = rhoH2O/mwH2O;    % mol/m^3
  dpH2dH  = 1/hH2;           % bar/(mol/m^3)

  % G-values
  GH     = 0.10*(1-exp(-presH2/0.1));        %  molecule/100eV
  GOH    = 0.35*(1-exp(-presH2/0.3));        %  molecule/100eV
  dGHdH  =          exp(-presH2/0.1)*dpH2dH; %
(molecule/100eV)/(mol/m^3)
  dGOHdH = 0.35/0.3*exp(-presH2/0.3)*dpH2dH; %
(molecule/100eV)/(mol/m^3)

  % Other
  dN       = 4.75e-3/penD;                                  %  m/m
  v1       = ratk2/concH2O;                                 %  m^3/mol
  dlam0    = v1*rhoH2O/eV/Na*rad.*(GH+GOH)/1e2;             %  1/s
  dk       = DO2/penD^2;                                    %  1/s
  dkH2O2   = DH2O2/penD^2;                                  %  1/s
  ddlam0dH = v1*rhoH2O/eV/Na*rad.*(dGHdH+dGOHdH)/1e2; %
(1/s)/(mol/m^3)

  B    = cO2*v1 - dN*dlam0/dk - 1;
  dBdO = v1;
  dBdH = -dN*ddlam0dH/dk;

  X    = 0.5*(B+sqrt(B.*B-4*cO2));
```

```
  dXdO = 0.5*(dBdO+0.5*(2*B.*dBdO-8*cO2)./sqrt(B.*B-4*cO2));
  dXdH = 0.5*(dBdH+0.5*(2*B.*dBdH      )./sqrt(B.*B-4*cO2));

  dlam    =  dlam0./(1+X);              %  1/s
  ddlamdO = -dlam0.*dXdO./(1+X).^2;     % (1/s)/(mol/m^3)
  ddlamdH = -dlam0.*dXdH./(1+X).^2;     % (1/s)/(mol/m^3)

  % Results
  dNom = (dkH2O2 + ratk1*dN*dlam);
  Gval =  dkH2O2./dNom;                          %  molecule/100eV
  Gval =  Gval*rhoH2O/Na/eV/1e2;                 %  mol/(J/kg)/m^3

  dcO2 = -dkH2O2*(ratk1*dN*ddlamdO)./dNom.^2;   %
(molecule/100eV)/(mol/m^3)
  dcO2 =  dcO2*rhoH2O/Na/eV/1e2;                %
(mol/(J/kg)/m^3)/(mol/m^3)

  dcH2 = -dkH2O2*(ratk1*dN*ddlamdH)./dNom.^2;   %
(molecule/100eV)/(mol/m^3)
  dcH2 =  dcH2*rhoH2O/Na/eV/1e2;                %
(mol/(J/kg)/m^3)/(mol/m^3)

  return

end

%*********************************************************************
*****



%*********************************************************************
*****
```